Studies of Ion Kinetic Effects in Shock-Driven Inertial Confinement Fusion Implosions at OMEGA and the NIF and Magnetic Reconnection Using Laser-Produced Plasmas at OMEGA

ARCHIVES
MASSACHUSETTS INSTITUTE OF TECHNOLOGY
NOV 10 2014
LIBRARIES

by

Michael Jonathan Rosenberg

B.A., Physics, Swarthmore College (2008)

Submitted to the Department of Physics
in partial fulfillment of the requirements for the degree of

Doctor of Philosophy

at the

MASSACHUSETTS INSTITUTE OF TECHNOLOGY

September 2014

© Massachusetts Institute of Technology 2014. All rights reserved.

Signature redacted

Author ....
Department of Physics
August 8, 2014

Signature redacted

Certified by ....
Richard Petrasso
Division Head, High Energy Density Physics
MIT Plasma Science and Fusion Center
Thesis Supervisor

Signature redacted

Certified by.. ....
Miklos Porkolab
Professor of Physics
Thesis Co-Supervisor

Signature redacted

Accepted by ....
Krishna Rajagopal
Professor of Physics
Associate Department Head for Education

Studies of
Ion Kinetic Effects in Shock-Driven Inertial Confinement Fusion Implosions at OMEGA and the NIF
and Magnetic Reconnection Using Laser-Produced Plasmas at OMEGA

by
Michael Jonathan Rosenberg

Submitted to the Department of Physics
on August 8, 2014, in partial fulfillment of the
requirements for the degree of
Doctor of Philosophy

Abstract

Studies of ion kinetic effects during the shock-convergence phase of inertial confinement fusion (ICF) implosions and magnetic reconnection in strongly-driven, laser-produced plasmas have been facilitated by the use of shock-driven ICF implosions and diagnosed using both mature and newly-developed nuclear diagnostics.

Ion kinetic effects that are likely to be significant early in ICF implosions, as strong shocks create a high-temperature, moderate-density plasma with an ion mean free path approximately the size of the fuel region, have, for the first time, been explored in a comprehensive experimental campaign. These experiments at the OMEGA laser facility, in which the ion mean free path was systematically varied in a series of shock-driven implosions, have demonstrated that measured fusion yields are increasingly discrepant relative to the predictions of hydrodynamic codes with increasing ion mean free path. The enhanced transport of fuel ions out of the hot plasma region and the reduction in fusion reactivity due to the depletion of high-energy tail ions are responsible. These effects have also been inferred in shock-driven implosions at the National Ignition Facility.

The universal plasma phenomenon of magnetic reconnection has been explored in strongly-driven, high-β laser-produced plasmas, driving reconnection in a regime relevant to astrophysical environments, such as the Earth's magnetopause. Using shock-driven ICF implosions as a proton source to probe magnetic fields, the first systematic laboratory experiments to study asymmetric magnetic reconnection have been conducted. These experiments have shown that the rate of reconnection in this strongly flow-driven system is dictated by the flow velocity and is largely insensitive to initial asymmetries in density, ram pressure, and geometry. Related experiments have probed the collision of parallel magnetic fields to assess the effect of strong flows on magnetic fields in the absence of reconnection. Experiments using high-resolution proton radiography have revealed small-scale electron jets that demonstrate the importance of two-fluid effects in permitting a fast reconnection even when reconnection is driven by strong plasma flows.

This work has improved understanding and spurred further experimental and theoretical inquiry into kinetic ion behavior in ICF implosions and magnetic reconnection in regimes rarely accessed in the laboratory.

Thesis Supervisor: Richard Petrasso
Title: Division Head, High Energy Density Physics
MIT Plasma Science and Fusion Center

Thesis Co-Supervisor: Miklos Porkolab
Title: Professor of Physics

Acknowledgments

Working in the High Energy Density Physics Division at MIT has been an exhilirating and educational experience, and I owe much gratitude to the senior scientists who have helped shape my experience. First and foremost, I thank my advisor, Richard Petrasso, for laying the groundwork and giving me the opportunity to be a part of this exciting research endeavor, and for bringing together extensive collaborations in support of my work. His constant enthusiasm, encouragement, and support has been instrumental. I thank Chikang Li for his valuable scientific insight, probing questions, and guidance on several experiments and papers. I thank Johan Frenje for his significant feedback on many papers and presentations. And I thank Fredrick Séguin for developing a lot of the infrastructure that enables so much of what we do, and for his invaluable feedback and suggestions on clarity of communication.

I am also grateful to many students, postdocs, scientists, and staff at MIT for their help and support. It has been a pleasure to work with and learn from my compatriots in the HEDP Division, including Daniel Casey, Mario Manuel, Nareg Sinenian, Maria Gatu Johnson, Hong Sio, Caleb Waugh, and, in particular, my officemates Hans Rinderknecht and Alex Zylstra. I owe tremendous thanks to Jocelyn Schaeffer, Irina Cashen, Robert Frankel, and Ernie Doeg for their careful and expedient procsssing of CR-39 data used in this work.

This work would not have been possible without many eager and helpful collaborators across a number of institutions. The bulk of the experimental work that comprises this thesis was conducted at the Laboratory for Laser Energtics (LLE) at the University of Rochester. I thank LLE scientists Craig Sangster, David Meyerhofer, Riccardo Betti, and Valeri Goncharov for their feedback and input in helping to elevate the quality of my research. I also thank the many scientists who assisted me with critical experimental and diagnostic support – Wolf Seka, Dustin Froula, Vladimir Glebov, Christian Stoeckl, Fred Marshall, and several others – as well as several LLE scientists who provided key simulation support, including Jacques Delettrez, Pat McKenty, and Igor Igumenshchev. In addition, I am grateful to the staff at LLE who help maintain that great facility and enable this experimental work, including Sam Morse, Steve Stagnitto, David Canning, as well as Michelle McCluskey and Joe Katz, who provided immensely valuable assistance with diagnostic setup on hectic shot days, and Michelle Evans, who assembled many complicated targets for my experiments. I thank also scientists at Lawrence Livermore National Laboratory (LLNL): Nino Landen and Andy Mackinnon, who have provided valuable feedback on my work and fostered our group's involvement at the NIF. I thank many collaborators who have provided valuable theoretical insight into my studies of ion kinetic effects, including Peter Amendt and Claudio Bellei (LLNL), Nels Hoffman and Grisha Kagan (Los Alamos National Laboratory), and Stefano Atzeni (Universitá di Roma "La Sapienza"). In addition, I thank Will Fox (Princeton Plasma Physics Laboratory), my conduit to the magnetic reconnection community, for many illuminating discussions and critical insight gleaned from his simulations.

I thank the funding agencies within the U.S. Department of Energy (DOE) and the National Nuclear Security Administration (NNSA) for supporting my research, as well as the National Laser

Users Facility (NLUF) program, which has provided crucial and ample opportunities for experiments at LLE, which comprise a lot of the research in this thesis.

I thank the members of my thesis committee, Miklos Porkolab, Earl Marmar, and Rob Simcoe, for their guidance, support, and excellent questions, which have helped to elevate the quality of this thesis.

As we are much more than our professional personas, I also owe enormous thanks on a personal level to the many family and friends who have supported me in this challenging endeavor. I thank my parents, Henry Rosenberg and Shelley Fellner-Rosenberg, whose unwavering pride and encouragement have set me on the path to get where I am today. And finally, I thank my wonderful fiancée, Rachel VanCott. Her humor, patience, and love have been a constant buoy of support.

Contents

Acknowledgments **5**

List of Publications **11**

List of Figures **13**

List of Tables **19**

1 Introduction to Inertial Confinement Fusion **23**

1.1 Nuclear Fusion 23

1.1.1 Criteria for Self-heating and Ignition 26

1.1.2 Controlled Fusion Methods 27

1.2 Laser-Driven Inertial Confinement Fusion (ICF) 28

1.2.1 Overview 28

1.2.2 Confinement and Compression for Hot-Spot Ignition 29

1.2.3 Typical Implosion Conditions 31

1.2.4 Laser Drive Schemes 33

1.3 Laser Facilities 35

1.3.1 Omega Laser Facility 35

1.3.2 National Ignition Facility 36

1.4 Shock-Driven Exploding Pusher ICF Implosions 37

1.5 Thesis Overview 39

1.6 References 40

2 Fusion Product Diagnostics for ICF Implosions **45**

2.1 Nuclear Spectroscopy for Measurements of Ion Temperature and Areal Density 45

2.1.1 Ion Temperature Measurements 46

2.1.2 Areal Density Measurements 48

2.2 CR-39-Based and Other Nuclear Diagnostics 49

2.2.1 Properties of CR-39 50

2.2.2 Magnet-Based Charged-Particle Spectrometers 52

2.2.3 Wedge-Range-Filter Proton Spectrometers 53

2.2.4 Other Nuclear Diagnostics of ICF Implosions 54

2.3 MIT Linear Electrostatic Ion Accelerator (LEIA) for Development of Nuclear Diagnostics 56

2.4 Development of a Compact DD-Proton Spectrometer 57

2.4.1 Introduction 57

2.4.2 Design and Analysis Principles 58
2.4.3 Step Range Filter Data 59
2.4.4 Discussion of Applicability and Uncertainties 65
2.4.5 Conclusions and Applications 70
2.5 Proton Detection in CR-39 at High Fluence 71
2.5.1 Introduction 71
2.5.2 High-Fluence Proton Detection Using CR-39 72
2.5.3 Scattering Pinhole Detector for Extension of Proton Yield Upper Limit 77
2.5.4 Discussion and Applications 80
2.5.5 Conclusions 81
2.6 Summary 81
2.7 References 81

3 Studies of Ion Kinetic Effects in ICF Using Shock-Driven Implosions 85
3.1 Ion Kinetic Effects in ICF Implosions 86
3.2 Exploration of Hydro to Kinetic Regimes in Shock-Driven Implosions 91
3.2.1 Overview 92
3.2.2 Exploding-Pusher Experiments on OMEGA 93
3.2.3 Principal Experimental Results 94
3.2.4 Discussion of Kinetic Effects 98
3.2.5 Use of Burn Profile Measurements to Assess Ion Diffusion 103
3.2.6 Conclusions 103
3.3 Investigation of Ion Kinetic Effects in Exploding Pushers at the NIF 105
3.3.1 Additional Background on Exploding Pushers 105
3.3.2 NIF Exploding Pusher Experiments and Modeling 108
3.3.3 Experimental Measurements and Comparison to Simulations 110
3.3.4 Discussion of Ion Kinetic Effects in NIF Exploding Pushers 115
3.3.5 NIF Exploding Pushers as a Possible Proton Backlighter 120
3.3.6 Conclusions 121
3.4 Future Work on Kinetic Effects in ICF Implosions 121
3.5 Summary 123
3.6 References 123

4 Overview of Magnetic Reconnection 131
4.1 Introduction 131
4.2 Sweet-Parker Model of Magnetic Reconnection 131
4.3 Alternative Reconnection Models 133
4.3.1 Petschek Reconnection Model 133
4.3.2 Anomalous Resistivity 133
4.4 Two-Fluid (Hall) or Collisionless Reconnection 134
4.5 Magnetic Reconnection in Astrophysical and Laboratory Plasmas 135
4.6 Asymmetric Reconnection 138
4.7 Thesis Overview: Magnetic Reconnection 139
4.8 References 140

5 Diagnosing Laser-Plasma Magnetic Reconnection Experiments 143
5.1 Laser Generation of Magnetic Fields in Plasmas 143

5.2 Proton Radiography Techniques for Measurement of Electric and Magnetic Fields in Plasmas 146
  5.2.1 Exploding-Pusher Implosion Monoenergetic Proton Backlighting 149
  5.2.2 Target Normal Sheath Acceleration Proton Backlighting 153
5.3 Previous Magnetic Field Measurements in Laser-Produced Plasmas 155
5.4 Thomson Scattering Measurements of Electron and Ion Temperature in Plasmas 157
5.5 Characterization of Single and Colliding Laser-Produced Plasma Bubbles 159
  5.5.1 Introduction and Motivation 159
  5.5.2 Laser-Foil Experiments and Measurements 160
  5.5.3 Proton Radiography and Thomson Scattering Results 161
  5.5.4 Discussion of Thermal Evolution in Laser-Foil and Reconnection Experiments 166
  5.5.5 Conclusions 168
5.6 Summary 168
5.7 References 169

6 Dynamics of Magnetic Field Evolution and Reconnection in Symmetric and Asymmetric Colliding Laser-Produced Plasma Bubbles 175
6.1 A Laboratory Study of Asymmetric Magnetic Reconnection in Strongly-Driven Plasmas 176
  6.1.1 Motivation for Asymmetric Reconnection Experiments 177
  6.1.2 Asymmetric Reconnection Experiments on the OMEGA Laser 177
  6.1.3 Proton Radiography Data of Asymmetric Reconnection 179
  6.1.4 Discussion of Reconnection-relevant Plasma Parameters 181
  6.1.5 Use of PIC Simulations to Aid Interpretation of Experimental Results 182
  6.1.6 (Non-)Impact of 3D Effects on the Reconnection Rate 185
  6.1.7 Conclusions 186
6.2 Two-Fluid to Single-Fluid Magnetic Reconnection in Laser-Plasma Experiments 186
  6.2.1 Motivation for Two-Fluid Reconnection Experiments 187
  6.2.2 Reconnection Experiments and High-Resolution Proton Radiography Data on OMEGA-EP 188
  6.2.3 Discussion of Plasma Conditions and Reconnection Physics 189
  6.2.4 Conclusions 193
6.3 First Experiments Probing the Collision of Parallel Magnetic Fields in Laser-Produced Plasmas 193
  6.3.1 Motivation for Colliding Parallel Magnetic Fields 193
  6.3.2 Interacting Parallel Magnetic Fields Experiments 194
  6.3.3 Proton Radiography of Colliding Plasmas Carrying Parallel Magnetic Fields 195
  6.3.4 Discussion of Experimental Findings and Future Work 196
  6.3.5 Conclusions 198
6.4 Future Work 198
6.5 Summary 199
6.6 References 200

7 Conclusion 207

Appendices 211

A Addendum and Data from Shock-Driven Exploding Pusher Experiments on OMEGA and NIF 213

B Discussion of Fusion Product Linewidth Measurements 237

C Discussion of Ion Transport and "Diffusion" Under Long Mean Free Path Conditions 245

D Thomson Scattering Data from Laser-Foil and Magnetic Reconnection Experiments 249

E Addendum and Proton Radiography Data from Magnetic Reconnection Experiments 257

F Formulary and Discussion of Relevant Parameters in Kinetic Effects and Magnetic Reconnection Experiments 279

G Description of Simulation Terms 287

List of Publications

This dissertation is based on several peer-reviewed journal publications and manuscripts submitted and to be submitted for publication:

1. M. J. Rosenberg, J. S. Ross, C. K. Li *et al.*, "Characterization of single and colliding laser-produced plasma bubbles using thomson scattering and proton radiography," Phys. Rev. E, **86**, 056,407 (2012)
2. M. J. Rosenberg, F. H. Séguin, C. J. Waugh *et al.*, "Empirical assessment of the detection efficiency of cr-39 at high proton fluence and a compact, proton detector for high-fluence applications," Review of Scientific Instruments, **85**(4), 043302 (2014)
3. M. J. Rosenberg, H. G. Rinderknecht, N. M. Hoffman *et al.*, "Exploration of the transition from the hydrodynamiclike to the strongly kinetic regime in shock-driven implosions," Phys. Rev. Lett., **112**, 185,001 (2014)
4. M. J. Rosenberg *et al.*, "A laboratory study of asymmetric magnetic reconnection in strongly-driven plasmas," submitted to Nat. Commun. (2014)
5. M. J. Rosenberg *et al.*, "A compact proton spectrometer for measurement of the absolute dd proton spectrum from which yield and ρr are determined in thin-shell inertial-confinement-fusion implosions," submitted to Rev. Sci. Inst. (2014)
6. M. J. Rosenberg *et al.*, "Utilization of nif diagnostic development shots for investigation of ion kinetic effects in direct-drive exploding-pusher implosions," to be submitted to Phys. Plasmas (2014)
7. M. J. Rosenberg *et al.*, "Observation of two-fluid to single-fluid magnetic reconnection dynamics in strongly-driven laser-plasma experiments," to be submitted to Phys. Rev. Lett. (2014)
8. M. J. Rosenberg *et al.*, "First experiments probing the collision of parallel magnetic fields using laser-produced plasmas," to be submitted to Phys. Rev. Lett. (2014)

List of Figures

1.1 Binding energy per nucleon as a function of atomic mass. 24
1.2 Cross sections for DT, DD, and D^{3}He fusion reactions as a function of center-of-mass reactant energy. 25
1.3 Lawson-like criterion for fusion ignition based on areal density and ion temperature in ICF implosions 30
1.4 Typical capsule used in hot-spot ignition experiments 31
1.5 Isobaric conditions at stagnation in hot-spot ignition implosions 32
1.6 High- and low-mode implosion asymmetries 33
1.7 Diagram of direct-drive and indirect-drive ICF 33
1.8 The OMEGA and OMEGA-EP laser systems 35
1.9 The NIF laser system 36
1.10 Converging shocks in exploding-pusher and hot-spot ignition implosions 37
1.11 Lagrangian mass trajectories and D^{3}He burn in an exploding pusher 38

2.1 Sample primary D^{3}He-proton spectrum for T$_i$ measurement 47
2.2 Reactivity ratio of DD and D^{3}He reactions 48
2.3 Sample primary D^{3}He-alpha spectrum 49
2.4 Sample secondary D^{3}He-proton spectrum 50
2.5 Track formation process in CR-39 51
2.6 Proton tracks in CR-39 51
2.7 Track diameter as a function of proton energy 52
2.8 Charged Particle Spectrometer (CPS) magnet and proton trajectories 53
2.9 Principle of the Wedge-Range-Filter (WRF) proton spectrometer 54
2.10 Conceptual illustration of penumbral imaging of the fusion burn profile 55
2.11 Cartoon schematic of MIT Linear ELectrostatic Ion Accelerator (LEIA) 57
2.12 Design of the step range filter (SRF) proton spectrometer 59
2.13 Example simulated proton spectra through SRF filters 60
2.14 Experimental setup for SRF development on LEIA 60
2.15 DD-proton signal on the SRF in experiments on LEIA 62
2.16 Illustration of degeneracy in inferred proton energy and linewidth in SRF data . . . 63
2.17 DD-proton signal obtained using the "thin" SRF on three D^{3}He-filled thin-glass-shell implosions on OMEGA 63
2.18 DD-proton spectrum from OMEGA shot 70561 transmitted through the SRF filters 64
2.19 DD-proton signal obtained using the "thick" SRF on NIF shot N130129 65
2.20 SRF-inferred DD-proton spectrum from NIF shot N130129, transmitted through each of the four SRF filters 66
2.21 Proton transmission through SRF filters as a function of energy 67
2.22 SRF linewidth uncertainty as a function of energy and linewidth 69
2.23 Microscope images of proton tracks at moderate and high fluence 72

2.24 Detection efficiency for 2-4-MeV protons at high fluence 73
2.25 Diagram of experiments on the Linear Electrostatic Ion Accelerator (LEIA) 74
2.26 Measured DD-proton fluence as a function of etch time for different incident proton fluences 75
2.27 Microscope images of D^3He proton tracks from the wedge-range-filter (WRF) spectrometer on NIF shot N110722 76
2.28 WRF-inferred D^3He-p yields as a function of etch time at high fluence on NIF implosions 76
2.29 WRF-inferred D^3He-p energy and linewidth as a function of etch time at high fluence on NIF implosions 77
2.30 Pinhole plus scattering foil for reduction of proton fluence on the CR-39 78
2.31 Scattering pinhole data obtained on LEIA 78
2.32 Scattering pinhole setup and data obtained on OMEGA shot 70400 79

3.1 Hydrodynamic models and kinetic and multi-ion extensions 86
3.2 Conceptual depiction of the kinetic Guderley model 88
3.3 Ion distribution function modified by Knudsen tail ion loss 90
3.4 Gamow peak calculation for Maxwellian and Knudsen-modified distribution functions 91
3.5 DT fusion reactivity reduction due to Knudsen layer effects 92
3.6 Lagrangian mass-element trajectories in a DUED simulation of an exploding pusher from the kinetic effects experiments 94
3.7 Ion density, temperature, and mean free path as a function of initial gas density . . . 95
3.8 Measured yields, yield-over-clean, ion temperatures, and bang time as a function of initial gas density 96
3.9 Measured and simulated yields as a function of initial gas density 97
3.10 Yield-over-clean relative to DUED as a function of the ratio of ion-ion mean free path to the minimum shell radius 98
3.11 DD yield-over-clean and ion temperature in DUED and the kinetic Guderley model . 100
3.12 Measured yields in comparison to the reduced ion kinetic model and clean hydrodynamics simulations 101
3.13 Measured and simulated surface brightness profiles of proton emission in OMEGA exploding pushers 104
3.14 Summary of OMEGA exploding pusher results relevant to experiments at the NIF . 107
3.15 Measured primary and secondary D^3He proton spectra from NIF exploding pushers 108
3.16 LILAC simulation of NIF D^3He exploding pusher N110722 110
3.17 Measured DD and D^3He yields in NIF exploding pushers as a function of DRACO-simulated yield 112
3.18 Yield-over-clean as a function of measured ion temperature in NIF exploding pushers 113
3.19 X-ray self-emission image of the imploded core in NIF D_2 exploding pusher N121128 114
3.20 pTOF signal obtained on NIF exploding pushers 115
3.21 Yield-over-clean as a function of Knudsen number for NIF exploding pushers 117
3.22 DD YOC vs. Knudsen number for exploding pushers on NIF and OMEGA 119
3.23 D^3He-p yield and energy as a function of polar angle on NIF shot N121128 121

4.1 Sweet-Parker model of magnetic reconnection 132
4.2 Two-fluid (Hall) model of magnetic reconnection 135
4.3 Magnetic reconnection at the Earth's dayside magnetopause 137
4.4 Magnetic reconnection as the cause of solar flares 138

4.5 Asymmetric magnetic reconnection configuration 139

5.1 Self-generated magnetic fields in laser-foil interaction 144
5.2 LASNEX-simulated magnetic field profiles in laser-foil experiment 145
5.3 Principle of proton radiography 146
5.4 Synthetic proton radigraphy of a magnetic field structure 148
5.5 Conceptual illustration of proton deflection and resulting proton fluence 149
5.6 Monoenergetic proton radiography 150
5.7 Proton fluence and energy images in monoenergetic proton radiography experiments 151
5.8 Grid-based monoenergetic proton radiography 152
5.9 Target normal sheath acceleration (TNSA) proton radiography 154
5.10 Experiment identifying magnetic fields around laser-produced plasma bubbles 156
5.11 Generic experimental setup for Thomson scattering measurements 157
5.12 Example Thomson scattering spectrum and notable features 158
5.13 Experimental setup for Thomson-scattering measurements in laser-foil experiments . 160
5.14 Proton radiography setup for single and colliding laser-produced plasma bubbles . . 161
5.15 Proton radiography images of single and colliding laser-produced plasma bubbles . . 162
5.16 Streaked Thomson scattering spectral images from single and colliding plasma bubbles 163
5.17 Thomson scattering spectra in colliding plasma bubbles (OMEGA shot 46931) . . . 163
5.18 Thomson-scattering-measured electron and ion temperatures in single and interacting plasma bubbles 165
5.19 Comparison of electron and ion temperatures in single versus colliding plasma bubbles 166

6.1 Plasma β and collisionality in astrophysical and laboratory magnetic reconnection . 176
6.2 Magnetic field configurations at the magnetopause and in the asymmetric reconnection experiments. 178
6.3 Proton radiography images and path-integrated magnetic field strength in asymmetric reconnection experiments 180
6.4 Magnetic flux in laser-plasma reconnection experiments 181
6.5 Measured flux annihilated in symmetric and asymmetric reconnection experiments . 182
6.6 Measured and PIC-simulated results for symmetric and asymmetric reconnection . . 184
6.7 Illustration of out-of-plane fields imposed by asymmetric plasma bubble geometry . 185
6.8 Experimental setup for proton radiography of magnetic reconnection experiments on OMEGA-EP 188
6.9 Proton radiography images obtained on OMEGA-EP at different sample times . . . 189
6.10 DRACO-simulated profiles in OMEGA-EP reconnection experiments 192
6.11 DRACO-simulated parameters around the reconnection region as a function of time . 193
6.12 Proton radiography setup for colliding plasmas carrying parallel magnetic fields . . . 194
6.13 Proton radiography images and path-integrated magnetic field strength in the interaction of parallel magnetic fields 196
6.14 Lineouts of path-integrated magnetic field strength in collision of parallel magnetic fields 197
6.15 Simulated magnetic fields in a 2D PIC simulation of colliding plasmas carrying parallel magnetic fields 197

A.1 LILAC simulations of exploding pushers on OMEGA 216
A.2 Scattered light data from an exploding pusher implosion on OMEGA 220

A.3 X-ray framing camera (XRFC) self-emission images of an exploding pusher implosion on OMEGA 221
A.4 X-ray spectrum from an exploding pusher implosion on OMEGA 221
A.5 Fusion-product spectra from a D^{3}He exploding pusher implosion on OMEGA 222
A.6 Measured yields as a function of initial gas density in exploding pusher implosions on OMEGA 223
A.7 Measured ion temperatures as a function of initial gas density in OMEGA exploding pushers 224
A.8 Measured fuel ρR on exploding pusher implosions on OMEGA 224
A.9 Measured and DUED-simulated bang times as a function of initial gas density on OMEGA exploding pushers 225
A.10 Measured and HYADES-simulated burn durations as a function of initial gas density on OMEGA exploding pushers 226
A.11 Measured and HYADES-simulated fusion burn radii on OMEGA exploding pusher implosions 226
A.12 Example of fitting procedure for Reduced Ion Kinetic (RIK) model 228
A.13 Measured yields as a function of simulated yields for NIF exploding pushers 230
A.14 Measured ion temperatures as a function of simulated ion temperatures for NIF exploding pushers 231
A.15 Measured bang times as a function of simulated bang times for NIF exploding pushers 235

B.1 CPS-measured fusion-product spectra from a D^{3}He exploding pusher implosion on OMEGA 237
B.2 Linewidth-inferred ion temperatures in OMEGA exploding pushers 238
B.3 CPS slit images on radiochromic film 239
B.4 Measured and simulated ion temperatures as a function of initial gas density 241

D.1 Experimental setup for Thomson-scattering measurements in laser-foil experiments . 250
D.2 Streaked Thomson scattering spectral images from single and colliding plasma bubbles 250
D.3 Thomson scattering spectra obtained on OMEGA shot 46926 251
D.4 Thomson scattering spectra obtained on OMEGA shot 46927 251
D.5 Thomson scattering spectra obtained on OMEGA shot 46928 252
D.6 Thomson scattering spectra obtained on OMEGA shot 46929 252
D.7 Thomson scattering spectra obtained on OMEGA shot 46930 253
D.8 Thomson scattering spectra obtained on OMEGA shot 46931 253

E.1 To-scale depiction of experimental setup for asymmetric reconnection experiments on OMEGA 257
E.2 15-MeV- and 3-MeV-proton radiography images in asymmetric reconnection experiments 259
E.3 15-MeV- and 3-MeV-proton radiography images of duplicate asymmetric reconnection experiments 260
E.4 To-scale depiction of experimental setup for magnetic reconnection experiments on OMEGA-EP 262
E.5 Face-on TNSA proton radiography images of reconnection experiments on OMEGA-EP 263
E.6 Side-on TNSA proton radiography images of reconnection experiments on OMEGA-EP 264
E.7 Face-on and side-on high-resolution proton radiography images of reconnecting plasma bubbles on OMEGA-EP 265

E.8 Measured and synthetic face-on proton radiography images and inferred magnetic field structures in reconnection experiments on OMEGA-EP 266
E.9 Measured and synthetic proton radiograph showing "double-Y" feature in EP reconnection experiments 267
E.10 To-scale depiction of experimental setup for side-on radiography of magnetic reconnection experiments on OMEGA 268
E.11 Side-on mononergetic proton radiography of magnetic reconnection experiments on OMEGA 269
E.12 To-scale depiction of experimental setup for colliding parallel magnetic fields experiments on OMEGA 270
E.13 Mononergetic proton radiography of colliding parallel magnetic fields on OMEGA . 271
E.14 15-MeV-proton images in anti-parallel and parallel colliding magnetic fields experiments on OMEGA 272
E.15 Proton radiography images and maps of beamlet deflection and path-integrated magnetic field strength in OMEGA experiments 273
E.16 Path-integrated field strength maps in anti-parallel and parallel colliding magnetic fields experiments on OMEGA 274
E.17 Lineout of path-integrated magnetic field strength used to infer magnetic flux in anti-parallel and parallel magnetic fields experiments 275
E.18 Fraction of possible magnetic flux annihilated for anti-parallel and parallel colliding magnetic fields in OMEGA experiments 276

List of Tables

1.1 Operating parameters for MCF and ICF. 27

2.1 Operating parameters for CPS, WRF, and the new SRF proton spectrometer 58
2.2 Measured and inferred quantities from LEIA tests of the SRF 61
2.3 SRF- and CPS-measured DD-proton yield, mean energy, and spectral width on three D^3He thin-glass-shell implosions on OMEGA 63
2.4 SRF-measured proton yields and ratios of proton signal on NIF shot N130129 64
2.5 Proton energy and linewidth bounds for SRF measurements 69

3.1 Key hydro-kinetic parameters in the hydrodynamic-like and strongly kinetic regimes 99
3.2 Capsule and laser parameters for exploding pusher experiments on NIF 109
3.3 Measured observables from NIF exploding pushers 111
3.4 Measured fuel ρR, total ρR, x-ray emission radius P0 and symmetry on NIF exploding pushers 115
3.5 Measured and DRACO-simulated bang times on NIF exploding pushers 116
3.6 Calculation of Knudsen number for NIF exploding pushers 117
3.7 Knudsen number calculation for shock phase in a variety of implosions 118
3.8 Measured D^3He-proton yield and energy at seven different WRF positions on N121128 120

4.1 Reconnection-relevant parameters in a variety of plasmas 136

5.1 Characteristics of radiochromic film stack used in TNSA backlighting 155
5.2 Summary of TNSA and exploding-pusher proton radiography characteristics 155

6.1 Plasma parameters for experimental and magnetopause reconnection environments . 178
6.2 Derived reconnection-relevant parameters for experimental and magnetopause environments 179
6.3 Scale parameters for PIC simulations of asymmetric magnetic reconnection 183
6.4 Estimates of magnetic-field quantities around the reconnection region in OMEGA-EP experiments 191
6.5 Reconnection-relevant parameters around the reconnection region in OMEGA-EP experiments 192

A.1 Experimental setup parameters for exploding pusher experiments on OMEGA 214
A.2 Principal experimental data from exploding pusher experiments on OMEGA 215
A.3 Additional experimental data from exploding pusher experiments on OMEGA 217
A.4 Ion collision parameters from exploding pusher experiments on OMEGA 218
A.5 Capsule and laser parameters for NIF exploding pushers 229

A.6 Measured observables from NIF exploding pushers 229
A.7 Measured and simulated fuel ρR in NIF exploding pushers 232
A.8 Measured secondary DT-n yields and inferred fuel ρR for NIF exploding pushers . . 233
A.9 Measured x-ray emission size and symmetry on NIF exploding pushers 234

B.1 CPS slit image widths from OMEGA exploding pusher experiments 240
B.2 Mechanisms that impact fusion product spectral widths 243

D.1 Time-dependent plasma conditions assumed or inferred from Thomson scattering spectra 254

E.1 Experimental setup parameters for asymmetric magnetic reconnection experiments on OMEGA 258
E.2 Magnetic field data for asymmetric magnetic reconnection experiments on OMEGA 261
E.3 Experimental setup parameters for magnetic reconnection experiments on OMEGA-EP 262
E.4 Experimental setup parameters for side-on radiography of magnetic reconnection experiments on OMEGA 268
E.5 Experimental setup parameters for asymmetric magnetic reconnection experiments on OMEGA 270
E.6 Magnetic field data for colliding parallel magnetic fields experiments on OMEGA . . 271

F.1 Plasma parameters relevant to experiments studying ion kinetic effects in ICF 283
F.2 Plasma parameters relevant to magnetic reconnection experiments using laser-produced plasmas 286

1

Introduction to Inertial Confinement Fusion

The first half of this thesis discusses experimental research and diagnostic techniques in laser-driven inertial confinement fusion (ICF). In this chapter, an overview of nuclear fusion is presented, as well as the goals and challenges associated with controlled fusion experiments designed to achieve energy gain in the laboratory. The physics of ICF implosions is discussed, including typical modes of operation and the experimental facilities where ICF and other laser-driven research is conducted.

Finally, a special class of ICF implosion, shock-driven "exploding pushers," are introduced. These implosions, either studied in themselves or used as a diagnostic tool, have driven the bulk of research contained in this thesis, both for ICF and for fundamental plasma physics.

1.1 Nuclear Fusion

Nuclear fusion is the process by which light ions combine to form heavier elements and release copious amounts of energy in the form of highly energetic nuclear or gamma ray products. In contrast to fission, in which heavy atoms break apart and release kiloelectron volts (keV) of energy, fusion reactions release megaelectron volts (MeV), a far greater energy yield. This energy release occurs as a consequence of the increasing binding energy per nucleon of light nuclei. Up through element 26, iron (Fe), fusion of light nuclei results in positive energy release, whereas elements heavier than iron can release energy when their nuclei break apart. Figure 1.1 shows the binding energy per nucleon, indicating the energy difference between two lighter nuclei (say, hydrogen) and a heavier nucleon (helium).

In order to achieve nuclear fusion and this large energy release, fusing nuclei must overcome the Coulomb repulsion of their respective positive charges. Classically, the energy required to overcome this potential barrier is of order ~MeV; however, the finite probability of quantum tunneling permits ions with energies of only ~keV to pass through the immense potential and settle into the opposing nucleus.

Hydrogen isotopes, with charge Z=1 and, therefore, a relatively small Coulomb potential, are the optimal fusion fuels. The solar $p-p$ chain, which produces most of the energy in the sun, relies on fusion of isotopes of hydrogen and helium. For controlled fusion experiments, reactions with the largest probability of occurring under conditions that are achievable in the laboratory are most widely used. Figure 1.2a shows the fusion cross section of several different reactions as a function of center-of-mass energy.[1] For laboratory fusion research, where reactant energies are typically 1-100 keV based on the ~keV ion temperatures that are achievable in fusion experiments, the DT fusion reaction

$$\mathrm{D} + \mathrm{T} \rightarrow \mathrm{n}\ (14.1\ \mathrm{MeV}) + \alpha(3.5\ \mathrm{MeV}) \tag{1.1}$$

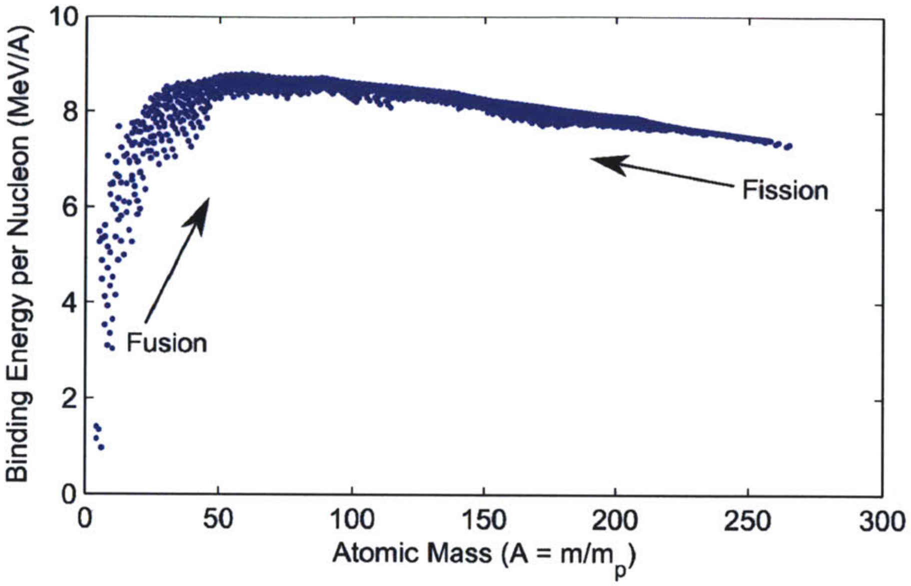

Figure 1.1. Binding energy per nucleon (MeV/A) as a function of atomic mass (A) [Source: BNL Atomic Mass Evaluation]. For elements lighter than iron (atomic mass 56), fusion produces a net energy gain. For elements heavier than iron, fission results in net energy release.

has the largest cross-section and therefore the largest probability of occurring. Other common reactions used in laboratory fusion research are DD

$$\mathrm{D} + \mathrm{D} \rightarrow \mathrm{n}\ (2.5\ \mathrm{MeV})\ +^3He(0.8\ \mathrm{MeV}){\sim}50\%,\ \text{and} \tag{1.2}$$

$$\mathrm{D} + \mathrm{D} \rightarrow \mathrm{p}\ (3.0\ \mathrm{MeV})\ +\mathrm{T}\ (1.0\ \mathrm{MeV})\ {\sim}50\%, \tag{1.3}$$

which have a similar energy dependence to DT, but a factor of ~100 lower cross-section, and D^{3}He,

$$\mathrm{D} +\ ^3He \rightarrow \mathrm{p}\ (14.7\ \mathrm{MeV})\ +\alpha(3.7\ \mathrm{MeV}). \tag{1.4}$$

The fusion reaction rate, which is generally desired to be maximum, is equal to the volume integral of the fusion cross-section multiplied by the center-of-mass velocity of the reactants and the product of their densities, such that

$$dY/dt \sim \int dV n_A n_B \sigma v, \tag{1.5}$$

where n_A is the density of reactant A and n_B is the density of reactant B, σ is the fusion cross-section and v is the center-of-mass velocity. Based on Figure 1.2a, it might seem feasible to accelerate deuterium beams to tens or hundreds of keV, direct them into a deuterated or tritiated target, and generate copious fusion reactions. However, this method is severely inefficient, as most of the energy of the beam ions is lost to Coulomb collisions that heat the target and do not lead to fusion reactions.[2,3] The head-on collision of opposing ion beams is similarly afflicted with physical impracticalities, such as the unsuitably low densities in ion beams of reasonable currents,[2] rapid thermalization of beam ions, or beam-beam collision instabilities. Thus, to circumvent these issues,

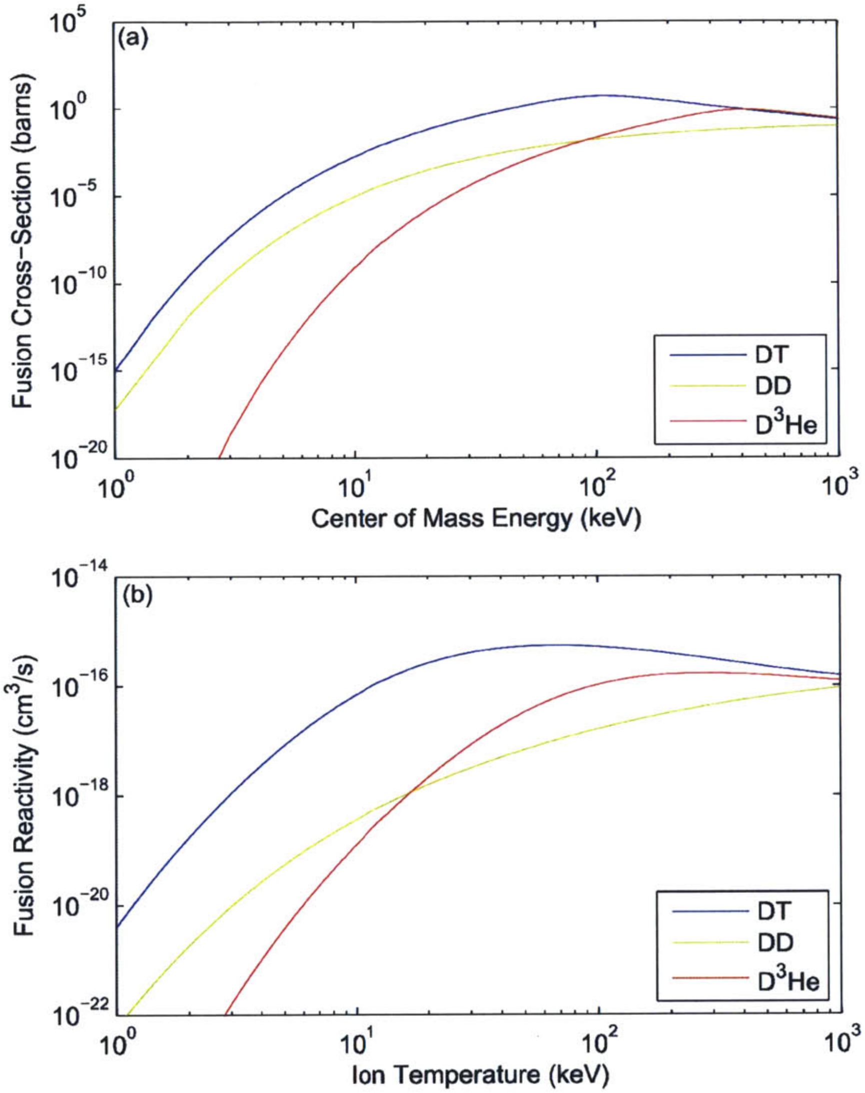

Figure 1.2. (a) Cross sections for DT, DD, and D^{3}He fusion reactions as a function of center-of-mass (CM) reactant energy and (b) Maxwellian-averaged fusion reactivities as a function of temperature. The DD curve represents the D(d,p)T branch [Source: ENDFVII.1 library].

experiments designed to achieve net fusion energy gain in a controlled setting have focused on producing hot, confined plasmas.

In confined fusion experiments, where the hot plasma can be described as a Maxwellian distribution with a given temperature, the product of the fusion cross-section and the center-of-mass velocity can be averaged as

$$\langle \sigma v \rangle = \int d^3 v \sigma(v) e^{-\frac{mv^2}{2kT}}, \tag{1.6}$$

where T is the temperature of the plasma (specifically, the ions). The product $\langle \sigma v \rangle$ is known as the fusion reactivity, and is a function of ion temperature in a Maxwellian plasma. The reactivities of DT, DD, and D^3He fusion reactions as a function of ion temperature are shown in Figure 1.2b. For laboratory experiments in which the confined plasma has temperatures of order 10 keV, DT is the most reactive fusion fuel.

In order to achieve substantial fusion reactions and possible energy gain, the plasma must achieve a sufficient density and temperature over a sufficiently large volume and long confinement time. Following equation 1.5,

$$dY/dt \sim n^2 \langle \sigma v \rangle V_{burn}, \tag{1.7}$$

where V_{burn} is the volume over which fusion reactions occur. In order to create a self-sustaining reaction to ignite a significant fraction of the fuel and achieve net energy gain, the energy deposited into the fuel by charged fusion products must exceed energy losses due to radiation and thermal conduction. In DT fusion, this energy deposition is in the form of 3.5-MeV alpha particles, which slow down on the electrons in the plasma and ultimately supply energy to the remaining fuel ions to instigate further fusion reactions.

1.1.1 Criteria for Self-heating and Ignition

The condition for self-sustainment of a fusion plasma, generally known as *ignition*, is when the rate of energy deposited by (charged) fusion products exceeds the rate of energy loss, generally to radiation or thermal conduction.[3] The rate of brehmsstrahlung radiation per unit volume in a deuterium-tritium plasma is proprtional to the square of the electron density and the inverse square root of the temperature, as

$$W_b = C_b n_e^2 T^{1/2}, \tag{1.8}$$

where C_b is a constant equivalent to 5.34×10^{-24} erg cm^3 s^{-1} keV$^{-1/2}$. In DT fusion, the energy deposited into the fuel comes from the confined 3.5-MeV alphas, which lose energy to electrons as they traverse the plasma. This alpha heating rate is proportional to the fusion reactivity, the reactant energy Q_α, and the product of the reactant densities, with

$$W_\alpha = n_D n_T \langle \sigma v \rangle Q_\alpha = \frac{1}{4} n^2 \langle \sigma v \rangle Q_\alpha. \tag{1.9}$$

The neutrons do not deposit much energy in the fuel itself and so their 14.1 MeV of energy do not contribute to the self-heating of the plasma. Having $W_\alpha > W_b$ is a necessary (but not sufficient) condition to achieve fusion ignition.

To describe the efficiency of a fusion power scheme, the quantity $Q = P_{fusion}/P_{aux}$ is defined as the ratio of fusion power released to auxiliary power supplied. In a steady-state reactor, alpha heating should balance energy loss mechanisms in such a way that auxiliary power can be eliminated and the reactor operates at $Q = \infty$, the strictest definition of thermonuclear ignition. In a pulsed fusion system, such as in inertial confinement fusion, a driver delivers energy E_d in a rapid burst, producing the necessary conditions for copious fusion reactions and generating fusion energy E_{fus}.

The energy gain $G = E_{fus}/E_d$ is the ratio of these quantities, where $G = 1$ denotes breakeven and $G \gg 1$ is considered the desired "high gain".

Instantaneous steady-state operation requires a balance of power inputs and losses, with the losses equivalent to the sum of bremsstrahlung radiation and the diffusive loss of thermal energy from the hot plasma. This diffusive power loss per unit volume for a hydrogen plasma is

$$W_{dif} = 3nk_BT/\tau_E, \tag{1.10}$$

where k_B is Boltmann's constant and τ_E is the energy confinement time, the characteristic diffusion time for the plasma internal energy. The balance of power losses and sources is expressed as

$$W_b + W_{dif} = W_{aux} + W_\alpha = \left(\frac{5}{Q} + 1\right) W_\alpha. \tag{1.11}$$

Substituting in equations 1.8, 1.9, and 1.10 for the various power terms, the criterion for power balance is

$$n\tau_E = \frac{3k_BT}{\frac{1}{4}[\frac{5}{Q} + 1]Q_\alpha\langle\sigma v\rangle - C_bT^{1/2}}. \tag{1.12}$$

The right-hand side is only a function of temperature, and so this equation sets a fairly simplified relation between density, confinement time, and temperature. This condition is known as the Lawson criterion, and establishes a baseline for fusion reactor operation in terms of the confinement parameter $n\tau_E$ – the left-hand side must exceed the right-hand side. Though it is formulated in terms of steady-state quantities, it can be adapted for pulsed fusion systems like ICF, as described in Section 1.2.2. In particular, it will be shown that this condition on $n\tau_E$ is equivalent to a condition on the areal density ρR in inertial confinement fusion implosions.

1.1.2 Controlled Fusion Methods

Two dominant areas of laboratory fusion research, designed to achieve self-sustaining reactions and energy gain in hot (~10 keV), confined plasmas are magnetic confinement fusion (MCF) and inertial confinement fusion (ICF). In MCF, the plasma is confined in steady state by strong magnetic fields which tie ions to field lines and prevent losses to the wall of the chamber in order to extend the confinement time. In ICF, the plasma is confined by its own inertia – the inward implosion of a spherical mass of fuel before its dissipation. ICF is a pulsed fusion scheme which relies on compression of the fuel to extremely high densities over a very short duration.

Table 1.1. Operating parameters for MCF and ICF.

Parameter	MCF	ICF
Density (cm^{-3})	10^{14}	10^{25}
Temperature (keV)	10	10
Confinement Time (s)	10^{3}	10^{-9}
Volume (cm^3)	10^{9}	10^{-6}

Each method satisfies the Lawson criterion, but in rather different ways. While MCF uses tenuous plasmas at modest densities, but long confinement times (and large volumes), ICF plasmas are extremely dense, but with very short confinement times (and very small volumes). A comparison of the relevant operating parameters of MCF and ICF is shown in Table 1.1. The first part of this thesis discusses aspects of laser-driven inertial confinement fusion, described in the following sections.

1.2 Laser-Driven Inertial Confinement Fusion (ICF)

Inertial confinement fusion requires rapid compression of fusion fuel to extreme densities ($\sim 10^{25}$ cm^{-3}) and high temperatures ($\sim$10 keV). These conditions can be achieved through the use of laser or laser-produced x-ray drive. This section describes basic principles of laser-driven ICF, modes of operation, and challenges towards achieving ignition.

1.2.1 Overview

While the principle of inertial confinement fusion originated in the weapons programs of the 1950s, ICF research began in earnest after the invention of the laser in 1960. Initial research demonstrated the necessity of operating at high compression, and early work proposed the usage of pulsed laser systems to implode capsules to produce microscopic fusion ignition in a similar manner to a fission-driven fusion device. The declassification of ICF research in 1972 precipitated an expansion of the research effort. The seminal publication by Nuckolls *et al.*[4] described the fundamental issues that must be overcome in order to achieve controlled thermonuclear ignition in the laboratory, principally related to the required factor of 10^4 compression in density of the fusion fuel. It was thought that high gain would require laser energies of 0.1-1 MJ, but that energy breakeven would be possible with as little as 1 kJ of laser energy. High compression allows for ignition with a smaller fuel mass and, consequently, a smaller laser drive. Furthermore, for high compression and greater confinement of the fuel ions, energetic, charged fusion products are stopped in the fuel as well, providing additional heating that drives further reactions. This process of ignition is necessary for high energy gain.

Nuckolls *et al.* described the necessity of pressures well in excess of 10^{10} atm to implode and compress the fuel to sufficiently high density and to couple implosion velocity to internal energy (temperature) in the final plasma. This pressure is achievable through the laser or x-ray ablation of shell material which, in a manner similar to a rocket, propels the remaining shell and fuel inward at velocities of several hundred μm/ns. In order to achieve high compression, the fuel must be kept at a state close to Fermi degenerate, such that the compression process is nearly isentropic and the fuel can be compressed to very high densities without pushing back too strongly against the incoming material. The radiation pulse must be optimally shaped to produce such an isentropic compression, and Nuckolls *et al.* described a pulse shape consisting of ten distinct pulses.

This principle has been applied in recent high-compression experiments, where carefully tuned "pickets"[5] of laser power launch shocks into the fuel in order to set a low adiabat (α), the ratio of fuel pressure to the minimum, Fermi degenerate pressure. A typical adiabat is in the range $\alpha \sim 1.5$-2 (the point design[6] for an ICF ignition implosion at the National Ignition Facility uses an adiabat of $\alpha = 1.4$). Suprathermal electrons in the corona, produced by laser-plasma instabilities, can preheat the fuel in a manner that increases the fuel adiabat and degrades the compression. These instabilities can be mitigated by operating in a regime of radiation intensity below the threshold for instability onset, or by doping the shell with high-Z atoms, which increases the amount of benign inverse bremsstrahlung absorption of the laser energy.

Implosion symmetry and shell stability were also discussed by Nuckolls *et al.*, expounding on the importance of obtaining hydrodynamic behavior as close as possible to spherical symmetry in order to achieve optimal implosion conditions and maximum energy coupling into the fuel. The requirement of a 10^4 compression in density – a factor of ~20 convergence in radius – demands that the implosion radius be uniform to much better than 1/20 of the initial radius and that the implosion velocity be uniform to much better than 5% over the capsule. Such uniformity requires a symmetric drive, with irradiation from many directions. Asymmetries inherent in the irradiation may be mitigated somewhat in the absorption process. Light propagates only as far as the critical density surface, the radius at which $\omega_r = n_e e^2/m_e \epsilon_0$, where ω_r is the angular frequency of the radiation source and n_e is the density. The transport of energy from the critical surface to the ablation front by electrons heated by inverse bremsstrahlung absorption smooths the inherent irradiation non-uniformity and reduces drive asymmetries. Hydrodynamic stability of the shell is paramount to maintain the necessary 1D behavior. In particular, with the large density gradients and acceleration, both at the ablation front and later during the deceleration of the shell, the Rayleigh-Taylor instability may produce spikes of cold shell material into the hot fuel which would quench fusion burn. Maintaining sufficiently high compression while mitigating hydrodynamic instabilities is a key challenge in ICF research.

1.2.2 Confinement and Compression for Hot-Spot Ignition

The need for high compression stems from the required confinement of fuel ions responsible for initiating fusion burn. The confinement time of fuel ions τ_c is

$$\tau_c = R_f/C_s, \tag{1.13}$$

where R_f is the fuel radius and $C_s = \sqrt{2k_BT/m}$ is the sound speed. As described earlier, the confinement parameter $n\tau$ needs to exceed a certain function of temperature, representing energy gains and losses, in order to sustain fusion burn. This parameter can be expressed as

$$n\tau_c = \frac{nR_f}{C_s} = \frac{\rho R_f}{mC_s}. \tag{1.14}$$

The quantity ρR_f, the fuel areal density, is a critical parameter describing the compression of the fuel and determines the efficiency of fusion burn.[3]

The Lawson criterion, describing the necessary relation between $n\tau$ and temperature in order to achieve fusion ignition (Equation 1.12), can therefore be re-expressed in terms of a condition on ρR in an inertial confinement fusion implosion. The final ρR must exceed a certain function of temperature so that energy gains outpace energy losses. On the basis of analytical theory and 1D simulations, it has been found that this condition, for DT fuels, is approximately

$$\rho R_f > \left(\frac{4.4}{T_i}\right)^{2.2}, \tag{1.15}$$

where ρR_f in g/cm^2 and T_i in keV are evaluated around peak fusion production, ignoring the effects of alpha heating.[7] This relation is illustrated in Figure 1.3. Sufficiently high ρR_f and T_i are required to ignite an ICF implosion. Typical designs for ICF ignition at the National Ignition Facility have a total areal density of ~1.8-2.0 g/cm^2,[8] and, therefore, temperatures around T_i~3.0-3.5 keV.

The efficiency of fusion burn is defined as the ratio of ions that undergo fusion to the total number of fuel ions, with

$$\Phi = N_{fusion}/N_{total}, \tag{1.16}$$

Figure 1.3. Lawson-like criterion for fusion ignition based on areal density (ρR_f) and ion temperature (T_i) around peak compression and fusion production in ICF ignition implosions (Equation 1.15). This curve, dependent on the ρR_f and T_i that are achieved in 1D simulations that exclude alpha heating, indicates where ignition is marginally likely to occur, as described by Betti *et al.*[7]

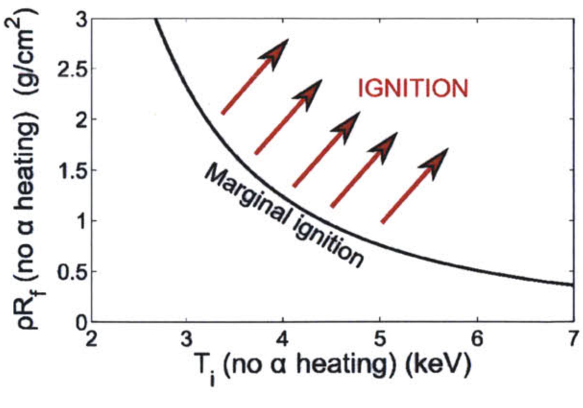

where $N_{total} \sim nV_0$ and V_0 is the total fuel volume. The number of fusing ions is

$$N_{fusion} \sim \frac{n^2\langle\sigma v\rangle V_0 R_f}{C_s}, \tag{1.17}$$

and the burn efficiency in the limit of little fuel depletion can be expressed as

$$\Phi \sim \frac{n^2\langle\sigma v\rangle V_0 R_f}{C_s n V_0} \sim \frac{\rho R_f \langle\sigma v\rangle}{m C_s}. \tag{1.18}$$

Thus, the fraction of fusing fuel ions is directly proportional to ρR_f. Accounting for fuel depletion, the burnup fraction is

$$\Phi \sim \frac{\rho R_f}{\rho R_f + H_B}, \tag{1.19}$$

where the burn parameter $H_B \sim C_s m/\langle\sigma v\rangle$ is the denominator in equation 1.18. The burn parameter for DT fuel in the range of 10-100 keV is ~7-10 g/cm^2, such that in order to achieve a burn fraction of order 30%, a fuel ρR of 3 g/cm^2 is required.

Energy considerations make it less desirable to heat the entire fuel mass uniformly and instead it is preferable to heat a small mass of the fuel to thermonuclear conditions to initiate fusion burn, with the balance of the fuel at sufficient areal density to be heated by energy deposition from charged fusion products. A uniform mass of DT at an areal density of 3 g/cm^2 or a mass density of 1000 g/cm^3 over a sphere of radius 30 μm, at a temperature of 10 keV, contains 800 kJ of internal energy. This energy, which would have to be coupled into the implosion, is a significant fraction of the total energy in the most powerful laser drive system (i.e. at the National Ignition Facility) and impossible to achieve under practical circumstances. However, if the implosion is designed in such a way that only a small fraction (~1-3%) of the fuel mass had to be heated by the drive, with the rest heated by energetic fusion products, much less energy is required to be coupled into the core plasma. This is the principle behind hot-spot ignition.

In hot-spot ignition, a hot, low-density gas is surrounded by a cooler, high-density layer of fuel (with an inert ablator nearly blown away by the time of peak fusion production). The hot spot consists of gas at a density of ~40 g/cm^3, a temperature of 10 keV, and an areal density of ρR_{HS} ~0.3 g/cm^2. The requirement on the hot-spot areal density is also set by the need to stop alpha particles in DT fuel within the hot spot to initiate an expanding wave of fusion burn. The range of a 3.5-MeV alpha particle in 10 keV DT is exactly this value, ~0.3 g/cm^2. The total internal energy in the hot spot is a much more achievable ~25 kJ, requiring a drive efficiency of only a few percent on a MJ-class laser system. The surrounding cold fuel is only 0.2-0.4 keV, but at a density of ~400 g/cm^3 and ρR_{cold} ~2 g/cm^2, it has sufficient areal density to burn a significant fraction of the fuel.

1.2.3 Typical Implosion Conditions

A typical hot-spot ignition implosion, as described by Atzeni and Meyer-ter-Vehn,[3] occurs as follows. The initial capsule consists of three sections, as illustrated in Figure 1.4. The inner-most section is DT gas, at a density of roughly 0.3 mg/cm^3, surrounded by a layer of cryogenic, solid DT at ~0.2 g/cm^3. This inner gas, as well as blowoff into the gas from the initially solid material, eventually forms the hot spot. The initial solid DT layer forms the dense fuel into which the fusion burn wave eventually propagates. These fuel layers are surrounded by an ablator, typically plastic (CH) or pure carbon at solid densities ~1-3 g/cm^3. Ignition-scale capsules currently in use at the National Ignition Facility are typically ~1.1 mm in radius, with a ~90-μm-thick ablator surrounding a solid DT layer that is 70 μm thick.[9]

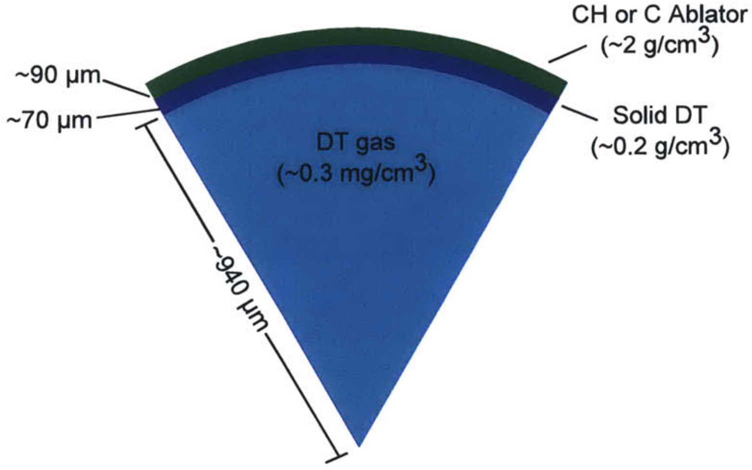

Figure 1.4. Typical capsule used in hot-spot ignition experiments at the National Ignition Facility. A CH or carbon ablator surrounds two separate fuel layers: a solid layer of high-density DT, which will comprise the main fuel, and a core of DT gas, which will largely comprise the hot spot.

In order to precisely set the conditions in both the hot spot and in the cold, dense fuel to optimize compression, several shocks are launched that set the fuel adiabat. The adiabat is defined as $\alpha = P/P_{Fermi}$, the ratio of pressure to Fermi-degenerate pressure as a function of density and temperature. This measure of entropy, constant during the desired isentropic compression (desired so as to not further increase the internal energy of the fuel), ostensibly determines the achievable increase in density as a function of ablation pressure. Since the goal is to maximize density (and areal density) for a given pressure, it is ideal to have an adiabat as low as possible. Ignition experiments are designed for an adiabat of α ~1.5-2. The use of several spherically-converging shocks, timed to coalesce at the inner surface of the solid DT layer, allows for near-arbitrarily high compression, as opposed to a single shock which can maximally increase the density by a factor of 4. The resulting shock propagates into the low-density gas, adding significant heat and entropy, and ultimately forming the high-temperature hot spot. Shocks in ICF implosions are discussed further in Section 1.4, Chapter 3, and Appendix A.

The shocks are typically launched by several small "pickets" of laser power early in the pulse,[5] which are followed by a rise in laser intensity, constituting the main part of the pulse and the beginning of ablative drive. Radiation absorbed at the critical density surface is conducted by electrons to the ablation front, where the heating of shell material causes ablator ions to be driven radially outward. This ablation is tantamount to a spherical rocket, which propels the remaining mass inward. For ignition-relevant implosions, the shell reaches an implosion velocity of ~300 μm/ns. The final energy density in the hot spot, heated and compressed by PdV work imparted by the imploding shell, scales strongly with the implosion velocity, with the final hot spot temperature scaling as ($T_i \propto V^{5/4}$).[7] By the end of the laser pulse, the shell is nearly completely ablated and the shell and cold fuel coast to the center.

Shortly before the shell reaches its minimum radius, the strong, spherically converging shock rebounds off the origin and expands back outward toward the shell. The shock wave reaching the shell begins the deceleration process. During this phase, the temperature of the hot spot is rapidly heated by the conversion of shell kinetic energy to gas internal energy, and this heating rate exceeds losses due to thermal conduction and radiation. The enormous pressure in the hot spot, >200 Gbar, prevents further compression and the implosion stagnates. Stagnation is characterized by near-isobaric conditions, with the moderate-density, high-temperature hot spot at ~40 g/cm^3 and T_i ~10 keV balanced by the ultra-high density, low-temperature outer fuel layer at ~500 g/cm^3 and T_i ~0.5 keV. This isobaric condition in a typical hot-spot ignition implosion is illustrated in Figure 1.5. By the time isobaric conditions are achieved and stagnation occurs, the shell has converged by a factor of 20 or greater in radius.

Figure 1.5. Simulated temperature (solid blue), density (dashed black), and pressure (dotted red) profiles around stagnation in a typical hot-spot ignition implosion, as depicted by Atzeni and Meyer-ter-Vehn.[3] The low-density, high-temperature hot spot sparks the initial fusion reactions, whose products deposit energy in the surrounding high-density, (initially) low-temperature fuel.

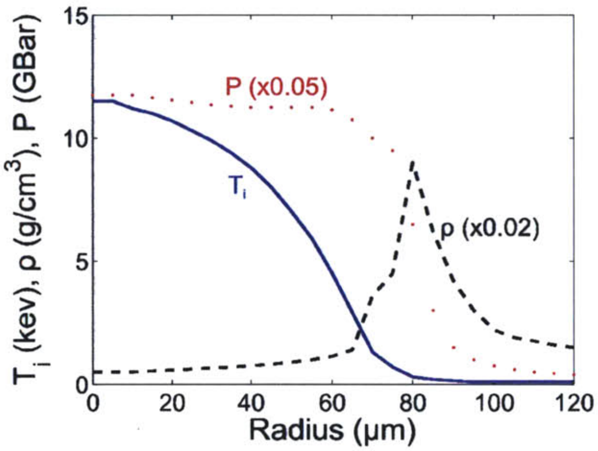

Initial fusion reactions occur in the hot spot, and DT alphas completely deposit their energy throughout the low-density region, igniting a wave of fusion burn that propagates into the cold fuel at a speed of ~500 μm/ns. According to simulations of ICF implosions that account for alpha heating, temperatures in the fuel can reach 100 keV, at pressures as high as 10 Tbar.[3] Burn occurs over a duration of ~50 ps.

Stability considerations during the implosion are also important and set limits on parameters such as the implosion aspect ratio (the ratio of shell radius to shell thickness) and the implosion velocity. Hydrodynamic instablities such as Rayleigh-Taylor are prone to develop in the presence of large pressure or density gradients in a rapidly imploding and accelerating system. Instabilities can be seeded at the ablation front by non-uniform energy deposition due to irradiation asymmetries or by perturbations on the surface of the capsule. Spikes of plasma that develop during medium to high-mode ($l > 10$) instability growth and are amplified by convergence can effectively reduce the hot-spot size and, more damagingly, introduce cold, high-Z material into the hot spot, which radiates, loses heat, and quenches ignition. If the shell or cold fuel layer are too thin, it is easier for hydrodynamic instabilities to break through into the hot spot. Low-mode drive asymmetries can produce a non-spherical implosion and lead to the inefficient transfer of shell kinetic energy to hot-spot thermal energy. Symmetry – and the tradeoff between potential high-mode and low-mode perturbations – is a major factor in weighing the two radiation-driven ICF drive schemes, direct drive and indirect drive, as discussed in the following section. Figure 1.6 illustrates high- and low-mode implosion asymmetries in an ICF implosion.

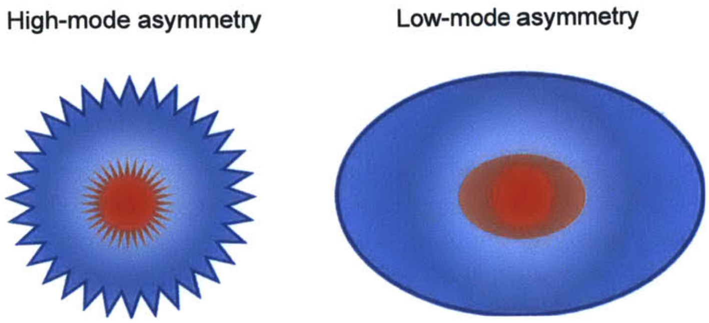

Figure 1.6. High-mode (left) and low-mode (right) asymmetries in ICF implosions. High-mode asymmetries introduce mix of cold fuel and shell material into the hot spot, degrading burn. Low-mode asymmetries, resulting in a non-spherical implosion, prevent the efficient coupling of implosion kinetic energy into the hot spot.

1.2.4 Laser Drive Schemes

Laser-driven inertial-confinement fusion ignition is being pursued primarily through two different drive schemes – direct drive, in which laser energy is absorbed directly by the imploding capsule, and indirect drive, in which laser light irradiates the inner surface of a high-Z hohlraum that surrounds the capsule, bathing the capsule in x-ray radiation. These drive mechanisms are illustrated in Figure 1.7, and the challenges surrounding the pursuit of ICF ignition are described in this section.

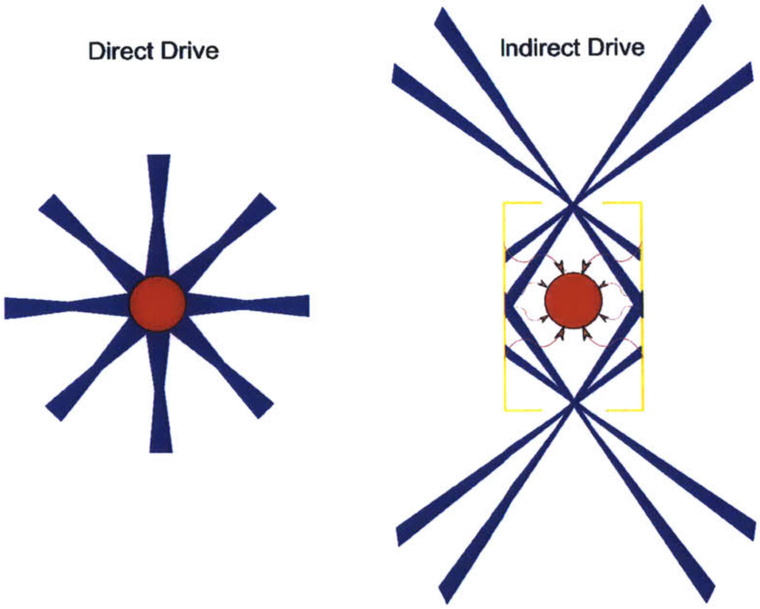

Figure 1.7. Diagram of direct-drive (left) and indirect-drive (right) ICF. In direct drive, lasers directly illuminate the outer layer of an ICF capsule. In indirect drive, lasers illuminate the inner surface of a cylindrical, high-Z hohlraum, which converts laser energy to x-rays. These x-rays then illuminate the capsule and drive the implosion.

Direct Drive

In direct-drive inertial confinement fusion, lasers directly ablate the outer shell layers. Laser light at a wavelength of 351 nm is absorbed at the critical surface, defined as the location where the plasma frequency becomes larger than the laser frequency, at a critical density n_c of 9×10^{21} cm^{-3}. Laser energy is absorbed collisionally by electrons in a process known as inverse bremsstrahlung absorption, and energy is subsequently coupled to the ions by electron-ion collisions. The critical surface is typically ~100 μm from the ablation surface, where shell material is blown outward, driving the rest of the capsule inward. Electrons transport energy from the critical surface to the ablation front, driving the implosion.

The ablation pressure, which ought to be large in order to generate a fast implosion velocity, is a moderate function of laser intensity, as

$$p_a \propto (I/\lambda_L)^{2/3}, \tag{1.20}$$

where I is the laser intensity and λ_L the wavelength.[10] On the other hand, for laser intensities that are too high, laser-plasma interaction (LPI) instabilities develop that can have deleterious effects on implosion performance. These instabilities involve the coupling of laser energy to both light and plasma waves[11] and produce suprathermal electrons that can preheat the cold fuel, increase the adiabat, and degrade the compression. Stimulated Raman Scattering (SRS) represents the decay of an incident light wave into a scattered light wave and an electron plasma wave, and occurs at densities up to the quarter-critical density ($<n_c/4$). Stimulated Brillouin Scattering (SBS) is the decay of an incident light wave into a scattered light wave and an ion acoustic wave, and occurs up to the critical density ($<n_c$). Two-Plasmon Decay (TPD) is the decay of an incident light wave into two electron plasma waves, and occurs very close to the quarter-critical density. In general, these instabilities occur due to current generated by the motion of electrons in the electric field of the incident light, which drives plasms waves and may consequently impact the local electric field in an unstable configuration. For higher laser intensities, stronger currents are induced, which are necessary to maintain the instability. In particular, the threshold for TPD is a laser intensity $I \gtrsim 5\times10^{14}$ W/cm^2. The crashing of the resulting plasma waves produces high-energy electrons, which can harmfully preheat the fuel and increase the fuel adiabat.

Direct-drive ICF has a fairly high efficiency in terms of coupling laser light into the ablator plasma, with laser absorption fractions typically ~50%.[12] However, the direct illumination of the capsule, with many overlapping beam spots across the capsule necessarily introduces high-mode irradiation asymmetries, which may seed hydrodynamic instability growth. On the other hand, low-mode asymmetries are fairly non-existent for systems with >20 uniformly-positioned beams (including the 60-beam OMEGA laser), and implosions are more likely to be roughly spherical.

Indirect Drive

In indirect-drive ICF, lasers irradiate the inner surface of a high-Z *hohlraum*, which re-radiates much of the energy as x-rays with typical radiation temperatures around 300 eV.[13] By virtue of the higher drive radiation frequency, the x-ray energy is absorbed as a much higher critical density, which consequently positions the critical surface closer to the ablation surface and reduces the distance over which electrons must transport energy to the ablation front. Despite the improved electron transport and reduced occurrence of LPI in the shell corona,[1] indirect-drive has the distinct disadvantage of a very low efficiency in converting laser light to useful kinetic energy in the implosion. The conversion efficiency of laser energy to x-ray energy is <70%, and the capsule only "sees" a small fraction of that, such that the total coupling efficiency between the laser drive and the capsule is ~10%.

Indirect drive has the advantage of smoothing out high-mode illumination non-uniformities that are a concern in direct-drive implosions. However, as an essentially cylindrical drive of a spherical target, is prone to low-mode asymmetries, producing prolate or oblate implosions. These low-mode implosion asymmetries produce non-useful shell and fuel kinetic energy that is not efficiently coupled into hot-spot thermal energy and must be avoided in order to increase the chances of achieving ignition.

---

[1] LPI does, however, impact the coupling of laser energy to the walls of the hohlraum in the first place, with typically ~15% of that light scattered away.

1.3 Laser Facilities

Experiments in inertial-confinement fusion and high-energy-density physics[14,15] are conducted at two preeminent laser facilities, the Omega Laser Facilty at the Laboratory for Laser Energetics (LLE) at the University of Rochester and the National Ignition Facility at Lawrence Livermore National Laboratory.

1.3.1 Omega Laser Facility

The Omega Laser Facility at LLE houses both the 60-beam OMEGA[16] and the 4-beam OMEGA-EP[17] laser systems. OMEGA was designed for direct-drive ICF experiments, with its 60 beams oriented in an icosahedral, "soccer ball" pattern of hexagons and pentagons in such a way that minimizes drive asymmetry. The OMEGA laser is designed to deliver up to 500 J per beam (up to 30 kJ toal) at a wavelength of 351 nm (3ω light for a fundamental wavelength of 1054 nm) in a variety of pulse shapes from ~400 ps to ~3 ns. The peak power is 0.5 TW per beam, 30 TW total. The laser and target bays that comprise OMEGA are illustrated on the left side of Figure 1.8.

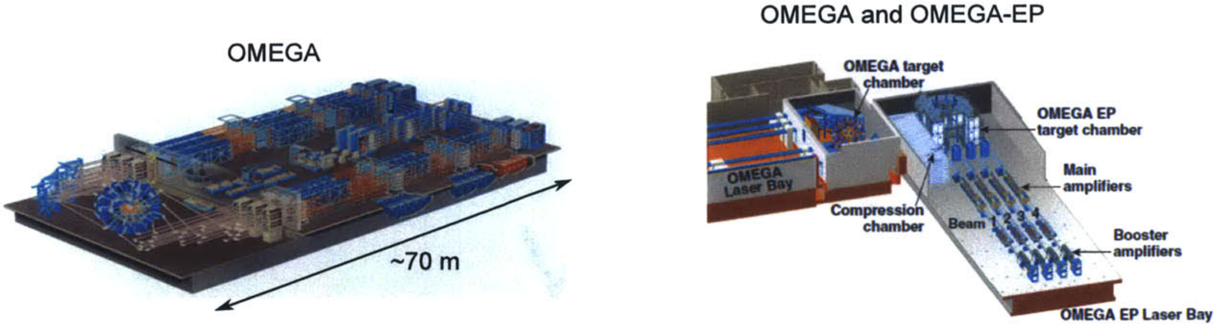

Figure 1.8. OMEGA and OMEGA-EP laser and target bays. In the OMEGA laser system (left), 60 beams are amplified several times before being directed into the target bay. The OMEGA-EP laser system (right) consists of 4 beams, one of which can be directed into the OMEGA target chamber during joint shot operations. Schematics credit: LLE staff.

OMEGA-EP (right side of Figure 1.8) is a 4-beam system designed to operate in a combination of short-pulse (~ps) and long-pulse (~ns) modes, with the short-pulse beams operated at the fundamental wavelength of 1054 nm (1ω) and the long-pulse beams operated at 3ω. Up to two short-pulse beams, 1-100 ps in duration, may be utilized in a single shot. Short pulse Beam 1 can deliver up to 50 J in 0.7 ps or 850 J in 10 ps, while short pulse Beam 2 can deliver 400 J in 0.7 ps or 1500 J in 10 ps. Design specifications call for up to 700 J in 0.7 ps or 2600 J in 10 ps for both short-pulse beams. Any of the four beams can be configured for long-pulse use, 0.1-10 ns, and their maximum energy output varies with pulse duration, from 100 J in 0.1 ns to ~1000 J in 1 ns to 4000 J in 10 ns. OMEGA-EP provides a very versatile platform for probing both long time scale (~ns) and short time scale (~ps) physics relevant to HED plasmas and short-pulse laser-plasma interactions. Additionally, in "joint" configuration, one short-pulse beam from OMEGA-EP can be directed into the OMEGA chamber. One such use of the OMEGA-EP beam in this mode is as a source of backlighter protons in OMEGA implosion experiments.[18]

1.3.2 National Ignition Facility

The National Ignition Facility (NIF) laser system,[19] illustrated in Figure 1.9, consists of 192 beams, divided into 48 "quads" of 4 beams each, to deliver up to 1.8 MJ at a peak power of 500 TW. Typical laser pulses range from ~1.4-20 ns in duration. Configured for indirect-drive ICF experiments and the irradiation of the inner surface of cylindrical hohlraums, the beams are arranged into 4 rings at each of 23°, 30°, 45°, and 50° relative to the hohlraum axis. The laser power and wavelength can be adjusted from one ring to the next in order to optimize low-mode implosion symmetry. Beam pointing can be adjusted slightly to allow for different experimental configurations, including for polar direct drive (PDD), where the NIF beams are repointed for direct irradiation of an ICF capsule, with most of the laser energy directed towards the poles of the capsule.[20,21]

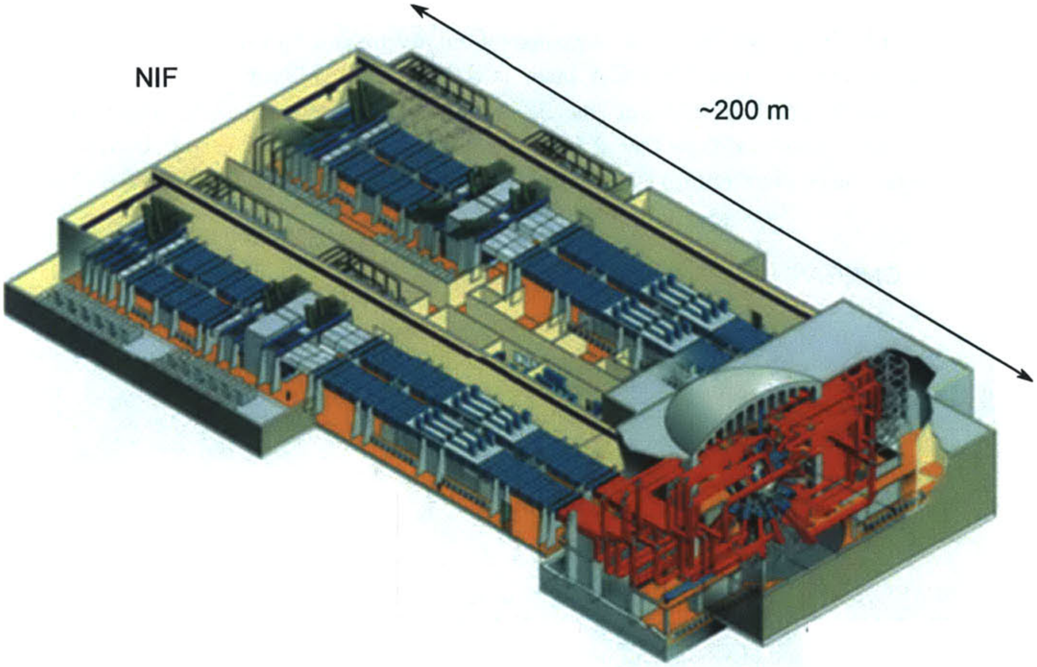

Figure 1.9. NIF laser and target bays. Forty-eight "quads" of beams, 192 beams in total, are amplified several times before being directed into the target chamber. Schematic credit: LLNL staff.

Typical indirect-drive ICF experiments on NIF utilize Au or depleted uranium (DU) hohlraums of length ~10 mm and diameter ~5.75 mm, with a laser entrance hole at each end comprising the inner ~50% in radius of the lid of the hohlraum. Ignition-relevant capsules are a shell approximately 2.1 mm in diameter, consisting of a CH ablator surrounding a DT ice layer and a core of DT gas. Surrogate, room-temperature experiments replace the ice layer with a thicker ablator that is roughly hydrodynamically equivalent and usually replace the DT gas with D_2 or D^3He for diagnostic and radiation safety purposes. These surrogate implosions are a reasonable substitute for assessing the physics of ablator performance, measuring the implosion velocity, and assessing the shell symmetry. Polar-direct-drive exploding-pusher implosions on NIF, predominantly for the purpose of diagnostic calibration, use glass shells of diameter 1.5 mm or 2.1 mm and either DT, D_2, or D^3He gas depending on which nuclear diagnostics are to be calibrated. Recently, ablatively-driven PDD experiments have begun to be performed, in anticipation of the assessment of PDD as a means of achieving ICF ignition.

1.4 Shock-Driven Exploding Pusher ICF Implosions

As discussed in Section 1.2, shocks play an important role in determining the initial fuel conditions in ICF implosions. In hot-spot ignition implosions, a series of shocks coalesce in the cold fuel, setting the fuel entropy and thus dictating the compressibility. The propagation of a strong shock into the gas increases the density and temperature in the gas, culminating with shock convergence and rebound, which sets the initial hot-spot conditions before peak compression. A special class of implosions, known colloquially as "exploding pushers," are driven almost exclusively by a strong shock launched into the gas early in the implosion. These implosions isolate the physics of shock convergence in ICF implosions. Figure 1.10 depicts simulations of converging shocks in an exploding pusher on OMEGA (14.6 kJ, 0.4 mg/cm^3 D^3He, 2.3 μm-thick, SiO_2) in comparison to an ignition implosion. In both cases, high Mach number ($M > 10$) shocks, at a speed of ~2000 μm/ns in the exploding pusher and ~500 μm/ns in the ignition implosion propagate through tenuous gases, of density ~0.3-0.4 mg/cm^2. Therefore, exploding pusher implosions are an excellent experiment to study the physics of shock propagation, shock convergence, and hot-spot formation as relevant to ignition implosions.

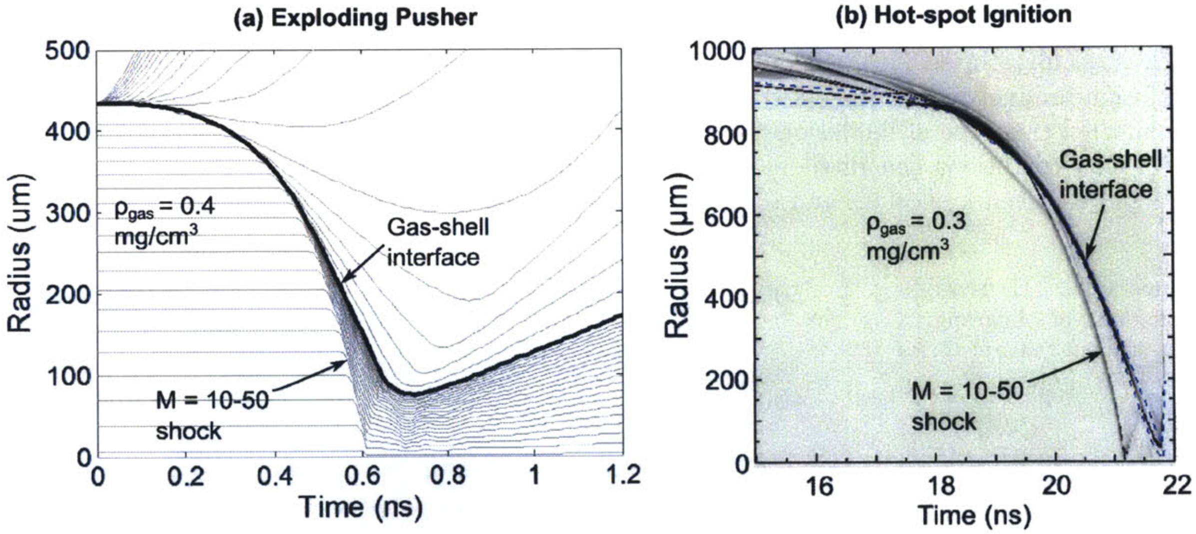

Figure 1.10. (a) 1D HYADES-simulated Lagrangian mass-element trajectories in an OMEGA exploding pusher, illustrating the rapid shock convergence, and (b) simulated pressure gradient (typically representing shock trajectories) in a hot-spot ignition implosion (simulation and plot by H. Robey, LLNL). Exploding pushers generate strong ($M \gg 1$) shocks in diffuse gas in a similar manner to the early stages of hot-spot ignition implosions and produce conditions after shock convergence relevant to hot-spot generation in ignition experiments.

Historically, exploding pushers were among the first implosions studied in ICF research and get their name from the rapid heating and explosion of the thin (typically glass) shell, which consequently launches the shock into the gas. Early exploding pushers[22–25] typically used lasers of very high intensity (>10^{15} W/cm^2), such that laser-plasma instabilities developed and generated hot electrons, which immediately penetrated and heated the thin shell, causing it to explode. The traditional picture of an exploding pusher is one where half the shell mass is expelled outward and half the shell mass is propelled inward. Recent exploding-pusher experiments utilize larger capsules and therefore lower laser intensities, where LPI was not as significant and the shell was heated instead somewhat more slowly by the self-radiation within the shell. This style of exploding pusher behaves slightly more ablatively, but still drives the implosion by means of a high-Mach-number (M ~15) shock that increases the density and temperature of the resulting plasma.

A 1D radiation-hydrodynamics HYADES simulation of a typical exploding pusher shot on the OMEGA laser facility is depicted in Figure 1.11. This implosion was driven by 60 beams in a 0.6-ns pulse, delivering 14.6 kJ of 351 nm laser energy to a SiO_2 capsule 840 μm in outer diameter and 2.2 μm thick with a mass density of 2.2 g/cm^2, filled with 8.2 atm (1.1 mg/cm^3) D^3He in a 50:50 atomic mixture. At first, the shock (relatively) slowly traverses the solid shell at a velocity of 30 μm/ns, a Mach number of M ~10, assuming an effective electron temperature of T_e ~0.1 eV and therefore a sound speed of 3 μm/ns ahead of the shock. By t = 100 ps, the shock breaks out into the gas and moves inward slightly ahead of the imploding fuel-shell interface. By the time the shock reaches half the initial shell radius at r = 210 μm, the shock is moving very rapidly, ~1500 μm/ns, for a Mach number of M ~10-50, depending on assumptions about the electron temperature in the unshocked gas, typically 10-30 eV. The shock converges around t = 620 ps and strongly rebounds at ~1000 μm/ns, a Mach number of M ~2, as the electron temperature ahead of the rebounding shock is T_e ~3 keV. The heating imparted by the rebounding shock elevates the ion temperature upward of 20 keV, initiating D^3He reactions along and immediately behind the shock trajectory. In an ideal exploding pusher, all of the yield is produced during shock rebound and fusion product measurements are sensitive only to plasma conditions immediately after shock rebound. In this type of implosion, such measurements can directly assess the shock physics and the plasma conditions generated by strong converging and rebounding shocks, relevant to both these shock-driven implosions and to ignition-relevant, ablatively-driven implosions.

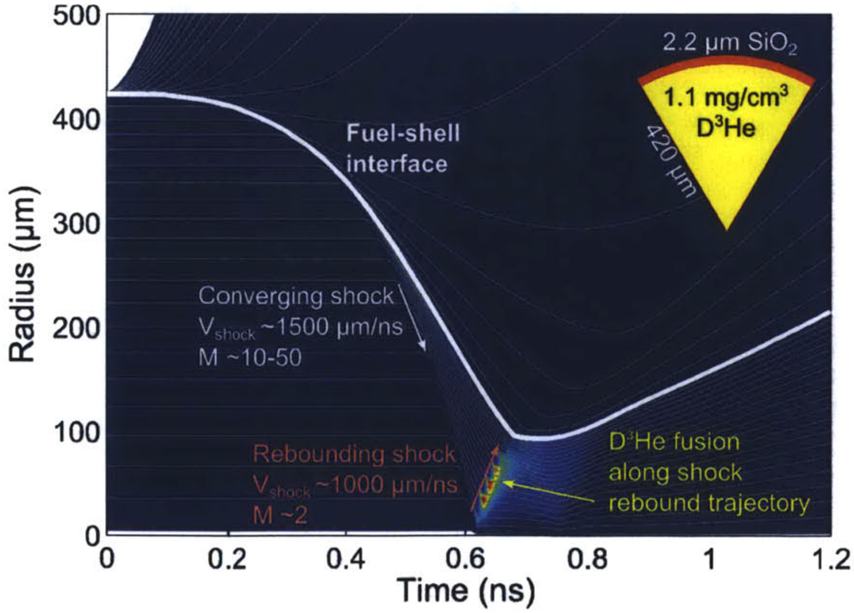

Figure 1.11. 1D HYADES simulation of Lagrangian mass-element trajectories (grey lines) in an exploding pusher with a 2.2 μm thick, 840 μm diameter, 2.2 g/cm^2 SiO_2 shell filled with 8.2 atm (1.1 mg/cm^3) D^3He. A strong shock converges and then rebounds at the center of the capsule, producing D^3He fusion along the shock rebound trajectory.

One key aspect of the post-shock phase in both ablatively-driven implosions and exploding-pusher implosions is the prevalence of ion kinetic effects. Around the time of fusion production in the exploding pusher discussed above, known colloquially as "shock flash," the ion density is $\sim 2.5\times10^{22}$ cm^{-3} and the ion temperature is T_i ~18 keV, such that the average ion-ion mean free path is ~60 μm, a significant fraction of the fuel radius. Thus, the fuel conditions are poorly described by hydrodynamics and a kinetic description of the implosion is necessary. Exploding pushers, with typically high ion temperatures as a result of the strong shock convergence, are a test bed for the physics of kinetic effects in ICF implosions. By virtue of the long ion-ion collision times (τ_{D3He} ~200 ps), a multiple-ion picture can be important.[2] The timescale for ions to diffuse out of the hot spot after shock convergence can also be fairly short, on the order of ~100 ps, suggesting that ion mean free path effects are significant. This ion kinetic physics, which is present in the early phases of hot-spot ignition implosions, can be studied in simpler, purely shock-driven exploding pushers, as discussed later in this thesis.

1.5 Thesis Overview

The first part of this thesis discusses diagnostic development and the use of shock-driven exploding pushers to study kinetic effects in laser-driven inertial confinement fusion implosions.

Chapter 2 discusses existing and new fusion-product diagnostics for measurements of fusion yield, burn-averaged ion temperatures, fuel and shell ρR, burn history, and spatial burn profiles. Among these diagostics are a newly-developed, compact DD-proton spectrometer for measurement of the DD-proton yield and implosion areal density in exploding pusher implosions on OMEGA and NIF and a novel instrument that effectively extends the yield operating range for DD-proton yield measurements in thin-shell implosions on NIF.

Chapter 3 expands on the discussion of the shock-convergence phase of ICF implosions and the ion kinetic effects that are prevalent during that phase, and how shock-driven implosions offer a simple experimental platform to study kinetic effects relevant to the early phases of ignition implosions. Shock-driven implosions experiments were performed on OMEGA and NIF and their results demonstrate deficiencies in hydrodynamics simulations as ion kinetic effects become significant. The first concerted, systematic experimental campaign to study ion kinetic effects in ICF implosions varied the mean-free-path in shock-driven implosions on OMEGA, and produced a strong trend of worsening yield agreement with hydrodynamic models with increasing mean-free-path. These results demonstrate that the hydrodynamic description was becoming increasingly invalid. The results are explained by the rapid diffusion of hot fuel ions and the preferential escape of suprathermal ions that would otherwise be responsible for fusion reactions. Exploding pusher experiments on NIF are also suggestive of ion kinetic effects becoming important as the ion-ion mean free path approaches a measurable fraction of the radius of the implosion.

The second part of this thesis discusses the study magnetic reconnection using laser-produced plasmas, using exploding pushers (and other proton sources) as a diagnostic tool to probe the collision of plasmas carrying magnetic fields.

Chapter 4 introduces the concept of magnetic reconnection, the rearranging of magnetic topology in a plasma, including basic theory and typical applications.

Chapter 5 describes the generation of magnetic fields in laser-produced plasmas and their application in experiments to study magnetic reconnection. Techniques used to probe these plasmas are discussed, including proton radiography measurements of electric and magnetic fields and Thomson scattering measurements of electron and ion temperatures. Early laser-plasma magnetic reconnection experiments showed annihilation of MG magnetic fields. Newly presented Thomson scattering measurements show that the magnetic reconnection dynamics do not significantly alter the thermal properties of this $\beta\sim 8$ plasma.

---

[2] Similarly, electron-ion collision times are long, τ_{ei} ~300 ps, such that electron-ion equilibration is a significant effect that can be studied through measurements of electron and ion temperatures in these implosions.

Chapter 6 discusses novel experiments using proton radiography to probe magnetic reconnection in symmetric and asymmetric plasma collisions. Among these are the first concerted laboratory experiments to study asymmetric magnetic reconnection, by introducing an asymmetry in the plasma bubble size, density, temperature, and flow velocity across the reconnection region. These asymmetric experiments demonstrated a comparable annihilation of magnetic flux as in similar, symmetric experiments. In these strongly-driven reconnection experiments, the rate of magnetic flux annihilation is determined by the plasma flow velocity and appears insensitive to local plasma conditions or asymmetries. High-resolution proton radiographs show detailed structure of magnetic fields around laser-produced plasma bubbles and their reconnection. Reconnection-induced electron jets are observed early in time, signifying a fast, two-fluid reconnection process; however, the persistence of strong magnetic fields late in time and the evolution of plasma conditions indicates a transition to a slower, single-fluid reconnection regime. Experiments designed such that colliding magnetic fields are parallel (as opposed to anti-parallel as in the reconnection experiments) show magnetic field deformation and pileup in absence of reconnection.

Chapter 7 summarizes and concludes the thesis.

1.6 References

1. H.-S. Bosch and G. M. Hale, "Improved formulas for fusion cross-sections and thermal reactivities," Nuclear Fusion, **32**(4), 611 – 631 (1992).
2. R. F. Post, "Controlled fusion research - an application of the physics of high temperature plasmas," Rev. Mod. Phys., **28**(3), 338–362 (1956).
3. S. Atzeni and J. Meyer-Ter-Vehn, *The Physics of Inertial Fusion: Beam Plasma Interaction, Hydrodynamics, Hot Dense Matter*, International Series of Monographs on Physics, (Oxford University Press, 2004).
4. J. Nuckolls, L. Wood, A. Thiessen *et al.*, "Laser compression of matter to super-high densities: Thermonuclear (ctr) applications," Nature, **239**, 139–142 (1972).
5. V. N. Goncharov, J. P. Knauer, P. W. McKenty *et al.*, "Improved performance of direct-drive inertial confinement fusion target designs with adiabat shaping using an intensity picket," Phys. Plasmas, **10**(5), 1906–1918 (2003).
6. S. W. Haan, J. D. Lindl, D. A. Callahan *et al.*, "Point design targets, specifications, and requirements for the 2010 ignition campaign on the national ignition facility," Physics of Plasmas, **18**(5), 051001 (2011).
7. R. Betti, P. Y. Chang, B. K. Spears *et al.*, "Thermonuclear ignition in inertial confinement fusion and comparison with magnetic confinement," Physics of Plasmas, **17**(5), 058102 (2010).
8. J. D. Lindl, P. Amendt, R. L. Berger *et al.*, "The physics basis for ignition using indirect-drive targets on the national ignition facility," Phys. Plasmas, **11**(2), 340–491 (2004).
9. H. F. Robey, J. D. Moody, P. M. Celliers *et al.*, "Measurement of high-pressure shock waves in cryogenic deuterium-tritium ice layered capsule implosions on nif," Phys. Rev. Lett., **111**, 065,003 (2013).
10. R. Fabbro, B. Faral, J. Virmont *et al.*, "Experimental study of ablation pressures and target velocities obtained in 0.26 mu m wavelength laser experiments in planar geometry," Physics of Fluids, **28**(11), 3414–3423 (1985).
11. W. Kruer, *The Physics Of Laser Plasma Interactions*, Frontiers in Physics, (Westview Press, 2003).
12. W. Seka, D. H. Edgell, J. P. Knauer *et al.*, "Time-resolved absorption in cryogenic and room-temperature direct-drive implosions," Physics of Plasmas, **15**(5), 056312 (2008).
13. J. Lindl, "Development of the indirect-drive approach to inertial confinement fusion and the target physics basis for ignition and gain," Phys. Plasmas, **2**(11), 3933–4024 (1995).
14. R. C. Davidson, *Frontiers in High Energy Density Physics*, (National Academies Press, Washington, DC, 2003).
15. R. P. Drake, *High-Energy-Density Physics*, (Springer Press, New York, 2006).

16. T. R. Boehly, D. L. Brown, R. S. Craxton *et al.*, "Initial performance results of the omega laser system," Opt. Commun., **133**, 495–506 (1997).
17. L. J. Waxer, D. N. Maywar, J. H. Kelly *et al.*, "High-energy petawatt capability for the omega laser," Opt. Photonics News, **16**(30) (2005).
18. A. B. Zylstra, C. K. Li, H. G. Rinderknecht *et al.*, "Using high-intensity laser-generated energetic protons to radiograph directly driven implosions," Rev. Sci. Inst., **83**(013511) (2012).
19. G. Miller, E. Moses and C. Wuest, "The national ignition facility," Opt. Eng., **43**, 2841 (2004).
20. S. Skupsky, J. A. Marozas, R. S. Craxton *et al.*, "Polar direct drive in the national ignition facility," Phys. Plasmas, **11**(5), 2763–2770 (2004).
21. P. B. Radha, F. J. Marshall, J. A. Marozas *et al.*, "Polar-drive implosions on omega and the national ignition facility," Phys. Plasmas, **20**(056306) (2013).
22. H. Brysk and P. Hammerling, "Dt fusion with microshells," Phys. Rev. Lett., **34**(8), 502–503 (1975).
23. E. K. Storm, H. G. Ahlstrom, M. J. Boyle *et al.*, "Laser fusion experiments at 4 tw," Phys. Rev. Lett., **40**(24), 1570–1573 (1978).
24. M. D. Rosen and J. H. Nuckolls, "Exploding pusher performance – a theoretical model," Phys. Fluids, **22**(7), 1393–1396 (1979).
25. B. Ahlborn and M. H. Key, "Scaling laws for laser driven exploding pusher targets," Plasma Physics, **23**(5), 435–447 (1981).

2

Fusion Product Diagnostics for ICF Implosions

Fusion products provide a wealth of information about the conditions in ICF implosions. The yield of nuclear products is sensitive to the temperature and density at the time when the reaction rate is greatest. The reaction history gives information on the dynamics of the implosion, principally the implosion velocity in terms of the convergence of a shock front or shell. The spectra of the nuclear products can be used to diagnose plasma conditions such as the ion temperature or areal density. The use of existing and newly-developed fusion product diagnostics of ICF implosions is the subject of this chapter. This chapter is organized as follows.

First, an overview of previously-developed and well-established nuclear diagnostics is presented: Section 2.1 discusses the use of nuclear measurements and spectroscopy as a means of diagnosing yield, ion temperature, and areal density in ICF implosions; Section 2.2 describes the properties of CR-39 nuclear track detectors and their usage in fusion-product spectroscopy and other nuclear diagnostics; Section 2.3 discusses the MIT Linear Electrostatic Ion Accelerator (LEIA) and its operation as a test-bed for development of ICF nuclear diagnostics.

Second, the development of two new nuclear diagnostics as part of the research for this thesis is discussed: Section 2.4 describes the development of a new compact, CR-39-based DD-proton spectrometer for measurement of yield and areal density in thin-shell implosions on OMEGA and NIF; Section 2.5 discusses evaluation and extension of the proton yield range of operation through development of a new CR-39-based DD-proton detector for high-fluence applications.

2.1 Nuclear Spectroscopy for Measurements of Ion Temperature and Areal Density

In addition to providing the yield of the implosion, a quantity of general interest in ICF, nuclear measurements are a powerful tool for determining the plasma conditions at the most important time in ICF implosions – the period when fusion reactions occur.[1] The fusion products most frequently measured in ICF implosions are the neutrons and protons from DD reactions

$$\mathrm{D} + \mathrm{D} \rightarrow \mathrm{n}\ (2.5\ \mathrm{MeV}) + {}^{3}\mathrm{He}(0.8\ \mathrm{MeV})\ [\sim 50\%], \text{ and} \tag{2.1}$$

$$\mathrm{D} + \mathrm{D} \rightarrow \mathrm{p}\ (3.0\ \mathrm{MeV}) + \mathrm{T}\ (1.0\ \mathrm{MeV})\ [\sim 50\%], \tag{2.2}$$

the protons and alpha particles from D^{3}He reactions

$$\mathrm{D} + {}^{3}\mathrm{He} \rightarrow \mathrm{p}\ (14.7\ \mathrm{MeV}) + \alpha(3.7\ \mathrm{MeV}), \tag{2.3}$$

and the neutrons and alpha particles from DT reactions

$$\mathrm{D} + \mathrm{T} \rightarrow \mathrm{n}\ (14.1\ \mathrm{MeV}) + \alpha(3.5\ \mathrm{MeV}). \tag{2.4}$$

Each of these products are born in a line at the specified energies, with a spectral shape determined by conditions in the implosion. As will be discussed in the following sections, by measuring the characteristics of the resulting spectra, it is possible to ascertain conditions in the hot spot and in the converged shell.

2.1.1 Ion Temperature Measurements

The birth widths of fusion product spectra are determined primarily by the Doppler broadening of the spectra due to the finite energy of the reactants, with $\sigma_D^2 = XT_i$, where σ_D is the Doppler width, T_i is the fusion burn-averaged ion temperature, and X is a constant. For both the spectral width and the ion temperature in keV, $X = 5630$ for DT reactions, 1510 for DD reactions (proton branch), and 5880 for D^{3}He reactions.[2,3,1] Those relations hold for both products in the specified reaction, so that in absence of other sources of broadening, (for example) the D^{3}He-proton spectrum has the same width as the D^{3}He-α spectrum. Under conditions where thermal broadening dominates the width of the fusion product spectrum, the linewidth is a direct measurement of the ion temperature, as weighted over the spatiotemporal burn region of that particular reaction. A sample D^{3}He-proton spectrum from which an ion temperature is inferred is shown in Figure 2.1. For this shot, OMEGA shot 61089, a thin-glass exploding pusher, a D^{3}He-burn-averaged ion temperature of T_i~17 keV is inferred from the Doppler width of σ~315 keV.

The inference of ion temperature from the width of fusion-product spectra can be complicated by other sources of spectral broadening. While the primary peak of fusion neutron spectra is largely insensitive to implosion conditions, save for bulk flow velocities,[4] charged fusion products can gain or lose energy and, consequently, experience spectral broadening, as a result of non-thermal effects. In thick-shell implosions, the significant ρR causes an overall energy downshift (see Section 2.1.2) as well as broadening of the spectrum due to dispersion, straggling, a time-varying energy downshift, and the differential path-length experienced by fusion products born at different locations in the implosion. As a result, this temperature measurement is only reliable using protons or alphas when ρR-related broadening is minimal in comparison to thermal broadening. This is typically the case for ρR<20 mg/cm^2 and T_i>10 keV,[5] as in most thin-shell exploding-pusher implosions as discussed in Chapter 3. Time-varying electric fields around the capsule[6] can also broaden charged fusion-product spectra by imparting a varying energy upshift over the duration of fusion reactions. These time-varying fields are ideally avoided, or measured and accounted for, in experiments where an ion temperature measurement is desired from spectral information.

As will be discussed in Chapter 3, the widths of fusion-product spectra are also modified by changes to the ion distribution function. In particular, when the ion distribution function is no longer Maxwellian, the relationship between the spectral width and the effective ion temperature is altered. The spectra become narrower when high-energy ions are preferentially removed from the distribution function, and can become broader if there is an increase in population of the high-energy tail. These considerations are typically not included in spectral analysis, and ongoing research is directed towards understanding and accounting for these effects. Other effects that can impact the interpretation of fusion-product spectral widths for measurement of the ion temperature are radial or turbulent bulk flows,[7,8] which can broaden the spectrum in a manner similar to thermal Doppler broadening. This is discussed further in Appendix B.

In mixed-fuel reactions, the ion temperature can also be determined by the ratio of yields of

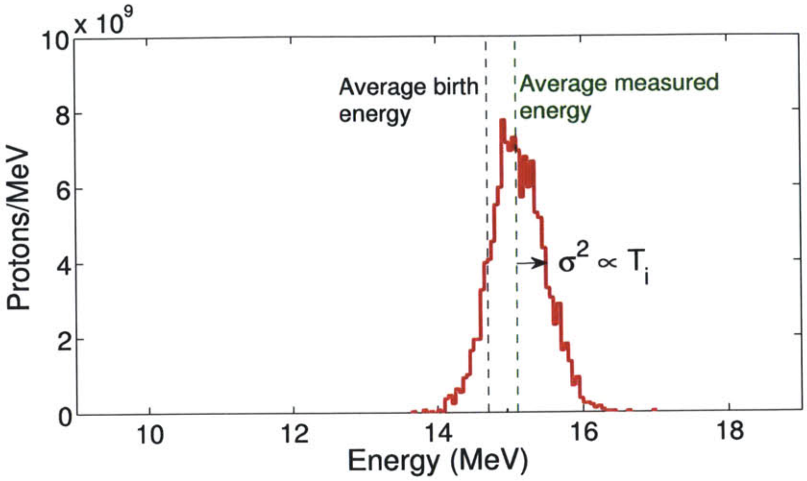

Figure 2.1. Measured primary D^3He-proton spectrum from OMEGA thin-glass shell exploding pusher implosion 61089. Since this implosion had very little compression, there was a negligible amount of line broadening due to proton ranging effects, and the measured linewidth is a direct measurement of the burn-averaged ion temperature. A temperature of T_i~17 keV is inferred from the Doppler width of σ~315 keV. This proton spectrum is slightly upshifted relative to its birth energy due to capsule charging effects.

two different reactions whose fusion reactivities have different sensitivities to ion temperature.[5] The DD and D^3He yields scale as

$$Y_{DD} = \frac{1}{2} n_D^2 \langle\sigma v\rangle_{DD} V_{DD} \tau_{DD}, \text{ and} \tag{2.5}$$

$$Y_{D^3He} = n_D n_{^3He} \langle\sigma v\rangle_{D^3He} V_{D^3He} \tau_{D^3He}, \tag{2.6}$$

where V is the average burn volume for each reaction and τ is the burn duration. Assuming $V_{DD} \sim V_{D^3He}$ and $\tau_{DD} \sim \tau_{D^3He}$, the ratio of DD to D^3He yields is

$$Y_{DD}/Y_{D^3He} \sim \frac{1}{2} \frac{n_D}{n_{^3He}} \frac{\langle\sigma v\rangle_{DD}}{\langle\sigma v\rangle_{D^3He}}, \tag{2.7}$$

so that

$$2 \frac{n_{^3He}}{n_D} \frac{Y_{DD}}{Y_{D^3He}} \sim \frac{\langle\sigma v\rangle_{DD}}{\langle\sigma v\rangle_{D^3He}}. \tag{2.8}$$

The quantity on the right hand side of equation 2.8 is a strong function of the ion temperature. Given known or measured quantities on the left-hand side, the mixture of D and ^3He and the measured yields, the ion temperature can be readily inferred. The DD/D^3He reactivity ratio as a function of ion temperature is shown in Figure 2.2.

Both of these ion temperature measurement techniques are used to characterize conditions in ICF implosions. The Doppler width of the fusion neutron spectra is used widely on OMEGA and NIF in cryogenic, ignition-relevant implosions.[9,10] In the thin-shell implosions discussed throughout this work, charged fusion-product spectra are used to measure the ion temperature averaged over one or more fusion burn regions. The yield-ratio method is also used, though predominantly for confirmation, since it is sensitive to two burn regions simultaneously and thus does not directly probe an easily identifiable region of the plasma.

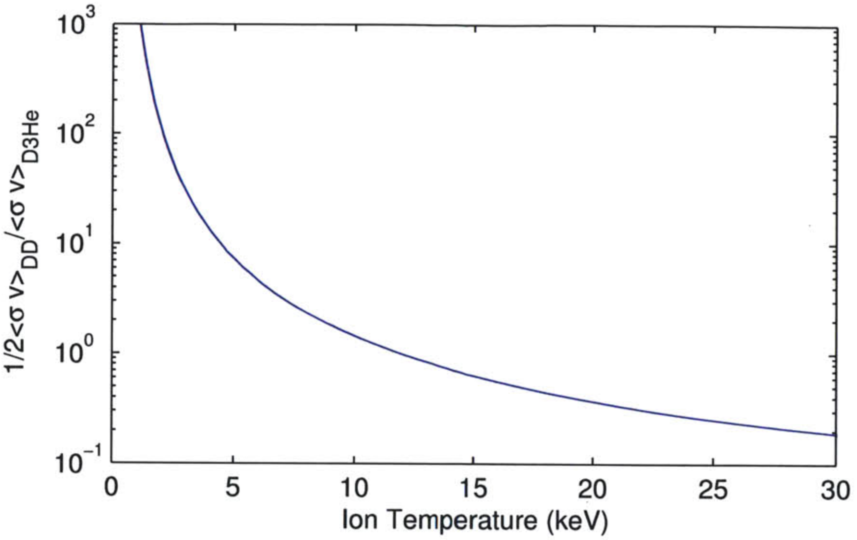

Figure 2.2. Reactivity ratio of DD and D^{3}He reactions for a 1:1 D:^{3}He fuel mixtur. Given a measured ratio of DD and D^{3}He yields, a yield-averaged ion temperature can be inferred.

2.1.2 Areal Density Measurements

As discussed in Chapter 1, the areal density (ρR) is a key parameter describing the degree of compression and the confinement of the fuel ions. The areal density around times of fusion production can be inferred from the spectra of both charged and neutral fusion products. Charged fusion products, such as the protons from DD and D^{3}He reactions and the alpha particles from DT reactions, lose energy as they collide with electrons in the fuel and the shell. That energy loss can be measured and directly correlated to the total areal density in the implosion. For a particle born at energy E_0, the resulting energy E_f is a function of the areal density (ρR) traversed as

$$E_f = E_0 - \int_0^{\rho R_{total}} \left[\frac{dE}{d\rho R}(E)\right] d\rho R, \tag{2.9}$$

where $\frac{dE}{d\rho R}$ is the stopping power of the plasma, describing the incremental loss in energy per incremental amount of ρR, and is itself a function of energy. As long as the stopping power is known approximately for the plasma conditions in the implosion – it depends weakly on the density and moderately on the electron temperature – a measurement of the average energy of the charged particles exiting the implosion in contrast to their birth energy is sufficient to infer the total ρR. An example of this measurement, using D^{3}He alphas on OMEGA exploding pusher shot 69069, is shown in Figure 2.3. A total ρR of ~3 mg/cm^2 is inferred based on the dowshift of the D^{3}He-α spectrum from a birth energy of 3.67 MeV to a final average energy of 2.95 MeV.

Neutrons, instead of being slowed gradually over many small-angle collisions which downshift the entire spectrum, undergo discrete large-angle scattering events which decrease the neutron energy and populate the spectrum with "downscattered" neutrons at energies significantly below the birth energy. The fraction of downscattered neutrons, expressed as a ratio of downscattered to unscattered neutrons comprising the primary peak, is proportional to the total ρR.[11]

The ρR of the fuel alone can be determined from the yield of secondary fusion products, which

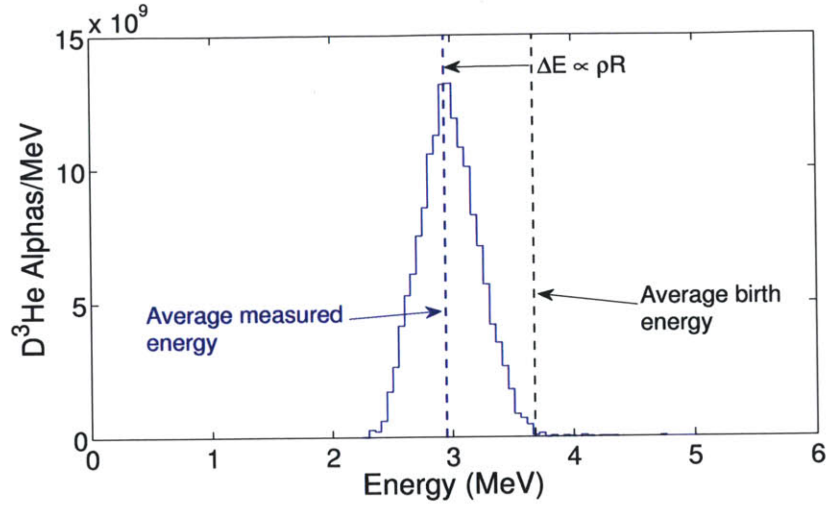

Figure 2.3. Measured primary D^3He-α spectrum obtained on OMEGA D^3He glass-shell implosion 69069. The downshift in the mean energy of the alpha spectrum, from a birth energy of 3.67 MeV to a measured energy of 2.95 MeV, is used to infer a total ρR of ~3 mg/cm^2.

are produced from the in-flight reaction of primary fusion products and ambient fuel ions.[12–14] This technique is frequently utilized in implosions with D_2 gas, which produce primary T (1.0 MeV) and ^{3}He (0.8 MeV) products as in equations 2.2 and 2.1. These fusion products lose energy as they traverse the fuel and have a finite probability of reacting with D ions, via the reactions

$$D + T(< 1.0 \text{ MeV}) \rightarrow \alpha(6.7\text{-}1.4 \text{ MeV}) + n\ (11.9\text{-}17.2 \text{ MeV}), \text{ and} \tag{2.10}$$

$$D + ^3He(< 0.8 \text{ MeV}) \rightarrow \alpha(6.6\text{-}1.7 \text{ MeV}) + p\ (12.6\text{-}17.5 \text{ MeV}). \tag{2.11}$$

For fuel ρR small enough that the secondary reactant is not ranged out in the fuel, the ratio of secondary to primary fusion yields is proportional to the fuel ρR.[12,13] When the fuel ρR is large enough, the production of secondary particles saturates as the ^{3}He or T ions are ranged out and no further secondary reactions occur with additional fuel ρR. When this happens, the ratio of secondary to primary yields is a function of the range of the ^{3}He or T ion in the plasma, which depends solely on the electron temperature. The linear regime, where the secondary to primary yield ratio is directly proportional to the fuel ρR, extends up to ~10 mg/cm^2 for secondary D^3He protons and up to ~100 mg/cm^2 for secondary DT neutrons for an electron temperature $T_e \lesssim 3$ keV, as in most implosions. Additionally, as with primary D^3He protons, the energy downshift in the secondary D^3He-proton spectrum can be used to infer the total ρR. Such a secondary D^3He-proton spectrum is shown in Figure 2.4. On NIF D_2-filled exploding pusher shot N110131, a fuel ρR of 4.6 mg/cm^2 is inferred from the ratio of secondary D^3He-p to primary DD-n yield, while a total ρR of 23 mg/cm^2 is inferred from the average energy downshift of the D^3He-p spectrum.

2.2 CR-39-Based and Other Nuclear Diagnostics

One of the most versatile methods for detecting fusion products is with the solid-state nuclear track detector CR-39,[15] which records information about charged-particle energies and also provides information about the location of nuclei incidet on the detector surface. CR-39 is used in a variety of

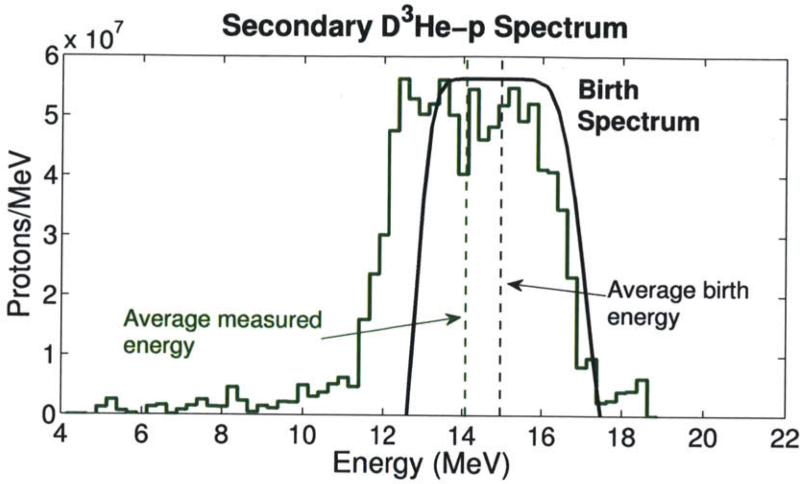

Figure 2.4. Measured secondary D^{3}He-proton spectrum obtained on NIF D_2 glass-shell implosion N110131. For this implosion with a fuel ρR <10 mg/cm^2 (it is ~4.6 mg/cm^2), the ratio of secondary proton yield (Y_{2p}) to primary neutron yield (Y_{1n}) is proportional to the fuel ρR. The downshift in energy from the birth spectrum is used to infer the total ρR ~23 mg/cm^2.

nuclear diagnostics, including charged-particle spectrometers. Other widely-used nuclear diagnostic techniques are also discussed.

2.2.1 Properties of CR-39

CR-39 is sensitive to charged particles, which deposit energy and leave a trail of damage in the form of broken molecular bonds along the ion path. When the CR-39 is exposed to a hot sodium hydroxide solution, the surface material is etched away. The bulk of the CR-39 etched at a bulk etch rate V_b, while the tracks with damage left by the energetic ions are etched away at a faster rate V_t, such that the damage trails produce conical pits. Before etching, damage trails are of order ~nm in diameter; after 6 hours of etching in 80° C 6N NaOH, protons, tritons, and alpha particle tracks are of order 3-25 μm, with the diameter proportional to the energy deposition rate into the CR-39 and inversely proportional to the energy of the incident particle.[16,17] The track formation process described above is illustrated in Figure 2.5.

After etching, the tracks are visible under standard optical microscopes at a magnification of 10-100x. Figure 2.6 shows tracks produced by 1.5-MeV protons which have been etched in 80° C 6N NaOH, standard etchant conditions, for 2 hours. Tracks left by charged particles are distinguished from intrinsic background – defects in the CR-39 that appear vaguely similar to real tracks – on the basis of the track diameter, darkness (typically referred to as "contrast"), and eccentricity. Intrinsic background signal is generally small in diameter and light in contrast. Longer etching permits greater differentiation between real charged-particle tracks, which become larger and darker, and intrinsic noise. As CR-39 reveals local tracks, rather than a bulk, integrated signal, it is also used to record positional information. This property makes CR-39 valuable in charged-particle spectroscopy (and, as discussed in Chapter 5, radiography).

Track appearance encodes information about the energy and identity of incident particles. For a particular piece of CR-39 at a given etch time, particles at higher charge and atomic mass, such as alpha particles, appear larger and usually darker than particles at lower charge and mass, such

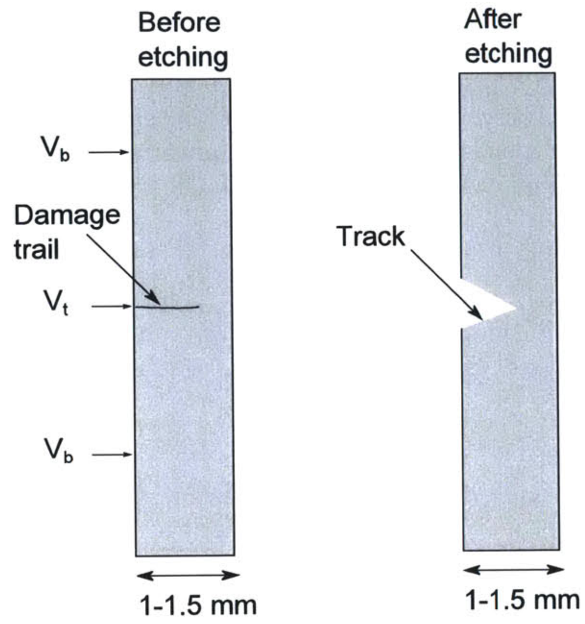
Before etching
After etching
V_b
Damage trail
V_t
V_b
Track
1-1.5 mm
1-1.5 mm

Figure 2.5. Track formation process in CR-39. A damage trail left by an energetic particle – typically protons, tritons, or alpha particles at 1-8 MeV – is etched out at a track etch rate V_t, while the bulk of the CR-39 is etched at a slower bulk etch rate V_b, resulting in a track microns in diameter. The diagram is egregiously not to scale.

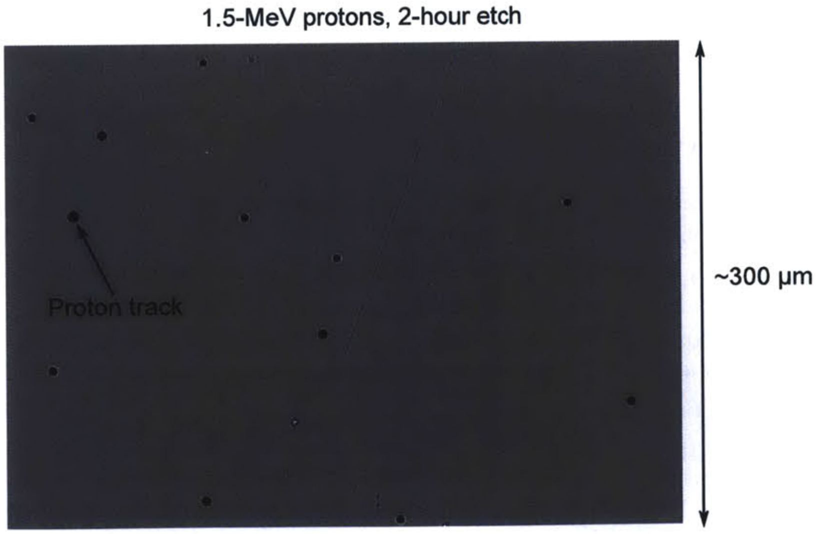
1.5-MeV protons, 2-hour etch
Proton track
~300 μm

Figure 2.6. Proton tracks in CR-39, viewed at 40x magnification. After 2 hours of etching in 80° C 6N NaOH, 1.5-MeV-proton tracks appear dark, highly circular, and with a diameter of ~5.3 μm.

as protons. For a given incident particle type, the track diameter – proportional to the energy deposition rate near the CR-39 surface – can be used to infer the energy of that particle when it struck the CR-39. For protons, the track diameter has a maximum slightly above the Bragg peak, around ~0.5 MeV, and falls off inversely at higher energies.[16,17] Figure 2.7 shows a sample curve of track diameter as a function of proton energy, using data originally published by Sinenian *et al.*[17] The ideal range for using track diameters to infer proton energies is 1.5-4 MeV, away from the Bragg peak and where the diameter vs. energy curve is smooth, but not too shallow, such that an uncertainty in the measured diameter corresponds to only a modest uncertainty in the inferred particle energy. Both the spatial sensitivity and energy sensitivity make CR-39 a powerful detection medium for charged-particle spectroscopy.

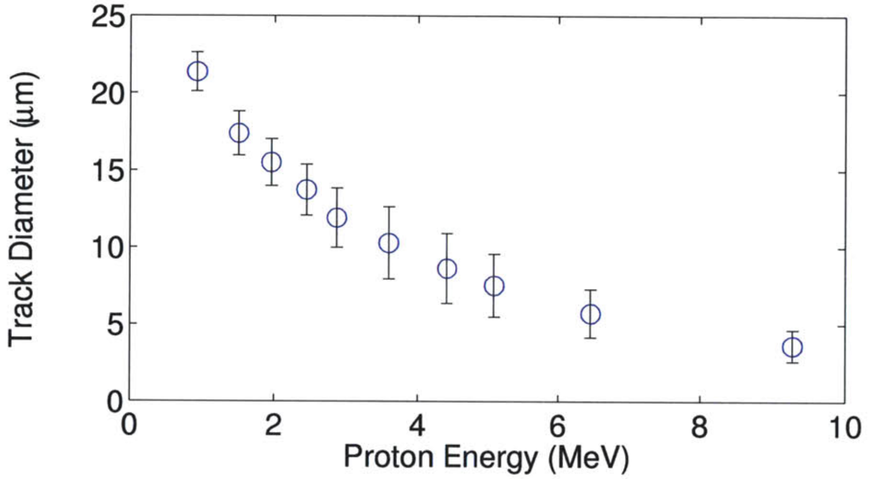

Figure 2.7. Track diameter as a function of proton energy after 6 hours of etching in an 80° C 6N NaOH solution. Error bars denote the standard deviation in measured track diameter over a batch of CR-39 and reflect piece-to-piece variation in the CR-39 response. This data was originally published by Sinenian *et al.*[17]

2.2.2 Magnet-Based Charged-Particle Spectrometers

Magnet-based charged-particle spectrometers leverage the spatial sensitivity afforded by CR-39 to infer energies of incident particles from positions of tracks on the detector.[1,6,16] Two such Charged Particle Spectrometers (CPS) are installed permanently on the OMEGA target chamber for measurements of charged fusion products and ablator ions at proton-equivalent energies of 0.1-30 MeV. A schematic of the CPS magnet and proton trajectories is illustrated in Figure 2.8. CR-39 detectors are placed at the focal plane to cover the specified range of charged-particle energies, and the position of tracks on CR-39 is used to reconstruct the spectrum of incident particles. CPS is used predominantly for measurements of D^3He protons and alphas, DD protons and tritons, DT alphas, ablator ions,[18] and "knock-on" protons produced by the recoil of DT neutrons with protons in the shell of CH implosions.[19] For example, the D^3He-alpha spectrum shown in Figure 2.3 was obtained using CPS 2.

CPS uses apertures of different widths to allow for operation at a wide range of nuclear yields, from as low as the 4π equivalent of $\sim 10^8$ fusion protons to as high as $\sim 10^{14}$ ablator ions. The smallest apertures have a spectral response width that is much narrower than the Doppler width

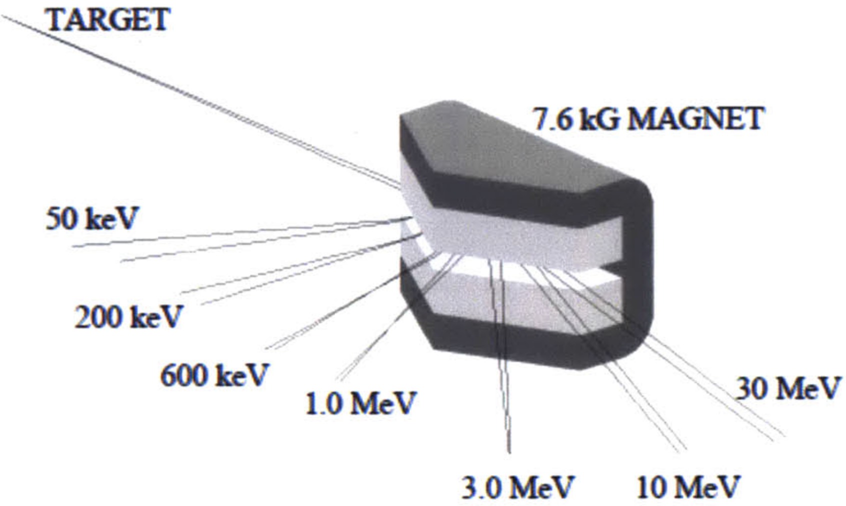

Figure 2.8. Magnet and proton trajectories for the Charged Particle Spectrometer (CPS) used on OMEGA. This diagram was originally presented by Hicks.[1]

of fusion-product spectra, and therefore introduce only small uncertainties to measurements of ion temperature from the spectral width. CPS provides simultaneous measurements of several different fusion-product spectra from which yield, ion temperature, and ρR can be inferred, reducing overall measurement uncertainty. This capability has also enabled detailed studies of capsule charging, based on the energy upshift experienced by four different charged fusion products,[6] and similarly makes possible the assessment of models of energetic ion stopping power in ICF-relevant plasmas.[20]

2.2.3 Wedge-Range-Filter Proton Spectrometers

Another instrument utilized for charged-particle spectroscopy is the Wedge Range Filter (WRF) proton spectrometer,[16,21] which measures proton spectra in the range 4-20 MeV. They are compact (~5 cm) and designed to be fielded at multiple locations around the OMEGA and NIF target chambers.[22] The WRF concept is illustrated in Figure 2.9. A wedge of aluminum or zirconia is placed in front of a piece of CR-39. Incident protons are ranged through different thicknesses of filter material, losing an amount of energy that is proportional to the filter thickness. The protons then leave tracks in the CR-39. Based on the diameter of the proton track (d) – which is determined by the proton energy when it struck the CR-39 (E_1) – and the position on the CR-39 (x), which tells how much filter material the proton passed through on its way to the detector ($t(x)$), the incident energy of the proton (E_0) is inferred. With thousands of protons incident on the detector, a spectrum can be reconstructed. Both the primary D^{3}He-proton spectrum in Figure 2.1 and the secondary D^{3}He-proton spectrum in Figure 2.4 were obtained using WRFs.

Like other charged-particle spectrometers, WRFs are used to measure total ρR, such as on NIF implosions filled with D^{3}He gas,[22] fuel ρR on OMEGA and NIF D$_2$-filled implosions,[14,23] and ion temperature on thin-shell implosions where the width of the D^{3}He-p line is dominated by thermal broadening.[24] As many of these spectrometers can be fielded at different locations during a single experiment, they allow for measurements of D^{3}He-proton energy anisotropy and, therefore, measurement of ρR asymmetries.[25,26] The uncertainty in WRF energy measurements is ~±150 keV, which roughly translates to a relative uncertainty in total ρR of ~±6 mg/cm^2 for a

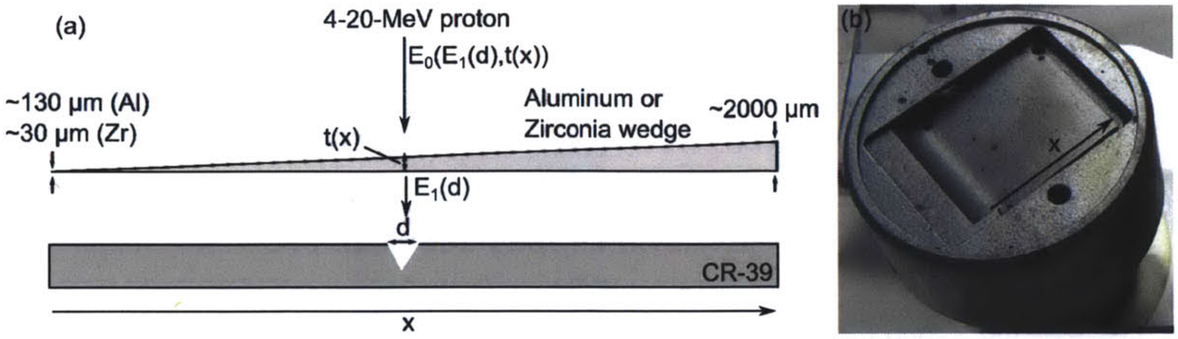

Figure 2.9. (a) Principle of the WRF proton spectrometer and (b) photograph of an Al WRF in use at the NIF. Protons incident on the detector pass through a filter thickness t, which is a known function of the resulting track position on the CR-39 x. The track diameter d is used to infer the energy E_1 of the proton after passing through the filter, upon striking the CR-39. The incident energy E_0, a function from the post-filter energy E_1 and ranging through material thickness t, is therefore inferred from the measured track diameter d and position x.

measurement based on the downshift of ~15-MeV protons. This uncertainty is small enough to resolve observed low-mode ρR asymmetries on NIF implosions.[22,26] The instrumental broadening for a 14.7-MeV proton line is ~150 keV for aluminum WRFs and ~250 keV for zirconia, which are smaller than the Doppler broadening of the D^{3}He-p line at an ion temperature of ~10 keV. Therefore, in high-temperature implosions with negligible other sources of broadening, WRFs offer a reliable means of measuring T_i from the Doppler width of the D^{3}He-p spectrum.

2.2.4 Other Nuclear Diagnostics of ICF Implosions

The diagnostics discussed so far have used charged-particle spectroscopy to measure nuclear yields, burn-averaged ion temperatures and areal densities. Below, some other diagnostic techniques and observables in ICF implosions are discussed, as well as their application toward understanding implosion physics.

Proton Core Imaging

The spatial profile of fusion product emission contains information about the ion density and ion temperature profiles at the time of peak fusion reactions. The proton core imaging system (PCIS)[27–29] utilizes either penumbral imaging, as illustrated in Figure 2.10, or mesh imaging to reconstruct the radial burn profile and produce 2D images of the surface brightness of proton emission. The system is typically used to detect DD and D^{3}He protons, though in theory any charged particle – including D^{3}He or DT alphas – could be used. In the penumbral imaging system, the emitted particles pass through an aperture with a diameter ~2 mm and onto a CR-39 detector, filtered appropriately to detect the given fusion product. The resulting image on the CR-39, an example of which using D^{3}He protons is shown on the right side of Figure 2.10, shows the projection of the circular aperture as a flat fluence of protons across the center, which falls off rapidly at the edge. The penumbra reflects the finite source size, as the derivative of the proton fluence is proportional to the profile of surface brightness. In experiments such as those described in Chapter 3 and Appendix A, PCIS measurements of DD and D^{3}He burn profiles offer a powerful constraint on models of ICF implosions.

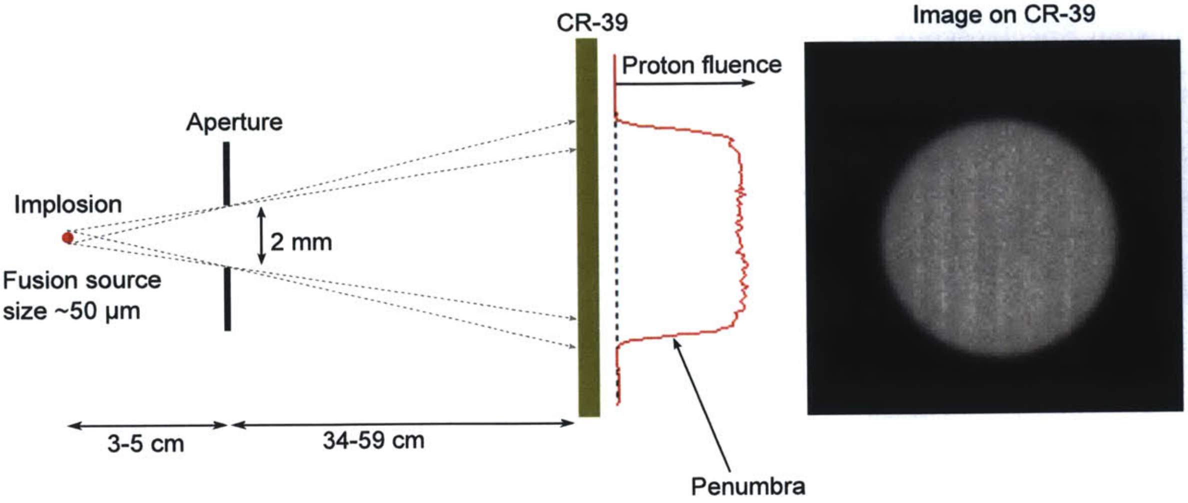

Figure 2.10. Conceptual illustration of penumbral imaging of the fusion burn profile, the basis for the proton core imaging system (PCIS). The projected image of a macroscopic aperture is produced by charged fusion products incident on CR-39. The finite source size creates a drop in proton fluence over a finite width at the edge of the image, and the derivative of the fluence is related to the projected profile of the surface brightness. Magnifications of 12-20 are typically used. A sample D^{3}He proton image (from OMEGA shot 69057) is shown on the right.

Burn History Measurements

In addition to the spatial burn profile, the temporal burn history is used to assess implosion dynamics, as the bang time – the time of peak fusion production – is sensitive to the implosion velocity and therefore to the energy coupling into the implosion. The neutron temporal diagnostic (NTD)[30,31] and proton temporal diagnostic (PTD)[32] are scintillator-based systems. Fusion neutrons or protons deposit energy in a scintillator, which emit light in a pulse whose response time is short relative to the duration of the particle impulse onto the detector. The resulting signal is then deconvolved to infer the reaction history in the implosion, which is processed to give the absolute bang time and a rough yield as well as the shape of the burn history curve. Absolute bang-time uncertainties are typically ~±50-75 ps. A modification to the PTD system (dualPTD) allows for simultaneous measurement of the DD-n and D^{3}He-p bang times on D^{3}He implosions, in which the relative bang-time differential will be measured to ±10 ps. These relative burn history measurements may be sensitive to species separation effects in mixed-fuel implosions.

The particle time-of-flight (pTOF) diagnostic, which is in regular operation on NIF[33] and has also been used on OMEGA, is a direct electronic detection system. Energetic nuclei deposit energy in a diamond substrate, which generates electron-hole pairs. An applied bias voltage across the diamond sweeps out charge and produces pulses of current. Though the rise time is too long to encode information about the shape of the burn history curve, pTOF records bang-times using a wide variety of particles, including DT neutrons, DD neutrons, and D^{3}He protons. An upgrade to pTOF (MagPTOF) will make the detector more robust to large x-ray fluxes experienced on NIF indirect-drive implosions. MagPTOF will uniquely be able to measure the shock bang-time using D^{3}He protons on NIF surrogate implosions.

Neutron Spectroscopy

Fusion neutrons produced in DT and DD reactions are also used to diagnose yield, ion temperature, and ρR in ICF implosions. As discussed in Section 2.1.1, the width of neutron spectra can be used to infer ion temperature. Unlike protons transiting the capsule which lose energy continuously over many collisions, neutrons undergo discrete scattering events which reduce the neutron energy and populate a region in the spectrum several MeV below the birth energy. The ratio of the number of these downscattered neutrons to the unscattered neutrons at the birth energy is related to the probability of scattering and is used to infer the total ρR. As discussed in Section 2.1.2, in D_2 implosions, the ratio of secondary DT-neutron yield to primary DD-neutron yield is a measure of the fuel ρR.[12,13]

One technique for neutron spectrometry is time-of-flight measurements. The neutron time-of-flight (nTOF)[34] diagnostics in place at OMEGA and NIF utilize similar principles as the pTOF to reconstruct the DD or DT neutron spectrum, rather than to infer a bang time. The magnetic recoil spectrometer (MRS)[35,11,36] is a magnet-based spectrometer that uses a CH or CD conversion foil to elastically scatter DT neutrons and produce recoil protons or deuterons, which are momentum analyzed by a permanent magnet. With a similar principle to CPS, the location of proton or deuteron tracks on CR-39 detectors are used to infer the recoil particle spectra and the incident neutron spectrum, to infer the neutron yield, burn-averaged T_i, and total ρR.

2.3 MIT Linear Electrostatic Ion Accelerator (LEIA) for Development of Nuclear Diagnostics

The MIT Linear Electrostatic Ion Accelerator (LEIA)[37] is a fusion-product source for development and calibration of nuclear diagnostics, including, primarily, CR-39-based instruments for measurements discussed above. Illustrated in Figure 2.11, LEIA consists of an RF oscillator which generates a deuterium or ^{3}He plasma, a probe power supply at several kV which drives ions out of the source, and an electrostatic potential ramp up to 150 kV, which accelerates ions into an erbium deuteride (ErD_2) target. Thus, the accelerator drives D ions at energies of 0-150 keV into deuterium ions in the target, producing typically $\sim 10^6$ DD reactions per second, providing DD protons, neutrons, tritons, and ^{3}He products to test nuclear diagnostics that will be used on ICF facilities. A ^{3}He beam can be used to embed ^{3}He ions in the target, such that when a D beam is incident on the target, up to $\sim 10^5$ D^{3}He reactions per second occur, generating D^{3}He protons and alphas. A surface barrier detector (SBD) measures the energy of individual fusion products and determines the absolute particle yield, which is essential in the characterization of CR-39 response and in the development and calibration of CR-39-based charged-particle diagnostics.

In particular, D^{3}He and DD protons have been used to assess the sensitivity of CR-39 in terms of the diameter of particle tracks, as a function of proton energy and etch conditions.[17] Experiments on LEIA have also studied the loss of sensitivity of CR-39 as a function of exposure to vacuum, as occurs in the usage of CR-39-based diagnostics on NIF.[38] Data obtained on LEIA have also been used in studies of enhancing the energy dynamic range of CR-39-based detectors[39] and in evaluating an analytical model of track overlap on CR-39.[40] LEIA has served as the calibration site for scores of WRF proton spectrometers that have been implemented on OMEGA and NIF,[16,21] and has also been used in the evalution and development of CR-39-based DD-neutron detectors.[41] As will be described in Sections 2.4 and 2.5, LEIA has been essential in the development of a new DD-proton spectrometer[42] and the assessment and mitigation of excessively high particle fluences[43] for CR-39-based diagnostics on ICF facilties.

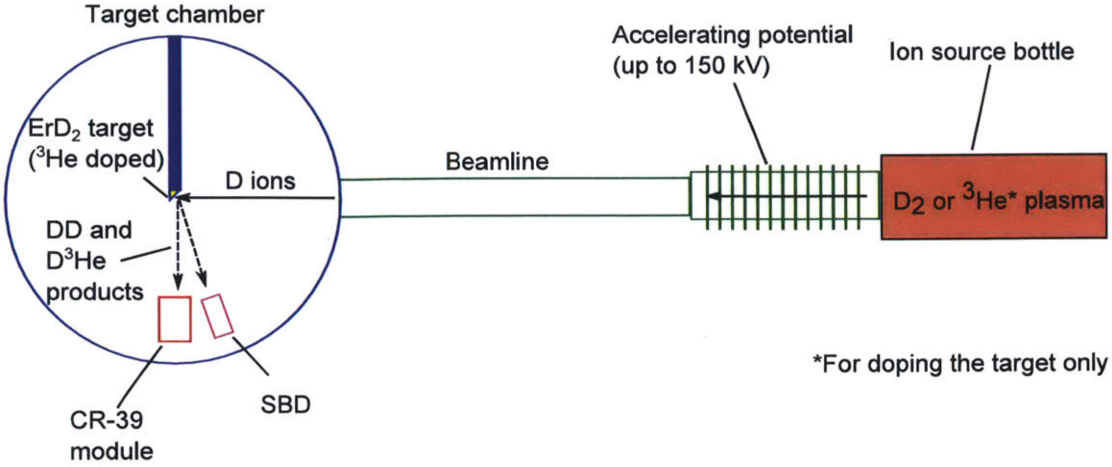

Figure 2.11. Cartoon schematic of MIT Linear Electrostatic Ion Accelerator (LEIA).[37] A beam of deuterium (D) ions is extracted from the ion source bottle and accelerated through a potential of up to 150 kV. The ions slam into the ErD_2 target, doped with ^{3}He, producing DD and D^3He reactions. The resulting charged fusion products are detected by a CR-39-based detector and a surface barrier detector (SBD).

2.4 A Compact Proton Spectrometer for DD Yield and ρR Measurements in Thin-Shell Inertial-Confinement-Fusion Implosions

In order to increase the versatility of low-energy proton spectrometers, a compact, step range filter (SRF) proton spectrometer has been developed for measurement of the DD yield and ρR in thin-shell inertial confinement fusion implosions filled with D_2 or D^3He gas. Using a series of stepped tantalum range filters, this spectrometer is sensitive to protons in the range 1-9 MeV, and the signal behind each filter can be used to reconstruct a Gaussian spectrum, with the mean energy and linewidth generally well constrained for proton spectra around ~1-3 MeV. This spectrometer has been developed using the LEIA fusion-product source and applied to experiments on the OMEGA laser facility and the National Ignition Facility (NIF). Modeling of the proton slowing in the filters is necessary to reconstruct the spectrum, and uncertainties of ±10% in yield and ±120 keV in proton energy (~±4 mg/cm^2 in ρR based on the energy downshift of DD protons) are estimated for typical conditions. This DD-proton detector can be used for *in situ* calibration of DD-neutron yield diagnostics on NIF. The work described in this section has been submitted to *Review of Scientific Instruments.*[42]

2.4.1 Introduction

As described above, charged-particle spectroscopy is a powerful diagnostic tool in inertial confinement fusion (ICF) research for assessing implosion conditions, such as the fusion yield (Y), areal density (ρR), and ion temperature (T_i).[44,5,13,45] Several diagnostic techniques have been used, including magnet-based spectrometers[44,1,46] and ranging filters,[16] with detection substrates consisting of image plates[47] and the solid-state nuclear track detector CR-39.[16]

Though the existing suite of charged-particle spectrometers is able to detect protons over a wide range of energies, from ~0.1 to ~30 MeV, and at a variety of incident particle fluences,[43] there are limitations to their usage that render them unavailable for certain applications. In particular, the charged particle spectrometers (CPS)[1,16] operated on the OMEGA laser facility[48] are at fixed port positions and effectively limited to proton yields above 10^8. The wedge range filter (WRF) proton spectrometers[16,21] are compact and portable, and can be fielded at multiple positions simultaneously around the OMEGA or NIF[49] target chamber, but their energy range for proton detection is limited to 4-20 MeV. The operating parameters of existing proton spectrometers on OMEGA and NIF, in comparison to the step range filter (SRF) presented in this work, are summarized in Table 2.1.

Table 2.1. Operating parameters under typical conditions for the charged particle spectrometers (CPS),[1,16] wedge range filter (WRF) proton spectrometers,[16,21] and the new step range filter (SRF) proton spectrometer. CPS has a wide energy range, but is limited to two fixed positions on OMEGA. The WRFs are portable, but are limited to proton energies above 4 MeV. The SRF combines the portability of the WRF with a lower energy range. It should be noted that though the current SRF is limited to proton spectral measurements in the range of ~1-3 MeV, it is capable of detecting protons up to ~9 MeV.

Spectrometer	Facility	Location (max. #)	Energy Range	Yield Range
Charged-Particle Spectrometer (CPS)	OMEGA	Fixed (2)	0.1-30 MeV	$\sim10^8$-10^{13}
Wedge Range Filter (WRF)	OMEGA	Portable (~10)	4-20 MeV	$\sim10^6$-10^{11}
	NIF	Portable (~8)	4-20 MeV	$\sim10^7$-10^{12}
Step Range Filter (SRF)	OMEGA	Portable (~10)	1-3 MeV	$\sim10^6$-10^{11}
	NIF	Portable (~8)	1-3 MeV	$\sim10^7$-10^{12}

The SRF combines the ease-of-use advantages of the WRFs with the ability to measure proton spectra at energies as low as 1 MeV. Using steps of thin tantalum foils in front of a piece of CR-39, protons in the range of 1-9 MeV can be detected. For low-energy (~1-3 MeV) protons produced via the DD reaction,

$$\mathrm{D} + \mathrm{D} \rightarrow \mathrm{T}(1.01\ \mathrm{MeV}) + \mathrm{p}(3.02\ \mathrm{MeV}), \tag{2.12}$$

the SRF can be used to measure the energy downshift of the proton spectrum, from which the total ρR is inferred. This detector is intended to diagnose thin-shell, deuterium-filled (D_2 or D^3He) implosions with a ρR less than 30 mg/cm^2, at which point the protons are ranged out. In addition to having utility in physics studies of shock-driven implosions,[23] these proton detectors can be used for an *in situ* calibration of DD-neutron detectors on OMEGA or NIF,[50] using a technique described by Waugh *et al.*[51]

2.4.2 Design and Analysis Principles

The SRF detector, designed to fit into a WRF spectrometer casing, consists of a thick aluminum frame (background plate), to which are adhered steps of thin tantalum filters, followed by a piece of CR-39. Photographs of a sample SRF setup and a cartoon front view of the foils, as seen from an implosion, are shown in Figure 2.12. Two separate designs have been implemented to make spectral measurements at slightly different energy ranges: a thicker set of foils, with quadrants covered by nominally 10, 14, 19, and 23 μm of tantalum, and a thinner set of foils, with quadrants covered by nominally 5, 10, 15, and 20 μm of tantalum. These particular filters were chosen to optimize measurement of DD protons in the energy range ~1-3 MeV. The SRF is conceptually similar to the wedge range filter (WRF) proton spectrometers,[16,21,22] which use a continuous ramp, rather than discrete steps of different thicknesses. In each design, the aluminum background plate is 3180 μm thick to fully stop protons up to 25 MeV and to provide a region for characterization of intrinsic background in the CR-39.[1]

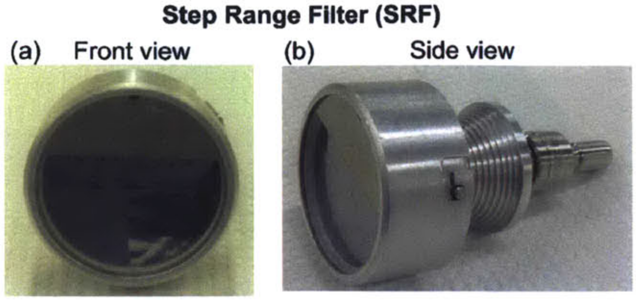

Figure 2.12. (a) Front and (b) side view of a representative step range filter (SRF) setup. Two different configurations, the (c) thick and (d) thin SRF, have been developed. The thickness of the different tantanlum filters is indicated. The aluminum background plate, 3180 μm thick, covers the upper ~1/3 of the module and provides a background region on the CR-39 behind the filter stack.

(c) Thick SRF filters (d) Thin SRF filters

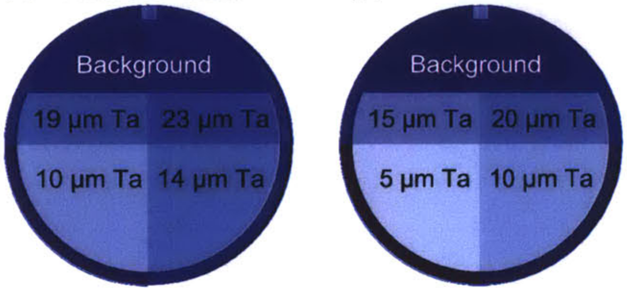

The proton signal measured behind the four step filters is used to infer the total proton yield and to construct a spectrum based on modeling of the energy ranging through each Ta foil. Consider an example using the thick detector package, with an incident Gaussian proton spectrum at a peak energy of E_0 = 2.5 MeV and a spectral width of σ = 0.25 MeV, representative of a downshifted DD-proton spectrum. Figure 2.13 shows this incident spectrum (black) and the resulting spectra (red) after ranging through the different Ta filters. The SRIM stopping power tables[52] were used for these calculations, as well as a zeroth order treatment of energy straggling, which further broadens the spectrum. 100% of the protons pass through the 10-μm Ta foil above the ~100 keV detection cutoff.[16] 99% are detected by the CR-39 behind the 14-μm-thick foil. The 19-μm foil permits 57% of the protons to be detected, while the 23-μm foil permits only 7% of the protons. The number of protons detected per cm^2 behind each filter, S_{10}, S_{14}, S_{19}, and S_{23}, are used to constrain the three parameters describing a Gaussian spectrum – the total yield Y, mean energy E_0, and the spectral width σ. Thus, in contrast to the WRF, which uses information about the number and diameter of proton tracks behind a filter with a continuous range of thicknesses, the SRF infers properties of the proton spectrum simply from the number of proton tracks behind discrete filters of different thicknesses. This analysis principle using four filters applies for any 3-parameter model spectrum, though for simplicity, the interpretation and discussion of the SRF results herein assume a Gaussian spectrum. For DD-protons around ~1-3 MeV, affected by a small energy downshift, the assumption of a Gaussian spectrum is usually valid.

2.4.3 Step Range Filter Data

The SRF proton spectrometer has been tested on the Linear Electrostatic Ion Accelerator (LEIA)[37] and used to diagnose thin-shell D_2 and D^3He-filled implosions at OMEGA and the NIF.

---

[1] Intrinsic background in the CR-39 consists of small defects which can appear to have similar characteristics as real proton tracks and must be discriminated away or subtracted out from the measured signal.

Figure 2.13. Simulated proton spectra behind 10 μm, 14 μm, 19 μm, and 23 μm Ta filters (red curves). The black curve represents the incident proton spectrum, with an average energy of 2.5 MeV and a Gaussian σ of 0.25 MeV. The CR-39 detection cutoff energy is 0.1 MeV.

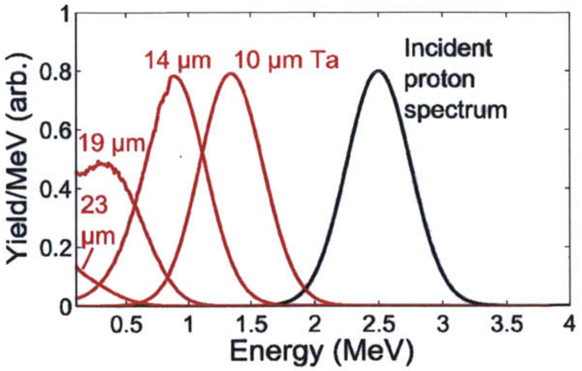

Demonstration of the SRF Principle Using LEIA

Figure 2.14. Diagram of experimental setup on the Linear Electrostatic Ion Accelerator (LEIA). A deuteron beam incident on a ErD_2 target generates DD protons, which are detected by both a surface barrier detector (SBD) and the SRF. Aluminum filters are used sometimes to range down DD protons to lower energies, as discussed in the text.

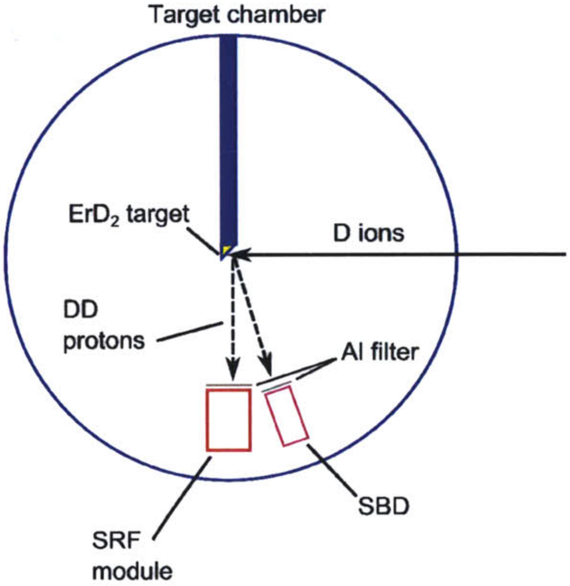

Initial testing of the SRF was conducted on LEIA, as depicted schematically in Figure 2.14.[37] LEIA generates a beam of deuterons at energies up to 150 keV, which impinges on an ErD_2 target. The resulting DD fusion reactions (Equation 2.12) produce a spectrum of protons around 3.0 MeV, which are detected by the SRF and by a surface barrier detector (SBD) that records the energy and number of individual particles. Having an independent measurement of the DD-p energy[2] and yield allows for careful verification and uncertainty assessment of the SRF measurements.

Experiments on LEIA demonstrate the sensitivity of the SRF to proton spectra of different average energies. Figure 2.15 shows the resulting signal based on the proton fluence transmitted through each filter for a variety of incident proton spectra, ranging from $E_0 = 3.04$ MeV to $E_0 = 1.80$ MeV. The lower proton energies, measured by the SBD, are achieved by placing an additional filter in front of the SRF to range down DD protons that are born at 3.04 MeV.

At $E_0 = 3.04$ MeV (no additional filtering), nearly all protons pass through each filter and are detected on the CR-39. Only 5% fewer protons are detected behind the 19-μm and 23-μm filters than behind the 10-μm and 14-μm filters, though this measured loss of protons is only slightly outside of measurement uncertainty. Protons at the low-energy tail of the spectrum are ranged out in the thicker filters.

---

[2] The SBD is energy-calibrated using α particles produced by the decay of ^{226}Ra. The proton energy incident on the SRF is detremined by the SBD on separate LEIA experiments, with the SBD placed in the SRF position, and filtered with the appropriate additional filtering.

At $E_0 = 2.13$ MeV (~40 additional μm Al filtering), all protons are ranged out by the 23-μm filter, while 98% of protons are ranged out in the 19-μm filter. The 14-μm filter permits 98% of the protons, within measurement uncertainty of 100%, while the 10-μm filter transmits 100% of the protons.

At $E_0 = 1.92$ MeV (~45 μm additional Al filtering), no protons are detected behind the 23-μm or 19-μm filters, 88% of protons are detected behind the 14-μm filter, and 100% of the protons are detected behind the 10-μm filter.

The data using 1.80-MeV protons (~50 additional μm Al filtering) further illustrates the effects of ranging, as only 71% of protons are detected behind the 14-μm filter and 100% of the protons are detected behind the 10-μm filter. For these fairly narrow spectra, σ~0.10-0.13 MeV as measured by the SBD, the ranging out of part of the proton spectrum is observed behind only a single filter at a time. As at most one filter transmits a non-zero, non-unity fraction of the protons, the relative signal behind each filter is a sensitive measurement of the average energy of the proton spectrum.

These data have been analyzed using the SRF analysis technique (inferring the incident proton spectra based on the measured signal ratios) to compare to the known, SBD-measured spectral parameters. By contrasting the SBD spectral measurements to the SRF data, it is possible to estimate the uncertainties in the SRF-determined incident proton energy. A summary of the SRF-inferred spectral quantities and measured proton signals, and actual, SBD-measured spectral quantities, is presented in Table 2.2. Given an incident proton mean energy and spectral width, a model of proton ranging[52] through each of the SRF filters produces modeled proton spectra and modeled proton signal behind each filter. The model used to analyze the LEIA data includes spectral dispersion and a zeroth order treatment of energy straggling.

Table 2.2. Measured SRF ratios of proton signal behind each of the four filters and the SRF-inferred average energy and spectral width based on modeling of spectral ranging through the different filters in LEIA experiments. The SBD-measured average energy and spectral width are shown for comparison. The difference between the SBD and SRF energy measurement helps identify uncertainties in the SRF analysis. Uncertainty in the SRF-inferred E_0 and σ represents degeneracy between those two quantities, as the two fitting parameters need to match only one proton signal ratio (the others being either 0 or ~1 and, therefore, not highly sensitive to the incident proton energy). The overall difference between the SBD-measured E_0 and the SRF-inferred E_0 characterizes uncertainty in the SRF measurement, which is ~100 keV. The uncertainty estimates are discussed in more detail in Section 2.4.4.

SRF Measured Proton Signal Ratios			SRF E_0	SRF σ	SBD E_0	SBD σ
S_{14}/S_{10}	S_{19}/S_{10}	S_{23}/S_{10}	(MeV)	(MeV)	(MeV)	(MeV)
0.99	0.95	0.94	3.10±0.05	0.10±0.03	3.04	0.10
0.98	0.02	0	2.13±0.03	0.11±0.02	2.13	0.11
0.88	0	0	2.04±0.04	0.12±0.03	1.92	0.12
0.71	0	0	1.97±0.03	0.13±0.05	1.80	0.13

The SRF data taken on LEIA show that the analysis captures the incident proton energy as measured by the SBD to within 150 keV, and to within 50 keV at energies of 2-3 MeV. It is shown in Section 2.4.4 that this ~100 keV error in the SRF energy measurement is roughly consistent with the energy uncertainty determined from uncertainty inherent in the modeling. Some of the uncertainty in the SRF-inferred energy based on the signal ratios stems from the degeneracy between E_0 and σ

when matching one signal ratio. For example, in the 1.92 MeV experiment, it is only necessary to match one relative signal ratio (S_{14}/S_{10}) with two incident spectral parameters (E_0 and σ). The ranging model is able to produce $S_{14}/S_{10} = 0.88$ for several combinations of (E_0,σ) centered around (2.04, 0.12) MeV, within ±0.04 MeV for both E_0 and σ. This degeneracy issue is illustrated in Figure 2.16. It is a particular concern for inferring narrow spectra, as discussed further in Section 2.4.4.

Additionally, it is inferred from the spectral modeling that in these experiments, all protons are detected behind the 10-μm Ta filter, which means that the yield of the incident protons is simply that inferred behind the 10-μm Ta filter. Even though only one ratio is used and there is some degeneracy between E_0 and σ, the range of possible solutions is constrained by the fact that none of them allow for any fraction of the spectrum to be ranged out in the 10-μm Ta filter. For broader spectra, often observed at OMEGA and, especially, in NIF implosions, there can be multiple filters that allow through a non-zero, non-unity fraction of protons. Under these conditions, the inferred proton energy and linewidth are simultaneously constrained by multiple signal ratios. For a sufficiently low incident proton mean energy or sufficiently broad incident spectrum, a fraction of the proton spectrum may be ranged out even in the thinnest (e.g. 10-μm) Ta filter and modeling is necessary to infer the incident proton yield.

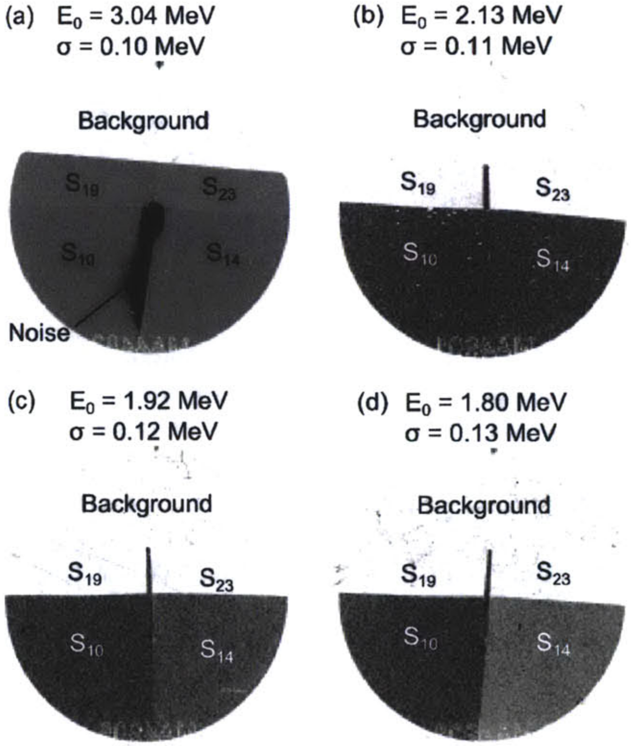

Figure 2.15. SRF DD-proton signal obtained on LEIA for incident mean proton energies of (a) 3.04 MeV, (b) 2.13 MeV, (c) 1.92 MeV, (d) 1.80 MeV, as determined by the SBD. Darker signifies a greater proton fluence. As the proton energy decreases, the relative signal between each window changes: S_{14}/S_{10} decreases as a larger fraction of the protons is ranged out in the 14-μm Ta filter. The relative signal ratios are presented in Table 2.2.

Use on OMEGA and NIF Implosions

The SRF was also used to diagnose thin-glass-shell exploding pusher ICF implosions at OMEGA and the NIF. Three experiments at OMEGA used ~850-μm diameter, ~2.3-μm-thick SiO_2 shells filled with ~15 atm D^3He gas, imploded by 13.8-15.8 kJ laser energy in a ~0.6 ns laser pulse. These implosions generated 2-3×10^{10} DD protons with an average energy of 3.1 MeV, which were detected by the "thin" SRF configuration at a distance of 175 cm from the implosion. At this

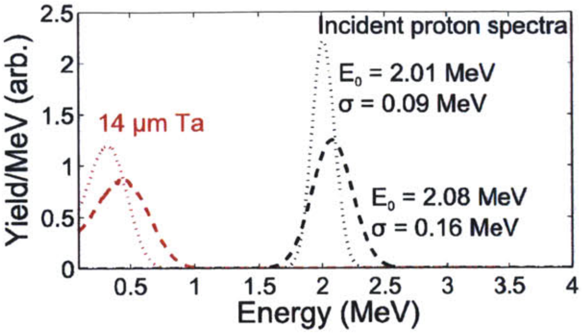

Figure 2.16. Simulated proton spectra incident on the SRF (black) and transmitted through the 14 μm Ta filter (red). For both a higher-energy, broader spectrum (dashed, $E_0 = 2.08$ MeV, $\sigma = 0.16$ MeV) and a lower-energy, narrower spectrum (dotted, $E_0 = 2.01$ MeV, $\sigma = 0.09$ MeV), 88% of the protons are transmitted through the 14 μm Ta filter. Thus, there is a degeneracy in inferring both E_0 and σ from one relative signal ratio (S_{14}/S_{10}).

position, the fluence was 5-8×10^4 protons per cm^2 at the SRF spectrometer. On these implosions, and in general, 14.7-MeV D^3He protons were not detected by the SRF, as they pass through the CR-39 at an energy above the upper limit for proton detection.

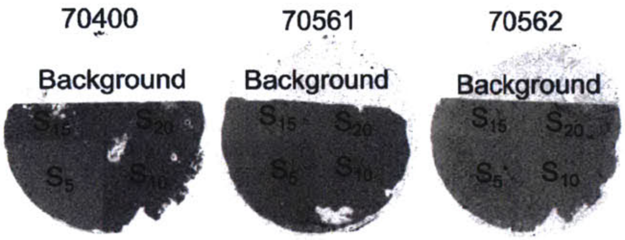

Figure 2.17. DD-proton signal measured using the "thin" SRF (5, 10, 15, 20-μm Ta filters) on three D^3He-filled thin-glass-shell implosions on OMEGA (shots 70400, 70561, 70562). Dark signifies a greater proton fluence. In each experiment, the proton spectrum exiting the implosion has a mean energy ~3.1 MeV, energetic enough that the entire spectrum is transmitted through each filter. The 5-μm Ta filter also transmits D^3He-α particles, which on shot 70400 produced significant track overlap[40] and loss of ~20% of the proton signal.

Table 2.3. SRF- and CPS-measured DD-proton yield, mean energy, and spectral width for three D^3He thin-glass-shell implosions at OMEGA (Ω). The SRF-inferred E_0 and σ are bounds, based on a combination of energy and spectral width at which at least 95% of the proton spectrum is transmitted through the 20-μm Ta filter. Though the energy lower bound is fairly rigid, if the proton spectrum had a significantly higher energy, it could also permit a wider upper-limit on the spectral width.

Ω	SRF Measured Proton Yields				SRF E_0	SRF σ	CPS Yield	CPS E_0	CPS σ
Shot	Y_5	Y_{10}	Y_{15}	Y_{20}	(MeV)	(MeV)		(MeV)	(MeV)
70400	2.05×10^{10}	2.55×10^{10}	2.45×10^{10}	2.52×10^{10}	>2.84	<0.15	2.71×10^{10}	3.18	0.14
70561	2.74×10^{10}	3.01×10^{10}	2.61×10^{10}	2.89×10^{10}	>2.84	<0.15	3.06×10^{10}	3.10	0.13
70562	1.91×10^{10}	1.82×10^{10}	1.77×10^{10}	1.84×10^{10}	>2.84	<0.15	2.73×10^{10}	3.14	0.13

DD-proton signal images obtained on three implosions on OMEGA, shots 70400, 70561, and 70562, are shown in Figure 2.17. All three images show a near-uniform proton signal behind the four different filters, which were made of 5 μm, 10 μm, 15 μm, and 20 μm thick Ta. On shot 70400, the signal behind the 5-μm Ta filter shows a reduced proton signal as a result of track overlap,[40] between D^3He-α and the DD protons. On the two subsequent shots, 70561 and 70562, the data were processed in such a fashion that track overlap behind the 5-μm Ta filter was insignificant. On all three shots, ablator ions[18,53] were at a sufficiently low energy to not interfere with the proton measurements, as will be discussed further in Section 2.4.4. The fact that a nearly identical fluence was observed behind each filter suggests that no significant part of the proton spectrum was ranged out in any of the filters. The incident proton mean energy and spectral width can therefore be constrained to those solutions that permit 100% of protons through the 20-μm Ta filter. Furthermore, the determination of the proton yield is straightforward, and can be computed directly based on the measured proton signal behind any of the filters. For example, on shot 70400, the proton fluence behind the 10-μm Ta filter fluence was $S_{10} = 6.63\times10^4/\text{cm}^2$. With the detector at a distance of 175 cm from the implosion, the proton yield inferred behind the 10-μm Ta filter is therefore $Y_{10} = S_{10}[4\pi(175)^2] = 2.55 \times 10^{10}$, which is in reasonable agreement with a separate DD-proton yield measurement of 2.71×10^{10} (see Table 2.3).

The inferred proton yields, mean proton energy, and linewidth are summarized in Table 2.3. The results are compared to measurements obtained on the same shots using the charged-particle spectrometers (CPS).[1,16] The CPS measurements are averages from two different spectrometers, CPS1 and CPS2, and as shown in Table 2.3, the SRF-determined mean energy and linewidth agree with the CPS measurements. Differences in observed yield between different lines of sight may be due to electric and/or magnetic fields around the implosion that produce spatial anisotropies in charged fusion product fluence.[6] The CPS-measured DD-proton spectrum on shot O70561 was used as the incident spectrum on the SRF, and the spectrum behind each filter is shown in Figure 2.18. For the incident mean proton energy of E_0 = 3.10 MeV and spectral width σ = 0.13 MeV, none of the protons are ranged out by any of the filters, as concluded from the SRF data.

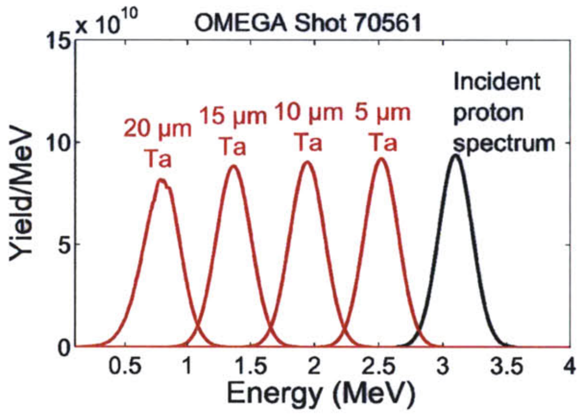

Figure 2.18. CPS-measured DD-proton spectrum from OMEGA shot 70561, transmitted through each of the four filters of the "thin" SRF. The incident spectrum has a mean proton energy of E_0 = 3.10 MeV, with a spectral width of σ = 0.13 MeV. The resulting proton spectra (red) ranged through the 5 μm, 10 μm, 15 μm, and 20 μm Ta (thick SRF filters) are shown. 100% of the protons are transmitted through every filter, as demonstrated in the SRF measurement.

Table 2.4. SRF-measured proton yields through each of the 10-μm, 14-μm, 19-μm, and 23-μm Ta filters, and ratios of proton signal behind each of the four windows, on NIF shot N130129. The average values are used to infer the incident DD-proton yield, mean energy, and spectral width (see Figure 2.20).

Detector	SRF Measured Proton Yields				SRF Signal Ratios					
Position	Y_{10}	Y_{14}	Y_{19}	Y_{23}	S_{14}/S_{10}	S_{19}/S_{10}	S_{23}/S_{10}			
Position 1	1.78×10^{11}	1.22×10^{11}	2.42×10^{10}	2.85×10^{9}	0.69	0.14	0.016	SRF Inferred		
Position 2	2.02×10^{11}	1.49×10^{11}	2.52×10^{10}	2.34×10^{9}	0.74	0.13	0.012	Yield	E_0	σ
Position 4	2.17×10^{11}	1.53×10^{11}	2.98×10^{10}	3.18×10^{9}	0.71	0.14	0.015		(MeV)	(MeV)
Average	1.99×10^{11}	1.41×10^{11}	2.64×10^{10}	2.79×10^{9}	0.71	0.13	0.014	2.07×10^{11}	2.05	0.34

The "thick" SRF configuration was used to measure the DD-proton spectrum from a D_2-filled, thin-glass-shell implosion at the NIF. The experiment (shot N130129) used a 4.6-μm-thick, 1533-μm diameter SiO_2 capsule filled with 10 atm D_2 gas, which was driven by 51 kJ laser energy in a ~1.4 ns pulse in the polar-direct-drive[54,55] configuration.[3] A DD(-neutron) yield of 2.5×10^{11} was measured by neutron time-of-flight (nTOF) detectors[34,56] and indium activation.[50] As this implosion had a total areal density of ~18 mg/cm^2, as inferred from the downshift of secondary proton spectra measured by WRF spectrometers,[13,16] the DD protons escaped the implosion and were detected by the SRF.

---

[3] This exploding pusher experiment on NIF, and several others, will be discussed in Chapter 3 in the context of exploring ion kinetic effects using shock-driven ICF implosions.

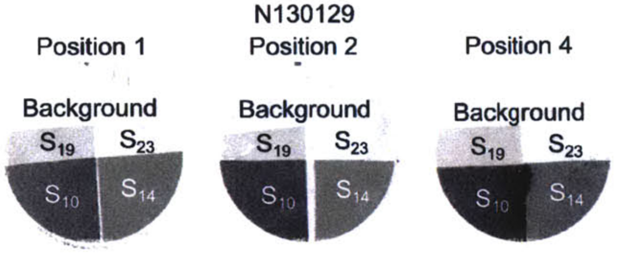

Figure 2.19. DD-proton signal obtained at three different detector positions using the "thick" SRF (10, 14, 19, 23-μm Ta filters) on NIF direct-drive D_2-filled thin-glass shell shot N130129. Dark signifies a greater proton fluence. A similar absolute fluence level and ratio of proton signals is observed at each detector. The gradation in fluence across the different windows, with a finite fraction of the proton spectrum permitted behind multiple windows, indicates a fairly broad proton spectrum.

Three "thick" SRFs were fielded in close proximity to each other at a distance of 375 cm from the implosion; the proton fluence images are shown in Figure 2.19 and the raw proton yield measurements behind each filter and signal ratios are summarized in Table 2.4. Each SRF shows a gradually decreasing fluence of protons with increasing filter thickness. On average, the ratio of proton signal behind the 14-μm filter to that behind the 10-μm filter is $S_{14}/S_{10} = 0.71$, while $S_{19}/S_{10} = 0.13$ and $S_{23}/S_{10} = 0.014$. This reduction in fluence across the different filters, in contrast to sharp cutoffs in fluence demonstrated in tests at the LEIA accelerator, indicates a fairly broad DD-proton spectrum. Analysis of this data and the determination of the total proton yield, incident mean energy, and spectral width are summarized at the bottom of Table 2.4, with the resulting spectra shown in Figure 2.20.

Because three spectral parameters (total yield, mean energy, and spectral width) are fit by four measured quantities, the inferred spectrum is constrained. Based on the relative signal ratios of $S_{14}/S_{10} = 0.71$, $S_{19}/S_{10} = 0.13$ and $S_{23}/S_{10} = 0.014$, a mean incident proton energy of $E_0 = 2.05$ MeV and a spectral width of $\sigma = 0.34$ MeV are inferred. The resulting simulated signal ratios of $S_{14}/S_{10} = 0.71$, $S_{19}/S_{10} = 0.13$ and $S_{23}/S_{10} = 0.008$ are in good agreement with the measured values, to within uncertainties in proton signal measurement and spectral modeling. The mean proton energy in particular is well-constrained, as deviations in energy up to only 0.04 MeV are permitted before an additional deviation of 10% in the relative proton signal is produced, larger than the measured yield uncertainty. Based on the proton energy downshift in the implosion, to 2.05 MeV, from the birth DD-proton energy of 3.02 MeV, a total ρR of 13$\pm$3 mg/cm^2 is inferred, in agreement with the measured total ρR from the downshift of secondary D^3He protons, 18$\pm$5 mg/cm^2. Thus, the SRF proton spectrometer can be used as a ρR diagnostic on implosions with deuterium fuel and sufficiently low ρR (<30 mg/cm^2).

2.4.4 Discussion of Applicability and Uncertainties

Experiments at the accelerator-based DD-p source (LEIA) and at OMEGA and the NIF demonstrate the utility of the SRF for determination of the DD proton spectrum in the energy range of ~1-3 MeV. These data also help identify uncertainties in the inference of proton yield, the mean proton energy, and the Gaussian spectral width.

Yield Uncertainty

The uncertainty in the SRF-measured proton yield is largely dictated by the degree to which spectral modeling is required to infer the incident proton yield. For incident spectra where the thinnest filter comfortably transmits the entire spectrum, the yield uncertainty is limited by counting statistics

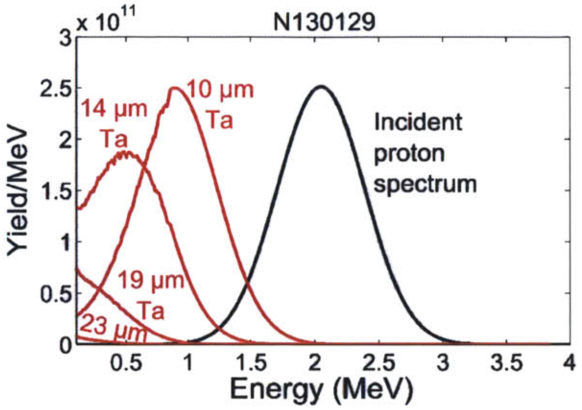

Figure 2.20. SRF-inferred DD-proton spectrum from NIF shot N130129, transmitted through each of the four filters of the "thick" SRF. The incident spectrum has a mean proton energy of $E_0 = 2.05$ MeV, with a spectral width of $\sigma = 0.34$ MeV. The resulting proton spectra (red) ranged through each of 10 μm, 14 μm, 19 μm, and 23 μm Ta (thick SRF filters), above the CR-39 detection cutoff energy of 0.1 MeV, are shown. A decreasing fraction of the proton spectrum is transmitted through the increasingly thick filters.

in the CR-39 (typically $\sim\pm1\%$ for protons at a fluence of $10^4/\mathrm{cm}^2$ over the $\sim$cm^2 area covered by each window) and by uncertainties inherent in analysis of proton tracks in CR-39, typically ~3-5%.[4] This condition – conservatively, greater than 99.9% of the proton spectrum transmitted through the 10-μm Ta filter for the "thick" SRF – is satisfied when, for example, E_0>1.81 MeV for σ<0.12 MeV or when E_0>2.35 MeV for σ<0.34 MeV (spectral widths chosen to span those observed on LEIA, OMEGA, and NIF). These conditions are illustrated in part in Figure 2.21, which shows the simulated proton transmission (or signal) through the different filters of the "thick" SRF. For the "thin" SRF, >99.9% of the proton spectrum is transmitted through the 5-μm filter when, e.g., E_0>1.23 MeV for σ<0.12 MeV or when E_0>1.90 MeV for σ<0.34 MeV. These energy ranges for 100% proton transmission through the thinnest filters are consistent with the analysis of SRF data from the LEIA and OMEGA experiments.

The N130129 data is an example of a spectrum where modeling is required to infer the incident proton yield, as a fraction of the spectrum was ranged out even in the thinnest (10-μm Ta) filter. In that case, uncertainty in the modeling itself contributes to the overall yield uncertainty. The objective of the modeling is to determine what fraction of the proton spectrum is detected and, thus, to correct for the fraction of protons that is ranged out. With a perfect understanding of the ranging process through the filters, this uncertainty would be negligible. However, uncertainty in the filter thickness[5] contributes to the uncertainty in the modeled ratio of yield through the 10-μm filter to the actual yield (Y_{10}/Y_{actual}). The actual yield is inferred based on the measured Y_{10} and the modeling-inferred Y_{actual}/Y_{10} ratio, which is constrained by the measured signal ratios S_{14}/S_{10}, S_{19}/S_{10}, and S_{23}/S_{10}. In the case of N130129, adding 1 μm to the thickness of the 10-μm filter only slightly changes the relative signal ratios (S_{14}/S_{10} from 0.71 to 0.74, versus measured 0.71; S_{19}/S_{10} from 0.13 to 0.13, versus measured 0.13; S_{23}/S_{10} from 0.008 to 0.008, versus measured 0.014), while Y_{10}/Y_{actual} decreases from 0.97 to 0.93. Similarly, removing 1 μm from the thickness of the 10-μm filter only slightly changes the relative signal ratios (S_{14}/S_{10} from 0.71 to 0.70, versus measured 0.71; S_{19}/S_{10} from 0.13 to 0.13, versus measured 0.13; S_{23}/S_{10} from 0.008 to 0.008, versus measured 0.014), while Y_{10}/Y_{actual} increases from 0.97 to 0.99. Therefore, this change to the modeling based on the bounds of measurement uncertainty of the filter thickness causes a barely-perceptible shift in the modeled signal ratios, but produces a ±4% change in the inferred yield. The uncertainty in the inferred yield resulting from uncertainties in the modeling must be addressed on a case-by-case basis, but should be no greater than of order ±5-10%. This uncertainty is added in quadrature to

---

[4] Particle fluence anisotropies can also contribute an additional uncertainty to the overall measured yield uncertainty, but these can be minimized in an appropriately-designed implosion where the protons are emitted $\gtrsim$ns after the end of the laser pulse.[51]

[5] The thickness of each SRF filter is measured individually, with a conservative uncertainty of ±1 μm.

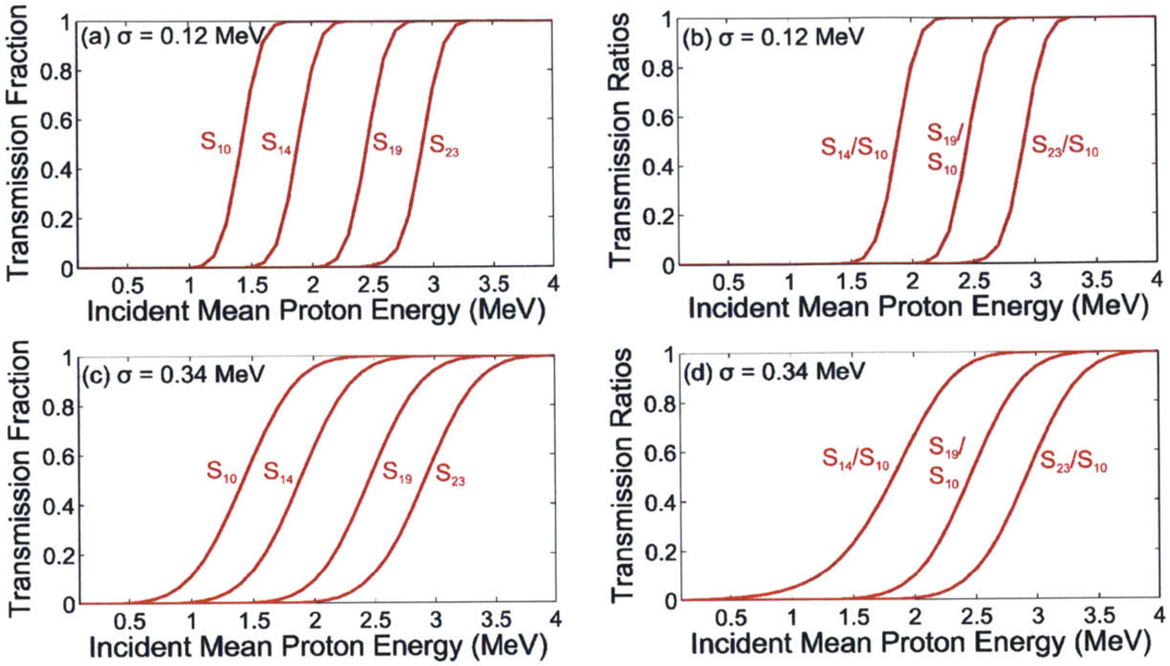

Figure 2.21. (a),(c) Fraction of protons transmitted through thick SRF filters (10 μm, 14 μm, 19 μm, and 23 μm Ta) and (b),(d) ratio of protons transmitted through the filters as a function of incident mean proton energy, for $\sigma = 0.12$ MeV (top) and $\sigma = 0.34$ MeV (bottom). A decreasing fraction of the proton spectrum is transmitted through the increasingly thick filters.

the uncertainties in proton track counting as discussed above.

Energy Uncertainty

The ability to infer a mean proton energy likewise depends on the proton energy relative to the proton range in the different filters. When all protons are transmitted through the different filters (and the relative signal ratios are all 1), only a lower limit on the mean proton energy can be established, as was the case in the OMEGA data. A conservative upper limit on the energy range at which the mean energy can be determined is set by the energy at which a detectable loss of transmission can be observed through the thickest filter in the SRF, either 23 μm Ta for the current "thick" version or 20 μm Ta for the "thin" version. For purposes of this study, a detectable loss of transmission is considered to be below 97% of the protons transmitted (allowing for 3% uncertainty in the measured signal behind each filter). For the thick SRF, 97% transmission through 23 μm Ta is achieved when, e.g., $E_0 = 3.18$ MeV for $\sigma<0.12$ MeV (Figure 2.21a) or when $E_0 = 3.57$ MeV for $\sigma<0.34$ MeV (Figure 2.21c). The LEIA data shown in Figure 2.15a, at a mean energy of $E_0 = 3.04$ MeV, is an example that is coming close to the limit below which a mean energy can be precisely inferred. For energies above these values, it is impossible to determine the exact mean energy. For the thin SRF, 97% transmission through 20 μm Ta is achieved when, e.g., $E_0 = 2.82$ MeV for $\sigma<0.12$ MeV or when $E_0 = 3.23$ MeV for $\sigma<0.34$ MeV. The OMEGA data shown in Figure 2.17 are all above this energy limit and, thus, the most information that can be inferred is that the mean energy is >2.84 MeV (for $\sigma \lesssim 0.15$ MeV). The use of thicker filters can extend the range of energies at which an accurate energy measurement can be made (beyond simply establishing a lower limit). For those spectra where only one filter transmits less than 100% of the proton spectrum, there is a degeneracy in inferring two spectral quantities (mean energy and spectral width) from only one relative signal ratio. Under these conditions, the inferred mean energy can be constrained by reasonable bounds on the spectral width (if known) or by the energy at which the second thickest filter begins to range out a detectable fraction of the spectrum.

The mean proton energy measurement is well-constrained when one or more filters transmits a fraction of the proton spectrum. As shown in Figure 2.21a,c, this condition is satisfied when the incident mean energy is ~1-3 MeV. This is evident in the LEIA data shown in Figure 2.15b-d, where incident proton energy differences of 100-200 keV cause differences in the relative signal ratios (S_{14}/S_{10} in particular) of 10-20%, considerably larger than the uncertainty in proton track counting on the CR-39. This sensitivity is also illustrated by the slopes of the relative transmission (or signal) ratio curves in Figure 2.21b,d. Thus, the random uncertainty in the analysis (inferring E_0 based on the relative signal ratio) based on the ±3-5% random uncertainty in the proton signal measurement is ~±50 keV. Allowing for up to a ±1 μm filter thickness uncertainty, the corresponding random uncertainty in the E_0 inferred from the modeling is ~±110 keV. The total energy uncertainty is around ±120 keV,[6] of order the difference between the SBD-measured and SRF-inferred energy values as shown in Table 2.2. This energy uncertainty is equivalent to an uncertainty of ~±4 mg/cm^2 in a total ρR measurement based on the energy downshift of the DD-proton spectrum.

Linewidth Uncertainty

To simultaneously constrain both the mean proton energy and spectral width, it is necessary to have multiple windows where a measurable fraction of the incident proton spectrum has been ranged out. When the proton energy is too high and only the thickest filter transmits a fraction of the proton spectrum, there is a degeneracy between the mean energy and spectral width, as alluded to above. Under those circumstances, the relative signal ratio is much more sensitive to the mean energy than to the spectral width, resulting in a well-constrained mean energy, while the spectral width is poorly constrained. Thus, a spectral width measurement is only possible for the "thick" SRF when E_0<2.71 MeV (based on <97% of protons transmitted through the 19-μm Ta filter for σ = 0.12 MeV, see Figure 2.21a) or for the "thin" SRF when E_0<2.24 MeV (based on <97% of protons transmitted through the 15-μm Ta filter for σ = 0.12 MeV). The spectral width is most accurately inferred when the spectrum is broad enough (typically for σ>0.12 MeV) that there is significant overlap in energy space between the spectra ranged through different filters. This can also be understood as there being more than one window with a non-zero, non-unity fraction of the spectrum. If only one window at a time (and not the thickest filter) shows a non-zero, non-unity signal relative to the other windows, the spectral width can be constrained to $\sigma \lesssim 0.12$ MeV for the present designs with ~4-5-μm Ta filtering differences between windows. This narrow-spectrum condition was present in the LEIA data presented in Section 2.4.3. A different SRF design with more filters and less incremental filtering between windows could potentially be used to measure the linewidth of narrower spectra. A summary of the proton mean energy and spectral width bounds for SRF measurements of the proton yield, mean energy, and spectral width, for different values of the mean energy and spectral width, is presented in Table 2.5.

When the proton spectrum is broad enough and sufficiently low in energy that signal behind multiple filters is a fraction of the number of incident protons (for example, in the N130129 data), the uncertainty in the inferred spectral width is based on the uncertainty in the relative signal ratios used to infer σ. As an illustrative example, the data from N130129 ($S_{14}/S_{10} = 0.71$, S_{19}/S_{10}

---

[6] This energy uncertainty is roughly comparable to that of the WRF proton spectrometer used at a higher energy range,[16,21,22] 4-20 MeV, in contrast to the ~1-3 MeV range for energy measurement using the present SRF spectrometer.

Table 2.5. Summary of proton mean energy and spectral width bounds for SRF measurement of the proton yield, mean energy E_0, and spectral width σ. These are based on the "thick" SRF, with filters consisting of 10 μm, 14 μm, 19 μm, and 23 μm Ta. The energy ranges for the "thin" SRF are slightly lower, as discussed in the text.

Observable	E_0 range (σ limit)	Comments on analysis
Yield	$1.81<E_0<9$ MeV ($\sigma<0.12$ MeV)	No modeling required
Yield	$1<E_0<1.81$ MeV ($\sigma>0.12$ MeV)	Inferred from modeling
Yield	$2.35<E_0<9$ MeV ($\sigma<0.34$ MeV)	No modeling required
Yield	$1<E_0<2.35$ MeV ($\sigma>0.34$ MeV)	Inferred from modeling
Mean Energy (E_0)	$2.71<E_0<3.18$ MeV ($\sigma<0.12$ MeV)	Measurement possible; E_0/σ degeneracy
Mean Energy (E_0)	$1<E_0<2.71$ MeV ($\sigma>0.12$ MeV)	Measurement well constrained
Mean Energy (E_0)	$3.10<E_0<3.57$ MeV ($\sigma<0.34$ MeV)	Measurement possible; E_0/σ degeneracy
Mean Energy (E_0)	$1<E_0<3.10$ MeV ($\sigma>0.34$ MeV)	Measurement well constrained
Spectral Width (σ)	$1<E_0<2.71$ MeV ($\sigma>0.12$ MeV)	Measurement well constrained
Spectral Width (σ)	$1<E_0<3.10$ MeV ($\sigma>0.34$ MeV)	Measurement well constrained

$= 0.13$, $S_{23}/S_{10} = 0.014$) is analyzed to infer $E_0 = 2.05$ MeV and $\sigma = 0.34$ MeV, with modeled signal ratios of $S_{14}/S_{10} = 0.71$, $S_{19}/S_{10} = 0.13$, $S_{23}/S_{10} = 0.008$ (Section 2.4.3). If the modeled σ were changed to 0.37 MeV, the modeled signal ratios become $S_{14}/S_{10} = 0.70$, $S_{19}/S_{10} = 0.15$, $S_{23}/S_{10} = 0.014$. Conversely, for $\sigma = 0.31$ MeV, the modeled signal ratios become $S_{14}/S_{10} = 0.72$, $S_{19}/S_{10} = 0.11$, $S_{23}/S_{10} = 0.005$. Thus, a 0.03 MeV difference on top of $\sigma = 0.34$ MeV corresponds to a ~15% departure for S_{19}/S_{10} and a ~50% difference in S_{23}/S_{10}. These differences are well outside of the uncertainty of the raw proton signal measurement. Therefore, a reasonable, conservative estimate of the uncertainty in the spectral width under such conditions is ~±50 keV. The approximate uncertainty in σ based on this kind of analysis is shown in Figure 2.22. The uncertainty in σ is inferred as the variation in the modeled σ that produces a ±0.03 change in any of the modeled signal ratios (S_{14}/S_{10}, S_{19}/S_{10}, and S_{23}/S_{10}). This analysis represents the maximum difference in σ that produces a non-observable (within measured signal uncertainties) change in the signal ratios. Typical uncertainty in σ over the energy range of interest is ~±20-60 keV. Uncertainty in the filter thickness primarily translates to an uncertainty in the mean energy and does not substantially contribute to uncertainty in the inferred spectral width.

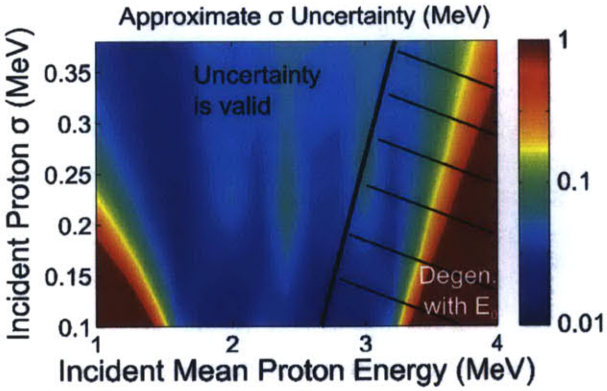

Figure 2.22. Approximate uncertainty in the inferred σ using the thick SRF as a function of incident proton mean energy and σ. This uncertainty calculation is based on the variation in the modeled σ that produces a maximum variation of ±0.03 in any of the modeled proton signal ratios (S_{14}/S_{10}, S_{19}/S_{10}, and S_{23}/S_{10}). To the right of the thick black line, there is a degeneracy between the inferred E_0 and σ, so that the linewidth cannot be uniquely inferred.

Comments on Energy Range: Ablator Ions and CR-39 Upper Energy Limit for Proton Detection

It has been established that the SRF operates effectively as a spectrometer for proton spectra in the range ~1-3 MeV. This energy range is limited on the low end by the presence of "ablator" protons, which are accelerated to energies up to ~1 MeV by electric fields in the corona of ICF implosions for a variety of shell materials.[18,53] The yield of these ablator protons is much higher than the fusion-generated proton yields, and thus ablator ions overwhelm the DD-proton signal if not properly filtered. Based on the OMEGA (NIF) data using the thin (thick) SRF, it is determined that for the laser drive conditions in those experiments, with an intensity of $\sim 10^{15}$ ($\sim 5\times 10^{14}$) W/cm^2, the ablator protons were at low enough energies, <0.8 MeV (<1.3 MeV), to be ranged out in the 5-μm (10-μm) Ta filter and, therefore, did not impact the detection of DD protons. If the SRF filtering were made thinner in an attempt to detect lower-energy protons, the ablator protons may be able to pass through the filters and wash out the fusion proton signal.

The energy upper-limit for SRF operation is dictated primarily by the thickest filtering. As CR-39 can detect protons at 100% efficiency up to ~8 MeV, the upper energy limit for simply detecting protons is the maximum incident energy of a proton such that, when ranged through the thickest SRF filter, it emerges on the CR-39 at an energy no greater than ~8 MeV. For the current SRF configurations, with thickest filters of 20 μm and 23 μm Ta, that energy upper limit for detecting protons and measuring a proton yield is ~9 MeV. As discussed above, this energy limit is not the same as that for spectroscopy, which relies on a differential in proton signal between different windows; for the current configurations, the upper limit for measuring the mean proton energy is ~3 MeV. In principle, both of these energy upper-limits can be increased by the use of additional or thicker filters.

2.4.5 Conclusions and Applications

A compact step range filter (SRF) proton spectrometer has been designed and implemented at OMEGA and the NIF for a yield, mean energy, and spectral width determination for the DD-proton spectrum in the energy range ~1-3 MeV. Unlike other low-energy proton spectrometers used on ICF facilities, the SRF is highly portable and can be fielded at multiple positions around the implosion inside the target chamber. This instrument is a lower-energy analogue of the well-established WRF proton spectrometer, which operates in the energy range of 4-20 MeV. The SRF has been tested on LEIA and in implosions at OMEGA and the NIF. These experiments have demonstrated the sensitivity of the detector response to the mean proton energy and width of the incident spectrum. For a proton spectrum with a mean energy $E_0<3$ MeV, a typical uncertainty in the mean energy is $\sim\pm 0.12$ MeV. For a sufficiently broad spectrum ($\sigma>0.12$ MeV) at a mean energy <2.7 MeV, the spectral width can be estimated with an uncertainty of $\sim\pm 50$ keV.

The SRF was designed for diagnosis of thin-glass-shell ICF implosions (<30 mg/cm^2) with deuterium in the fuel (either D_2 or D^3He gas), which produce DD protons at a birth energy of ~3.02 MeV. Measurements of the DD fusion yield and spectral width provide information about the ion temperature in the implosion, while the energy downshift is proportional to the areal density (up to a ρR of ~30 mg/cm^2, at which point the DD protons are ranged out). This technique can be extended to higher energy ranges through the use of thicker filtering. The SRF could be of great value at the NIF for an *in situ* calibration of DD-neutron detectors.[56,50,51] With an appropriate change in filtering, the SRF can also be applied to the detection of D^3He- or DT-α particles in the energy range of 1-4 MeV. On D^3He-filled implosions, a second piece of CR-39 placed behind the first and filtered appropriately can be used to simultaneously detect D^3He protons. The SRF can also be adapted for measurement of the ^{3}He^{3}He-proton spectrum in fundamental nuclear science experiments.

2.5 Empirical Assessment of the Detection Efficiency of CR-39 at High Proton Fluence and a Compact, Proton Detector for High-Fluence Applications

A general concern for detecting nuclear products using CR-39 centers around the ability to detect individual particle tracks, which becomes difficult when the spatial density of those tracks is high. The CR-39 solid-state nuclear track detectors widely used in physics and in many inertial confinement fusion (ICF) experiments have 100% detection efficiency for ~0.5-8 MeV protons under most conditions. However, when the fluence of incident particles becomes too great, overlap of particle tracks leads to under-counting at typical processing conditions (5h etch in 6N NaOH at 80° C). Short etch times required to avoid overlap can cause under-counting as well, as tracks are not fully developed. Experiments have determined the minimum etch times for 100% detection of 1.7-4.3-MeV protons and established that for 2.4-MeV protons, relevant for detection of DD protons, the maximum fluence that can be detected using normal processing techniques is $\lesssim 3\times10^6$ cm^{-2}. A CR-39-based proton detector has been developed to mitigate issues related to high particle fluences on ICF facilities. Using a pinhole and scattering foil several mm in front of the CR-39, proton fluences at the CR-39 are reduced by more than a factor of ~50, increasing the operating yield upper limit by a comparable amount. The work described in this section has been published in *Review of Scientific Instruments.*[43]

2.5.1 Introduction

CR-39 solid-state nuclear track detectors are used in a variety of applications to detect charged particles based on damage trails left by incident particles depositing energy in the material.[15] In ICF research, CR-39-based diagnostics measure the fusion yield, ion temperature, areal density, and burn profile in imploding capsules,[6,5,16,35,29] as well as electric and magnetic fields in laser-driven high-energy-density physics experiments.[57–59]

Under normal conditions, tracks are counted individually with 100% detection efficiency with very little systematic error. However, when particle fluences become too high, tracks can overlap in such a way that detection software cannot distinguish them, and tracks are either not counted or are under-counted (when multiple tracks are recorded as zero or one track).[40] This situation can arise especially on high-yield applications such as exploding-pusher implosions for diagnostic calibration at the NIF[49] or the OMEGA laser facility[48] where detector positions are fixed.

Previous studies of the usage of CR-39 detectors in high-fluence applications have focused on details of track formation[60] and models of track overlap probability,[60,61,40] as well as the optical properties of CR-39 in the highly saturated regime.[62]

This work seeks to determine empirically the minimum etch time required for all tracks to become visible, to assess the fluence upper limit for 100% detection on CR-39 specifically for protons, and to establish a technique for extending the yield upper limit of operation of CR-39-based measurements by reducing the fluence at the CR-39 surface. Though this work specifically discusses proton detection, it can be extended to other energetic charged particles, including deuterons, tritons, and alpha particles. This study focuses on the protons produced in DD and D^{3}He reactions:

$$\mathrm{D}+\mathrm{D}\rightarrow \mathrm{T}(1.01\ \mathrm{MeV})+\mathrm{p}(3.02\ \mathrm{MeV}),\ \text{and} \tag{2.13}$$

$$D + {}^3\text{He} \rightarrow {}^4\text{He}(3.6\text{ MeV}) + \text{p}(14.7\text{ MeV}). \tag{2.14}$$

These reactions are used to characterize the yield, ion temperature, and ρR in certain classes of ICF implosions.

2.5.2 High-Fluence Proton Detection Using CR-39

As previously discussed, charged particles incident on the CR-39 leave trails of damage in the form of broken molecular bonds as energy is deposited along their trajectories. Etching the CR-39 in a 6N solution of sodium hydroxide (NaOH) at 80° C reveals the damage trails such that their diameters are of order microns and they are visible using standard microscope equipment with a typical magnification of 40x. Individual tracks are identified and recorded for use in charged-particle diagnostics. Protons of energy ∼0.5-8 MeV are detectable with a 100% efficiency under normal fluence circumstances.[16] The diameter of proton tracks has been determined empirically to be inversely correlated with the incident proton energy above ∼0.5 MeV,[7] such that lower-energy protons leave larger tracks.[16,17] When the particle fluence is high enough that tracks begin to overlap, they are not all counted, introducing errors into measurements that rely on the absolute number or diameter of particle tracks. Figure 2.23 illustrates proton tracks after 5-6 hours of etching under a 40x magnification. At a moderate fluence of 5×10^3 cm^{-2} (6 hours of etching), tracks are well-separated and are counted individually with insignificant overlap. At a high fluence of 2.4×10^5 cm^{-2} (5 hours of etching), many of the tracks (red) are overlapping and are not recorded by the track detection software. Algorithms to correctly detect and identifying multiple overlapping tracks have yet to be developed.

Figure 2.23. Microscope images of proton tracks at (a) a moderate fluence of 5×10^3 cm^{-2}, after a 6-hour etch, and (b) a high fluence of 2.4×10^5 cm^{-2}, after a 5-hour etch. At a high fluence and long etch time, track overlap causes undercounting of proton tracks and an erroneously low yield measurement. The yellow tracks are counted as single tracks, but the red tracks are ignored.

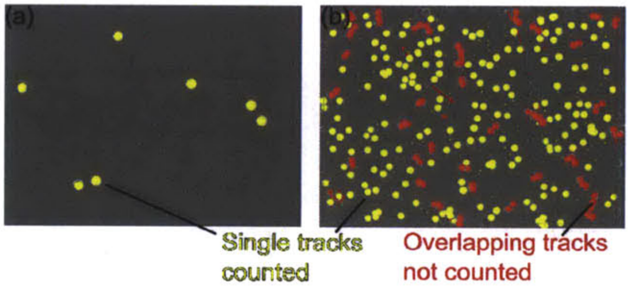

Experiments to assess the CR-39 detection efficiency under high-fluence conditions have been performed on LEIA,[37] as well as at OMEGA and the NIF. High fluence experiments have been conducted using aluminum-filtered CR-39 with DD and D^{3}He protons at a uniform track diameter and on wedge-filtered CR-39 with a continuum of D^{3}He-proton track diameters. As track overlap depends on the diameter of the proton tracks as well as their fluence, protons of different energies experience different degrees of overlap (lower-energy protons leave larger tracks are are more susceptible to overlap) and, consequently, have different fluence upper limits.

Flat-Filtered CR-39

Figure 2.24 illustrates the under-counting problem of protons of different energies as a function of etch time in high fluence conditions. On an exploding pusher experiment on OMEGA, shot 62409, a thin glass shell filled with D^{3}He gas was imploded with 30 kJ of laser energy in a 1-ns pulse; DD and D^{3}He protons were detected by CR-39 filtered by flat pieces of aluminum. With detectors at 175 cm away from the target, the 7.6$\times 10^{10}$ DD protons and 1.4$\times 10^{11}$ D^{3}He protons were measured at a fluence of 2.0$\times 10^5$ cm^{-2} and 3.7$\times 10^5$ cm^{-2}, respectively. DD protons (Figure 2.24a) were ranged through either 25 μm or 50 μm of Al, ending up at 2.7 or 2.0 MeV. D^{3}He protons were ranged through either 200 μm or 175 μm of Al, as well as ~1500 μm of CR-39, ending up at 3.8 or 4.3 MeV.

---

[7] The curve of proton track diameter as a function of incident proton energy has a similar shape to the curve of proton stopping power in CR-39, dE/dx as a function of proton energy E, though the empirically-observed peak in the "diameter versus energy" curve occurs around ∼0.5 MeV, while the Bragg-peak energy for proton stopping in CR-39 is around ∼0.1 MeV.[16,52]

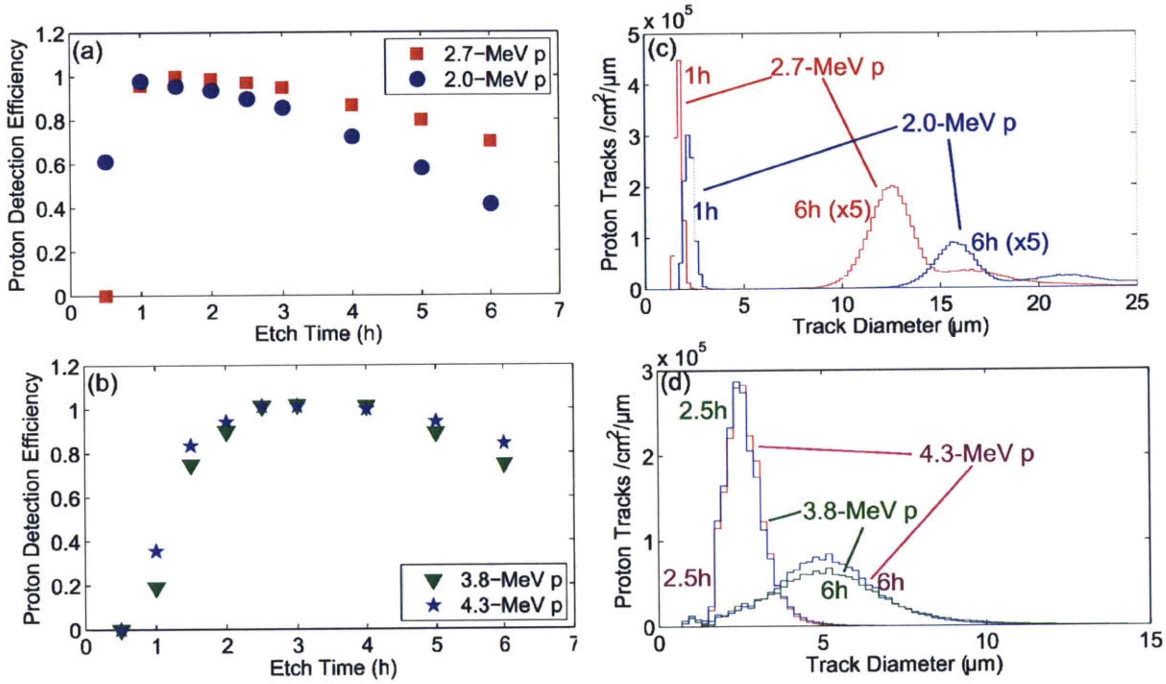

Figure 2.24. Detection efficiency for (a) 2.0- and 2.7-MeV protons at a fluence of 2.0$\times 10^5$ cm^{-2} and (b) 3.8- and 4.3-MeV protons at a fluence of 3.7$\times 10^5$ cm^{-2}. These data illustrate the under-counting of protons at short etch times, before all tracks are visible using the 40x magnification, and at long etch times, as track overlap prevents the counting of all proton tracks. The corresponding diameter histograms for (c) 2.0- and 2.7-MeV protons and (d) 3.8- and 4.3-MeV protons illustrate the growth and increasing overlap of tracks at long etch times. The long high-diameter tails for the 2.0- and 2.7-MeV-proton tracks in (c) are a consequence of multiple overlapping tracks being interpreted as one large track.

At short etch times, not all of the DD-proton tracks were visible, such that after a 0.5h etch, only 61% of the larger, 2.0-MeV-proton tracks and virtually none of the smaller 2.7-MeV-proton tracks were visible (Figure 2.24a). By a 1-hour etch, the inferred yield reached a maximum, as 100% of the tracks are being counted and track overlap is not yet significant. As the etch time is increased further, the inferred yield begins to drop – more rapidly for the larger, 2.0-MeV-proton tracks – as tracks begin to overlap and are not counted. By a 6-hour etch, only 42% of the 2.0-MeV-proton tracks and 70% of the 2.7-MeV-proton tracks are correctly counted. These results are reflected also in the diameter histograms (Figure 2.24c), as the 2.0-MeV protons are at larger diameters and more prone to track overlap, showing at a 6-hour etch a rather long high-diameter tail due to multiple overlapping tracks that are recorded as a single, large track. The trend of detection efficiency with etch time is similar for higher-energy, smaller-diameter D^{3}He protons. At a 1-hour etch, only 19% of 3.8-MeV-proton tracks and 35% of 4.3-MeV-proton tracks are counted (Figure 2.24b). Detection of 100% of the protons only occurs by a 2.5-hour etch – as evidenced by the plateau in detection efficiency – and, subsequently, track overlap diminishes the inferred yield at longer etch times. At a 6-hour etch, 73% of 4.3-MeV-proton tracks and 83% of 3.8-MeV-proton tracks are counted. Because of the relatively small difference in track diameters between 3.8-MeV protons and 4.3-MeV protons (Figure 2.24d), as the CR-39 response does not change substantially at high energy, there is not as much of a difference in the incidence of track overlap and reduction of detection efficiency.

This data can also be used to assess a model of track overlap, which predicts track overlap to increase linearly with the proton fluence and with the effective area of an average track.[40] For the 3.8-MeV-proton data at a 6h etch shown in Figure 2.24b and 2.24d, with a fluence of 3.7×10^5 cm^{-2} and a mean track diameter of 5.5 μm, the model predicts that 70% of tracks are not overlapping. This prediction is in excellent agreement with the 73% detection efficiency that was measured. However, the model has difficulty under conditions of extreme overlap, such as the 2.0-MeV-proton data at a 6-hour etch. At a fluence of 2.0×10^5 cm^{-2} and a mean track diameter (for the main peak) of 16 μm, the model predicts that only 22% of tracks are not subject to overlap, much lower than the measured detection efficiency of 42%. It is likely that a substantial fraction of the recorded tracks are actually multiple overlapping tracks recorded as a single track. This effect is encapsulated in the long high-diameter tails at a 6-hour etch in Figure 2.24c.

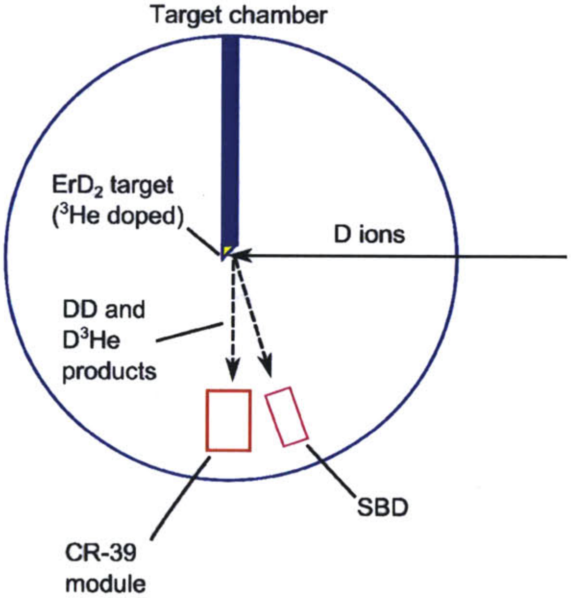

Figure 2.25. Diagram of experiments on LEIA. A deuteron beam impinges on a ^{3}He-doped, ErD$_2$ target, generating DD and D^{3}He protons, which are detected by both a surface barrier detector (SBD) and CR-39 detectors.

Experiments on LEIA, illustrated schematically in Figure 2.25 more closely assess the undercounting of proton tracks at short etch times. In these experiments, a deuterium beam incident on a ^{3}He-doped ErD$_2$ target produces DD and D^{3}He fusion products, which are detected by a surface barrier detector (SBD). The SBD provides confirmation of the expected nuclear production rate, for comparisn to CR-39-based measurements. Figure 2.26 shows measured proton fluences on the CR-39 as a function of etch time at fluences of (a) 3.2×10^5 cm^{-2}, (b) 6.4×10^5 cm^{-2}, and (c) 3.0×10^6 cm^{-2}. The actual fluences were measured with a surface barrier detector (SBD), providing an independent measure for comparison to the CR-39 data. The data indicate that by etch times of 0.75h or 1h, all of the 1.7-MeV- and 2.4-MeV-proton tracks are counted at fluences of 3.2×10^5 cm^{-2} and 6.4×10^5 cm^{-2}. However, at a 0.5h etch, when using a 40x magnification, only 17% of 2.4-MeV-proton and 87% of 1.7-MeV-proton tracks are counted. At the short etch times necessary to avoid track overlap in high fluence conditions, some of the proton tracks are not visible under typical scanning conditions. Use of the 100x magnification allows all tracks to be recorded at a 0.5h etch; however, scanning with the 100x objective is very time-consuming and is generally avoided.

These experiments demonstrate that when scanning with the 40x objective, an etch time of 1h is necessary to reveal all of the proton tracks. Thus, if track overlap becomes significant at earlier than a 1h etch, normal processing will not be able to achieve 100% detection efficiency. For example, at a fluence of 3.0×10^6 cm^{-2}, by a 1h etch, track overlap is already significant enough to reduce the detection efficiency to 88%. These results establish that at fluences at or above 3.0×10^6 cm^{-2}, 2.4-MeV protons cannot be counted at 100% efficiency using normal CR-39 processing techniques. This limit will also apply for protons at a lower energy, which have larger diameters and are therefore more susceptible to track overlap.[40]

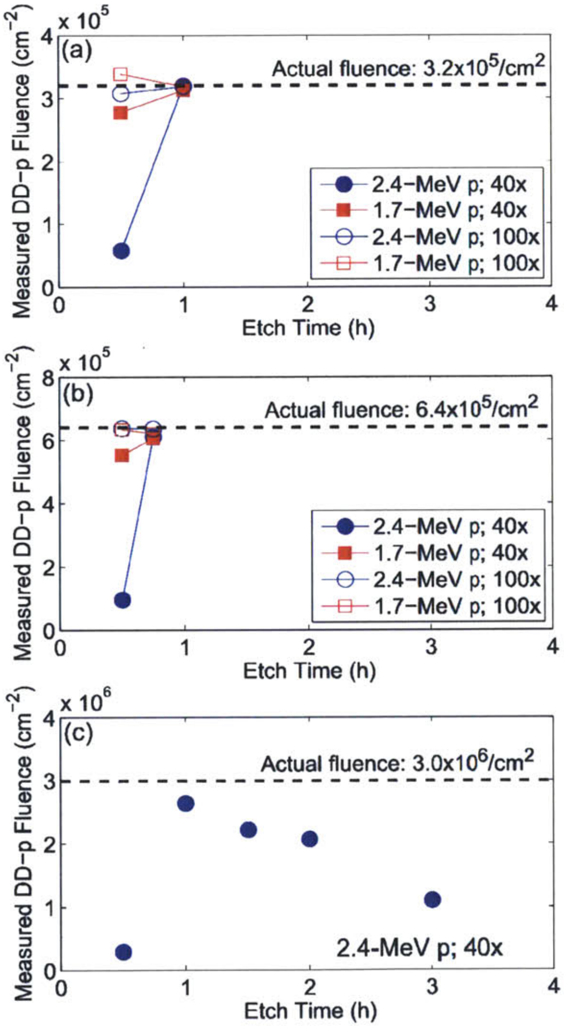

Figure 2.26. Measured DD-proton fluence as a function of etch time at fluence of (a) 3.2×10^5 cm^{-2}, (b) 6.4×10^5 cm^{-2}, and (c) 3.0×10^6 cm^{-2}. The actual fluence was measured using the SBD. Measurement uncertainty is approximately the size of the symbols.

Wedge-Filtered CR-39

CR-39 proton data obtained with wedge-range-filter (WRF) proton spectrometers[16,21,22] also display track overlap problems under certain conditions, which can impact measurements of yield, burn-averaged ion temperature, and areal density. NIF D^{3}He exploding pusher shot N110722 produced a yield of 1.35×10^{10} protons, and WRFs positioned 50 cm from the implosion were exposed to a fluence of 4.3×10^5 cm^{-2} protons. Images of tracks corresponding to protons likely at an energy of ~2-3 MeV incident on the CR-39, after being ranged through the aluminum wedge, are shown in Figure 2.27. After 2.5 hours of etching (Figure 2.27a), only 4% of proton tracks are overlapping, while after 5 hours of etching (Figure 2.27b) 48% of tracks are not counted due to track overlap.

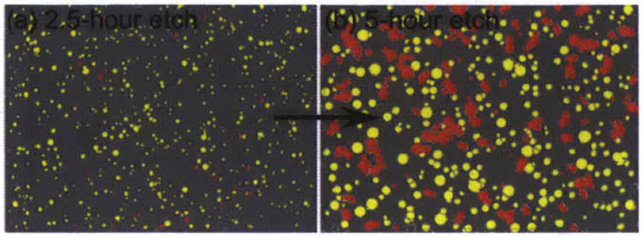

Figure 2.27. Microscope images of D^{3}He proton tracks from the wedge-range-filter (WRF) spectrometer on NIF shot N110722 at (a) a 2.5-hour etch, and (b) a 5-hour etch. The WRF was positioned at 50 cm from the implosion, resulting in a fluence of 4.3×10^5 cm^{-2}. The yellow tracks are counted as single tracks and the red overlapping tracks are ignored. These tracks correspond to protons likely at an energy of ~2-3 MeV incident on the CR-39, after being ranged through the aluminum wedge.

The inferred detection efficiency for 14.4-MeV protons ranged through the WRF are shown as a function of etch time for N110722 and similar D^{3}He exploding pusher N121128 in Figure 2.28. The tracks analyzed in the WRF data correspond to protons at an incident energy on the CR-39 of ~1-4 MeV. Both pieces of data show track under-counting at short etch times, albeit much more severely in the N121128 data, with only 34% of the tracks recorded at a 1-hour etch. This difference reflects differences in CR-39 sensitivity across different batches or individual pieces. The N110722 data, at a slightly lower fluence, has a more gradual decrease in the inferred yield and a more extended plateau, still counting 93% of its tracks by a 3.5-hour etch. The N121128 data shows a sharper retreat from the peak in the inferred yield, with an efficiency of 81% after a 3-hour etch and 63% after a 5-hour etch. The shape of the N121128 curve suggests that 6.5×10^5 cm^{-2} is very close to the fluence upper-limit for being able to detect 100% of protons using the WRF.

Figure 2.28. WRF-inferred D^{3}He-p yields, normalized to the actual yields, as a function of etch time for (a) NIF shot N110722, at a fluence of 4.3×10^5 cm^{-2}, and (b) NIF shot N121128, at a fluence of 6.5×10^5 cm^{-2}. The protons contributing to the WRF analysis had an incident energy on the CR-39 of ~1-4 MeV.

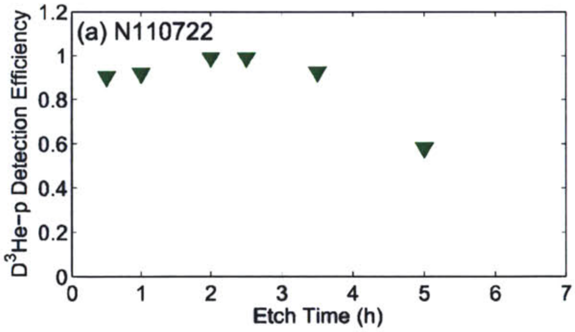

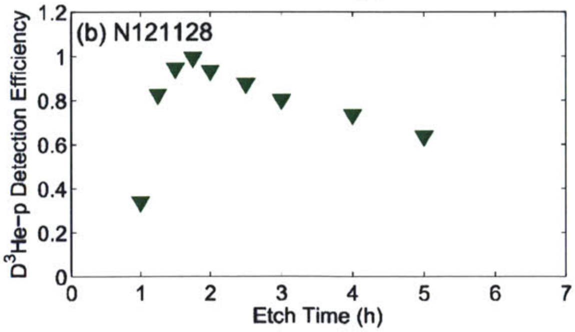

The impact of track overlap on spectral reconstruction is assessed in terms of the effect on WRF-measured D^{3}He-p mean energy and linewidth. The inferred proton energy and linewidth for NIF shots N110722 and N121128 are shown as a function of etch time (and, thus, as a function of increasing track overlap) in Figure 2.29. On both shots, the mean energy is fairly constant as a function of etch time, with minimal variation in the N110722 measurements, and only a ~90 keV decrease in the inferred proton energy from a 1.5h etch to a 5h etch in the N121128 measurements. Therefore, it can be concluded that in this regime of overlap, with the detection efficiency reduced by no more than 40%, the mean energy measurement is robust to overlap to within 100 keV. However, the spectral width does show some dependence on the degree of track overlap. In both the N110722 and N121128 data, the linewidth increases noticeably at longer etch times. On shot N110722, the measured linewidth increases from 325 keV to 385 keV between 2h and 5h; on shot N121128, the measured linewidth increases beyond a 3h etch, from 310 keV to 335 keV at a 5h etch. Under these conditions, the energy measurement is relatively unaffected, and therefore energy-based measurements of ρR are stable. However, ion temperature measurements based on the linewidth are impaired.

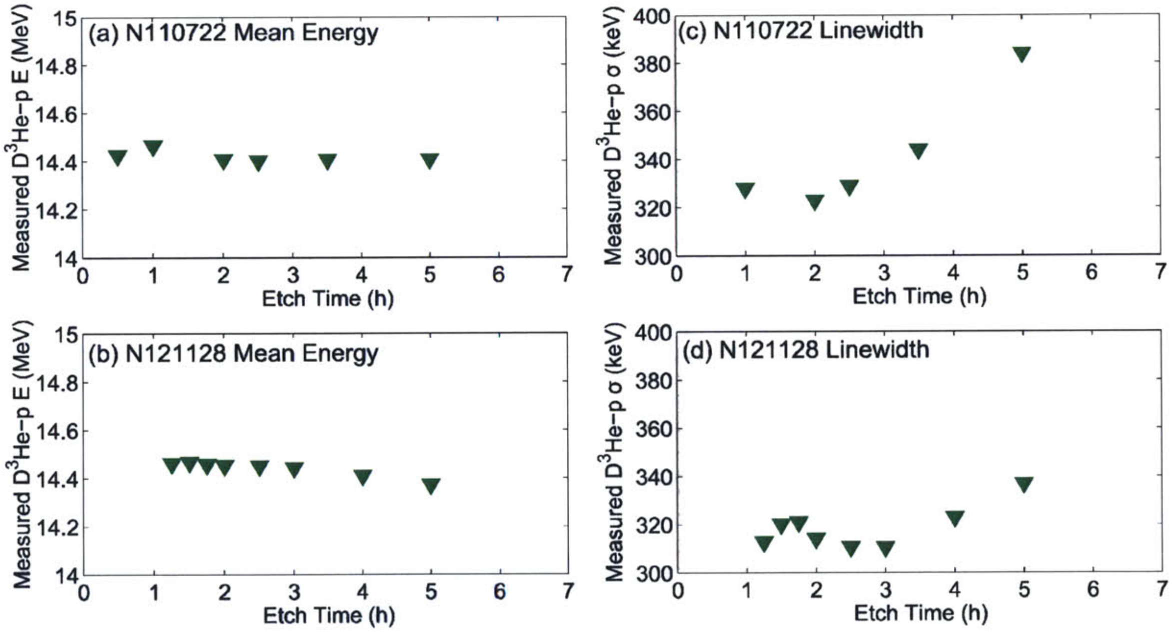

Figure 2.29. WRF-inferred D^{3}He-p (a-b) energy and (c-d) linewidth as a function of etch time for (a),(c) NIF shot N110722, at a fluence of 4.3×10^5 cm^{-2}, and (b),(d) NIF shot N121128, at a fluence of 6.5×10^5 cm^{-2}.

2.5.3 Scattering Pinhole Detector for Extension of Proton Yield Upper Limit

As demonstrated in Figure 2.26c, at a high enough fluence, above ~3×10^6 cm^{-2} 2.4-MeV protons, track overlap begins to occur before all tracks are countable using standard processing techniques. To operate in such high-fluence conditions, as is occasionally necessary on experiments at NIF, the proton fluence at the CR-39 surface must be reduced.

A pinhole and scattering foil displaced ~cm from the CR-39 can be utilized to reduce the fluence of protons at the CR-39 surface. The principle is illustrated schematically in Figure 2.30. Protons enter a small pinhole of diameter d ~100-300 μm, which at the fluences of interest (~10^6 cm^{-2})

allow ~500-5000 protons to pass through. A thin foil immediately behind and attached to the pinhole substrate scatters protons at an average angle θ_s (~5° for a 5 μm Ta foil). A spacer of length L ~cm between the pinhole substrate and the CR-39 allows the protons to disperse over an area of radius $\sim L\theta_s$, such that the proton fluence at the CR-39 is lower than that at the pinhole by a factor of $\sim(L\theta_s/d)^2$. For L ~1 cm, the fluence at the CR-39 can be reduced by a factor of ~50.

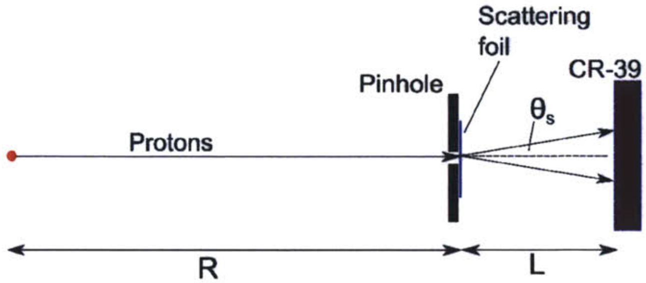

Figure 2.30. Pinhole plus scattering foil for reduction of proton fluence on the CR-39. Reducing the pinhole diameter, increasing the foil-CR-39 distance (L), and increasing the mean scattering angle θ_s all generate a greater fluence reduction factor.

This concept was tested on LEIA, which produced DD protons at a fluence of 1.3×10^6 cm^{-2} at the 200 μm-diameter pinhole. The resulting proton images on the CR-39, separated from the pinhole by 8.7 mm, are shown in Figure 2.31. Figure 2.31a shows that, in the absence of a scattering foil, the proton signal is highly concentrated over an area less than 1 mm at the center of the detector, at a fluence of 1.1×10^5 cm^{-2}. The finite size of the proton source reduces the fluence at the CR-39 to below that at the pinhole. The addition of a 5 μm Ta scattering foil behind the pinhole causes a noticeable difference in the proton signal at the CR-39 (Figure 2.31b). The proton signal is dispersed over several mm, such that the maximum fluence is reduced to 2.5×10^4 cm^{-2}, a factor of 50 lower than the incident fluence on the pinhole.

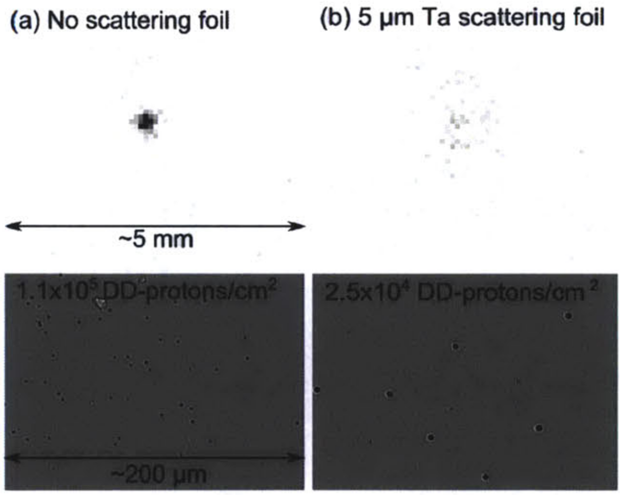

Figure 2.31. Scattering pinhole data obtained on LEIA, (a) without a scattering foil, showing a fluence at the CR-39 of 1.1×10^5 DD-protons per cm^2, at a 1-hour etch, and (b) with a 5 μm Ta scattering foil, resulting in a fluence of 2.5×10^4 DD-protons per cm^2 at the CR-39 at a 2-hour etch. The incident fluence scales are identical in both images. The nominal proton fluence at the pinhole is 1.3×10^6 cm^{-2}, and is greater than that at the CR-39 in the no-foil case because of the finite size of the proton source. With the scattering foil, the fluence is reduced by a factor of 50 below that incident on the pinhole.

A version of the detector with a 300 μm diameter pinhole in a 150 μm-thick Al substrate and a 10 μm Ta scattering foil was fielded on D^{3}He exploding pusher shot 70400 on OMEGA, as depicted in Figure 2.32. The implosion produced 2.8×10^{10} DD protons as inferred from the DD-neutron yield measured by the neutron time of flight (nTOF) suite.[34] With the pinhole positioned 35.4 cm from the implosion, the fluence of DD protons incident at the pinhole was 1.8×10^6 cm^{-2}, such that a 100% detection efficiency would be nearly impossible using conventional CR-39 processing methods. The resulting DD-proton signal on the CR-39 after a 2-hour etch shows a fairly diffuse signal spread over several mm (Figure 2.32d), much larger than the size of the pinhole, and roughly as expected based on a calculated mean scattering angle of ~7° and pinhole-CR-39 separation of

8.7 mm.[52] The maximum proton fluence was reduced from 1.8×10^6 cm^{-2} at the pinhole to 4.3×10^4 cm^{-2} at the CR-39, a factor of 40 reduction. The placement of the 10 μm Ta scattering foil 8.7 mm in front of the CR-39 did not result in a substantially different proton track diameter distribution than if the same 10 μm Ta foil were placed directly in front of the CR-39 (Figure 2.32f).

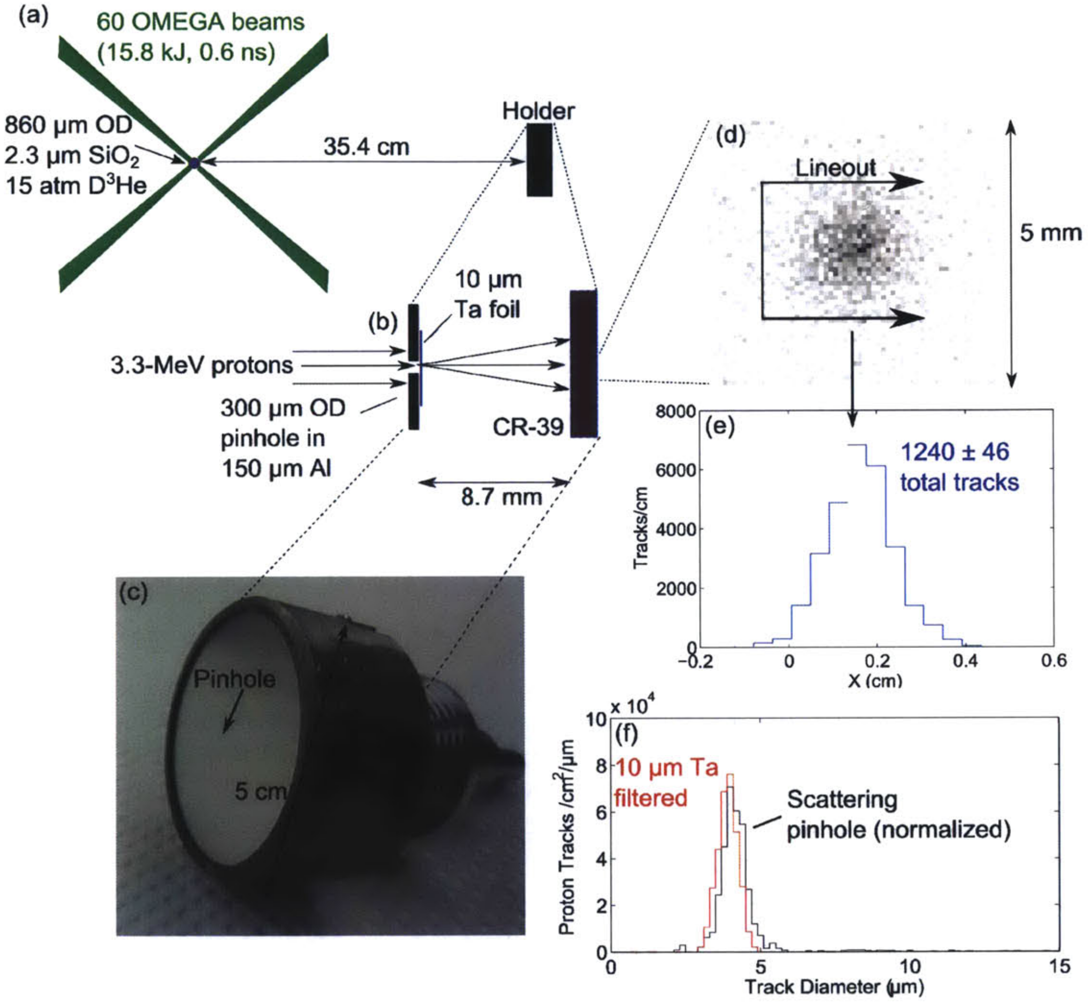
(a)
60 OMEGA beams
(15.8 kJ, 0.6 ns)
860 μm OD
2.3 μm SiO2
15 atm D3He
35.4 cm
Holder
(b)
10 μm
Ta foil
3.3-MeV protons
300 μm OD
pinhole in
150 μm Al
CR-39
8.7 mm
(c)
Pinhole
5 cm
(d)
Lineout
5 mm
(e)
1240 ± 46
total tracks
Tracks/cm
8000
6000
4000
2000
0
-0.2
0
0.2
0.4
0.6
X (cm)
(f)
x 10^4
10
8
6
4
2
0
10 μm Ta
filtered
Scattering
pinhole (normalized)
Proton Tracks /cm²/μm
0
5
10
15
Track Diameter (μm)

Figure 2.32. Scattering pinhole setup and data obtained on OMEGA shot 70400. (a) The detector package was fielded 35.4 cm from an implosion of a thin glass capsule filled with D^{3}He. (b) A 300 μm diameter pinhole followed by a 10 μm Ta foil was used to scatter 3.3-MeV protons produced in DD reactions onto the CR-39; (c) the detector package was housed inside the 5-cm diameter diagnostic module. The protons were dispersed (d) over an area several mm wide on the CR-39, reducing the incident fluence from 1.8×10^6 cm^{-2} at the pinhole to 4.3×10^4 cm^{-2} at the CR-39. The total number of tracks (e) was 1240±46. It was found (f) that the distribution of proton diameters generated by the scattering pinhole instrument, using a 10 μm Ta scattering foil, is nearly identical to that produced by a detector with a simple 10 μm Ta filter directly in front of the CR-39 after a 2-hour etch.

The total number of protons on the detector, as determined from the background-subtracted total under the peak in Figure 2.32, is 1240±46 (Figure 2.32e), where the uncertainty is due to choices of subtraction of intrinsic background in the CR-39. The inferred DD-proton yield and its total uncertainty are determined as follows. The number N of protons on the CR-39 is used to determine the DD-p fluence F at the pinhole, as $F = N/(\pi(d/2)^2)$, where d is the diameter of the pinhole. The total yield is therefore $Y = F(4\pi R^2)$, where R is the distance from the implosion to the pinhole. Thus,

$$Y = \frac{N}{\pi(d/2)^2} 4\pi R^2 \tag{2.15}$$

and the fractional uncertainty in the yield is

$$\frac{\Delta Y}{Y} = \sqrt{\left(\frac{\Delta N_{bkgd}}{N}\right)^2 + \left(\frac{\sqrt{N}}{N}\right)^2 + \left(2\frac{\Delta d}{d}\right)^2} \tag{2.16}$$

where the first term on the right-hand side represents the uncertainty due to intrinsic background, the second term represents the uncertainty due to raw counting statistics, and the third term represents the uncertainty in the pinhole diameter. The uncertainty in the distance from the pinhole to the implosion is <0.1% and can be neglected.

For $N = 1240$, $\Delta N_{bkgd} = 30$, $R = 35.4$ cm, $d = 300 \pm 10$ μm, $Y = 2.76 \pm 0.21 \times 10^{10}$, in excellent agreement with the nTOF-measured yield of 2.8×10^{10}. In this case, most of the yield uncertainty comes from uncertainty in the pinhole diameter (6.7% out of 7.6% total). For a smaller number of protons through the pinhole, the statistical and background-related uncertainties will be more significant.

2.5.4 Discussion and Applications

CR-39 proton data at energies of 1.7-4.3 MeV show that, in the absence of track overlap, 100% detection efficiency can be achieved under a 40x objective after as short as 0.75-2.5 hours of etching in a 6N NaOH solution at 80° C. The incident proton fluence limits the etch time for 100% detection, as track overlap limits the number of invidual proton tracks that are counted correctly. For 2.0-MeV protons at a fluence of 2.0×10^5 cm^{-2}, track overlap becomes significant (<95% detection efficiency) after only 2 hours of etching. Higher-energy protons that leave smaller tracks are slightly less susceptible to overlap, which only becomes significant for 4.3-MeV protons at 3.7×10^5 cm^{-2} after 5 hours of etching. For 2.4-MeV protons at a fluence of 3×10^6 cm^{-2}, track overlap occurs even before all tracks can be counted, such that it is impossible to achieve 100% detection efficiency. This establishes the fluence upper-limit for 100% detection of individual 2.4-MeV-proton tracks.

For proton fluences where normal processing techniques cannot achieve 100% detection efficiency, a detector based on a pinhole and scattering foil has been designed to reduce the fluence of protons incident on the CR-39 and effectively shift the range of operation of CR-39-based proton yield measurements. Proton fluences above the 100% efficiency limit are regularly achieved on D_2 exploding pusher experiments on NIF for calibration of DD-neutron diagnostics, where DD yields of up to 1×10^{12} produce proton fluences of 3×10^7 cm^{-2} at CR-39 detectors at a position 50 cm from the implosion, fixed due to hardware limitations. This fluence is well above that at which normal processing techniques can work. A scattering pinhole-based instrument, housed entirely within the module currently used for wedge range filter (WRF) proton spectrometers,[21] can reduce the proton fluence incident on the CR-39 by a factor of ~50, to ~6×10^5 cm^{-2}, which at energies of 1.7-2.4 MeV can be measured at 100% efficiency (Figure 2.26). This technique can also be applied for measurements of more energetic D^3He protons or for alpha particles produced in D^3He or DT implosions, and future work may also apply this fluence reduction technique to proton spectral measurements using the WRF spectrometer.

2.5.5 Conclusions

Empirical studies have established a fluence upper limit for 100% detection efficiency of protons in CR-39 of $\lesssim 3\times10^6$ cm^{-2} for 2.4-MeV protons. At higher fluences, the onset significant track overlap – preventing individual tracks from being distinguished and properly counted – occurs at etch times short enough that the tracks are not entirely detectable and 100% detection efficiency is never achieved. At the OMEGA and NIF laser facilities, fixed diagnostic positions sometimes force CR-39-based diagnostics to be fielded at distances where the proton fluence can exceed this fluence upper limit. For such circumstances, a pinhole and scattering-foil has been developed and implemented to reduce the fluence of DD protons at the CR-39 surface by a factor of ~40 or more. This detector package significantly extends the yield upper limit for DD-proton measurements on thin-shell implosions, and this technique can be further adapted to measurements of other fusion products.

2.6 Summary

Nuclear diagnostic techniques for measurement of yield, ion temperature, fuel and total areal density, burn profile, and burn history in ICF implosions have been presented. The use of these techniques will be discussed in Chapter 3 and Appendix A in the context of measuring implosion conditions in shock-driven exploding pushers. Additionally, two new charged-particle instruments have been presented: (1) the compact and portable ~1-3-MeV-proton step range filter (SRF) spectrometer, and (2) the "scattering pinhole" for measurement of fusion yield in high-particle-fluence environments. These instruments have enhanced the suite of nuclear diagnostics for use at the OMEGA and NIF laser facilities, particularly on exploding pusher implosions.

2.7 References

1. D. G. Hicks, *Charged-Particle Spectroscopy: A New Window on Inertial Confinement Fusion*, Ph.D. thesis, Massachusetts Institute of Technology (1999).
2. H. Brysk, "Fusion neutron energies and spectra," Plasma Physics, **15**(7), 611 – 617 (1973).
3. L. Ballabio, J. Kallne and G. Gorini, "Relativistic calculation of fusion product spectra for thermonuclear plasmas," Nucl. Fusion, **38**(11), 1723–1735 (1998).
4. M. Gatu Johnson, D. T. Casey, J. A. Frenje *et al.*, "Measurements of collective fuel velocities in deuterium-tritium exploding pusher and cryogenically layered deuterium-tritium implosions on the nif," Physics of Plasmas, **20**(4), 042707 (2013).
5. C. K. Li, D. G. Hicks, F. H. Séguin *et al.*, "D-^{3}he proton spectra for diagnosing shell ρr and fuel t_i of imploded capsules at omega," Phys. Plasmas, **7**(6), 2578–2584 (2000).
6. D. G. Hicks, C. K. Li, F. H. Séguin *et al.*, "Charged-particle acceleration and energy loss in laser-produces plasmas," Phys. Plasmas, **7**(12), 5106–5117 (2000).
7. B. Appelbe and J. Chittenden, "The production spectrum in fusion plasmas," Plasma Physics and Controlled Fusion, **53**(4), 045,002 (2011).
8. T. J. Murphy, "The effect of turbulent kinetic energy on inferred ion temperature from neutron spectra," Physics of Plasmas (1994-present), **21**(7), 072701 (2014).
9. T. C. Sangster, V. N. Goncharov, R. Betti *et al.*, "Improving cryogenic deuteriumtritium implosion performance on omega," Physics of Plasmas, **20**(5), 056317 (2013).
10. M. J. Edwards, P. K. Patel, J. D. Lindl *et al.*, "Progress towards ignition on the national ignition facility," Physics of Plasmas, **20**(7), 070501 (2013).
11. M. G. Johnson, J. A. Frenje, D. T. Casey *et al.*, "Neutron spectrometryan essential tool for diagnosing implosions at the national ignition facility," Review of Scientific Instruments, **83**(10), 10 (2012).

12. M. D. Cable and S. P. Hatchett, "Neutron spectra from inertial confinement fusion targets for measurement of fuel areal density and charged particle stopping powers," J. Appl. Phys., **62**(6), 2233–2236 (1987).
13. F. H. Séguin, C. K. Li, J. A. Frenje *et al.*, "Using secondary-proton spectra to study the compression and symmetry of deuterium-filled capsules at omega," Phys. Plasmas, **9**(6), 2525–2537 (2002).
14. S. Kurebayashi, J. A. Frenje, F. H. Séguin *et al.*, "Using nuclear data and monte carlo techniques to study areal density and mix in d_2 implosions," Phys. Plasmas, **12**, 032,703 (2005).
15. A. P. Fews and D. L. Henshaw, "High resolution alpha particle spectroscopy using CR-39 plastic track detector," Nuclear Instruments and Methods in Physics Research, **197**(2-3), 517–529 (1982).
16. F. H. Séguin, J. A. Frenje, C. K. Li *et al.*, "Spectrometry of charged particles from inertial-confinement-fusion plasmas," Review of Scientific Instruments, **74**(2) (2003).
17. N. Sinenian, M. J. Rosenberg, M. Manuel *et al.*, "The response of cr-39 nuclear track detector to 1-9 mev protons," Rev. Sci. Inst., **82**(103303) (2011).
18. D. G. Hicks, C. K. Li, F. H. Séguin *et al.*, "Observations of fast protons above 1 mev produced in direct-drive laser-fusion experiments," Physics of Plasmas, **8**(2) (2001).
19. J. A. Frenje, C. K. Li, F. H. Séguin *et al.*, "Diagnosing fuel r and r asymmetries in cryogenic deuterium-tritium implosions using charged-particle spectrometry at omega," Physics of Plasmas, **16**(4), 042704 (2009).
20. J. A. Frenje *et al.*, to be submitted to Phys. Rev. Lett. (2014).
21. F. H. Séguin, N. Sinenian, M. Rosenberg *et al.*, "Advances in compact proton spectrometers for inertial-confinement fusion and plasma nuclear sciencea)," Review of Scientific Instruments, **83**(10), 10 (2012).
22. A. B. Zylstra, J. A. Frenje, F. H. Séguin *et al.*, "Charged-particle spectroscopy for diagnosing shock r and strength in nif implosions," Review of Scientific Instruments, **83**(10), 10 (2012).
23. M. J. Rosenberg *et al.*, "Utilization of nif diagnostic development shots for investigation of ion kinetic effects in direct-drive exploding-pusher implosions," to be submitted to Phys. Plasmas (2014).
24. M. J. Rosenberg, H. G. Rinderknecht, N. M. Hoffman *et al.*, "Exploration of the transition from the hydrodynamiclike to the strongly kinetic regime in shock-driven implosions," Phys. Rev. Lett., **112**, 185,001 (2014).
25. C. K. Li, F. H. Sé, J. A. Frenje *et al.*, "Effects of nonuniform illumination on implosion asymmetry in direct-drive inertial confinement fusion," Phys. Rev. Lett., **92**(20), 205,001 (2004).
26. A. Zylstra *et al.*, submitted to Phys. Rev. Lett. (2014).
27. F. H. Séguin, J. L. Deciantis, J. A. Frenje *et al.*, "D^3he-proton emission imaging for inertial-confinement-fusion experiments (invited)," Rev. Sci. Inst., **75**(10), 3520–3525 (2004).
28. J. L. DeCiantis, F. H. Séguin, J. A. Frenje *et al.*, "Proton core imaging of the nuclear burn in inertial confinement fusion implosions," Rev. Sci. Inst., **77**(043503) (2006).
29. F. H. Séguin, J. L. DeCiantis, J. A. Frenje *et al.*, "Measured dependence of nuclear burn region size on implosion parameters in inertial confinement fusion experiments," Physics of Plasmas, **13**(8), 082704 (2006).
30. R. A. Lerche, D. W. Phillion and G. L. Tietbohl, "25 ps neutron detector for measuring icf-target burn history," Rev. Sci. Inst., **66**(1), 933–935 (1995).
31. C. Stoeckl, V. Y. Glebov, S. Roberts *et al.*, "Ten-inch manipulator-based neutron temporal diagnostic for cryogenic experiments on omega," Rev. Sci. Inst., **74**(3), 1713–1716 (2003).
32. J. A. Frenje, C. K. Li, F. H. Séguin *et al.*, "Measuring shock-bang timing and ρr evolution of d^3he implosions at omega," Phys. Plasmas, **11**(5), 2798–2805 (2004).
33. H. G. Rinderknecht, M. G. Johnson, A. B. Zylstra *et al.*, "A novel particle time of flight diagnostic for measurements of shock- and compression-bang times in d^3he and dt implosions at the nif," Rev. Sci. Inst., **83**(10D902) (2012).
34. V. Y. Glebov, C. Stoeckl, T. C. Sangster *et al.*, "Prototypes of national ignition facility neutron time-of-flight detectors tested on omega," Rev. Sci. Inst., **75**, 3559–3562 (2004).
35. J. A. Frenje, D. T. Casey, C. K. Li *et al.*, "First measurements of the absolute neutron spectrum using the magnetic recoil spectrometer at omega (invited)," Rev. Sci. Inst., **79**(10E502) (2008).
36. D. T. Casey, J. A. Frenje, M. G. Johnson *et al.*, "The magnetic recoil spectrometer for measurements of the absolute neutron spectrum at omega and the nif," Rev. Sci. Inst., **84**(043506) (2013).
37. N. Sinenian, M. J.-E. Manuel, A. B. Zylstra *et al.*, "Upgrade of the mit linear electrostatic ion accelerator (leia) for nuclear diagnostics development for omega, z, and nif," Rev. Sci. Inst., **83**(043502) (2012).

38. M. J.-E. Manuel, M. J. Rosenberg, N. Sinenian *et al.*, "Changes in cr-39 proton sensitivity due to prolonger exposure to high vacuums relevant to the national ignition facility and omega," Rev. Sci. Inst., **82**(095110) (2011).
39. A. B. Zylstra, H. G. Rinderknecht, N. Sinenian *et al.*, "Increasing the energy dynamic range of solid-state nuclear track detectors using multiple surfaces," Rev. Sci. Inst., **82**(083301) (2011).
40. A. B. Zylstra, J. A. Frenje, F. H. Séguin *et al.*, "A new model to account for track overlap in cr-39 data," Nuclear Instruments and Methods in Physics Research A., **681**, 84–90 (2012).
41. J. A. Frenje, C. K. Li, F. H. Séguin *et al.*, "Absolute measurements of neutron yields from dd and dt implosions at the omega laser facility using cr-39 track detectors," Review of Scientific Instruments, **73**(7) (2002).
42. M. J. Rosenberg *et al.*, "A compact proton spectrometer for measurement of the absolute dd proton spectrum from which yield and ρr are determined in thin-shell inertial-confinement-fusion implosions," submitted to Rev. Sci. Inst. (2014).
43. M. J. Rosenberg, F. H. Séguin, C. J. Waugh *et al.*, "Empirical assessment of the detection efficiency of cr-39 at high proton fluence and a compact, proton detector for high-fluence applications," Review of Scientific Instruments, **85**(4), 043302 (2014).
44. Y. Kitagawa, K. Tanaka, M. Nakai *et al.*, "Areal density measurement of imploded cryogenic target by energy peak shift of dd-produced protons," Physical review letters, **75**(17), 3130 (1995).
45. R. D. Petrasso, J. A. Frenje, C. Li *et al.*, "Measuring implosion dynamics through ρr evolution in inertial-confinement fusion experiments," Phys. Rev. Lett., **90**(9), 095,002 (2003).
46. J. Cobble, K. Flippo, D. Offermann *et al.*, "High-resolution thomson parabola for ion analysis," Review of Scientific Instruments, **82**(11), 113,504–113,504 (2011).
47. C. Freeman, G. Fiksel, C. Stoeckl *et al.*, "Calibration of a thomson parabola ion spectrometer and fujifilm imaging plate detectors for protons, deuterons, and alpha particles," Review of Scientific Instruments, **82**(7), 073,301–073,301 (2011).
48. T. R. Boehly, D. L. Brown, R. S. Craxton *et al.*, "Initial performance results of the omega laser system," Opt. Commun., **133**, 495–506 (1997).
49. G. Miller, E. Moses and C. Wuest, "The national ignition facility," Opt. Eng., **43**, 2841 (2004).
50. D. L. Bleuel, C. B. Yeamans, L. A. Bernstein *et al.*, "Neutron activation diagnostics at the national ignition facility (invited)," Rev. Sci. Inst., **83**(10D313) (2012).
51. C. J. Waugh, M. J. Rosenberg *et al.*, to be submitted to Review of Scientific Instruments (2014).
52. J. F. Ziegler, M. D. Ziegler and J. P. Biersack, "Srim–the stopping and range of ions in matter (2010)," Nuclear Instruments and Methods in Physics Research Section B: Beam Interactions with Materials and Atoms, **268**(11), 1818–1823 (2010).
53. N. Sinenian, A. B. Zylstra, M. J.-E. Manuel *et al.*, "Total energy loss to fast ablator-ions and target capacitance of direct-drive implosions on omega," Applied Physics Letters, **101**(11), 114102 (2012).
54. S. Skupsky, J. A. Marozas, R. S. Craxton *et al.*, "Polar direct drive in the national ignition facility," Phys. Plasmas, **11**(5), 2763–2770 (2004).
55. P. W. McKenty, R. S. Craxton, A. Shvydky *et al.*, "Evaluation of the first polar-drive, dt-gas-filled target implosions on the nif," Bull. Am. Phys. Soc., **55**(15) (2010).
56. V. Y. Glebov, D. D. Meyerhofer, T. C. Sangster *et al.*, "Development of nuclear diagnostics for the national ignition facility (invited)," Rev. Sci. Inst., **77**(10E715) (2006).
57. C. K. Li, F. H. Séguin, J. A. Frenje *et al.*, "Monoenergetic proton backlighter for measuring *e* and *b* fields and for radiographing implosions and high-energy density plasmas (invited)," Rev. Sci. Inst., **77**, 10E725 (2006).
58. J. R. Rygg, F. H. Séguin, C. K. Li *et al.*, "Proton radiography of inertial fusion implosions," Science, **319**, 1223–1225 (2008).
59. C. K. Li, F. H. Séguin, J. A. Frenje *et al.*, "Charged-particle probing of x-ray-driven inertial-fusion implosions," Science, **327**, 1231–1235 (2010).
60. T. Yamauchi, "Studies on the nuclear tracks in cr-39 plastics," Radiation Measurements, **36**, 73–81 (2003).
61. I. Rajta, E. Baradács, A. A. Bettiol *et al.*, "Optimization of particle fluence in micromachining of cr-39," Nuclear Instruments and Methods in Physics Research B., **231**, 384–388 (2005).
62. S. Gaillard, J. Fuchs, N. R.-L. Galloudec *et al.*, "Study of saturation of cr39 nuclear track detectors at high ion fluence and of associated artifact patterns," Rev. Sci. Inst., **78**(013304) (2007).

3

Studies of Ion Kinetic Effects in ICF Using Shock-Driven Implosions

As discussed in Chapter 1, shocks play an important role in determining the initial fuel conditions in ICF implosions. In hot-spot ignition implosions, a series of shocks coalesce in the cold fuel, setting the fuel entropy and thus dictating the compressibility. The propagation of a strong shock into the gas slightly increases the density and greatly increases the temperature in the gas, culminating with shock convergence and rebound, which sets the initial hot-spot conditions before peak compression. Notably, after shock convergence, the incipient hot-spot plasma is low-density ($n_i{\sim}10^{22}$ cm^{-3}) and high temperature ($T_i{\sim}10$ keV), such that the ion-ion mean free path λ_{ii} is of order $\sim$100 μm, approximately the size of the fuel region. For such conditions, the hydrodynamic assumptions built into the vast majority of codes used to simulate ICF implosions are invalid, and long-mean-free-path (or "kinetic") effects become significant.

Non-hydrodynamic effects in the context of ICF, in particular deviations from a Maxwellian ion distribution, have been considered in prior theoretical work dating back several decades.[1–5] However, given that the phase of the implosion around peak compression, when ignition may occur, is strongly collisional and the hydrodynamic description is applicable, such effects have, until recently, largely been ignored by the ICF community. As will be discussed, for a more complete and accurate understanding of ICF implosion physics, a kinetic picture of the shock convergence phase is required.

As shown in Figure 3.1, there have been many recent advances in understanding of implosion processes that extend beyond those included in average-ion, hydrodynamic models. One of these avenues of research, examination of ion kinetic effects and the transition between hydrodynamic and kinetic regimes, using shock-driven exploding pusher implosions, is the subject of this chapter. The data presented in this chapter illustrate in quantitative detail how and under what conditions ion kinetic effects impact plasma conditions during the shock convergence phase of ICF implosions. This work represents the first systematic, experimental exploration of ion kinetic effects in inertial confinement fusion implosions, with the goal of improving understanding of the physical mechanisms, beyond those accounted for in mainline (hydrodynamic) ICF simulations, that become important during the shock phase of implosions.

This chapter is organized as follows: Section 3.1 introduces and expands on background of some of the specific long-mean-free-path effects that can impact the shock-convergence phase of ICF implosions; Section 3.2 describes the major contribution of this thesis to the field of ICF, the first comprehensive experimental campaign, on OMEGA, to explore the transition between hydrodynamic-like and strongly kinetic regimes using shock-driven exploding-pusher implosions, between a regime where the ion mean free path is short compared to the fuel radius and one

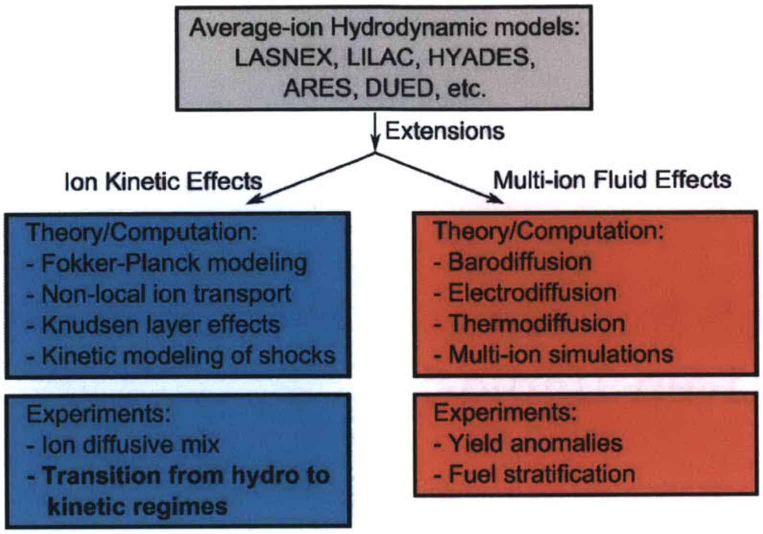
Average-ion Hydrodynamic models:
LASNEX, LILAC, HYADES,
ARES, DUED, etc.
Extensions
Ion Kinetic Effects
Multi-ion Fluid Effects
Theory/Computation:
- Fokker-Planck modeling
- Non-local ion transport
- Knudsen layer effects
- Kinetic modeling of shocks
Experiments:
- Ion diffusive mix
- Transition from hydro to kinetic regimes
Theory/Computation:
- Barodiffusion
- Electrodiffusion
- Thermodiffusion
- Multi-ion simulations
Experiments:
- Yield anomalies
- Fuel stratification

Figure 3.1. Hydrodynamic codes used to model ICF implosions and extensions beyond the average-ion, hydrodynamic picture. The LASNEX,[6] LILAC,[7] HYADES,[8] ARES,[9] and DUED[10] codes, as well as many others used in ICF simulations are average-ion fluid codes that do not account for kinetic or multiple-ion effects. Some theoretical work has explored kinetic and multi-ion fluid effects, including: Fokker-Planck modeling of ICF implosions,[11,12] inclusion of non-local ion transport,[13] Knudsen layer modification of the ion distribution function,[1,14–16] modeling of ion kinetic behavior around shock fronts, baro-,[17] electro-,[18] and thermodiffusion,[19] as well as multiple-ion-fluid simulations.[20]. Recent experimental work has resulted in the observation of yield anomalies in multiple-ion implosions,[21–23] and diffusion-related mix of fuel and shell ions.[24] The bulk of this chapter focuses on studies of ion kinetic effects using exploding pusher implosions, in particular probing the transition between "hydrodynamic" and "kinetic" regimes and inferring the onset, nature, and magnitude of ion kinetic effects.

where it is extremely long; Section 3.3 presents a complementary set of ride-along exploding pusher experiments on NIF, conducted as part of this thesis, that have been analyzed to infer evidence of ion kinetic effects.

3.1 Ion Kinetic Effects in ICF Implosions

The low-density, high-temperature conditions created by a strong converging shock in both ablatively-driven and shock-driven implosions lead to a breakdown of the assumptions underpinning the hydrodynamic description of the plasma. Non-hydrodynamic, or kinetic, effects can become important both (1) during shock convergence and (2) after shock rebound, during the "shock flash" phase of fusion production.

As the width of the converging shock is determined by the ion-ion mean free path, any improper treatment of long mean free path effects (e.g. in a hydrodynamic model) will fail to capture dynamics and energy coupling of the converging shock through the gas. For example, the actual width of the shock front, as dictated by the ion-ion mean free path λ_{ii}, can be larger than simulated by hydrodynamic models that do not incorporate real plasma viscosity and instead uses the numerical, von Neumann artificial viscosity. The use of real ion viscosity, as well as the non-local transport of gas ions ahead of the shock front smooths simulated shock profiles and ultimately leads to a reduction in simulated fusion yield by virtue of the weakened energy coupling.[25,13,26] This effect was demonstrated by Li *et al.*,[13] as shock-front profiles of mass density and ion temperature in 1D LILAC radiation-hydrodynamics simulations of an ablatively-driven implosion are smoothed by the inclusion of ion viscosity and non-local ion transport. The addition of these models produces a broader simulated shock front at lower temperature, with a pedestal of ion density extending ahead of the shock front toward the origin, in contrast to the sharp shock front produced in the nominal simulation. Hybrid hydrodynamic-kinetic (Fokker-Planck-based) models have also produced smoother profiles of density and temperature immediately after shock convergence and consequently produced lower shock-generated fusion yields than in hydrodynamic simulations.[5,11,12] The kinetic treatment produces a density profile that is more diffuse, rather than strongly peaked, at the origin, and a temperature profile that is much smoother than in the fluid simulation from which the kinetic simulation is initiated. As a consequence, the shock flash DD fusion yield is a factor of 5 lower than in the fluid simulation.[11] Both of these kinetic-based models produce results in better agreement with experimental data, and in doing so indicate that purely hydrodynamic models fail to capture important aspects of the shock convergence process.

An analytic model based on the Guderley solution[27] for a strong, spherically-converging shock has been developed by Amendt *et al.*[28] to estimate the loss of energy coupled to the gas on the basis of long ion-ion mean free paths during this converging shock phase. This model limits the thermal energy in the resulting hot-spot plasma to the thermal and kinetic energy in the incoming shock at the point where the shock front radius R_1 is equivalent to the ion-ion mean free path at the shock front (λ_1).[28] This effect is illustrated conceptually in Figure 3.2. Early in time, the shock front radius R_1 is greater than the ion-ion mean free path λ_{ii}. At some point, λ_{ii} equals the shock front radius, and the shock front is effectively smeared out all the way to the origin. At this point, the shock is unable to couple additional energy to the gas, and the final thermal energy density in the gas is constrained to the thermal energy density and ram pressure in the post-shocked gas. The final energy density in the plasma is determined to be

$$(Z+1)\frac{3}{2}n_F k_B T_F = \frac{1}{2}\rho_s V_s^2 + (Z+1)\frac{3}{2}n_1 k_B T_1 \tag{3.1}$$

where the right-hand side is evaluated at a radius $R_1 = \lambda_1$ and ρ_s is the mass density in the shock front, V_s is the post-shock velocity, Z is the average ion charge, n_1 (T_1) is the incoming post-shock ion number density (ion temperature), and n_F (T_F) is the final ion number density (ion temperature) after shock rebound. As the shock converges to a radius equivalent to the local λ_{ii} in the shock front, the shock front width becomes larger than its radius and the ions are no longer effectively confined.

In the hydrodynamic limit, where the minimum shell radius R_{shell} is greater than the radius at which the incoming shock radius equals the shock-front mean free path ($R_{shell} > R_1 \sim \lambda_1$), the kinetic correction to the Guderley model temperature is not applied. In those experiments where $\lambda_1 > R_{shell}$, the kinetic model is applied to limit the resulting ion temperature, according to equation 3.4, and, therefore, the fusion yield. The kinetic Guderley model YOC trend is determined by the trend in the ratio of kinetic-limited final ion temperature to the Guderley-model ion temperature that would have occurred without this limitation, as the DD YOC $\propto(T_{F,kinetic}/T_{F,hydro})^{2.5}$, with the absolute YOC normalized to match the YOC in the hydrodynamic regime. As shown in Section 3.2, this Guderley model, which accounts for the weakened energy coupling as a result of long mean-free-path effects at the converging shock front, can explain quantitatively a trend of diminished yield with longer mean free path in exploding pusher experiments on OMEGA.

Kinetic effects are significant as well in the post-shock heated gas. After shock convergence and rebound, ion densities of order 10^{22} cm^{-3} and ion temperatures of order 10 keV produce ion-ion

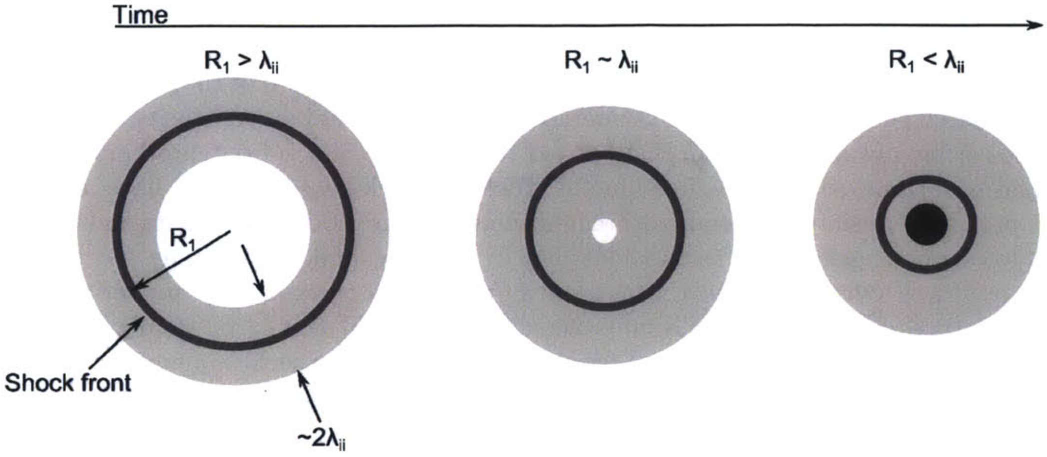

Figure 3.2. Conceptual depiction of the kinetic Guderley model.[28] Early in time, the shock front radius R_1 is greater than the ion-ion mean free path λ_{ii}. At some point, λ_{ii} equals the shock front radius, and the shock front is effectively smeared out all the way to the origin. At this point, the shock is unable to couple additional energy to the gas, and the final thermal energy in the gas is constrained to the thermal and ram-pressure energy in the post-shocked gas. As a consequence, the long ion-ion mean free paths that arise during shock convergence limit the resulting hot-spot energy. This model was developed by Amendt *et al.*[28]

mean free paths for a Maxwellian-averaged DT fuel ion around λ_{ii} ~250 μm, a few times larger than the radius of the fuel. These ions will readily diffuse out of the fuel, as the timescale for ion diffusion under such conditions, assuming a 100 μm inner shell radius (R_{shell}), is $\tau_{diff} = R_{shell}^2/(\frac{1}{3}\lambda_{ii}v_{ti})$~140 ps,[1] roughly the same order as the typical fusion burn duration ~100 ps. The ratio of burn duration to ion diffusion time $R_\tau \equiv \tau_{burn}/\tau_{diff}$ is a key figure of merit for the importance of ion kinetic effects around the time of fusion production. When $R_\tau \gtrsim 1$, ion diffusion should be significant.

For fusion considerations, the ions at the high-energy tail of the Maxwellian distribution are most important, and those ions with an energy near the Gamow-peak energy (see Appendix F), the most probable ion energy to undergo fusion,[2] are even more susceptible to long mean-free-path effects. As a simple illustration, for an equimolar D^{3}He plasma at n_i = 10^{22} cm^{-3} and T_i = 10 keV, the Gamow-peak energy is 29.1 keV for DD fusion and 49.1 keV for D^{3}He fusion, such that the main fusing ions are much more energetic than an average ion at the thermal energy. It should be cautioned that the Gamow-peak energy is a center-of-mass energy and not the energy of an individual ion, so the following discussion of Gamow-peak ions is intended to be illustrative, rather than rigorous. A more precise relation between the center-of-mass Gamow peak energy and the energy of individual reactant ions is presented in Appendix F. While the geometric mean of Maxwellian-averaged mean free paths for D and ^{3}He ions is 56 μm, the mean free path for D ions at the DD Gamow peak energy is 284 μm, while the mean free paths for D and ^{3}He ions, respectively, at the D^{3}He Gamow peak energy are 807 μm and 183 μm. Therefore, the ions responsible for fusion are even less confined than the average thermal ion and may escape into the shell. This effect, the Knudsen layer loss of high-energy ions, can significantly affect the distribution function and energy transport in the plasma and suppress the fusion reactivity.[1–3,14,15]

---

[1] For this calculation, the ion diffusion time is taken as the geometric mean of diffusion times for different ion species, D and T, with the thermal velocity v_{ti} and ion mean free path λ_{ii} calculated separately for each ion.

[2] The Gamow peak forms as a result of competing trends of the increasing fusion cross-section with center-of-mass energy and the decreasing population of ions with energy according to a Maxwellian distrubition.

The modification of ion distribution functions due to Knudsen ion losses in a D^{3}He fuel[15] is shown in Figure 3.3. The Knudsen number $N_K \equiv \lambda_{ii}/R_{shell}$, the ratio of Maxwellian-averaged ion mean free path to the distance to the shell, parameterizes the significance of this effect. It is another key figure of merit for the importance of ion kinetic effects, the spatial analogue of the R_τ parameter. For $N_K>1$, the ion population is significantly reduced for $\epsilon \equiv mv^2/2kT>2$. Considering that the center-of-mass Gamow peak energy for fusion reactions occurs typically at $\epsilon\sim2.9$ for DD fusion and ~4.9 for D^{3}He fusion at an ion temperature of 10 keV, the fusion reactivity is greatly reduced even at a more modest Knudsen number of $N_K = 0.2$. Under these conditions, which are easily achieved during the shock phase of ICF implosions, half of $\epsilon = 4.9$ ions are lost to the shell.

Figure 3.4 illustrates in greater detail how the reduction in tail-ion population impacts the fusion reactivity. Based on the DD fusion cross-section and distribution function in a 10 keV plasma, the Gamow peak energy – the most probable center-of-mass energy at which colliding ions will undergo fusion – is at several times the thermal energy, so the loss of high-energy tail ions due to Knudsen layer effects significantly reduces the overall probability of fusion. The relative probability of fusion per center-of-mass energy $g(E)$ is the product of the ion distribution function, which in the Maxwellian case scales like $f(E)\propto\exp(-E/kT)$, and the fusion cross section, which scales like $\sigma(E)\propto\exp(-(E_G/E)^{1/2})$, related to the probability of quantum tunneling into the opposing ion to allow for fusion.[29] The Gamow energy E_G, the scale energy for quantum tunneling, should not to be confused with the energy of the Gamow peak E_{Gp}, the most probable center-of-mass energy at which a fusion reaction will occur. In the Maxwellian case, for an ion temperature of 10 keV, the bulk of fusion occurs between ions at the center-of-mass Gamow peak energy of $E_{Gp} = 29.1$ keV, nearly three times more energetic than an ion at the thermal energy. Knudsen layer losses of energetic tail ions significantly deplete the ion population at the Gamow peak energy, reducing the peak energy[3] and, most significantly, reducing the overall probability of fusion (area under the $g*(E)$ curve). A preliminary model of this effect[14] applied to DT fuels suggests that even for $N_K \sim 0.1$ in a $T_i = 10$ keV plasma, the DT reactivity may be reduced by a factor of 4. For $N_K > 1$, the predicted reactivity reduction is extreme, a factor of 40 or more.

The magnitude of reactivity reduction due to tail ion depletion using an updated Knudsen layer model, as presented by Albright *et al.*,[15] is shown in Figure 3.5. As the Knudsen number increases (say, as a consequence of decreasing density) at a given ion temperature, the DT fusion reactivity decreases substantially. For $T_i = 10$ keV, a Knudsen number of $N_K = 0.006$ produces a 4% reduction in reactivity, while $N_K = 0.12$ produces a 50% reactivity reduction. For Knudsen numbers approaching or exceeding unity, the fusion reactivity can be reduced by factors of 2-5 or more. Even at Knudsen numbers of order $N_K\sim0.01$-0.1, ion kinetic effects start to become important and ought to be considered. This Knudsen layer fusion reactivity reduction effect is observed in exploding pusher implosions with D^{3}He gas, as described in Section 3.2.

A preliminary simulation technique to assess ion kinetic effects, which will later be discussed in Section 3.2 in the context of interpreting exploding pusher experiments, has been developed by Hoffman *et al.* to build into a radiation-hydrodynamics code models of Knudsen reactivity reduction, ion diffusion, and enhanced ion thermal conduction.[30] At each time step in the hydro simulation, profiles of ion density and ion temperature, and the fusion reactivity within each zone, are modified according to these kinetic ion transport models that are generally not accounted for in mainline ICF codes. Multipliers on each of the relevant transport coefficients: the ion-ion collision time, Knudsen number, and ion heat flux, are constrained by fits to experimental data on a case-

---

[3] Because the spectrum of the resulting fusion products depends on the average energy of the reacting ions, the Knudsen loss of high-energy ions and consequent reduction in energy of the Gamow peak will produce a narrower fusion product spectrum than would otherwise be expected for a given effective ion temperature. As was alluded to in Chapter 2, this effect impacts the inference of ion temperature from the width of fusion product spectra.

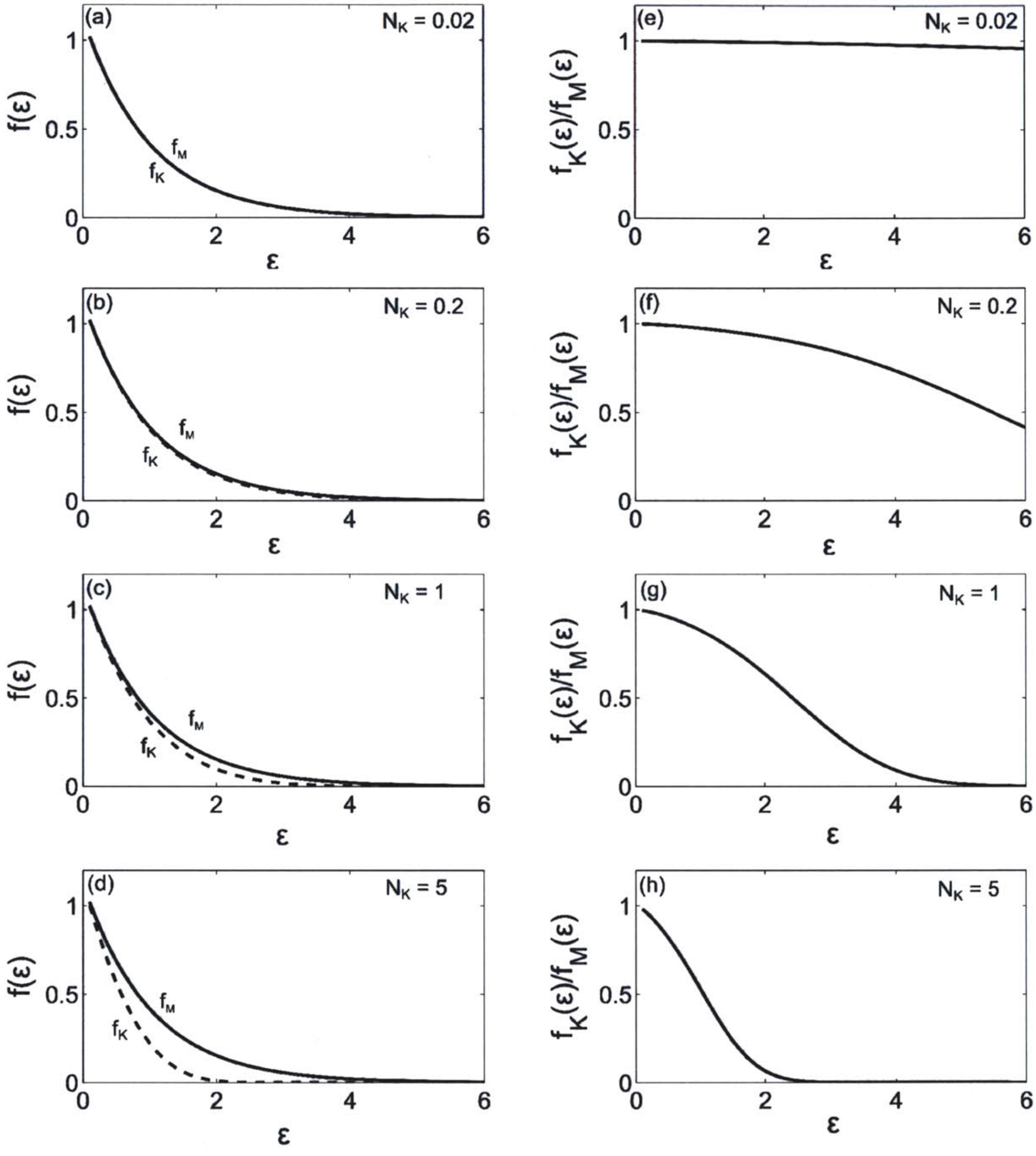

Figure 3.3. (a)-(d) Maxwellian (f_M, solid) and Knudsen-modified (f_K, dashed) ion distribution functions for an average D^3He ion at different Knudsen numbers (N_K).[14] As the Knudsen number increases, the loss of high-energy tail ions becomes more apparent, especially at ion energies $\epsilon \equiv mv^2/2kT > 2$ for $N_K > 1$. The loss of high-energy ions is reflected more clearly in the ratio (e)-(h) of Knudsen to Maxwellian distribution functions.

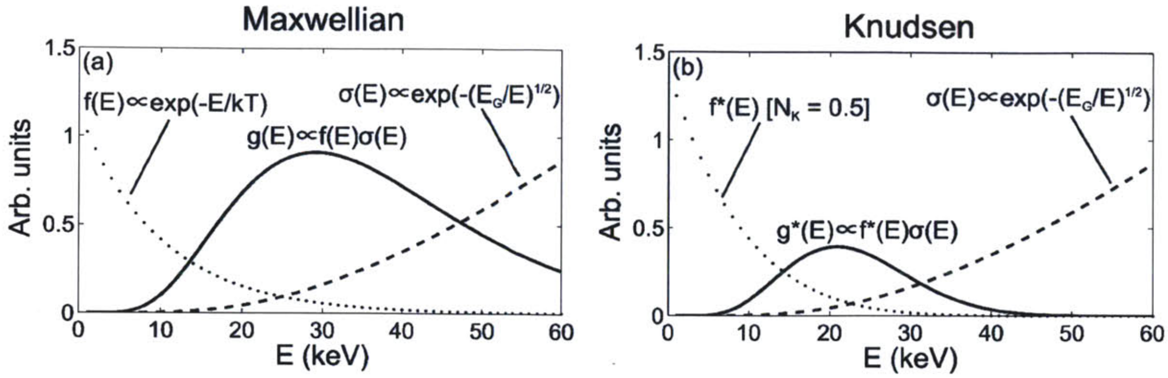

Figure 3.4. Gamow peak calculation for (a) Maxwellian and (b) Knudsen-modified distribution functions in a 10 keV DD plasma. In each, the distribution function $f(E)$ (dotted lines) is a decreasing function of center-of-mass energy E, while the DD fusion cross-section $\sigma(E)$ (dashed lines) is an increasing function of energy relative to the Gamow energy E_G. Their product $g(E)$ (solid lines) determines the rate of fusion percolliding ion center-of-mass energy, and the area under the curve is proportional to the total reaction rate, significantly less for the Knudsen-modified case (Knudsen number $N_K = 0.5$).

by-case basis. As such, this reduced ion kinetic (RIK) model is not a first-principles model, nor is it a self-consistent or truly kinetic treatment, but it does allow for a rough assessment of ion kinetic effects in a tractable simulation framework that extends beyond well-benchmarked hydrodynamic codes.

Both the broadening of the shock front early in time and the non-hydrodynamic behavior prevalent in the core after shock convergence could adversely impact implosion performance in ICF generally, beyond merely during the shock phase. Though the ion mean free path around the time of peak convergence in an ignition implosion is considerably shorter than during shock convergence, it is conceivable that "kinetic" conditions in the incipient hot-spot affect later implosion performance. Non-local ion transport of particles and heat, which is significant during shock convergence, may impact the conditions preceding the main compression phase. Knudsen tail ion depletion can perturb the core plasma after shock convergence and may also affect the fusion reactivity even at compression burn if 3D mix is significant and the effective surface area of the hot-spot/cold-fuel interface is large. Investigation of the degree to which ion kinetic effects at shock convergence impact the main compression phase is an active and ongoing area of research.

The following sections describe studies which have quantitatively assessed the importance of ion kinetic effects during the shock phase of ICF implosions, using shock-driven, exploding pusher implosions.

3.2 Exploration of the Transition from the Hydrodynamic-like to the Strongly Kinetic Regime in Shock-Driven Implosions

Toward investigating the impact of ion kinetic effects, clear evidence of the transition from hydrodynamic-like to strongly kinetic conditions in shock-driven implosions has been, for the first time, revealed and quantitatively assessed. Implosions with a range of initial equimolar D^3He gas densities show that as the density is decreased, hydrodynamic simulations strongly diverge from and increasingly overpredict the observed nuclear yields, from a factor of ~2 at 3.1 mg/cm^3 to a factor of 100 at 0.14 mg/cm^3. (The corresponding Knudsen number, the ratio of ion mean-free-path to minimum

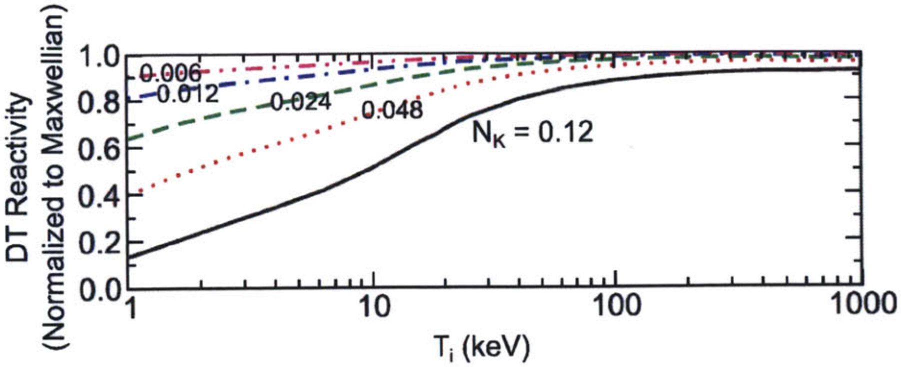

Figure 3.5. DT fusion reactivity reduction due to Knudsen layer effects. At a given ion temperature, the reactivity relative to the typical Maxwellian-averaged reactivity is a decreasing function of Knudsen number N_K. As N_K approaches a significant fraction of unity, and even by $N_K = 0.12$, the reactivity reduction becomes substantial. Knudsen numbers around or above 0.3 are clearly in a regime where ion kinetic effects are present, as is relevant to experiments discussed later in this chapter. This figure was modified from the version published by Albright *et al.*[15]

shell radius, varied from 0.3 to 9; similarly, the ratio of fusion burn duration to ion diffusion time, another figure of merit of kinetic effects, varied from 0.3 to 14.) This result is shown to be unrelated to the effects of hydrodynamic mix. As a first step to garner insight into this transition, the reduced ion kinetic (RIK) model that includes gradient-diffusion and loss-term approximations to several transport processes was implemented within the framework of a 1D radiation-transport code. After empirical calibration, the RIK simulations reproduce the observed yield trends, largely as a result of ion diffusion and the depletion of the reacting tail ions. This work has been published in *Physical Review Letters.*[31]

3.2.1 Overview

As discussed previously, inertial confinement fusion (ICF) implosions, whether for ignition[32] or non-ignition[33,34] experiments, are nearly exclusively modeled as hydrodynamic in nature with a single average-ion fluid and fluid electrons.[29,35] However, in the early phase of virtually all inertial fusion implosions, strong shocks are launched into the capsule where they increase in strength and speed as they converge to the center and abruptly and significantly increase the ion temperature in the central plasma region. In this process, and in the rebound of the shock from the center, which initiates a burst of fusion reactions (i.e. the fusion shock burn or shock flash[36]), the mean-free-path for ion-ion collisions can become, especially for lower-density fueled implosions, sufficiently long that both the shock front itself and the resulting central plasma are inadequately described by hydrodynamic modeling. This process and the transition of regimes from hydrodynamic-like to strongly kinetic are the focus of this section.

Recent kinetic and multiple-ion-fluid simulations have begun to explore deviations from average-ion hydrodynamic models, particularly during the shock phase of implosions when such effects are potentially paramount. For example, in an effort to explain observed yield anomalies in multiple-ion fuels of D^{3}He, DT, and DT^{3}He,[21,23,22] researchers have investigated multiple-ion-fluid effects[17,18,20] as well as utilized a hybrid fluid-kinetic model.[11,12] Other modeling work has included ion viscosity and non-local ion transport[13] in order to reduce discrepancies with shock-generated nuclear yields. Very recently a model for Knudsen layer losses of energetic ions,[14] based in part on earlier work,[2] was explored for a variety of plastic capsule implosions with relatively thick walls, all largely ablatively-driven (not shock-driven), and with THD fuel. In their work, inclusion of non-Maxwellian effects and a turbulent mix model brought their simulated yields into better agreement with measurements.

In contrast to previous studies, this work represents a comprehensive experimental effort to isolate and carefully explore ion kinetic effects in shock-driven implosions by systematically varying the ion-ion mean-free-path relative to the minimum shell radius, i.e. from a regime where the hydrodynamic description is approximately valid to one where it is strongly violated. To achieve this goal, this experimental campaign used virtually identical glass capsules and laser drive conditions; varied only the fill density of equimolar D^3He (from 3.1 to 0.14 mg/cm^3); and made the most comprehensive set of diagnostic measurements possible so as to achieve the most credible hydro-kinetic parameters and to allow, in the future, the highest-fidelity comparison to simulations. The experimental measurements include absolute yields for both DD and D^3He reactions

$$\mathrm{D} + \mathrm{D} \rightarrow {}^3\mathrm{He}(0.82\ \mathrm{MeV}) + \mathrm{n}(2.45\ \mathrm{MeV}) \tag{3.2}$$

$$\mathrm{D} + {}^3\mathrm{He} \rightarrow \alpha(3.6\ \mathrm{MeV}) + \mathrm{p}(14.7\ \mathrm{MeV}); \tag{3.3}$$

burn-averaged ion temperatures (T_i) for both DD and D^3He reactions; scattered light from the implosion drive; x-ray images of the imploding capsule for determination of the convergence (and the minimum shell radius); secondary nuclear yield measurements to infer the fuel areal density and convergence; and bang times and, usually, burn durations from both DD and D^3He reactions. As will be shown, even the shock burn duration, when compared to ion diffusion times (inferred from this collection of experimental measurements), is insightful and is an excellent figure-of-merit for understanding the transition from hydrodynamic to strongly kinetic regimes (see Table 3.1). It is demonstrated that standard and well-known hydrodynamic simulations[7,10,8] are increasingly discrepant with experimental results as the ion mean-free-path becomes larger than the minimum shell radius.

3.2.2 Exploding-Pusher Experiments on OMEGA

A series of glass-shell exploding pusher implosions were performed on the OMEGA laser facility.[37] The capsules had an outer diameter of 860±12 μm, a wall thickness of 2.3±0.1 μm, a density of 2.15 g/cm^3, and were filled with a range of fill densities of equimolar D^3He gas, from 3.1 to 0.14 mg/cm^3. The capsules were imploded by 59 or 60 symmetrically-pointed beams, delivering 14.6 kJ in a 0.6-ns pulse. Details of the experimental setup are summarized in Appendix A.

Rapid laser absorption in the thin SiO_2 ablator caused a strong, spherically-converging shock to be launched into the gas with a resulting Mach number of $M{\sim}15$. As the shock rebounds at the center of the implosion, DD and D^3He fusion burn is initiated along the shock rebound trajectory.

Radiation-hydrodynamic simulations were performed using three well-known and benchmarked hydrodynamic simulation codes: LILAC,[7] HYADES,[8] and DUED.[10] As will be shown in Figure 3.9, all three gave very similar predictions in this campaign and, as a representative case, the 1D version of the 2D Lagrangian DUED code[10,38] is utilized herein; it includes flux-limited electron thermal transport with a flux limiter of $f = 0.07$ and non-LTE opacities. (Some of the physics included in these simulations is described further in Appendix G.) Laser absorption is modeled by inverse bremsstrahlung with laser refraction and a 10% reduction in the input laser energy so that the time-averaged simulated absorbed laser fraction matches experimental measurements by full aperture backcsatter stations (FABS).[39] Ion viscosity is included. The DUED simulation of an implosion with 1.1 mg/cm^3 D^3He is shown in Figure 3.6. Lagrangian mass-element trajectories as a function of time show a rapidly converging shock, which rebounds at ~0.7 ns.

Figure 3.6. Lagrangian mass-element trajectories in 1D DUED simulations of an implosion with 1.1 mg/cm^3 D^{3}He. The laser pulse is a square pulse, about 0.6 ns in duration.

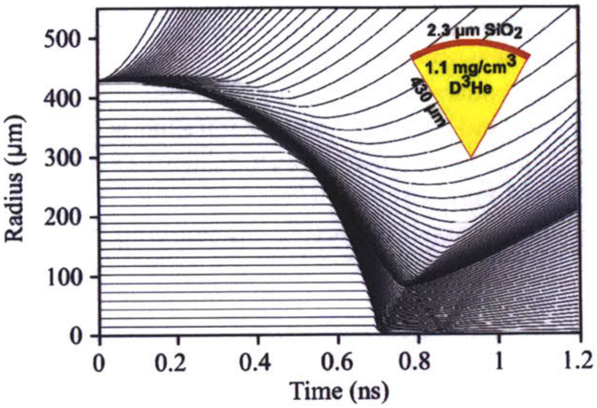

To characterize these implosions, the experimentally-determined ion density, D^{3}He-burn-averaged ion temperature, and estimated ion-ion mean free path around bang time across the range of initial gas densities are shown in Figure 3.7. These plots illustrate how the plasma conditions differ across the implosions with different initial gas densities in a way that creates a large variation in ion-ion mean free path, from the hydrodynamic-like (high density) to the strongly kinetic (low density) regime.

For decreasing initial gas density, the Maxwellian-average mean-free-path for ion-ion collisions around nuclear bang time, based on measured quantities, varied from ~40 μm to ~800 μm, from a regime that is reasonably hydrodynamic-like to one that is strongly kinetic. This is reflected in the Knudsen number $N_K \equiv \lambda_{ii}/R_{shell}$, the ratio of ion mean-free-path to minimum shell radius, which varied from ~0.3 to 9. The Knudsen number is another figure-of-merit for studies of hydrodynamic and kinetic behavior. In a broader context, this near single-parameter study allows for a quantitative assessment of long mean-free-path effects in a regime comparable to the early phases of cryogenically layered hot-spot ignition implosions, in which a M~10-50 shock converges in a DT gas of initial density 0.3 mg/cm^3.[41,32]

3.2.3 Principal Experimental Results

Measured DD and D^{3}He yields, Doppler-broadening-inferred burn-averaged ion temperatures (T_i), and DD bang time, the time of peak fusion production, are compared to post-processed DUED-predicted values in Figure 3.8. DD yields and burn-averaged T_i were measured using the neutron time of flight (nTOF), suite[42] while D^{3}He yields and burn-averaged T_i were measured using wedge-range-filter (WRF) proton spectrometers and charged particle spectrometers (CPS).[43] Excellent agreement observed between the spectral widths of the D^{3}He-α and D^{3}He-p spectra (see Appendix A) gives a high degree of confidence in the D^{3}He-burn-averaged ion temperature measurement. The DD bang times were measured using the neutron temporal diagnostic (NTD).[44] Uncertainties in measured yields are ~±10%, while the uncertainty in the DD-burn-averaged T_i is ±0.5 keV, and the uncertainty in the D^{3}He-burn-averaged T_i is ±2 keV. The absolute uncertainty in DD-neutron bang time is ±50 ps.

DUED-simulated DD and D^{3}He yields are slowly varying as the initial gas density is decreased, increasing in the case of D^{3}He, as the decrease in density is balanced or overcome by an increase in temperature and fusion reactivity. In contrast, the measured yields decrease dramatically at low density. This discrepancy in trends is reflected in the yield-over-clean (YOC), the ratio of

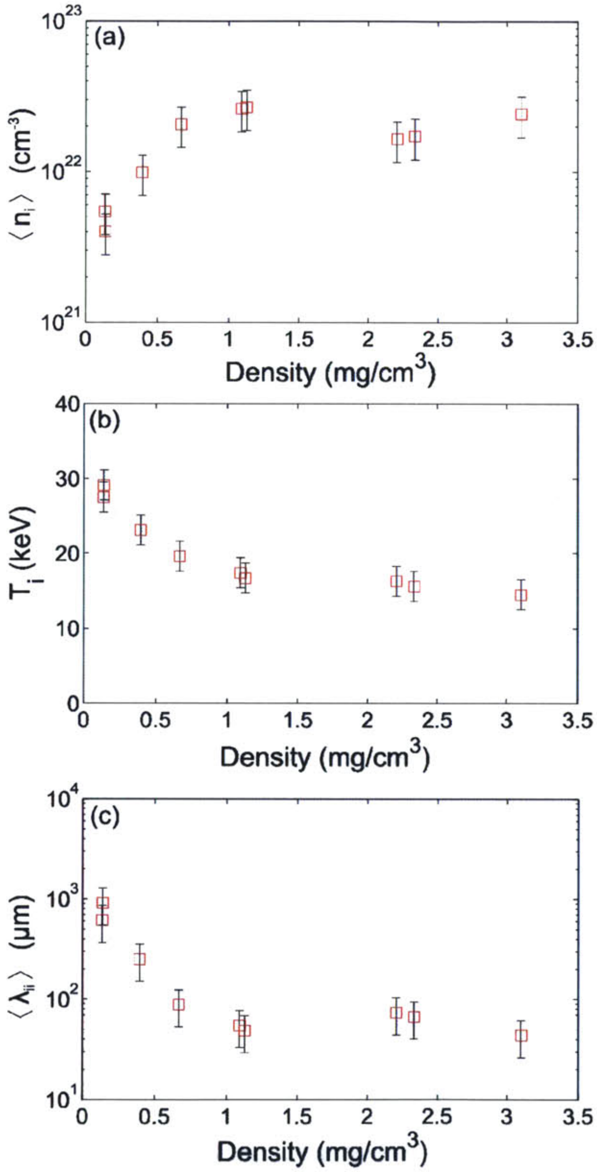

Figure 3.7. Measured (a) ion density, (b) ion temperature, and (c) ion-ion mean free path as a function of initial gas density. The ion density was inferred either from the secondary-yield-measured fuel ρR[40] or from the measured shell convergence. The ion temperature is the D^{3}He-burn-averaged ion temperature inferred from the linewidth of the D^{3}He-p spectrum. The ion-ion mean free path is given by the ion density and a yield-averaged ion temperature of both DD and D^{3}He (slightly different than the D^{3}He-burn-averaged ion temperatures shown in (b)). These plots illustrate how the plasma conditions differ across the implosions with different initial gas densities in a way that creates a large variation in ion-ion mean free path.

Figure 3.8. Measured and DUED-simulated DD and D^3He (a) yields, (b) yields-over-clean (YOC) relative to DUED simulations, (c) measured and DUED-simulated burn-averaged ion temperatures, and (d) measured and DUED-simulated DD bang time as a function of initial gas density. The initial gas density in cryogenically layered ignition experiments, 0.3 mg/cm^3,[32] is indicated with the dotted vertical line. This indicates that such ignition implosions during the shock convergence phase are in the kinetic regime. Two separate experiments were performed at 0.14 mg/cm^3 with nearly identical results, indicating excellent repeatability.

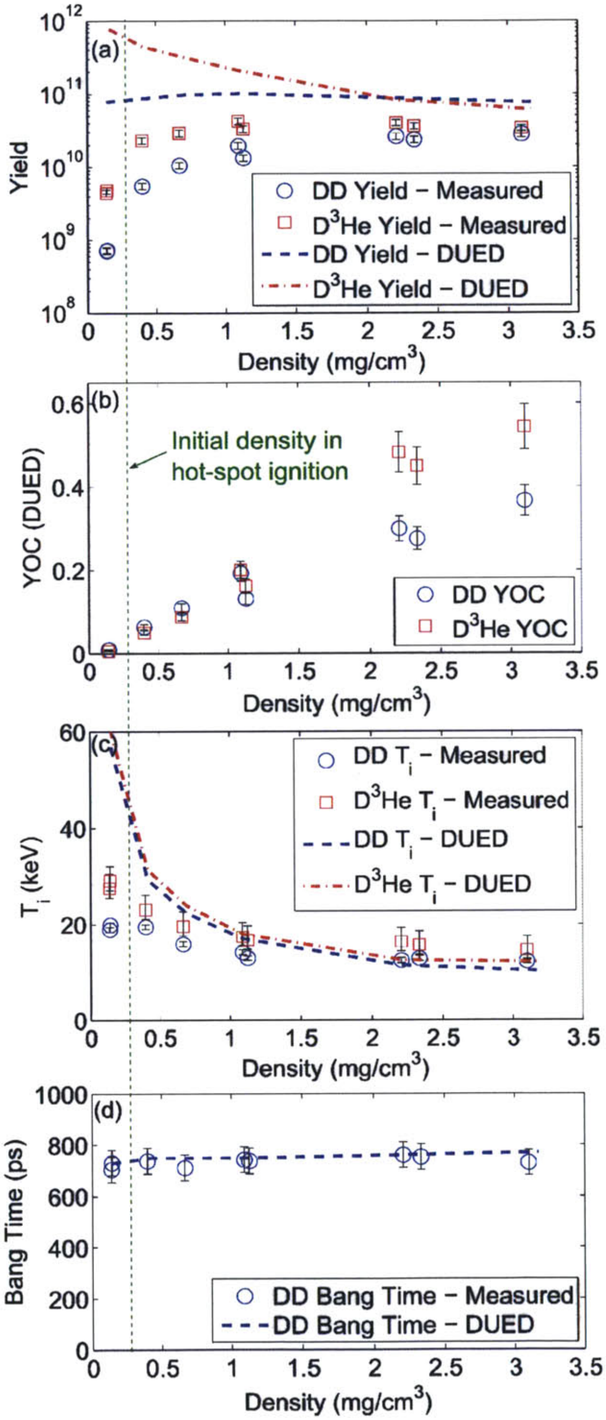

measured yields to yields simulated by 1D ("clean") hydrodynamic simulations that do not include a turbulent mix model or kinetic effects. This decrease in YOC is especially notable below ~1.7 mg/cm^3 and reflects the weakening confinement of fuel ions as the ion mean-free-path becomes significant relative to the shell radius. Above ~1.7 mg/cm^3, representing a more hydrodynamic-like regime, the YOC reaches ~0.35 for DD and ~0.5 for D^{3}He yields. Even in the "hydrodynamic" limit of these experiments, the YOC fails to reach unity. As will be discussed in Section 3.2.4, the Knudsen number in these high-density experiments is an already-elevated N_K~0.3, in a regime where ion kinetic effects are starting to have an impact on fusion production. It will be shown in Section 3.3 that these results match the findings of exploding pusher experiments at the NIF, where ion kinetic effects are starting to have an influence on fusion yields at N_K~0.3. For N_K<0.1, and certainly by N_K~0.01, the impact of ion kinetic effects is significantly diminished.

To demonstrate that these yield results are universal to ICF hydrodynamic simulations and not merely specific to DUED, the yields simulated by four different hydrodynamic codes – DUED, LILAC, HYADES, and the hydrodynamic simulation underlying the RIK model – are shown in Figure 3.9. To within a factor of ~2-3, the different codes give the same predictions for the DD and D^{3}He yields, and they all show similar trends of yield as a function of initial gas density. As a result, DUED appears to be a fair representative of the many different hydrodynamic codes used to model these experiments, and a comparison of the experimental results to any of the simulations would produce the same conclusions.

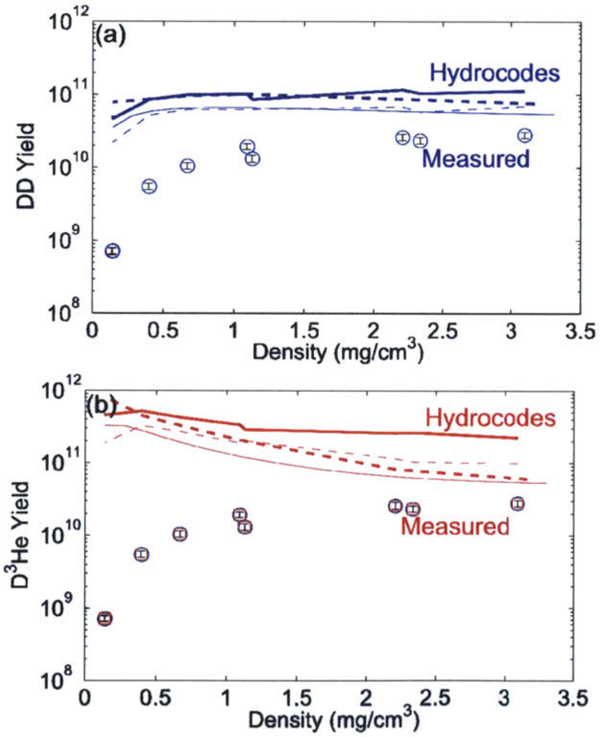

Figure 3.9. Measured and simulated (a) DD and (b) D^{3}He yields as a function of initial gas density. The yields predicted by the various codes, DUED (thick dotted line), LILAC (thick solid line), HYADES (thin dashed line), and the hydrodynamic simulation underlying the RIK model (thin solid line) are within a factor of ~2-3 of each other and show similar trends with initial gas density. Thus, the conclusions that are drawn from comparing the measured yields (markers) to the simulations are the same for each of the different hydrocodes.

Both the measured and DUED-simulated ion temperatures increase as gas density is decreased, suggesting that more energy is coupled to each ion at lower gas density; however, the trend in T_i is much stronger in simulation than in the experiment. Also, the difference between DD and D^{3}He burn-averaged ion temperatures indicates the presence of temperature gradients in the fuel, though based on the long ion-ion collision times in more strongly kinetic experiments (~900 ps at the lowest gas density) this difference may also partly reflect a difference in temperatures between

^{3}He and D ions.

The measured DD bang time is relatively independent of gas density and also matches the DUED predictions. This approximate invariance is reasonable, given that the shock decouples from the shell only ~300 ps before shock rebound (Figure 3.6), such that the higher-velocity shock in the low-density implosion reaches the center only slightly earlier than the lower-velocity shock in the high-density implosion.

A compendium of measurements from these experiments, as well as additional data not discussed here, including multiple fusion-product spectra, x-ray images, scattered light measurements, and fusion burn profiles, are presented in Appendix A.

3.2.4 Discussion of Kinetic Effects

In order to qualitatively understand the strong decrease in YOC, this general trend is recast in terms of the Maxwellian-averaged ion-ion mean-free-path, where $\lambda_{ii} \propto T_i^2/n_i$.[4] As the initial fill density is decreased from 3.1 to 0.14 mg/cm^3, the ion density after shock convergence decreases from ~2×10^{22} to ~5×10^{21}.[5] Concurrently with the decrease in ion density, the ion temperature (a yield-weighted average of DD- and D^{3}He-burn-averaged ion temperatures) increases from 14 keV to 28 keV, such that over the range of the experiment, λ_{ii} varies from ~40 μm at high density to ~800 μm at low density. At high density, the ion-ion mean-free-path is ~$0.3R_{shell}$, where R_{shell} is the x-ray-framing-camera (XRFC)[45] estimated minimum shell radius ~130 μm. At high density, the Knudsen number N_K~0.3, and a hydrodynamic description is more valid. At low density, λ_{ii}~$9R_{shell}$ (N_K~9), with R_{shell} ~85 μm, such that the hydrodynamic description is severely invalid and long ion mean-free-path effects, as reflected by the large Knudsen number, are significant (see Table 3.1).

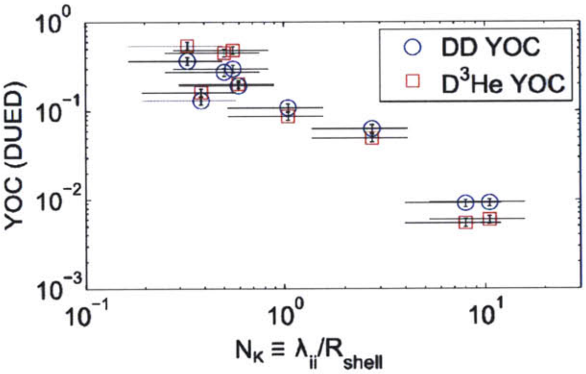

Figure 3.10. Yield-over-clean (YOC) relative to 1D DUED simulations for both DD and D^{3}He reactions as a function of the Knudsen number, the ratio of the ion-ion mean-free-path (at bang time) to the measured minimum shell radius.

The DD and D^{3}He YOC relative to DUED simulations (originally plotted as a function of initial gas density in Figure 3.8b) are now shown as a function of $N_K \equiv \lambda_{ii}/R_{shell}$ in Figure 3.10. Both the DD and D^{3}He YOC show a dramatic trend of decreasing YOC with increasing N_K, from YOC$_{DD}$ ~0.35 and YOC$_{D^3He}$ ~0.50 at N_K~0.3 to YOC$_{DD}$ ~0.009 and YOC$_{D^3He}$ ~0.006 at N_K~9. The hydrodynamic code does an increasingly poor job matching the measured yields as the conditions in the implosion become strongly kinetic.

---

[4] The ion-ion mean-free-path used throughout is the geometric mean of D and ^{3}He mean-free-paths, inferred from measured quantities (see Appendix F).

[5] The ion density is inferred either from the fuel ρR as measured by the ratio of secondary DT-neutron yield to primary DD-neutron yield[40] or from the minimum shell radius as estimated from x-ray framing camera (XRFC) images.[45] The decrease in initial gas density is offset partially by an increase in shell convergence, though convergence effects and the significance of hydrodynamic instabilities and mix is, as will be shown, minimal

An important issue is whether the observed YOC trend could be a result of hydrodynamic mix increasingly quenching the yield as the initial fuel density decreases, as might well be expected in ablatively-driven implosions. A fall-line analysis[46] using hydrodynamics simulations indicates that hydrodynamic fuel-shell mix cannot substantially account for this trend, as should be expected for these low-convergence (convergence ratio ~4-5), shock-driven implosions in which there is virtually no deceleration phase.[6] Eliminating hydro-simulated yield generated outside of the radius corresponding to 20% of the distance from the fuel-shell interface to the fall-line (the maximum-velocity trajectory of the fuel-shell interface) models a near-worst-case reduction of fusion yield. This analysis assumes that the shell is entirely mixed with the fuel in that volume and fusion reactions are completely quenched. At 3.1 mg/cm^3, the reduction in yield due to mix is negligible, while even at 0.14 mg/cm^3, mix accounts for at most a factor of 2 yield reduction. Hydrodynamic mix falls short then by at least a factor of 20 in explaining the factor of 40 difference in YOC observed between 0.14 mg/cm^3 and 3.1 mg/cm^3.

In a similar vein, and again based solely on experimental measurements, the ratio R_τ of the fusion burn duration to the ion diffusion time is calculated. R_τ is another figure of merit for describing hydrodynamic-kinetic regimes. The characteristic diffusion timescale based on the ion mean-free-path and thermal velocity, $\tau_{diff} = R^2_{shell}/(\frac{1}{3}\lambda_{ii}v_{ti})$, is ~10 ps for D ions and ~40 ps for ^{3}He ions at 0.14 mg/cm^3. These diffusion times are substantially shorter than the duration of fusion burn, ~120 ps for D^{3}He fusion and ~140 ps for DD fusion. Conversely, in the hydrodynamic-like regime (3.1 mg/cm^3), τ_{diff} is ~600 ps for D ions and 2400 ps for ^{3}He, such that diffusion is insignificant over the duration of fusion burn, ~200 ps for DD fusion and ~160 ps for D^{3}He fusion. As shown in Table 3.1, R_τ varies from ~0.3 to ~14 for DD and from ~0.07 to ~3 for D^{3}He fusion. Similar to the Knudsen number, R_τ reflects this transition from hydrodynamic-like to strongly kinetic. When $R_\tau \gtrsim 1$, ion diffusion must be important, and this will not be adequately accounted for in the standard hydrodynamic models.

Table 3.1. Key hydro-kinetic parameters, all inferred from measured quantities, in the hydrodynamic-like and strongly kinetic regimes, including the initial gas density, the yield-averaged ion temperature, the average ion-ion mean-free-path at bang time, the minimum shell radius, the Knudsen number, the DD (D^{3}He) burn duration, the D (^{3}He) ion diffusion time, and the ratio of DD (D^{3}He) burn duration to D (^{3}He) diffusion time.

Initial gas density (mg/cm^3)	$\langle T_i \rangle$ (keV)	λ_{ii} (μm)	R_{shell} (μm)	N_K	$\tau_{burn,DD}$ ($\tau_{burn,D3He}$) (ps)	$\tau_{diff,D}$ ($\tau_{diff,3He}$) (ps)	$R_{\tau,DD}$ ($R_{\tau,D3He}$)
3.1	14	~40	~130	~0.3	~200 (~160)	~600 (~2400)	~0.3 (~0.07)
0.14	28	~800	~85	~9	~140[7] (~120)	~10 (~40)	~14 (~3)

A kinetic-based analytic model of the implosion that accounts for the reduced energy coupling into the plasma after shock convergence is able to explain the measured yield trend. As described earlier, based on the Guderley solution of a strong, spherically-converging shock,[27] this model limits the thermal energy in the resulting hot-spot plasma to the thermal and kinetic energy in the incoming shock at the point where the shock front radius R_1 is equivalent to the ion-ion mean free path at the shock front (λ_1).[28] The final energy density in the plasma is determined to be

$$(Z+1)\frac{3}{2}n_F k_B T_F = \frac{1}{2}\rho_s V_s^2 + (Z+1)\frac{3}{2}n_1 k_B T_1 \qquad (3.4)$$

where the right-hand side is evaluated at a radius $R_1 = \lambda_1$ and ρ_s is the mass density in the shock front, V_s is the shock velocity, Z is the average ion charge, n_1 (T_1) is the incoming post-shock ion number density (ion temperature), and n_F (T_F) is the final ion number density (ion temperature) after shock rebound. As the shock converges to a radius equivalent to the local λ_{ii} in the shock front, the shock front width becomes larger than its radius and the ions are no longer effectively confined.

---

[6] In the deceleration phase of ablatively-driven implosions, Rayleigh-Taylor instabilities can introduce substantial mix, degrading implosion performance and reducing fusion yields.

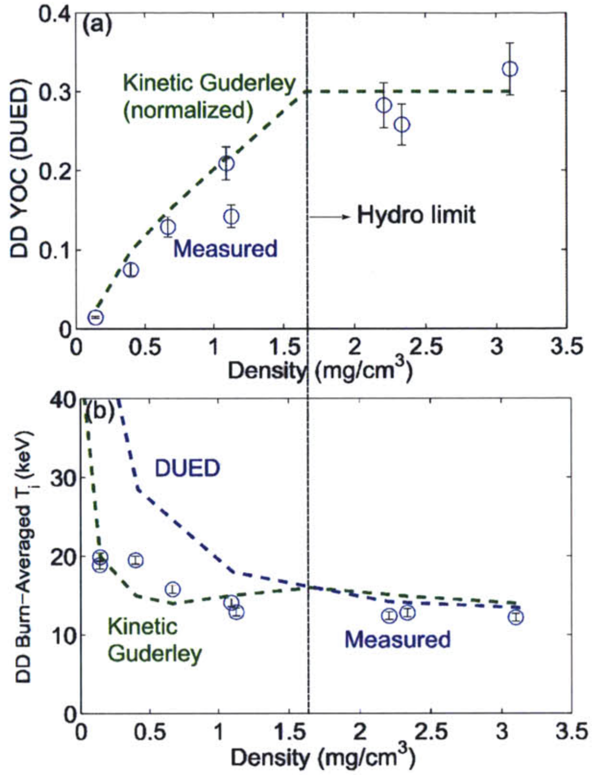

Figure 3.11. (a) DD yield-over-clean (YOC) and (b) DD burn-averaged ion temperature in DUED and the kinetic Guderley model. The kinetic Guderley model YOC is normalized to the value in the hydro regime, with the physics of the model expressed in the YOC trend in the kinetic regime.

The hydrodynamic limit is where the minimum shell radius R_{shell} is greater than the radius at which the incoming shock radius equals the shock-front mean free path ($R_{shell} > R_1 \sim \lambda_1$) and kinetic effects are ignored. In those experiments where $\lambda_1 > R_{shell}$, the kinetic model limits the resulting ion temperature and, therefore, the fusion yield. The kinetic Guderley model YOC trend is determined by the trend in the ratio of kinetic-limited final ion temperature to the ion temperature that would have occurred without this limitation, with the absolute YOC normalized to match the YOC in the hydrodynamic regime. The measured DD YOC and DD-burn-averaged ion temperatures are contrasted to hydrodynamic and kinetic Guderley model predictions in Figure 3.11. For initial fill densities below 1.7 mg/cm^3, where $\lambda_1 > R_{shell}$ and the kinetic model is applied, the model YOC normalized to the YOC in the hydrodynamic limit closely follows the measured DD YOC trend (Figure 3.11a). The kinetic-modeled ion temperatures also more closely match the data than do DUED predictions (Figure 3.11b). This Guderley model, which accounts for the weakened energy coupling as a result of long mean-free-path effects, can explain quantitatively the trend of diminished yield with longer mean free path.

As a computational step to begin exploring this hydro-kinetic transition, the previously-described reduced ion kinetic (RIK) model that includes gradient-diffusion and loss-term approximations to several transport processes was implemented within a 1D radiation-hydrodynamics code.[30] This model includes the effects of kinetic transport of ion mass, momentum, and thermal energy, and reduction in fusion reactivity owing to Knudsen-layer modification of ion-distribution tails when the ion mean-free-path around bang time approaches the shell radius.[14,15] The model requires empiri-

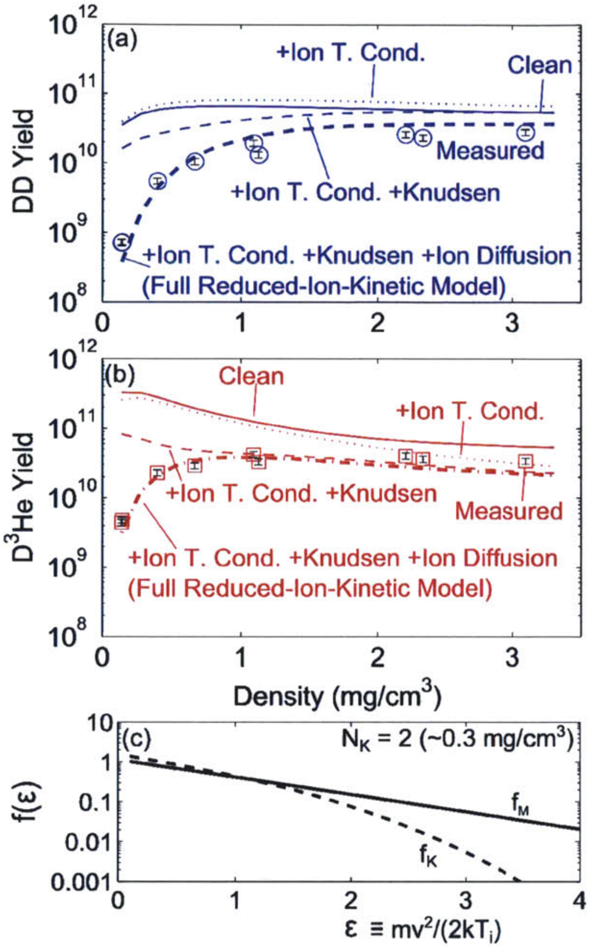

Figure 3.12. Measured (a) DD and (b) D^3He yields (symbols) in comparison to the reduced ion kinetic model (thick dashed lines) and to clean hydrodynamics simulations that ignored kinetic effects (thin solid lines). Also shown are yields from simulations that progressively added ion thermal conduction (thin dotted lines) and then Knudsen reactivity reduction (thin dashed lines) onto the clean simulations, with ion diffusion also included in the full reduced ion kinetic model (thick dashed lines). The difference between the curves shows the impact each individual kinetic effect has on the yields. The (c) Knudsen-modified ion distribution function (f_K, dashed),[15] area normalized to the original Maxwellian distribution function (f_M, solid), shows how tail ions are depleted for an average D^3He ion for a typical strongly-kinetic-regime ($\sim$0.3 mg/cm^3) Knudsen number of N_K=2.

cally determined parameters to calibrate its various flux terms. A single set of 5 model parameters is then constrained by the measured DD and D^3He yields, DD-burn-averaged T_i, DD bang time, and the laser absorption fraction over the entire data set (40 observables). A brief discussion of the RIK model and its fitting procedure is presented in Appendix A. These simulations used the nominal capsule diameter, shell thickness, and laser pulse parameters, varying only the initial fill density, as was done in the experiments. The code uses multigroup radiation diffusion, charged-fusion-product diffusion, flux-limited electron thermal diffusion ($f_e = 0.06$), and laser energy propagation via geometric ray tracing and deposition by inverse bremsstrahlung, with laser deposition and the flux limiter inferred from the observed bang time and absorption fraction.

Figure 3.12 shows the measured DD and D^3He yields in comparison to the reduced ion kinetic (RIK) model and the clean hydrodynamic simulation with kinetic effects turned off. Each kinetic effect – ion thermal conduction, reactivity reduction due to Knudsen modification of the ion distribution function, and ion diffusion – has been progressively implemented to show how each effect impacts the fusion yields over the density range. The measured yield trends are captured by the full reduced ion kinetic model over the entire density range. In contrast, the clean simulation shows a very different, flat trend, similar to that in DUED simulations (Figure 3.8a), though with slightly better agreement than DUED in the high-density limit due to a lower laser absorption fraction and electron flux limiter, which produce lower clean-simulated yields.

A breakdown of how each kinetic effect contributes to the overall reduction in fusion yield is illustrated in Figure 3.12a,b. Starting with a clean, hydrodynamic simulation, each kinetic effect is included one at a time, starting with enhanced ion thermal conduction, followed by Knudsen tail ion losses, and finally ion diffusion. The importance of each particular effect is determined by the best-fit model to the experimental results, with some uncertainty in the magnitude of each effect related to the quality of fit. As is discussed briefly in Appendix A, the chi-squared fit to this data set for the RIK model, which allows for variation in three kinetic-effect multipliers, is in reasonable agreement with the number of degrees of freedom. This indicates that the fit matches the data fairly accurately. The multipliers themselves are also reasonably well constrained.

The inclusion of ion thermal conduction actually produces a 10-20% *enhancement* of the DD yield in the high density limit, as thermal energy is efficiently conducted to larger radii, allowing for additional reactions. Conversely, ion thermal conduction causes a 20-50% decrease in the D^3He yield, as the high-temperature spike at the origin during shock convergence is smoothed out, suppressing the D^3He yield that is produced there in the pure hydrodynamic simulations. This effect is especially pronounced at high initial gas densities, as in those implosions an even larger fraction of D^3He reactions occur as a consequence of this temperature spike in the pure hydrodynamic simulations.

Knudsen tail ion losses cause an additional reduction in fusion yields, by 20-60% for DD yields and 20-70% for D^3He yields, with the largest effect – as expected – at the lowest initial gas density. In experiments where the ion-ion mean free path is longest, the high-energy tail ions are even more susceptible to non-confinement and escaping into the shell. The addition of ion diffusion further reduces the DD yield by 30% at high density and by a factor of 40 at low density and reduces the D^3He yield by only 5% at high density and a factor of 25 at low density. It is especially notable that ion diffusion has virtually no impact on the D^3He yield above an initial gas density of 1 mg/cm^3, but rapidly becomes important below that density. The increasing impact on the DD yield is somewhat more gradual, though also becoming more significant below 1 mg/cm^3. Overall, the addition of ion diffusion, the loss of confinement of ions even within the Maxwellian framework, is the most significant kinetic effect impacting fusion yields in these shock-driven, long-mean-free-path experiments.

It is also noteworthy and physically reasonable that for both DD and D^3He yields, as the experiments increase in Knudsen number (decrease in initial gas density), first tail ion loss effects are important, and then bulk ion diffusion becomes dominant. At smaller Knudsen numbers (N_K~0.3), the tail of the ion distribution function, with even longer mean free paths than the thermal average, is poorly confined, while bulk, thermal ions are still reasonably confined. However, for larger Knudsen numbers (N_K>1), the thermal ions themselves are poorly confined and readily escape into the shell. Thus, for increasing N_K, the importance of bulk ion diffusion relative to tail ion loss increases.

To summarize the RIK model results, the principal kinetic effects responsible for the reduction in yield are: firstly, the diffusion of ions out of the hot fuel region, which becomes especially significant at the lowest initial gas densities; and, secondly, the reduction in fusion reactivity due to the non-Maxwellian depletion of high-energy ions. Around a density of 0.3 mg/cm^3, representative of the strongly kinetic regime, reduced fusion reactivity due to Knudsen modification of the ion distribution function is reponsible for a factor of ~2.5 (~4) reduction in DD (D^3He) yield relative to the hydrodynamic model, while ion diffusion accounts for an additional factor of ~10 (~5) DD (D^3He) yield reduction. For a Knudsen number of $N_K = 2$, typical of the strongly kinetic regime around 0.3 mg/cm^3, the tail of the Knudsen-modified ion distribution function is significantly depleted relative to the corresponding Maxwellian ion distribution function, especially for normalized ion energies $\epsilon \equiv mv^2/2kT_i > 2$ (see Figure 3.12c). As the fusing reactant ions typically have energies well above the thermal energy, this depletion of high-energy ions due to long mean-free-paths can have a large impact on the fusion reactivity.

3.2.5 Use of Burn Profile Measurements to Assess Ion Diffusion

Additional evidence of the impact of ion diffusion is provided through a comparison of measured spatial burn profiles to burn profiles from another set of simulations, using hydrodynamic models with and without diffusion. As discussed in Chapter 2, the proton core imaging system (PCIS)[47,48] uses penumbral imaging to measure the DD-p and D^3He-p spatial burn profiles. The burn profiles have been measured across the range of initial gas densities in these experiments. Figure 3.13 shows measured profiles of 2D surface brightness (line-of-sight integral of radial burn profile) in comparison to hydro-simulated brightness profiles at 0.4 mg/cm^3, representative of the kinetic regime, and at 3.1 mg/cm^3, representative of the hydrodynamic regime.

Across the hydrodynamic and kinetic regimes, the measured DD and D^3He brightness profiles (and burn profiles) appear centrally peaked. In contrast, the pure hydrodynamic simulation predicts a profile that is peaked far from the center, near the gas-shell interface. However, the inclusion of classical ion diffusion in the simulations greatly reduces the overall fusion yield and preferentially eliminates yield produced near the gas-shell interface. As a consequence, the diffusion model produces simulated brightness profiles that are centrally peaked, in qualitative agreement with the measured brightness profiles. In the hydrodynamic regime, diffusion has a minimal impact on both the magnitude and shape of fusion burn profiles. Thus, the centrally-peaked measured brightness profiles are in good agreement with the simulated brightness profiles either with or without diffusion. These data confirm the interpretation of the experimental findings based on the yield results: ion kinetic effects, including ion diffusion, become substantial as the mean free path of the ions becomes large relative to the radius of the fuel region.

A remaining question is the nature of this effect: as diffusion entails the outward propagation of gas ions and the inward propagation of shell ions, which of those effects is dominant? The Knudsen layer picture requires high-energy gas ions to escape into the shell (this picture could also be thought to apply to bulk gas ions even within a Maxwellian framework). Alternatively, the observed diffusion effect could be the consequence of high-Z shell ions diffusing inward, reducing the gas temperature in that region, and quenching the yield. For Knudsen numbers $N_K \gg 1$, it may no longer make sense to discuss collisions between fuel ions, and the relevant ion-ion mean free path may be between the hot fuel ions and the cooler shell ions into which they are diffusing. The issue of characterizing a "diffusion" process under conditions of long ion mean free path in the fuel are discussed further in Appendix C. A possible experiment to address the question of diffusion across interfaces, with implosions using alternative shell materials, is proposed in Section 3.4.

3.2.6 Conclusions

In conclusion, a systematic and comprehensive set of experiments using shock-driven D^3He implosions, in which a wide array of diagnostics were employed, has demonstrated a dramatically increasing yield deficit, relative to hydrodynamic predictions, with decreasing initial gas density. This study methodically varied the Knudsen number N_K from 0.3 to 9; or the ratio of the fusion burn duration to the ion diffusion time, R_τ, from $\sim$0.3 to $\sim$14. Both dimesionless parameters, directly inferred from experimental measurements, indicate the degree of ion kinetic effects. Hydrodynamic mix cannot account for these observations. A kinetic Guderley shock model, which limits the final temperature in the plasma based on the energy contained in the shocked plasma when the shock converges to a radius equivalent to the ion-ion mean free path, reproduces the observed yield trend and agrees reasonably with measured ion temperatures. This simple kinetic

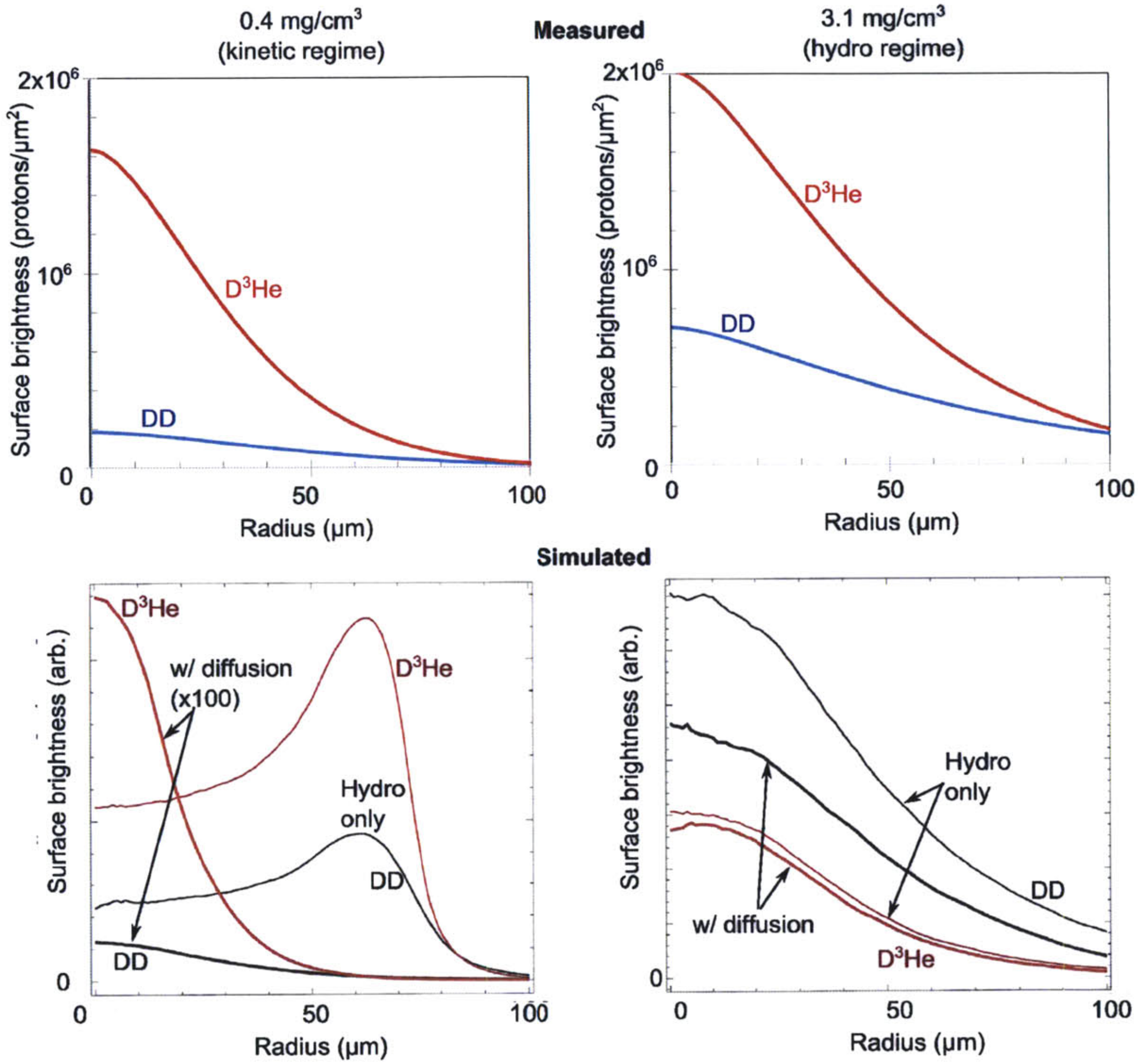

Figure 3.13. Measured and simulated surface brightness profiles of proton emission in OMEGA exploding pushers in the kinetic regime (0.4 mg/cm^3) and the hydrodynamic regime (3.1 mg/cm^3). The inclusion of ion diffusion in the simulations has a large impact in the kinetic regime, bringing modeled and measured profiles into qualitative agreement. In the hydrodynamic-like regime, ion diffusion has a minimal impact. These results confirm what was shown in the yield results.

model encapsulates the long-mean-free-path physics inherent in the converging shock front early in these implosions. As a computational step towards illuminating the role of ion kinetic effects, a model requiring empirically-calibrated parameters for determining the flux terms is utilized. This model incorporates ion transport and deviations from Maxwellian behavior within the framework of a radiation-hydrodynamics simulation, and it effectively captures the measured yield trends. In a separate set of simulations, the inclusion of ion diffusion is required to reproduce measured spatial fusion burn profiles in the long-mean-free-path regime, further confirming the importance of ion kinetic effects under such conditions. In a broader context, an important question concerns the potential role of kinetic effects in the evolution of ignition implosions at the National Ignition Facility.[32] Could the shock convergence phase, which mirrors low-density, shock-driven implosions discussed herein, impact the subsequent evolution of the compressional phase of the implosion, which is highly collisional and hydrodynamic in nature? It is possible that insight into this question could be culled by measuring, with high accuracy, the differential as well as the absolute timing of both shock and compression bang times in surrogate ignition capsules filled with D^{3}He,[49] as is being planned,[50,51] and contrasting these measurements to the predictions of hydrodynamic simulations used at the National Ignition Facility.

3.3 Utilization of NIF Diagnostic Development Shots for Investigation of Ion Kinetic Effects in Direct-Drive Exploding-Pusher Implosions

Shock-driven exploding pushers have also been studied at the National Ignition Facility to gain insight into the impact of ion kinetic effects during the shock convergence phase of ICF implosions. Ride-along measurements of yield, ion temperature, areal density (ρR), shell convergence, and bang time have been made on experiments designed for diagnostic calibration at the NIF. These measurements, which were obtained on D$_2$ and D^{3}He thin-glass-shell implosions, probe the shock convergence phase of ICF implosions, a critical stage in hot-spot ignition experiments. The data complement previous studies of kinetic effects in shock-driven implosions on OMEGA, described above. Ion temperature and fuel ρR inferred from fusion-product spectroscopy are used to estimate the ion-ion mean free path in the gas. A trend of decreasing yields relative to the predictions of 2D DRACO hydrodynamics simulations with increasing Knudsen number (the ratio of ion-ion mean free path to minimum shell radius) suggests that ion kinetic effects are increasingly impacting the hot fuel region, in general agreement with previous results. The long mean free path conditions giving rise to ion kinetic effects in the gas are often prevalent during the shock phase of both exploding pushers and ablatively-driven implosions. In addition, a D^{3}He exploding pusher shot (N121128) demonstrates that a monoenergetic proton source could easily be implemented at the NIF for backlighting a broad range of high energy density (HED) experiments in which fields and flows are manifest, a technique which has been used widely on OMEGA, and which will be elaborated on in Chapter 5. This work will be submitted to *Physics of Plasmas.*[52]

3.3.1 Additional Background on Exploding Pushers

Thin, spherical glass shells were among the first capsules used in laser-driven inertial confinement fusion (ICF) research.[53–56] Known as "exploding pushers", these implosions are characterized by rapid heating of the thin shell, which explodes and drives a shock wave into the fuel. This shock wave compresses and heats the gas as it converges at the center of the capsule, and produces fusion reactions as it rebounds back through the fuel. This type of implosion is contrasted against implosions designed to achieve ignition and energy gain, which are driven by the ablation of outer shell material and subsequent hydrodynamic compression of the fuel. These ablatively-driven implosions are currently under study at the National Ignition Facility (NIF) in the indirect-drive configuration.[57,58,49,59,32,33] Because shock-driven exploding-pusher implosions are mainly 1-D in nature and less sensitive to the complex hydrodynamic processes that characterize ablatively-driven implosions, they are an ideal experiment to isolate and study the physics of strong, spherically-converging shocks and hot-spot formation in ICF implosions.

Understanding the conditions generated by strong shocks in ICF implosions is crucial for achieving hot-spot ignition,[60,61] in which shock waves launched into the fuel set the entropy, temperature, and density of the fuel before the main compression stage sets off fusion burn.[58,59] In related experiments, measurements of the fusion yield, fuel ion temperature (T_i), areal density (ρR), and fusion reaction history during the shock rebound phase can provide information about the state of the implosion several hundred picoseconds before peak compression and help to constrain models of the implosion.[62,63]

While some previous studies of the shock convergence phase of ICF implosions have used thick-shell CH capsules in ablatively-driven implosions,[64,36,65–69] the implosion dynamics and measured observables in exploding pushers are sensitive predominantly to shock physics and not to mix and 3-D effects. Recent experiments have used glass-shell implosions to study the effects of dopants on implosion dynamics,[70–73] non-equilibrium plasmas,[74] and the effect of adding ^{3}He fuel on implosion performance.[22,75] Though some of these experiments reported data for a distinctive shock phase, many of the experiments were in a more compression-dominated regime than the present experiments. Those experiments were designed to probe a particular aspect of implosion physics (e.g. how changing the dopant concentration affects radiation properties) and not the overall dynamics of the implosion around shock convergence.

The experiments discussed herein provide a more direct study of the physics of shock convergence in exploding-pusher implosions, where fusion is driven largely by shock heating and long ion mean free path effects may be important. These experiments produced a copious amount of DD and D^{3}He reactions and allow for a comprehensive characterization of the implosions: concurrently with two separate fusion yields, two different burn-averaged ion temperatures are measured. Fuel ρR in D_2 implosions and total ρR in both D_2 and D^{3}He implosions are measured at shock burn. X-ray images of the imploding shell and core provide information on implosion shape and convergence, while both x-ray and nuclear bang-time measurements assess the energy coupling of the shock into the gas. This study employs 2-D DRACO radiation-hydrodynamics simulations[76,77] for comparison to experimental data. Inferring the physics of shock propagation in ICF implosions is simplified in exploding pushers relative to ablatively-driven implosions, as ablation and compression do not play as significant a role in producing fusion yield.

Shock-driven, low-convergence exploding-pusher implosions are not strongly degraded by fuel-shell mix as are ablatively-driven implosions. They are also a reliable source of fusion products insensitive to capsule and laser illumination uniformity.[36] Exploding pushers have been used extensively as a fusion product source for diagnostic development,[78] for charged-particle radiography of ICF implosions,[79] hohlraums,[80] and laser-foil interactions,[81,82] and for nuclear physics experiments at ICF- and solar-relevant conditions.[83,23,84] The use of exploding pushers, such as those discussed in this work, as a proton backlighter on NIF has been proposed. Studying shock-driven implosions both advances understanding of the shock convergence phase of ICF implosions and enables development of scientific platforms that utilize exploding pushers.

As discussed above, in Section 3.2, exploding pushers are an excellent platform to probe kinetic effects, which can be significant during the shock-convergence phase of ICF implosions. Kinetic effects are important in these moderate-density, high-temperature implosions where the mean free path for ion-ion collisions approaches the size of the burn region. Previous experimental work has investigated kinetic effects in shock-driven implosions and demonstrated the significance of ion diffusion and other long-mean-free-path effects that are not modeled in hydrodynamic codes.[31,24] A systematic study showing the breakdown of hydrodynamic models (in this particular case the 1D radiation-hydrodynamics code DUED[10]) with increasing ion-ion mean free path, described in Section 3.2, is summarized again in Figure 3.14. In this previously-discussed series of exploding pushers on OMEGA with a variety of initial gas densities, the ion-ion mean free path λ_{ii} and the Knudsen number $N_K \equiv \lambda_{ii}/R_{shell}$, the ratio of mean free path to minimum shell radius and a key figure of merit of ion kinetic effects, were varied from a regime that is reasonably hydrodynamic-like ($N_K<1$) to a regime that is strongly kinetic ($N_K \gg 1$). The trend of increasing deviation from hydrodynamic models with increasing Knudsen number indicated the influence of ion kinetic effects. In agreement with this picture, another recent study by Le Pape *et al.* shows that in a high-density, low-temperature, short-mean-free-path, $N_K \ll 1$) indirect-drive exploding pusher implosion, hydrodynamic codes are able to reproduce with high fidelity the experimental results.[85] In concert, these studies indicate that the ion-ion mean free path and the Knudsen number is a strong determinant of the applicability of hydrodynamic models.

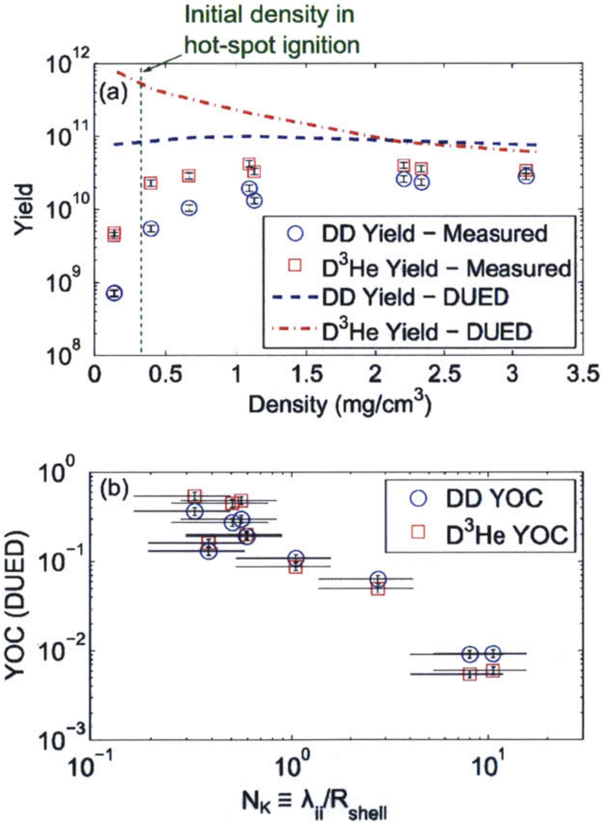

Figure 3.14. Previously-reported (a) measured and 1D DUED-simulated[10] DD and D^{3}He yields as a function of initial gas density and (b) yield-over-clean (YOC) relative to DUED simulations for both DD and D^{3}He reactions as a function of the Knudsen number, the ratio of the ion-ion mean-free-path (at bang time) to the measured minimum shell radius in exploding pusher implosions on OMEGA.[37] This data was originally presented in Section 3.2.[31] The initial gas density in cryogenically layered ignition experiments, 0.3 mg/cm^3,[32] is indicated with the dotted vertical line in (a). These results show that ion kinetic effects become important as a strong function of the Knudsen number. These expreiments help frame the present exploding-pusher experiments at the NIF.

To further investigate whether the trends observed in these prior experiments apply generally, under quite different experimental conditions (larger capsules, asymmetric illumination, oblate implosions), data were obtained, in a ride-along mode, on polar-direct-drive exploding pusher shots at the NIF that were conducted for diagnostic development and calibration. In addition, given the scarcity of NIF shots for non-programmatic purposes, it is important to cull as much information and physics insight possible from these diagnostic development shots. These experiments produced copious DD and D^{3}He reactions, allowing for characterization of the implosions through measurement of two separate fusion yields, two different burn-averaged ion temperatures, fuel ρR in D$_2$ implosions and total ρR in both D$_2$ and D^{3}He implosions, x-ray images of the imploding shell and core, and x-ray and nuclear bang-times. This study employs 2D DRACO radiation-hydrodynamics simulations[76,77] for comparison to experimental data. In this work, the experimentally-inferred ion-ion mean free path $\lambda_{ii} \propto T_i^2/n_i Z^4$ (where T_i is the ion temperature, n_i is the ion density, and Z is the ion charge)[8] is compared to the minimum shell radius R_{shell} to describe the degree of ion kinetic behavior, as in prior work.[31] The Knudsen number $N_K \equiv \lambda_{ii}/R_{shell}$ is used to describe when ion kinetic effects become important, as they do when this parameter approaches a significant fraction of unity. It is observed that the fusion yield relative to DRACO predictions varies inversely with the experimentally-determined N_K, suggesting that ion kinetic effects are beginning to degrade implosion performance. These results dovetail with the findings of the previous experiments, where an increasing discrepancy relative to hydrodynamic codes is observed with increasing Knudsen number, as will be shown in Figure 3.22.

3.3.2 NIF Exploding Pusher Experiments and Modeling

DD and D^{3}He fusion yield, burn-averaged ion temperatures, fuel and total ρR, implosion convergence and symmetry, and bang time were measured in exploding-pusher implosions at the National Ignition Facility (NIF).[86] Experiments were conducted with ~192 laser beams pointed in the polar direct drive configuration,[87,88] delivering 40-130 kJ onto a capsule in a 1.4- or 2.0-ns ramp pulse. The experiments, conducted primarily for diagnostic calibration,[89,90] used glass shells with a 1530-1680-μm diameter and a thickness of 4.1-4.6 μm, filled with 10-12 atm. of D$_2$, D^{3}He, or HD^{3}He gas. Some experimental parameters are summarized in Table 3.2 and Appendix A.

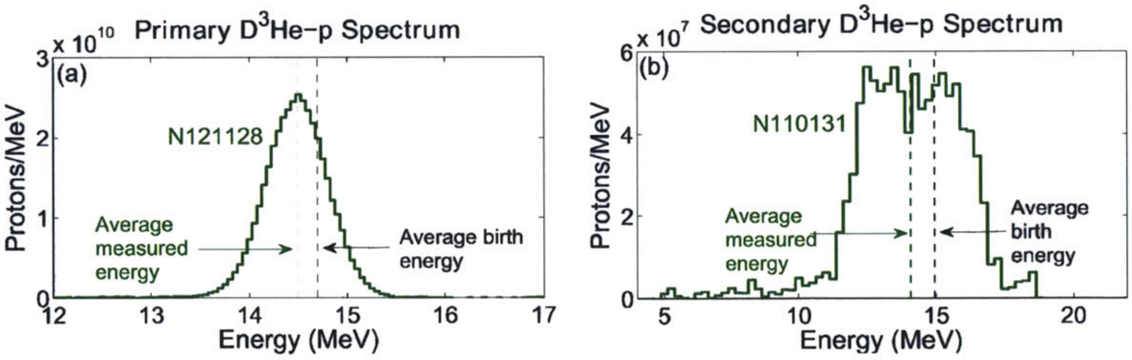

Figure 3.15. (a) Measured primary D^{3}He-proton spectrum from D^{3}He exploding-pusher shot N121128 and (b) measured secondary D^{3}He-proton spectrum from D$_2$ exploding-pusher shot N110131. From the primary spectrum (a), the D^{3}He yield, D^{3}He-burn-averaged ion temperature (related to the spectral width as $T_i \propto \sigma^2$), and total ρR (proportional to energy downshift) are inferred. From the secondary spectrum (b), the total ρR is inferred from the energy downshift, while the ratio of secondary D^{3}He-proton to primary DD-neutron yield is proportional to the fuel ρR for $\rho R \leq 10$ mg/cm^2 (for T_e ~5 keV). Note the difference in energy-axis scale, as the secondary spectrum is much broader than the primary spectrum.

---

[8] The total ion mean free path in a multiple-ion plasma is based on the total collision rate of a test ion on each population of ions (for example: D on D + D on ^{3}He; ^{3}He on D + ^{3}He on ^{3}He). In terms of mean free paths, $\lambda_{Di}^{-1} = \lambda_{DD}^{-1} + \lambda_{D^3He}^{-1}$; $\lambda_{^3Hei}^{-1} = \lambda_{^3HeD}^{-1} + \lambda_{^3He^3He}^{-1}$. The overall ion mean free path is taken as the geometric mean, $\lambda_{ii} = \sqrt{\lambda_{Di}\lambda_{^3Hei}}$. These calculations are further discussed in Appendix F.

The primary nuclear reactions used to diagnose the exploding-pusher implosions are:

$$D + D \rightarrow {}^{3}\mathrm{He}(0.82\ \mathrm{MeV}) + \mathrm{n}(2.45\ \mathrm{MeV}), \tag{3.5}$$

$$D + D \rightarrow \mathrm{T}(1.01\ \mathrm{MeV}) + \mathrm{p}(3.02\ \mathrm{MeV}), \text{and} \tag{3.6}$$

$$D + {}^{3}\mathrm{He} \rightarrow \alpha(3.6\ \mathrm{MeV}) + \mathrm{p}(14.7\ \mathrm{MeV}). \tag{3.7}$$

Neutron time-of-flight (nTOF) detectors[42,91] and proton spectroscopy[43,92,50] were used to measure DD and D^3He yields and burn-averaged ion temperatures, and a particle time-of-flight (pTOF)[51] detector was used to measure bang time. The yield of the secondary D^3He protons was used to determine fuel ρR in D_2 implosions.[40] These protons are produced in D_2 gas-filled implosions when ^3He fusion products (see equation 3.5) react with the thermal D fuel ions

$$^{3}\mathrm{He}(\leq 0.82\ \mathrm{MeV}) + D \rightarrow \alpha + \mathrm{p}(12.6 - 17.5\ \mathrm{MeV}). \tag{3.8}$$

The ratio of the secondary D^3He-proton to primary DD-neutron yield is proportional to the fuel ρR for fuel ρR below ~10 mg/cm^2.[93,94] At higher fuel ρR values, the technique is saturated. For D^3He (D_2) gas-filled implosions, the energy downshift of the primary (secondary) D^3He-proton spectrum is used to infer the total ρR.[50] Sample primary and secondary D^3He-proton spectra are shown in Figure 3.15. From the primary spectrum, the D^3He yield, D^3He-burn-averaged ion temperature, and total ρR are inferred; from the secondary spectrum, the fuel ρR and total ρR are inferred. These measurements are discussed further in Section 3.3.3.

Table 3.2. Capsule and laser parameters for exploding pushers used in this study, including: capsule outer diameter d; shell thickness Δr; total laser energy; approximate laser pulse duration; D_2 fill pressure; and ^3He fill pressure.

NIF Shot Number	d (μm)	Δr (μm)	Energy (kJ)	Pulse (ps)	D_2 fill (atm.)	^3He fill (atm.)
N100823	1567	4.1	80.0	~2100	1.4	10.5[9]
N110131	1555	4.5	52.0	~2100	10.0	
N110722	1536	4.1	42.7	~1400	3.3	5.3
N120328	1555	4.4	130.6	~2100	9.9	
N121128	1682	4.3	43.4	~1400	3.3	5.8
N130129	1533	4.6	51.4	~1400	10.0	

For illustrative purposes, a 1D LILAC[95,7] simulation of mass-element trajectories and time-dependent temperature and fusion burn rates is shown in Figure 3.16 for a typical D^3He gas-filled exploding-pusher implosion at the NIF (shot N110722). Fusion reactions are initiated primarily along the shock rebound trajectory(~1.8-2.0 ns), well before peak compression (~2.2 ns).

Primarily, the 2D hydrocode DRACO[76,77] was used to simulate these NIF exploding-pusher experiments. The use of 2D simulations is especially pertinent in these experiments, where the polar direct drive (PDD) imposes an illumination asymmetry. 3D ray tracing is used to model inverse bremsstrahlung absorption of laser energy, and material equations of state were taken from SESAME tables. A flux-limited Spitzer thermal conductivity was used, with a flux limiter of 0.06. (Some of the physics included in these simulations is described further in Appendix G.) DRACO simulations of ablatively-driven PDD experiments at the OMEGA laser facility[37] were in good agreement with measured x-ray radiographs and ρR.[96,97] DRACO simulations have also been found to reproduce experimental yield, shell shape, and ρR in symmetrically-driven cryogenic implosions

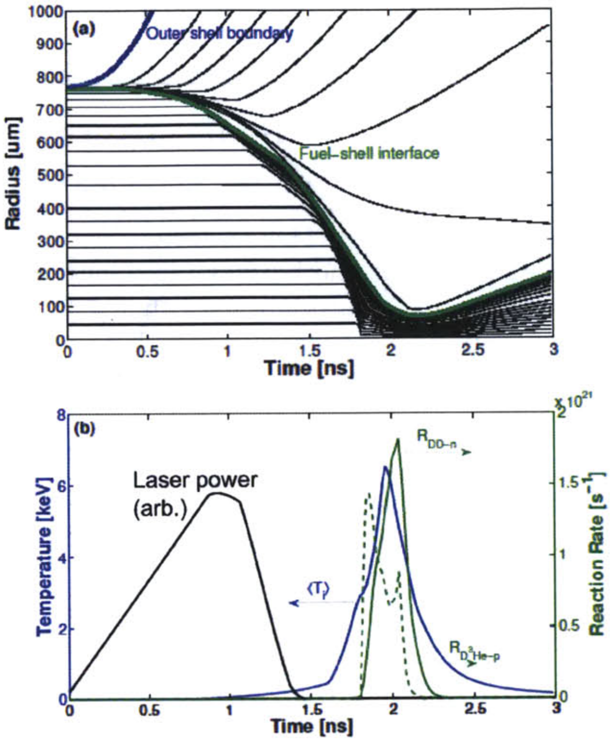

Figure 3.16. Illustrative 1D LILAC-simluated (a) Lagrangian mass element trajectories (black), (b) volume-averaged fuel ion temperature (blue), and rates of DD burn (green - solid) and D^3He burn (green - dashed) as a function of time in NIF D^3He exploding-pusher shot N110722 (4.1-μm-thick shell, 1536-μm diameter, 8.6 atm). A representative 1.4-ns-ramp laser pulse, approximately like that used in shot N110722, is also shown.

at OMEGA.[98–100] To properly simulate the laser-absorption process and reproduce the implosion velocity and shape in these exploding-pusher implosions, it is sometimes necessary to include models of non-local electron transport (NLET)[101] and cross-beam energy transfer (CBET).[102,103] Including CBET has been found to be necessary to reproduce implosion shape for higher laser intensities (laser energy >100 kJ for these NIF exploding pushers).[103] Observables such as yield, ion temperature, ρR, bang time, and shell convergence and symmetry are calculated from the "nominal" DRACO simulations and DRACO simulations that include NLET and/or CBET, as appropriate.

3.3.3 Experimental Measurements and Comparison to Simulations

In this section, the measured fusion yields, burn-averaged ion temperatures, fuel and shell ρR, bang times, shell convergence, and shape are presented and, in some cases, compared to DRACO-simulated values. It will be shown later that deviations from DRACO yield predictions are suggestive of ion kinetic effects. Experimental measurements are summarized in Table 3.3. Supplementary data and comparison to other simulations are presented in Appendix A.

Yield

DD-neutron yields were measured using the neutron time-of-flight (nTOF)[42,91] diagnostic suite and DD-proton yields were measured using the solid-state nuclear track detector CR-39,[43] with an overall yield uncertainty of ∼±15%. The D^3He-proton yields were measured using wedge-range-filter proton spectrometers (WRFs).[43,92,50] A sample WRF primary D^3He-proton spectrum is shown in Figure 3.15a for shot N121128. The measured D^3He yields shown in Figure 3.17b are averages of several measurements that each have an uncertainty of ∼±15%. The overall uncertainty in the yield measurement on a given shot is ∼±10%

Table 3.3. Measured observables from these exploding pushers, including: DD yield; D^3He yield; DD-burn-averaged ion temperature; D^3He-burn-averaged ion temperature; bang time (x: x-ray, p: D^3He-proton, n: DD-neutron); fuel ρR; and total ρR.

NIF Shot Number	Y_{DD}	Y_{D^3He}	T_{iDD} (keV)	T_{iD^3He} (keV)	Bang Time (ps)	Fuel ρR (mg/cm^2)	Total ρR (mg/cm^2)
N100823	1.38×10^{10}	2.32×10^{10}	10.5	16.2			13
N110131	3.01×10^{11}		5.4		2430 (x)	4.6	23
N110722	2.85×10^{10}	1.30×10^{10}	8.8	15.1	1910 (x)		11
N120328	1.00×10^{12}		11.4		1770 (x)	3.6	
N121128	7.27×10^{10}	2.09×10^{10}	7.1	11.0	1880 (p)		9
N130129	2.50×10^{11}		4.0		2470 (n)	4.6	18

A comparison of measured and DRACO-simulated DD yields from D_2- and D^3He-gas-filled exploding pushers (Figure 3.17a) reveals that experimental values cluster around a yield-over-clean (YOC) ~0.5-0.6. The NLET-CBET DRACO simulations have a YOC closer to 1. The experimental and DRACO-simulated data show that the D^3He yield is, on average, 0.27 of the nominal 2D DRACO simulated value (with a standard deviation of 0.20). Overall, the observed implosion performance relative to simulations is slightly worse for pure D_2 and higher-yield (higher-T_i) implosions. As will be discussed below and in Section 3.3.4, these results are consistent with influence of ion kinetic effects, which reduce the yield relative to hydrodynamics simulations in implosions with higher T_i, lower Z, and, thus, longer ion mean free paths.

Ion Temperature

In order to explore trends within the yield data to elucidate the possible role of ion kinetic effects, the yield results are presented in comparison to measured burn-averaged ion temperatures. The DD-burn-averaged ion-temperature was measured by nTOFs and the D^3He-burn-averaged ion temperature was determined from the Doppler width of the measured D^3He proton spectrum (see Figure 3.15a), as measured by WRFs.[104,105,43] In NIF exploding-pusher implosions, the measured D^3He-proton linewidth is dominated by thermal broadening.[10] Other capsule-related broadening effects (e.g. ρR evolution and implosion geometry) account for a broadening of $\sigma\sim100$ keV in NIF exploding pusher implosions,[11] and are subtracted in quadrature from the measured linewidth. Additional broadening effects that are difficult to quantify on a shot-by-shot basis are not accounted for in this analysis, and thus set an upper limit on the Doppler-inferred ion temperature. However, the Doppler broadening of the D^3He-proton spectrum should be considered a reliable measure of the D^3He-burn-averaged temperature. Uncertainties in the different measurements are ~0.5 keV for the nTOF DD-burn-averaged temperature and ~2 keV for the D^3He-burn-averaged temperature.

The measured DD and D^3He burn-averaged temperatures are compared to the DRACO YOCs in Figure 3.18. Both sets of data show a trend of decreasing YOC with increasing burn-averaged T_i over the range of 4 to 15 keV, with a more apparent trend among the D^3He data. In Section 3.3.4 this YOC trend will be expressed in terms of the Knudsen number $N_K \propto (T_i^2/n_i Z^4)/R_{shell}$ in a way that indicates ion kinetic effects may be responsible.

---

[10] Instrumental broadening for aluminum WRFs used at NIF is $\sigma\sim$130-170 keV, while a typical thermal Doppler width of the D^3He-p spectrum is $\sigma\sim$250 keV.

[11] This broadening arises from differential proton slowing due to different amounts of ρR across the burn duration and different path lengths for protons traversing the shell and sampling different effective amounts of ρR, and is modeled based on the measured ρR and simulated burn duration, assuming uniform proton emission throughout the fuel.

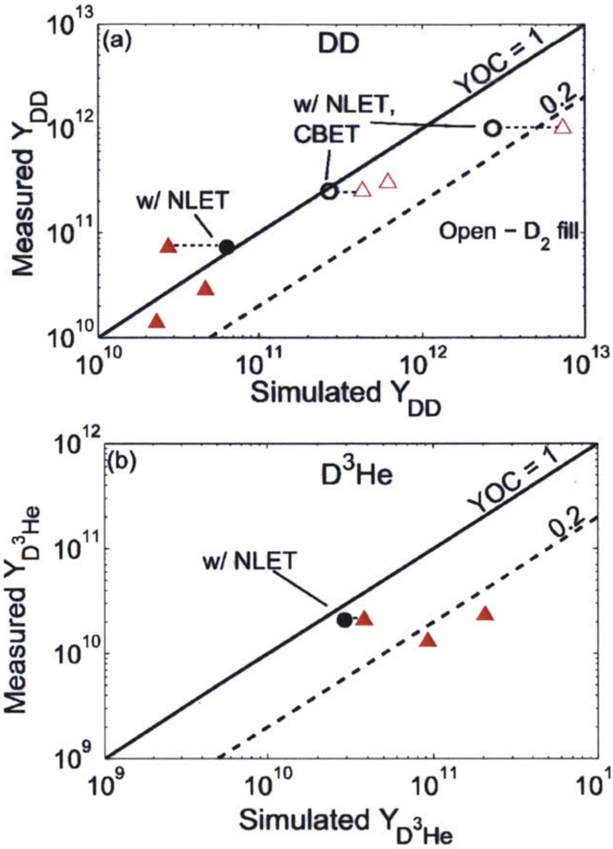

Figure 3.17. (a) Measured DD yield and (b) D^3He yield as a function of DRACO-simulated yield. Open markers denote D_2-gas-filled implosions, while filled markers denote D^3He-gas-filled implosions. The red triangles represent nominal DRACO simulations, while the black circles are DRACO simulations that have included non-local electron transport and cross-beam energy transfer. Dotted horizontal lines connect multiple simulations of the same shot. Yield-over-clean (YOC) values of 1 (solid line) and 0.2 (dashed line) are indicated. The measured yields are averaged over several measurements on each shot, each with individual uncertainties of ~±15%. The overall error on each data point is ~±10-15%

As an aside, the measured difference between DD-burn-averaged and D^3He-burn-averaged ion temperatures (x-axis values shown in Figures 3.18a and 3.18b) is not a sign of diagnostic disagreement, but rather is symptomatic of profiles and temporal evolution of density and temperature throughout the burn. Relative to the DD fusion reactivity, the D^3He reactivity has a stronger temperature dependence and is weighted more strongly by the hotter regions of the implosion. Ion temperature gradients therefore produce measurable differences in the burn-averaged ion temperatures of different reactions.

ρR and Convergence

Measurements of fuel ρR, total ρR, and shell convergence provide information about the fuel assembly in these low-convergence, shock-driven implosions, and can be used to help identify the approximate ion density n_i, ion mean free path λ_{ii}, and minimum shell radius R_{shell}. The ratio of these lengths, $N_K \equiv \lambda_{ii}/R_{shell}$, is a key figure-of-merit for the assessment of ion kinetic effects, as discussed further in Section 3.3.4.

As discussed previously in Section 3.3.2, the fuel ρR is inferred from the ratio of secondary D^3He-p to primary DD-n yields in D_2 implosions. For shot N110131, a secondary-proton yield of $2.0\pm0.5\times10^8$ (see Figure 3.15b) and a primary DD-neutron yield of $3.0\pm0.3\times10^{11}$ gives a fuel ρR of 4.6 ± 1.1 mg/cm^2, using a model of uniform fusion production throughout the fuel.[93] Similar measurements give a fuel ρR of 3.6 ± 1.1 mg/cm^2 for shot N120328 and 4.6 ± 1.1 mg/cm^2 for shot N130129. These fuel ρR measurements are used to estimate the implosion convergence ratio, as $C = (\rho R_f/\rho R_{f0})^{1/2}$, where ρR_{f0} is the initial fuel areal density. With ρR_{f0}~0.13 mg/cm^2 for these

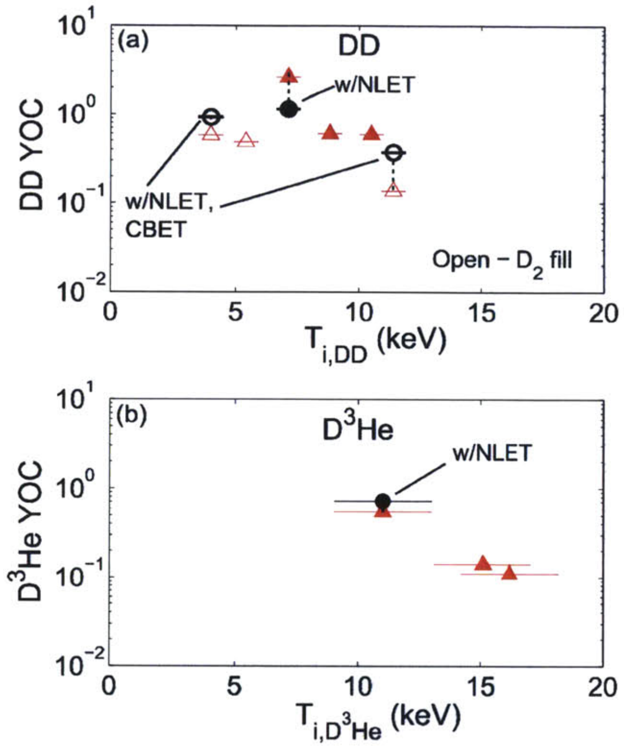

Figure 3.18. (a) DD YOC as a function of the measured DD-burn-averaged ion temperature ($T_{i,DD}$) and (b) D^3He YOC as a function of the measured D^3He-burn-averaged ion temperature ($T_{i,D3He}$). The red triangles represent nominal DRACO simulations, while the black circles are DRACO simulations that have included nonlocal electron transport and cross-beam energy transfer. Dotted vertical lines connect multiple simulations of the same shot.

three D_2-filled implosions, convergence ratios of ~5.3-6.0 are inferred. These measurements will be used subsequently in Section 3.3.4 to estimate the ion density and, ultimately, the ion mean free path in these exploding pushers around bang time.

Total ρR data is not directly used to evaluate hydrodynamic-kinetic parameters, but is presented for completeness and as a consistency check on the approximate convergence ratios inferred from the fuel ρR measurements. As first discussed in Section 3.3.2 and shown in Figure 3.15, the total ρR is inferred from the energy downshift of the secondary or primary D^3He-proton spectrum. Assuming an average secondary-proton birth energy of 14.96 MeV and measured energies of 14.08 ±0.15 MeV on the equator and an average energy of 14.33±0.15 MeV on the pole, total ρR of ~26±5 and ~19±5 mg/cm^2, respectively, are inferred for shot N110131 (Figure 3.15b). An average total ρR of 18±5 mg/cm^2 is inferred on D_2 shot N130129, while no total ρR measurement is possible for shot N120328 as the spectrum is net upshifted relative to the birth energy.[12] For D^3He-filled implosions, the birth energy of the primary D^3He-p spectrum is taken to be 14.7 MeV. D^3He shot N121128 was measured to have a total ρR of 9±4 mg/cm^2 (see Figure 3.15a), while a total ρR of 13±4 mg/cm^2 was obtained on shot N100823 and 11±4 mg/cm^2 was measured on shot N110722. These total ρR values, generally 10-20 mg/cm^2, are a factor of 10-20 greater than the initial ρR in the shell of ~1 mg/cm^2. The shell ρR data are roughly consistent with the convergence ratio of ~6 that was inferred from the fuel ρR, when allowing for some blowoff of outer shell material.[13]

---

[12] The measurement of total ρR from energy downshift in the D^3He-p spectrum is sometimes complicated by the presence of radial electric fields around the capsule that cause an upshift in proton energy upon leaving the capsule,[106] such that the downshift-inferred total ρR is a lower limit on the actual ρR in the implosion. However, when the laser intensity is below $\sim 4\times10^{14}$ W/cm^2 or when the nuclear bang time is well after the end of the laser pulse, electric-field upshifts are diminished and the birth energy is well known. This is the case on five of the six experiments used in this study, with shot N120328 the only exception.

[13] The convergence ratio is related to the shell ρR as $C \sim \sqrt{\rho R_{sf}/(1-f)\rho R_{s0}}$, where ρR_{sf} (ρR_{s0}) is the final

X-ray emission gives a sense of the core size around bang time and may be used to estimate the implosion convergence and the length scale of the fuel, which can be compared to λ_{ii} to evaluate the likely impact of ion kinetic effects. Gated x-ray imaging diagnostics, the hardened gated x-ray imager (hGXI)[107] and the gated x-ray detector (GXD),[108] were used to capture images of the implosions. Figure 3.19 shows a measured x-ray emission image from the imploded core as captured by hGXI on shot N121128, ~100 ps before bang time. The image shows a core radius, expressed as the Legendre mode P0 of ~168 μm and an oblateness, characterized by a Legendre P2/P0, of ~-0.13. This oblateness, present across this set of implosions as a consequence of the polar drive (with the x-ray P2/P0 ranging from -0.09 to -0.33 oblate, and also evident in the total ρR asymmetry obtained on shot N110131), shows significant differences from previous, symmetrically-driven implosions on OMEGA,[31] which did not measurably deviate from spherical symmetry. The oblateness also demonstrates the importance of using a 2D code such as DRACO for comparison to experimental results. DRACO simulations that include NLET[103] adequately capture the implosion shape for shot N121128.

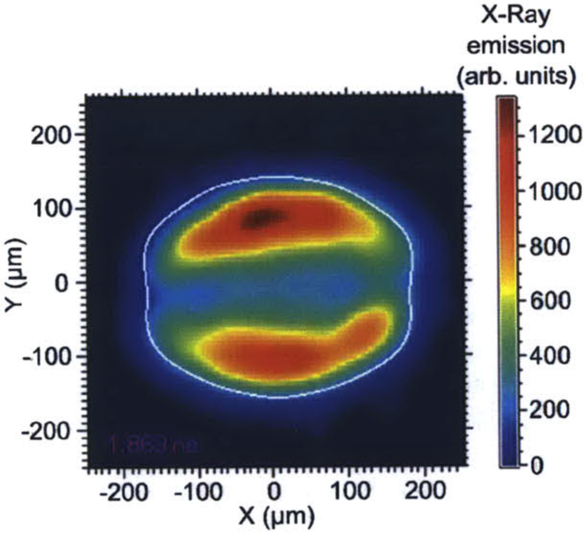

Figure 3.19. hGXI x-ray self-emission of the imploded core ~100 ps before bang time in D^{3}He exploding-pusher shot N121128. The image, with 10% peak emission contour (white line) indicated, shows an average P0 ~168 μm and a P2/P0 ~-0.13 (13% oblate). The measured radius R_{shell} is used as a scale length of the implosion in calculation of the Knudsen number $N_K \equiv \lambda_{ii}/R_{shell}$.

A summary of the measured fuel ρR, total ρR, implosion size, and symmetry is presented in Table 3.4. The P0 values across this set of exploding pushers imply convergence ratios of ~4-8, roughly in agreement with those inferred from the fuel ρR and total ρR. These convergence data are used in Section 3.3.4 to estimate the ion density and implosion radius in order to calculate key ion kinetic parameters in a manner similar to that described in Section 3.2.[31]

Bang Time

In order to assess the possible role of ion kinetic effects, it is important to determine that yield trends relative to DRACO are not the result of discrepancies in the energy coupling to the implosion. The energy coupling and, consequently, the implosion velocity, is assessed by measurements of nuclear and x-ray bang times – the times of peak fusion and x-ray production in the core. Bang time measurements using D^{3}He-protons and DD-neutrons were made by the particle time of flight (pTOF) diagnostic.[51] X-ray bang times were measured using the south pole bang time (SPBT)

(initial) shell ρR and f is the fraction of shell material that has been blown off (beyond the initial shell radius). For an approximate blowoff fraction of $f = 0.6$ and $\rho R_{sf}/\rho R_{s0}$ ~10-20, C~5-7, consistent with C~6 inferred from the fuel ρR data.

Table 3.4. Measured fuel ρR, total ρR, x-ray emission radius P0 (contour of 10% of maximum brightness for N121128), and relative magnitude of second Legendre mode (P2/P0), the dominant asymmetry in the implosion. This ratio quantifies the deviation in core shape from spherical symmetry, with a negative value signifying an oblate implosion. These measuremets are used to quantify the ion-ion mean free path and implosion size, to assess the likely impact of ion kinetic effects.

Shot	Fuel ρR	Total ρR	X-Ray	
	(mg/cm^2)	(mg/cm^2)	P0 (μm)	P2/P0
N100823		13±4		
N110131	4.6±1.1	23±5	89	-0.24
N110722		11±4	115	-0.33
N120328	3.6±1.0		182	-0.10
N121128		9±4	168	-0.13
N130129	4.6±1.1	18±5	94	-0.09

diagnostic[109] and gated x-ray imaging diagnostics, hGXI[107] and GXD.[108] These measured bang times are summarized and compared to DRACO-simulated DD-neutron bang times in Table 3.5. Uncertainty in the pTOF-measured DD-neutron bang time is ∼±120 ps, while the uncertainty in the D^{3}He-proton bang time measurements is ∼±100 ps. Uncertainty in the x-ray bang time is ∼±100 ps. pTOF traces used to infer nuclear bang times on shots N121128 and N130129 are shown in Figure 3.20. Comparing the nuclear bang times, the measured D^{3}He bang time on shot N121128, 1880±100 ps, is in reasonable agreement with the DRACO DD bang time of 2020 ps, while the measured DD bang time on shot N130129, 2470±120 ps, is in good agreement with the DRACO DD bang time of 2530 ps. The overall trend indicates that DRACO captures the basic implosion dynamics and energy coupling to these shock-driven implosions fairly well. Therefore, the trend in the yield data is likely not related to inaccurate modeling of overall implosion dynamics, and may be attributed to ion kinetic effects, as discussed in the following section.

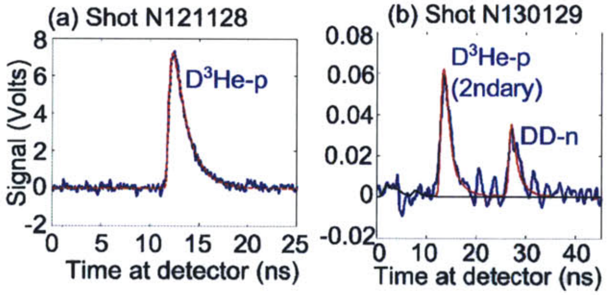

Figure 3.20. pTOF signal obtained on (a) D^{3}He shot N121128 and (b) D$_2$ shot N130129, used to infer nuclear bang times.

3.3.4 Discussion of Ion Kinetic Effects in NIF Exploding Pushers

Though the experimental bang times compare reasonably well with DRACO simulations, indicating that the overall implosion dynamics and energy coupling in these shock-driven implosions are modeled fairly accurately, trends within the nuclear yield data point to ion kinetic effects impacting fusion production. To estimate the significance of ion kinetic effects, the ion-ion mean free path around bang time, λ_{ii}, which varies in these implosions on the basis of the fuel composition (Z), T_i, and n_i, is evaluated. The ion temperature is taken as the DD-burn-averaged T_i in D$_2$ implosions and the yield-weighted average of the DD- and D^{3}He-burn-averaged ion temperature in D^{3}He implosions. The ion density is estimated from the measured fuel ρR as $n_i = n_{i0}(\rho R_f/\rho R_{f0})^{3/2}$,

Table 3.5. Measured nuclear and x-ray bang times and DRACO-simulated DD-n bang times. The nuclear measurements were made using D^3He protons (p) on N121128 and with DD neutrons (n) on N130129.

Shot	Measured Bang Times		DRACO Bang Time
	Nuclear (ps)	X-Ray (ps)	Nuclear (DD-n) (ps)
N110131		2430	2650
N110722		1910	2150
N120328		1770	1990
N121128	1880 (p)	2000	2020
N130129	2470 (n)		2530

assuming mass conservation and spherical symmetry, where n_{i0} and ρR_{f0} are the initial gas ion density and the initial fuel ρR, respectively. This calculation is performed directly for D_2 shots on which fuel ρR data was obtained, and a similar implied convergence ratio (~6) is also assumed for the D^3He shots. These experimental quantities are used to estimate λ_{ii} around bang time, which is compared to the minimum shell radius R_{shell} as given by the x-ray P0.

As shown in Figure 3.21, the Knudsen number $N_K \equiv \lambda_{ii}/R_{shell}$ varies by a factor of ~7 over these exploding-pusher implosions, largely as a consequence of different fuel ion Z and ion temperature. For $N_K \ll 1$, the implosion behaves more hydrodynamically, whereas for $N_K \gtrsim 0.3$, kinetic effects start to become significant (as observed in experiments on OMEGA described in Section 3.2). The moderate-temperature, D^3He-filled shot N121128 is the most hydrodynamic-like implosion, where $T_i = 8.0$ keV, $n_i \sim 7\times10^{22}$ cm^{-3}, and $Z = 1.47$, resulting in a λ_{ii} of ~6 μm.[14] Under these conditions, and with $R_{shell} = 150$ μm, N_K is ~0.04 for N121128. In contrast, the high-temperature, D_2-filled shot N120328 is the most kinetic-like implosion, where $T_i = 11.4$ keV, $n_i \sim 7\times10^{22}$ cm^{-3}, and Z = 1, resulting in a λ_{ii} of ~50 μm. In this case, $R_{shell} = 180$ μm and N_K is ~0.3. Parameters used to calculate the experimentally-inferred Knudsen numbers are summarized in Table 3.6, and YOC values are shown as a function of the experimentally-inferred Knudsen numbers in Figure 3.21. For both DD and D^3He yields, each set of simulations shows a trend of decreasing YOC with increasing N_K. For the NLET-CBET DRACO simulations, DD YOC ~1 for N_K ~0.04 (N121128, the most hydrodynamic-like implosion), while DD YOC ~0.4 at N_K ~0.3 (N120328, the most kinetic-like implosion). Notably, as shown in Figure 3.22, this most kinetic-like implosion among the NIF PDD data set overlaps in both N_K and YOC with the most hydrodynamic-like implosion in the OMEGA direct-drive exploding-pusher set (Section 3.2). As the DRACO hydrodynamics code does not account for kinetic effects, ion mean free path effects such as enhanced ion diffusion and Knudsen reactivity reduction due to modification of the ion distribution function[2,14,15] may account for this trend. It has been shown previously that kinetic effects reduce shock yields in exploding pushers, and do so more strongly with increasing Knudsen number.[31]

For these largely shock-driven implosions, hydrodynamic mix at the fuel-shell interface is very unlikely to explain the trend of decreasing YOC with increasing Knudsen number. In order for mix to explain this trend, the most "kinetic" implosion, N120328, would have to be the most susceptible to mix, to be driven by compression more so than the other implosions. However, by virtue of having the highest measured DD-burn-averaged ion temperature – a strong signature of shock heating – it is likely that this shot is the most predominantly shock-driven, with fusion reactions generated along the shock rebound trajectory. It is therefore unlikely that this shot is preferentially susceptible

---

[14] Following the earlier discussion, the individual ion mean free paths $\lambda_{DD}\sim52$ μm, $\lambda_{D^3He}\sim13$ μm, $\lambda_{^3HeD}\sim16$ μm, $\lambda_{^3He^3He}\sim4$ μm, so that $\lambda_{Di}^{-1}\sim11$ μm, $\lambda_{^3Hei}^{-1}\sim3$ μm and $\lambda_{ii}\sim6$ μm.

Table 3.6. Estimates of ion density, ion temperature, mean ion charge, minimum shell radius, Maxwellian-averaged mean free path for ion-ion collisions, and Knudsen number. The ion-ion mean free path and, therefore, the Knudsen number, varies largely as a consequence of variations in ion temperature and in gas composition ($\langle Z \rangle$).

NIF Shot #	n_i (cm^{-3})	T_i (keV)	$\langle Z \rangle$	λ_{ii} (μm)	R_{shell} (μm)	N_K
N110131	11×10^{22}	5.4	1	9	89	0.1
N110722	6×10^{22}	10.8	1.44	12	115	0.1
N120328	7×10^{22}	11.4	1	50	182	0.3
N121128	7×10^{22}	8.0	1.47	6	150	0.04
N130129	11×10^{22}	4.0	1	5	94	0.05

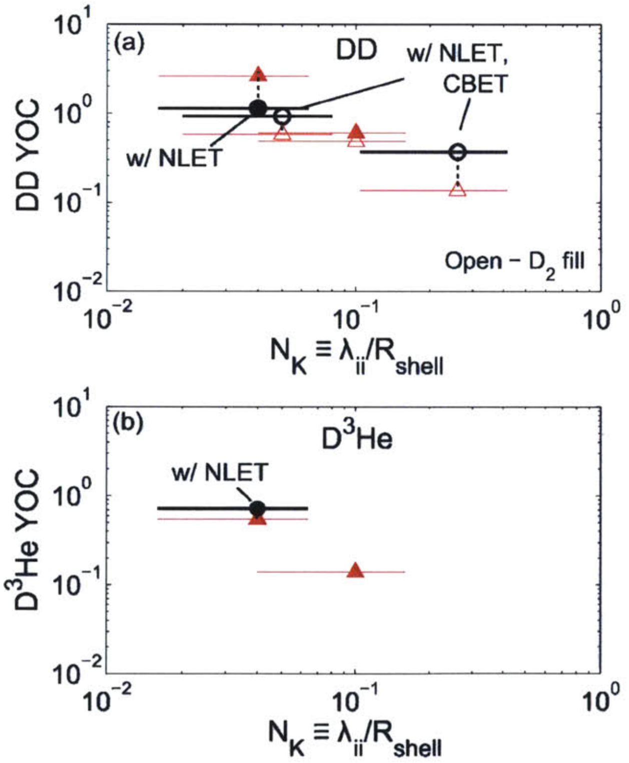

Figure 3.21. (a) DD and (b) D^{3}He YOC as a function of the Knudsen number (N_K)– the ratio of ion-ion mean free path (λ_{ii}) to minimum shell radius (R_{shell}). The red triangles represent comparison to nominal DRACO simulations, while the black circles represent comparison to DRACO simulations that include NLET and/or CBET to more accurately simulate the implosion shape. Dotted vertical lines connect multiple simulations of the same shot. The trend of decreasing YOC with increasing λ_{ii}/R_{shell} across all simulations suggests that kinetic effects are starting to impact the experimental yields.

to the deleterious effects of mix, and in fact it may be even less compressively-driven (and less susceptible to mix) than the other implosions in this study.[15] Preliminary 2D ARES simulations[9] that include a KL mix model[110] indicate that mix does not have a significant impact on simulated yields and that a trend of lower yield-over-simulated (YOS) for higher-N_K implosions persists. As mix does not appear able to account for the trend of decreasing YOC with increasing Knudsen number, ion kinetic effects, rather than mix, are inferred as the likely explanation.

Table 3.7. Estimates of ion density, ion temperature, mean ion charge, gas composition, Maxwellian-averaged mean free path for ion-ion collisions, and Knudsen number after shock convergence for: a strongly-kinetic exploding pusher on OMEGA (Section 3.2); a NIF direct-drive exploding pusher from this study; a strongly hydrodynamic-like indirect-drive exploding pusher on NIF from Le Pape *et al.*;[85], and an ignition-relevant implosion. The parameters corresponding to hot-spot conditions during the compression phase of an ignition implosion are also presented. The three exploding pusher cases span the regimes of strongly kinetic to strongly hydrodynamic-like. For the exploding pushers, the ion density and ion temperature are estimated from experimental measurements, while for the NIF ignition-relevant shock phase case, they are taken from hydrodynamic simulations of a surrogate implosion, near the center of the implosion immediately after shock convergence. The NIF ignition compression phase case is an estimate based on recent NIF experiments.[111] In both shot N120328 (the most kinetic-like of the NIF direct-drive exploding pushers presented here) and the shock phase of the NIF ignition-relevant implosion, λ_{ii} ~50 μm, which approaches the size of the burn region (~100 μm) in the ignition-relevant case (N_K ~0.5).

Implosion	n_i (cm^{-3})	T_i (keV)	$\langle Z \rangle$	Fuel	λ_{ii} (μm)	N_K
Rosenberg *et al.*	4×10^{21}	28	1.5	D^{3}He	900	10
N120328	7×10^{22}	11.4	1	DD	50	0.3
Le Pape *et al.*	3×10^{23}	3.5	1	DD	2	0.01
NIF Ignition (shock phase)	~6×10^{22}	~10	1	DT	~45	~0.5
NIF Ignition (compr. phase)	10^{25}	4	1	DT	0.1	0.002

The results of these NIF direct-drive exploding-pusher experiments fit with those previously observed in direct-drive exploding pushers at higher N_K on OMEGA (Section 3.2)[31] and indirect-drive exploding pushers at much lower N_K on NIF.[85] Table 3.7 shows the ion-ion mean free path and Knudsen number in each of these exploding pusher experiments, as well as shortly (~100 ps) after shock convergence in a surrogate, ignition-relevant implosion on NIF and during the peak compression phase of a NIF ignition-relevant implosion. In the OMEGA experiments (Section 3.2),[31] the YOC was found to be a strong inverse function of N_K for $0.3\lesssim N_K \lesssim 10$; in the NIF indirect-drive exploding pushers (Le Pape *et al.*),[85] YOC~1, near-perfect agreement with hydrodynamic models, was obtained on implosions with N_K~0.01. The present NIF direct-drive exploding-pusher experiments span the N_K space in between those extremes and demonstrate that the deviation from hydrodynamic models becomes noticeable between $0.1\lesssim N_K \lesssim 0.3$. This trend in YOC as a function of N_K over the different experimental campaigns is illustrated in Figure 3.22, showing a consistent picture of the onset of ion kinetic effects with increasing Knudsen number, despite radically different drive conditions. The entire range of exploding pusher data shown in Figure 3.22 spans three orders of magnitude, between regimes of very low (10^{-2}) and very high (10) Knudsen numbers. While the OMEGA direct-drive experiments were conducted in a comprehensive, systematic way, the NIF experiments, conducted in a ride-along mode, produced a somewhat more complex set of data. However, in concert, these different experimental campaigns show how the discrepancy relative to hydrodynamic codes with increasing Knudsen number begins to be observed.

---

[15] In addition, a fall-line analysis[46] of 1D LILAC simulations, representing the worst-case application of hydrodynamic mix to a 1D model, indicates that mix fails to account for the trend of decreasing YOC with increasing Knudsen number. In this toy model, the shell, instead of smoothly decelerating, breaks apart and completely mixes into the fuel, quenching burn above the line in radius-time space corresponding to the maximum shell velocity (100% penetration fraction). When this model is applied, the trend of decreasing YOC with increasing N_K persists, with a yield-over-fall-line (YOF)~0.75 at N_K ~0.04 (most hydrodynamic-like implosion, shot N121128) and YOF~0.12 at N_K ~0.3 (most kinetic-like implosion, shot N120328).

Additionally, in both the N120328 exploding-pusher example and the NIF ignition case, λ_{ii}~50 μm after shock convergence, an appreciable fraction of the size of the hot spot. Under those conditions, ion diffusion may significantly alter the density profiles, and Knudsen layer effects may allow the higher-energy ions to escape the hot-spot region. Knudsen layer effects[14] may also be important even at the compression phase in ignition implosions, where asymmetries (or 3D effects) amplify the surface area of the fuel-shell interface, allowing for significant loss of energetic ions even a modest ion-ion mean free path.

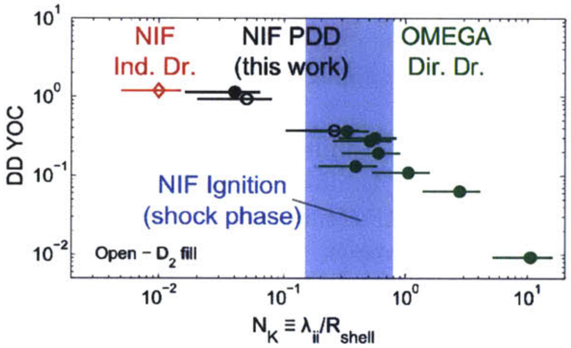

Figure 3.22. DD YOC as a function of the Knudsen number (N_K) for an indirect-drive exploding pusher on NIF (red diamond),[85] three polar-direct-drive (PDD) exploding pushers on NIF described in this section for which optimal DRACO simulations (including non-local electron transport and/or cross-beam energy transfer) were performed, from left to right, shots N121128, N130129, and N120328 (black circles), and direct-drive exploding pushers on OMEGA (green circles). Filled markers represent D^3He-filled implosions, while open markers denote D_2-filled implosions. Though the drive conditions are quite different, these experiments show a unified picture of the increasing impact of ion kinetic effects as a function of increasing Knudsen number above $N_K \gtrsim 0.1$. A band centered around $N_K = 0.5$ shows the approximate Knudsen number at the center of a NIF ignition-relevant implosion immediately after shock convergence..

In a NIF ignition implosion, the continued shell convergence after shock rebound greatly increases the fuel ion density, reducing λ_{ii} and N_K and producing much more hydrodynamic-like conditions around peak compression. The question that will be addressed in the future is: could the kinetic-like conditions during the shock convergence phase, including multiple-ion effects,[23,20] have any lingering manifestations and effects on the subsequent compression phase, which is strongly hydrodynamic-like (as shown in Table 3.7)? Ongoing and future experiments will explore this open question. Measurements of the relative and absolute timing of shock and compression bang time on surrogate implosions the NIF, as have been recently obtained and will be obtained routinely in the future,[112] may shed light on this issue.

Further studies will investigate aspects of the shock convergence phase of ICF implosions using exploding pushers, where ion kinetic effects are likely to be important. Yield anomalies in mixed-fuel exploding pushers will be explored and may elucidate species separation during shock convergence.[20] A comparison of exploding-pusher data to a hybrid kinetic treatment like that of Larroche[11,12] is an important continuation of this study. That theoretical work shows that kinetic simulations produce weaker and smoother profiles of temperatures and density near shock-bang time than hydrodynamic simulations, as the shock front is broadened to $\sim\lambda_{ii}$. Exploding-pusher experiments conducted in the indirect-drive configuration[85] will continue to be studied. These experiments in particular more closely approximate the process of shock convergence and shock burn as it occurs in NIF indirect-drive implosions.

3.3.5 NIF Exploding Pushers as a Possible Proton Backlighter

Additionally, characterization of these implosions aids development of exploding pushers as a monoenergetic proton source at NIF. As will be discussed in Chapter 5, exploding pushers have been shown to be a reliable source of fusion products insensitive to capsule and laser illumination uniformity[36] and have been used extensively at the OMEGA laser facility[37] as a fusion product source for charged-particle radiography of ICF implosions,[79] hohlraums,[80] and laser-foil interactions,[81] and for studies of stopping power in laser-generated plasmas. The use of exploding pushers, such as those discussed in this work, as a proton backlighter on NIF has been proposed. These data provide a promising first step toward development of this technique at the NIF. Studying exploding-pusher implosions both advances understanding of the shock convergence phase of ICF implosions, during which ion kinetic effects can be prevalent, and also enables development of scientific platforms that utilize exploding pushers.

Of particular importance for proton backlighting is the spatial uniformity of both the emitted proton fluence and the emitted proton energy. Measurements of the uniformity of the D^3He-proton spectrum on exploding pusher shot N121128, based on seven WRFs (three near the equator (90,78) and four near the pole (0,0) relative to the NIF geometry) are shown in Table 3.8 and illustrated visually in Figure 3.23. The spectrum shown in Figure 3.15a is taken from the Equator-1 WRF.

Table 3.8. Measured D^3He-proton yield and energy at seven different WRF positions (including their distance from the implosion) on D^3He exploding pusher shot N121128. The measurements on the equator were conducted at a fairly high fluence of protons (6×10^5 cm^{-2}),[113] and the capability to measure the D^3He-p energy using WRFs at significantly higher fluences has been developed.[114] The random energy uncertainty for each measurement is $\sim\pm60$ keV, while the random yield uncertainty for each measurement is $\sim\pm5\%$. Excellent uniformity of the emitted proton fluence and energy show that this implosion has great utility as a monoenergetic proton source. Even with many fewer beams, as required in a proton backlighting experiment, such isotropy in proton fluence and energy is achievable.

WRF Position	Dist. (cm)	D^3He-p Yield (10^{10})	D^3He-p Energy (MeV)
Equator-1	50	2.01	14.39
Equator-3	50	2.17	14.34
Equator-4	50	2.14	14.40
Eq. Avg.		2.11	14.38
Pole-1	200	2.00	14.54
Pole-2	200	2.05	14.49
Pole-3	200	2.11	14.36
Pole-4	200	2.15	14.45
Pole Avg.		2.08	14.46

These data show that the emitted D^3He-proton spectrum was extremely uniform in both fluence and energy on shot N121128. The average fluence variation is <2% from pole to equator, with a 3% standard deviation overall. The energy varies by only 80 keV between the polar and equatorial measurements, with an overall standard deviation of 65 keV. Thus, shot N121128 illustrates the potential for a highly uniform source of protons in both fluence and energy. While all 192 beams were used to drive this implosion, in a proton backlighting experiment many fewer beams would be used, as some beams are necessary to drive the subject. Even under such conditions, excellent uniformity in proton fluence and energy can be achieved. An implosion with this degree of proton emission uniformity could simultaneously backlight multiple experiments. Additionally, such excellent proton energy isotropy would enable studies of proton stopping power in laser-generated plasmas, which rely on an assumption of protons of identical energy emitted along different lines of sight. Importantly, as shown in Figure 3.20, pTOF can be used to measure the D^{3}He-proton bang time, necessary to identify the time at which protons sample the subject.

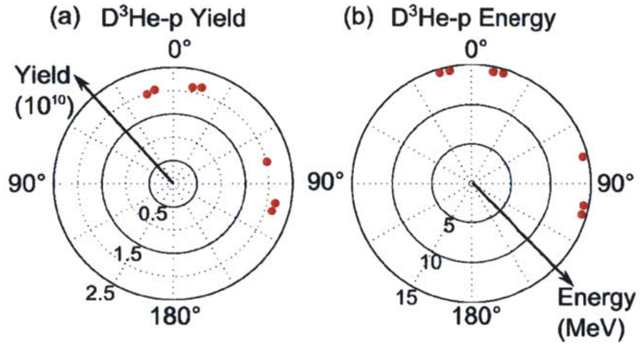

Figure 3.23. WRF-measured D^{3}He-p (a) yield and (b) energy as a function of polar angle on NIF for shot N121128. Excellent uniformity is observed, to ~±3% in inferred yield and ~±70 keV (~±0.5%) in energy, smaller than measurement uncertainties.

3.3.6 Conclusions

In order to fully exploit diagnostic development shots at the NIF, ride-along measurements of fusion yield, fuel ion temperature, ρR, convergence, and bang time have been presented for polar-direct-drive, D$_2$ and D^{3}He exploding-pusher implosions. These data are used to probe the physics of the shock convergence phase of implosions relevant both to shock-driven, exploding-pusher implosions and to ablatively-driven implosions, when ion kinetic effects can be important. The data have been compared to 2D DRACO hydrodynamic simulations and show a notable trend of decreasing YOC with increasing Knudsen number ($N_K \equiv \lambda_{ii}/R_{shell}$). This trend is suggestive of ion kinetic effects, and is consistent with the results of previous experiments at much higher and much lower Knudsen number, even though these implosions used different capsules and polar-direct-drive illumination. This work also motivates the continued development of kinetic models of ICF implosions, which may be especially pertinent at the high-temperature, moderate-density conditions present at shock burn in both exploding pushers and the shock-convergence phase of ablatively-driven implosions.

3.4 Future Work on Kinetic Effects in ICF Implosions

Future experimental work to investigate ion kinetic effects in ICF implosions will focus on fleshing out in greater detail the nature and significance of these effects during the shock-convergence phase and also attempting to assess the impact they have on the later, compression phase and ignition.

The Knudsen layer effect will be examined in greater depth. Additional experiments under similar conditions to the exploding pusher implosions described in Section 3.2 will use various fuels to more widely test the model of reactivity reduction. Other reactions of interest, beyond the D^{3}He and DD reactions studied in this work, include DT, of obvious interest due to its usage in ignition-relevant implosions, and ^{3}He^{3}He, relevant to studies of stellar nucleosynthesis using

ICF implosoions. Fusion product spectroscopy will be analyzed more closely to possibly infer modifications of the reactant ion distribution function from the shape of the fusion product spectra. Though it is highly challenging to deduce conclusively, direct observation of a depletion of high-energy ions from the distribution function would constitute an enormous leap toward understanding this effect and its manifestation in ICF implosions.

Additional experiments will further constrain models of ion diffusion. Previous studies, conducted in parallel to those described here, have observed for the first time non-hydrodynamic mix between CD shell ions and ^{3}He fuel ions as a likely consequence of strong ion diffusion in thin-shell implosions.[24] The same ion diffusion models used to interpret the experimental results described in Section 3.2 have been applied to these CD shell experiments and can reasonably explain the results. In future experiments, an inert shell layer (likely CH) of various thicknesses will be inserted between the shell deuterons and the fuel ^{3}He ions, to determine how far ions have to diffuse in order to produce significant diffusive mix. Additionally, implosions with pure CH shells, rather than SiO_2, will assess the shell-Z-dependence of ion diffusion in implosions where the fuel ion-ion mean free path is long relative to the fuel radius. Relatedly, the effect of diffusion between multiple ion species (such as D and T or D and ^{3}He), which is a likely contributor to yield anomalies observed in such mixed-fuel implosions,[21,23,22] will continue to be studied.

Having established and quantified the significance of these effects in the context of purely shock-driven implosions, the next major step will be to determine, experimentally and/or theoretically, the degree to which these effects can impact the later, compressional stage of implosions and possibly impact ignition. To that end, two new diagnostics are being developed to measure simultaneously the burn histories of D^{3}He protons and DD neutrons, which can either manifest as (1) two shock-burns (DD-n and D^{3}He-p in D^{3}He-filled exploding pusher implosions (to study species separation efffects alluded to above) or (2) as separate shock and compression burns in D^{3}He-filled ablatively-driven implosions. The first such instrument, dualPTD, is an enhancement of the current PTD[66] on OMEGA and measures highly accurate burn history differentials necessary to resolve multi-ion effects that can impact the relative burn histories of different reactions. This instrument can resolve the relative burn history on the order of tens of ps, approximately the expected scale of multiple-ion or species-separation effects. The second instrument, MagPTOF, is an upgrade to the current pTOF[51] in operation at the NIF, and will measure the bang time of shock-flash D^{3}He-p and compression-burn DD-n. It is plausible that any impact that the "kinetic" shock phase has on the later compression phase may manifest in a discrepancy between the MagPTOF-measured and hydro-simulated differential in bang time between shock burn and compression burn. However, given that the bang times on OMEGA exploding pushers were found to be fairly insensitive to kinetic effects (independent of initial gas density or Knudsen number) and reasonably modeled by hydro simulations (Section 3.2), and that bang times in exploding pushers on NIF were also reasonably well-simulated by hydro models (Section 3.3), it is possible that the relative shock/compression bang times will not be sensitive to the presence of ion kinetic effects.

Additionally, on the theoretical front, using the present exploding pusher data to constrain or benchmark models of ion kinetic effects, it will be possible to apply those models to simulation of ignition-relevant implosions. By comparing a well-benchmarked model that includes ion kinetic effects to a model that excludes them, it is possible to predict the degree to which these kinetic effects may impact an ignition implosion. The question that must be addressed is: do these shock-phase ion kinetic effects have a lingering manifestation and impact during the subsequent compression phase? The answer to this question determines the possible impact that the work presented in this chapter has on ongoing efforts to achieve ICF ignition at the NIF.

If it becomes apparent that kinetic effects present during the shock phase have a deleterious impact on implosion performance at peak compression (e.g. through high energy ions excaping the hot spot and preheating and increasing the adiabat of the cold fuel layer, degrading compression), then steps must be taken to mitigate these effects. Such mitigation would likely require avoiding the low-density, high-temperature conditions present early in time that give rise to kinetic effects. In such a scenario, it may be necessary to avoid launching strong shocks through that initial low-density gas. For example, in the alternative ignition scheme of shock ignition,[115] a strong shock is launched into the fuel only at the end of the implosion, rather than early in the implosion as in hot-spot ignition. In addition to avoiding generating the long mean free path conditions that give rise to ion kinetic effects, it may also be possible to design an implosion, in the framework of hot-spot ignition or otherwise, that is not susceptible to the particular effect that is found to be harmful. Ongoing and future work seeks to identify what, if any, those harmful kinetic effects are.

3.5 Summary

The significance of ion kinetic effects during the shock-convergence phase of ICF implosions has, for the first time, been assessed in a systematic experimental campaign. These effects include the diffusion of ions out of the fuel region and deviation from a Maxwellian distribution as a consequence of long ion mean free paths. Both of these effects may potentially impact implosion performance, through modification of hydrodynamic profiles or depletion of reacting ions. Experiments at the OMEGA and NIF laser facilities have explored these effects in shock-driven exploding pusher implosions that isolate the "kinetic" shock-convergence phase. On OMEGA, a comprehensive set of experiments explored the transition between hydrodynamic-like and strongly-kinetic conditions and produced an increasing deviation from the predictions of hydrodynamic simulations with increasingly kinetic conditions. Models that attempt to account for these long-mean-free-path effects better reproduce the experimental results. On NIF, ride-along data obtained on exploding pusher implosions point to the onset of ion kinetic effects in implosions where the ion-ion mean free path around the time of peak fusion production approaches the size of the fuel region. The results of these experiments suggest that ion kinetic effects are likely to be significant during the shock phase of a variety of ICF implosions, including ignition-relevant implosions, and opens up new avenues of inquiry into the physics relevant to the high-temperature, low-density conditions present early in ICF implosions. Future work will explore these effects in greater detail and assess the degree to which kinetic effects prevalent during the shock phase affect the later, hydrodynamic-like, compression phase during which ignition may occur.

3.6 References

1. D. B. Henderson, "Burn characteristics of marginal deuterium-tritium microspheres," Phys. Rev. Lett., **33**(19), 1142–1144 (1974).
2. A. G. Petschek and D. B. Henderson, "Influence of high-energy ion loss on dt reaction rate in laser fusion pellets," Nucl. Fusion, **19**(12), 1678–1680 (1979).
3. T. Nishikawa, H. Takabe and K. Mima, "Ion kinetic effect on fusion reaction rate," Jpn. J. Appl. Phys., **28**(10), 2004–2010 (1989).
4. T. Yabe and K. A. Tanaka, "Long ion mean-free path and nonequilibrium radiation effects on high-aspect-ratio laser-driven implosions," Laser Part. Beams, **7**(2), 259–266 (1989).
5. F. Vidal, J. P. Matte, M. Cadanova *et al.*, "Spherical ion kinetic simulations of dt implosions," Phys. Rev. E, **52**(4), 4568–4571 (1995).
6. J. A. Harte, W. E. Alley, D. S. Bailey *et al.*, "Lasnex – a 2-d physics code for modeling icf," UCRL-LR-105821-96-4, pages 150–164 (1996).
7. J. Delettrez, "Thermal electron transport in direct-drive laser fusion," Can. J. Phys., **64**, 932 (1986).

8. J. T. Larsen and S. M. Lane, "Hyades - a plasma hydrodynamics code for dense plasma studies," J. Quant. Spectrosc. Radiat. Transfer, **51**(12), 179–186 (1994).
9. J. Pino, J. Greenough, R. Tipton *et al.*, "2d simulations of cd mix capsules," Bull. Am. Phys. Soc., **58**(16) (2013).
10. S. Atzeni, "2-d lagrangian studies of symmetry and stability of laser fusion targets," Computer Physics Communications, **43**(1), 107 – 124 (1986).
11. O. Larroche, "Kinetic simulations and fuel ion transport in icf target implosions," Eur. Phys. J. D, **27**, 131–146 (2003).
12. O. Larroche, "Ion fokker-planck simulation of d-^{3}he gas target implosions," Phys. Plasmas, **19**(122706) (2012).
13. D. Li, V. N. Goncharov, I. V. Igumenshchev *et al.*, "Modeling ion heat transport in icf targets," Bull. Am. Phys. Soc., **52**(11) (2007).
14. K. Molvig, N. M. Hoffman, B. J. Albright *et al.*, "Knudsen layer reduction of fusion reactivity," Phys. Rev. Lett., **109**(095001) (2012).
15. B. J. Albright, K. Molvig, C.-K. Huang *et al.*, "Revised knudsen-layer reduction of fusion reactivity," Physics of Plasmas, **20**(12), 122705 (2013).
16. X.-Z. Tang, C. J. McDevitt, Z. Guo *et al.*, "A hybrid model for coupling kinetic corrections of fusion reactivity to hydrodynamic implosion simulations," Physics of Plasmas, **21**(3), 032706 (2014).
17. P. Amendt, O. L. Landen, H. F. Robey *et al.*, "Plasma barodiffusion in inertial-confinement-fusion implosions: Application to observed yield anomalies in themonuclear fuel mixtures," Phys. Rev. Lett., **105**, 115,005 (2010).
18. G. Kagan and X.-Z. Tang, "Electro-diffusion in a plasma with two ion species," Phys. Plasmas, **19**, 082,709 (2012).
19. G. Kagan and X.-Z. Tang, "Thermo-diffusion in inertially confined plasmas," Physics Letters A, **378**(21), 1531 – 1535 (2014).
20. C. Bellei, P. A. Amendt, S. C. Wilks *et al.*, "Species separation in inertial confinement fusion fuels," Phys. Plasmas, **20**, 012,701 (2013).
21. J. R. Rygg, J. A. Frenje, C. K. Li *et al.*, "Tests of the hydrodynamic equivalence of direct-drive implosions with different d2 and 3he mixtures," Phys. Plasmas, **13**, 052,702 (2006).
22. H. W. Herrmann, J. R. Langenbrunner, J. M. Mack *et al.*, "Anomalous yield reduction in direct-drive deuterium/tritium implosions due to ^{3}he addition," Phys. Plasmas, **16**, 056,312 (2009).
23. D. T. Casey, J. A. Frenje, M. G. Johnson *et al.*, "Evidence for stratification of deuterium-tritium fuel in inertial confinement fusion implosions," Phys. Rev. Lett., **108**, 075,002 (2012).
24. H. G. Rinderknecht, H. Sio, C. K. Li *et al.*, "First observations of nonhydrodynamic mix at the fuel-shell interface in shock-driven inertial confinement implosions," Phys. Rev. Lett., **112**, 135,001 (2014).
25. D. Li, V. N. Goncharov, I. V. Igumenshchev *et al.*, "Modeling ion heat transport in icf targets," Bull. Am. Phys. Soc., **51**, 342 (2007).
26. S. Skpusky, V. N. Goncharov and D. Li, "Nonlocal ion-heat transport and viscosity in icf implosions using a quasi-monte carlo approach," Bull. Am. Phys. Soc., **52**(10) (2007).
27. G. Guderley, "Strong spherical and cylindrical compression shocks in the vicinity of spherical centers and cylinder axes," Luftfahrtforschung, **19**(9), 302–312 (1942).
28. P. Amendt, C. Bellei, S. Wilks *et al.*, "On the onset of kinetic effects in icf implosions," Bull. Am. Phys. Soc., **58**(16) (2013).
29. S. Atzeni and J. Meyer-Ter-Vehn, *The Physics of Inertial Fusion: Beam Plasma Interaction, Hydrodynamics, Hot Dense Matter*, International Series of Monographs on Physics, (Oxford University Press, 2004).
30. N. Hoffman *et al.*, "Validating kinetic models in a fluid code using data from high-knudsen-number capsule implosions," Bull. Am. Phys. Soc., **58**(16) (2013).
31. M. J. Rosenberg, H. G. Rinderknecht, N. M. Hoffman *et al.*, "Exploration of the transition from the hydrodynamiclike to the strongly kinetic regime in shock-driven implosions," Phys. Rev. Lett., **112**, 185,001 (2014).
32. M. J. Edwards, P. K. Patel, J. D. Lindl *et al.*, "Progress towards ignition on the national ignition facility," Physics of Plasmas, **20**(7), 070501 (2013).
33. T. R. Dittrich, O. A. Hurricane, D. A. Callahan *et al.*, "Design of a high-foot high-adiabat icf capsule for the national ignition facility," Phys. Rev. Lett., **112**, 055,002 (2014).

34. T. C. Sangster, V. N. Goncharov, R. Betti *et al.*, "Improving cryogenic deuteriumtritium implosion performance on omega," Physics of Plasmas, **20**(5), 056317 (2013).
35. J. Lindl, "Development of the indirect-drive approach to inertial confinement fusion and the target physics basis for ignition and gain," Phys. Plasmas, **2**(11), 3933–4024 (1995).
36. J. R. Rygg, J. A. Frenje, C. K. Li *et al.*, "Observations of the collapse of asymmetrically driven convergent shocks," Phys. Plasmas, **15**, 034,505 (2008).
37. T. R. Boehly, D. L. Brown, R. S. Craxton *et al.*, "Initial performance results of the omega laser system," Opt. Commun., **133**, 495–506 (1997).
38. S. Atzeni, A. Schiavi, F. Califano *et al.*, "Fluid and kinetic simulation of inertial confinement fusion plasmas," Computer physics communications, **169**(1), 153–159 (2005).
39. W. Seka, H. A. Baldis, J. Fuchs *et al.*, "Multibeam stimulated brillouin scattering from hot, solid-target plasmas," Phys. Rev. Lett., **89**(17), 175,002 (2002).
40. M. D. Cable and S. P. Hatchett, "Neutron spectra from inertial confinement fusion targets for measurement of fuel areal density and charged particle stopping powers," J. Appl. Phys., **62**(6), 2233–2236 (1987).
41. J. D. Lindl, P. Amendt, R. L. Berger *et al.*, "The physics basis for ignition using indirect-drive targets on the national ignition facility," Phys. Plasmas, **11**(2), 340–491 (2004).
42. V. Y. Glebov, C. Stoeckl, T. C. Sangster *et al.*, "Prototypes of national ignition facility neutron time-of-flight detectors tested on omega," Rev. Sci. Inst., **75**, 3559–3562 (2004).
43. F. H. Séguin, J. A. Frenje, C. K. Li *et al.*, "Spectrometry of charged particles from inertial-confinement-fusion plasmas," Review of Scientific Instruments, **74**(2) (2003).
44. C. Stoeckl, V. Y. Glebov, S. Roberts *et al.*, "Ten-inch manipulator-based neutron temporal diagnostic for cryogenic experiments on omega," Rev. Sci. Inst., **74**(3), 1713–1716 (2003).
45. D. K. Bradley, P. M. Bell, O. L. Landen *et al.*, "Development and characterization of a pair of 30-40 ps x-ray framing cameras," Rev. Sci. Inst., **66**(1), 716–718 (1995).
46. P. Amendt, J. D. Colvin, R. E. Tipton *et al.*, "Indirect-drive noncryogenic double-shell ignition targets for the national ignition facility: Design and analysis," Phys. Plasmas, **9**(5), 2221–2233 (2002).
47. F. H. Séguin, J. L. Deciantis, J. A. Frenje *et al.*, "D^{3}he-proton emission imaging for inertial-confinement-fusion experiments (invited)," Rev. Sci. Inst., **75**(10), 3520–3525 (2004).
48. F. H. Séguin, J. L. DeCiantis, J. A. Frenje *et al.*, "Measured dependence of nuclear burn region size on implosion parameters in inertial confinement fusion experiments," Physics of Plasmas, **13**(8), 082704 (2006).
49. D. G. Hicks, N. B. Meezan, E. L. Dewald *et al.*, "Implosion dynamics measurements at the national ignition facility," Plasma Physics, **19**, 122,702 (2012).
50. A. B. Zylstra, J. A. Frenje, F. H. Séguin *et al.*, "Charged-particle spectroscopy for diagnosing shock r and strength in nif implosions," Review of Scientific Instruments, **83**(10), 10 (2012).
51. H. G. Rinderknecht, M. G. Johnson, A. B. Zylstra *et al.*, "A novel particle time of flight diagnostic for measurements of shock- and compression-bang times in d^{3}he and dt implosions at the nif," Rev. Sci. Inst., **83**(10D902) (2012).
52. M. J. Rosenberg *et al.*, "Utilization of nif diagnostic development shots for investigation of ion kinetic effects in direct-drive exploding-pusher implosions," to be submitted to Phys. Plasmas (2014).
53. H. Brysk and P. Hammerling, "Dt fusion with microshells," Phys. Rev. Lett., **34**(8), 502–503 (1975).
54. E. K. Storm, H. G. Ahlstrom, M. J. Boyle *et al.*, "Laser fusion experiments at 4 tw," Phys. Rev. Lett., **40**(24), 1570–1573 (1978).
55. M. D. Rosen and J. H. Nuckolls, "Exploding pusher performance – a theoretical model," Phys. Fluids, **22**(7), 1393–1396 (1979).
56. B. Ahlborn and M. H. Key, "Scaling laws for laser driven exploding pusher targets," Plasma Physics, **23**(5), 435–447 (1981).
57. S. H. Glenzer *et al.*, "Cryogenic thermonuclear fuel implosions on the national ignition facility," Plasma Physics, **19**, 056,318 (2012).
58. H. F. Robey *et al.*, "Precision shock tuning on the national ignition facility," Phys. Rev. Lett., **108**(122702) (2012).

59. A. J. Mackinnon *et al.*, "Assembly of high-areal-density deuterium-tritium fuel from indirectly driven cryogenic implosions," Phys. Rev. Lett., **108**(21), 215,005 (2012).
60. J. Nuckolls, L. Wood, A. Thiessen *et al.*, "Laser compression of matter to super-high densities: Thermonuclear (ctr) applications," Nature, **239**, 139–142 (1972).
61. J. Lindl, R. McCrory and E. Campbell, "Progress toward ignition and burn propagation in inertial confinement fusion," Physics Today, **45**, 32–40 (1992).
62. A. B. Zylstra *et al.*, submitted to Phys. Rev. Lett. (2014).
63. A. B. Zylstra *et al.*, to be submitted to Phys. Plasmas (2014).
64. J. R. Rygg, J. A. Frenje, C. K. Li *et al.*, "Electron-ion thermal equilibration after spherical shock collapse," Phys. Rev. E, **80**, 026,403 (2009).
65. J. R. Rygg, *Shock Convergence and Mix Dynamics in Inertial Confinement Fusion*, Ph.D. thesis, Massachusetts Institute of Technology (2006).
66. J. A. Frenje, C. K. Li, F. H. Séguin *et al.*, "Measuring shock-bang timing and ρr evolution of d^{3}he implosions at omega," Phys. Plasmas, **11**(5), 2798–2805 (2004).
67. R. D. Petrasso, J. A. Frenje, C. Li *et al.*, "Measuring implosion dynamics through ρr evolution in inertial-confinement fusion experiments," Phys. Rev. Lett., **90**(9), 095,002 (2003).
68. V. N. Goncharov, J. P. Knauer, P. W. McKenty *et al.*, "Improved performance of direct-drive inertial confinement fusion target designs with adiabat shaping using an intensity picket," Phys. Plasmas, **10**(5), 1906–1918 (2003).
69. V. N. Goncharov, O. V. Gotchev, E. Vianello *et al.*, "Early stage of implosions in inertial confinement fusion: Shock timing and perturbation evolution," Phys. Plasmas, **13**(1), 012,702 (2006).
70. E. S. Dodd, J. F. Benage, G. A. Kyrala *et al.*, "The effects of laser absorption on direct-drive capsule experiments at omega," Phys. Plasmas, **19**, 042,703 (2012).
71. D. C. Wilson, G. A. Kyrala, J. F. B. Jr. *et al.*, "The effects of pre-mix on burn in icf capsules," J. Phys. Conf. Ser., **112**, 022,015 (2008).
72. W. J. Garbett, S. James, G. A. Kyrala *et al.*, "Constraining fundamental plasma physics processes using doped capsule inplosions," J. Phys. Conf. Ser., **112**, 022,016 (2008).
73. G. A. Kyrala, D. C. Wilson, J. F. Benage *et al.*, "Effect of higher z dopants on implosion dynamics: X-ray spectroscopy," High Energy Density Physics, **3**, 163–168 (2007).
74. A. R. Miles, H.-K. Chhung, R. Heeter *et al.*, "Numerical simulation of thin-shell direct drive dhe3-filled capsules fielded at omega," Phys. Plasmas, **19**, 072,702 (2012).
75. W. J. Garbett, C. J. Horsfield, H. W. Herrmann *et al.*, "Modelling the effect of ^{3}he in direct drive capsule implosions," J. Phys. Conf. Ser., **244**, 022,001 (2010).
76. D. Keller, T. J. B. Collins, J. A. Delettrez *et al.*, "*DRACO* - a new multidimensional hydrocode," Bull. Am. Phys. Soc., **44**(37) (1999).
77. P. B. Radha, V. N. Goncharov, T. J. B. Collins *et al.*, "Two-dimensional simulations of plastic-shell, direct-drive implosions on omega," Phys. Plasmas, **12**(032702) (2005).
78. D. L. Bleuel, C. B. Yeamans, L. A. Bernstein *et al.*, "Neutron activation diagnostics at the national ignition facility (invited)," Rev. Sci. Inst., **83**(10D313) (2012).
79. J. R. Rygg, F. H. Séguin, C. K. Li *et al.*, "Proton radiography of inertial fusion implosions," Science, **319**, 1223–1225 (2008).
80. C. K. Li, F. H. Séguin, J. A. Frenje *et al.*, "Charged-particle probing of x-ray-driven inertial-fusion implosions," Science, **327**, 1231–1235 (2010).
81. C. K. Li, F. H. Séguin, J. A. Frenje *et al.*, "Measuring *e* and *b* fields in laser-produced plasmas with monoenergetic proton radiography," Phys. Rev. Lett., **97**, 135,003 (2006).
82. C. K. Li, F. H. Séguin, J. A. Frenje *et al.*, "Observation of the decay dynamics and instabilities of megagauss field structures in laser-produced plasmas," Phys. Rev. Lett., **99**, 015,001 (2007).
83. J. A. Frenje, C. K. Li, F. H. Séguin *et al.*, "Measurements of the differential cross sections for the elastic n-^{3}h and n-^{2}h scattering at 14.1 mev by using an inertial confinement fusion facility," Phys. Rev. Lett., **107**, 122,502 (2011).
84. Y. Kim, J. M. Mack, H. W. Herrmann *et al.*, "Determination of the deuterium-tritium branching ratio based on inertial confinement fusion implosions," Phys. Rev. C, **85**, 061,601(R) (2012).

85. S. Le Pape, L. Divol, L. Berzak Hopkins *et al.*, "Observation of a reflected shock in an indirectly driven spherical implosion at the national ignition facility," Phys. Rev. Lett., **112**, 225,002 (2014).
86. G. Miller, E. Moses and C. Wuest, "The national ignition facility," Opt. Eng., **43**, 2841 (2004).
87. S. Skupsky, J. A. Marozas, R. S. Craxton *et al.*, "Polar direct drive in the national ignition facility," Phys. Plasmas, **11**(5), 2763–2770 (2004).
88. P. W. McKenty, R. S. Craxton, A. Shvydky *et al.*, "Evaluation of the first polar-drive, dt-gas-filled target implosions on the nif," Bull. Am. Phys. Soc., **55**(15) (2010).
89. A. Mackinnon, S. L. Pape, R. Wallace *et al.*, "Using exploding pusher targets to commission diagnostics for the national ignition facility," Bull. Am. Phys. Soc., **55**(15) (2010).
90. S. L. Pape, A. Mackinnon, P. McKenty *et al.*, "Nuclear diagnostic commissioning for the national ignition campaign," Bull. Am. Phys. Soc., **56**(16) (2011).
91. V. Y. Glebov, D. D. Meyerhofer, T. C. Sangster *et al.*, "Development of nuclear diagnostics for the national ignition facility (invited)," Rev. Sci. Inst., **77**(10E715) (2006).
92. F. H. Séguin, N. Sinenian, M. Rosenberg *et al.*, "Advances in compact proton spectrometers for inertial-confinement fusion and plasma nuclear sciencea)," Review of Scientific Instruments, **83**(10), 10 (2012).
93. F. H. Séguin, C. K. Li, J. A. Frenje *et al.*, "Using secondary-proton spectra to study the compression and symmetry of deuterium-filled capsules at omega," Phys. Plasmas, **9**(6), 2525–2537 (2002).
94. S. Kurebayashi, J. A. Frenje, F. H. Séguin *et al.*, "Using nuclear data and monte carlo techniques to study areal density and mix in d_2 implosions," Phys. Plasmas, **12**, 032,703 (2005).
95. J. Delettrez, R. Epstein, M. C. Richardson *et al.*, "Effect of laser illumination nonuniformity on the analysis of time-resolved x-ray measurements in uv spherical transport experiments," Phys. Rev. A, **36**(8), 3926–3934 (1987).
96. J. A. Marozas, F. J. Marshall, R. S. Craxton *et al.*, "Polar-direct-drive simulations and experiments," Phys. Plasmas, **13**(056311) (2006).
97. P. B. Radha, F. J. Marshall, J. A. Marozas *et al.*, "Polar-drive implosions on omega and the national ignition facility," Phys. Plasmas, **20**(056306) (2013).
98. P. W. McKenty, T. C. Sangster, M. Alexander *et al.*, "Direct-drive cryogenic target implosion performance on omega," Phys. Plasmas, **11**(5), 2790–2797 (2004).
99. F. J. Marshall, R. S. Craxton, J. A. Delettrez *et al.*, "Direct-drive, cryogenic target implosions on omega," Phys. Plasmas, **12**(056302) (2005).
100. S. X. Hu, B. Militzer, V. N. Goncharov *et al.*, "Strong coupling and degeneracy effects in inertial confinement fusion implosions," Phys. Rev. Lett., **104**, 235,003 (2010).
101. D. Cao, J. Chenhall, G. Moses *et al.*, "Numerically robust and efficient nonlocal electron transport in 2d draco simulations," Bull. Am. Phys. Soc., **58**(16) (2013).
102. P. Michel, L. Divol, E. A. Williams *et al.*, "Tuning the implosion symmetry of icf targets via controlled crossed-beam energy transfer," Phys. Rev. Lett., **102**, 025,004 (2009).
103. P. W. McKenty, F. J. Marshall, M. Hohenberger *et al.*, "Evaluation of the effects of cross-beam energy transfer in nif polar-drive exploding-pusher experiments," Bull. Am. Phys. Soc., **58**(16) (2013).
104. D. G. Hicks, *Charged-Particle Spectroscopy: A New Window on Inertial Confinement Fusion*, Ph.D. thesis, Massachusetts Institute of Technology (1999).
105. C. K. Li, D. G. Hicks, F. H. Séguin *et al.*, "D-^{3}he proton spectra for diagnosing shell ρr and fuel t_i of imploded capsules at omega," Phys. Plasmas, **7**(6), 2578–2584 (2000).
106. D. G. Hicks, C. K. Li, F. H. Séguin *et al.*, "Charged-particle acceleration and energy loss in laser-produces plasmas," Phys. Plasmas, **7**(12), 5106–5117 (2000).
107. S. Glenn, J. Koch, D. K. Bradley *et al.*, "A hardened gated x-ray imaging diagnostic for inertial confinement fusion experiments at the national ignition facility," Rev. Sci. Inst., **81**(10E539) (2010).
108. G. A. Kyrala, S. Dixit, S. Glenzer *et al.*, "Measuring symmetry of implosions in cryogenic *Hohlraums* at the nif using gated x-ray detectors (invited)," Rev. Sci. Inst., **81**(10E316) (2010).
109. D. H. Edgell, D. K. Bradley, E. J. Bond *et al.*, "South pole bang-time diagnostic on the national ignition facility (invited)," Rev. Sci. Inst., **83**(10E119) (2012).

110. G. Dimonte and R. Tipton, "K-l turbulence model for the self-similar growth of the rayleigh-taylor and richtmyer-meshkov instabilities," Physics of Fluids, **18**(8), 085101 (2006).

111. O. Hurricane, D. Callahan, D. Casey *et al.*, "Fuel gain exceeding unity in an inertially confined fusion implosion," Nature, **506**, 343–348 (2014).

112. H. G. Rinderknecht, H. Sio, J. A. Frenje *et al.*, "A magnetic particle time-of-flight (magptof) diagnostic for measurements of shock- and compression-bang time at the nif (invited)a)," Review of Scientific Instruments, **85**(11), 11 (2014).

113. M. J. Rosenberg, F. H. Séguin, C. J. Waugh *et al.*, "Empirical assessment of the detection efficiency of cr-39 at high proton fluence and a compact, proton detector for high-fluence applications," Review of Scientific Instruments, **85**(4), 043302 (2014).

114. H. Sio *et al.*, submitted to Rev. Sci. Inst. (2014).

115. R. Betti, C. D. Zhou, K. S. Anderson *et al.*, "Shock ignition of thermonuclear fuel with high areal density," Phys. Rev. Lett., **98**, 155,001 (2007).

4

Overview of Magnetic Reconnection

Up to this point, exploding pusher ICF implosions have been discussed as surrogates for studying the shock-convergence phase of ICF implosions, for development of ICF diagnostics, and for studying ion kinetic effects as they manifest in ICF implosions. A further use for exploding pushers, as a proton source and diagnostic tool to probe fundamental plasma physics phenomena, will be discussed in Chapter 5. In this chapter, the ubiquitous and universally-prevalent plasma phenomenon of magnetic reconnection is introduced. In Chapters 5 and 6, studies of magnetic reconnection using laser-produced plasmas are described, including the use of an exploding-pusher-based proton source and other diagnostic techniques to measure the evolution of fields, flows, and thermal properties.

4.1 Introduction

Magnetic reconnection[1–3] is the change in magnetic topology in the presence of a plasma, typically as oppositely-directed magnetic fields merge, annihilate, and release energy in the form of plasma heating and energetic particles ejected from the reconnection region. It is thought to be the dominant mechanism for energy release in the solar corona,[4] responsible for solar flares and coronal mass ejections. Magnetic reconnection also occurs around the magnetosphere of the Earth on both the day side (magnetopause)[5] and the night side (magnetotail),[6] and is responsible for the occurrence of *auroras* in the Earth's atmosphere as energetic particles stream down magnetic field lines to the Earth's surface. Reconnection occurs at many astrophysical scales at any location separating magnetized plasmas of different origins, including at the boundary between the solar magnetic field and the interstellar medium,[7] and possibly between galaxy clusters.[8] Magnetic reconnection is also a critical phenomenon in magnetic-confinement-fusion devices[9] and even in inertial-fusion hohlraums,[10] where laser-produced magnetic fields interact. This chapter provides an overview of magnetic reconnection concepts, astrophysical occurrences, and some laboratory investigations, as background for the presentation in Chapters 5 and 6 of studies of magnetic reconnection using laser-produced plasmas.

4.2 Sweet-Parker Model of Magnetic Reconnection

A simple, two-dimensional model for magnetic reconnection in collisional plasmas described by the equations of magnetohydrodynamics (MHD) was developed by Sweet and Parker in 1957.[11,12] Figure 4.1 illustrates this model, with plasma carrying oppositely-directed magnetic fields of magnitude B into the reconnection region or current sheet of half-length L at inflow speed V_{in}. The layer over which magnetic fields are annihilated has half-width δ, and plasma is ejected out of the end of the layer at speed V_{out}. The outflow speed is derived based on the assumption that the energy density of the annihilating magnetic fields, $B^2/2\mu_0$ is entirely converted to plasma kinetic energy density, $\frac{1}{2}\rho V_{out}^2$, where ρ is the mass density of the plasma. The outflow speed is therefore equal to the Alfvén speed, $V_{out} = V_A = B/\sqrt{\mu_0 \rho}$. By conservation of mass, ignoring compressibility, $V_{in}L = V_{out}\delta$, such that the inflow speed is $V_{in} = V_A(\delta/L)$. The inflow speed, typically a small fraction of the Alfvén speed, dictates the rate of magnetic field annihilation and is considered to be analogous to the reconnection rate.

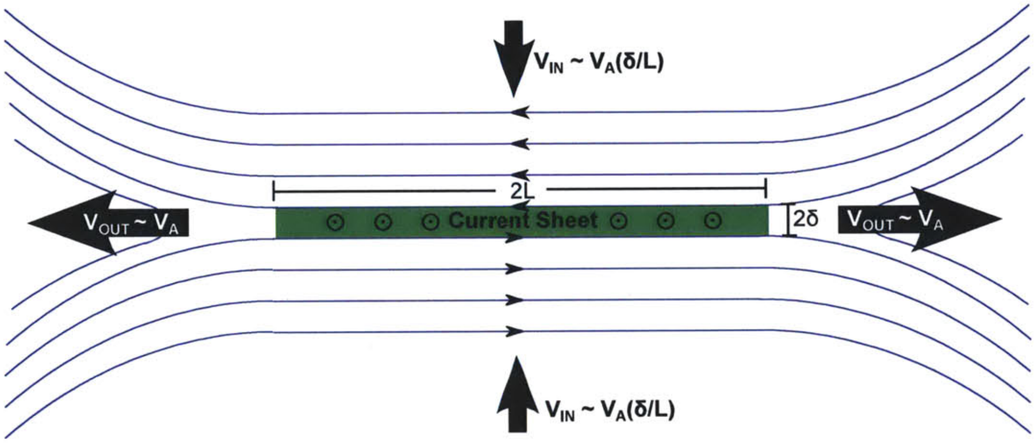

Figure 4.1. Sweet-Parker reconnection model with an elongated current sheet and relatively slow inflow. Plasma is ejected out of the reconnection region at a velocity close to the Alfvén speed V_A.

The resistive MHD model allows for a precise prediction of the reconnection inflow speed in this collisional, Sweet-Parker model. It is defined by the Ohm's law equation

$$\mathbf{E} + \mathbf{v} \times \mathbf{B} = \eta \mathbf{J}, \tag{4.1}$$

where η is the resistivity of the plasma and $\mathbf{J}$ the current. Ideal MHD, where the resistive term is negligible and the field lines are "frozen in" to the plasma, is considered to apply outside the narrow current sheet. Within the current sheet, resistivity is required to break and reconnect magnetic field lines and produce a rearrangement of magnetic topology. Inside the current sheet, the electric field is negligible, such that $V_{in}B \sim \eta J$. Based on Faraday's law, the current which gives rise to the opposing magnetic fields scales like $\mu_0 J \sim B/\delta$. Solving for the inflow velocity, $V_{in} \sim \eta/\delta\mu_0$ or $V_{in} \sim V_A\sqrt{\eta/\mu_0 L V_A}$. The quantity

$$S = \mu_0 L V_A/\eta \tag{4.2}$$

is known as the Lundquist number, and represents the ratio of diffusive to Alfvén timescales. Thus, $\delta/L = V_{in}/V_A \sim 1/\sqrt{S}$. Most astrophysical systems have very large Lundquist numbers, of order 10^{10} or greater. Therefore, the Sweet-Parker model of magnetic reconnection predicts a very slow inflow, only a miniscule fraction of the Alfvén speed. The Sweet-Parker-based reconnection rate has been demosntrated to be much too slow to match astrophysical observations. For example, a time scale for reconnection-related solar flares is predicted to be on the order of years by the Sweet-Parker model; in actuality, they occur on a time scale of minutes or hours. In most discussions of reconnection, the baseline models that are considered and compared to new findings are the Sweet-Parker model and the two-fluid (Hall) or collisionless model presented later, in Section sec:Collisionless. For completeness, a few alternative models are presented below.

4.3 Alternative Reconnection Models

The classical Sweet-Parker model, with its typically long, thin current sheet, and resultant slow inflow speed, does not permit the fast rates of reconnection that appear to be prevalent in and astrophysical and laboratory contexts. In order to resolve this disparity, other models have been proposed within the MHD framework, either to alter the scaling of V_{in} to remove unfavorable dependences on the Lundquist number (i.e. the $1/\sqrt{S}$ scaling, which for typical large values of S stifles reconnection rates in the Sweet-Parker model) or to increase the factors that reduce the Lundquist number (i.e. the plasma resistivity).

4.3.1 Petschek Reconnection Model

The Petschek model[13] greatly enhances the reconnection rate by effectively reducing the length of the current sheet and allowing for significantly faster inflow. This model posits that the reconnection of magnetic fields occurs not over the full length of the reconnection region $2L$, but rather over a shorter region of length $2L'$. By decreasing the aspect ratio of the dissipation region, the ratio of inflow to outflow speeds and, consequently, the reconnection rate, is enhanced. The remainder of the reconnection region is occupied by slow shocks which accelerate plasma outside the short diffusion region up to the Alfvén speed. The seemingly arbitrary length L' was chosen to be the minimum value at which the current produced by these shocks remains small relative to the current which is responsible for the reconnecting magnetic fields. The resulting scaling for the current sheet length is $L' \sim L/S(\ln(S))^2$.[14] Thus, the reconnection rate, instead of scaling as $V_A/\sqrt{S}$, scales as $V_A/\ln(S)$.

Unfortunately for the Petschek model, the diffusion region half-length L' is not actually a free parameter, but instead is limited by the constraint that the magnetic field in the slow shock region must be constantly replenished, and this regeneration becomes weaker as L' is reduced. As it turns out, the Petschek length L' is constrained to the Sweet-Parker length L, and no gain in reconnection rate is achieved.[14] A resolution to this conflict based on an enhanced and spatially-dependent resistivity, which restores some of the reconnection rate gains in the Petschek model, is presented below.

4.3.2 Anomalous Resistivity

Instability-related enhancement of resistivity, known as anomalous resistivity,[14] offers a way to enhance the reconnection rate in both Sweet-Parker and Petschek models, and to allow the Petschek model to be faster than Sweet-Parker. The lower hybrid instability is prone to develop in the presence of a large difference between electron and ion velocities, corresponding to a critical current J_c. This critical current is exceeded, and the lower-hybrid instability excited, when the current layer half-thickness δ is smaller than a critical thickness $\delta_c = B/\mu_0 J$. When the Sweet-Parker current sheet thickness is smaller than this critical thickness, the instability produces copious resistive heating, which generates pressure that effectively expands the current sheet until the instability turns off. Thus, the current sheet thickness is pegged to the critical thickness δ_c – larger than the Sweet-Parker thickness – and the current sheet aspect ratio is consequently enhanced. Therefore, the reconnection inflow speed (the rate of reconnection) is increased.

Anomalous resistivity also revives the utility of the Petschek model as a unique solution distinct from the Sweet-Parker model. A spatially-dependent and current-dependent resistivity complicates the model for generation of magnetic fields to replace those swept away in the Petschek picture.[14] The inflow velocity is dependent on the difference between the resistivity at the center of the current sheet η_0 and the resistivity at the end of the diffusion region η', as $V_{in} \sim (\eta_0 - \eta')/\delta_c$. Based on a linear relationship between the resistivity and the current, it is found that $(\eta_0 - \eta') \sim (L'^2/L^2)(B/\delta_c)(d\eta/dJ)$ and $(V_{in}/V_A)^3 \sim B/(V_A L^2)(d\eta/dJ)$. Therefore, the Petschek inflow velocity in the anomalous resistivity model is $V_{in} = V_A(\delta_c/LS^*)^{1/3}$, where S^* is a modified Lundquist number accounting for the anomalous resistivity, which is typically several orders of magnitude greater than the usual Spitzer resistivity. The increase in current sheet thickness, decrease in Lundquist number, and weaker exponent in the scaling conspire to increase the Petschek reconnection rate to much faster than allowed by classical Sweet-Parker theory and closer in line with observations.

4.4 Two-Fluid (Hall) or Collisionless Reconnection

Two-fluid effects (also referred to as Hall effects) offer a simpler mechanism by which the theoretical reconnection rate can be enhanced, above those found in the collisional, resistive-MHD Sweet-Parker theory and closer to values observed in nature.[2] The models discussed in the previous sections all fall under the umbrella of magnetohydrodynamics, where the plasma is described as a single fluid with ions and electrons closely bound to each other. However, when the scale length of interest – the width of the current sheet – becomes smaller than the ion gyroradius ρ_i or the ion inertial length $d_i = c/\omega_{pi}$ (equivalent to the ion gyroradius of an ion at the Alfvén speed), the ions are no longer tied to the field lines and the magnetic fields are bound only to the electron fluid. The two-fluid reconnection regime is generally considered to be when the Sweet-Parker current sheet width δ_{SP} is smaller than the ion inertial length d_i. As it turns out, this condition for two-fluid reconnection ($\delta_{SP}/d_i < 1$) is fairly close to the condition that the electron mean-free-path λ_e is larger than the current sheet half-length L; therefore, two-fluid reconnection is also considered to be collisionless reconnection.

On scales smaller than d_i, the demagnetized ions act predominantly as a neutralizing background, and the electrons are responsible for transporting the magnetic flux into the reconnection region. Mathematically, this two-fluid treatment differs from the resistive MHD model by the inclusion of the Hall ($\mathbf{J} \times \mathbf{B}$) term in Ohm's law

$$\mathbf{E} + \mathbf{v} \times \mathbf{B} - \mathbf{J} \times \mathbf{B}/en_e = \eta\mathbf{J}. \tag{4.3}$$

When the electron flow decouples from the ion flow, reconnection takes place only over a small region where the electrons are demagnetized, on a much smaller scale than the ion demagnetization region, as shown in Figure 4.2. Electrons flow vertically into the thin current sheet and then rapidly turn outward in the outflow direction. The electron current effectively arises due to the need to maintain quasineutrality as the electron density is reduced in regions where magnetic field lines become more diffuse near the electron diffusion region.[15] The resulting in-plane current generates an out-of-plane magnetic field following Ampere's Law.[15,16] Based on the direction of the current, this out-of-plane magnetic field takes a characteristic quadrupolar configuration. The orientation of the quadrupolar field is determined by the inflow and outflow directions only, regardless of the direction of the reconnecting magnetic field.[15] A bipolar in-plane electric field also develops, directed vertically toward the reconnection layer.[15] These fields are important signatures of two-fluid reconnection and have been observed in spacecraft measurements of the Earth's magnetosphere[17] and in some laboratory experiments.[18,3] Another key signature of two-fluid reconnection is high-speed electron jets that stream out of the reconnection region in the outflow direction,[19] the observation of which in laser-plasma reconnection experiments will be discussed in Chapter 6.

Importantly, this two-fluid reconnection model permits a much faster reconnection, as the aspect

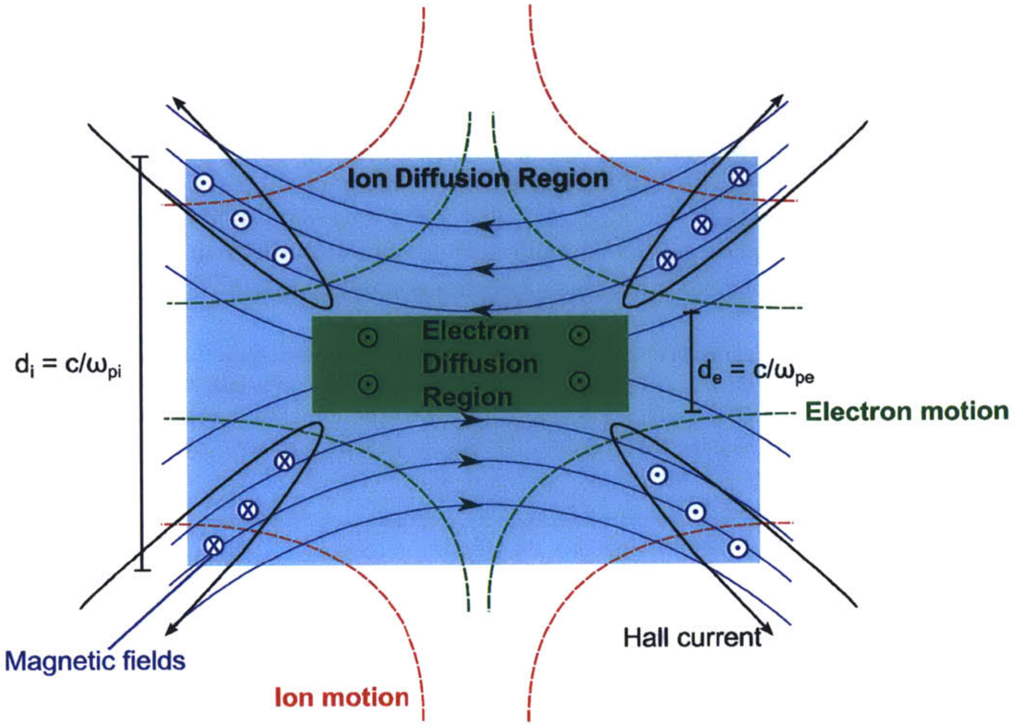

Figure 4.2. Two-fluid (Hall) reconnection model. Ions decouple from the field lines on length scales shorter than $d_i = c/\omega_{pi}$, while the electron fluid carries the field lines into the electron diffusion region, where field lines break and reconnection occurs. In-plane currents (black) form, which produce a quadrupolar, out-of-plane magnetic field (blue).

ratio of the current sheet (length/width) is significantly reduced. The Ohm's law electric field in the out-of-plane direction, which is greatly enhanced by the Hall ($\mathbf{J} \times \mathbf{B}$) term, represents the motion or annihilation rate of magnetic flux, as $E = -d\Psi/dt$. Reconnection rates as high as $V_{in} = 0.1V_A$ or, equivalently, $\mathbf{E} = 0.1V_A B$, have been predicted in collisionless or Hall MHD simulations.[2,3] It has been observed experimentally that the reconnection rate scales inversely with the collisionality, becoming faster with increasing d_i/δ_{SP}.[18] Two-fluid effects, and observation of a transition from fast, two-fluid reconnection to slow, single-fluid reconnection are discussed in the context of laser-produced plasma experiments in Chapter 6.

4.5 Magnetic Reconnection in Astrophysical and Laboratory Plasmas

Magnetic reconnection occurs in nature and in the laboratory in a variety of regimes, with densities and magnetic field strengths that vary by tens of orders of magnitude. Consequently, reconnection-relevant dimensionless parameters like the Lundquist number S, the collisionality parameter δ_{SP}/d_i, and the plasma β, the ratio of thermal to magnetic energy density, vary substantially and introduce very different reconnection physics. A summary of conditions in astrophysical and experimental reconnection environments, based on the discussion in Ji *et al.*[20] and its references, is shown in Table 4.1. Included in this table are conditions for reconnection in the solar corona, where flares are prominent, at the Earth's dayside magnetopause, in the interstellar medium, in the laboratory plasma of the Versatile Toroidal Facility (VTF),[21] where reconnection experiments are conducted, and in plasmas produced by the interaction of $\sim 10^{14}$ W/cm^2 lasers with solid targets.[22] These parameters will also be illustrated graphically in Figure 6.1. Another relevant descriptor, not commonly referenced, but particularly relevant to laser-plasma experiments and the magnetopause, is the ratio of flow velocity (V_{flow}) to Alfvén speed (V_A). This parameter describes how strongly the magnetic fields are driven together: for $V_{flow}/V_A>1$, the fields are said to be strongly driven, as they are advected faster than the speed at which magnetic fields can naturally rearrange themselves. This condition is an important aspect of laser-plasma reconnection experiments discussed in Chapter 6.

Table 4.1. Estimates of the plasma scale size, electron density, magnetic field strength, and the resulting dimensionless parameters: plasma β, the ratio of thermal to magnetic pressure; the Lundquist number S; and the ratio of the Sweet-Parker current sheet width (δ_{SP}) to the ion skin depth (d_i), which dictates the collisionality. Many of these values are taken from Ji *et al.*,[20] which contains a much more extensive list of plasma environments.

Location	Scale (m)	n_e (m^{-3})	B (T)	β	S	δ_{SP}/d_i
Solar corona	10^7	10^{15}	0.02	0.0002	10^{13}	10
Dayside magnetopause	6×10^7	10^7	10^{-7}	1	10^{14}	0.0001
Interstellar medium	5×10^{19}	10^5	10^{-9}	0.1	10^{20}	2000
VTF experiment	0.4	10^{18}	0.1	0.005	1000	0.2
Laser-produced plasma	0.001	10^{26}	50	10	500	1

Reconnection occurs in a variety of plasma environments at different plasma β, varying from on the order of 10^{-4} – magnetic-field dominated – in parts of the solar corona to as high as $\sim$100 – hydrodynamically dominated – at the boundary between the heliosphere and the interstellar medium.[7] Certain locations in the solar photosphere[23] and the dayside magnetopause of the Earth and other planets[24–26] also achieve values of $\beta>1$. One local, naturally-occurring example of reconnection is at the dayside magnetopause, as illustrated in Figure 4.3. The northward-facing magnetic field in the Earth's magnetosphere is impinged upon by the sometimes southward-facing magnetic field in the solar wind plasma, in this context known as the magnetosheath. Outflow from reconnection around the Earth's magnetosphere is responsible for the appearance of the *aurora*. Spacecraft observation of one magnetopause reconnection event[17] showed that the magnetosheath plasma had a density of 8 cm^{-3} and a magnetic field strength of 80 nT, while the Earth's magnetosphere plasma had a density of 2 cm^{-3} and a magnetic field of 80 nT. Typical plasma β is $\sim$5 in the magnetosheath and <1 in the magnetosphere, producing an asymmetric, high-β reconnection. Asymmetric reconnection is discussed in more detail in Section 4.6 and experiments exploring asymmetric reconnection using laser-produced plasmas is discussed in Chapter 6. While laboratory plasmas such as in VTF[21] or the Magnetic Reconnection Experiment (MRX)[27] have lower plasma β, of order 0.01-0.1, typical β in laser-produced plasmas are $\sim$10.[28] In combination, this wide variety of laboratory plasmas allows exploration of the physics of reconnection in several different astrophysical contexts, from magnetically-dominated to hydrodynamically-dominated.

As described earlier, the Lundquist number S is the ratio of resistive to Alfvén timescales and determines the aspect ratio of the Sweet-Parker current sheet ($\delta_{SP}/L = 1/\sqrt{S}$) and the reconnection inflow rate V_{in}/V_A. The large Lundquist numbers found in many astrophysical contexts and the resulting slow Sweet-Parker-predicted reconnection rate led to the search for fast reconnection models. Furthermore, for very high Lundquist numbers, above $\sim 10^4$, the reconnection layer is

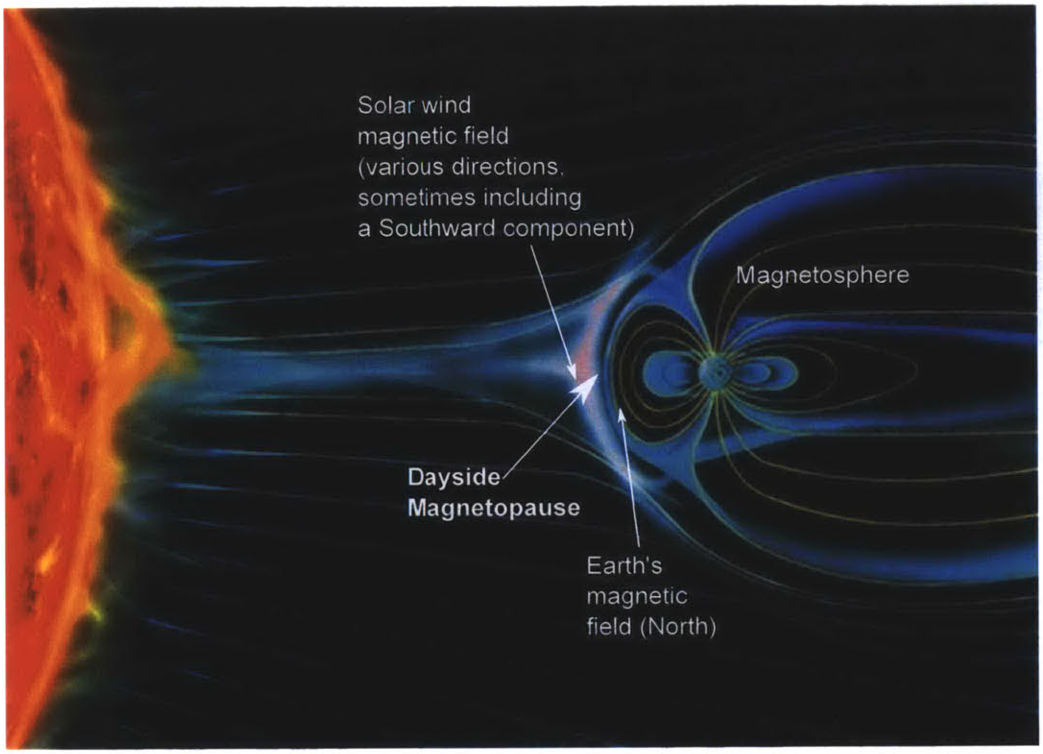

Figure 4.3. Magnetic reconnection at the Earth's dayside magnetopause, where the Earth's northward magnetic field interacts with the magnetic field carried by the solar wind, which can contain a southward component. Illustration credit: NASA

prone to breaking up into multiple current sheets, with magnetic islands or plasmoids ultimately ejected out of the layer.[20] This plasmoid-mediated reconnection is thought to be responsible for coronal mass ejections on the sun, with reconnection outflow ejected away from the solar surface. The outflow toward the surface of the sun is responsible for the appearance of coronal loops on the solar surface, as plasma is heated along reconnected magnetic field lines. This process is illustrated in NASA images in Figure 4.4. The solar corona, with a Lundquist number of $S{\sim}10^{13}$, is well into the plasmoid-dominated regime of reconnection.

In addition to occurring in different regimes of plasma β and Lundquist number, reconnection also occurs in very disparate regimes of collisionality. Among the astrophysical environments listed in Table 4.1, the interstellar medium and solar corona fall into the collisional regime, while the magnetopause is highly collisionless. Collisionless reconnection is fairly well reproduced in the VTF experiment, and laser-produced plasmas are also generally considered collisionless for the purposes of reconnection studies. It should be noted that in the laser-produced plasma, because $\beta{>}1$, the length scale for ion demagnetization, the ion gyroradius ρ_i, is greater than the ion inertial length d_i by a factor of $\sim\sqrt{\beta}$ (see Appendix F), and the plasma is somewhat less collisional than is suggested by the ratio δ_{SP}/d_i. For certain high-β conditions, δ_{SP}/ρ_i is a more relevant collisionality metric. Signatures of collisionless reconnection, such as out-of-plane quadrupolar magnetic fields and fast electron jets, have been observed in spacecraft measurements of the magnetopause[29,19] and the magnetotail (night side of the magnetopause)[30] and in the laboratory.[18]

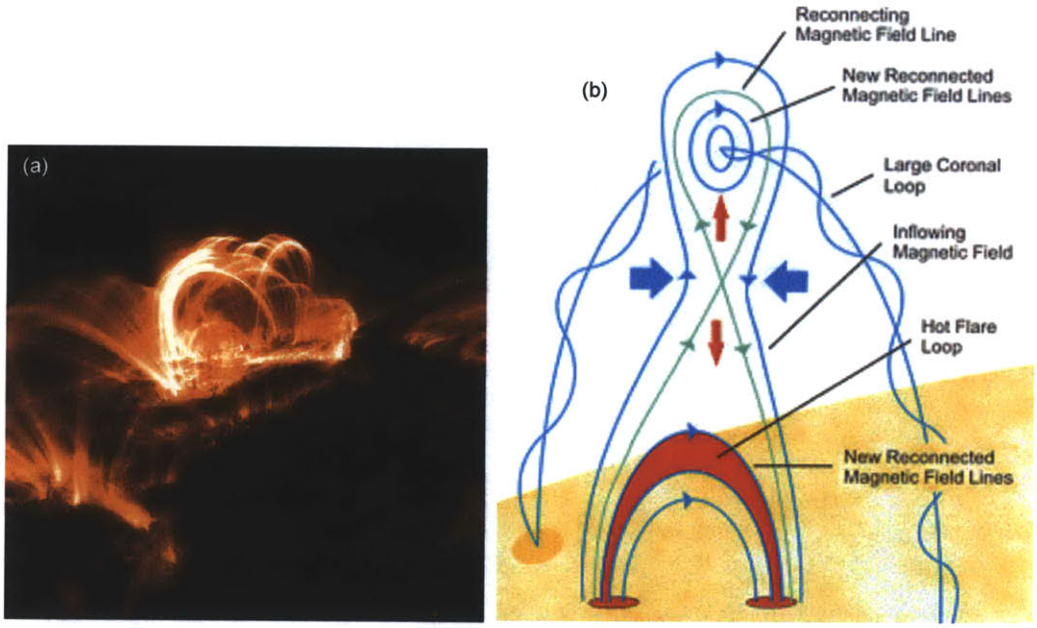
(a)
(b)
Reconnecting Magnetic Field Line
New Reconnected Magnetic Field Lines
Large Coronal Loop
Inflowing Magnetic Field
Hot Flare Loop
New Reconnected Magnetic Field Lines

Figure 4.4. Magnetic reconnection in the context of solar flares. The hot flare loop, as seen in an x-ray image obtained by the TRACE satellite (a), is plasma flowing along the reconnected field lines to the solar surface, as illustrated in (b). Image and cartoon credit: NASA.

4.6 Asymmetric Reconnection

To this point, models of reconection have been discussed in the context of perfect symmetry across the current sheet. However, reconnection more frequently occurs in the universe under conditions of asymmetric inflow, with differences in plasma density, magnetic field strength, inflow velocity, or ram pressure across the current sheet. Notable examples of asymmetric reconnection are at the Earth's magnetopause,[31,32] the magnetotail,[6] the solar atmosphere,[33] and the heliopause.[7] Asymmetric magnetic reconnection can occur at any boundary between magnetically-separated plasmas of different origins. Asymmetric *outflow* reconnection, with asymmetries along (rather than across) the current sheet, occurs in the context of solar flares.[34]

Asymmetric reconnection has recently begun to be studied theoretically. An extension of the Sweet-Parker model has provided a scaling law for the reconnection rate and outflow speed for asymmetric inflow reconnection,[35] finding that the effective magnetic field strength and Alfvén speed are hybrid quatities based on B and ρ on either side of the current sheet. The outflow velocity scales as

$$V_{out}^2 \sim \frac{B_1 B_2 (B_1 + B_2)}{\rho_1 B_2 + \rho_2 B_1}, \tag{4.4}$$

where B_1 (B_2) is the magnetic field strength and ρ_1 (ρ_2) is the plasma density on the upper (lower) side of the current sheet. Under symmetric conditions, the outflow speed reduces to $V_{out} \sim B/\sqrt{\rho} \sim V_A$, the Alfvén speed. The reconnection rate expressed as the reconnection electric field, scales as

$$E \sim \frac{B_1 B_2}{B_1 + B_2} V_{out} \frac{2\delta}{L}. \tag{4.5}$$

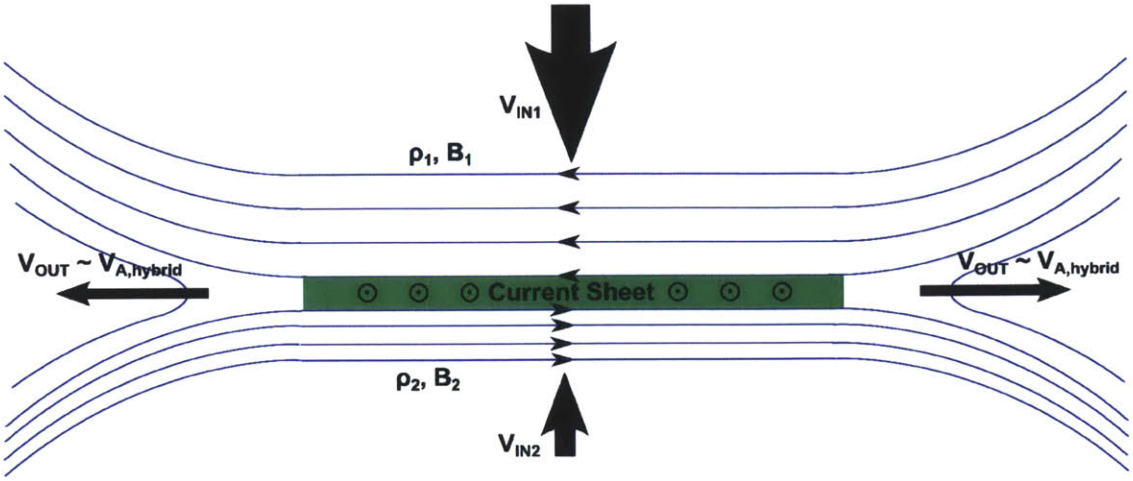

Figure 4.5. Asymmetric magnetic reconnection configuration. In this example, the magnetic field is stronger on the lower side of the current sheet ($B_2 > B_1$), while the inflow velocity is greater on the upper side of the current sheet ($V_{in1} > V_{in2}$) in order to maintain a equivalent annihilation rate of magnetic flux. In a general reconnection configuration, the plasma densities on either side of the current sheet (ρ_1, ρ_2) are likely to be different as well. The outflow speed V_{out} is equivalent to a hybrid Alfvén speed (Equation 4.4).

For symmetric conditions, this scaling reduces to the usual relation $E \sim BV_A\delta/L$. A Sweet-Parker-like asymmetric reconnection configuration is depicted in Figure 4.5. Several collisional and collisionless simulation studies have explored aspects of asymmetric reconnection and have generally confirmed the scalings predicted by the Sweet-Parker-like model.[36–40] A key theoretical finding is that, unlike in symmetric reconnection, in a reconnection geometry with asymmetries in density and magnetic field strength across the current sheet, the plasma stagnation point is no longer colocated with the magnetic null point, such that plasma can fow across the X-point. Additionally, in the presence of an out-of-plane "guide" magnetic field, asymmetric configurations at high plasma β are prone to a suppression of reconnection by diamagetic drift of the X-line occurring faster than the outflow speed.[41,42] This phenomenon has been proposed to suppress reconnection in high-β asymmetric evironments such as at the magnetopause.[43] Asymmetric reconnection has also been hypothesized to produce an additional in-plane electric field as a consequence of different Larmor radii ρ_i and ion inertial lengths d_i on either side of the current sheet.[44]

To date, asymmetric reconnection has received little concerted experimental attention. The first dedicated experimental campaign to study asymmetric magnetic reconnection, using strongly-driven, $\beta > 1$, laser-produced plasmas, is discussed in Chapter 6.

4.7 Thesis Overview: Magnetic Reconnection

The second part of this thesis discusses studies of magnetic reconnection using laser-produced plasmas.

Chapter 5 describes the generation of magnetic fields in laser-produced plasmas and their application in experiments to study magnetic reconnection. Techniques used to probe these plasmas are discussed, including proton radiography for measurements of electric and magnetic fields and Thomson scattering for measurements of electron and ion temperatures. A proton radiography technique using D^{3}He-filled exploding pushers as a monoenergetic proton source is described. Early laser-plasma magnetic field and reconnection experiments that showed annihilation of MG magnetic fields are summarized. Finally, newly-presented Thomson scattering measurements of laser-plasma reconnection experiments show that the magnetic reconnection dynamics do not significantly alter the thermal properties of this $\beta\sim 8$ plasma.

Chapter 6 discusses several new experiments using proton radiography to probe magnetic reconnection in the symmetric and asymmetric collision of laser-produced plasmas. The first systematic, laboratory experiments to study asymmetric magnetic reconnection are presented. It is shown that experiments that introduced an asymmetry in the plasma bubble size, density, and pressure across the reconnection region demonstrate a similar annihilation of magnetic flux as in comparable, symmetric experiments. In these strongly-driven reconnection experiments, the rate of flux anihilation is found to be dictated by the plasma flow velocity and thus insensitive to initial plasma conditions and asymmetries. High-resolution proton radiographs show detailed structure of electric and magnetic fields around laser-produced plasma bubbles and their reconnection, including in-plane (reconnection-induced) jets. A slowing of the reconnection rate is observed as strong magnetic fields persist as the plasma transitions from the collisionless to the collisional regime. Experiments configured to produce a strong collision of parallel magnetic fields (as opposed to anti-parallel in reconnection experiments) show magnetic field deformation in the absence of reconnection.

4.8 References

1. D. Biskamp, "Magnetic reconnection via current sheets," Phys. Fluids, **29**(5), 1520–1531 (1986).
2. E. G. Zweibel and M. Yamada, "Magnetic reconnection in astrophysical and laboratory plasmas," Annu. Rev. Astron. Astrophys., **47**, 291–332 (2009).
3. M. Yamada, R. Kulsrud and H. Ji, "Magnetic reconnection," Rev. Mod. Phys., **82**(1), 603–664 (2010).
4. S. Tsuneta, "Structure and dynamics of magnetic reconnection in a solar flare," Astrophys. J., **456**, 840–849 (1996).
5. B. U. O. Sonnerup, G. Paschmann, I. Papamastorakis *et al.*, "Evidence for magnetic field reconnection at the earth's magnetopause," J. Geophys. Res., **86**(A12), 10,049–10,067 (1981).
6. M. Oieroset, T. D. Phan and M. Fujimoto, "Wind observations of asymmetric magnetic reconnection in the distant magnetotail," Geophys. Res. Lett., **31**(L12801) (2004).
7. M. Opher, J. F. Drake, K. M. Schoeffler *et al.*, "Is the magnetic field in the heliosheath laminar or a turbulent sea of bubbles?" Astrophys. J., **734**(71) (2011).
8. M. W. Kunz, A. A. Scheknochihin, S. C. Cowley *et al.*, "A thermally stable heating mechanism for the intracluster medium: turbulence, magnetic fields and plasma instabilities," Mon. Not. R. Astron. Soc., **410**, 2446–2457 (2011).
9. J. A. Wesson, "Sawtooth reconnection," Nucl. Fusion, **30**(12), 2545–2549 (1990).
10. J. Lindl, "Development of the indirect-drive approach to inertial confinement fusion and the target physics basis for ignition and gain," Phys. Plasmas, **2**(11), 3933–4024 (1995).
11. P. A. Sweet, page 123, (Cambridge University Press, New York, 1958).
12. E. N. Parker, "Sweet's mechanism for merging magnetic fields in conducting fluids," J. Geophys. Res., **62**, 509–520 (1957).
13. H. E. Petschek, "Magnetic field annihilation," Proceedings of AAS-NASA Symposium on Physics of Solar Flares, NASA Spec. Publ., **SP-50**(425) (1964).
14. R. M. Kulsrud, "Magnetic reconnection: Sweet-parker versus petschek," Earth Planets Space, **53**, 417–422 (2001).
15. D. A. Uzdensky and R. M. Kulsrud, "Physical origin of the quadrupole out-of-plane magnetic field in hall-magnetohydrodynamic reconnection," Phys. Plasmas, **13**(062305) (2006).
16. A. Le, J. Egedal, W. Daughton *et al.*, "Magnitude of the hall fields during magnetic reconnection," Geophys. Res. Lett., **37**(L03106) (2010).
17. F. S. Mozer, S. D. Bale and T. D. Phan, "Evidence of diffusion regions at a subsolar magnetopause crossing," Phys. Rev. Lett., **89**(1), 015,002 (2002).

18. M. Yamada, Y. Ren, H. Ji *et al.*, "Experimental study of two-fluid effects on magnetic reconnection in a laboratory plasma with variable collisionality," Phys. Plasmas, **13**(052119) (2006).
19. T. D. Phan, J. F. Drake, M. A. Shay *et al.*, "Evidence for an elongated (>60 ion skin depths) electron diffusion region during fast magnetic reconnection," Phys. Rev. Lett., **99**, 255,002 (2007).
20. H. Ji and W. Daughton, "Phase diagram for magnetic reconnection in heliophysical, astrophysical, and laboratory plasmas," Phys. Plasmas, **18**(111207) (2011).
21. J. Egedal, W. Fox, N. Katz *et al.*, "Laboratory observations of spontaneous magnetic reconnection," Phys. Rev. Lett., **98**(015003) (2007).
22. C. K. Li, F. H. Séguin, J. A. Frenje *et al.*, "Observation of megagauss-field topology changes due to magnetic reconnection in laser-produced plasmas," Phys. Rev. Lett., **99**, 055,001 (2007).
23. Y. E. Litvinenko, "Photospheric magnetic reconnection and canceling magnetic features on the sun," Astrophys. J., **515**, 435–440 (1999).
24. G. Paschmann, I. Papamastorakis, W. Baumjohann *et al.*, J. Geophys. Res., **91**(A10), 11,099–11,115 (1986).
25. T.-D. Phan, G. Paschmann, W. Baumjohann *et al.*, "The magnetosheath region adjacent to the dayside magnetopause: Ampte/irm observations," J. Geophys. Res., **99**(A1), 121–141 (1994).
26. A. Masters, J. P. Eastwood, M. Swisdak *et al.*, "The importance of plasma β conditions for magnetic reconnection at saturn's magnetopause," Geophys. Res. Lett., **39**(L08103) (2012).
27. H. Ji, M. Yamada, S. Hsu *et al.*, "Experimental test of the sweet-parker model of magnetic reconnection," Phys. Rev. Lett., **80**(15), 3256–3259 (1998).
28. M. J. Rosenberg, J. S. Ross, C. K. Li *et al.*, "Characterization of single and colliding laser-produced plasma bubbles using thomson scattering and proton radiography," Phys. Rev. E, **86**, 056,407 (2012).
29. X. H. Deng and H. Matsumoto, "Rapid magnetic reconnection in the earth's magnetosphere mediated by whistler waves," Nature, **410**, 557–560 (2001).
30. M. Oieroset, T. D. Phan, M. Fujimoto *et al.*, "In situ detection of collisionless reconnection in the earth's magnetotail," Nature, **412**, 414–417 (2001).
31. F. S. Mozer, V. Angelopoulos, J. Bonnell *et al.*, "Themis observations of modified hall fields in asymmetric magnetic field reconnection," Geophys. Res. Lett., **35**(L17S04) (2008).
32. F. S.Mozer, P. L. Pritchett, J. Bonnell *et al.*, "Observations and simulations of asymmetric magnetic field reconnection," J. Geophys. Res., **113**(A00C03) (2008).
33. J. T. Karpen, S. K. Antiochos, C. R. DeVore *et al.*, "Dynamic responses to magnetic reconnection in solar arcades," Astrophys. J., **495**, 491–501 (1998).
34. N. A. Murphy, M. P. Miralles, C. L. Pope *et al.*, "Asymmetric magnetic reconnection in solar flare and coronal mass ejection current sheets," Astrophys. J., **751**(1) (2012).
35. P. A. Cassak and M. A. Shay, "Scaling of asymmetric magnetic reconnection: General theory and collisional simulations," Physics of Plasmas, **14**(10), 102114 (2007).
36. J. E. Borovsky and M. Hesse, "The reconnection of magnetic fields between plasmas with different densities: Scaling relations," Physics of Plasmas, **14**(10), 102309 (2007).
37. P. A. Cassak and M. A. Shay, "Scaling of asymmetric hall magnetic reconnection," Geophys. Res. Lett., **35**(L19102) (2008).
38. P. L. Pritchett, "Collisionless magnetic reconnection in an asymmetric current sheet," J. Geophys. Res., **113**(A06210) (2008).
39. J. Birn, J. E. Borovsky and M. Hesse, "Properties of asymmetric magnetic reconnection," Phys. Plasmas, **15**(032101) (2008).
40. J. Birn, J. E. Borovsky, M. Hesse *et al.*, "Scaling of asymmetric reconnection in compressible plasmas," Phys. Plasmas, **17**(052108) (2010).
41. M. Swisdak, B. N. Rogers, J. F. Drake *et al.*, "Diamagnetic suppresion of component magnetic reconnection at the magnetopause," J. Geophys. Res., **108**(A5) (2003).
42. M. Swisdak, M. Opher, J. F. Drake *et al.*, "The vector direction of the interstellar magnetic field outside the heliosphere," Astrophys. J., **710**, 1769–1775 (2010).
43. T. D. Phan, J. T. Gosling, G. Paschmann *et al.*, "The dependence of magnetic reconnection on plasma β and magnetic shear: Evidence from solar wind observations," Astrophys. J. Lett., **719**, L199–L203 (2010).
44. K. Malakit, M. A. Shay, P. A. Cassak *et al.*, "New electric field in asymmetric magnetic reconnection," Phys. Rev. Lett., **111**, 135,001 (2013).

5

Diagnosing Laser-Plasma Magnetic Reconnection Experiments

Laser-produced plasmas are an excellent, controlled, laboratory environment in which to study the physics of magnetic reconnection, relevant to its widespread occurrence in astrophysical plasmas. In this chapter, an overview of experimental conditions and well-established diagnostics of laser-plasma reconnection experiments is presented.

First, in Section 5.1, background on the generation and interaction of magnetic fields in laser-produced plasmas is presented. Then, the diagnostic technique of proton radiography, used to image and measure electric and magnetic fields in laser-produced plasmas, is discussed (Sections 5.2 and 5.3), including the use of exploding pusher implosions as a monoenergetic proton source. The use of Thomson scattering as a means to measure local conditions in laser-plasma experiments is introduced in Section 5.4.

Finally, the chapter concludes with the presentation of a new study, conducted as part of this thesis, that combines previously-presented proton radiography results with newly-analyzed Thomson scattering data to characterize comprehensively the magentic and thermal properties of laser-produced plasma bubbles and the magnetic reconnection of bubble pairs (Section 5.5). The experimental data show that the electron and ion temperatures of the plasma are largely unchanged in the strongly-driven magnetic reconnection of high-β plasmas. These results constitute a significant contribution to the field of plasma physics and help guide new studies of magnetic reconnection using laser produced plasmas (Chapter 6).

5.1 Laser Generation of Magnetic Fields in Plasmas

The generation of magnetic fields by the interaction of intense ($\sim 10^{14}$ W/cm^2) lasers with matter was first observed in 1971.[1] Measurements using magnetic probes,[1] Faraday rotation,[2] interferometry,[3] x-ray imaging,[4] and, later, proton radigraphy,[5,6] have confirmed the existence of megagauss (MG) magnetic fields around expanding plumes or bubbles of plasma created by laser ablation of solid targets. Two-fluid theory identifies the source of these self-generated magnetic fields as non-parallel gradients in electron density n_e and electron temperature T_e. Starting with the electron momentum equation in absence of an initial magnetic field, the electric field is balanced principally by the electron pressure gradient,[7] as

$$\mathbf{E} = -\frac{\nabla p_e}{n_e e}, \tag{5.1}$$

where p_e is the electron pressure, n_e is the electron density and e is the electron charge. The curl of this electric field gives rise to a changing magnetic field, as dictated by Faraday's law,

$$\frac{\partial \mathbf{B}}{\partial t} = -\nabla \times \mathbf{E} = \nabla \times \left(\frac{\nabla p_e}{n_e e} \right) = \frac{\nabla T_e \times \nabla n_e}{n_e e}, \tag{5.2}$$

where T_e is the electron temperature. The generation of magnetic fields according to $\partial \mathbf{B}/\partial t \propto \nabla T_e \times \nabla n_e$ is known as the Biermann battery mechanism.

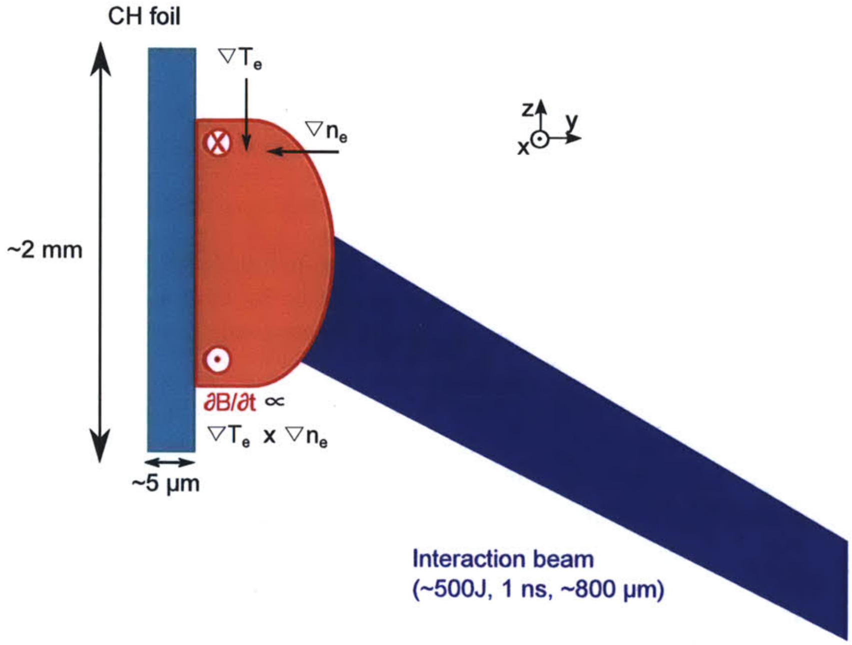

Figure 5.1. Self-generated magnetic fields in laser-foil interaction. A density gradient in the -y direction and a temperature gradient radially inward (-z direction at the top of the bubble and +z direction at the bottom) produces an azimuthal magnetic field at the perimeter of an expanding plasma bubble. Typical conditions for OMEGA experiments[6,8] are given.

Figure 5.1 illustrates how non-parallel gradients in electron temperature and electron density generate magnetic fields around the laser spot of a laser-foil interaction. The ablation of plasma off of the foil surface creates a gradient in density back toward the foil surface in the direction of the incident laser (-y direction). The laser spot itself creates a cylindrically radially inward gradient of electron temperature toward the center of the hemispherical plasma bubble. These gradients are most strongly non-parallel at the perimeter of the expanding plasma bubble, and for typical laser-foil interaction conditions, the magnetic fields occupy a thin ribbon of thickness ~100 μm. The azimuthal direction of these fields is also consistent with an effective current in the laser propagation direction (-y direction) as electrons stream away from the foil (+y direction) more rapidly than the ions.

Figure 5.2 shows 2D MHD LASNEX[9–12] simulations of profiles of magnetic field strength in a laser-foil experiment on OMEGA, with 500 J in a 1-ns pulse and an 800-μm spot size incident on a 5-μm thick CH foil. As shown by Li *et al.*[13] after laser shutoff around t = 1.1 ns, the perimeter of the bubble starts to become more diffuse as it expands radially as well as vertically away from the foil surface. Typical electron densities are $n_e \sim 10^{20}$ cm^{-3} at the perimeter of the bubble, where magnetic fields are strongest, and up to $\sim 10^{22}$ cm^{-3} at the bubble center, near the foil. The strongest electron density gradient is toward the foil, in the -y direction. The plasma also cools significantly during its expansion, with temperatures early in time of $T_e \sim 1.2$ keV near the bubble center and ~0.7 keV at the perimeter (with a strong, radially-inward gradient), and only ~0.5 keV later in time. Magnetic fields in a thin skin at the bubble perimeter with a near-constant magnitude of ~0.5 MG are advected with the plasma expansion and flow in both the radial (Z) and vertical (Y) directions.

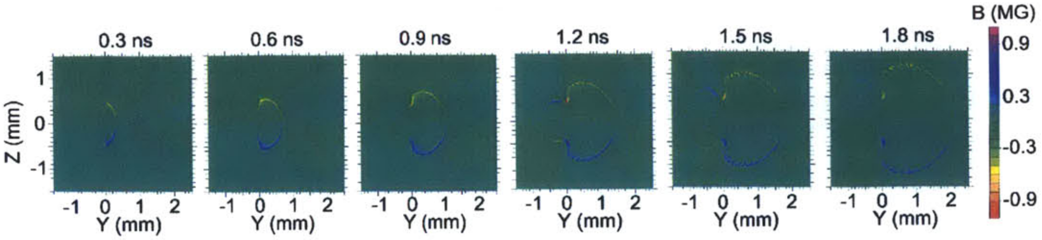

Figure 5.2. LASNEX-simulated magnetic field profiles in a laser-foil experiment on OMEGA, for 500 J in a 1-ns pulse and an 800-μm spot size incident on a 5-μm thick CH foil from the right side.[13] The evolution of this cylindrically-symmetric laser-produced plasma bubble shows a near-constant magnetic field strength (~0.5 MG) that is advected radially outward and away from the foil.

In addition to the generation of magnetic fields due to gradients in temperature and density, the magnetic fields evolve largely as a consequence of advection with the plasma flow. The effects of advection and diffusion of fields are described by the inclusion of additional terms in Ohm's law. Including plasma flow and resistive effects in equation 5.1 yields

$$\mathbf{E} = -\frac{\nabla p_e}{n_e e} - \mathbf{V}_e \times \mathbf{B} + \frac{\mathbf{R}_e}{n_e e}, \tag{5.3}$$

where $\mathbf{V}_e$ is the bulk flow velocity of the electron fluid and $\mathbf{R}_e$ is the force imparted on the electrons. Writing this frictional force as $\mathbf{R}_e = n_e e \eta \mathbf{J}$, where η is the resistivity and $\mathbf{J} = n_e e(\mathbf{V}_i - \mathbf{V}_e)$ is the plasma current, the generalized Ohm's law is derived as

$$\mathbf{E} = \frac{\mathbf{J} \times \mathbf{B} - \nabla p_e}{n_e e} - \mathbf{V}_i \times \mathbf{B} = -\frac{\nabla p_e}{n_e e} - \mathbf{V}_e \times \mathbf{B}. \tag{5.4}$$

The current or electron velocity term corresponds to the Hall effect, though in a plasma that does not already contain a magnetic field it does not contribute to electric field generation.

Faraday's law can be expressed in more detail by taking the curl of equation 5.4, such that

$$\frac{\partial \mathbf{B}}{\partial t} \approx -\nabla \times \left(\frac{\mathbf{J} \times \mathbf{B} - \nabla p_e}{n_e e} - \mathbf{V}_i \times \mathbf{B} - \frac{\mathbf{R}}{n_e e} \right), \tag{5.5}$$

where $\mathbf{R}$ accounts for resistive frictional effects. The important terms in the magnetic field evolution equation are

$$\frac{\partial \mathbf{B}}{\partial t} \approx \nabla \times \left(\frac{\nabla p_e}{n_e e} \right) + \nabla \times (\mathbf{V}_i \times \mathbf{B}) + \frac{\eta}{\mu_0} \nabla^2 \mathbf{B}, \tag{5.6}$$

where the resistive contributions have been expressed in terms of a current, the curl of which yields the Laplacian of the magnetic field. The curl of the pressure gradient is the so-called Biermann battery source term described earlier, while the ion velocity term dictates advection of the magnetic field with the fluid, and the resistive term represents the diffusion of magnetic fields. The relative importance of flow in comparison to diffusion over the length scale L is expressed in terms of the magnetic Reynolds number

$$Rm = \frac{\mu_0 L V_i}{\eta}. \tag{5.7}$$

For $Rm \gg 1$, the magnetic fields are advected with the fluid flow; whereas for $Rm \ll 1$, the magnetic field diffuses rapidly relative to bulk plasma motion. At early times in laser-foil experiments, the plasma is hot enough ($\sim$1 keV) that resistivity is fairly insignificant and the magnetic Reynolds number is $Rm \sim 2000$. The magnetic fields are effectively advected with the expansion of the plasma bubble. Later in time as the plasma cools and expansion slows, the resistivity increases and becomes larger than the flow. At these late time, instabilities have been observed, which are attribute to resistive effects.[8,14]

5.2 Proton Radiography Techniques for Measurement of Electric and Magnetic Fields in Plasmas

Electric and magnetic fields generated in laser-produced plasmas have been probed and measured using the diagnostic technique of proton radiography.[5,15] The principle of the technique relies on measuring the deflection of backlighter protons according to the Lorentz force

$$\mathbf{F} = q\mathbf{E} + q\mathbf{v} \times \mathbf{B}, \tag{5.8}$$

where q is the proton charge and $\mathbf{v}$ is the proton velocity. A generic illustration of proton radiography is shown in Figure 5.3.

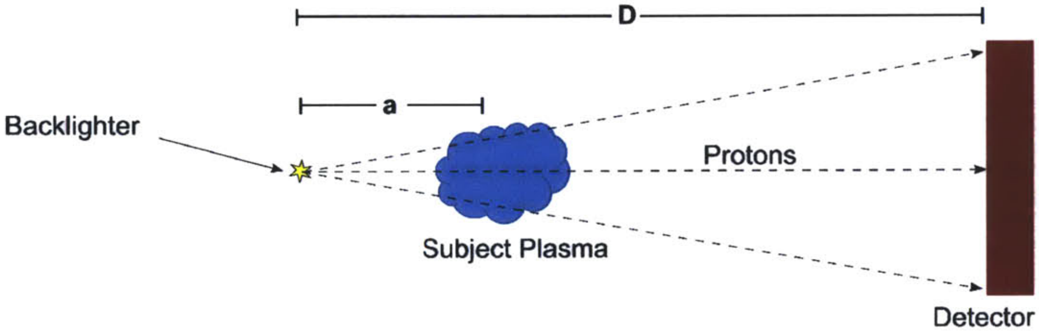

Figure 5.3. Principle of proton radiography. Protons are emitted from a small source volume and sample a subject plasma a distance a from the backlighter. The protons are deflected by electric and magnetic fields in the plasma and their positions recorded on a detector, typically radiochromic film (RCF) or CR-39, positionted a distance $D \gg a$ from the backlighter. The magnification is D/a.

The deflection angle for a proton of velocity v_p passing through an electric field $\mathbf{E}$ can be determined by calculating the transverse momentum imparted on the proton, as

$$m_p \frac{dv_\perp}{dt} = qE_\perp, \tag{5.9}$$

where the subscript $_\perp$ denotes perpendicular relative to the incident proton velocity. Considering the proton path length through the plasma is $dl = v_p dt$, the perpendicular velocity can be expressed as

$$v_\perp m_p v_p = qE_\perp, \text{ or} \tag{5.10}$$

$$v_\perp / v_p = \frac{q}{2E_p} \int E_\perp dl, \tag{5.11}$$

where $E_p = m_p v_p^2/2$ is the proton energy. The left-hand side represents the tangent of the deflection angle θ, so that the proton-path-integrated electric field strength is

$$\int E_{\perp} dl = \frac{2E_p}{q} \tan\theta. \tag{5.12}$$

In terms of the geometry of the experiment, the relationship between the apparent linear displacement at the detector ξ and the path-integrated perpendicular electric field is

$$\int E_{\perp} dl = \frac{2E_p}{q} \frac{\xi}{D-a}. \tag{5.13}$$

Given a measured displacement at the detector and knowing the proton energy allows precise, quantitative measurement of the perpendicular electric field strength integrated along the proton trajectory. Even without a tightly-constrained proton energy, useful information on electric (or magnetic) field structures and rough magnitudes can be obtained.

The magnetic deflection is derived similarly, starting at the force equation

$$m_p \frac{dv_{\perp}}{dt} = q\mathbf{v}_p \times \mathbf{B}. \tag{5.14}$$

A straightforward substitution $\mathbf{dl} = \mathbf{v}_p dt$ leads to

$$v_{\perp} = -\frac{q}{m_p} \int \mathbf{B} \times \mathbf{dl}. \tag{5.15}$$

The deflection is in the direction perpendicular to the magnetic field and proportional to the magnetic field component perpendicular to the incident proton velocity. In terms of the measured displacement at the detector ξ and the deflection angle θ, for small θ where $\sin\theta \sim \tan\theta \sim \theta$,

$$\int \mathbf{B} \times \mathbf{dl} = -\frac{m_p v_p}{q} \sin\theta = -\frac{m_p v_p}{q} \frac{\xi}{D-a}. \tag{5.16}$$

Again, given a known proton energy (or velocity) and a measured displacement, the path-integrated field strength can be inferred at high quantitative accuracy.

One concern with this technique is the fact that without *a priori* knowledge of whether the fields are electric or magnetic, there is a degeneracy in extracting the field type from the measured deflection. Are the fields causing the proton deflection electric or magnetic? This problem is rectified either (1) in experiments where multiple proton energies are used at once, because deflection due to electric and magnetic fields have different energy scalings – $\xi_E \propto 1/E_p$ and $\xi_B \propto 1/\sqrt{E_p}$, or (2) in experiments that change the geometry of the radiography.[16]

In general, proton radiography is robust to depth of focus issues, which can plague other types of imaging systems sensitive to focusing or defocusing of particles or photons (where sharp images are obtained only at a particular distance from the focusing source). Figure 5.4 depicts synthetic proton radiographs produced by varying aspects of the experimental geometry, principally the distance between the backlighter and the detector. The images are generated by proton ray tracing through the indicated path-integrated magnetic field structure, roughly reminiscent of a laser-plasma magnetic reconnection experiment. In each of the first three synthetic radiographs, the backlighter protons are deflected inward toward the center of the magnetic field structures. Variation of the backlighter-detector distance from 6 to 24 cm (from a magnification of M = 8.5 to M = 31, given a backlighter-subject distance of 0.8 cm) does not qualitatively change the appearance of proton fluence structures, with only very small quantitative differences in the peak proton fluence magnitude at the detector. For M ≫1, the magnetic deflection behaves like a projection system, not changing the shape, but merely the size of the resulting image. This allows great flexibility in experimental design, in order to optimize other aspects of the radiography (e.g. the proton fluence at the detector). Only in situations with parallel incoming proton rays or a small magnification (M∼1) does the shape of the corresponding proton fluence image depend on the distance between the subject and the detector.

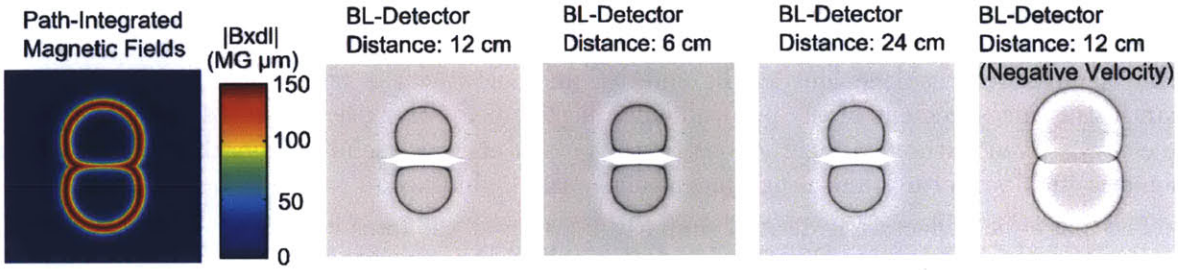

Figure 5.4. Synthetic proton radigraphy of a magnetic field structure, illustrating how differences in the backlighter-detector distance do not qualitatively change the appearance of proton fluence structures at the detector. The difference between inward deflection and outward deflection, due to the reversal of direction of the backlighter protons ("negative velocity") is also illustrated. This example uses near-azimuthal magnetic fields centered around two different bubbles, as in laser-plasma reconnection experiments, with a peak path-integrated magnetic field strength of 150 MG μm. The synthetic radiographs are produced via proton ray tracing, with 23.8-MeV protons and a backlighter-subject distance of 0.8 cm.

The appearance of light and dark features – deficits and enhancements of proton fluence – are, to zeroth order, projections of the gradient in proton deflection resulting from the gradient in path-integrated electric or magnetic field strength.[15] Considering proton deflection in a single dimension, the relation between the position of a proton ray at the object x_0 and at the image x is given by

$$x = x_0 + \frac{D}{a}x_0 + D\alpha_x, \tag{5.17}$$

where α_x is the angular deflection induced by electric or magnetic fields. For $D \gg a$, the first term can be neglected and the system can be treated as a projection system, as discussed above. The intensity of proton signal at the detector I is related to the intensity incident on the object I_0 as

$$I_0/I = \left(\frac{\partial x}{\partial x_0}\right) \sim \left[1 + \frac{D}{a} + D\frac{\partial \alpha_x}{\partial x_0}\right]. \tag{5.18}$$

For a large magnification and small proton deflection, the proton intensity at the detector is simply

$$I/I_0 \sim \left[1 - a\frac{\partial \alpha_x}{\partial x_0}\right]. \tag{5.19}$$

This equation is expressed in terms of the position at the object; equation 5.17 can be used to convert the object-plane coordinates into the image-plane coordinates. For small proton deflections, the image-plane position x is simply proportional to the object plane position x_0, so the modulations in proton fluence at the detector are simply projections of the gradient in deflection angle (with modification to that simple projection determined by the angular deflection). The deflection angle is related to path-integrated electric and magnetic field magnitudes, based on equations 5.12 and

5.16, as

$$\alpha_x = \frac{q}{2E_p} \int E_\perp dl \tag{5.20}$$

and

$$\alpha_x = \frac{q}{m_p v_p} \int \mathbf{B} \times \mathbf{dl}. \tag{5.21}$$

Thus, the intensity of proton fluence features is largely a function of the gradient in path-integrated electric or magnetic field strength. These effects are illustrated conceptually in Figure 5.5.

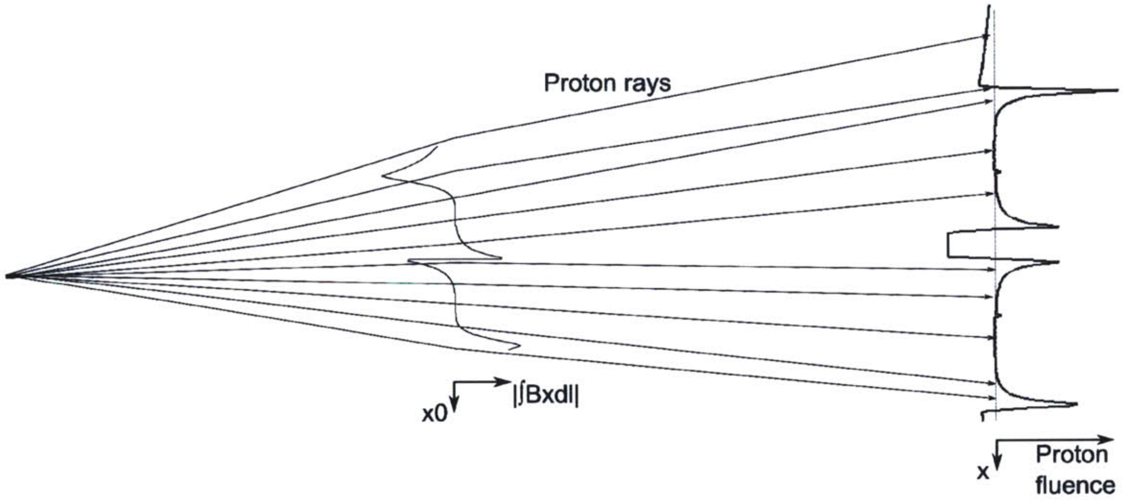

Figure 5.5. Conceptual illustration of proton deflection and the resulting proton fluence based on proton ray tracing through a path-integrated magnetic field structure. In general, regions of strong gradients in path-integrated magnetic field strength at the object plane (x_0) correspond to peaks and valleys in proton fluence at the image plane (x). In reality, the magnification is much greater than depicted.

5.2.1 Exploding-Pusher Implosion Monoenergetic Proton Backlighting

One proton backlighting technique utilizes D^3He exploding-pusher implosions, of the type studied in detail to explore kinetic effects (as discussed in Chapter 3), to generate an isotropic burst of monoenergetic DD and D^3He protons at 3 and 15 MeV, respectively.[17,18] The properties of this backlighter are dictated by the implosion dynamics and fusion production. A typical backlighter implosion on OMEGA uses a 420-μm diameter, 2-μm thick SiO_2 shell filled with 18 atm of equimolar D^3He gas. This capsule is imploded by 18-30 beams, delivering 9-12 kJ quasi-symmetrically on the capsule in a 1-ns pulse. The implosion generates $\sim 10^8$-10^9 DD protons and $\sim 5\times10^7$-5×10^8 D^3He protons over a period of $\sim$100 ps and with a source size of $\sim$50 μm.[17] This backlighter is isotropic, such that multiple experiments can be backlit simultaneously in different directions. In Chapter 3 it was discussed how exploding pusher data obtained in ride-along mode at the NIF are being used towards the development of this backlighting technique at that facility.

Because of the monoenergetic nature of the fusion products, with $\Delta E/E$ of order 2%, very precise quantitative information on electric and magnetic fields can be gleaned from the measured deflection of backlighter protons. Furthermore, because protons of two distinct energies sample the same plasma (albeit at slightly different times because of the difference in time-of-flight), it is possible to break the degeneracy to determine whether the field in question is electric or magnetic. CR-39 nuclear track detectors are configured in a two-piece stack to detect the DD and D^3He

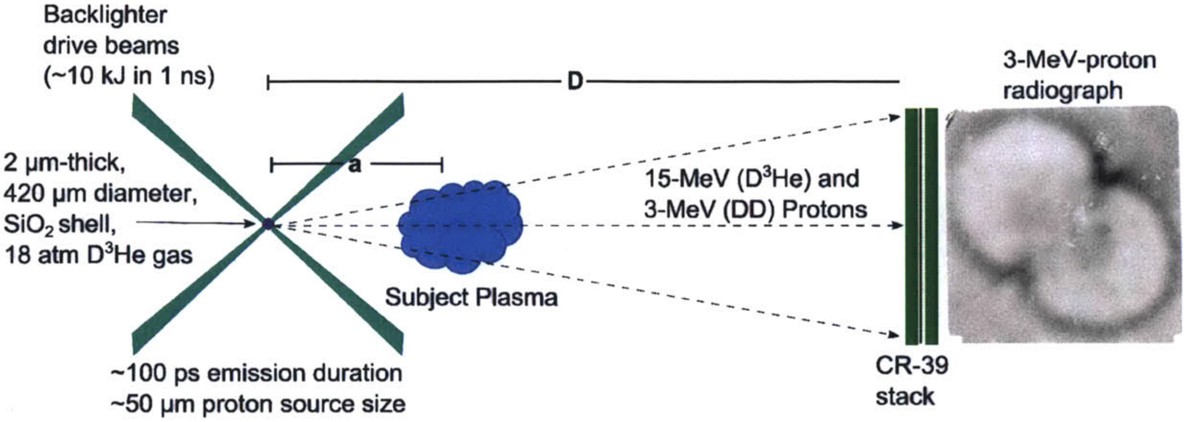

Figure 5.6. Monoenergetic proton radiography using a thin glass-shell, exploding pusher implosion with D^3He gas to produce a $\sim$100 ps burst of monoenergetic 15-MeV (D^3He) and 3-MeV (DD) protons with a $\sim$50 μm source size. A sample 3-MeV-proton radiograph of magnetic fields around colliding and reconnecting laser-produced plasma bubbles is shown, with dark representing greater proton fluence.

protons at optimal energies. This proton backlighting technique is illustrated in Figure 5.6, with a sample 3-MeV-proton radiograph of colliding and reconnecting laser-produced plasma bubbles. The 3-MeV-proton radiography image is obtained on the front piece of CR-39, filtered by 7.5 μm of tantalum to range out low-energy ablator ions and to attenuate x-rays. 15-MeV-proton radiographs are obtained on the second piece of CR-39, additionally filtered by the first piece of 1500 μm thick CR-39, plus 200 μm of aluminum.

This proton radiography technique also presents the unique advantage of being able to measure the energy of the protons through the diameter of the tracks left in the CR-39.[19] Based on the well-known birth energy and the energy-resolving capabilites of the CR-39, it is possible to determine the relative amount of energy downshift. This makes it possible to probe mass structures, or to determine the path-integrated density ρL between the backlighter and the detector. Most valuably, if it is determined that protons passing through the subject plasma do not lose significant energy, any deflection of backlighter protons can be attributed to electric and magnetic fields and not to mass scattering, which would cause a downshift in backlighter proton energy.

The potency of this technique, using simultaneous images of proton fluence and proton energy, is illustrated in Figure 5.7. In a 15-MeV-proton fluence image of an unimploded ICF capsule (with a cone embedded in the shell), a significant deficit of protons is observed in a circular pattern corresponding to the limb of the shell (Figure 5.7a).[20] The proton energy image (Figure 5.7c) shows an identical circular pattern of reduced proton energy. In combination, these images indicate that the protons have been scattered by mass structures (namely, the solid-density CH shell), causing both an angular scattering and a loss of energy. In contrast, a laser-foil experiment provides an example of proton fluence structures uncorrelated with proton energy structures. In Figure 5.7b, 15-MeV-proton fluence modulations are observed at both the center and the perimeter of a laser-produced plasma bubble. However, the proton energy image (Figure 5.7d), shows no structure at the center of the image and little structure at the perimeter. Because the proton fluence structures show no analog in the proton energy image, it can be inferred that electromagnetic fields, and not mass scattering, are responsible for the proton fluence structures in the image obtained in the laser-foil experiment.

For many laser-plasma experiments, including magnetic reconnection experiments discussed in

Chapter 6, with typical plasma densities of ~10^{20} cm^{-3} over length scales of order ~mm, mass scattering has a negligible effect on proton radiography. The magnitude of scattering is similar to that of the original cold target in those particular experiments, a 5 μm thick foil of ~1.1 g/cm^3 CH, which produces an average scattering angle of only ~0.05° for 15-MeV protons. This mass-related scattering is small compared to typical scattering angles due to ~MG magnetic fields, of order ~1°. It has been shown that the cold-matter approximation is reasonable for calculations of mass scattering in plasmas for this type of experiment.[18]

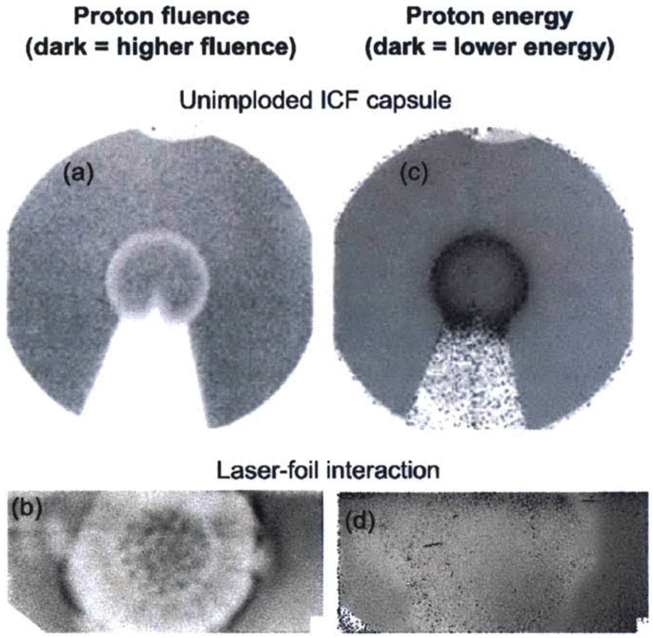

Figure 5.7. Proton (a),(b) fluence and (c),(d) energy images in monoenergetic proton radiography experiments, imaging an unimploded ICF capsule (cone-in-shell) and a laser-foil interaction. In the ICF capsule, both the 15-MeV-proton fluence and energy (images originally published by Rygg *et al.*[20]) are reduced at the limb of the capsule due to mass scattering of the backlighter protons. In contrast, in the laser-foil interaction, the proton energy is unchanged despite fluctuations in the proton fluence. Thus, it is inferred that fields, not scattering, are responsible for the fluence modulations.

In some experiments, a metallic mesh is placed on one side of the subject plasma to divide the proton fluence into a grid of discrete beamlets, to enable an accurate, quantitative inference of path-integrated field strength maps. An illustration of grid-based radiography with the monoenergetic proton backlighter is shown in Figure 5.8. A typical mesh is 60 μm thick Ni, with a 150 μm period. 3-MeV protons that directly strike the front of the mesh are ranged out (the range of a 3-MeV proton in nickel is ~45 μm). However, there is a fraction of 3-MeV protons that graze the surface of the mesh and pass through only a short length of nickel. These protons experience significant angular scattering. For example, 3-MeV protons that pass through 10 μm Ni experience scattering of, on average 3.4°. This is a fairly large angle, compared to the angle subtended by the grid spacing, ~1° (150 μm spacing at a distance of 1 cm from the backlighter). As a result, the partial scattering of 3-MeV protons smears out the grid structure in the image (see Figure 5.8b), though large-scale proton deflection due to fields is still observed (see Figure 5.8c). Ideal grid images are obtained using 15-MeV protons. These protons are not stopped in the Ni mesh, but rather are slowed enough that they are ranged out in the 200-μm Al filter immediately in front of the second piece of CR-39 (the piece that detects the 15-MeV protons). Partial scattering is not a concern for these higher-energy protons (<0.5° scattering angle for the small fraction of "grazing" 15-MeV that pass through only 10 μm of the Ni mesh) and sharp grid images are obtained (see Figure 5.8d).

The use of individual beamlets, easier to identify and locate than a continuous flux of protons, is used to precisely and quantitatively measure the proton deflection. Equations 5.13 and 5.16 show how the measured deflection ξ relates to the path-integrated magnitude of electric and magnetic fields. In combination with the monoenergetic backlighter, this technique is a powerful tool for ob-

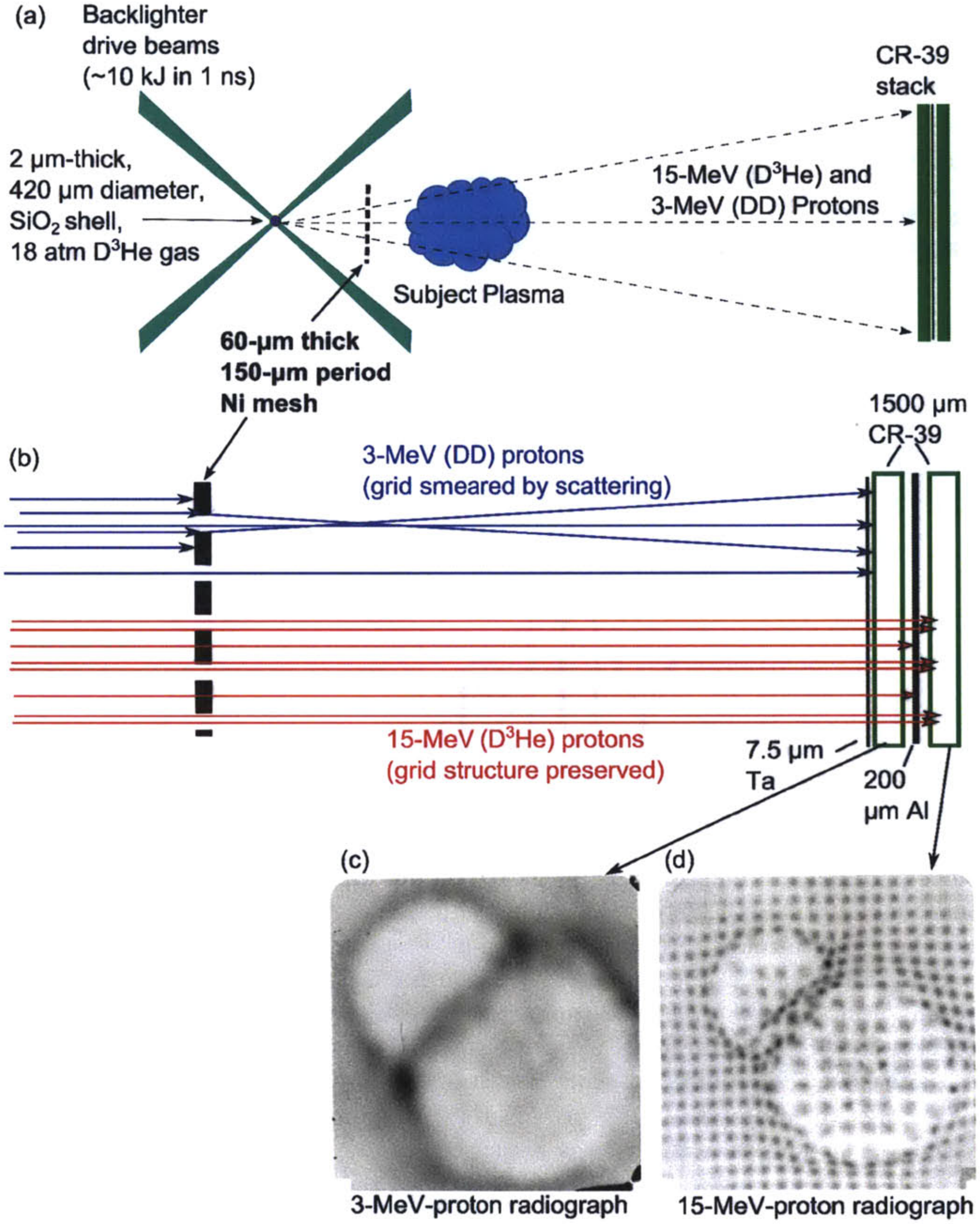
(a)
Backlighter drive beams (~10 kJ in 1 ns)
CR-39 stack
2 μm-thick, 420 μm diameter, SiO$_2$ shell, 18 atm D^{3}He gas
15-MeV (D^{3}He) and 3-MeV (DD) Protons
Subject Plasma
60-μm thick 150-μm period Ni mesh
(b)
1500 μm CR-39
3-MeV (DD) protons (grid smeared by scattering)
15-MeV (D^{3}He) protons (grid structure preserved)
7.5 μm Ta
200 μm Al
(c)
(d)
3-MeV-proton radiograph
15-MeV-proton radiograph

Figure 5.8. Grid-based monoenergetic proton radiography. In this example, a magnetic reconnection experiment later discussed in Chapter 6, (a) a 60-μm thick Ni mesh with a 150-μm period is placed between the backlighter source and the experiment. A zoomed in view (b) of the proton trajectories through the mesh and the detector (ignoring deflection at the subject) illustrates how the 3-MeV DD protons (blue) are completely stopped in the mesh, but at oblique incidence can scatter off the mesh and smear out the grid structure. In contrast, the 15-MeV D^{3}He protons (red) scatter very little, and those protons that pass through the mesh are subsequently ranged out in the filtering in front of the CR-39, leaving a sharp grid structure. Resulting (c) 3-MeV and (d) 15-MeV proton radiographs demonstrate these effects.

taining highly accurate measurements of local path-integrated electric and magnetic field strengths in laser-produced plasmas. With grid-based radiography, there is the added consideration of potential ambiguity between beamlets – the question of which beamlet corresponds to which initial grid location. It is ideal to construct the experiment such that the apparent deflection of beamlets is smaller than the grid spacing, or at least that the difference in proton beamlet deflection from one grid point to the next is smaller than the grid spacing. In cases where ambiguity of grid-beamlet pairing becomes an issue, it may be possible to resolve the degeneracy using synthetic radiography, as the strong magnetic-field gradients necessary to produce such ambiguity likely leave other signatures in proton fluence (e.g. stretching or shrinking of proton beamlets) beyond the information contained simply in the beamlet centroid location. The 150-μm period mesh used in most experiments is sufficiently spaced relative to beamlet deflections in order to minimize beamlet ambiguity.

This exploding-pusher-based, monoenergetic proton radiography technique has been used previously to study electric and, predominantly, magnetic fields in laser-foil experiments,[6,16] and to identify instabilities and observe magnetic field decay dynamics in laser-produced plasmas.[8,14] Other experiments have used monoenergetic proton radiography to probe large electric fields in imploding ICF capsules[20,21] and filamentary structure in the coronal plasma.[20,22] Several experiments have investigated detailed field structures in indirect-drive hohlraums, including jets and plasma blow-off in vacuum and gas-filled hohlraums.[23–25] Monoenergetic proton radiography has also been used to study magnetic fields around laser-produced plasma jets and jet interactions,[26] the Rayleigh-Taylor instability in laser-produced plasmas,[27] and another instability-related field structures.[28] This technique has also been used to make the first quantitative measurements of magnetic reconnection in laser-produced plasmas.[13] These studies of magnetic reconnection using proton radiography have been greatly expanded upon in this work, as will be described in Chapter 6. Details of some previous proton radiography studies of, specifically, *magnetic* fields in laser-foil interactions are discussed in the Section 5.3.

5.2.2 Target Normal Sheath Acceleration Proton Backlighting

Another proton backlighting technique utilizes a high-intensity (~10^{19} W/cm^2) laser-foil interaction to accelerate protons up to energies of 0-50 MeV, or greater.[29,30] The target normal sheath acceleration (TNSA) mechanism works by irradiating a thin, high-Z (typically Au) foil in such a way that high-energy electrons are ejected from the back surface (non-irradiated side) of the foil. The absence of these electrons sets up a strong potential sheath in which contaminant protons are accelerated. An exponentially-decaying spectrum of protons is produced,[29] and the protons are typically focused in a cone around the direction of propagation of the incident laser, with a larger cone half-angle for less energetic protons and a smaller cone half-angle for highly energetic protons. These half-angles range from ~5° for protons >35 MeV to ~20° for protons >17 MeV,[29] though under typical radiography conditions these angle are larger than the angle required to image the entire subject.

The protons are typically detected by a stack of radiochromic film (RCF),[31] where the resulting optical density of the film is correlated to the deposited dose of protons. Each film is sensitive predominantly to protons of a different energy, with the greatest energy sensitivity around the Bragg peak of that film. The sensitivity full-width at half maximum (FWHM) on a given film is of order ~200 keV.[32] Thus, each film is sensitive protons over a finite range of energies. This slightly complicates quantitative inference of electric and magnetic field structures from the measured proton fluence in a way that is not true of proton radiography with a monoenergetic source (as discussed in the previous section). Another consideration for obtaining high-quality images is the intensity of proton fluence on the film. With too little fluence, images are not visible; with too much fluence, the film saturates and features are swamped out.

This proton backlighting technique has been used to study electric and magnetic fields in laser-foil interactions,[33,34] laser-wire interactions,[35] hohlraum experiments,[36] and studies of the Rayleigh-Taylor instability.[37] Some experiments have used this proton radiography technique to image magnetic reconnection experiments in laser-produced plasmas.[38,39] Recent experiments studying magnetic reconnection using TNSA proton backlighting are discussed in Chapter 6.

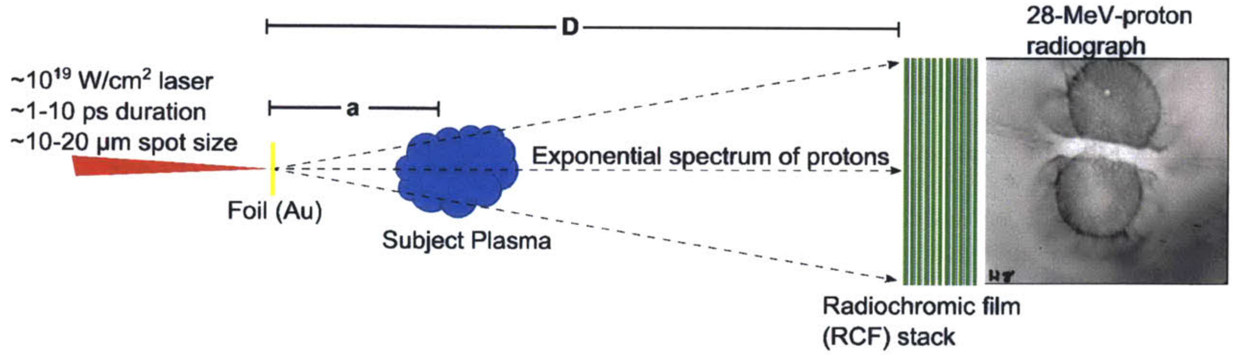

Figure 5.9. Proton radiography using the target normal sheath acceleration mechanism. Protons are accelerated away from a foil irradiated by an intense ($\sim 10^{19}$ W/cm^2) laser with a 1-10 ps duration and a 10-20 μm spot size. The protons consist of an exponentially decaying spectrum and are detected by a stack of radiochromic film (RCF). A sample 28-MeV-proton radiography image of colliding and reconnecting plasma bubbles is shown, with dark representing a greater proton-induced dose. Rings of high proton fluence appear as a consequence of gradients in path-integrated magnetic field strength at the perimeter of the plasma bubbles, as protons passing through regions of different field strength are deflected to the same location at the film.

TNSA proton radiography used in magnetic reconnection experiments in this work were performed at the OMEGA-EP laser facility.[40] A typical setup for TNSA proton radiography is illustrated in Figure 5.9. Experiments on OMEGA-EP utilized a 10 μm thick Au foil irradiated by a laser pulse of a variety of laser energies: either a 1-ps pulse, with laser energies of 200-400 J or a 10-ps pulse, with laser energies up to 850 J.[32] The 1-ps pulse, with a higher laser power, produced more energetic protons, upward of 50 MeV, with optimal images produced by protons in the range of 15-30 MeV. A face-on radiograph of laser-produced plasma bubbles undergoing magnetic reconnection, obtained using these laser parameters, is shown in Figure 5.9. This configuration was more useful for looking at stronger fields, as the higher proton energy allows for a more modest proton deflection, easier to measure. The 10-ps pulse produced protons at energies up to $\sim$35 MeV, with the most useful images with protons at 10-20 MeV, more sensitive to weaker field structures.

In these experiments, twelve pieces of RCF film were filtered so that the individual pieces of film had proton energies of greatest sensitivity spaced out by 2-10 MeV, with times of flight between the different films separated by 10-60 ps. Table 5.1 indicates the proton energies of greatest sensitivity for this commonly-used film pack and corresponding times-of-flight for each proton energy, for a typical backlighter-subject distance of 8 mm.

The spatial and temporal resolution of this proton backlighting technique are determined largely by the laser properties. The laser spot size and, thus, the proton source size for TNSA proton backlighting on OMEGA-EP is typically $\sim$10-20 μm. This size effectively sets the spatial resolution of the images. For $\sim$mm-scale plasmas in typical laser-plasma experiments, this resolution is

Film	Energy (MeV)	Time-of-Flight (ns)
1	4.7	0.38
2	7.1	0.31
3	8.9	0.28
4	10.5	0.25
5	14.8	0.21
6	18.3	0.19
7	23.8	0.17
8	28.4	0.16
9	36.0	0.14
10	42.5	0.13
11	51.0	0.12
12	60.9	0.11

Table 5.1. Characteristics of radiochromic film stack used in TNSA backlighting, including the proton energy of greatest probability and time-of-flight for a backlighter-subject distance of 8 mm as used in magnetic reconnection experiments.

sufficient to resolve highly detailed structures (as illustrated in the sample image in Figure 5.9. The temporal resolution, dictated by the duration of the laser pulse, is of order ~1-10ps, much shorter than scale times in laser-plasma experiments that are driven by ~ns lasers.

The characteristic parameters and relative advantages and disadvantages of exploding-pusher (monoenergetic) and TNSA proton backlighting are summarized in Table 5.2. In summary, TNSA backlighting offers superior temporal and spatial resolution, necessary to discern small-scale features, while the monoenergetic, exploding-pusher backlighter allows for greater quantitativeness in inferring path-integrated electric or magnetic field magnitudes over larger-scale structures, aided as well by better spatial uniformity of the proton emission.

Table 5.2. Characteristics of TNSA and exploding-pusher proton backlighting.

Characteristic	TNSA	Exploding-Pusher
Backlighter Target	Planar Foil	Spherical Capsule
Laser drive	200-850 J/1-10 ps	10 kJ/1 ns
Proton source size	10-20 μm	50 μm
Proton source duration	1-10 ps	100 ps
Proton emission	Directional	Isotropic
Proton spectrum	Exponential	Monoenergetic

5.3 Previous Magnetic Field Measurements in Laser-Produced Plasmas

Both exploding-pusher and TNSA proton backlighting techniques have been used to measure magnetic fields in laser-foil interactions, likely generated by the Biermann battery mechanism as described in Section 5.1.[6,8,16,33,34] These experiments set the stage for new magnetic reconnection experiments using laser-produced plasmas, as will be discussed in Chapter 6. Monoenergetic proton radiography revealed magnetic fields of order ~0.5 MG for laser-foil interactions with a 500 J, 1 ns pulse and an 800 μm spot size incident on a 5 μm thick CH foil.[6] LASNEX simulations, which estimated a magnetic field strength of 0.5 MG, were postprocessed to produce synthetic proton images which matched large-scale features in the data quite accurately.[6,8] These results also give confidence in the LASNEX predictions of magnetic field evolution. Different field structures were produced with the usage of different phase plates, which changed the beam spatial profile.[6]

Evolution of this single laser-produced plasma bubble revealed a near-linear radial expansion velocity of ~500 μm/ns, which was generally well-modeled by LASNEX while the laser was on.[8] However, the development of instabilities at the plasma bubble perimeter after the laser turned off and the plasma cooled and became more resistive caused deviations from the predictions of the 2D MHD simulation. The magnetic field, which remained constant in magnitude despite the expansion and the increase in path-integrated field strength, was found to decay faster than predicted. The evolution of proton images reflecting the magnetic field structure is shown in the next section in conjunction with Thomson scattering measurements of electron and ion temperatures in identical experiments.

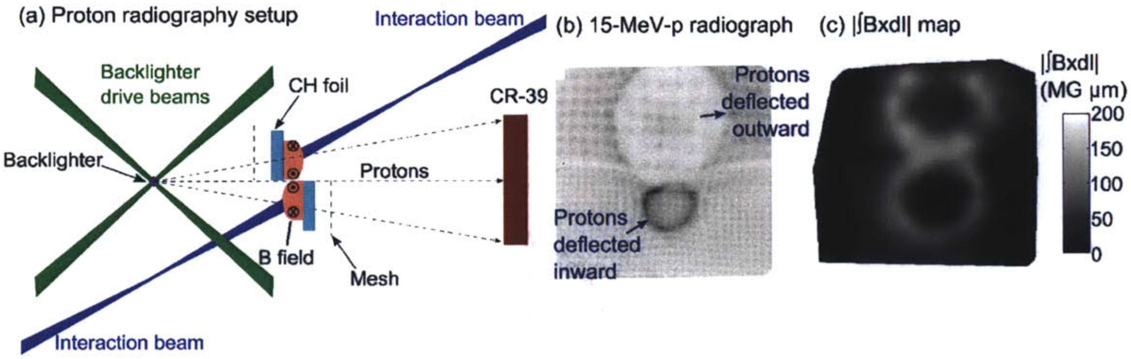

Figure 5.10. Experiment demonstrating magnetic fields around laser-produced plasma bubbles. Azimuthal magnetic fields cause an outward deflection of backlighter protons at the upper side of the foil and an inward deflection of protons at the lower side of the foil. If the field were electric, the protons would be deflected identically on each side of the foil.

Unequivocal demonstration of the identity of the magnetic (as opposed to electric) fields was accomplished by turning around the radiography axis relative to the incident laser pulse and observing a reversal in the field-induced proton deflection.[16] Two lasers from opposite direction were incident on a foil, one parallel and one anti-parallel to the direction of proton propagation from the backlighter to the detector. The azimuthal magnetic fields around plasma bubble associated with the laser coming from the detector side deflected protons radially outward, while the magnetic fields around the plasma bubble associated with the laser coming from the backlighter deflected protons radially inward. A similar, newly-conducted experiment that illustrates this effect is shown in Figure 5.10 (and also discussed in Chapter 6 and Appendix E). If the fields were instead radial electric fields, the protons would be deflected the same way on either half of the foil. These magnetic fields have been observed also in experiments using TNSA backlighting.[33,34] The collision of adjacent expanding plasma bubbles produces a magnetic reconnection geometry at the interaction point,[38,13,41,39] and in several of these experiments proton radiography has been used to image the magnetic field structures and their reconnection. Recent experiments using both exploding-pusher and TNSA proton radiograpy to probe magnetic reconnection experiments in laser-produced plasmas are described in Chapter 6.

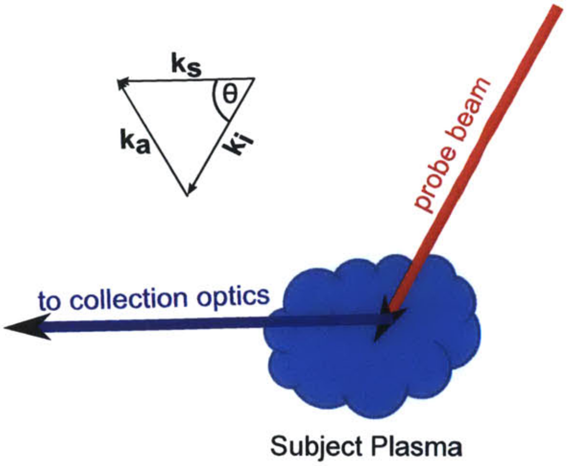

Figure 5.11. Generic experimental setup for Thomson scattering measurements. The probe beam is incident with wave vector $\mathbf{k}_i$ and is scattered by angle θ, directed toward the collection optics at wave vector $\mathbf{k}_s$. The scattering wave vector is $\mathbf{k}_a = \mathbf{k}_s - \mathbf{k}_i$.

5.4 Thomson Scattering Measurements of Electron and Ion Temperature in Plasmas

While proton radiography is used to measure electric and magnetic fields, other diagostic techniques are required to precisely identify plasma conditions. Thomson scattering is a powerful tool for measuring parameters such as electron temperature, ion temperature, electron density, flow velocity, and average charge state in laser-produced plasmas.[42] Incident probe light scattered off of electrons forms a characteristic spectral shape that is sensitive to many different properties of the plasma. Over length scales longer than the Debye length λ_D, plasma motion behaves collectively, and for scattering wavevectors k_a such that $\alpha \equiv 1/k_a\lambda_D > 1$, this collective motion is probed in what is termed coherent Thomson scattering. Light scattered off of electrons in ion acoustic or electron plasma waves contains information about the collective properties of the scattering plasma. A typical Thomson scattering setup is illustrated in Figure 5.11.

The power radiated into solid angle $d\Omega$ over the scattered frequency range $d\omega_s$ at position $\mathbf{R}$ can be expressed as[42,43]

$$P_s(\mathbf{R},\omega_s)d\Omega d\omega_s = P_i r_0^2 d\Omega d\omega_s/(2\pi A)(1+2\omega/\omega_i)n_e S(\mathbf{k}_a,\omega), \tag{5.22}$$

where P_i is the incident probe beam power, $r_0 = e^2/m_e c^2$ (cgs units) is the classical electron radius, A is the cross-sectional area of the Thomson scattering volume, and n_e is the electron density. The scattering wave vector $\mathbf{k}_a = \mathbf{k}_s - \mathbf{k}_i$ and the frequency $\omega = \omega_s - \omega_i$, where the subscript s denotes a scattered quantity and the subscript i denotes an incident quantity. $S(\mathbf{k},\omega)$, known as the spectral density function, contains the physics of the scattering process and is expressed as

$$S(\mathbf{k}_a,\omega) = \frac{2\pi}{k}(1-\chi_e/\epsilon)^2 f_{e0}\left(\frac{\omega}{k}\right) + \sum_j \frac{2\pi}{k}\frac{Z_j^2 N_j}{N}\left(\frac{\chi_e}{\epsilon}\right)^2 f_{i0}\left(\frac{\omega}{k}\right). \tag{5.23}$$

The summation over j denotes different ion species, N_j is the number density of the jth ion, and $N = \sum_j N_j Z_j$. The electron and ion distribution functions are f_{e0} and f_{i0}, and $\epsilon = 1 + \chi_e + \chi_i$ is the dielectric function, where χ_e (χ_i) is the electron (ion) susceptibility.

For scattering off of ion acoustic waves, the mode of Thomson scattering exploited in this study (Section 5.5),[44] there is a resonance close to the scattering frequency and the ion acoustic frequency,

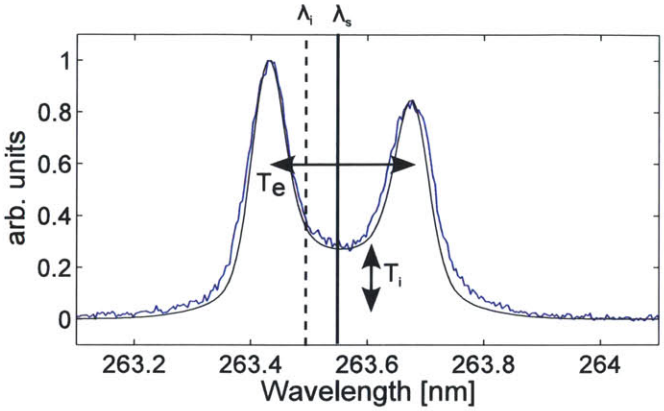

Figure 5.12. Example of a Thomson scattering spectrum. The shift of the centroid λ_s from the incident wavelength λ_i denotes a Doppler shift relative to the scattering wave vector. The separation of the two peaks is most sensitive to the electron temperature, while the amplitude of the region between them is sensitive to the ion temperature. The density is proportional to the total scattered power. The blue line denotes measured data, while the black line is a fit, as presented in Section 5.5.

such that[45]

$$\omega_a = \pm k_a \sqrt{\frac{\kappa_b T_e}{M}\left[\frac{Z}{1+k^2\lambda_D^2}+\frac{3T_i}{T_e}\right]}. \tag{5.24}$$

The scattered frequency depends on the electron temperature T_e, the ion mass M, the average ion charge Z, and the ion temperature T_i. Light is scattered by ion acoustic waves propagating with and against the scattering direction, with a wavelength separation of

$$\frac{\Delta\lambda}{\lambda_i} = \frac{4}{c}\sin\left(\frac{\theta}{2}\right)\sqrt{\frac{\kappa_b T_e}{M}\left[\frac{Z}{1+k^2\lambda_D^2}+\frac{3T_i}{T_e}\right]}, \tag{5.25}$$

where the substitution $k_a = 2k_i \sin(\theta/2)$ has been made in equation 5.24 based on the scattering angle θ. As is evident in equation 5.25, the wavelength difference of the two peaks in the spectrum is sensitive to plasma conditions. A Thomson scattering spectrum showing ion acoustic features in a CH plasma, depicted in Figure 5.12 (an example of the data presented in Section 5.5), illustrates how the spectrum is sensitive to electron and ion temperatures. The wavelength separation depends predominantly on the electron temperature, while the spectral shape and, in particular, the amplitude of the plateau region between the two peaks, is sensitive also to the ion temperature. The overall shift in the center of the spectrum is proportional to the flow velocity along the scattering direction.

This technique has been used to diagnose a variety of laser-produced plasmas, including laser foil interactions,[46] plasma jets,[47] ICF hohlraums,[48] magnetically reconnecting plasma plumes,[38] and collisionless shocks.[49] Spatially or temporally-resolved measurements are used to evaluate changing plasma conditions throughout an experiment, and a well-focused probe beam and small collection apertures allow for highly localized measurements, with Thomson scattering volumes as small as 50 μm on a side.[45] Thomson scattering probe beams typically operate in the visible or ultraviolet part of the electromagnetic spectrum, for example with wavelengths of 263.5 or 527 nm (4ω or 2ω light for a fundamental laser wavelength of 1054 nm). These beams can propagate up to the critical density of the plasma $n_c = m_e\epsilon_0\omega^2/e^2$ (mks units), which for a 4ω probe beam is 1.6×10^{22} cm^{-3}. For probing denser plasmas, x-ray Thomson scattering[50] operates at photon energies of several keV (a factor of ~1000 higher frequency than obtained with lasers) and consequently is able to penetrate up to densities of 10^{28} cm^{-3}.

The following section describes a set of experiments in which newly-analyzed Thomson scattering measurements, in combination with proton radiography data, have been used to assess the properties of expanding hemispherical plasma bubbles produced in laser-foil interactions, as well as the magnetic reconnection of colliding pairs of plasma bubbles.

5.5 Characterization of Single and Colliding Laser-Produced Plasma Bubbles Using Thomson Scattering and Proton Radiography

Time-resolved measurements of electron and ion temperature using Thomson scattering have been combined with proton radiography data for comprehensive characterization of individual laser-produced plasma bubbles or the interaction of bubble pairs, where reconnection of azimuthal magnetic fields occurs. Measurements of ion and electron temperatures agree with LASNEX simulations of single plasma bubbles, which include the physics of magnetic fields. There is negligible difference in temperatures between a single plasma bubble and the interaction region of bubble pairs, though the ion temperature may be slightly higher due to the collision of expanding plasmas. These results are consistent with reconnection in a $\beta \sim 8$ plasma, where the release of magnetic energy (<5% of electron thermal energy) does not appreciably affect the hydrodynamics. This work has been published in *Physical Review E.*[44]

5.5.1 Introduction and Motivation

Characterization of laser-produced plasmas is important in a variety of experiments relevant to both inertial confinement fusion and basic plasma physics, where measurements of the temperature and magnetic field evolution are critical to understanding the plasma dynamics.[51,52,2,53] Such plasmas are especially relevant in indirect-drive inertial confinement fusion, where multiple lasers irradiate the inside of a cylindrical hohlraum.[54] Previously, Thomson scattering[42] has been used to diagnose the temperature evolution of laser-produced plasmas, both in indirect-drive hohlraums[48] and in planar laser-foil experiments.[55,38]

One particular scientific application of laser-foil interactions is the study of self-generated azimuthal magnetic fields around laser-produced expanding, hemispherical plasma bubbles[1,56] and their reconnection. Magnetic reconnection[57] has been explored traditionally in the context of astrophysical plasmas,[58,59] or in the laboratory with plasmas at low density ($\sim 10^{12}$-10^{14} cm^{-3}) and low plasma β, the ratio of thermal energy density to magnetic energy density ($\sim$0.001-0.1).[60,61] [1] Recent experiments have assessed the evolution and reconnnection of magnetic fields in the high-energy-density regime,[62,63] through the interaction of multiple laser-produced plasma bubbles.[13,38,41,39,64] Several of these experiments have utilized the proton radiography technique[5] to probe these laser-produced plasma bubbles, producing quantitative data on the strength of laser-generated magnetic fields.[8,13,38,41,16,39] Though some measurements of electron and ion temperature have been made in these experiments,[38] a comprehensive, time-resolved set of measurements had yet to be published.

In this study, Thomson-scattering measurements have been used to characterize the temperature evolution at different times and locations in the laser-produced plasma bubbles and in the interaction region of bubble pairs. The data offers a comprehensive, time-resolved set of measurements of local electron and ion temperatures in single and interacting laser-produced plasma bubbles, in conjunction with proton radiography data used to infer magnetic fields. Measurements of electron and ion temperatures in the reconnection region of laser-generated magnetic fields provide unique information on the temperature evolution in a high-β reconnection event. By juxtaposing temperature data in the reconnection region to comparable data in the single bubble experiment, it is possible to infer the role of magnetic reconnection and the hydrodynamic collision of the two bubbles in shaping the thermal properties of the plasma.

---

[1] In astrophysical plasmas, the regimes in which reconnection takes place can vary quite substantially. Electron densities range from 10^{-1} cm^{-3} in the Earth's magnetotail to 10^{11} cm^{-3} in the solar chromosphere, while plasma betas range from $\sim 10^{-4}$ in the solar corona to $\sim$1 at the Earth's magnetopause to $\sim$100 in the solar photosphere.

5.5.2 Laser-Foil Experiments and Measurements

Laser-foil experiments were conducted at the OMEGA laser facility.[65] In each experiment, a 5-μm CH foil was irradiated by one or two 351 nm (3ω) beams in a 1-ns pulse with 500 J/beam and SG4 phase plates, producing an 800 μm spot size with a 4th-order supergaussian profile.[66] For the dual-beam reconnection experiments, laser spots were separated by 1.2-1.4 mm. In separate experiments, monoenergetic proton radiography data[6] and 4ω Thomson scattering data[45] were obtained for the single or pair of laser-foil interactions. These experiments provide complementary information on the evolution of magnetic fields and ion and electron temperatures both in laser-produced plasma bubbles and in the magnetic reconnection of bubble pairs.

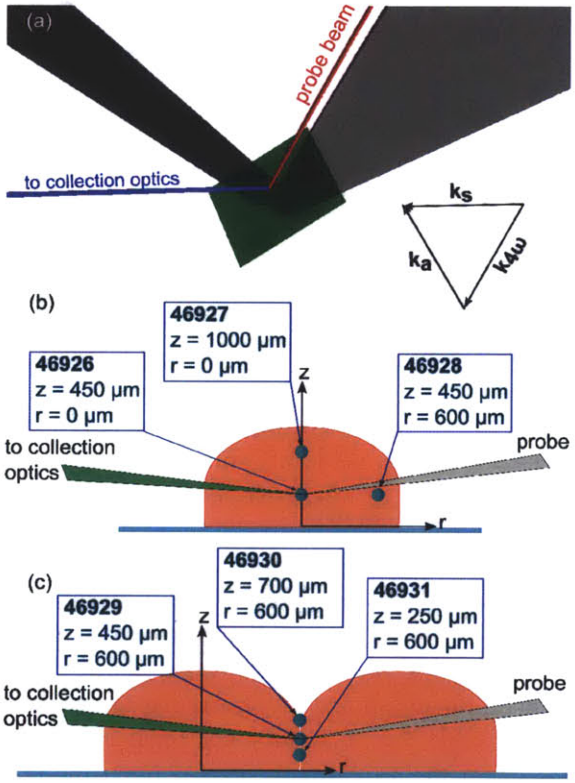

Figure 5.13. Experimental setup for the Thomson-scattering experiments (a). In these experiments, the Thomson-scattering probe beam was incident at a 79° angle relative to the foil normal (z-axis), nearly parallel to the foil surface, while the detector was at 37° to the normal, such that the scattering angle was 63° and the scattering vector 21° to the foil normal. Locations probed are shown for (b) single bubble experiments and (c) reconnection experiments.

The setup for the Thomson-scattering experiments is shown in Figure 5.13. The Thomson-scattering technique utilizes a frequency-quadrupled (263.5 nm) probe beam and a streaked detector system for time-resolved measurements of the scattered light spectrum, from which electron and ion temperature histories are inferred for the laser-produced plasma.[45] On different shots, the probe beam was focused onto three different locations in each of the (b) single bubble and (c) interacting bubble geometry. The Thomson-scattering volume can be described as a cylinder approximately 60 μm in diameter and $\sim$75 μm in length, providing a local measurement of the plasma conditions.[45]

From the spectrum of light scattered by ion-acoustic fluctuations the electron and ion temperature can be determined.[42] To first order, the electron temperature is proportional to the square of the wavelength shift of the probe beam; the spectral shape of ion-acoustic features is sensitive also to the ion temperature.[48] The electron density can also be inferred from the absolute magnitude of the scattered light spectrum, but density measurements were not obtained in this study.

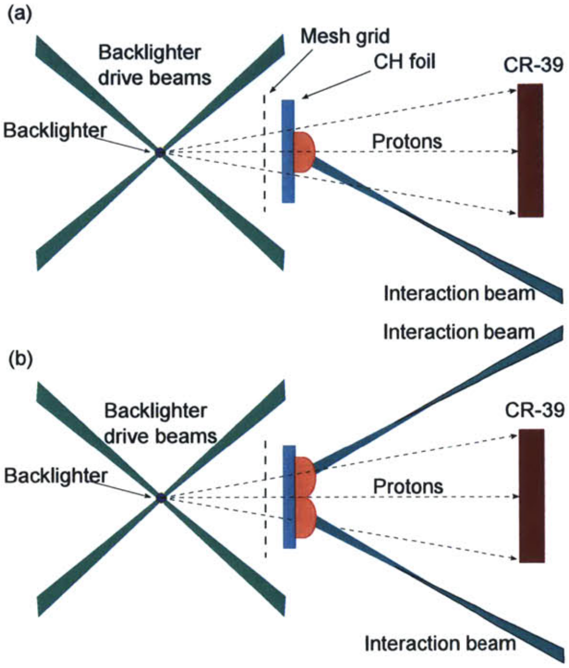

Figure 5.14. Proton radiography setup for (a) the single bubble experiments and (b) the reconnection experiments. The distance between the backlighter and the CH foil is 15 mm, while the distance between the mesh grid and the foil is 2 mm. These experiments, the first using this configuration, were originally reported by Li *et al.*[8,13]

The proton radiography setup is shown in Figure 5.14 for both (a) the single laser-foil experiments and (b) the dual laser-foil (reconnection) experiments. A D^3He-filled, thin-glass-shell exploding-pusher backlighter capsule was illuminated by 20 OMEGA beams, delivering 8.5 kJ in a 1-ns pulse and producing monoenergetic 3- and 15-MeV protons from respective DD and D^3He fusion reactions. These backlighter protons were divided by a mesh grid into discrete beamlets before sampling the laser-produced CH plasma. The proton beamlets were then deflected by magnetic fields surrounding the plasma plasma bubbles and their positions were recorded using CR-39. Given the known proton energy as measured by proton spectrometers,[19] the measured deflection of each beamlet was used to infer quantitatively the path-integrated magnetic field strength through the plasma. The absolute timing of the proton arrival at the plasma was determined by the proton temporal diagnostic (PTD),[67] which measures the time of proton emission from the backlighter. These proton radiography experiments were described originally by Li *et al.* for single laser-produced plasma bubbles[8] and for the interaction of multiple bubbles.[13] Though the Thomson-scattering measurements and the proton radiography data were obtained on different shots, the experiments used comparable laser and target parameters.

5.5.3 Proton Radiography and Thomson Scattering Results

Images of both individual and interacting plasma bubbles, using 15-MeV protons, are shown in Figure 5.15. These images, which have been published previously, reveal the evolution and reconnection of magnetic fields around laser-produced plasma bubbles.[8,13] The published images are used here to illustrate the location of Thomson-scattering regions in the nearly identical experiments conducted in this work. In the single bubble images (Figure 5.15a), Thomson scattering regions are located either at the center of the bubble (red star, r=0, z=450 and 1000 μm) or towards the

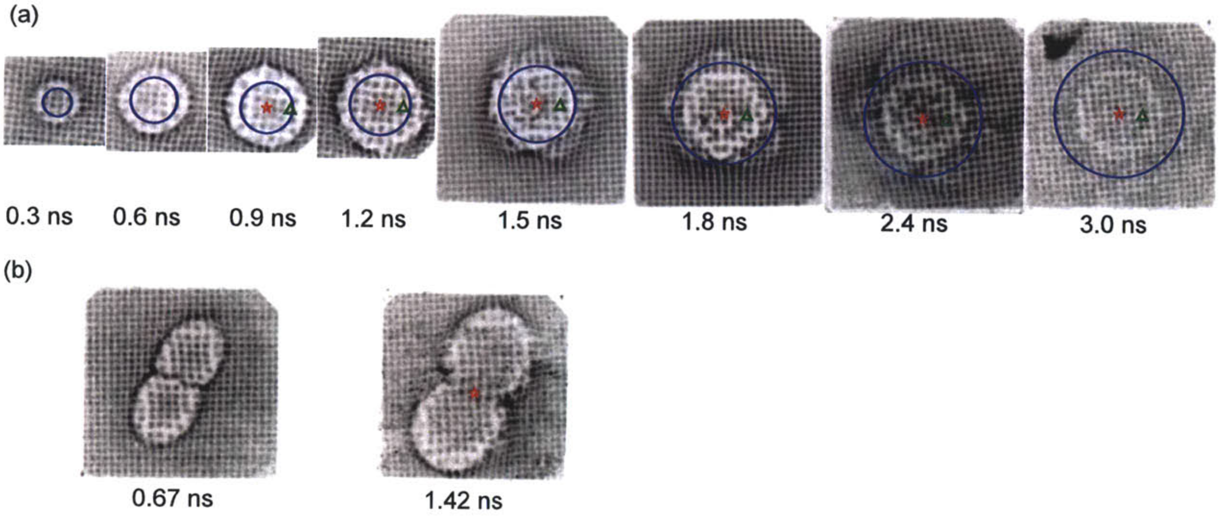

Figure 5.15. 15-MeV-proton radiography images of (a) single laser-produced plasma bubbles and (b) interacting plasma bubbles undergoing magnetic reconnection. The approximate bubble size is indicated in the single bubble images (blue circle), and the location of Thomson scattering regions are shown at r=0 (red star, for both z=450 μm and z=1000 μm) and at r=600 μm (green triangle, for z=450 μm) for t>0.9 ns. In the interacting bubbles experiments, the Thomson scattering regions are located in the reconnection layer at r=600 μm (red star, for z=250 μm, z=450 μm, and z=700 μm). These images were first published by Li *et al.*[8,13]

bubble edge (green triangle, r=600 μm, z=450 μm). The approximate bubble size (blue circle) is shown to illustrate the location of the bubble perimeter relative to the outer Thomson-scattering region. Note that the bubble edge is not the location of beamlet pileup, since that feature is the result of proton deflection and does not represent the actual radius of the bubble. The sample times indicated for the proton radiography images were obtained using PTD. Since the bubble has expanded beyond a radius of 600 μm by t=0.9 ns, the Thomson-scattering data at r=600 μm obtained for t>0.9 ns are well within the bubble perimeter.

Thomson-scattering measurements in the reconnection experiments (Figure 5.15b) were all made in the center of the reconnection region, at the midpoint between the bubble centers (red star, at z=250, 450, and 700 μm). As shown in the first reconnection image, the interaction of the two plasma bubbles has already begun at t=0.67 ns. Thomson scattering measurements of the interacting plasma bubbles were made from t~0.8-3.1 ns, so the data are obtained when the bubbles are interacting and their magnetic fields reconnecting.

Streaked Thomson-scattering spectra are shown in Figure 5.16, for each of the experimental geometries depicted in Figure 5.13. These images show the time evolution of scattered light spectra and reflect changes in the plasma conditions at the particular locations in the experiments. Wavelength shifts in both features reflect changes in the plasma flow, while changes in the inter-line spacing indicate evolution of the electron temperature.[42] Lineouts are taken to produce spectra at different times throughout the experiment from which the time history of electron and ion temperatures is inferred.

The times chosen for spectral analysis in shot 46931 are shown at the bottom right of Figure 5.16. Each lineout integrates over 120 ps to reduce the statistical noise in the spectrum. The relative timing of the spectral snapshots within a particular shot is known to ±50 ps, while the absolute uncertainty in the timing is ±100 ps. The resulting spectra and their fits are shown in Figure

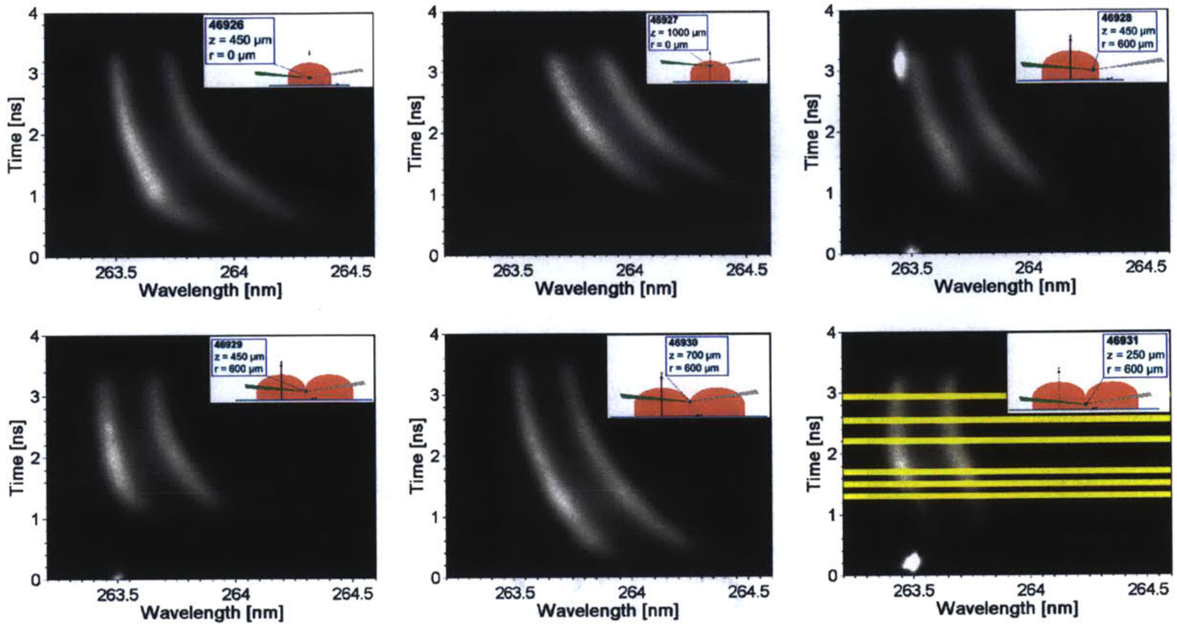

Figure 5.16. Streaked Thomson scattering spectra from single bubble experiments (top) and interacting bubble experiments (bottom), at the locations depicted in Figure 5.13. The horizontal yellow bars in the bottom-right image indicate the times that were chosen for spectral analysis for shot 46931. For improved statistics, the spectra were integrated over 120 ps at each lineout, as indicated by the width of the bars. The resulting lineouts are shown in Figure 5.17.

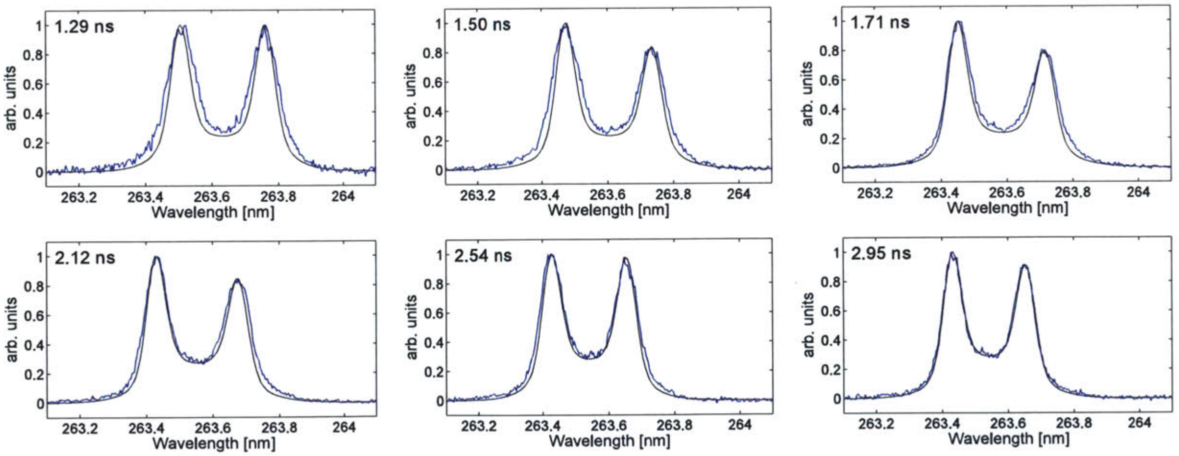

Figure 5.17. Measured spectra (jagged blue curves) and their fits (smooth black curves) obtained from six lineouts of the streaked image on shot 46931 shown in Figure 5.16. Changes in the interline spacing and the ratio of trough to peak amplitude depict evolution of the electron and ion temperatures at (r=600 μm, z=250 μm) in the interaction region of the colliding plasmas. Additional broadening of measured spectral features in comparison to their fits may be due to spatial gradients in electron and ion temperature across the Thomson scattering volume.

5.17. The fitted spectra are convolutions of the Thomson scattering form factor and the estimated instrumental response function, represented by a Gaussian of full-width at half maximum 0.055 nm. Additional broadening of the measured spectral features not accounted for by the fits may be due to spatial gradients of electron and ion temperatures across the finite Thomson scattering volume. Uncertainties in the inferred electron and ion temperatures are based on the quality of fit. A compendium of Thomson scattering spectra and the assumed and inferred plasma conditions is presented in Appendix D.

Measurements of the time-dependent electron and ion temperatures at three locations in the single bubble plasma are shown on the left side of Figure 5.18 and compared to temperatures predicted by two-dimensional (2D) LASNEX[9] hydrodynamics simulations at the appropriate location. The LASNEX simulations used in this study include the physics of magnetic fields and their generation from nonparallel gradients in electron temperature and electron density.[10,12] The simulations include flux-limited electron diffusion and the Braginskii cross-field transport terms, which may modify hydrodynamic profiles.[11] The inclusion of magnetic fields has little effect (<10%) on LASNEX predictions of electron and ion temperatures over the time when Thomson scattering measurements were obtained.

The overall electron temperature behavior agrees with LASNEX simulations. The electron temperature at each location decreases after the laser turns off around t~1 ns, with the magnitude and time-scale of decay generally matching those predicted by LASNEX over the period 1<t<2 ns. Beyond t~2 ns, the measured electron temperatures level off around 300 eV, while the simulated electron temperatures continue to decrease. This discrepancy may be caused by slight heating of the plasma by the probe beam at late times, which is not accounted for in the LASNEX simulations. Deposition of 30 J of laser energy over 3 ns, in a volume the width of the Thomson scattering region and length the approximate size of the plasma bubble, can be expected to account for of order ~100 eV of heating, in comparison to the ~keV heating provided by the 500 J/1 ns drive beam spread out over the 800 μm spots size. At t~1.5 ns, the measured electron temperatures appear slightly lower than LASNEX predictions. Such a discrepancy would be consistent with the previous observation of magnetic fields around a single plasma bubble decaying faster than predicted.[8] That result could be explained by the measured electron temperature being lower than the simulated temperature, which would produce a faster diffusion of magnetic fields.

The ion temperature measurements also agree with LASNEX simulations. In some experiments, the early-time ion temperatures are higher than predicted, though there is a large uncertainty in those measurements due to relatively poor fits to the measured spectrum. As the ion temperature is inferred from the ratio of trough to peak amplitude in the scattered light spectrum, its uncertainty is especially sensitive to the looseness of fit caused by temperature gradients across the Thomson scattering volume. In all three single-bubble experiments at t>1.5 ns, the timing of the ion temperature evolution matches LASNEX predictions, consistent with what was observed for the electron temperatures.

Thomson scattering measurements of electron and ion temperatures in the reconnection region of the colliding plasma bubbles are shown on the right side of Figure 5.18. At each height in the reconnection layer, the electron temperature decreases after the laser has turned off. At z=450 μm and z=700 μm, the ion temperature decreases monotonically, while at z=250 μm, there is a slight increase in the ion temperature for 1<t<1.7 ns before it decreases. Since the interacting plasmas bubbles are inherently three-dimensional, 2D LASNEX simulations are not applicable for these experiments.

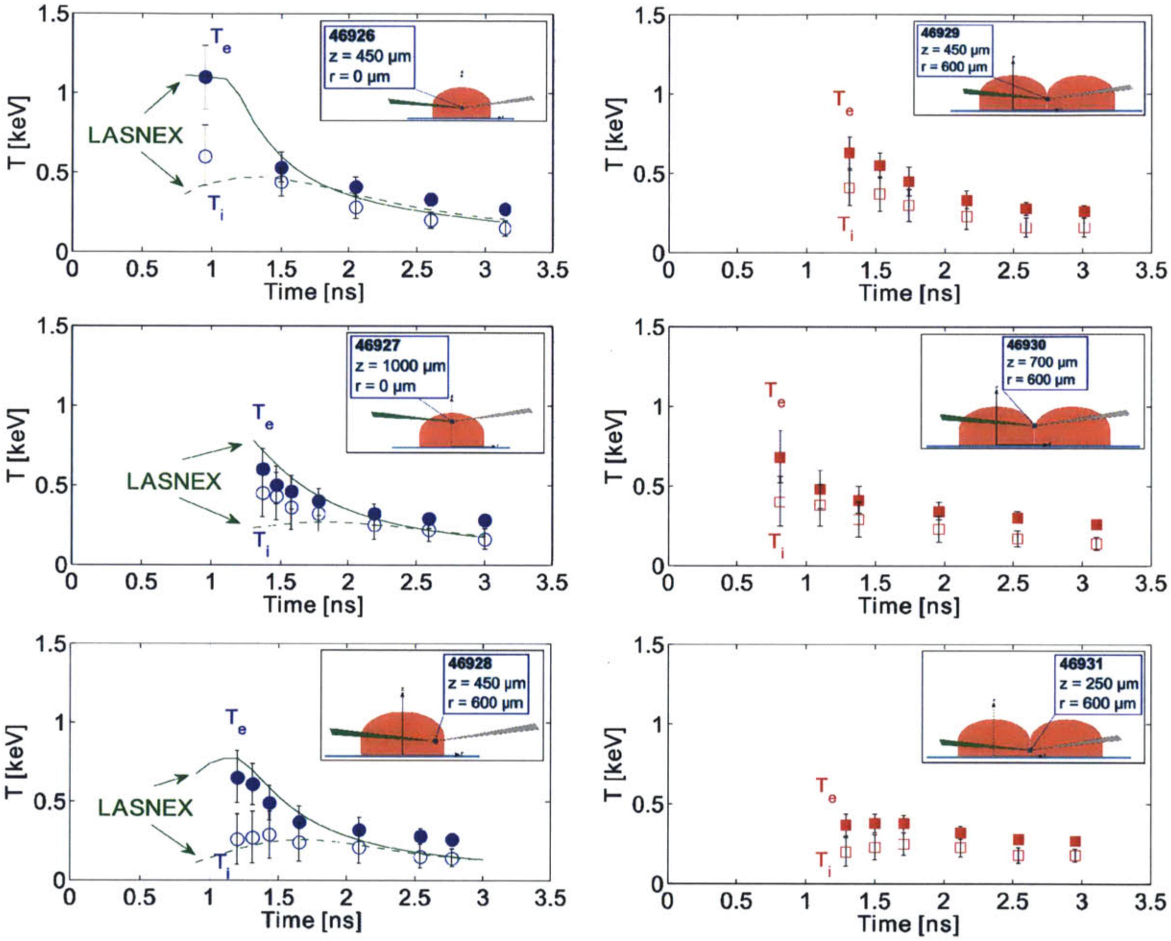

Figure 5.18. Simultaneous, time-dependent Thomson scattering measurements of electron temperatures (filled markers) and ion temperatures (open markers) at different positions in the single bubble (left) and interacting bubbles (right). Single bubble data are compared to LASNEX predictions of electron temperature (solid lines) and ion temperatures (dashed lines). Comparisons between measured electron and ion temperatures demonstrate differences in electron-ion thermal equilibration at different locations and times in these experiments, as discussed in Section 5.5.4.

5.5.4 Discussion of Thermal Evolution in Laser-Foil and Reconnection Experiments

The single bubble electron and ion temperature data are well-modeled by LASNEX and depict the convection and cooling of the laser-produced plasma bubble in the period after laser shutoff, as the bubble is allowed to expand into the ambient vacuum. Measured electron and ion temperatures at fixed points in the experimental geometry level off at late times, as hotter plasma near the bubble center is convected through the Thomson scattering regions. At all three locations in the single plasma bubble, the measured electron temperature at t>2 ns is greater than LASNEX predictions, possibly due to continued heating of the plasma by the Thomson scattering probe beam. It should be noted that the late-time comparison of experimental data to LASNEX simulations is complicated also by the emergence of instabilities, which breaks the 2D bubble symmetry after the laser turns off around t∼1.2 ns.[8]

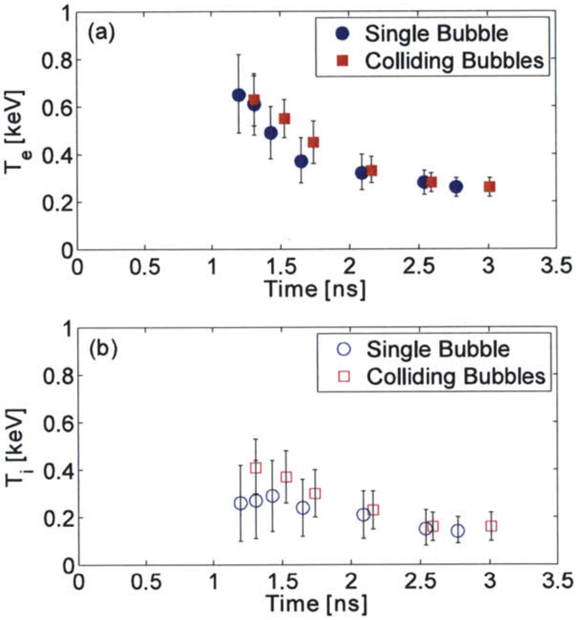

Figure 5.19. Comparison of time-dependent (a) electron temperature and (b) ion temperature for single plasma bubbles (blue circles) and colliding plasma bubbles (red squares) after the bubble collision around t∼0.7 ns. There is a negligible difference in temperatures between the single bubble and colliding-bubbles case, though the ion temperature around t=1.3 ns is ∼50% higher in the colliding-bubble case (barely within uncertainty). These results are consistent with a hydrodynamic collision of plasma bubbles at $\beta \gg 1$.

Having measurements of the conditions in both single and interacting plasma bubbles allows assessment of the effect of the plasma collision and magnetic reconnection on the energetics of the system. A comparison of time-dependent electron and ion temperatures measured at (r=600 μm, z=450 μm) in the single bubble case versus the interacting bubbles case is shown in Figure 5.19. As shown in Figure 5.19a, there is a negligible difference in the electron temperature history between the single bubble and reconnection cases during the time when magnetic reconnection is occurring between the two bubbles. Thus, the magnetic field energy released during reconnection does not noticeably raise the electron temperature. This result is in contrast to the findings of Nilson *et al.*,[38] where an increase in the electron temperature to 1.7 keV was inferred from Thomson scattering measurements in the reconnection region of laser-produced plasma bubbles. The minimal impact of magnetic reconnection on the electron temperature of the plasma is expected for reconnection at high plasma β, where the magnetic pressure is small in comparison to the hydrodynamic pressure of the plasma.

The ion temperature histories (Figure 5.19b) are nearly identical given the large uncertainties at early times, though the appearance of a slightly higher T_i in the colliding bubbles case at t∼1.3 ns is suggestive of a hydrodynamic collision of plasmas, independent of magnetic reconnection.[68] The ion-ion mean free path under these conditions is approximately 1 μm, so the plasma is collisional and some kinetic energy from the colliding plasmas is expected to be transferred to ion thermal energy.

These data can also be used to more precisely identify the plasma β for these laser-produced plasmas, the ratio of thermal to magnetic pressure, defined as

$$\beta = \frac{n_i k T_i + n_e k T_e}{B^2/2\mu_0}, \tag{5.26}$$

where n_i (n_e) and T_i (T_e) are the ion (electron) density and temperature, and B is the magnetic field strength. LASNEX simulations give an approximate electron density, while Thomson scattering and proton radiography data give the temperatures and the magnetic field strength, respectively. Since each of the measurements is performed locally and at different times, care must be taken to ensure that appropriate values are used. For example, proton radiography data provide snapshots of the magnetic-field strength at the expanding bubble perimeter where the magnetic fields are concentrated, while Thomson scattering data are taken at fixed locations (e.g. r=600 μm).

At t=0.91 ns in the single bubble experiment, the bubble perimeter is located at r=700 μm, just outside the Thomson scattering region at r=600 μm. At t=1.20 ns, the earliest Thomson scattering measurement at that location gives T_e=0.65 keV and T_i=0.26 keV at (r=600 μm, z=450 μm). These temperatures, and the ~0.5 MG magnetic field inferred from the proton radiography data are approximately representative of the plasma conditions at the bubble perimeter at t=0.9-1.2 ns and r=600-700 μm. Along with the LASNEX-predicted electron density of 7×10^{19} cm^{-3}, these parameters are used to estimate β~8. Therefore, the magnetic energy density is approximately one eighth of the total thermal energy density at the bubble perimeter.

Similarly, the expansion velocity of the plasma bubble can be used to infer the ratio of plasma thermal energy to kinetic energy of the expanding plasma bubble. For a bubble expansion velocity of V~500 μm/ns, as inferred from proton radiography data[8] and consistent with the Doppler shifts in the Thomson-scattering spectra, there is approximately 3 times as much energy contained in the kinetic energy density (ram pressure) of the expanding bubble ($\frac{1}{2}n_i m_i V^2$) as there is contained in the thermal energy density ($n_i k T_i + n_e k T_e$), and about 25 times as much energy density as in the magnetic fields ($B^2/2\mu_0$). These results reinforce the picture of plasma bubble interaction where the dynamics is dominated by hydrodynamic processes, even though energy is released by the reconnection of large magnetic fields. At the high densities present in these experiments, the maximum energy released by the dissipation of 0.5 MG magnetic fields sets an upper bound on the increase in electron temperature of ~80 eV. The actual energy released is estimated to be lower,[13] corresponding to an electron temperature increase of only ~20 eV. Each of these estimates is negligible compared to the measured electron temperature of 650 eV.

The conditions under which magnetic reconnection occurs can be further specified by comparing timescales of different physical processes in the plasma bubbles prior to their collision. The magnetic Reynolds number (R_m), the ratio of resistive to flow timescales, is ~2000, affirming that advection is the dominant mechanism in transporting the magnetic fields to the reconnection layer. Under such conditions, stretching of magnetic field lines[69] and pileup of magnetic flux may occur, as is predicted in colliding plasma bubbles.[64] However, the Thomson-scattering data indicate that even if the magnetic field strength is enhanced locally, the release of magnetic energy is insufficient to appreciably increase the electron temperature. The Lundquist number (S), the ratio of resistive to Alfvén crossing times, is ~400 for this reconnection event, small enough to produce a fairly stable reconnection.

The simultaneous, time-resolved measurements of electron and ion temperatures shown in Figure 5.18 hint at the process of thermal equilibration between species at different locations in the expanding plasma bubble. It should be emphasized that these time-dependent measurements are not tracking a parcel of plasma, but rather sampling different locations in the bubble geometry as they pass through the fixed Thomson scattering region (e.g. at r=600 μm, z=450 μm).

In the single bubble case, at each of (r=0, z=450 μm), (r=0, z=1000 μm), and (r=600 μm, z=450 μm), the electron temperature is greater than the ion temperature at t~1.2 ns by a factor of ~1.5-2.5, due to the preferential absorption of laser light by the electrons. As the central region of the plasma bubble expands through the Thomson scattering regions, the electrons and ions move closer to equilibrium, such that by t~1.8 ns, the temperatures are within 25% of each other. The difference between electron and ion temperatures in the colliding bubbles experiments is not substantially different from the single bubble case, and temperatures approach each other gradually for t>1 ns. In both sets of experiments, the electron and ion temperatures never quite equilibrate. This result may be due to the absorption of energy from the Thomson scattering probe beam, which preferentially heats the electrons.

For a CH plasma at $n_e \sim 10^{20}$ cm^{-3} and $T_e \sim 650$ eV, conditions near the bubble perimeter (r=600 μm, z=450 μm) at early times, the electron-ion equilibration time is $\tau_{eq} \sim 4$ ns. As this timescale is longer than the duration of the experiment, it is unlikely that the perimeter plasma experiences significant thermal equilibration. The appearance of equilibration is more likely a consequence of the convection of plasma from denser regions at the center of the bubble, where an electron density of $\sim 5\times10^{20}$ cm^{-3} is predicted at early times. The equilibration time under those conditions is closer to $\tau_{eq} \sim 1$ ns, so some thermal equilibration likely has occurred by the time that plasma passes through the Thomson scattering region.

5.5.5 Conclusions

Time-resolved electron and ion temperature data have been presented for single and colliding plasma bubbles generated by laser-foil interactions. These data have been combined with magnetic field data to produce a comprehensive picture of the thermal and magnetic evolution of both individual plasma bubbles and the magnetic reconnection of interacting bubble pairs. The single-bubble electron and ion temperature data are in good agreement with LASNEX simulations.

Comparison of the temperature data between the single bubble and the interacting bubbles elucidates the impact of magnetic reconnection and hydrodynamic collision on the thermal properties of the plasma. The temperature data reveal a negligible difference between the single bubble and the reconnection case, though the ion temperature may be slightly higher at early times in the bubble collision. These results are consistent with the hydrodynamic collision of plasma bubbles at $\beta \gg 1$, where magnetic reconnection does not appreciably alter the dynamics and the estimated increase in electron temperature due to the release of magnetic energy is <5% of the total. A comparison of the energy sources in the system corroborates this picture: the kinetic energy density of the expanding bubble is ~3 times its thermal energy density and ~25 times its magnetic energy density. These data help guide subsequent studies of magnetic reconnection, discussed in Chapter 6, and future basic plasma physics experiments using laser-foil interactions.

5.6 Summary

The generation of electric- and magnetic-field-carrying plasmas by the interaction of intense lasers with solid targets and techniques for diagnosing laser-plasma experiments have been presented. Proton radiography is a valuable tool for probing electric and magnetic field structures, while

Thomson scattering provides a wealth of information about local plasma conditions, particularly electron and ion temperatures. These techniques have been newly applied to characterize magnetic-field and thermal evolution of both individual laser-produced plasma bubbles and the magnetic reconnection of interacting bubble pairs. It has been shown that the electron temperature is not substantially increased as a consequence of magnetic reconnection in these colliding laser-produced plasmas. This result is expected in light of the fact that most of the energy of the system consists of thermal or bulk kinetic (ram-pressure) energy, with magnetic energy only a small contribution ($\beta \gg 1$). These results are valuable in helping understand the energetics of reconnection in high-β plasmas, relevant to astrophysical environments, as well as for guiding further experiments to study magnetic reconnection using laser-produced plasmas. In the following chapter (Chapter 6), both exploding-pusher proton backlighting and TNSA proton backlighting are applied to new experiments probing the interaction and reconnection of ~MG magnetic fields in laser-plasma experiments.

5.7 References

1. J. A. Stamper, K. Papadopoulos, R. N. Sudan *et al.*, "Spontaneous magnetic fields in laser-produced plasmas," Phys. Rev. Lett., **26**(17), 1012–1015 (1971).
2. J. A. Stamper and B. H. Ripin, "Faraday-rotation measurements of megagauss magnetic fields in laser-produced plasmas," Phys. Rev. Lett., **34**(3), 138–141 (1975).
3. A. Raven, O. Willi and P. T. Rumsby, "Megagauss magnetic field profiles in laser-produced plasmas," Phys. Rev. Lett., **41**(8), 554–557 (1978).
4. M. A. Yates, D. B. van Hulsteyn, H. Rutkowski *et al.*, "Experimental evidence for self-generated magnetic fields and remote energy deposition in laser-irradiated targets," Phys. Rev. Lett., **49**(23), 1012–1015 (1982).
5. A. J. Mackinnon, P. K. Patel, R. P. Town *et al.*, "Proton radiography as an electromagnetic field and density perturbation diagnostic (invited)," Rev. Sci. Inst., **75**(10), 3531–3536 (2004).
6. C. K. Li, F. H. Séguin, J. A. Frenje *et al.*, "Measuring *e* and *b* fields in laser-produced plasmas with monoenergetic proton radiography," Phys. Rev. Lett., **97**, 135,003 (2006).
7. M. G. Haines, "Magnetic-field generation in laser fusion and hot-electron transport," Can. J. Phys., **64**, 912 (1986).
8. C. K. Li, F. H. Séguin, J. A. Frenje *et al.*, "Observation of the decay dynamics and instabilities of megagauss field structures in laser-produced plasmas," Phys. Rev. Lett., **99**, 015,001 (2007).
9. G. B. Zimmerman and W. L. Kreur, "Numerical simulation of laser-initiated fusion," Comments Plasma Phys. Control. Fusion, **2**(51) (1975).
10. P. D. Nielsen and G. B. Zimmerman, Lawrence Livermore National Laboratory Report No. UCRL-53123 (1981).
11. J. A. Harte, W. E. Alley, D. S. Bailey *et al.*, "Lasnex – a 2-d physics code for modeling icf," UCRL-LR-105821-96-4, pages 150–164 (1996).
12. R. P. J. Town *et al.*, "Calculating and measuring self-generated magnetic fields in hohlraums," Bull. Am. Phys. Soc., **50**(123) (2005).
13. C. K. Li, F. H. Séguin, J. A. Frenje *et al.*, "Observation of megagauss-field topology changes due to magnetic reconnection in laser-produced plasmas," Phys. Rev. Lett., **99**, 055,001 (2007).
14. C. K. Li, J. A. Frenje, R. D. Petrasso *et al.*, "Pressure-driven, resistive magnetohydrodynamic interchange instabilities in laser-produced high-energy-density plasmas," Phys. Rev. E, **80**, 016,407 (2009).
15. N. L. Kugland, D. D. Ryutov, C. Plechaty *et al.*, "Invited article: Relation between electric and magnetic field structures and their proton-beam images," Rev. Sci. Inst., **83**, 101,301 (2012).
16. R. D. Petrasso, C. K. Li, F. H. Seguin *et al.*, "Lorentz mapping of magnetic fields in hot dense plasmas," Phys. Rev. Lett., **103**, 085,001 (2009).
17. C. K. Li, F. H. Séguin, J. A. Frenje *et al.*, "Monoenergetic proton backlighter for measuring *e* and *b* fields and for radiographing implosions and high-energy density plasmas (invited)," Rev. Sci. Inst., **77**, 10E725 (2006).

18. M. J.-E. Manuel, A. B. Zylstra, H. G. Rinderknecht *et al.*, "Source characterization and modeling development for monoenergetic-proton radiography experiments on omega," Rev. Sci. Inst., **83**, 063,506 (2012).
19. F. H. Séguin, J. A. Frenje, C. K. Li *et al.*, "Spectrometry of charged particles from inertial-confinement-fusion plasmas," Review of Scientific Instruments, **74**(2) (2003).
20. J. R. Rygg, F. H. Séguin, C. K. Li *et al.*, "Proton radiography of inertial fusion implosions," Science, **319**, 1223–1225 (2008).
21. C. K. Li, F. H. Séguin, J. R. Rygg *et al.*, "Monoenergetic-proton-radiography measurements of implosion dynamics in direct-drive inertial-confinement fusion," Phys. Rev. Lett., **100**, 225,001 (2008).
22. F. H. Séguin, C. K. Li, M. J.-E. Manuel *et al.*, "Time evolution of filamentation and self-generated fields in the coronae of directly driven inertial-confinement fusion capsules," Phys. Plasmas, **19**(012701) (2012).
23. C. K. Li, F. H. Séguin, J. A. Frenje *et al.*, "Observations of electromagnetic fields and plasma flow in hohlraums with proton radiography," Phys. Rev. Lett., **102**, 205,001 (2009).
24. C. K. Li, F. H. Séguin, J. A. Frenje *et al.*, "Charged-particle probing of x-ray-driven inertial-fusion implosions," Science, **327**, 1231–1235 (2010).
25. C. K. Li, F. H. Séguin, J. A. Frenje *et al.*, "Impeding hohlraum plasma stagnation in inertial-confinement fusion," Phys. Rev. Lett., **108**, 025,001 (2012).
26. C. K. Li, D. D. Ryutov, S. X. Hu *et al.*, "Structure and dynamics of colliding plasma jets," Phys. Rev. Lett., **111**, 235,003 (2013).
27. M. J.-E. Manuel, C. K. Li, F. H. Séguin *et al.*, "First measurements of rayleigh-taylor-induced magnetic fields in laser-produced plasmas," Phys. Rev. Lett., **108**, 255,006 (2012).
28. M. J.-E. Manuel, C. K. Li, F. H. Séguin *et al.*, "Instability-driven electromagnetic fields in coronal plasmas," Phys. Plasmas, **20**(056301) (2012).
29. R. A. Snavely, M. H. Key, S. P. Hatchett *et al.*, "Intense high-energy proton beams from petawatt-laser irradiation of solids," Phys. Rev. Lett., **85**(14), 2945–2948 (2000).
30. S. P. Hatchett, C. G. Brown, T. E. Cowan *et al.*, "Electron, photon, and ion beams from the relativistic interaction of petawatt laser pulses with solid targets," Phys. Plasmas, **7**(5), 2076–2082 (2000).
31. D. S. Hey, M. H. Key, A. J. Mackinnon *et al.*, "Use of gafchromic film to diagnose laser generated proton beams," Rev. Sci. Inst., **79**(053501) (2008).
32. A. B. Zylstra, J. A. Frenje, F. H. Séguin *et al.*, "Charged-particle spectroscopy for diagnosing shock r and strength in nif implosions," Review of Scientific Instruments, **83**(10), 10 (2012).
33. C. A. Cecchetti, M. Borghesi, J. Fuchs *et al.*, "Magnetic field measurements in laser-produced plasmas via proton deflectometry," Phys. Plasmas, **16**, 043,102 (2009).
34. S. L. Pape, P. Patel, S. Chen *et al.*, "Proton radiography of magnetic fields in a laser-produced plasma," High Energy Density Physics, **6**, 365–367 (2010).
35. *39th EPS Conference and 16th Int. Congress on Plasma Physics*, P1.176.
36. M. Borghesi, G. Sarri, C. A. Cecchetti *et al.*, "Progress in proton radiography for diagnosis of icf-relevant plasmas," Laser Part. Beams, **28**, 277–284 (2010).
37. L. Gao, P. M. Nilson, I. V. Igumenshchev *et al.*, "Magnetic field generation by the rayleigh-taylor instability in laser-driven planar plastic targets," Phys. Rev. Lett., **109**(115001) (2012).
38. P. M. Nilson, L. Willingale, M. C. Kaluza *et al.*, "Magnetic reconnection and plasma dynamics in two-beam laser-solid interactions," Phys. Rev. Lett., **97**, 255,001 (2006).
39. L. Willingale, P. M. Nilson, M. C. Kaluza *et al.*, "Proton deflectometry of a magnetic reconnection geometry," Phys. Plasmas, **17**, 043,104 (2010).
40. L. J. Waxer, D. N. Maywar, J. H. Kelly *et al.*, "High-energy petawatt capability for the omega laser," Opt. Photonics News, **16**(30) (2005).
41. P. M. Nilson, L. Willingale, M. C. Kaluza *et al.*, "Bidirectional jet formation during driven magnetic reconnection in two-beam laser-plasma interactions," Phys. Plasmas, **15**, 092,701 (2008).
42. D. H. Froula, S. H. Glenzer, J. N. C. Luhmann *et al.*, *Plasma Scattering of Electromagnetic Radiation*, (Academic Press, Burlington, Massachusetts, 2011), second edition.
43. J. S. Ross, S. H. Glenzer, J. P. Palastro *et al.*, "Thomson-scattering measurements in the collective and noncollective regimes in laser produced plasmas," Rev. Sci. Inst., **81**(10D523) (2010).

44. M. J. Rosenberg, J. S. Ross, C. K. Li *et al.*, "Characterization of single and colliding laser-produced plasma bubbles using thomson scattering and proton radiography," Phys. Rev. E, **86**, 056,407 (2012).
45. D. H. Froula, J. S. Ross, L. Divol *et al.*, "Thomson-scattering techniques to diagnose local electron and ion temperatures, density, and plasma wave amplitudes in laser produced plasmas (invited)," Rev. Sci. Inst., **77**(10E522) (2006).
46. S. H. Glenzer, W. Rozmus, B. J. MacGowan *et al.*, "Thomson scattering from high-z laser-produced plasmas," Phys. Rev. Lett., **82**(1), 97–100 (1999).
47. G. Gregori, J. Schein, P. Schwendinger *et al.*, "Thomson scattering measurements in atmospheric plasma jets," Phys. Rev. E, **59**(2), 2286–2291 (1999).
48. D. H. Froula, J. S. Ross, L. Divol *et al.*, "Thomson-scattering measurements of high electron temperature hohlraums plasmas for laser-plasma interaction studies," Phys. Plasmas, **13**, 052,704 (2006).
49. J. S. Ross, S. H. Glenzer, P. Amendt *et al.*, "Characterizing counter-streaming interpenetrating plasmas relevant to astrophysical collisionless shocks," Phys. Plasmas, **19** (2012).
50. S. H. Glenzer and R. Redmer, "X-ray thomson scattering in high energy density plasmas," Rev. Mod. Phys., **81**(4), 1625–1663 (2009).
51. P. K. Carroll and E. T. Kennedy, "Laser-produced plasmas," Contemp. Phys., **22**(1), 61–96 (1981).
52. P. T. Rumsby and J. W. M. Paul, "Temperature and density of an expanding laser produced plasma," Phys. Plasmas, **16**(3), 247–260 (1974).
53. S. P. Regan, D. K. Bradley, A. V. Chirokikh *et al.*, "Laser-plasma interactions in long-scale-length plasmas under direct-drive national ignition facility conditions," Phys. Plasmas, **6**(5), 2072–2080 (1999).
54. J. Lindl, "Development of the indirect-drive approach to inertial confinement fusion and the target physics basis for ignition and gain," Phys. Plasmas, **2**(11), 3933–4024 (1995).
55. S. H. Glenzer, W. E. Alley, K. G. Estabrook *et al.*, "Thomson scattering from laser plasmas," Phys. Plasmas, **6**(5), 2117–2128 (1999).
56. M. G. Haines, "Saturation mechanisms for the generated magnetic field in nonuniform laser-matter irradiation," Phys. Rev. Lett., **78**(2), 254–257 (1997).
57. D. Biskamp, *Magnetic Reconnection in Plasmas*, (Cambridge University Press, Cambridge, UK, 2000).
58. S. Tsuneta, "Structure and dynamics of magnetic reconnection in a solar flare," Astrophys. J., **456**, 840–849 (1996).
59. B. U. O. Sonnerup, G. Paschmann, I. Papamastorakis *et al.*, "Evidence for magnetic field reconnection at the earth's magnetopause," J. Geophys. Res., **86**(A12), 10,049–10,067 (1981).
60. J. Egedal, W. Fox, N. Katz *et al.*, "Laboratory observations of spontaneous magnetic reconnection," Phys. Rev. Lett., **98**(015003) (2007).
61. H. Ji, M. Yamada, S. Hsu *et al.*, "Experimental test of the sweet-parker model of magnetic reconnection," Phys. Rev. Lett., **80**(15), 3256–3259 (1998).
62. R. C. Davidson, *Frontiers in High Energy Density Physics*, (National Academies Press, Washington, DC, 2003).
63. R. P. Drake, *High-Energy-Density Physics*, (Springer Press, New York, 2006).
64. W. Fox, A. Bhattacharjee and K. Germaschewski, "Fast magnetic reconnection in laser-produced plasma bubbles," Phys. Rev. Lett., **106**, 215,003 (2011).
65. T. R. Boehly, D. L. Brown, R. S. Craxton *et al.*, "Initial performance results of the omega laser system," Opt. Commun., **133**, 495–506 (1997).
66. H. T. Powell and T. J. Kessler, *Laser Coherence Control: Technology and Applications*, (SPIE, Bellingham, WA, 1993).
67. J. A. Frenje, C. K. Li, F. H. Séguin *et al.*, "Measuring shock-bang timing and ρr evolution of d^{3}he implosions at omega," Phys. Plasmas, **11**(5), 2798–2805 (2004).
68. O. Rancu, P. Renaudin, C. Chenais-Popovics *et al.*, "Experimental evidence of interpenetration and high ion temperature in colliding plasmas," Phys. Rev. Lett., **75**(21), 3854–3857 (1995).
69. G. Gregori, F. Miniati, D. Ryu *et al.*, "Three-dimensional magnetohydrodynamic numerical simulations of cloud-wind interactions," Astrophys. J., **543**, 775–786 (2000).

6

Dynamics of Magnetic Field Evolution and Reconnection in Symmetric and Asymmetric Colliding Laser-Produced Plasma Bubbles

As discussed in Chapter 4, magnetic reconnection is a pervasive phenomenon in the universe, affecting plasma dynamics in the solar corona, the Earth's magetosphere, magnetic-fusion devices, and a variety of other astrophysical and laboratory environments. Laser-produced plasmas offer a controlled laboratory setting in which the physics of magnetic reconnection can be studied. In Chapter 5 it was discussed how the interaction of lasers with foil targets produces magnetized plasmas in the strongly-driven (ram pressure>magnetic pressure), high-β (thermal pressure>magnetic pressure) regime, and that these plasmas can be driven together to produce magnetic reconnection. This chapter presents three new proton radiography studies of the interaction and reconnection of magnetic fields in laser-plasma experiments.

Together these experiments constitute new experimental explorations of magnetic reconnection in a regime rarely accessed in the laboratory, with relevance to fundamental reconnection physics as well as to specific astrophysical cases. Figure 6.1 illustrates the plasma β and collisionality in laser-plasma reconnection experiments, in comparison to astrophysical cases and to other, more typical laboratory reconnection experiments. These parameters were originally presented in Table 4.1. In particular, laser-plasma experiments probe reconnection in a regime defined by high plasma β and the importance of collisionless effects, relevant to the Earth's magnetopause. Additionally, as is somewhat related to the high β, both the laser-plasma experiments and the magnetopause are characterized by very strong plasma flows driving the reconnection. This regime of strongly-driven reconnection is not typically studied in the laboratory. Additionally, the asymmetric plasma conditions present at the magnetopause (different plasma conditions on either side of the current sheet) can be reproduced in laser-plasma experiments, but have to date been ignored in laboratory work. The work described in this chapter, with new investigations of magnetic reconnection in the little-explored regimes achieved in laser-plasma experiments, constitute a significant contribution to the field of plasma physics.

This chapter is organized as follows: Section 6.1 discusses the first dedicated experiments to study specifically *asymmetric* magnetic reconnection in the laboratory, using monoenergetic proton radiography to measure the rate of magnetic flux annihilation in otherwise comparable asymmetric and symmetric laser-generated plasma experiments; Section 6.2 describes laser-plasma reconnection experiments imaged by high-resolution proton radiography to reveal details of the reconnection region, including electron jets and bulk magnetic field structures, and to illustrate a transition from the two-fluid to the single-fluid regime of reconnection; and Section 6.3 presents a novel set

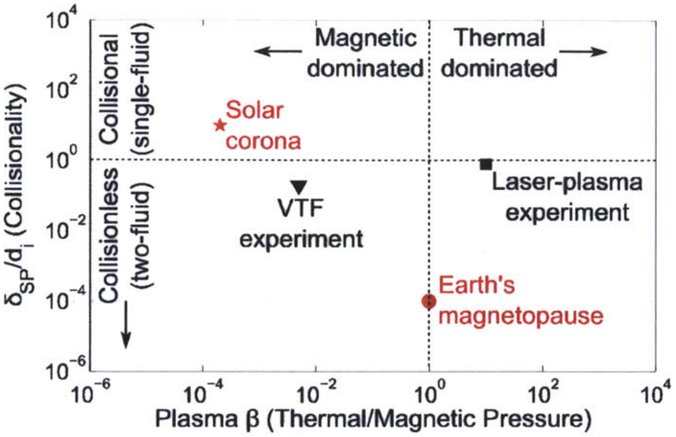

Figure 6.1. Plasma β and collisionality (δ_{SP}/d_i) in astrophysical and laboratory magnetic reconnection. Red points denote astrophysical reconnection cases (solar corona, star; Earth's magnetopause, circle), while black points denote laboratory experiments (VTF, triangle; laser-plasma experiments, square). In particular, laser-plasma experiments access regimes of reconnection relevant to the Earth's magnetopause, as both are characterized by fair high plasma β and are susceptible to collisionless reconnection effects. Not shown, but particularly important, are the facts that, like the magnetopause, laser-plasma experiments have very strong plasma inflows and also can be driven asymmetrically (see Section 6.1).

of experiments probing the strongly-driven collision of *parallel* magnetic fields that do not undergo reconnection. In summary, these high-β laser-plasma experiments generate new insight into the physics of strongly-driven, two-fluid reconnection (characterized by decoupled ions and electrons), relevant to magnetic reconnection in astrophysics.

6.1 A Laboratory Study of Asymmetric Magnetic Reconnection in Strongly-Driven Plasmas

Magnetic reconnection, the annihilation and rearrangement of magnetic fields in a plasma, is a universal phenomenon that frequently occurs when two plasmas collide with oppositely-directed field lines forced together. In most natural circumstances the collision is asymmetric (the two plasmas having different properties), but the vast majority of theoretical and experimental work to date has been limited to symmetric configurations. In addition, the regime of strongly-driven magnetic reconnection, where the ram pressure of the plasma dominates the magnetic pressure as it does in several important astrophysics and space physics environments, has also received little experimental attention. To remedy this important lack of experimental data, we designed experiments to probe magnetic field structures and their reconnection in asymmetric, strongly-driven, laser-generated plasmas. The strongly-driven reconnection of MG magnetic fields around asymmetric, $\beta \sim 10$ laser-produced plasmas (asymmetry factor of ~ 2 in scale, ~ 1.5 in density, ~ 3 in magnetic flux) has been imaged using monoenergetic proton radiography. Asymmetric experiments demonstrate a super-Alfvénic reconnection rate only 20% slower than in comparable symmetric experiments, consistent with 2D PIC simulations and analytical scalings of this collisionless reconnection. The results show that the rate of magnetic flux annihilation is dictated by the relative flow velocities of the opposing plasmas that drive magnetic fields and is insensitive to initial asymmetries. Additionally, even though three-dimensional magnetic field structures that arise due to asymmetries are predicted to interfere with the small-scale electron flows mediating reconnection, they have minimal impact on the rate of reconnection as a consequence of the strong flows. This work has been submitted to *Nature Communications.*[1]

6.1.1 Motivation for Asymmetric Reconnection Experiments

Magnetic reconnection[2,3] is a pervasive phenomenon in the universe. In astrophysics, it is thought to be a key mechanism for energy release in the solar corona and in solar flares, and it is important at the Earth's dayside magnetopause (see Figure 6.2a). In an earthbound context, it allows for fast reconfiguration of the confining magnetic field and consequent energy loss in magnetized-fusion devices.[4] Reconnection most frequently occurs in these environments, and in fact universally in nature, in configurations where there is an asymmetry in the plasma density, temperature, magnetic field strength, geometry, and/or flow across the reconnection layer. In the magnetopause, for example, a strong solar wind drives reconnection across an asymmetric boundary, with differences of a factor of $\sim$0.3 in density and $\sim$7 in magnetic field strength. The plasma thermal β (ratio of thermal to magnetic pressure) is $\sim$0.1 at the high-field, low-density magnetosphere and $\sim$1 at the low-field, high-density magnetosheath, and the plasma ram pressure β_{ram} (ratio of ram to magnetic pressure) is $\sim$50 on the solar-wind side, signifying a strongly-driven reconnection.[5–7] Despite the prevalence of asymmetry in nature, it is only recently that studies have begun to explore its effects on reconnection, primarily in analytic theory[8] and in numerical simulations of collisional[8,9] and collisionless plasmas,[10–13] as discussed in Chapter 4. Some experimental work has been performed with spacecraft measurements of the Earth's magnetopause,[14,15] but presented here is the first comprehensive laboratory effort to isolate and study the effects of asymmetry on magnetic reconnection, using strongly-driven colliding plasmas.

Magnetic fields generated by the interaction of $\sim 10^{14}$ W/cm^2 lasers with solid targets have been measured experimentally,[16,17] and recent experiments have utilized the proton radiography technique[18] to image and quantify magnetic fields around the symmetric interaction of multiple laser-produced plasma bubbles.[19,20] Some experiments have demonstrated the annihilation of magnetic fields and other signatures of magnetic reconnection.[19–21] One experiment introduced an asymmetry in the magnetic field strength, though the magnetic fields and their annihilation were not measured directly.[21] In the present experiments, monoenergetic proton radiography[22,23] has probed the asymmetric interaction of magnetic field-carrying laser-produced plasmas. These experiments drove reconnection between plasma bubbles at different stages in their evolution – with differences in geometry, density, ram pressure, and total magnetic flux. This set of experiments provides the first quantitative measurements of magnetic flux annihilation and the reconnection rate between asymmetric plasmas in the laser-produced, strongly-driven, or high-energy-density plasma regime,[24] relevant to several astrophysical environments. It is demonstrated that the reconnection rate in these asymmetric experiments is affected neither by the asymmetry in density or ram pressure across the current sheet, nor by out-of-plane fields that arise due to the asymmetries in flow velocity and geometry, which modify the electron flow. The rate of magnetic flux annihilation due to reconnection is found to be equivalent to the opposing flow velocity of the colliding plasmas in both symmetric and asymmetric experiments.

6.1.2 Asymmetric Reconnection Experiments on the OMEGA Laser

The experiments were conducted at the OMEGA laser facility.[25] As shown in Figure 6.2c, each experiment involved two 500-J beams of 351-nm laser light striking a 5-μm-thick, 1.11 g/cm^3, 1:1 C:H parylene foil for 1 ns and focused into 800-μm spots separated by 1.4 mm. The interaction of each laser beam with the foil produced an expanding, hemispherical plasma bubble with an azimuthal magnetic field of $\sim$0.5 MG concentrated at its perimeter,[26] where the plasma β was $\sim$10. Unlike previous investigations of reconnection in symmetric laser-produced plasma configurations,[19–21] these experiments additionally introduced a delay (Δt) between the two beams incident

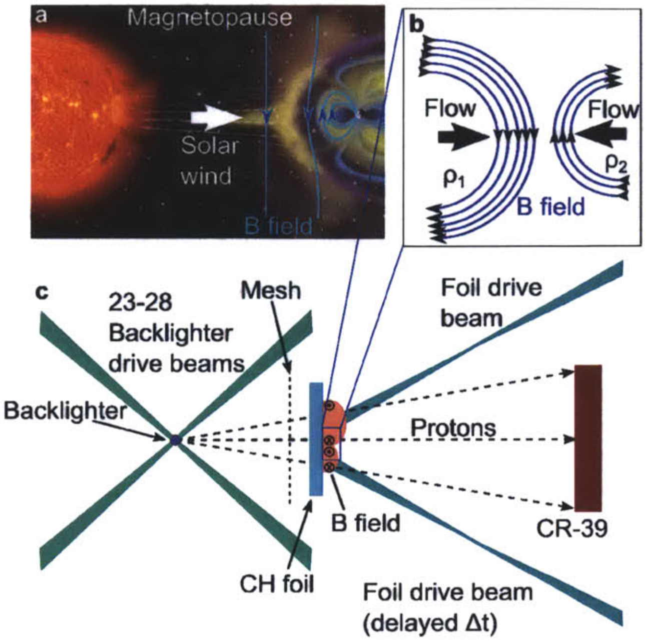

Figure 6.2. (a) Magnetic fields at the magnetopause, where the solar wind drives asymmetric reconnection between the interplanetary magnetic field and the Earth's magnetosphere, bear similarities to (b) magnetic fields and flows in the asymmetric reconnection experiments. (c) In the experiments, the distance between the backlighter capsule and the CH foil was 1 cm, while the distance between the mesh and the foil was 0.2 cm. The distance between the backlighter and the CR-39 proton detector was 27-28 cm, so the magnification was M=27-28. The relative timing of laser onset of the two foil drive beams was varied from Δt=0 to Δt=0.7 ns.

on the foil. This enables study of the interaction between plasma bubbles that are at different stages in their evolution, with differences in geometry, temperature, density, ram pressure ($\frac{1}{2}\rho V^2$, where ρ is the plasma density and V the bulk flow velocity), and total magnetic flux. The magnetic Reynolds number Rm (a measure of the strength of flow relative to magnetic diffusive processes) is ~3000, indicating that the magnetic field was frozen into the flowing plasma, as it is in most astrophysical contexts (where $Rm \gg 1$). Consequently, the magnetic fields were largely advected with the outward radial flow of the plasma bubbles, which expanded into each other and drove their oppositely-directed magnetic fields to interact. The resultant magnetic field configuration (Figure 6.2b) has strong similarities to that of the magnetopause (6.2a); a quantitative comparison of plasma conditions and reconnection-relevant parameters for the two contexts is presented in Tables 6.1 and 6.2.

Table 6.1. Plasma parameters for experimental and magnetopause reconnection environments, including the electron density (n_e), the mass density (ρ), the electron temperature (T_e), the magnetic field strength (B), the average ion charge ($\langle Z\rangle$), the flow velocity (V_{flow}), the sound speed (C_s), and the length scale (L_{scale}), which can be roughly equated to the current sheet length. Experimental parameters are representative conditions just prior to the onset of reconnection (though conditions evolve significantly throughout the experiment), while magnetopause conditions are based on Refs. [6] and [27] and their references and are representative of typical values and the degree of asymmetry between the solar wind and magnetosphere sides.

Location	n_e (cm^{-3})	ρ (g/cm^3)	T_e (eV)	B (T)	$\langle Z\rangle$	V_{flow} (μm/ns)	C_s (μm/ns)	L_{scale} (μm)
Exp.(Symmetric)	7×10^{19}	2.2×10^{-4}	700	50	3.5	450	250	800
Exp. (Asymm. - large)	12×10^{19}	3.7×10^{-4}	550	50	3.5	450	220	1200
Exp. (Asymm. - small)	4×10^{19}	1.2×10^{-4}	900	50	3.5	450	280	400
M'pause (Solar wind)	7	1×10^{-23}	15	7×10^{-9}	1	400	50	10^{16}
M'pause (M'sphere)	2	0.3×10^{-23}	300	5×10^{-8}	1	50	200	10^{14}

The magnetic field structures and the rates of magnetic reconnection in the experiments were

Table 6.2. Derived reconnection-relevant parameters for experimental and magnetopause environments based on the plasma parameters described in Table 6.1, including the ratio of thermal pressure to magnetic pressure (β), the ratio of ram pressure to magnetic pressure (β_{ram}), the Alfvén speed (V_A), the magnetic Reynolds number (Rm), the Lundquist number (S), the ion inertial length (d_i), and the ratio of Sweet-Parker current sheet width to ion inertial length (δ_{SP}/d_i), a parameter describing the importance of two-fluid or collisionless reconnection effects.

Location	β	β_{ram}	V_A (μm/ns)	Rm	S	d_i (μm)	δ_{SP}/d_i
Experiment (Symmetric)	8	22	100	3000	600	40	0.9
Experiment (Asymm. - large bubble)	11	38	70	3000	500	30	1.9
Experiment (Asymm. - small bubble)	6	13	130	2000	600	50	0.3
Magnetopause (Solar wind)	1	48	60	2×10^{14}	3×10^{13}	10^{11}	0.02
Magnetopause (Magnetosphere)	0.1	0.004	800	2×10^{13}	3×10^{14}	2×10^{11}	3×10^{-5}

studied using monoenergetic proton radiography.[22,23] To generate backlighter protons, a spherical glass capsule with a 420-μm diameter and a 2 μm-thick wall, filled with 18 atm of D^{3}He gas, was imploded by 23-28 OMEGA lasers, delivering 11-12 kJ in a 1-ns pulse. The implosion produced an isotropic burst of monoenergetic 15-MeV D^{3}He protons. The protons were divided by a 150-μm-period, 60-μm-thick Ni mesh into discrete beamlets, which sampled the plasma and were detected using CR-39. The resultant proton radiographs allow measurements of the deflections of individual proton beamlets due to magnetic fields around the laser-produced plasma bubbles, as shown in Figure 6.3a, where individual images are organized according to both the duration of time since the plasma bubbles began to interact (t_{int}) and the difference in onset time between the two foil drive beams (Δt) in the experiment. The absolute time of proton emission from the backlighter was measured using the particle temporal diagnostic (PTD).[28] Experimental setup parameters are further summarized in Appendix E.

6.1.3 Proton Radiography Data of Asymmetric Reconnection

The most salient feature in the images of Figure 6.3a is the deflection of proton beamlets away from the center of each bubble due to the azimuthal magnetic field at each bubble's perimeter. In addition, there are distortions in the beamlet distributions in the image regions corresponding to the interaction of the two bubbles, where there are bubble deformation and reconnection of magnetic fields. In all cases, the proton-path-integrated magnetic field strength can be determined from the magnitude of the beamlet deflections ξ relative to where they would have been in the image plane in the absence of fields: $|\int \mathbf{B}\times d\mathbf{l}| = \xi m_p v_p/(qA)$, where m_p (v_p) is the proton mass (velocity), q is the proton charge, and A is the foil-detector distance.[20] Resulting maps of path-integrated magnetic field are shown in Figure 6.3b. Additional details of the path-integrated field map reconstruction are presented in Appendix E. At the later times, most of the field maps show annihilation of magnetic flux and the deformation of magnetic field structures in the reconnection region.

The line-integral of path-integrated field strength is equivalent to the magnetic flux, and the amount of flux annihilated $\Delta\Phi_{ann}$ is inferred as the difference between the sum of the flux at the perimeters of both plasma bubbles and the total flux in the interaction region. The calculation of magnetic flux is illustrated in Figure 6.4. Since flux ($\Phi = B * dA = |B \times dl| ds$) is the quantity of interest in these experiments as far as the measurement of the reconnection rate, it does not matter exactly what the magnetic field strength is, nor the exact scale height dl, but rather their product. Therefore, this calculation avoids the difficulty of exactly determining B from a measurement of

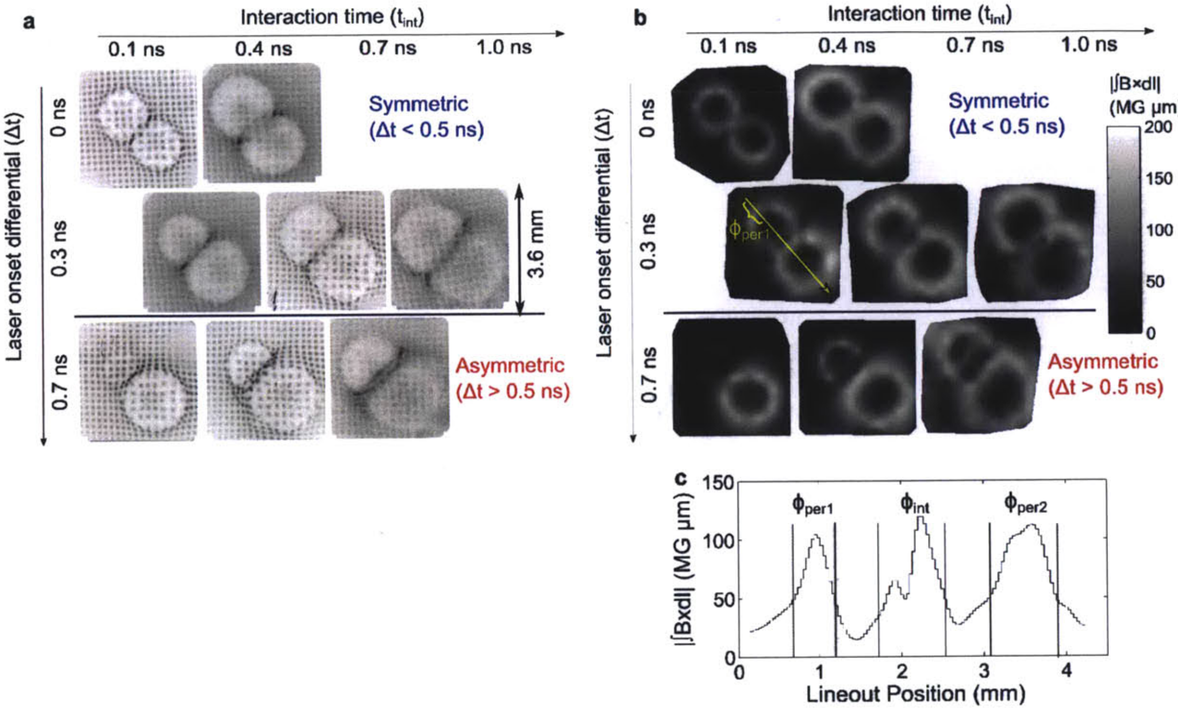

Figure 6.3. (a) 15-MeV-proton images and (b) inferred path-integrated magnetic field strength maps at different interaction times $t_{int.}$ (since the beginning of bubble interaction) and for differing amounts of bubble asymmetry as parameterized by the laser onset differential Δt (the difference in onset times of the two bubble-generating beams) Each image covers a field of view (at the foil) of 3.6 mm by 3.6 mm. (c) A sample lineout of $|\int \mathbf{B}\times d\mathbf{l}|$, is integrated along the yellow arrow to measure the magnetic flux Φ.

$|\int \mathbf{B}\times d\mathbf{l}|$.

The total magnetic flux annihilated in the reconnection region was calculated as $\Delta\Phi_{ann} = (\Phi_{per1} + \Phi_{per2}) - \Phi_{int}$, where Φ_{per1} and Φ_{per2} were the fluxes at the perimeters of the individual plasma bubbles and Φ_{int} was the total flux measured in the interaction region, where reconnection occurred. The flux in each case was measured as a line-integral of the path-integrated field strength (see Figure 6.3c or 6.4). The bubble expansion speed V_b, as estimated based on the radius of the outer extent of magnetic-field structure around an individual bubble, is a relatively constant 450 μm/ns over the duration of the experiment. This flow velocity is much larger than the typical Alfvén speed V_{A0}, the speed at which ions can rearrange the magnetic field structure, which is $\sim$100 μm/ns at the perimeters of the expanding plasma bubbles just prior to their collision. Consequently, and in contrast to many previous experiments,[29] magnetic reconnection was strongly driven, with the plasma bubbles driven together faster than the natural velocity at which the magnetic fields can adjust. Magnetic field measurements from these experiments are summarized in Appendix E.

The measured annihilated flux is compared to the flux advected into the reconnection region based on the constant flow velocity V_b in Figure 6.5. This flow-based total flux scales as $2V_b t_{int}|\int \mathbf{B}\times d\mathbf{l}|$, where V_b is the measured radial expansion velocity; t_{int} is the duration of time since the bubbles began to collide; and $|\int \mathbf{B}\times d\mathbf{l}|$ is the measured path-integrated magnetic field strength through the perimeter of the smaller bubble. (The larger bubble carries some magnetic fields that are unopposed by the smaller bubble.) For the more symmetric plasma interactions, the amount of flux annihilated increases with time to $\Delta\Phi_{ann} = 88\pm20$ MG μm mm at $t_{int} = 0.85$ ns; in comparison to the flux available for reconnection, twice the flux contained in the smaller bubble,

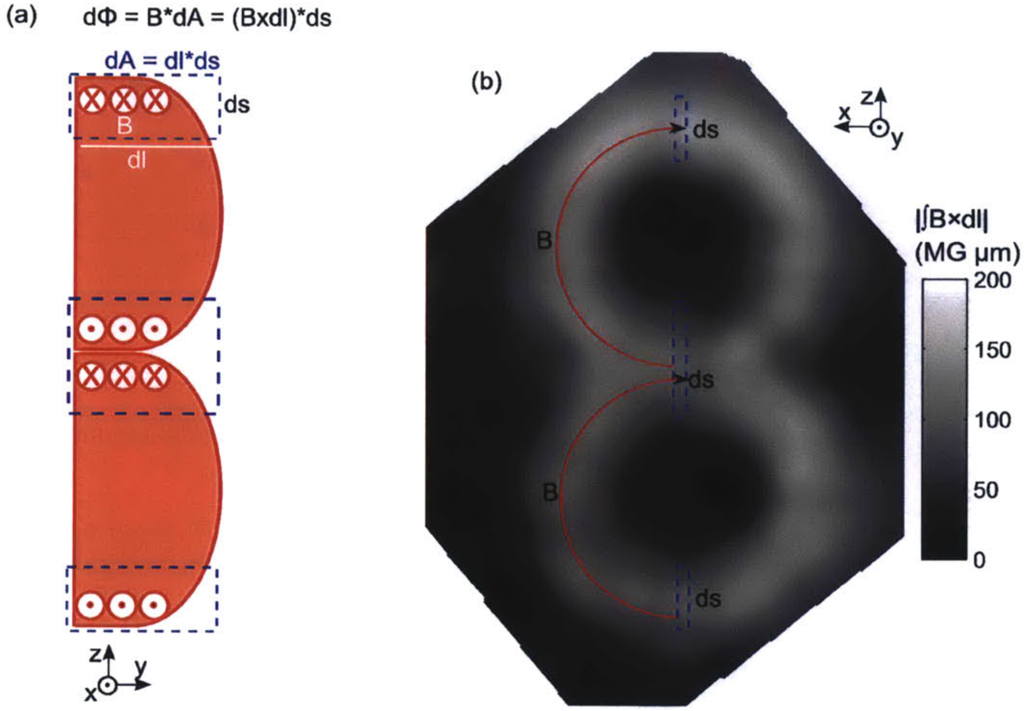

Figure 6.4. (a) Cartoon of magnetic fields and flux in laser-plasma reconnection experiments and (b) image of path-integrated magnetic field strength to illustrate the calculation of magnetic flux. The magnetic flux is the in-plane line integral of the path-integrated magnetic field strength, as $\Phi = |B \times dl|ds$.

68±20% was annihilated. The more asymmetric cases show only slightly less flux annihilation, with $\Delta\Phi_{ann} = 62\pm20$ MG μm mm at $t_{int} = 0.72$ ns, and 51±19% of the available flux. This is equivalent to an average reconnection rate of ~100 MG μm mm/ns in the symmetric experiments and ~85 MG μm mm/ns in the asymmetric experiments. In both symmetric and asymmetric cases, the rate of reconnection was nearly equivalent to the flow-based rate, as the total flux annihilated $\Delta\Phi_{ann}$ is $\sim 2V_b t_{int}|\int \mathbf{B}\times\mathbf{dl}|$. In contrast, this rate is much faster than that expected based on the nominal Alfvén speed, as $\Delta\Phi_{ann}\sim 10V_{A0}t_{int}|\int \mathbf{B}\times\mathbf{dl}|$. Furthermore, reconnection in the asymmetric experiments was only ~20% slower than in the symmetric experiments, an essentially insignificant difference. It can therefore be concluded that the reconnection rate was governed primarily by the relative velocities of incoming and opposing plasmas, independent of the plasma asymmetry.

6.1.4 Discussion of Reconnection-relevant Plasma Parameters

Calculation of the plasma parameters in the experiments shows that the magnetic reconnection was strongly driven and that two-fluid effects (decoupled ions and electrons) were important. To estimate the key plasma parameters we used measurements and simulated quantities from other recent, similar experiments. Thomson-scattering measurements of local plasma conditions, discussed in Chapter 5, indicated an electron temperature $T_{e0}\sim 0.7$ keV at the plasma bubble perimeter just prior to interaction in a typical symmetric experiment.[30] The electron density, as predicted by LASNEX radiation-hydrodynamics simulations[31,17] of individual laser-produced plasma bubbles, was $n_{e0}\sim 7\times10^{19}$ cm^{-3}. In addition, the magnetic field strength at the perimeter of each bubble was ~0.5 MG, as predicted by LASNEX and confirmed by experimental data.[32] These numbers imply that the ratio of thermal pressure to magnetic pressure was $\beta \equiv n_e kT_e/(B^2/2\mu_0)\sim 8$, while the ratio

Figure 6.5. Measured annihilated flux versus the expected annihilated flux based on the flow velocity. The thin, dotted line denotes the annihilated flux based on the flow velocity, while the thick, dashed line indicates the annihilated flux based on a nominal Alfvénic reconnection rate ($\Delta\Phi = V_{A0}t_{int}|\int \mathbf{B}\times\mathbf{dl}|$). Error bars principally denote uncertainty in the boundaries of the magnetic flux regions and the magnitude of proton beamlet deflections.

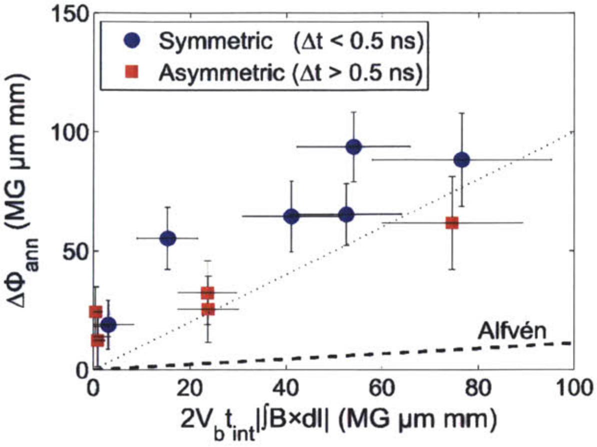

of ram pressure to magnetic pressure was $\beta_{ram} \equiv \frac{1}{2}\rho V^2/(B^2/2\mu_0){\sim}22$. It is noted again that the reconnection was strongly driven, by virtue of $\beta_{ram} \gg 1$, or, equivalently, $V_b \gg V_A$, as previously discussed.

As discussed in Chapter 4, the significance of two-fluid reconnection effects in the experiments is assessed by comparing the length scale for electron-ion decoupling to the width of the reconnection region. The ion inertial length, the distance over which electrons and ions decouple in a plasma, was $d_i \equiv c/\omega_{pi} {\sim} 40$ μm, where ω_{pi} is the frequency of ion oscillations in a plasma. Based on the radiographs, the length L of the boundary layer current sheet was ~800 μm, while the Lundquist number, the ratio of diffusive to Alfvén timescales, was $S \equiv \mu_0 L V_{A0}/\eta {\sim} 600$, where η is the plasma resistivity. As a result, the current sheet width in the experiments, as predicted by Sweet-Parker reconnection theory,[33,34] was $\delta_{SP} \equiv L/\sqrt{S}$ ~35 μm and therefore $\delta_{SP}/d_i {\sim} 0.9$. The ion gyroradius ρ_i in the experiment was approximately equal to the ion inertial length of ~40 μm. On length scales shorter than d_i or ρ_i the ions are demagnetized, while the electrons remain tightly bound to the magnetic field lines and electron flow carries magnetic flux into the annihilation region. The conditions in the experiments, with $\delta_{SP}/d_i \lesssim 1$, were far different from those required for a single-fluid reconnection model, which requires that $\delta_{SP}/d_i \gg 1$. All of these parameters evolved with time throughout these highly dynamic experiments, but, on the whole, collisionless or two-fluid effects were important in the reconnection process just as they are in magnetopause reconnection (where electron densities of ~10 cm^{-3} and magnetic field strengths of ~10 nT imply $\delta_{SP}/d_i {\sim} 10^{-3}$).

6.1.5 Use of PIC Simulations to Aid Interpretation of Experimental Results

In order to help interpret the physics in these experiments, two-dimensional numerical simulations were performed. First, the azimuthally symmetric 2D structure and evolution of each individual bubble was simulated with 2D DRACO[35] and LASNEX[36] radiation-hydrodynamics codes. At the point in time when the individual bubbles were about to collide, the conditions in both bubbles (radial profiles of density, temperature, magnetic field strength, and flow velocity) on a plane parallel to the foil were recorded. These were then used as initial conditions for further simulation through the bubble-interaction phase using the 2D, planar particle-in-cell (PIC) code PSC in a manner previously applied to other experiments involving reconnection in laser-driven plasmas.[37,38] The use of a PIC code, rather than a hydrodynamic code, is necessary during the interaction phase in order to capture the physics of two-fluid reconnection. The PIC simulations did not account for continued laser drive or for the self-generation of magnetic fields, nor – as a 2D simulation – did they account for the full 3-dimensional structure of the hemispherical plasma bubbles.

In basic agreement with the data (Figure 6.6a-b), the simulations show (Figure 6.6c-d) the emergence of a reconnection layer in the interaction region, the annihilation of magnetic fields, and the deformation of the plasma bubbles due to their hydrodynamic collision. The ribbons of path-integrated fields in the measured data are much thicker than the ribbons of magnetic field in the simulations as a result of the 3D shell structure of the plasma bubbles – the simulations represent only a single slice parallel to the foil. The simulated reconnection rates, expressed in Figure 6.6e in terms of the reconnection-related out-of-plane electric field (E_y), are nearly indistinguishable in the symmetric and asymmetric simulations. This result is consistent with experimental observations. Magnetic field amplification due to flux pileup up to a factor of 4 is observed in the simulations as a consequence of the strongly-driven interaction, as in previous modeling studies of related experiments.[38] Such pileup is difficult to detect in the measured path-integrated field maps, due to the coarse spatial resolution of the images as imposed by the mesh spacing. Flux pileup is predicted to occur on length scales of order ~50 μm, much shorter than the 150 μm mesh period. Notably, the simulations show a comparable degree of flux pileup in both symmetric and asymmetric cases, though pileup occurs inversely to the density or ram pressure asymmetry and slightly more weakly overall in the asymmetric simulation. This flux pileup likely explains the fast reconnection rates inferred from the measured magnetic flux data in symmetric and asymmetric experiments. This result indicates, in a manner consistent with prior symmetric simulations[37] and the experimental result discussed above, that the reconnection rate in a strongly-driven system is dependent more on the characteristics and strength of the drive mechanism – as determined by the flow velocity – than on ambient, "undriven" plasma conditions and asymmetries.

Table 6.3. Scale parameters for PIC simulations, based on the maximum initial electron density ($n_{e,init}$), the maximimum initial magnetic field strength (B_{init}, and the derived Alfvén speed ($V_{A,init}$), ion inertial length (d_{i0}), and sound speed (C_{s0}).

$n_{e,init}$ (cm^{-3})	B_{init} (T)	$V_{A,init}$ (μm/ns)	d_{i0} (μm)	C_{s0} (μm/ns)
6.8×10^{20}	50	31	11	250

The reconnection electric fields are predominantly attributable to the Hall $\boldsymbol{J_{Hall}}\times\boldsymbol{B}$ electromotive force and the electron pressure tensor in the current sheet, and they are driven at the periphery of the reconnection region by ion-driven magnetic-field advection $\boldsymbol{V_i}\times\boldsymbol{B}$. Similar magnitudes of the $\boldsymbol{V_i}\times\boldsymbol{B}$ term in the symmetric and asymmetric cases arise from the ram pressure around the current sheet, which is approximately equal in the symmetric and asymmetric simulations despite the large asymmetry between the two sides of the current sheet in the asymmetric case. This result suggests that the bulk plasma flows drive electrons to rearrange themselves in a way that produces a strong reconnection electric field and a rapid reconnection, and that this process is largely insensitive to asymmetries.

Remarkably, under a wide range of conditions reconnection occurs at the rate implied by the dynamics of the plasma bubble collision, with the local electron behavior dictated by the strong collision process. The reconnection rate produced in the simulations is also consistent with an analytic theory of asymmetric reconnection[8] based on a "hybrid" Alfvén speed and magnetic field strength (see Chapter 4) – inferred from the local density and magnetic field strength on each side of the current sheet – and the current-sheet aspect ratio (opening angle of the reconnection

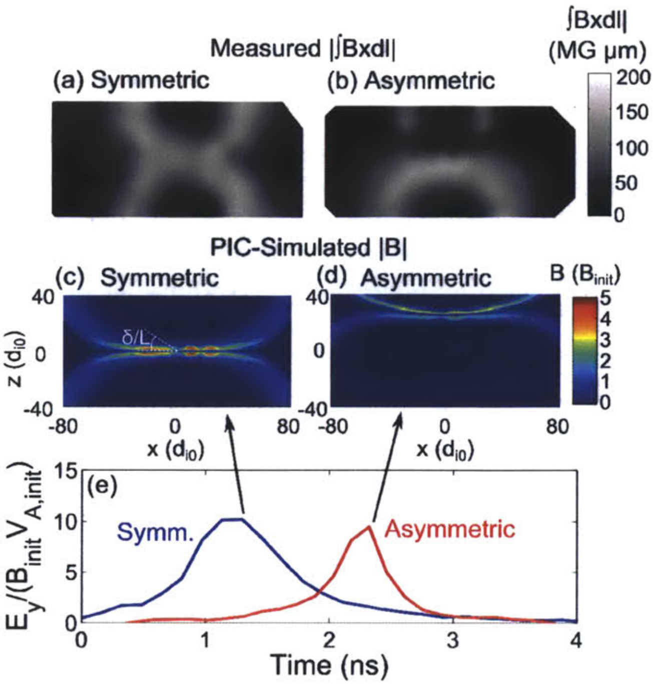

Figure 6.6. Measured and PIC-simulated results for symmetric and asymmetric reconnection. Measured images of $|\int \mathbf{B}\times d\mathbf{l}|$ in (a) symmetric and (b) asymmetric reconnection experiments. Simulated magnetic field strength in a plane parallel to the foil at the time of peak reconnection rate for the cases of (c) symmetric and (d) asymmetric interacting plasma bubbles. Spatial units are in terms of a nominal ion skin depth $d_{i0} = 11$ μm and the magnetic field strength is in terms of the peak initial magnetic field strength $B_{init} = 0.5$ MG. The simulated reconnection electric fields (e), normalized to initial magnetic field strength and Alfvén speed, are approximately equal in symmetric and asymmetric simulations, consistent with experimental results. The electric field is expressed in terms of B_{init} and the nominal Alfvén speed $V_{A,init} = 31$ μm/ns $\sim 1/3 V_{A0}$ in the simulation (based on B_{init} and the peak simulated density $n_{e,init} = 6.8\times10^{20}$ cm^{-3}), with these scale values used for normalization (see Table 6.3). The asymmetric simulation shows a delay in the onset of reconnection, because in this case it takes longer for sufficient pressure to build up on the small-bubble side to push back and drive reconnection. This effect is likely exaggerated in the simulation due to the lack of modeling of the continued laser drive, which in reality increases the pressure on the small-bubble side.

outflow). This model, independent of dissipation mechanism, gives a reconnection rate of

$$\frac{d\Phi}{dt} \sim E_r \sim \frac{B_1 B_2}{B_1 + B_2}\sqrt{\frac{B_1 B_2 (B_1 + B_2)}{\rho_1 B_2 + \rho_2 B_1}}\,\frac{\delta}{L}, \tag{6.1}$$

where ρ_1 (ρ_2) is the mass density and B_1 (B_2) is the magnetic field strength at the perimeter of the smaller (larger) plasma bubble, and δ/L is the generic current sheet aspect ratio. This is illustrated based on instantaneous, local conditions around the time of peak reconnection rate. The simulations show that the dynamically evolving asymmetry in the reconnection layer departs significantly from initial asymmetries: primarily, the initial asymmetry is one of plasma density, but as the system evolves and pressure balance is established around the layer the magnetic field asymmetry becomes dominant. At the peak reconnection rate in the symmetric simulation, based on the simulated density of 2.4×10^{-4} g/cm^3, magnetic field strength of 1.7 MG, and current sheet aspect ratio of 0.25, the analytic model predicts $E_y \sim 1.4\times10^7$ V/m, which compares favorably to the simulated $E_y \sim 1.6\times10^7$ V/m. Near the peak reconnection rate in the asymmetric simulation, based on simulated densities of 2.0×10^{-4} g/cm^3 (large bubble) and 1.6×10^{-4} g/cm^3 (small bubble), magnetic field strengths of 1.0 MG and 1.7 MG, and an aspect ratio of 0.29, the analytic model predicts $E_y \sim 1.0\times10^7$ V/m, close to the simulated $E_y \sim 0.8\times10^7$ V/m at that time. These experiments provide the first experimental evaluation of the reconnection rate scaling of Equation

6.1, albeit in an impulsive, strongly-driven system. Agreement with this steady-state model can only be considered suggestive, rather than explanatory, for this strongly-driven system. However, this picture suggests, in agreement with the experimental and simulated results, that under such strong external drive, the plasma conditions evolve to permit reconnection at the flow-based rate, regardless of the initial magnetic field, density, or ram pressure asymmetry. Future experiments under different drive conditions, may extensively explore the parameter space of magnetic-field and density asymmetry and more stringently assess this scaling.

6.1.6 (Non-)Impact of 3D Effects on the Reconnection Rate

Though the three-dimensional (3D) structure of the plasma bubble collisions is a notable feature of these experiments, in this particular geometry it was found that changes to the magnetic field structures due to 3D effects – primarily a tilt in the reconnection plane and out-of-plane velocity shear – have negligible impact on the reconnection rate in the strongly driven case. Figure 6.7 illustrates two asymmetric plasma bubbles and their magnetic fields just prior to the collision. Because the bubbles collide in such a way that the reconnection plane (y'=0) is not parallel to the foil (Y=0), the azimuthal magnetic fields have a component out of the reconnection plane, forming a bipolar field structure anti-symmetric about x'=0 with a magnitude $B_{y'}^{tilt} = B_0 \sin\theta$, where θ is the tilt angle between the foil and the reconnection plane and $B_0 \sim 0.5$ MG is the magnitude of the azimuthal magnetic field at the perimeter of each bubble. With $\theta \sim 25°$, $B_{y'}^{tilt} \sim 0.3 B_0$.

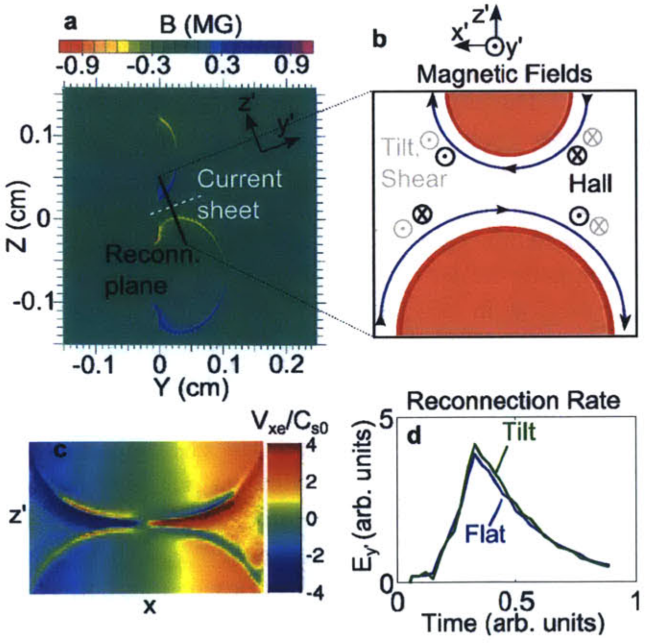

Figure 6.7. (a) LASNEX simulation of magnetic fields around asymmetric plasma bubbles just prior to their collision shows (b) how magnetic fields at the reconnection plane are produced, including the quadrupolar Hall magnetic fields (black) and out-of-plane fields due to the tilted reconnection plane and out-of-plane velocity shear across the current sheet (gray). 2D PIC simulations initiated with out-of-plane ("Tilt") fields show (c) modified electron flows but (d) a reconnection rate identical to those without external out-of-plane fields ("Flat").

Additionally, LASNEX simulations indicate that a rapid upward expansion of the small bubble ($V_{y,small} \sim 500$ μm/ns), in contrast to the weaker upward expansion of the large bubble at the interaction point ($V_{y,large} \sim 200$ μm/ns), creates a $\Delta V_{y'} \sim 270$ μm/ns out-of-plane velocity shear across the current sheet, leading to the generation of additional out-of-plane magnetic fields.[39] For $\Delta V_{y'} \sim 270$ μm/ns, $B_{z'} \sim 0.4 B_0$, and the velocity shear gradient spread out over ~ 400 μm, $B_{y'}^{shear} \sim 0.2 B_0$ in the same bipolar orientation as that caused by the reconnection plane tilt. Both of these effects are estimated to produce out-of-plane magnetic fields comparable to two-fluid or Hall reconnection out-of-plane magnetic fields (typically 0.1-0.5B_0[38]) that arise consistently with electron currents, indicating that these additional out-of-plane fields might have been expected to impact the reconnection process.

However, on the basis of the data, with reconnection occurring at a similar rate in symmetric and asymmetric experiments, it is inferred that these out-of-plane magnetic fields and their interference with Hall magnetic fields and electron currents have minimal net effect on the reconnection rate. The imposed out-of-plane magnetic fields enhance the electron inflow on the small-bubble side and stymie electron inflow on the large-bubble side due to the $\boldsymbol{J_{Hall}}\times\boldsymbol{B_{tilt}}$ force in the -z'-direction. 2D PIC simulations with additional out-of-plane "tilt" magnetic fields were conducted to assess this effect and have confirmed this result (Figure 6.7c), demonstrating enhanced electron flow on the upper side of the current sheet, reduced electron flow on the lower side, but no net change in the reconnection rate (Figure 6.7d). These simulations indicate that typical electron flow speeds related to the Hall current are approximately half of the bulk flow velocity $V_e{\sim}0.5V_b$. It is hypothesized that the minimal impact of the modification of electron flows on the reconnection rate is due to the reconnection process being strongly externally driven, as the small net fractional change in electron velocity $\Delta V_{e,net}{\lesssim}0.1V_e$ from the increase in V_e on one side and decrease on the other side is negligible in comparison to the large inflow speeds ($\Delta V_{e,net}{\ll}V_b$). Interestingly, these results bear on collisionless guide-field reconnection in strongly-driven systems, where small perturbations in the local physics due to out-of-plane fields may be overwhelmed by the strong drive mechanism, in contrast to tenuous, low-β, quasi-steady plasmas.[40]

6.1.7 Conclusions

Strongly-driven asymmetric magnetic reconnection has been comprehensively studied in the laboratory using colliding $\beta{\sim}10$ laser-produced plasmas. The super-Alfvénic annihilation of magnetic fields is observed to occur at nearly the same, flow-based rate in asymmetric and symmetric experiments. In support of these experiments, 2D PIC simulations indicate that near-equal reconnection electric fields, consistent with local electron physics at the current sheet, is supported and generated by bulk plasma flows into the reconnection region that are nearly equal, on average, in symmetric and asymmetric cases. Out-of-plane magnetic fields, due to the asymmetry in geometry and velocity shear, are predicted to modify electron flow in this two-fluid reconnection event, but are inferred to have minimal impact on the reconnection rate in this experiment. This result is due to the fact that the net change in inflow is small compared to the rapid inflow velocity in this strongly-driven system. Strongly-driven, two-fluid asymmetric magnetic reconnection such as studied in these experiments occurs in many astrophysics and space physics environments, most notably at the Earth's dayside magnetopause. The results of these experiments suggest that the rate of reconnection at the magnetopause may be dictated by the strength of the solar wind, rather than by the local, asymmetric, upstream plasma conditions. Future experiments with different drive conditions may explore a more extensive parameter space of asymmetries in magnetic-field strength, density, and drive.

6.2 Observation of Two-Fluid to Single-Fluid Magnetic Reconnection Dynamics in Strongly-Driven Laser-Plasma Experiments

As discussed in the context of asymmetric reconnection experiments, two-fluid physics is an important aspect of this regime of reconnection. In a separate set of experiments, evidence for a transition between the two-fluid and single-fluid regimes of magnetic reconnection has been observed in strongly-driven, laser-produced plasma experiments. High-resolution proton radiography has revealed unprecedented detail of electron flows as well as the evolution of large-scale self-generated magnetic field structures in the reconnection of colliding, $\beta\sim 20$ plasmas. Observation of supersonic, super-Alfvénic electron jets ($V_{jet}\sim 20V_A$) ejected from the reconnection region shows that two-fluid magnetic reconnection occurs early in time. The absence of this feature and the persistence of strong magnetic fields at late times, as well as the evolution of plasma conditions to a cooler, denser, more collisional state, demonstrates that the reconnection process slows down as the system enters the single-fluid regime of reconnection. This work will be submitted to *Physical Review Letters.*[41]

6.2.1 Motivation for Two-Fluid Reconnection Experiments

Magnetic reconnection[2] is a ubiquitous phenomenon in space[42,43] and laboratory[4] plasmas, where oppositely-directed magnetic fields undergo a modification of field-line topology and release magnetic energy. As previously discussed, when the scale width of the reconnection region is smaller than the ion inertial length ($d_i \equiv c/\omega_{pi}$), electrons and ions decouple, and the reconnection process is governed by electron flows, rather than the entire plasma fluid. This two-fluid reconnection (otherwise known as Hall reconnection or collisionless reconnection) is a common occurrence in astrophysics[44] and it has been studied in tenuous, quasi-steady plasma experiments.[45,46]

In contrast to those near-steady-state, low-density experiments, reconnection of magnetic fields in strongly-driven (ram pressure>magnetic pressure), $\beta>1$ (total thermal pressure>magnetic pressure) plasmas occurs frequently in astrophysics, impacting dynamics of plasmas in the solar photosphere[47] and at the heliopause.[48] Moreover, strongly-drive, two-fluid reconnection at high β is especially pertinent at the dayside magnetopause of the Earth and other planets.[15,49] To date, there has been little laboratory investigation of the physics of two-fluid reconnection in the $\beta>1$, strongly-driven plasma regime.

This work provides the first direct observation of two-fluid reconnection features alongside bulk magnetic field measurements in a strongly-driven, $\beta\sim 20$ plasma experiment, showing compelling evidence of a transition from a two-fluid magnetic reconnection regime to a single-fluid regime. These experiments were conducted using laser-produced plasmas, a well-established platform for studies of high-β magnetic reconnection. Prior experiments have examined the annihilation of magnetic fields,[20,50,1] thermal properties of the plasma,[19,30] plasma jets,[19,51,21,52] and energetic electrons produced during reconnection.[53] Particle-in-cell simulations have predicted that two-fluid physics plays a significant role in determining the reconnection rate in these strongly-driven, quasi-collisionless systems.[37]In the present experiments, high-resolution proton radiography has produced images of unprecedented detail and clarity of colliding laser-produced plasmas where the reconnection of magnetic fields is occurring. These images reveal electron jets and large-scale magnetic fields undergoing reconnection. These electron jets, a signature of two-fluid reconnection, emerge early in time when the plasma is in a collisionless regime. Later in time, as the plasma becomes collisional, the jet structure disappears and strong magnetic fields persist around the reconnection region. Hydrodynamic simulations show that throughout the plasma collision process, the plasma cools and becomes denser, so that the resistivity increases and the current sheet width becomes appreciably longer than the ion inertial length. These results demonstrate that the reconnection process transitions from a fast, two-fluid reconnection to a slow, single-fluid reconnection.

6.2.2 Reconnection Experiments and High-Resolution Proton Radiography Data on OMEGA-EP

Reconnection experiments using laser-produced plasmas were conducted at the OMEGA-EP laser facility.[54] In each experiment, depicted in Figure 6.8, a 12-μm-thick CH foil was irradiated by two 930-J, 1-ns laser pulses at a wavelength of 351 nm and with an 800-μm spot size (distributed phase plates were used to produce a smooth laser spot with a super-Gaussian exponent of 8). The laser spots were separated on the foil by 1.4 mm, each producing an expanding, hemispherical plasma bubble with an azimuthal magnetic field concentrated at its perimeter.[26] These plasmas expanded into each other, driving their oppositely-directed magnetic fields to interact and reconnect.

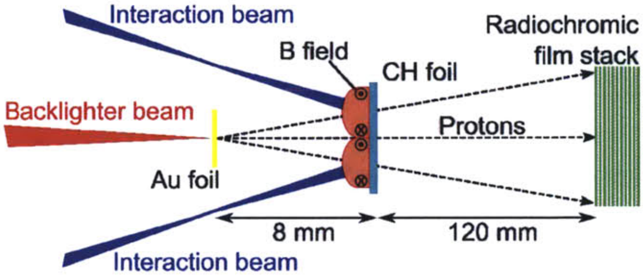

Figure 6.8. Proton radiography setup for reconnection experiments. The distance between the backlighterAu foils and the center of the CH foil was 8 mm, while the distance from the CH foil to the radiochromic film (RCF) stack was 120 mm, for a magnification of M=16. The relative timing between backlighter beam and the interaction beams was varied so that the backlighter protons sampled the plasma at different times in the interaction.

The reconnecting plasma bubbles were imaged using proton radiography. The deflection of protons was used to infer local magnetic field structures and currents, as well as the spatial scale of field-carrying features in the plasma.[18,55] Protons were generated by the target normal sheath acceleration (TNSA) mechanism,[56] introduced in Chapter 5, whereby a high-intensity ($\sim 10^{19}$ W/cm^2) laser incident on a foil accelerates protons to ~60 MeV in an exponentially-decaying spectrum.[57,58] The backlighter used a 190-J, 1-ps pulse with a 10-20 μm spot size, incident on a 10-μm-thick Au foil. This backlighter foil was positioned 8 mm from the CH target foil and parallel to it. Backlighter protons were deflected by magnetic fields around the target and detected by a stack of radiochromic film (RCF),[59] configured in such a way that the pieces of film in the stack were sensitive to protons at a variety of incident energies. The timing between the onset of the interaction beams and the onset of the backlighter beams was varied so that the protons sampled the plasma at different times in the plasma collision process. A summary of experimental parameters is presented in Appendix E.

Proton radiographs obtained with ~18-MeV and ~24-MeV protons are shown in Figure 6.9. The fluence modulations across the images are largely due to the deflection of backlighter protons by magnetic fields around the laser-produced plasma bubbles and in their interaction. The times indicated are between the onset of the interaction beams and the arrival of backlighter protons. Some aspects of the timing on each experiment were verified using the ultra-fast x-ray streak camera (UFXRSC)[60]. A compendium of proton radiography images, in both the face-on and side-on configuration, as well as discussion of additional features not presented here, is contained in Appendix E.

The images reveal several signatures of magnetic fields and the dynamics of reconnection. The most readily apparent feature is the pileup of protons in a circular pattern around each bubble due to their inward deflection by ~MG azimuthal magnetic fields at the bubble perimeters. For laser and backlighter proton propagation into the page, these magnetic fields are oriented clockwise. These fields are generated by the Biermann battery mechanism, arising due to non-parallel gradients in electron density (into the page) and electron temperature (radially inward toward the center of each plasma bubble), with $\partial \mathbf{B}/\partial t \propto \nabla T_e \times \nabla n_e$. In the region where the plasma bubbles collide and are

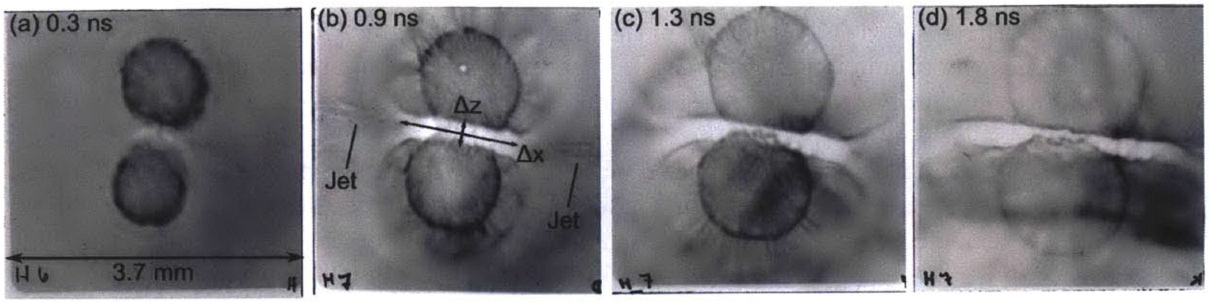

Figure 6.9. Proton radiography images at different times relative to the onset of the interaction beams, with dark areas representing greater proton fluence. The image at (a) 0.3 ns is produced by ~18-MeV protons, while the images at (b) 0.9 ns, (c) 1.3 ns, and (d) 1.8 ns are produced by ~24-MeV protons. Contrast has been optimized differently in each image to reveal details. The times indicated are between the onset of the interaction beams and the arrival of backlighter protons. Each image has a field of view at the foil ~3.7 mm on a side.

flattened against each other, protons are deflected away from the reconnection region toward the individual bubble centers due to the strong magnetic fields piled up just outside the current sheet. Electron jets ejected out of the reconnection region along the current sheet are visible early in time, at 0.9 ns. These evolution of these features, (1) the reconnection-induced electron jets and (2) the bulk magnetic fields in the interaction region, will be examined in greater detail to illustrate the transition from a two-fluid reconnection regime to a single-fluid regime.

6.2.3 Discussion of Plasma Conditions and Reconnection Physics

The collision of plasmas carrying oppositely-directed magnetic fields initially drove a two-fluid reconnection. Based on the electron density of $\sim 10^{20}$ cm^{-3} and temperature of ~1.3 keV at the perimeter of the expanding plasmas just prior to their collision, as estimated from 2D DRACO simulations,[35] the ion inertial length, a scale length for the decoupling of ions and electrons, was $d_i = c/\omega_{pi} \sim 30$ μm. Similarly, for a magnetic field strength of B ~0.55 MG (based on a lower bound on the measured field strength, as described later), the ion gyroradius, the length over which ions are bound to magnetic field lines, was $\rho_i \sim 40$ μm. On scales shorter than d_i or ρ_i, the ions are unmagnetized and the magnetic field is frozen in to the electron fluid, with the ions forming a neutralizing background. The width of the reconnection region based on Sweet-Parker (single-fluid) reconnection theory[33,34] is estimated to have been $\delta_{SP} = L/\sqrt{S} \sim 25$ μm, based on a current sheet length $L \sim 1$ mm and a Lundquist number, the ratio of diffusive to Alfvén timescales, of $S \sim 1800$. Consequently, as the ratios $\delta_{SP}/d_i \sim 0.8$ and $\delta_{SP}/\rho_i \sim 0.6$ were less than unity, the ions were decoupled from the electrons over the reconnection region and two-fluid reconnection effects are expected to be important during the initial collision of the plasmas. It is discussed later how, at late times, the increase in density and decrease in temperature altered the plasma conditions to a more collisional regime, where magnetic reconnection occurs in a slower, single-fluid process. Based on a DRACO-simulated inflow velocity of $V \sim 700$ μm/ns, the ratio of ram pressure ($\frac{1}{2}\rho V^2$) to magnetic pressure ($B^2/2\mu_0$) was ~60, so the reconnection process was strongly driven. Magnetic flux pileup as well as two-fluid effects are expected to be important in this strongly-driven system.[37]

The appearance of electron jets ejected from the reconnection region at 0.9 ns (Figure 6.9b) is conclusive evidence of a two-fluid reconnection early in time. Based on its appearance at t = 0.9 ns, stretching out of the field of view, it has propagated continuously at least 800 μm over a period of ~600 ps, at an in-plane velocity of $V_{jet} > 1300$ μm/ns. This jet velocity is considerably faster than the nominal ion Alfvén speed ($V_{jet}{\sim}20V_{A0}$), of the order of the electron Alfvén speed ($V_{jet}{\sim}0.3V_{Ae0}$), and several times the sound speed ($V_{jet}{\sim}5C_s$). The jet is well-collimated, with a total apparent width of 150 μm $\sim 5d_i$, of order the expected width of the current sheet. It appears to consist of multiple near-parallel strands, each of which is of order $\sim d_i$ in width. The electron jet extends at least $25d_i$ from the end of the collision region, similar to what has been observed in spacecraft observations of the Earth's magnetosheath.[61] An electron-Alfvénic jet of width $\sim d_i$ piercing the broader outflow region has been predicted in simulations of two-fluid reconnection[62] and arises self-consistently with in-plane currents typically ascribed to Hall reconnection physics. Its observation in these experiments is a compelling signature of a fast, continuous, two-fluid reconnection early in time.

The proton deflection within the jet structure allows for an inference of the in-plane magnetic field strength and, therefore, the out-of-plane current magnitude and electron density contained in the jet. The inferred properties of the jet provide further confirmation of a two-fluid reconnection picture at early times. The $\sim$50 μm apparent proton deflection due to magnetic fields associated with the jet current implies a path-integrated field strength of $\sim$15 MG μm, or a magnetic field strength of 0.05 MG for a $\sim$300 μm out-of-plane spatial extent of the field structure. The out-of-plane current consistent with that field over the 50 μm in-plane length scale is $\sim$1 kA. Based on that current and the cross-sectional area of $\sim$50 μm in-plane and $\sim$300 μm out of plane, the out-of-plane component of the current density is $J_y \sim 10^{11}$ A/m^2. Assuming that the out-of-plane electron velocity V_{ey} giving rise to this current is a fraction of the in-plane jet velocity, with $V_{ey} \sim 0.3V_{jet} \sim 500$ μm/ns, a jet electron density is inferred as $n_e = J_{ey}/(eV_{ey}) \sim 10^{18}$ cm^{-3}. The electron density in the jet is estimated to be two orders of magnitude lower than in the inflow plasma, indicating that only a small population of electrons is accelerated rapidly out of the current sheet. This characteristic of the super-Alfvénic electron outflow jet has been observed as well in spacecraft observations.[61]

The lack of a visible in-plane jet at t=1.3 ns or 1.8 ns suggests a weakening of the reconnection process around that time, as this signature of fast, collisionless reconnection is not apparent. The appearance of this two-fluid reconnection feature early in time and its absence late in time can be compared to the evolution of magnetic fields in the collision region to develop a more complete picture of the transition from two-fluid to single-fluid reconnection.

The persistence of magnetic fields around the current sheet at late times indicates a slowing of the rate of magnetic flux annihilation, as the plasma enters collisional a regime characterized by slow, single-fluid reconnection. The large-scale proton fluence features in the interaction region illustrate the bulk magnetic fields around the current sheet, and their evolution is used to estimate the annihilation of magnetic flux due to reconnection. In particular, the magnetic field strength and total magnetic flux around the reconnection layer is inferred from width of the proton fluence deficit Δz in the interaction region (as shown in Figure 6.9b). At t=0.9 ns, Δz is $\sim$280 μm at the foil in the 24-MeV-proton image, and is found to be $\sim$280 μm as well in the image produced by 36-MeV protons, the highest energy for which a usable image was obtained. As discussed below, the highest proton energy is used to establish the largest possible lower bound on the path-integrated magnetic field magnitude. The proton-path-integrated field strength at the center of the proton deficit region is inferred on the basis that protons directed through the center of the current sheet were deflected at least to the boundary of the proton deficit region. Quantitatively, this lower limit is inferred as

$$|\textstyle\int \mathbf{B} \times \mathbf{dl}| > \frac{m_p v_p}{q} \frac{L}{a(L-a)} |\boldsymbol{\xi}|, \tag{6.2}$$

where v_p is the velocity of protons at 36 MeV, the most likely proton energy on that film, L (a) is the backlighter-film (backlighter-foil) distance, and $\xi=\Delta z/2$ is the apparent proton deflection at the foil, the 140 μm half-width of the proton deficit region. For these conditions, $|\int \mathbf{B}\times\mathbf{dl}|$ >160 MG μm on either side of the current sheet For a characteristic out-of-plane height for the magnetic field structure of dl $\sim$300 μm, a reasonable assumption for early times in this class of laser-plasma experiment[32] and qualitatively consistent with the plasma bubble scale height in DRACO simulations, a magnetic field strength of $B>0.55$ MG is inferred. The length and width of this proton fluence feature and resulting estimates of magnetic-field quantities in the reconnection region as a function of time are summarized in Table 6.4.

Table 6.4. Estimates of magnetic-field quantities around the reconnection region at different times based on 36-MeV-proton images, including the full width of the proton fluence deficit region Δz, a lower bound on the inferred path-integrated field strength $|\int \mathbf{B}\times\mathbf{dl}|$, the approximate characteristic out-of-plane height of the magnetic field structure dl, a lower bound on the approximate magnetic field strength B, and the length of the reconnection region Δx.

Time (ns)	Δz (μm)	$\|\int \mathbf{B}\times\mathbf{dl}\|$ (MG μm)	dl (μm)	B (MG)	Δx (μm)
0.9	275±15	>160±15	~300	$\gtrsim$0.55	1450±130
1.3	275±15	>160±15	~500	$\gtrsim$0.30	1950±130
1.8	305±20	>180±20	~700	$\gtrsim$0.25	2800±190

As is evident in the images in Figure 6.9, the overall appearance and width of the proton deflection pattern around the reconnection region does not significantly change between 0.9 ns and 1.8 ns, indicating relatively slow reconnection dynamics late in time as the plasma becomes more collisional. Notably, this feature appears quite stable as it lengthens, becoming reminiscent of a Sweet-Parker current sheet in the collisional reconnection picture. The current sheet persists much longer than would be expected based on an annihilation of magnetic fields at the plasma flow velocity, which has been observed in previous experiments (Section 6.1). For a proton deficit region width of $\Delta z\sim 280$ μm and a plasma flow velocity of V $\sim$700 μm/ns, the time for the plasma to cross the reconnectio region unimpeded is only ~0.4 ns. However, the current sheet persists for at least 0.9 ns, and more likely for 1-2 ns, suggesting that a slow dissipation mechanism prevents reconnection from occurring at the flow-based rate. There is a negligible change in the path-integrated magnetic field strength around the reconnection region, and the magnetic fields driven into the interaction region are simply squeezed along the elongating collision midplane. A slowing of the reconnection rate is consistent with the lack of visible electron jets or other signatures of two-fluid reconnection.

The slowing of reconnection after $t=0.9$ ns is related to an increase in collisionality and resistivity in the reconnection layer after the laser is off, as the plasma cools,[32,30] but continues to be advected into the collision region. Density and temperature profiles at early and late times from a DRACO mockup of colliding plasmas with an identical laser drive to that used in the experiments (albeit restricted to 2D azimuthal symmetry – with a hemispherical plasma bubble effectively interacting with a surrounding plasma torus) are shown in Figure 6.10. Side-on proton radiography images obtained at identical times corroborate the DRACO dynamical picture. The density surrounding the collision region increases from $\sim 10^{20}$ cm^{-3} at 0.9 ns to $\sim 6\times 10^{20}$ cm^{-3} at 1.8 ns, while the temperature decreases from $T_e\sim 1300$ eV at 0.9 ns to ~700 eV at 1.8 ns. The Lundquist number decreases from $\gtrsim$1800 to $\gtrsim$400, so the current sheet becomes more stable against the plasmoid instability[63] and the Sweet-Parker current sheet width increases. The Lundquist number is given as a lower bound based on the lower bound on the measured magnetic field strength; it scales as $S\propto B$. The concurrent increase in collisionality causes the plasma to transition from a two-fluid

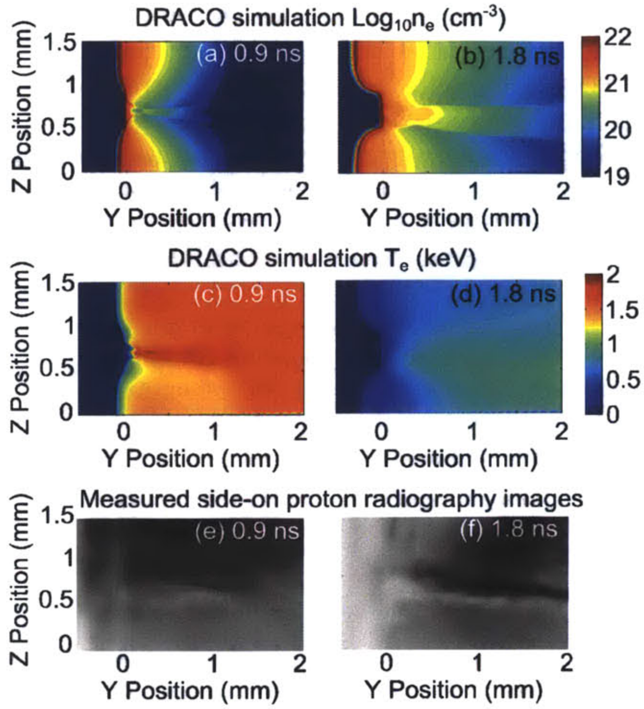

Figure 6.10. Simulated electron density [temperature] profiles at (a) [(c)] 0.9 ns and (b) [(d)] 1.8 ns from a DRACO mockup of the experiment, slightly modified to adhere to 2D azimuthal symmetry (centered on Z = 0). Laser beams are incident from the right, with a laser spot centered on Z = 0, and a ring-shaped laser spot with an identical profile centered on Z = 1.4 mm. This quirk in simulation geometry contributes to some slight asymmetries across the midplane. Near the collision region, the density increases and the temperature decreases substantially with time, causing the plasma to become collisional late in time. Measured side-on proton radiography images at (e) 0.9 ns and (f) 1.8 ns qualitatively confirm the dynamics of the DRACO simulations.

regime of reconnection to a single-fluid regime. The Sweet-Parker current sheet width increases to $\delta_{SP}\lesssim 150$ μm and the ion skin depth decreases to $d_i\sim 13$ μm, while the ion gyroradius increases slightly to $\rho_i\lesssim 70$ μm. As a result, δ_{SP}/d_i increases from $\lesssim 0.8$ to $\lesssim 12$ and δ_{SP}/ρ_i increases from $\gtrsim 0.6$ to $\gtrsim 2.3$. Figure 6.11 illustrates the evolution of the DRACO-simulated electron density and electron temperature, and bounds on the Lundquist number (lower bound) and the ratio δ_{SP}/d_i (upper bound) based on those parameters and the lower-bound magnetic field strength estimated from the proton radiography data. These parameters are also summarized at early (collisionless) and late (collisional) times in Table 6.5. As the plasma becomes collisional late in time ($\delta_{SP}/d_i > 1$), two-fluid mechanisms that enable a fast reconnection shut down. It has been observed previously in tenuous plasma experiments that the reconnection rate slows significantly as the plasma becomes more collisional[45]; the present data provide the first evidence of this process in a high-β, strongly-driven plasma.

Table 6.5. Reconnection-relevant plasma parameters around the reconnection region at early times (~0.6-0.9 ns) and late times (~1.8 ns) as the plasma transitions from a two-fluid regime to a single-fluid regime of reconnection, including the electron density (n_e), the electron temperature (T_e), the ion temperature (T_i), the magnetic field strength (B) lower bound, the length scale (L), the which can be roughly equated to the current sheet length, the flow velocity (V), the ion Larmor radius (ρ_i) upper bound , the ratio of total thermal pressure to magnetic pressure (β) upper bound, the ratio of ram pressure to magnetic pressure (β_{ram}) uppr bound, the Lundquist number (S) lower bound, the ion inertial length (d_i), the ratio of Sweet-Parker current sheet width to ion inertial length (δ_{SP}/d_i) upper bound, and the ratio of Sweet-Parker current sheet width to the ion Larmor radius (δ_{SP}/ρ_i) lower bound, two parameters that set the regime of single-fluid or two-fluid reconnection. The density and temperature are based on DRACO simulations, while the magnetic field strength lower bound and current sheet length are estimated from the proton radiography data.

Time	n_e (cm^{-3})	T_e (eV)	T_i (eV)	B (T)	L (μm)	V (μm/ns)	ρ_i (μm)	β	β_{ram}	S	d_i (μm)	δ_{SP}/d_i	δ_{SP}/ρ_i
~0.6-0.9 ns	1×10^{20}	1300	800	$\gtrsim 55$	1000	700	$\lesssim 40$	$\lesssim 20$	$\lesssim 60$	$\gtrsim 1800$	30	$\lesssim 0.8$	$\gtrsim 0.6$
~1.8 ns	6×10^{20}	700	500	$\gtrsim 25$	3100	200	$\lesssim 70$	$\lesssim 330$	$\lesssim 150$	$\gtrsim 400$	13	$\lesssim 12$	$\gtrsim 2.3$

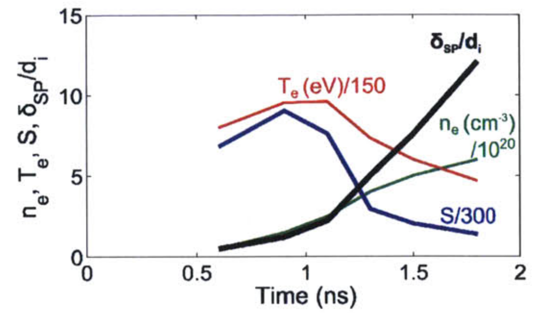

Figure 6.11. DRACO-simulated electron density (n_e, green) and electron temperature (T_e, red) around the collision region as a function of time. As the density increases and the temperature decreases, the Lundquist number (S, blue) decreases and the collisionality (δ_{SP}/d_i, thick black) increases and the plasma enters the regime of single-fluid reconnection.

6.2.4 Conclusions

In summary, these data demonstrate experimentally that collisionality is an important parameter dictating the rate of reconnection even in plasmas where reconnection is driven by strong plasma flows. The transition between a fast, collisionless, two-fluid regime of reconnection and a slow, collisional, single-fluid regime has been inferred. High-resolution proton radiography has revealed a supersonic, super-Alfvénic electron outflow jet early in the strongly-driven reconnection of ~MG magnetic fields in β~20 laser-produced plasmas. The observation of this feature provides strong evidence that a two-fluid reconnection takes place early in time when the plasma is collisionless. Later in time, the evolution of plasma conditions to a cooler, denser, more collisional state causes the reconnection rate to slow, as observed in the stability of late-time magnetic field structures. These findings are relevant to strongly-driven, high-β, two-fluid reconnection in astrophysical environments such as the magnetopause, as well as to reconnection more generally across a range of collisionality regimes.

6.3 First Experiments Probing the Collision of Parallel Magnetic Fields in Laser-Produced Plasmas

In order to understand the strongly-driven reconnection of magnetic fields in laser-plasma experiments, it is important to capture the hydrodynamic processes involved. To isolate and investigate these effects, novel experiments to study the strongly-driven collision of *parallel* magnetic fields in β~10, laser-produced plasmas have been conducted using monoenergetic proton radiography. These experiments were designed to probe the process of magnetic flux pileup, relevant to the strongly-driven interaction of magnetic fields in plasmas at a variety of magnetic shear angles in astrophysical and laboratory environments, including in the reconnection of anti-parallel magnetic fields where the reconnection inflow is dominated by strong plasma flows. The magnetic flux is found to be slightly compressed in the collision region, though with a weaker flux compression and amplification of the magnetic field strength than is predicted by 2D PIC simulations, as a consequence of the 3D collision geometry. Future experiments may drive a stronger collision and further explore the parameter space of magnetic field interactions in plasmas. This work will be submitted to *Physical Review Letters.*[64]

6.3.1 Motivation for Colliding Parallel Magnetic Fields

The dynamics of interacting and colliding plasmas carrying magnetic fields is a universal problem that appears at any boundary between magnetically separated plasmas. When magnetic fields are squeezed together in an anti-parallel configuration, field lines are prone to breaking and rearranging their topology in a manner that reduces the stored magnetic energy. This process of magnetic reconnection has been studied extensively in analytical theory,[33,34] computational studies,[65] spacecraft observations,[66] and laboratory experiments.[29,3] Much less discussed, but equally prevalent in the universe, is the interaction of magnetic fields that are predominantly parallel, where field structures are modified, but reconnection or annihilation of magnetic fields is minimal. This phenomenon occurs frequently at the dayside magnetopause, where the solar wind strongly drives a magnetic field into the Earth's magnetosphere. The interaction of solar-wind and magnetospheric plasmas occurs with their magnetic fields at a variety of shear angles,[67] including nearly parallel.[68,69]

This work presents the first laboratory experiments designed to study magnetic field deformation in the strongly-driven collision of *parallel* magnetic fields in a high-β plasma. Previous experiments exploring the interaction of anti-parallel magnetic fields in high-β, laser-produced plasmas, such as those described in the previous sections, have demonstrated signatures of magnetic reconnection[19–21,52] and observed an extremely fast rate of magnetic flux annihilation.[20,1] The nominally super-Alfvénic reconnection has been attributed to the pileup of magnetic flux during the collision process, which amplifies the local magnetic field strength and the Alfvén speed.[37] In this strongly-driven system, where the bulk flow velocity is significantly larger than the Alfvén speed and, equivalently, ram pressure dominates magnetic pressure, the fields are forced together faster than they can naturally rearrange themselves. The present experiments provide a test bed for investigating the physics of flux pileup as relevant both to astrophysical environments and their laboratory counterparts in a configuration where magnetic annihilation is unlikely to occur, by probing the magnetic field structures in the collision of parallel magnetic fields. It is observed that the magnetic flux is slightly compressed in the collision region, though a larger flux compression and amplification of the magnetic field strength is predicted by two-dimensional (2D) PIC simulations, suggesting that three-dimensional (3D) dynamics are an important consideration.

6.3.2 Interacting Parallel Magnetic Fields Experiments

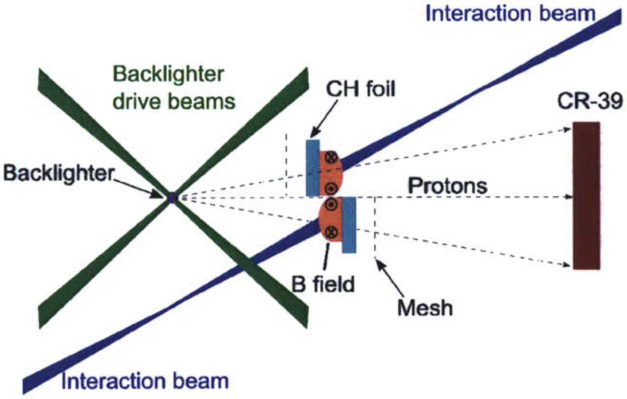

Figure 6.12. Proton radiography setup for colliding plasmas carrying parallel magnetic fields. The distance between the backlighter capsule and the interaction point was 10 mm, while each foil was 0.5 mm from the center; the distance between the mesh grid and the foil was 2 mm for the backlighter-facing mesh and 2.5 mm for the detector-facing mesh. In these parallel fields experiments, the distance between the backlighter and the detector was 270 mm such that the magnification was M ~27.

Laser-plasma experiments to study colliding parallel magnetic fields were conducted at the OMEGA laser facility.[25] In each experiment, depicted in Figure 6.12, two oppositely-directed 500-J, 1-ns laser pulses at a wavelength of 351 nm and with an 800-μm spot size were each incident on separate 5-μm-thick CH foils. Each laser-foil interaction generated an expanding, hemispherical plasma bubble, with ~0.5 MG toroidal magnetic fields advected with the expansion of the plasma bubble and concentrated at its perimeter.[26] Two parallel foils were separated by 1 mm in the direction normal to their surface and offset laterally. The laser spots were incident 0.7 mm from the edge of the foil, such that symmetric plasma bubbles expanding from each surface would collide at the point of radius of 700 μm and a height of 500 μm. The expanding azimuthal magnetic field structures are parallel at the point where they interact. A summary of experimental parameters is presented in Appendix E.

As shown in Chapter 5, the perimeter of the plasma bubbles at the initial collision point is characterized by an electron density of $n_{e0}{\sim}7{\times}10^{19}$ cm^{-3} and an electron temperature of $T_{e0}{\sim}0.65$ keV,[30] with a magnetic field strength of ~0.5 MG. As a result, the ratio of thermal pressure to magnetic pressure is $\beta{\sim}8$. Additionally, the radial expansion velocity $V_r{\sim}500$ μm/ns implies a ratio of ram pressure ($\frac{1}{2}\rho V_r^2$) to magnetic pressure of $\beta_{ram}{\sim}22$, so the magnetic field does not significantly perturb the dynamics and is merely advected with the plasma flow. As a consequence of this condition, equivalent to the flow velocity being much faster than the nominal Alfvén speed ($V_{A0}{\sim}100$ μm/ns), it is said that the interaction of magnetic fields is strongly driven. A typical magnetic Reynolds number is $Rm{\sim}2000$, signifying that advection dominates diffusive processes, with the magnetic fields largely frozen in to the plasma flow. These experimental conditions are in a regime of β, β_{ram}, and Rm relevant to strongly-driven, small-shear-angle magnetic field interactions at the magnetopause.

The interacting magnetic fields were imaged using monoenergetic proton radiography.[22,23] A spherical glass backlighter capsule with a 420-μm diameter and a 2 μm-thick wall, filled with 18 atm of D^{3}He gas, was imploded by 22 OMEGA beams, delivering 11 kJ in a 1-ns pulse. This implosion generated an isotropic burst of monoenergetic 15-MeV protons from the D^{3}He fusion. The fluence of protons was divided by a 150-μm-period Ni mesh into discrete beamlets, which sampled the plasma. The measured deflection of each beamlet was used to infer the local path-integrated magnetic field strength ($|\int \mathbf{B}\times d\mathbf{l}|$). The timing between the onset of the interaction beams and the onset of the backlighter drive beams was varied so that the backlighter protons sampled the plasma at different times in the collision process.

6.3.3 Proton Radiography of Colliding Plasmas Carrying Parallel Magnetic Fields

15-MeV-proton radiography images of colliding, laser-produced plasmas are shown in Figure 6.13a. These images demonstrate the deflection of proton beamlets due to magnetic fields concentrated at the perimeter of the plasma bubbles and in their interaction. The plasma bubble at the top (bottom) half of each image has azimuthal magnetic fields that are oriented clockwise (counterclockwise) when looking toward the backlighter from the detector, and the proton beamlets are deflected radially outward (inward). This effect has been observed previously in laser-foil experiments with lasers incident on opposite sides of the same foil, but with no interaction between the plasma bubbles.[26] Where the plasma bubbles collide, the magnetic fields are parallel, both deflecting protons downward. The grid structure on each side of the image has a different apparent size due to the different magnifications of the two pieces of mesh. The mesh for the top-half bubble is 1.3 mm from the backlighter, while the mesh for the bottom-half bubble is 0.75 mm from the backlighter.

The proton fluence structures evolve as a result of the generation, growth, and interaction of magnetic field structures. In the top half of the images, the apparent bubble size (the radius of high proton fluence) increases rapidly due to the radial expansion of the bubble and the strengthening of the path-integrated magnetic fields. In the bottom half of the images, the apparent bubble size does not change significantly due to competition between the radial expansion and the generation of additional magnetic fields. In the interaction region, the proton fluence structures are modified by the collision of the bubbles and the deformation of their magnetic field structures. The proton fluence in the interaction region is more complex than a superposition of proton deflection from

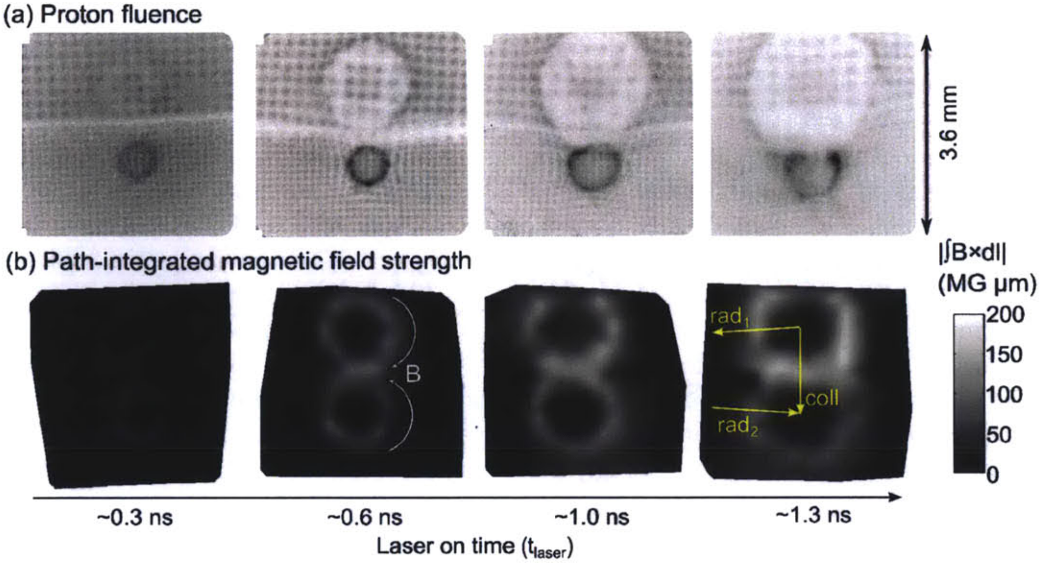

Figure 6.13. (a) 15-MeV-proton radiography images and (b) inferred path-integrated magnetic field strength at different times relative to the onset of the interaction beams. In the proton fluence images, dark areas representing greater proton fluence. Each image has a field of view at the foil ~3.6 mm on a side. The plasma bubbles are nominally symmetric and carry parallel magnetic fields into their interaction. Lineouts are taken through the collision region ("coll") and radially around each individual bubble ("rad$_1$" and "rad$_2$") at 1.3 ns, as discussed in Figure 6.14.

either bubble, indicating that the path-integrated magnetic field structure is modified.

Maps of path-integrated magnetic field strength inferred from proton deflection are shown in Figure 6.13b, directly illustrating the evolution and collision of magnetic field structures. The magnetic field structures are nearly identical on both sides, as expected for identically-driven plasma bubbles. The maps show that path-integrated field strength and total magnetic flux increase throughout the 1-ns laser pulse as magnetic fields are continuously generated. The outer extent of the field structures expands radially at ~500 μm/ns. The field map is cut off at the top bubble as those proton beamlets are deflected entirely out of the field of view. A nearly radially-symmetric profile of path-integrated magnetic field strength is observed at the plasma bubble perimeters, as observed in previously-discussed experiments.

The interaction region of the plasma bubbles shows a slight enhancement of the path-integrated magnetic field strength, due to a weak pileup of magnetic flux. Lineouts of path-integrated magnetic field strength (Figure 6.14) show that $|\int \mathbf{B}\times d\mathbf{l}|$ is enhanced and slightly narrower in the collision region of the plasma bubbles, in comparison to a mere superposition of radial profiles of $|\int \mathbf{B}\times d\mathbf{l}|$ from each bubble. This result indicates that a slight compression of magnetic flux is occurring. The total magnetic flux is roughly preserved, as there is minimal reconnection of magnetic fields in this small-shear-angle collision. Additional discussion of these experiments in contrast to experiments probing the interaction and reconnection of anti-parallel magnetic fields (from Section 6.1) is presented in Appendix E.

6.3.4 Discussion of Experimental Findings and Future Work

In similar experiments measuring the annihilation of antiparallel magnetic fields, a factor of 4 magnetic field amplification due to flux pileup is predicted to account for the nominally super-

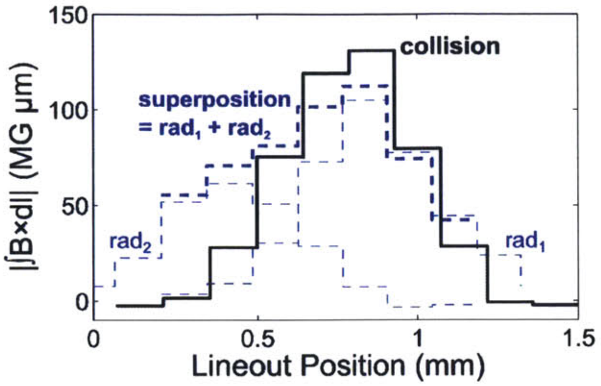

Figure 6.14. Lineouts of path-integrated magnetic field strength ($|\int \mathbf{B}\times d\mathbf{l}|$) through the collision region and radially through each individual bubble, as indicated in Figure 6.13b. The path-integrated magnetic field strength in the interaction region (thick solid line) is slightly greater and more sharply peaked than a simple superposition of radial profiles from individual profiles (thick dashed line), indicating that a collision of magnetic field structures has occurred.

Alfvénic rate of reconnection.[1] It is likely that, in comparison to those experiments, the collision produced in these experiments with parallel magnetic fields is somewhat weaker, at a more glancing incidence, as the interaction point is farther from the laser focal spot and, consequently, farther from the generation of the bubble expansion and drive mechanism. The deformation of magnetic field structures is expected to be less forceful in this configuration than with two bubbles generated on the same side of a foil.

Particle-in-cell (PIC) simulations were used to illustrate the expected magnitude of flux pileup in a two-dimensional (2D) view of this strong collision of parallel magetic fields. These simulations, which model a 2D slice in the plane of the magnetic fields (roughly parallel to the foil surfaces), were initiated based on azimuthally symmetric 2D DRACO[35] and 2D LASNEX[36] radiation-hydrodynamics simulations of a single laser-foil interaction. The in-plane profiles of density, temperature, flow velocity, and magnetic field strength of a single bubble were used as initial conditions in the PIC simulations, which predict the interaction process in these colliding plasmas carrying annuli of parallel magnetic fields. The PIC simulations do not account for the continued laser drive or self-generation of magnetic fields and represent only a 2D slice through the 3D interaction geometry, but represent qualitatively the collision process and the resulting deformation of magnetic field structures.

Snapshots of the magnetic field strength in the collision of parallel magnetic fields (Figure 6.15), as in the experiments, illustrate the local amplification of magnetic field strength. The magnetic field strength is enhanced in the collision region by a factor of ~3 as the ribbon of magnetic field is reduced in squeezed by the opposing ram pressure between the two plasma bubbles. The total magnetic flux is conserved and the magnetic energy is enhanced. This result is qualitatively similar to the experimental results, where a modification of path-integrated magnetic field profiles occurs, despite a conservation of total magnetic flux. However, the 2D simulation shows a more substantial increase in the local magnetic field strength than is observed experimentally. This difference is likely the consequence of 3D dynamics in the experiments, as plasma is allowed to flow in directions perpendicular to the plane of the magnetic fields. In contrast, the simulations force a strong in-plane flux compression.

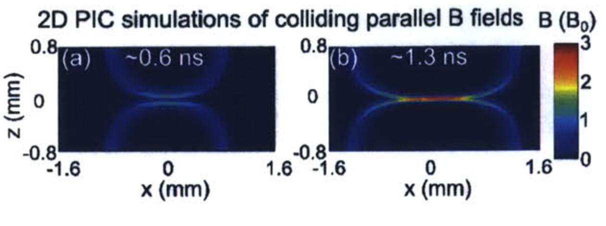

Figure 6.15. Simulated magnetic fields in a 2D PIC simulation of colliding plasmas carrying parallel magnetic fields. These simulations show a pileup of magnetic flux, but an absence of magnetic reconnection, in qualitative agreement with the data. However, the magnitude of pileup is stronger in the simulation.

The results of these experiments, showing evidence of pileup – but no reconnection – of magnetic fields, are consistent with observations and theory of magnetic reconnection at small shear angles, such as occurs within the solar wind and at the magnetopause. High β plasmas such as are produced in these experiments are highly prohibitive of magnetic reconnection at small shear angles. It has been observed that reconnection is inhibited for sufficiently small magnetic shear angles or sufficiently high plasma β or $\Delta\beta$ across the current sheet.[15] In the present experiments, the magnetic shear angle is nearly zero at the center of the collision and <10° at the periphery of the interaction layer. Though signatures of reconnection have been observed at magnetic shear angles as small as 4°,[69] the solar wind environment in which they appeared is at sufficiently low β to permit reconnection. The plasma bubbles in the experiments are nominally symmetric about the interaction layer; however, because $\beta{\sim}10$, even an incidental 10% asymmetry corresponds to a $\Delta\beta{\sim}1$, large enough to suppress reconnection up to a shear angle of ~30°.

This innovative experimental design can be further optimized in order to generate conditions and probe physics relevant to small-magnetic-shear-angle plasma interactions in astrophysics and to understand strongly-driven magnetic reconnection experiments in the laboratory. In order to produce a more forceful collision and closely study flux pileup over a range of collision strengths, the relative position of the foils may be varied to generate different profiles of radial expansion velocity at the interaction plane. It is expected that by decreasing the spatial offset in the direction perpedicular to the two foils, such that the bubbles collide at a position closer to each foil surface where the radial flow velocity is greater, the interaction will be even more strongly driven, with a larger ratio of flow velocity to nominal Alfvén speed. In addition, increasing the lateral separation between the foils parallel to the foil surface will reduce the nominal density and nominal Alfvén speed at the collision point and allow for a test of the rate at which magnetic fields deform and pile up. Obtaining radiographs from the direction parallel to the foils may aid in discrimination of path integration effects and determination of 3D evolution of the plasma bubbles and their field structures.

6.3.5 Conclusions

In summary, experiments have been conducted to probe the strongly-driven collision of parallel magnetic fields in laser-produced plasmas. These experiments show a slight compression of magnetic flux, but not as strong as in 2D PIC simulations, as 3D dynamics of the plasma interaction allow for a more glancing collision of magnetic fields. These experiments can be further optimized to study small-shear-angle magnetic field interactions as occurs in astrophysics and the strong pileup and amplification of magnetic fields as relevant to strongly-driven magnetic reconnection experiments where the reconnection rate is partially determined by the magnitude of flux pileup.

6.4 Future Work

The experimental magnetic reconnection work described here can be greatly expanded upon to further probe the parameter space of plasma conditions, collision asymmetries, and magnetic topologies.

One widespread area of interest in the magnetic reconnection community centers on the study of guide-field reconnection, with an externally-imposed magnetic field perpendicular to the reconnection plane. These conditions are prevalent in astrophysical environments such as the magnetopause, as well as in magnetic fusion devices. External magnetic fields can be applied to magnetic reconnection experiments using laser-produced plasmas, through the use of the magneto-inertial fusion electrical discharge system (MIFEDS)[70] on the OMEGA and OMEGA-EP laser facilities. The scaling of the reconnection rate and modification to the plasma collision and reconnection dynamics in the presence of a guide field can be studied and compared to the no-guide-field results described in Sections 6.1-6.3.

In particular, the impact of diamagnetic drift in the context of asymmetric, guide-field reconnection can be assessed. This theory postulates that in an asymmetric, high-β, guide-field reconnection, the large pressure gradient across the reconnection layer and the out-of-plane magnetic field produce a strong drift ($v_{drift} \propto \nabla p \times \boldsymbol{B}$) of the reconnection X-line.[71,72] When the drift velocity is faster than the Alfvén speed, reconnection is suppressed. This picture has been used to interpret spacecraft observations of reconnection at various magnetic shear angles,[15] but has not been evaluated in controlled experiments in the laboratory. Using the same asymmetric reconnection configuration as described in Section 6.1, and adding the MIFEDS-generated out-of-plane field, it will be possible to sweep relevant parameters and determine the degree to which reconnection is inhibited as a result of diamagnetic drift. The use of MIFEDS fields directed in the reconnection plane will also allow for studies of magnetic reconnection under various in-plane magnetic shear angles.

The regime of strongly-driven, $\beta > 1$ reconnection can be further explored by driving the plasma bubbles differently and modifying the initial profiles of density, flow velocity, and magnetic field strength. Driving a stronger magnetic field would allow for studies of reconnection in the $\beta \sim 1$ regime, where the magnetic pressure begins to have a significant impact on the overall dynamics. More generally, a wider parameter sweep of initial conditions would permit evaluation of reconnection-rate scalings in the strongly-driven regime. For example, the Cassak-Shay scaling[8,10] for the reconnection rate based on the magnetic field strength and density in an asymmetric reconnection can be more widely assessed. In addition, further experiments can determine the range of conditions under which the flow velocity dictates the reconnection rate, as discussed in Section 6.1, and possibly probe the boundaries of the strongly-driven reconnection regime. The effect of the strong flows on the reconnection dynamics can be studied in further experiments on the collision of parallel magnetic fields, expanding on those discussed in Section 6.3. Using gridless, higher-resolution proton radiography and altering the experimental geometry to drive a stronger collision, it may be possible to directly and unequivocally observe flux pileup, which ought to be a significant effect in strongly-driven magnetic reconnection.

Additional measurements may be used to further probe some of the details of reconnection physics. Energetic particles produced by magnetic reconnection has long been a subject of interest. The use of electron and ion spectroscopy along the direction of reconnection outflows will allow for additional study of energy conversion mechanisms and channels, as well as the overall energy balance between flow, thermal, magnetic, and particle kinetic energy. To that end, Thomson scattering (see Chapter 5) can be further utilized to probe electron and ion temperatures, as well as the electron density and bulk flow velocities, in the reconnection inflow and outflow regions. These measurements can also help to constrain the total energy contained in reconnection outflow jets, such as those discussed in Section 6.2.

6.5 Summary

The dynamics of magnetic field interaction and reconnection in a variety of experimental geometries has been studied in strongly-driven ($\beta_{ram} \gg 1$), high-β, laser-produced plasmas.

The first systematic laboratory exploration of asymmetric magnetic reconnection has shown that the strongly-driven collision of anti-parallel magnetic fields produces magnetic flux annihilation at the rate dictated by the plasma flow velocity, and that this rate of reconnection is the same for symmetric and asymmetric plasma conditions across the current sheet. This result has implications for strongly-driven (asymmetric) reconnection such as occurs at the Earth's magnetopause, suggesting that the rate of magnetic reconnection is a function of the strength of plasma flows and is insensitive to upstream plasma conditions and asymmetries.

In separate experiments, the observation of reconnection-induced electron jets early in time, but a persistence of strong magnetic fields late in time, points to a shift in regimes from a fast, two-fluid reconnection to a slow, single-fluid reconnection as the plasma conditions evolve to become more collisional. This result demonstrates experimentally that even in a strongly-driven system, the dissipation mechanism is important and – as in other regimes of reconnection – a fast, two-fluid process is necessary to allow for rapid reconfiguration of the magnetic fields and a release of magnetic energy.

The collision of plasmas carrying parallel magnetic fields has been investigated to study the effects of flux pileup, which are thought to mediate the strongly-driven interaction of magnetic fields in a variety of magnetic topologies. A somewhat weaker flux compression is observed than is expected in a 2D collision picture, showing that 3D dynamics produce a more complicated interaction and allow for greater freedom in the motion of the magnetic field lines.

These experiments have implications for reconnection physics in a variety of astrophysical or laboratory settings, including the strongly-driven interaction of magnetic fields between the solar wind and the Earth's magnetosphere.

6.6 References

1. M. J. Rosenberg *et al.*, "A laboratory study of asymmetric magnetic reconnection in strongly-driven plasmas," submitted to Nat. Commun. (2014).
2. D. Biskamp, *Magnetic Reconnection in Plasmas*, (Cambridge University Press, Cambridge, UK, 2000).
3. M. Yamada, R. Kulsrud and H. Ji, "Magnetic reconnection," Rev. Mod. Phys., **82**(1), 603–664 (2010).
4. J. A. Wesson, "Sawtooth reconnection," Nucl. Fusion, **30**(12), 2545–2549 (1990).
5. T.-D. Phan, G. Paschmann, W. Baumjohann *et al.*, "The magnetosheath region adjacent to the dayside magnetopause: Ampte/irm observations," J. Geophys. Res., **99**(A1), 121–141 (1994).
6. F. S. Mozer, S. D. Bale and T. D. Phan, "Evidence of diffusion regions at a subsolar magnetopause crossing," Phys. Rev. Lett., **89**(1), 015,002 (2002).
7. J. Eastwood, T. Phan, M. Øieroset *et al.*, "Influence of asymmetries and guide fields on the magnetic reconnection diffusion region in collisionless space plasmas," Plasma Physics and Controlled Fusion, **55**(12), 124,001 (2013).
8. P. A. Cassak and M. A. Shay, "Scaling of asymmetric magnetic reconnection: General theory and collisional simulations," Physics of Plasmas, **14**(10), 102114 (2007).
9. J. E. Borovsky and M. Hesse, "The reconnection of magnetic fields between plasmas with different densities: Scaling relations," Physics of Plasmas, **14**(10), 102309 (2007).
10. P. A. Cassak and M. A. Shay, "Scaling of asymmetric hall magnetic reconnection," Geophys. Res. Lett., **35**(L19102) (2008).
11. P. L. Pritchett, "Collisionless magnetic reconnection in an asymmetric current sheet," J. Geophys. Res., **113**(A06210) (2008).
12. K. G. Tanaka, A. Retino, Y. Asano *et al.*, "Effect on magnetic reconnection of a density asymmetry across the current sheet," Ann. Geophys., **26**, 2471–2483 (2008).
13. K. Malakit, M. A. Shay, P. A. Cassak *et al.*, "New electric field in asymmetric magnetic reconnection," Phys. Rev. Lett., **111**, 135,001 (2013).
14. F. S. Mozer, V. Angelopoulos, J. Bonnell *et al.*, "Themis observations of modified hall fields in asymmetric magnetic field reconnection," Geophys. Res. Lett., **35**(L17S04) (2008).

15. T. D. Phan, J. T. Gosling, G. Paschmann *et al.*, "The dependence of magnetic reconnection on plasma β and magnetic shear: Evidence from solar wind observations," Astrophys. J. Lett., **719**, L199–L203 (2010).
16. M. A. Yates, D. B. van Hulsteyn, H. Rutkowski *et al.*, "Experimental evidence for self-generated magnetic fields and remote energy deposition in laser-irradiated targets," Phys. Rev. Lett., **49**(23), 1012–1015 (1982).
17. C. K. Li, F. H. Séguin, J. A. Frenje *et al.*, "Measuring *e* and *b* fields in laser-produced plasmas with monoenergetic proton radiography," Phys. Rev. Lett., **97**, 135,003 (2006).
18. A. J. Mackinnon, P. K. Patel, R. P. Town *et al.*, "Proton radiography as an electromagnetic field and density perturbation diagnostic (invited)," Rev. Sci. Inst., **75**(10), 3531–3536 (2004).
19. P. M. Nilson, L. Willingale, M. C. Kaluza *et al.*, "Magnetic reconnection and plasma dynamics in two-beam laser-solid interactions," Phys. Rev. Lett., **97**, 255,001 (2006).
20. C. K. Li, F. H. Séguin, J. A. Frenje *et al.*, "Observation of megagauss-field topology changes due to magnetic reconnection in laser-produced plasmas," Phys. Rev. Lett., **99**, 055,001 (2007).
21. J. Zhong, Y. Li, X. Wang *et al.*, "Modelling loop-top x-ray source and reconnection outflows in solar flares with intense lasers," Nature Physics, **6**, 984–987 (2010).
22. C. K. Li, F. H. Séguin, J. A. Frenje *et al.*, "Monoenergetic proton backlighter for measuring *e* and *b* fields and for radiographing implosions and high-energy density plasmas (invited)," Rev. Sci. Inst., **77**, 10E725 (2006).
23. M. J.-E. Manuel, A. B. Zylstra, H. G. Rinderknecht *et al.*, "Source characterization and modeling development for monoenergetic-proton radiography experiments on omega," Rev. Sci. Inst., **83**, 063,506 (2012).
24. R. C. Davidson, *Frontiers in High Energy Density Physics*, (National Academies Press, Washington, DC, 2003).
25. T. R. Boehly, D. L. Brown, R. S. Craxton *et al.*, "Initial performance results of the omega laser system," Opt. Commun., **133**, 495–506 (1997).
26. R. D. Petrasso, C. K. Li, F. H. Seguin *et al.*, "Lorentz mapping of magnetic fields in hot dense plasmas," Phys. Rev. Lett., **103**, 085,001 (2009).
27. H. Ji and W. Daughton, "Phase diagram for magnetic reconnection in heliophysical, astrophysical, and laboratory plasmas," Phys. Plasmas, **18**(111207) (2011).
28. J. A. Frenje, C. K. Li, F. H. Séguin *et al.*, "Measuring shock-bang timing and ρr evolution of d^{3}he implosions at omega," Phys. Plasmas, **11**(5), 2798–2805 (2004).
29. H. Ji, M. Yamada, S. Hsu *et al.*, "Experimental test of the sweet-parker model of magnetic reconnection," Phys. Rev. Lett., **80**(15), 3256–3259 (1998).
30. M. J. Rosenberg, J. S. Ross, C. K. Li *et al.*, "Characterization of single and colliding laser-produced plasma bubbles using thomson scattering and proton radiography," Phys. Rev. E, **86**, 056,407 (2012).
31. R. P. J. Town *et al.*, "Calculating and measuring self-generated magnetic fields in hohlraums," Bull. Am. Phys. Soc., **50**(123) (2005).
32. C. K. Li, F. H. Séguin, J. A. Frenje *et al.*, "Observation of the decay dynamics and instabilities of megagauss field structures in laser-produced plasmas," Phys. Rev. Lett., **99**, 015,001 (2007).
33. P. A. Sweet, page 123, (Cambridge University Press, New York, 1958).
34. E. N. Parker, "Sweet's mechanism for merging magnetic fields in conducting fluids," J. Geophys. Res., **62**, 509–520 (1957).
35. D. Keller, T. J. B. Collins, J. A. Delettrez *et al.*, "*DRACO* - a new multidimensional hydrocode," Bull. Am. Phys. Soc., **44**(37) (1999).
36. G. B. Zimmerman and W. L. Kreur, "Numerical simulation of laser-initiated fusion," Comments Plasma Phys. Control. Fusion, **2**(51) (1975).
37. W. Fox, A. Bhattacharjee and K. Germaschewski, "Fast magnetic reconnection in laser-produced plasma bubbles," Phys. Rev. Lett., **106**, 215,003 (2011).
38. W. Fox, A. Bhattacharjee and K. Germaschewski, "Magnetic reconnection in high-energy-density laser-produced plasmas," Phys. Plasmas, **19**, 056,309 (2012).
39. J. Wang, C. Xiao and X. Wang, "Effects of out-of-plane shear flows on fast reconnection in a two-dimensional hall magnetohydrodynamics model," Phys. Plasmas, **19**, 032,905 (2012).
40. T. D. Tharp, M. Yamada, H. Ji *et al.*, "Quantitative study of guide-field effects on hall reconnection in a laboratory plasma," Phys. Rev. Lett., **109(**165002) (2012).

41. M. J. Rosenberg *et al.*, "Observation of two-fluid to single-fluid magnetic reconnection dynamics in strongly-driven laser-plasma experiments," to be submitted to Phys. Rev. Lett. (2014).
42. B. U. O. Sonnerup, G. Paschmann, I. Papamastorakis *et al.*, "Evidence for magnetic field reconnection at the earth's magnetopause," J. Geophys. Res., **86**(A12), 10,049–10,067 (1981).
43. S. Tsuneta, "Structure and dynamics of magnetic reconnection in a solar flare," Astrophys. J., **456**, 840–849 (1996).
44. M. Oieroset, T. D. Phan, M. Fujimoto *et al.*, "In situ detection of collisionless reconnection in the earth's magnetotail," Nature, **412**, 414–417 (2001).
45. M. Yamada, Y. Ren, H. Ji *et al.*, "Experimental study of two-fluid effects on magnetic reconnection in a laboratory plasma with variable collisionality," Phys. Plasmas, **13**(052119) (2006).
46. Y. Ren, M. Yamada, H. Ji *et al.*, "Identification of the electron-diffusion region during magnetic reconnection in a laboratory plasma," Phys. Rev. Lett., **101**(8), 85,003 (2008).
47. Y. E. Litvinenko, "Photospheric magnetic reconnection and canceling magnetic features on the sun," Astrophys. J., **515**, 435–440 (1999).
48. M. Opher, J. F. Drake, K. M. Schoeffler *et al.*, "Is the magnetic field in the heliosheath laminar or a turbulent sea of bubbles?" Astrophys. J., **734**(71) (2011).
49. M. Desroche, F. Bagenal, P. A. Delamere *et al.*, "Conditions at the expanded jovian magnetopause and implications for the solar wind interaction," J. Geophys. Res., **117**(A07202) (2012).
50. L. Willingale, P. M. Nilson, M. C. Kaluza *et al.*, "Proton deflectometry of a magnetic reconnection geometry," Phys. Plasmas, **17**, 043,104 (2010).
51. P. M. Nilson, L. Willingale, M. C. Kaluza *et al.*, "Bidirectional jet formation during driven magnetic reconnection in two-beam laser-plasma interactions," Phys. Plasmas, **15**, 092,701 (2008).
52. Q.-L. Dong, S.-J. Wang, Q.-M. Lu *et al.*, "Plasmoid ejection and secondary current sheet generation from magnetic reconnection in laser-plasma interaction," Phys. Rev. Lett., **108**, 215,001 (2012).
53. Q.-L. Dong, D.-W. Yuan, S.-J. Wang *et al.*, "Energetic electron generation by magnetic reconnection in laboratory laser-plasma interactions," J. Plasma Physics, **78**(4), 497–500 (2012).
54. L. J. Waxer, D. N. Maywar, J. H. Kelly *et al.*, "High-energy petawatt capability for the omega laser," Opt. Photonics News, **16**(30) (2005).
55. N. L. Kugland, D. D. Ryutov, C. Plechaty *et al.*, "Invited article: Relation between electric and magnetic field structures and their proton-beam images," Rev. Sci. Inst., **83**, 101,301 (2012).
56. S. P. Hatchett, C. G. Brown, T. E. Cowan *et al.*, "Electron, photon, and ion beams from the relativistic interaction of petawatt laser pulses with solid targets," Phys. Plasmas, **7**(5), 2076–2082 (2000).
57. R. A. Snavely, M. H. Key, S. P. Hatchett *et al.*, "Intense high-energy proton beams from petawatt-laser irradiation of solids," Phys. Rev. Lett., **85**(14), 2945–2948 (2000).
58. A. B. Zylstra, J. A. Frenje, F. H. Séguin *et al.*, "Charged-particle spectroscopy for diagnosing shock r and strength in nif implosions," Review of Scientific Instruments, **83**(10), 10 (2012).
59. D. S. Hey, M. H. Key, A. J. Mackinnon *et al.*, "Use of gafchromic film to diagnose laser generated proton beams," Rev. Sci. Inst., **79**(053501) (2008).
60. C. Stoeckl *et al.*, Bull. Am. Phys. Soc., **52**(67) (2007).
61. T. D. Phan, J. F. Drake, M. A. Shay *et al.*, "Evidence for an elongated (>60 ion skin depths) electron diffusion region during fast magnetic reconnection," Phys. Rev. Lett., **99**, 255,002 (2007).
62. M. A. Shay, J. F. Drake and M. Swisdak, "Two-scale structure of the electron dissipation region during collisionless magnetic reconnection," Phys. Rev. Lett., **99**, 155,002 (2007).
63. Y.-M. Huang, A. Bhattacharjee and B. P. Sullivan, "Onset of fast reconnection in hall magnetohydrodynamics mediated by the plasmoid instability," Physics of Plasmas, **18**(7), 072109 (2011).
64. M. J. Rosenberg *et al.*, "First experiments probing the collision of parallel magnetic fields using laser-produced plasmas," to be submitted to Phys. Rev. Lett. (2014).
65. J. Birn, J. F. Drake, M. A. Shay *et al.*, "Geospace environmental modeling (gem) magnetic reconnection challenge," Journal of Geophysical Research: Space Physics, **106**(A3), 3715–3719 (2001).
66. T. Phan, L. Kistler, B. Klecker *et al.*, "Extended magnetic reconnection at the earth's magnetopause from detection of bi-directional jets," Nature, **404**(6780), 848–850 (2000).

67. S. Cowley, "A qualitative study of the reconnection between the earth's magnetic field and an interplanetary field of arbitrary orientation," Radio Science, **8**(11), 903–913 (1973).

68. G. Paschmann, B. Sonnerup, I. Papamastorakis *et al.*, "The magnetopause and boundary layer for small magnetic shear: Convection electric fields and reconnection," Geophysical Research Letters, **17**(11), 1829–1832 (1990).

69. J. T. Gosling and T. D. Phan, "Magnetic reconnection in the solar wind at current sheets associated with extremely small field shear angles," Astrophys. J., **763**(L39) (2013).

70. O. V. Gotchev, J. P. Knauer, P. Y. Chang *et al.*, "Seeding magnetic fields for laser-driven flux compression in high-energy-density plasmas," Review of Scientific Instruments, **80**(4), 043504 (2009).

71. M. Swisdak, B. N. Rogers, J. F. Drake *et al.*, "Diamagnetic suppresion of component magnetic reconnection at the magnetopause," J. Geophys. Res., **108**(A5) (2003).

72. M. Swisdak, M. Opher, J. F. Drake *et al.*, "The vector direction of the interstellar magnetic field outside the heliosphere," Astrophys. J., **710**, 1769–1775 (2010).

7

Conclusion

In this thesis, experimental studies of ion kinetic effects during the shock-convergence phase of ICF implosions as well as magnetic reconnection in laser-produced plasmas have been driven by shock-driven ICF implosions. In the first case, the implosions themselves were used to generate conditions where long ion mean free path effects were significant; these ion kinetic effects were investigated in a systematic series of experiments. In the second case, the implosions were one type of proton source used to backlight magnetic fields in the collision and reconnection of laser-generated plasmas, a unique regime of magnetic reconnection experiments relevant to certain astrophysical environments. This experimental work was conducted principally through the use of well-devleoped nuclear diagnostic techniques, including fusion-product spectroscopy and proton radiography.

In addition, two new instruments were developed through the course of this work (Chapter 2): (1) a "scattering pinhole," which extends the yield upper-limit of operation of CR-39-based charged-particle diagostics for use at OMEGA and the NIF, and (2) the compact Step Range Filter proton spectrometer, which provides spectral information about fusion protons in the energy range 1-3 MeV in a small and easily portable package. These instruments were developed, tested, and validated at the LEIA facility, and implemented in experiments at OMEGA and the NIF. These instruments enhance the suite of nuclear diagnostics available for operation at these facilities, which were used in this thesis in experiments to study kinetic effects in ICF implosions and magnetic reconnection using laser-produced plasmas.

The significance of ion kinetic effects during the shock-convergence phase of ICF implosions was extensively investigated (Chapter 3). Experiments studying kinetic effects used predominantly shock-driven exploding pusher implosions, which isolate the shock phase of implosions and generate high-temperature, moderate-density conditions under which ion kinetic effects are likely to become important. In a comprehensive series of experiments on OMEGA, the initial density of D^3He gas within a thin glass shell was varied from $\sim$3.1 mg/cm^2 to $\sim$0.14 mg/cm^2 in order to explore, for the first time, the transition from hydrodynamic to kinetic conditions. Over this density range, the ratio of ion mean free path to minimum shell radius was varied from $\sim$0.3 to $\sim$9 (and the ratio of the duration of fusion burn to the ion diffusion time varied from$\sim$0.3 to $\sim$14), from a regime where kinetic effects were less significant to a regime where kinetic effects were dominant. An increasing discrepancy between measured and hydrodynamic-modeled fusion yields (from a factor of $\sim$2 discrepancy in the hydrodynamic-like regime to a factor of $\sim$100 discrepancy in the strongly kinetic regime) indicated that the hydrodynamic model fails to capture essential physics when the ion mean free path becomes long compared to implosion scales. A reduced-ion-kinetic model, which incorporates into a hydrodynamic code models of ion diffusion, enhanced ion thermal conduction, and Knudsen-layer modification of the ion distribution tail, is better able to reproduce the measured trends. It is inferred that a reduction in fusion reactivity due to the preferential escape of high-energy tail ions and the bulk diffusion of thermal ions out of the fuel are principally responsible for the dramatic reduction in yield in the strongly kinetic regime.

Ion kinetic effects were also explored in ride-along exploding pusher experiments at the NIF. Though not as systematic as the OMEGA campaign, these NIF experiments also show trends of increasing deviation from hydrodynamic-model predictions with increasing ion mean free path, pointing to the influence of ion kinetic effects. In total, these results suggest that ion kinetic effects are likely to be significant during the shock phase of a variety of ICF implosions, including ignition-relevant implosions. Future work will explore these effects in greater detail and assess the degree to which kinetic effects prevalent during the shock phase affect the later, hydrodynamic-like, compression phase.

The universal phenomenon of magnetic reconnection has been studied in laser-produced plasma experiments. These experiments strongly drove reconnection between colliding, $\beta>1$ plasmas carrying ~MG magnetic fields, a little-explored regime of reconnection with relevance to astrophysics. These laser-plasma experiments were probed using exploding-pusher-driven, monoenergetic proton radiography, which imaged magnetic field structures, and Thomson scattering, which probed local plasma conditions, including electron and ion temperatures. These techniques were applied to characterize magnetic-field and thermal evolution of both individual laser-produced plasma bubbles and the magnetic reconnection of colliding bubble pairs. It was shown (Chapter 5) that the electron temperature is not substantially increased ($<10\%$) as a consequence of magnetic reconnection in these colliding laser-produced plasmas. This result was expected in light of the fact that most of the energy of the system consists of thermal or ram pressure energy, with magnetic energy only a small contribution ($\beta\gg1$ and $\beta_{ram}\gg1$). The results of these experiments were also used to identify the regime of and to interpret new magnetic reconnection experiments building on prior work. In these new experiments, proton radiography was used to explore the interaction and reconnection of magnetic fields in a variety of topologies using laser-generated plasmas (Chapter 6).

Using shock-driven ICF implosions as a proton source to probe magnetic fields, the first systematic experiments were performed to study asymmetric magnetic reconnection in the laboratory. By driving two expanding plasma bubbles asymmetrically (one earlier than the other), these experiments produced a collision of plasmas with an asymmetry in density, geometry, ram pressure, and total magnetic flux across the reconnection layer. This strongly-driven asymmetric reconnection at $\beta\gtrsim1$ is analogous to magnetic reconnection at the Earth's magnetopause. Through a quantitative analysis of the magnetic flux annihilated in the plasma collision, it was determined that the reconnection rates were: (1) identical in comparable asymmetric and symmetric experiments, (2) much faster than explained by a nominal Alfvén speed, and (3) at a rate dictated by the flow velocity. These results showed that in this strongly-driven system (flow velocity $\gg$ Alfvén speed or $\beta_{ram}\gg1$), the reconnection rate was dictated by the flow velocity and insensitive to the initial, local plasma conditions. Particle-in-cell simulations based on experimental conditions suggested that the local conditions were modified by the strong external flows in a way that allowed for electron currents to permit a two-fluid reconnection at the flow-based rate. Flux pileup – the local amplification of magnetic fields in a strongly-driven system – is likely to play a role. It was also found that asymmetries in geometry, which produced additional out-of-plane magnetic field structures, did not appreciably impact the reconnection rate.

Additional laser-plasma experiments investigated the role of two-fluid effects (decoupled electrons and ions) in strongly-driven magnetic reconnection and explored the collision of plasmas carrying parallel magnetic fields in absence of reconnection. On OMEGA-EP, high-resolution TNSA proton radiography produced images of colliding and reconnecting laser-produced plasma bubbles of unprecedented detail and clarity, revealing small-scale electron jets that are a clear signature of two-fluid magnetic reconnection. These experiments also revealed a slowing of the reconnection rate late in time as the plasma became more collisional, demonstrating that the collisionality of the plasma and the mechanism of magnetic reconnection is important even in the strongly-driven regime where the system is dominated by fluid flows.

The effect of this strong drive, in absence of reconnection, was probed using monoenergetic proton radiography on OMEGA, in experiments that altered the geometry of the colliding plasma bubbles so that the magnetic fields collide in a parallel orientation. These experiments were motivated both by a desire to understand magnetic dynamics and flux pileup in a strongly-driven system and by strongly-driven, small-magnetic-shear reconnection that can occur at the magnetopause or other interfaces between magnetic fields of different origins. It was observed that the magnetic flux is preserved (as expected) in the collision of parallel magnetic fields and that reconnection is minimal. Future experiments will probe at higher resolution a stronger collision of plasmas where flux pileup is expected to be directly observed.

The work presented in this thesis has helped to advance the use and application of shock-driven ICF implosoins, to open key areas of experimental inquiry into the role of kinetic effects in inertial confinement fusion implosions, and to extend understanding of the nature of magnetic reconnection in the strongly-driven, high-β plasma regime.

Appendix A

Addendum and Data from Shock-Driven Exploding Pusher Experiments on OMEGA and NIF

Experimental setup information and data obtained in exploding pusher experiments on OMEGA and NIF are presented in this appendix, including a variety of measurements that expand on those shown in Chapter 3. Additional discussion of these measurements not previously discussed is included. First is a brief discussion of strong shocks in plasmas, which characterize both these exploding-pusher implosions and the shock-convergence phase of ignition-relevant implosions.

A.1 Defining Strong Shocks Relevant to ICF Implosions

Strong shocks are a defining characteristic of the early phases of ICF implosion. A strong shock is traditionally defined as one with a very high Mach number M, where the speed of the shock front is much faster than the thermal speed in the upstream plasma. Under these conditions, the density jump across the shock front approaches the maximum ratio of $\rho_2/\rho_1 = 4$ for a $\gamma = 5/3$ gas, where γ is the ratio of specific heats. More generally, the ratio of densities across the shock front can be expressed in terms of the Mach number as[1]

$$\frac{\rho_2}{\rho_1} = \frac{M^2(\gamma+1)}{M^2(\gamma-1)+2}. \tag{A.1}$$

In the strong shock ($M\gg1$) limit, the familiar ratio $\rho_2/\rho_1 = 4$ is recovered for $\gamma = 5/3$. To more quantitatively assess the conditions under which a shock is considered "strong", define such a condition as being when the density ratio across the shock front is >80-90% of the maximum, or $\rho_2/\rho_1>3.2\text{-}3.6$. Solving equation A.1 for M, it is determined that $\rho_2/\rho_1 = 3.2$ for $M\sim3.5$ or $\rho_2/\rho_1 = 3.6$ for $M\sim5.2$. Thus, a "strong" shock can be defined as one with $M\gtrsim3\text{-}5$.

In the context of ICF implosions, the initial converging shock has a typical Mach number of $M\sim10\text{-}50$ (as the upstream gas is quite cool, of order tens of eV). This initial shock is well into the "strong" shock regime. Conversely, the rebounding shock, which traverses an already-shocked plasma with a temperature of several keV, has a Mach number of only ~2, and is considered a fairly weak shock.

A.2 Experimental Setup and Data from Exploding Pusher Experiments on OMEGA

Experimental parameters from exploding pusher experiments on OMEGA[2] are shown in Table A.1. All experiments used a laser pulse with ~100 ps rise and fall times, and a 600 ps flat top, with smoothing by spectral dispersion (SSD), distributed phase plates (DPP) with a ~800 μm spot size and a super-Gaussian exponent of 4 (SG4). All shots used 60 beams, except 69058, 69061, 69069, and 69070, which used 59 beams in order to enable a background measurement of laser "blowby" for scattered light diagnostics. The capsules were "drop tower" SiO_2 glass at a density of 2.2 g/cm^3.

Table A.1. Experimental setup parameters for exploding pusher experiments on OMEGA, including the OMEGA shot number, incident laser energy, capsule diameter, capsule thickness, D_2 gas pressure, and ^{3}He gas pressure.

Shot	Laser Energy E (kJ)	Capsule OD (μm)	Capsule Thickness (μm)	D_2 Pressure (atm)	^{3}He Pressure (atm)
69055	14.6	854	2.2	8.37	14.13
69057	14.5	869	2.2	5.70	11.24
69058	14.6	835	2.4	5.70	10.32
69059	14.7	867	2.2	8.37	—
69060	14.7	874	2.4	3.45	~0.8[1]
69061	14.3	840	2.2	2.56	5.61
69063	14.9	858	2.3	2.56	5.36
69064	15.0	861	2.3	1.61	3.23
69066	14.8	868	2.3	0.96	1.92
69067	14.7	859	2.3	0.34	0.68
69068	14.5	845	2.4	0.34	0.66
69069	6.7	867	2.2	8.37	18.24
69070	6.7	867	2.3	0.96	1.91

Principal experimental data are summarized in Table A.2, including laser absorption, fusion yields, burn-averaged ion temperatures, and bang time. Ion temperatures are inferred from the Doppler width of DD-n and D^{3}He-p spectra assuming the relationship between spectral width and temperature appropriate for a Maxwellian ion distribution. Additional detailed data, particularly for shots at ~14.6 kJ laser energy, including burn durations and spatial sizes and data related to shell convergence and fuel ρR are shown in Table A.3. Ion collision parameters derived from experimental conditions mainly for the ~14.6 kJ shots are presented in Table A.4. The equations used to calculate various ion collision parameters, based largely on the NRL Plasma Formulary, are presented in Appendix F. For much of the work in Chapter 3 and in this appendix, the mean free paths for D^{3}He plasmas is taken to be the geometric mean of the individual mean free paths for D ions and ^{3}He ions.

---

[1] Capsule was supposed to have 6.73 atm ^{3}He, but leaked; approximate ^{3}He fill pressure inferred from measured yields and burn-averaged ion temperatures

[2] estimated from fuel ρR measurement

Table A.2. Experimental data from exploding pusher experiments on OMEGA, including the OMEGA shot number, laser absorption fraction measured by full aperture backscatter stations (FABS) with uncertainty ±0.02,[3] DD-n yield measured by nTOF with uncertainty ±10%,[4] D^{3}He-p yield measured by WRF proton spectrometers with uncertainty 10%,[5] DD-burn-averaged ion temperature from the Doppler width of the nTOF-measured DD-neutron signal with uncertainty ±0.5 keV, D^{3}He burn-averaged ion temperature from the Doppler width of D^{3}He fusion product spectra measured by CPS with uncertainty ±2 keV,[5] and the DD-neutron bang time measured by NTD[6] with uncertainty ±50 ps.

Shot	Laser Abs. Fraction	DD Yield	D^{3}He Yield	$T_{i,DD}$ (keV)	$T_{i,D3He}$ (keV)	DD Bang Time (ps)
69055	0.59	2.81×10^{10}	3.41×10^{10}	12.2	14.5	730
69057	0.57	2.35×10^{10}	3.51×10^{10}	12.8	15.6	752
69058	0.55	2.60×10^{10}	4.05×10^{10}	12.4	16.3	760
69059	0.57	1.41×10^{11}	—	12.4	—	688
69060	0.59	7.55×10^{10}	2.58×10^{10}	16.7	21.5	768
69061	0.60	1.32×10^{10}	3.30×10^{10}	12.9	16.7	738
69063	0.56	1.94×10^{10}	4.07×10^{10}	14.1	17.4	743
69064	0.56	1.05×10^{10}	2.96×10^{10}	15.8	19.6	711
69066	0.55	5.48×10^{9}	2.33×10^{10}	19.5	23.1	738
69067	0.56	7.24×10^{8}	5.42×10^{9}	19.9	29.1	731
69068	0.56	7.12×10^{8}	4.35×10^{9}	18.9	27.5	705
69069	0.72	1.22×10^{10}	7.65×10^{9}	8.3	10.4	961
69070	0.73	1.98×10^{9}	1.83×10^{9}	8.4	20.1	1017

A.3 Qualitative Presentation of OMEGA Exploding Pusher Simulations: Shock, Compression, and Fall-Line Analysis

A global picture of exploding pusher dynamics is provided by looking at simulated mass trajectories relative to the spatial and temporal occurrence of fusion burn in thin-shell implosions on OMEGA at a variety of initial D^{3}He gas densities. LILAC[10] simulations of two exploding pusher experiments described above and in Chapter 3, at the high-density and low-density extremes, are shown in Figure A.1. The overall mass element trajectories reveal subtle differences in implosion dynamics. Both cases show a converging shock that reaches the origin around 0.9 ns and rebound back toward the shell.

In the high-density case, shot 69055, the rebounding shock reaches the gas-shell interface at a radius of ~125 μm at 1.02 ns; the gas-shell interface is blown outward, halting compression. D^{3}He fusion reactions are generated along the shock rebound trajectory, far from the gas-shell interface. The greater initial gas density and resulting plasma pressure prevents shell convergence in a way that does not occur in the low-density case. In the low-density case, shot 69068, there is significantly greater convergence as a consequence of the increased ratio of shell mass (or momentum or ram pressure) to gas mass (or gas pressure). The rebounding shock only travels outward a short time and distance, and reaches the gas-shell interface at a radius of ~55 μm at 0.94 ns. In contrast to the high-density case, the shell does not immediately retreat, and continues to coverge to a minimum radius of ~45 μm. As a result, the D^{3}He fusion reactions are not produced exclusively along the shock rebound trajectory and some component of the burn is considered to be a result of compression.

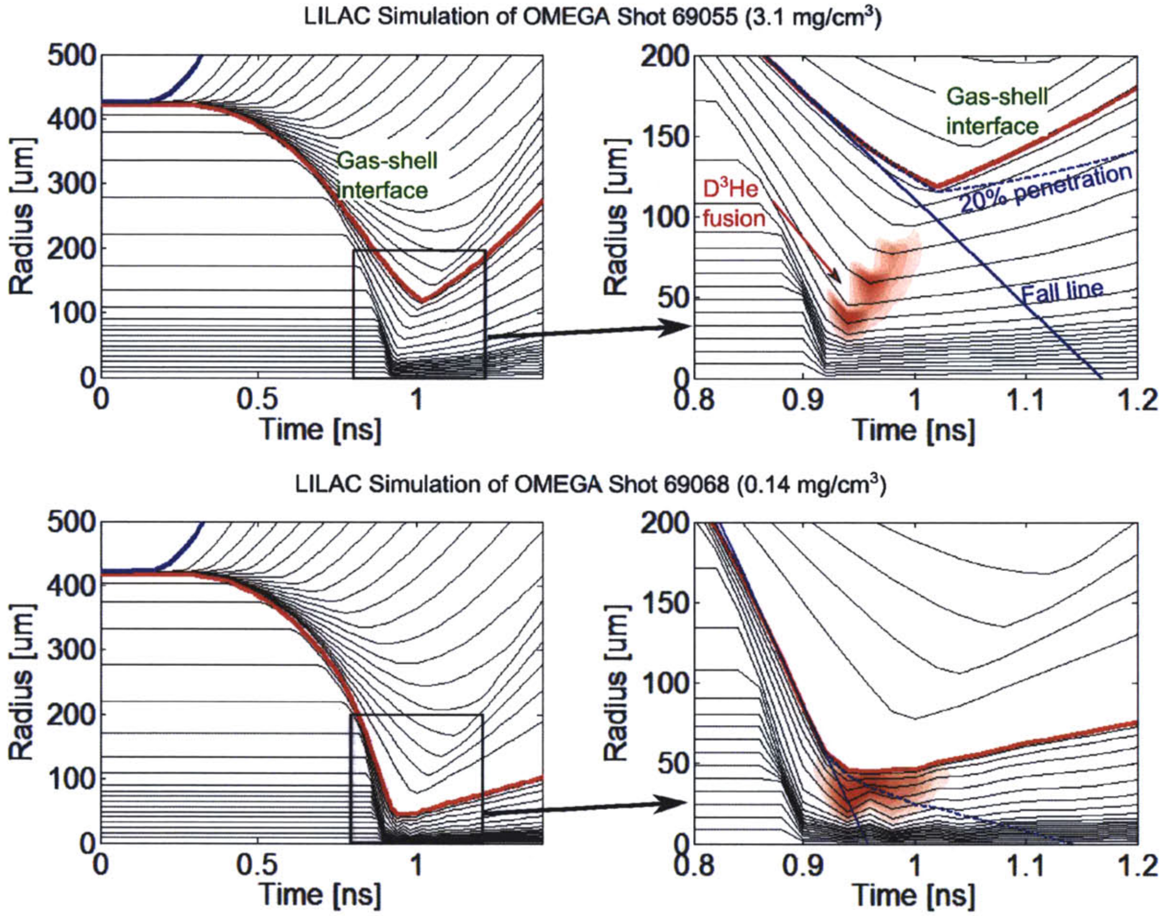

LILAC Simulation of OMEGA Shot 69055 (3.1 mg/cm^3)

LILAC Simulation of OMEGA Shot 69068 (0.14 mg/cm^3)

Figure A.1. LILAC simulations of exploding pushers on OMEGA. Mass element trajectories in a high-density (3.1 mg/cm^3, top) and low-density (0.14 mg/cm^3, bottom) reveal subtle differences in the overall hydrodynamics, as the high-density exploding pusher has a weaker convergence of the gas-shell interface and D^{3}He fusion reactions (red shade) entirely along the shock rebound trajectory. In contrast, the low-density implosion has a greater convergence and more volumetric fusion reactions. The fall line (right side, solid blue) represents the maximum velocity of the gas-shell interface and the 20% penetration line (right side, dashed blue) is 20% of the way from the gas-shell interface to the fall line and represents a reasonable depth of hydrodynamic mix (truncating yield above this line). The high-density implosion is unaffected by hydrodynamic mix, while the low-density implosion is somewhat more susceptible to hydrodynamic mix. However, even in the low-density case, hydrodynamic mix can account for at most a factor of 2 reduction in simulated yield, much smaller than the factor of 40 difference in yield over clean (YOC) between the high-density and low-density implosions.

Table A.3. Additional experimental data from exploding pusher experiments on OMEGA, including the OMEGA shot number, DD-n burn duration FWHM measured by NTD with uncertainty ∼±25 ps, D^{3}He-p burn duration FWHM measured by PTD with uncertainty ∼±25 ps, DD-p and D^{3}He-p spatial burn size FWHM as measured by PCIS with typical uncertainty ∼±5% except at the lowest gas pressures where it is ∼±10-20% due to statistics,[7] the minimum shell radius as inferred from XRFC[8] images with uncertainty ±20 μm, and the fuel ρR estimated from either secondary fusion yields[9] in surrogate experiments or the minimum shell radii, with uncertainty ±30%.

Shot	Burn Duration FWHM		Burn Size FWHM		Min. Shell	Fuel ρR
	DD (ps)	D^{3}He (ps)	DD (μm)	D^{3}He (μm)	Radius (μm)	(mg/cm^2)
69055	199	161		111	133[2]	1.5
69057	192	184	154	106		
69058	155	152		108	133	1.0
69059	190	—		—	108	1.1
69060	153	144		111	138	
69061	183	152	131	86	127	0.6
69063	201	157			92	1.1
69064	170	171	123	84	85	0.8
69066	213	146	112	76	92	0.4
69067		128	105	70	87	0.16
69068		122			77	0.19
69069	208	111				
69070		161				

As the dynamics of the high-density and low-density exploding pusher implosions are somewhat different, an appropriate question is whether these differences impact the interpretation of the experimental results in comparison to hydrodynamic simulations such as LILAC and others. In particular, as was briefly discussed in Chapter 3, a valid question is whether the precipitous drop in yield and in yield over clean (YOC) relative to hydrodynamic simulations with decreasing initial gas density is a consequence of hydrodynamic mix. A fall line analysis[11] shows that, while hydrodynamic mix can in principle account for some of the yield deficit in the low-density case, it is at most a factor of ∼2, well short of the factor of ∼40 necessary to explain the results.

As shown in the right column of Figure A.1, the fall line represents the trajectory corresponding to the maximum velocity of the gas-shell interface. This trajectory is the absolute upper limit of penetration of shell material into the gas as a result of hydrodynamic mix. A more realistic treatment of the potential extent of hydrodynamic mix is by using a finite penetration fraction, allowing shell material to propagate a certain fraction of the way from the gas-shell interface to the fall line. Based on theory of hydrodynamic instabilities and bubble or spike height at gas-shell interfaces,[12] a 20% penetration fraction, typically used for ablatively-driven implosions, is used a a near-worst-case treatment for these largely shock-driven implosions. In this fall line model, it is assumed that shell material mixes in completely down to the 20% penetration line and reactions produced above that line are quenched (as a result of high-Z material radiating away energy and drastically reducing the temperature). In the high-density case, all of the reactions occur below the 20% penetration line, and no simulated yield is eliminated due to mix. In the low-density case, roughly 50% of the D^{3}He reactions are generated above the 20% penetration line, and so it can be said that hydrodynamic mix can account for at worst 50% of the reduction in yield in the

Table A.4. Ion collision parameters from exploding pusher experiments on OMEGA, including the OMEGA shot number, ion density around bang time with ±30% uncertainty, yield-averaged ion temperature with ~±2 keV uncertainty, characteristic time for D on ^{3}He collisions, average ion-ion mean free path (geometric mean of D and ^{3}He mean free paths), and average Knudsen number, the ratio of ion-ion mean free path to minimum shell radius.

Shot	n_i (cm^{-3})	$\langle T_i \rangle$ (keV)	τ_{D3He} (ps)	$\langle \lambda_{ii} \rangle$ (μm)	$N_K \equiv \langle \lambda_{ii} \rangle / R_{shell}$
69055	2.4×10^{22}	13.5	92	44	0.33
69057	1.7×10^{22}	14.5	130	67	0.51
69058	1.7×10^{22}	14.8		74	0.56
69059	2.7×10^{22}			152	
69060					
69061	2.7×10^{22}	15.6	89	49	0.39
69063	2.6×10^{22}	16.3	99	55	0.60
69064	2.1×10^{22}	18.6	152	89	1.0
69066	1.0×10^{22}	22.4	394	252	2.7
69067	4.0×10^{21}	28.0		916	10.5
69068	5.4×10^{21}	26.3	893	615	8.0
69069					
69070					

low-density case.

Therefore, using this model, hydrodynamic mix can account for only up to a factor of 2 difference in YOC between the high-density and low-density case. However, the observed difference in YOC between the high-density and low-density exploding pushers is much greater, approximately a factor of 40. Therefore, a factor of $\gtrsim$20 difference in YOC is still unexplained by hydrodynamic mix. As discussed in Chapter 3, this YOC trend relative to hydro simulations is a strong function of ion-ion mean free path or Knudsen number, and is attributed to the increasing importance of un-modeled ion kinetic effects with an increase in those quantities.

An important question, given the stark differences in predicted hydrodynamic behavior between the high-density and low-density exploding pushers, is whether it can be determined experimentally whether such differences are real. Is there actually a compression component to the burn in the low-density case? Does hydrodynamic mix quench some of the otherwise-expected compression burn? Measurements of the fusion burn duration could potentially shed light on these issues. As will be shown in Section A.4, burn duration measurements were obtained on the experiments in question. The D^{3}He burn durations simulated by hydrodynamic simulations (e.g. LILAC or HYADES) show a trend of lengthening burn durations as a decreasing function of initial gas density. Essentially, as the compression component becomes more pronounced at low initial gas density, the duration of burn becomes longer in the hydrodynamic simulations. However, the PTD-measured[13] burn durations are largely insensitive to initial gas density. This result could indicate either (1) that the hydro-simulated burn was erroneously short in the high-density case (e.g. due to a unphysical spike in temperature and reactivity at the center immediately after shock convergence), or (2) that the hydro-simulated burn was erroneously long in the low-density case (e.g. because the convergence and compression itself was less than predicted, or because mix quenched the compression component). It may be difficult to deduce on the basis of burn history measurements alone whether mix was responsible for quenching any of the burn or whether there should not have been an expectation of seeing a compression component in the first place. X-ray spectroscopy of the shell ions could help deduce whether those shell ions were mixing into the fuel and reaching elevated temperatures, although there may be ambiguity about whether the presence of those shell ions in the fuel was the result of diffusive mix[14] or hydrodynamic mix. Additionally, measurements of bang time itself may also be impacted by the possible presence of compression burn or its truncation due to mix,[15] as bang times would be shifted earlier, along with the shortening of burn durations, if mix were quenching the otherwise late-time, compression-related burn.

A.4 Additional Data and Discussion of Exploding Pusher Experiments on OMEGA

Additional data and comparison to simulations of exploding pusher experiments on OMEGA, expanding on that presented in Chapter 3, is discussed in this section.

The significance and nature of ion kinetic effects is assessed through detailed measurements of plasma properties and dynamics in D^3He-filled, shock driven inertial confinement fusion implosions. Comprehensive measurements fusion yields, burn-averaged ion temperatures, fuel areal density, burn histories, burn profiles, and ablator conditions are presented and compared to hydrodynamic and kinetic models. The use of time- and space-dependent measurements will allow for reconstruction of a dynamic picture of the implosions. As discussed in Chapter 3, trends in these observables with ion mean free path are better captured by models that account for the loss of ion confinement and energy, especially due to enhanced ion diffusion and the loss of suprathermal ions largely responsible fusion reactions.

Measurements of fusion yields, burn-averaged ion temperatures, burn histories, and spatial burn profiles were made to characterize the implosions, and observables are compared to model predictions. These measurements utilized several fusion products, including the neutrons and protons from DD reactions

$$\mathrm{D} + \mathrm{D} \rightarrow {}^3\mathrm{He}(0.82\ \mathrm{MeV}) + \mathrm{n}(2.45\ \mathrm{MeV}) \tag{A.2}$$

$$\mathrm{D} + \mathrm{D} \rightarrow \mathrm{T}(1.01\ \mathrm{MeV}) + \mathrm{p}(3.02\ \mathrm{MeV}) \tag{A.3}$$

and protons from D^3He reactions

$$\mathrm{D} + {}^3\mathrm{He} \rightarrow \alpha(3.6\ \mathrm{MeV}) + \mathrm{p}(14.7\ \mathrm{MeV}). \tag{A.4}$$

Secondary D^3He reactions, whose fusion products are used to determine fuel ρR in D_2 implosions, are produced in D_2 implosions when ^3He fusion products (see equation A.2) react with ambient D fuel ions, in the reaction

$${}^3\mathrm{He}(\leq 0.82\ \mathrm{MeV}) + \mathrm{D} \rightarrow \alpha + \mathrm{p}(12.6 - 17.5\ \mathrm{MeV}). \tag{A.5}$$

The ratio of the resulting secondary D^3He-proton yield to the primary DD-neutron yield is proportional to the fuel ρR.[16,17]

Radiation-hydrodynamics simulations were performed using the DUED[18] and HYADES[19] codes, as well as another 1D fluid-based radiation-hydrodynamic code, on which the reduced ion kinetic (RIK) model is based.

A wide variety of measurements were obtained to diagnose coronal, shell, and fuel conditions.

A.4.1 Coronal and Shell Conditions

Conditions in the corona and the imploding shell have been assessed through the use of optical and x-ray diagnostics.

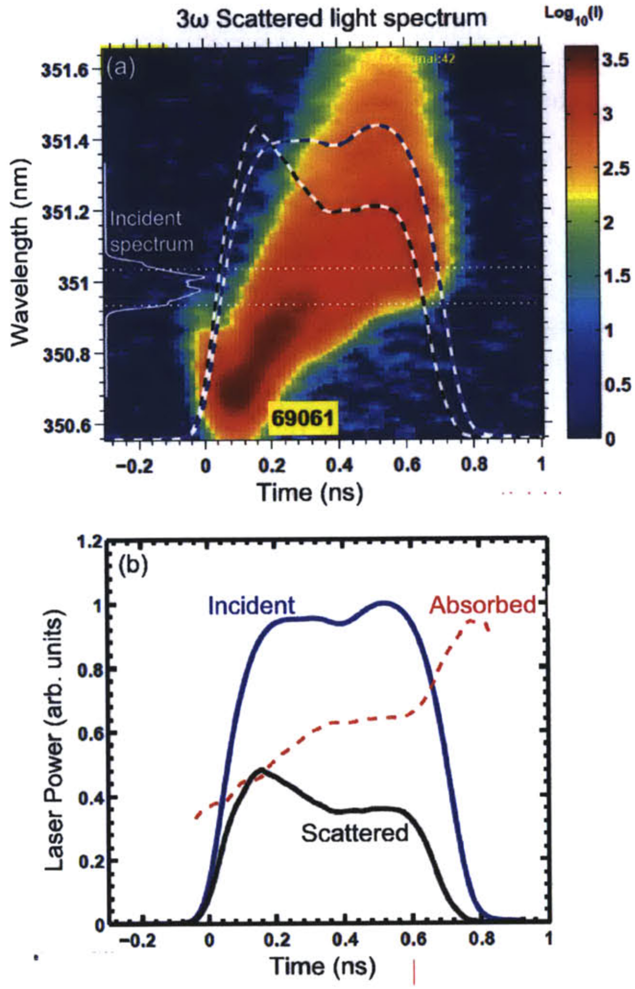

Figure A.2. Time-dependent (a) scattered light spectrum and (b) incident, scattered, and absorbed light around 351 nm for an imploding SiO_2 shell filled with 1.1 mg/cm^3 D^{3}He. The spectrum is blue-shifted early in the laser pulse as the coronal plasma is ablated outward and red-shifted late in the laser pulse as the shell implodes inward. The fraction of scattered light decreases later in the laser pulse. The time-integrated absorption fraction is 60% for this experiment, and 57±2% for the entire series of experiments.

Measurements of the laser absorption were provided by calorimetry and the full aperture backscatter stations (FABS),[3] which detect light from (primarily) stimulated Brillouin scattering (SBS), and also from stimulated Raman scattering (SRS) and two-plasmon decay (TPD). The time-dependent scattered light spectrum around the incident 3ω laser wavelength of 351 nm and the time-dependent laser absorption fraction in shot 69061, with 1.1 mg/cm^3 D^{3}He fill, are shown in Figure A.2. Early in the laser pulse, the scattered light spectrum (Figure A.2a) is blue-shifted relative to the incident wavelength, signifying the ablation of shell material and the radial expansion of the critical surface, up to which light is scattered by SBS. After $t = 0.3$ ns, the bulk of the scattered light becomes red-shifted with the imploding shell. The time-integrated SBS signal (A.2b) shows that the fraction of scattered light decreases slightly throughout the laser pulse, from ~0.48 to ~0.36, such that the average fraction of laser energy absorbed throughout the pulse is ~60%. Over the entire data set, with nominally identical laser and capsule conditions, the time-integrated laser absorption fraction was 57±2%.

As discussed in Chapter 3, measurements of the fraction of absorbed laser light were critical for guiding simulations of these shock-driven implosions. The time-integrated laser absorption fraction was used to constrain the reduced-ion-kinetic (RIK) simulations and was also used to validate DUED simulations, which predicted an absorption fraction in agreement with the measured values.

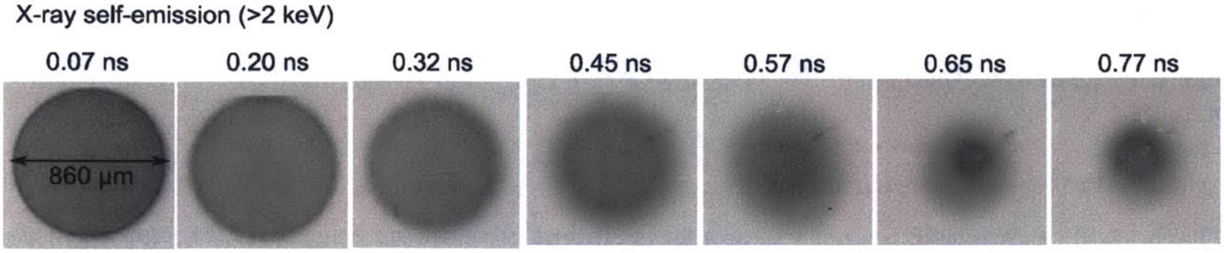

Figure A.3. X-ray framing camera (XRFC) self-emission images in an implosion of a glass shell filled with 1.1 mg/cm^3 D^{3}He (OMEGA shot 69063). The radius of peak emission reaches a minimum around t=0.65 ns, close to the measured bang time.

The position of the imploding shell as a function of time was obtained by x-ray framing camera measurements, which image the x-ray self-emission from the imploding glass shell. A sequence of x-ray framing camera (XRFC)[8] images at photon energies >2 keV obtained in the implosion of a 2.3 μm thick, 860 μm diameter glass shell filled with 1.1 mg/cm^3 of D^{3}He (OMEGA shot 69063) is shown in Figure A.3. Early in time the shell is clearly visible, with strong emission from the limb of the capsule as the electron density is concentrated in a thin shell. As the shell is ablated and implodes, the shell becomes more diffuse. The implosion accelerated rapidly between t = 0.32 and t = 0.57 ns, and the shell reaches a minimum radius between t = 0.65 ns and t = 0.72 ns. This time corresponds to the peak of the fusion reaction history. The radius of maximum emission increases late in the implosion as the shock heats and expands the fuel-shell interface. It is notable that throughout the implosion, the shell appears remarkably round and shows no indication of instability development, 2D structure, or large-scale breakup, confirming the picture of a 1D implosion. Over the series of experiments, the minimum shell radius as estimated from the x-ray emission decreases with decreasing initial gas density, from ~130 μm at 2.1 mg/cm^3 to ~80 at 0.14 mg/cm^3, though at small radius the structure becomes difficult to resolve. As described earlier, the minimum shell radius R_{shell} has been used to quantify the convergence for calculation of the Knudsen number $N_K \equiv \lambda_{ii}/R_{shell}$, a key figure of merit for ion kinetic effects.

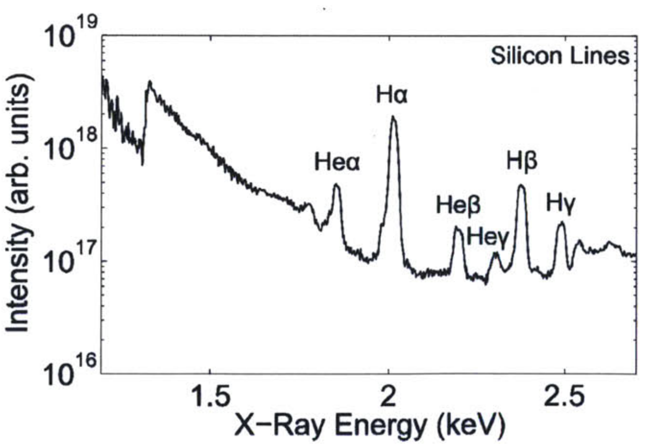

Figure A.4. X-ray spectrum between 1.2 and 2.7 keV of an imploding SiO$_2$ shell filled with 2.2 mg/cm^3 D^{3}He (OMEGA shot 69058). Spectral features primarily reflect silicon emission, including H-like and He-like lines. From the relative strength of the H-like lines in comparison to the He-like lines, a fairly hot plasma is inferred in the corona (T_e ~1-2 keV).

The x-ray spectrum emitted during the implosion yields information about conditions in the corona and the imploding shell, where the bulk of x-rays are emitted. A Rowland x-ray spectrometer has provided measurement of the time-integrated x-ray spectrum at photon energies between 1.2 and 2.7 keV.[20] The spectrum obtained in shot 69058, from an imploding 2.4-μm thick, 835 μm diameter SiO_2 shell filled with 2.2 mg/cm^3 D^{3}He, is shown in Figure A.4. The spectrum contains both continuum and line features, primarily corresponding to silicon emission. Several strong emission lines of H-like and He-like silicon are observed. The relative strength of the hydrogen-like lines relative to the helium-like lines indicates a fairly high temperature in the coronal shell material, ~1-2 keV.

A.4.2 Hot-Spot Conditions

Diagnosis of conditions in the hot fuel around bang time is conducted principally through measurements of fusion products, which are sensitive to profiles of ion density and ion temperature. Some of these data have been discussed previously, but many supplementary measurements are presented here.

Charged fusion-product spectra were measured by wedge-range-filter (WRF) proton spectrometers and magnet-based charged particle spectrometers CPS1 and CPS2.[5] These spectra are used to infer fusion yields and burn-averaged ion temperatures (T_i) from the Doppler width of the spectral lines. Additionally, DD yields and burn-averaged T_i were measured using the neutron time of flight (nTOF) suite.[4] CPS2-measured spectra from the DD protons in reaction A.3, and the D^{3}He protons and alphas in reaction A.4 are shown in Figure A.5. It will be shown that the D^{3}He-burn-averaged ion temperatures inferred from the spectral width of the D^{3}He-alpha and D^{3}He-proton spectra agree to within measurement uncertainty, providing additional confidence in the T_i measurement and demonstrating that ρR-related line broadening and electric-field-related line broadening are negligible.

Figure A.5. Fusion-product spectra of DD protons, D^{3}He alphas, and D^{3}He protons obtained using the magnet-based charged particle spectrometer CPS2 on an implosion with 0.67 mg/cm^3 D^{3}He (OMEGA shot 69064). These spectra are used to infer the fusion yield and also the burn-averaged ion temperatures from the width of the spectral lines.

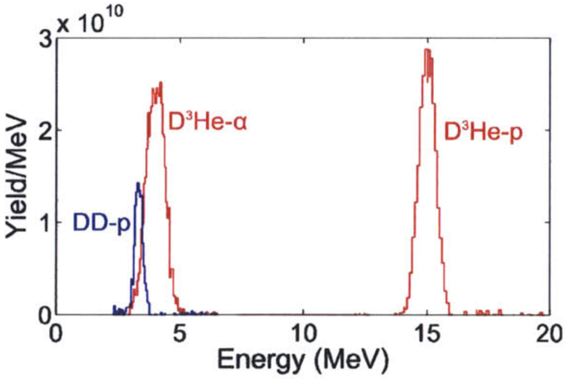

Measured DD and D^{3}He yields as a function of initial gas density are plotted in Figure A.6. For each reaction, multiple fusion product measurements are shown: the CPS1-measured DD-proton yields and nTOF-measured DD-neutron yields; and the WRF-measured D^{3}He-proton and CPS1-measured D^{3}He-α yields. The agreement between different measurements to within the ~10% uncertainty shows that the yield measurements are accurate. As shown previously, in Chapter 3, the measured yields are fairly insensitive to the initial gas density above 1 mg/cm^3, as the decrease in initial density is offset partially by an increase in shell convergence and an increase in the resulting ion temperature. The DD yield shows a slightly stronger dependence on the initial density, as it is less sensitive to the ion temperature and thus relatively more sensitive to the decrease in density. The D^{3}He yield is a near-constant ~4×10^{10} as low as 0.5 mg/cm^3. For reference, DUED-simulated yields are also plotted, showing a DD yield independent of initial gas density over the entire density range and a D^{3}He yield that actually increases with decreasing initial gas density. The increasing divergence of the simulated yields from the measured yields at low density occurs as the implosions become increasingly kinetic and the validity of the hydrodynamic model breaks down.

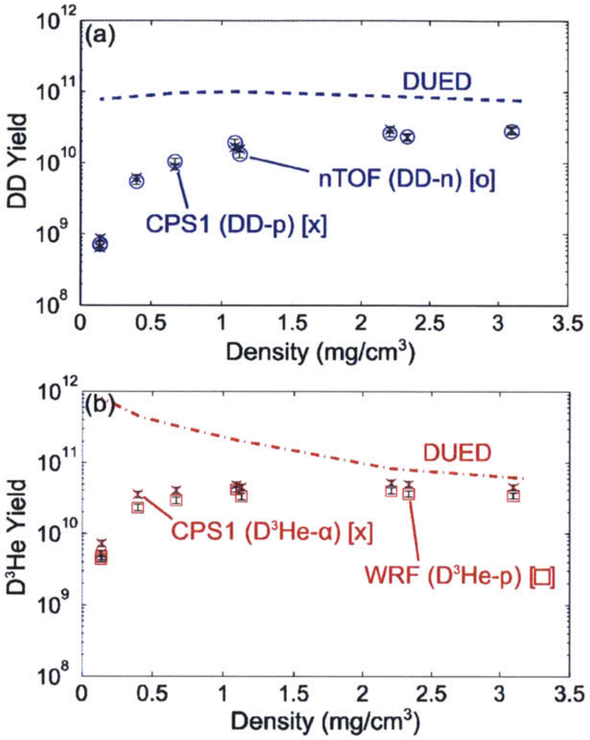

Figure A.6. Measured (a) DD and (b) D^3He yields as a function of initial D^3He gas density. The DD-neutron yields measured by nTOF (blue circles) are in excellent agreement with the DD-proton yields measured by CPS1 (blue x), and fall off rapidly below an initial gas density of 1 mg/cm^3. The WRF-measured D^3He-proton yields (red squares) are in good agreement with the CPS1-measured D^3He-α yields (red x) and fall off below 0.5 mg/cm^3. The DUED-simulated yields for both reactions are increasingly discrepant with the measured yields at low initial gas density as the implosions become more kinetic.

Ion temperature measurements from the Doppler width of DD and D^3He fusion products as a function of initial gas density are shown in Figure A.7. The DD-burn-averaged ion temperatures are inferred from DD-proton spectra as measured by CPS (average of two spectrometers) are in good overall agreement with the temperatures inferred from the nTOF-measured DD-neutron Doppler width. This agreement gives confidence to the direct relationship between the spectral width and ion temperature, and as stated above, that additional broadening of the proton spectrum due to electric field evolution[21] or ρR effects are negligible. The agreement of ion temperatures inferred from the D^3He-proton and D^3He-α spectra point to a similar conclusion. The measured DD-burn-averaged ion temperatures increase from 12 keV at 3.1 mg/cm^3 to 20 keV at 0.14 mg/cm^3, while the D^3He-burn-averaged ion temperatures show a similar trend with decreasing gas density, increasing from 15 to 30 keV. In both cases, the DUED-simulated burn-averaged ion temperatures are in fairly good agreement with the measurements at high initial gas density, but are much higher than the measurements at low initial gas density.[3]

The fuel ρR provides a rough measure of the average gas density after shock convergence and can be estimated both from the minimum radius of the converging shell and from the ratio of secondary to primary nuclear yields.[9] Assuming a spatially uniform fuel density, the fuel ρR around the time of peak fusion reactions, which coincides roughly with the maximum shell convergence, is $\rho\mathrm{R} \sim \rho\mathrm{R}_0\mathrm{C}^2$, where the convergence ratio $\mathrm{C} \equiv R_0/R_{min}$ is the ratio of the initial fuel radius to the final fuel radius. From the XRFC images, the radius of the fuel-shell interface R_{min} is estimated and used to compute the final fuel ρR. The fuel ρR has also been inferred from the ratio of the

---

[3] Though a direct comparison is not shown, it is noteworthy that the inclusion of ion viscosity in the model reduces the D^3He burn-averaged ion temperature at high density relative to a model that does not include viscosity, as the shock front is smoothed out and the temperature spike as the shock converges at the origin is less extreme.

Figure A.7. Measured (a) DD- and (b) D^3He-burn-averaged ion temperatures as a function of initial D^3He gas density. The DD-burn-averaged T_i measured by the nTOF DD-n Doppler width (blue circles) are in good agreement with the average of DD-burn-averaged T_i inferred from CPS1 and CPS2 (blue x) DD-proton spectra, and increase gradually with decreasing initial gas density. The CPS-measured D^3He-proton T_i (red squares) are in good agreement with the CPS1-measured D^3He-α yields (red x) and increase more rapidly than the DD-burn-averaged T_i at low density. The DUED-simulated burn-averaged ion temperatures for both reactions are increasingly discrepant with the measured ion temperatures at low initial gas density as the implosions become more kinetic.

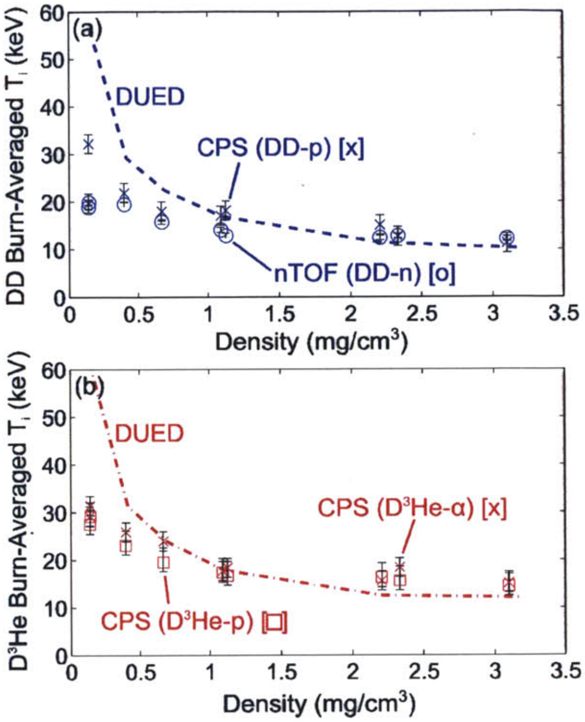

nTOF-measured secondary DT-neutron yield Y_{2n} to the primary DD-neutron yield Y_{1n} on pure D_2-filled shots hydroequivalent to the 3.1 mg/cm^3 and 0.40 mg/cm^3 in the present study. The convergence data is also used to estimate the ion density (n_i), as $n_i \sim n_{i0}C^3$, where n_{i0} is the initial ion number density, and ultimately the ion-ion mean free path $\lambda_{ii} \propto 1/n_i$.

Figure A.8. Measured fuel ρR inferred from estimates of the shell convergence (triangles) and from the ratio of secondary to primary neutron yields on hydroequivalent implosions (stars) as a function of initial gas density in comparison to DUED.

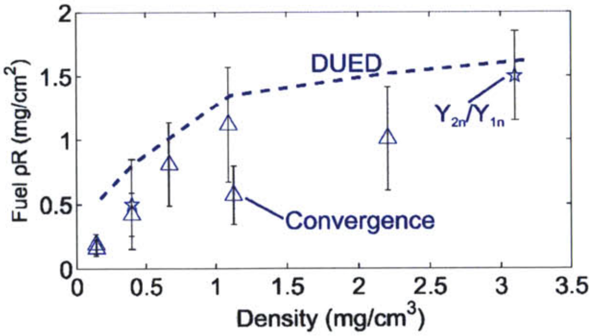

These fuel ρR measurements are compared to the DUED-predicted DD-burn-averaged fuel ρR in Figure A.8. A 40% uncertainty on the convergence-inferred fuel ρR is used, based on a 20% uncertainty in the minimum shell radius, while the uncertainty in the secondary-yield-inferred fuel ρR varies depending on neutron counting statistics. Both the data and the simulations show the expected trend of increasing fuel ρR with increasing initial gas density. The fact that the fuel ρR increases by only a factor of ~9 from low to high density, while the initial fuel ρR differed by a factor of 23, reflects a decrease in the shell convergence with increasing gas density. The trends in the data match those in the DUED simulations, though DUED slightly overestimates the fuel ρR. This discrepancy is especially pronounced at 0.14 mg/cm^3, where the predicted fuel ρR is a factor of ~3 higher than measured as a consequence of the higher predicted convergence ratio. The lack of confinement of fuel ions with extremely long mean free paths (λ_{ii}~250 μm at 0.40 mg/cm^3) may also contribute to this low fuel ρR or fuel density as inferred from the secondary yield measurement.

Burn histories help define implosion dynamics (based on the time of burn) and also set a scale time (i.e. the burn duration) to compare to relevant time scales like the ion diffusion time. The DD-n burn history was measured using the neutron temporal diagnostic (NTD)[6] and the D^{3}He-p burn history was measured using the proton temporal diagnostic (PTD).[13] The time of peak neutron emission (bang time) relative to the onset of the laser pulse is shown in Figure A.9 in comparison to DUED predictions (data originally presented in Chapter 3). The bang time is measured to be independent of initial gas density, in agreement with DUED, as well as other hydrodynamic codes. As the shock decouples and accelerates away from the shell only a few hundred ps before shock convergence, the faster shock velocity in the low-density limit does not result in an appreciably earlier bang time. Additionally, in the high-density case, the fusion reactions occur in a relatively small area close to the center of the implosion along the shock rebound trajectory, so that bang time occurs only ~20 ps after shock convergence, in comparison to a ~80 ps delay between shock convergence and bang time in the low-density implosions.

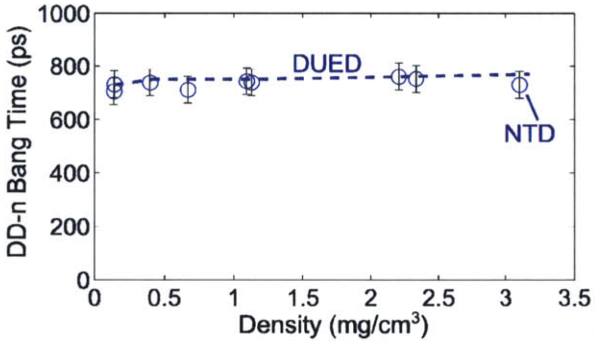

Figure A.9. Measured (blue circles) and DUED-simulated DD-neutron bang time as a function of initial gas density. The measured and simulated bang times are in good agreement, showing a negligible change in bang time with gas density.

The measured DD and D^{3}He burn durations, defined as the full-width at half maximum of the burn history, are contrasted to the burn durations predicted by HYADES simulations in Figure A.10. The measured and simulated DD burn durations are in reasonable agreement, showing negligible trend with initial gas density. The measured D^{3}He burn duration is also independent of initial gas density, but in contrast to the HYADES simulations, which show a decreasing burn duration with increasing initial gas density. While the simulations predict a very short D^{3}He burn duration at high density, ~50 ps, with much of the burn generated in a rapid burst of fusion reactions shortly after shock convergence, the data indicate a more gradual burn. The good agreement in burn duration between the data and hydrodynamic simulations under kinetic-like conditions at low pressure and poor agreement under hydrodynamic-like conditions at high pressure is somewhat contradictory to the yield and temperature results and is yet unexplained. As described in Chapter 3, the measured burn durations are used to calculate another figure of merit for ion kinetic effects, $R_\tau \equiv \tau_{burn}/\tau_{diff}$, the ratio of fusion burn durations to ion diffusion time. When this parameter is large, $R_\tau \gg 1$, as is the case in the strongly kinetic, low-density implosions, ion diffusion is a significant effect over the burn period.

Measurements of the time-integrated spatial burn profile shed light on profiles of ion density and temperature and, in conjunction with the measured burn history, can allow for construction of a dynamic picture of the implosion after shock convergence. The proton core imaging system (PCIS)[22,7] was used to diagnose radial profiles of the DD-proton and D^{3}He-proton emission and to determine the time-averaged burn radii of both reactions. The median burn radius (R_{burn}) – defined as the radius containing 50% of the burn – as a function of gas density is compared to

Figure A.10. NTD-measured DD (blue circles) and PTD-measured D^3He (red squares) burn duration as a function of initial gas density, in comparison to HYADES predictions. The measured burn durations are insensitive to gas density, while HYADES shows a very short D^3He burn duration at high density and a more extended burn at low density.

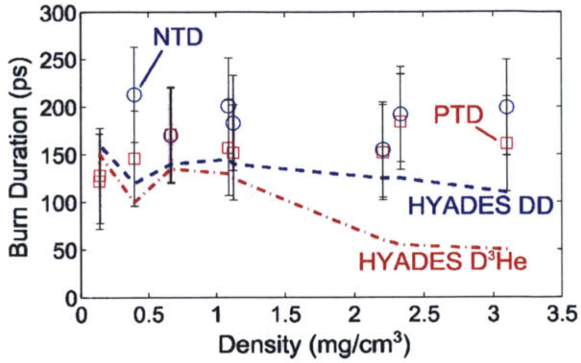

HYADES predictions in Figure A.11. Both measurements show a trend of increasing burn radius with increasing gas density; however, the HYADES simulations exhibit a peak in predicted burn radius in the middle of the density range, falling off at both high density and low density. Additionally, the data show a fairly constant differential between the DD and D^3He burn radii, widening slightly from $\Delta R_{burn} \equiv R_{burn,DD}$ - $R_{burn,D^3He} = 13$ μm at 0.14 mg/cm^3 to $\Delta R_{burn} = 24$ μm at 3.1 mg/cm^3. In contrast, the HYADES simulations show a much stronger trend in ΔR_{burn}, from 1 μm at 0.14 mg/cm^3 to 33 μm at 3.1 mg/cm^3.

Overall, the magnitude of the burn radii are in reasonable agreement with the HYADES predictions, though differences in the trends shed light on deficiencies in the hydrodynamic model. The D^3He burn radius data show a more diffuse burn region at high density than in HYADES. The high-density results corroborate the burn duration findings, where the hydrodyanmic simulation predicts a very strong burn in a small region and short duration after shock convergence, while the data indicate a more extended burn. This result partially explains the remaining discrepancy between measured and hydro-simulated yields even in the hydrodynamic regime. In the low-density, kinetic regime, the more centrally peaked measured D^3He burn region may signify the loss of ions especially close to the shell in a manner not captured by hydrodynamic codes that maintain a Maxwellian distribution. It was discussed in Chapter 3 how the measured burn profile shapes indicate that ion diffusion is a significant effect in the long-mean-free-path implosions.

Figure A.11. PCIS-measured DD (blue circles) and D^3He (red squares) median burn radii as a function of initial gas density, in comparison to HYADES predictions. The measured burn radii increase monotonically with increasing gas density, while the simulations peak in the middle of the density range.

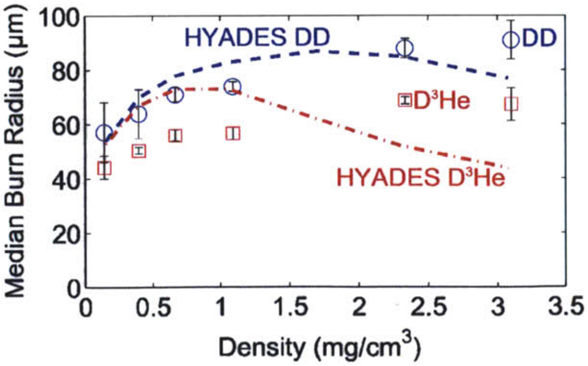

A.5 Notes on the Reduced Ion Kinetic Model and Fitting Procedure

The Reduced Ion Kinetic (RIK) model[23] was presented in Chapter 3 as a crude implementation of ion kinetic effects in the framework of a radiation-hydrodynamics code, and reasonably reproduced experimental results on OMEGA exploding pushers over a wide range of Knudsen numbers. As was briefly mentioned, the RIK simulations allow for five tunable parameters in order to produce the best fit to the data. While the simulations, therefore, are not an "out of the box" or first principles model, when they are suitably constrained by experimental data, it can be concluded that the model offers a reasonable representation of conditions in the experiments. The procedure by which those simulation free parameters are determined, and the resulting accuracy of the model, are discussed in this section.

The RIK model contains five free parameters, two that can be thought of as describing overall energy coupling and dynamics (the laser fraction f_{ls} and the electron thermal flux limiter f_e) and three that describe ion kinetic effects (the Knudsen number multiplier f_{Knu}, the ion mass transport or ion diffusion multiplier f_{idif}, and the ion thermal conduction multiplier f_{icnd}).[23] The goal of the model fitting routine is to find the location in the 5-dimensional parameter space of these different multipliers that most closely matches the experimental observables. In particular, as applied to these OMEGA experiments, the RIK model sought to match five observables, the DD yield, the D^3He yield, the DD-burn-averaged ion temperature, the DD bang time, and the laser absorption. (Note that the laser fraction multiplier f_{ls} is not the same as the absorbed laser energy, since the RIK model does account for laser refraction, which reduces the laser energy to an amount below that dictated by f_{ls}. For these experiments, it was found that the ideal fit is achieved by $f_{ls} = 0.63$, which produces a laser absorption fraction of 52%, slightly below the measured laser absorption of 57±4%.) The fit was applied simultaneously to match those five observables on eight shots, for a total of 40 observables constraining 5 free parameters. As such, the fit is considered to be well-constrained.

Quantitatively, the objective of the fitting procedure is to minimize the "chi-squared" parameter, which in this case is defined to be

$$\chi^2 \equiv \sum_{shots} \frac{\left(\log_{10}Y_{DD,obs} - \log_{10}Y_{DD,RIK}\right)^2}{\sigma^2_{\mathrm{logYDD}}} + \frac{\left(\log_{10}Y_{D3He,obs} - \log_{10}Y_{D3He,RIK}\right)^2}{\sigma^2_{\mathrm{logYD3He}}} + \frac{\left(T_{iDD,obs} - T_{iDD,RIK}\right)^2}{\sigma^2_{TiDD}} + \frac{\left(t_{bangDD,obs} - t_{bangDD,RIK}\right)^2}{\sigma^2_{tb}} + \frac{\left(f_{abs,obs} - f_{abs,RIK}\right)^2}{\sigma^2_{fabs}}, \quad \text{(A.6)}$$

where σ is the measurement uncertainty for each of the observables. For the OMEGA experiments, σ_{logYDD} and $\sigma_{\mathrm{logYD3He}}$ were taken to be the equivalent of 10% uncertainty, σ_{TiDD} was 0.5 keV, σ_{tb} was 50 ps, and σ_{fabs} was 0.04.

Figure A.12 illustrates this procedure in a simplified case, matching only one shot's worth of observables (five total) with two free parameters. In this case, limited to only shot 69057, a minimum $\chi \sim 2.5$ was obtained for $(f_{idif}, f_{icnd}) \sim (0.8, 1.0)$. This is a reasonable quality of fit for five observables and two free parameters. A jog of ~50% for f_{idif} or ~50% for f_{icnd} is permitted before χ increases by 1, setting a rough scale for the uncertainty in the model fit.

For the entire set of experiments, the model parameters that produced the best fit to the 40 experimental observables were $(f_{ls}, f_e, f_{Knu}, f_{idif}, f_{icnd}) = (0.63, 0.06, 0.1, 0.1, 4)$. It should be noted that, in contrast, the purely hydrodynamic simulations used multipliers of (0.63, 0.06, 0, 0, 1). For the 8-shot fit, the total χ^2 was fairly close to 40, signifying a reasonably good fit of the RIK model to the experimental data. On the basis of this good fit, it is therefore reasonable to extract information about the overall experimental dynamics and the nature and magnitude of ion kinetic effects from the RIK model predictions, as was described in Chapter 3.

By turning on each kinetic effect one at a time, as was shown in Figure 3.12, it was possible to deduce the impact of each specific effect. The difference between (0.63, 0.06, 0, 0, 1) and (0.63, 0.06, 0, 0, 4) illustrated the (modest) impact of enhanced ion thermal conduction; the difference between (0.63, 0.06, 0, 0, 4) and (0.63, 0.06, 0.1, 0, 4) showed the fairly substantial importance of Knudsen layer effects on the fusion reactivity; and the difference between (0.63, 0.06, 0.1, 0, 4) and (0.63, 0.06, 0.1, 0.1, 4) showed how ion diffusion affects the fusion yields.

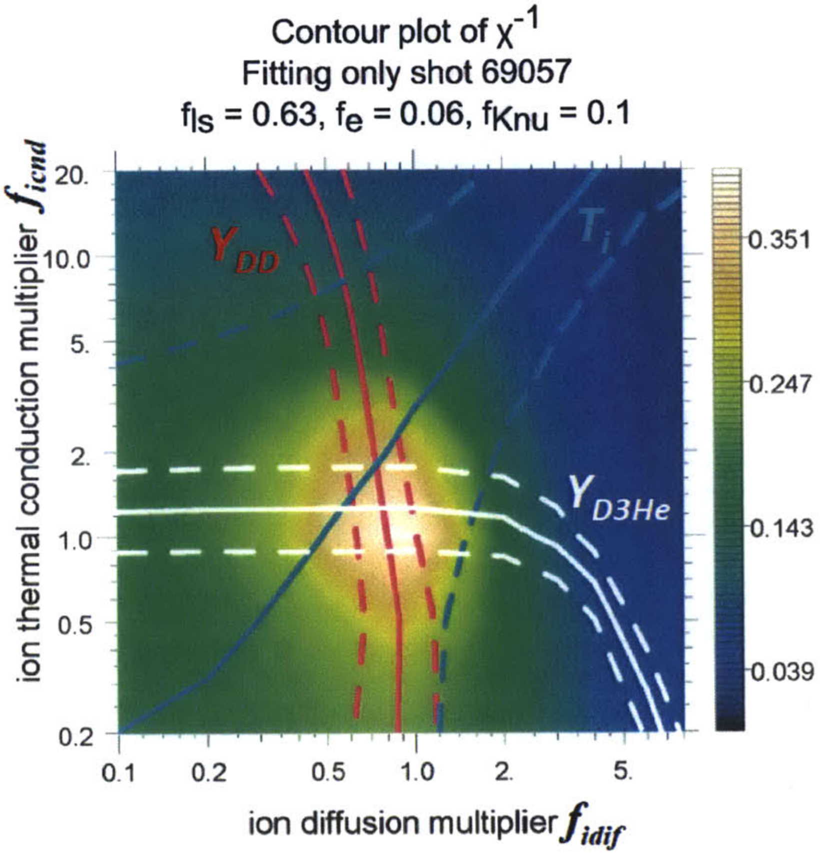

Figure A.12. Example of fitting procedure for Reduced Ion Kinetic (RIK) model, originally presented by Hoffman.[23] Contours of χ^{-1} reflect the goodness of fit to five observables (three shown) for shot 69057 as a function of tunable model parameters f_{idif} (ion diffusion) and f_{icnd} (ion thermal conduction). For the purposes of this exercise, multipliers on electron flux limiter ($f_e = 0.06$), laser fraction ($f_{ls} = 0.63$) and Knudsen number ($f_{Knu} = 0.1$) have been fixed. The solid reddish (bluish) [white] line represents the contour in (f_{idif},f_{icnd}) space over which the simulations are able to match exactly the measured DD yield (DD-burn-averaged ion temperature) [D^{3}He yield]. The dashed lines that bracket each of the solid lines represent a 1-σ deviation from the exact measured quantity, where σ is the uncertainty corresponding to that particular measurement. The goal of this process is to find the region in model-parameter space where χ^2 is minimized. In the case of this example, that corresponds to (f_{idif},f_{icnd}) ~ (0.8, 1.0); for the entire set of OMEGA experiments, all five model parameters were allowed to vary, and the fit was simultaneously constrained by 40 observables (5 observables each on 8 different shots).

A.6 Experimental Setup and Data from Exploding Pusher Experiments on NIF

Initially presented in Chapter 3, experimental parameters from exploding pusher experiments on NIF[24] are shown in Table A.5. All lasers used a ramp pulse with a ~1.2 ns ramp and either a ~0.7 ns flat top or a truncated, ~0.2 ns flat top, and a ~0.1 ns fall time. Beams were configured in the polar-direct-drive configuration to try to optimize implosion symmetry. All shots used 192 beams. Experimental measurements are summarized in Table A.6.

Table A.5. Capsule and laser parameters for exploding pushers used in this study, including: capsule outer diameter d; shell thickness Δr; total laser energy; approximate laser pulse duration; D_2 fill pressure; and ^{3}He fill pressure.

NIF Shot Number	d (μm)	Δr (μm)	Energy (kJ)	Pulse (ps)	D_2 fill (atm.)	^{3}He fill (atm.)
N100823	1567	4.1	80.0	~2100	1.4	10.5[4]
N110131	1555	4.5	52.0	~2100	10.0	
N110722	1536	4.1	42.7	~1400	3.3	5.3
N120328	1555	4.4	130.6	~2100	9.9	
N121128	1682	4.3	43.4	~1400	3.3	5.8
N130129	1533	4.6	51.4	~1400	10.0	

Table A.6. Measured observables from these exploding pushers, including: DD yield; D^{3}He yield; DD-burn-averaged ion temperature; D^{3}He-burn-averaged ion temperature; bang time (x: x-ray, p: D^{3}He-proton, n: DD-neutron); fuel ρR; total ρR; x-ray emission radius P0 (contour of 10% of maximum brightness for N121128), and relative magnitude of second Legendre mode (P2/P0).

NIF Shot Number	Y_{DD}	Y_{D^3He}	T_{iDD} (keV)	T_{iD^3He} (keV)	Bang Time (ps)	Fuel ρR (mg/cm^2)	Total ρR (mg/cm^2)	X-Ray P0 (μm)	X-Ray P2/P0
N100823	1.38×10^{10}	2.32×10^{10}	10.5	16.2			13		
N110131	3.01×10^{11}		5.4		2430 (x)	4.6	23	89	-0.24
N110722	2.85×10^{10}	1.30×10^{10}	8.8	15.1	1910 (x)		11	115	-0.33
N120328	1.00×10^{12}		11.4		1770 (x)	3.6		182	-0.10
N121128	7.27×10^{10}	2.09×10^{10}	7.1	11.0	1880 (p)		9	168	-0.13
N130129	2.50×10^{11}		4.0		2470 (n)	4.6	18	94	-0.09

A.7 Additional Discussion of Exploding Pusher Experiments on NIF

Additional data and comparison to simulations of exploding pusher experiments on NIF, expanding on that presented in Chapter 3, is discussed in this section.

In addition to 2D DRACO simulations, 1D LILAC radiation-hydrodynamic simulations[25,10] are used for comparison to the experimental data. LILAC includes the physics of laser absorption, radiative transport, and thermal transport through a flux-limited diffusion model.[26] All calculations in this work used a flux limiter of $f = 0.06$, which is a standard choice due to reasonable agreement demonstrated historically between implosion performance and model predictions. This flux-limited model has shown good agreement with Fokker-Planck models of laser-plasma interactions,[27] and while experiments have shown that the flux limiter best reproducing measured results changes throughout an implosion, $f = 0.06$ is close to the average value.[28] LILAC calculates the spatial and temporal profiles of ion and electron densities and temperatures, total pressure, fuel velocity, and positions of Lagrangian mass elements as functions of space and time. Fusion burn rates are computed in each cell based on the ion density, ion temperature, and Maxwellian-averaged fusion reactivities. A representative LILAC simulation of NIF D^3He exploding pusher shot N110722 was shown in Chapter 3.

A.7.1 Yield and Ion Temperature

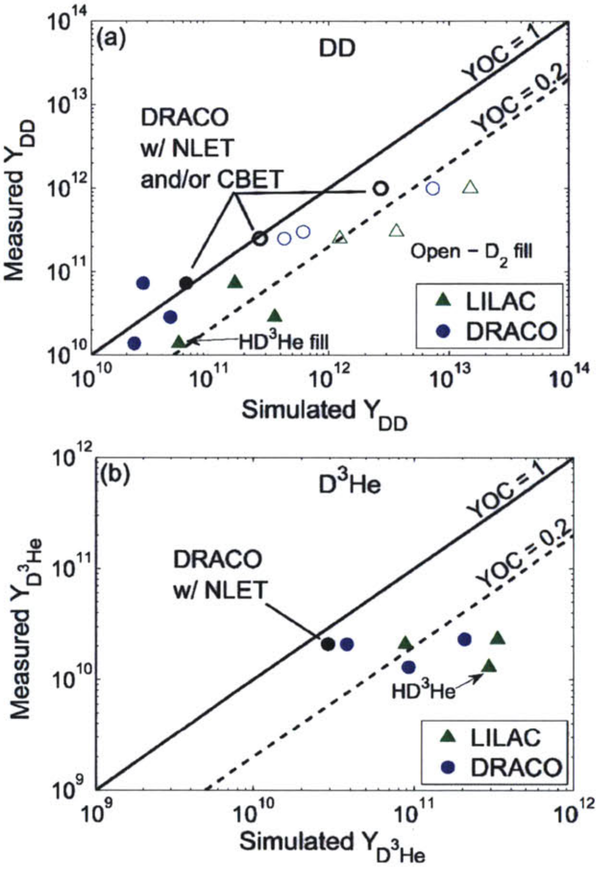

Figure A.13. (a) Measured DD yield and (b) D^3He yield as a function of LILAC-simulated (triangles) or DRACO-simulated (circles) yield. Open points denote D_2-gas-filled implosions, while filled points denote D^3He-gas-filled implosions. The blue circles represent nominal DRACO simulations, while the black circles are DRACO simulations that have included non-local electron transport and/or cross-beam energy transfer. Yield-over-clean (YOC) values of 1 (solid line) and 0.2 (dashed line) are indicated. The measured yields are averaged over several measurements on each shot, each with individual uncertainties of ~±15%. The overall error on each data point is ~±10-15%.

A comparison of measured and LILAC-simulated DD yields from D_2- and D^3He-gas-filled exploding pushers reveals that experimental values are around 19±13% of LILAC-predicted values for a large range of neutron yields (Figure A.13a). Kinetic effects such as Knudsen layer loss of energetic ions[29] may contribute to the yield deficit relative to this hydrodynamics simulation. As discussed earlier, implosion performance relative to simulations is slightly worse for pure D_2 and higher-yield (higher-T_i) implosions, which have longer ion-ion mean free paths, pointing to the possible influence of ion kinetic effects. The use of polar direct drive on NIF may affect capsule performance relative to 1D simulations which do not account for the 2D illumination. The use of 2D DRACO simulations in order to capture the effects of polar drive was discussed in Chapter 3. Measured DD yields are, on average, 84% of the nominal 2D DRACO predicted yield, but with a 82% standard deviation. Most of the data points cluster around YOC ~55-60%. The NLET-CBET DRACO simulations have a YOC closer to 1, though for both sets of DRACO simulations the lowest YOCs are again among the high-T_i, D_2-filled implosions with longer ion mean free paths. In each experiment, 2D considerations accounted for part of the measured yield deficit relative to 1D predictions, even though previous studies have shown that yields produced during the shock phase of implosions are insensitive to large initial drive non-uniformities.[30]

The data and LILAC simulations show that the D^{3}He yield for several NIF experiments is only 12% of their simulated values (with a 9% standard deviation). Because most D^{3}He reactions occur along the shock rebound trajectory, it is unlikely that issues related to compression yield on NIF exploding pusher simulations are relevant for D^{3}He yield calculations. However, like for the DD results, the 2D drive may partially explain the D^{3}He YOC. The measured D^{3}He yield is, on average, 27% of the nominal 2D DRACO simulated value, suggesting that 2D effects at least partially account for the yield deficit relative to 1D LILAC simulations. The inclusion of NLET partially improves DRACO agreement with the measured D^{3}He yield. Kinetic effects may be responsible for the D^{3}He YOC being lower than the DD YOC, both because the D^{3}He reactivity is more sensitive to temperature-reducing kinetic effects that weaken the shock rebound and because D^{3}He reactivity is more susceptible to tail ion loss effects.[29]

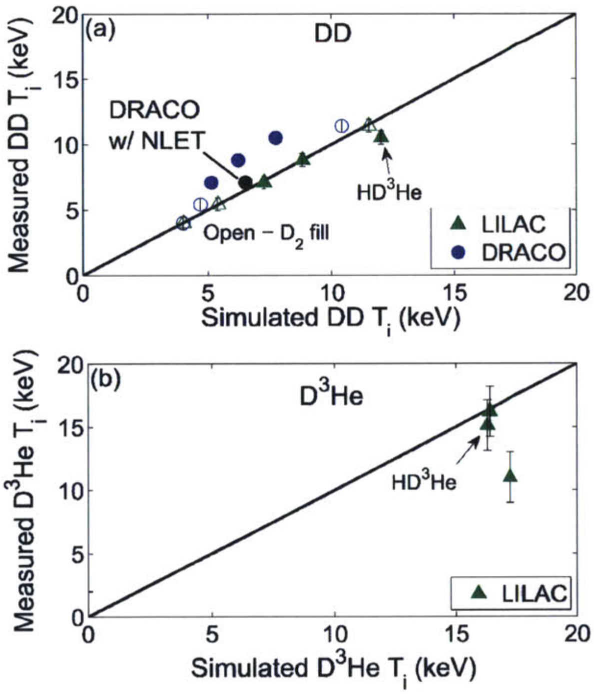

Figure A.14. Measured (a) DD-burn-averaged and (b) D^{3}He-burn-averaged ion temperatures versus the LILAC-simulated (triangles) and DRACO-simulated (circles) burn-averaged ion temperatures. The blue circles represent nominal DRACO simulations, while the black circle is a DRACO simulation that has included non-local electron transport.

The temperatures determined from the different burn-averaged measurements are contrasted to LILAC- and DRACO-simulated burn-averaged temperatures in Figure A.15. Excellent agreement is observed for the DD-burn-averaged ion temperatures (Figure A.15a.), and D^{3}He-burn-averaged ion temperatures are also found to be in good agreement with LILAC simulations on two of three experiments (Figure A.15b).

A.7.2 ρR, Convergence, and Bang Time

Fuel ρR

As discussed in Chapter 3, fuel ρR was inferred from the secondary D^{3}He-proton yield in D$_2$ implosions, and here the ρR is compared to simulated values. With a secondary-proton yield of

$(2.0\pm0.5)\times10^8$ and a primary DD-neutron yield of $3.0\pm0.3\times10^{11}$, a fuel ρR of 4.6 ± 1.1 mg/cm^2 is inferred for N110131 using a model of uniform fusion production throughout the fuel.[16] This measured fuel ρR is a factor of three lower than the LILAC-simulated fuel ρR of 14.5 mg/cm^2 and a factor of 2.5 lower than the nominal DRACO-simulated fuel ρR of 11 mg/cm^2. Table A.7 contrasts the fuel ρR data to simulated values. For the three D_2 exploding pushers, both LILAC and DRACO overestimate the burn-averaged fuel ρR, with 2D effects such as low-mode implosion asymmetry (if DRACO is properly modeling the asymmetries) accounting only partially for the discrepancy relative to the 1D simulation. These results suggest that the DD burn in those NIF exploding pusher implosions occurs at a lower fuel density than simulated by LILAC. This discrepancy could be explained by the code predicting too much yield around peak compression, which would skew the simulated fuel ρR higher. This density discrepancy may explain overall measured yields being lower than simulated by LILAC, with yield trends within the dataset (e.g. based on T_i or gas Z) attributed to ion kinetic effects, as described in the main text.

Table A.7. Measured and simulated DD-burn-averaged fuel ρR (mg/cm^2) in NIF D_2 exploding pushers.

Shot	Measured ρR_f (mg/cm^2)	LILAC	DRACO
N110131	4.6±1.1	14.5	11
N110328	3.6±1.0	13.8	11
N130129	4.6±1.1	10.2	7

Secondary DT-Neutron Data for Fuel ρR Estimates

In principle, the fuel ρR can also be inferred from the yield of secondary DT neutrons, an analogue to the secondary D^{3}He protons.[9,16] The secondary DT-neutron yields measured on the six NIF direct-drive exploding pushers used in this study, and the fuel ρR values naively inferred from the ratio of secondary DT-n to primary DD-n yields, are shown in Table A.8. The fuel ρR values are inferred assuming a uniform burn model (as for the secondary D^{3}He-p) and an electron temperature equivalent to the measured DD-burn-averaged ion temperature. Unlike for secondary D^{3}He protons, the yield of secondary DT neutrons is somewhat sensitive to the electron temperature, as the energetic triton must slow down significantly before being able to fuse with an ambient deuteron. This slowing process depends sensitively on the electron temperature. The inferred fuel ρR values are reasonable for D_2 shots N110131 and N130129, but are significantly discrepant from the fuel ρR inferred from secondary D^{3}He-p on D_2 shot N120328 and quite high relative to what would be expected on the three D^{3}He shots, N100823, N110722, and N121128.

Total or Shell ρR

The total ρR on shot N110131 is inferred from the downshift in the average energy of the secondary D^{3}He-proton spectrum.[16] There is some uncertainty in the measurement due to the presence of radial electric fields around the capsule that cause an upshift in proton energy upon leaving the capsule,[21] such that the downshift-inferred total ρR is a lower limit on the actual ρR in the implosion. However, when the laser intensity is below $\sim4\times10^{14}$ W/cm^2 or when the nuclear bang time is well after the end of the laser pulse, electric-field upshifts are diminished and the birth energy is well known. Assuming an average secondary-proton birth energy of 14.96 MeV and measured energies of 14.08 ±0.15 MeV on the equator and an average energy of 14.33±0.15 MeV on the pole, total ρR of $\sim26\pm5$ and $\sim19\pm5$ mg/cm^2, respectively, are inferred for shot N110131. Subtracting

Table A.8. Measured secondary DT-n yields and inferred fuel ρR for NIF exploding pushers. The inferred fuel ρR are reasonable for D_2 shots N110131 and N130129, but are generally high for the D^3He shots N100823, N110722, and N121128, and are low for D_2 shot N120328.

Shot	Measured DT-n Yield	Inferred Fuel ρR (mg/cm^2)
N100823	3.2×10^7	>100
N110131	8.6×10^7	3
N110722	3.3×10^7	12
N120328	12×10^7	1
N121128	5.0×10^7	8
N130129	7.6×10^7	3

the fuel ρR, which is assumed to be symmetric, the shell $\rho R \sim 21\pm5$ mg/cm^2 on the equator and $\sim 14\pm5$ mg/cm^2 on the pole are measured. These values are in good agreement on average with the LILAC-predicted 1D shell ρR of ~ 14 mg/cm^2 and also point to an oblate implosion, as confirmed by x-ray images. DRACO simulations also capture the total ρR accurately: D^3He shot N121128 was measured to have a total ρR of 9 ± 5 mg/cm^2, while DRACO predicted between 7 and 11 mg/cm^2 around bang time.

Discussion of the Relationship Between ρR and Convergence: Fuel, Shell, and Mass Conservation Issues

In Chapter 3, the measured fuel ρR was used to infer an approximate convergence ratio C as $C = (\rho R_f/\rho R_{f0})^{1/2}$, where ρR_f is the fuel areal density around bang time and ρR_{f0} is the initial fuel areal density. As part of that discussion, the ratio of final to initial shell areal density was used as well to corroborate the inference of C. The precise relation between the convergence ratio and the ratio of final to initial shell ρR is presented below.

Assume that the shell is fairly thin, with thickness Δ_s and radius R_s, so that the shell volume can be approximated as $4\pi R_s^2\Delta_s$ and the shell density can be written as $\rho_s{\sim}N_s m_{si}/(4\pi R_s^2\Delta_s)$, where N_s is the total number of shell ions and m_{si} is the mass of an average shell ion. The shell ρR can therefore be expressed as $\rho R_s{\sim}\rho_s\Delta_s{\sim}N_s m_{si}/(4\pi R_s^2)$. Thus, the ratio between final shell ρR and initial shell ρR is $\rho R_{sf}/\rho R_{s0}{\sim}(N_{sf}m_{si}/N_{s0}m_{si})(4\pi R_{s0}^2/4\pi R_{sf}^2){\sim}(N_{sf}/N_{s0})(R_{s0}/R_{sf})^2$. As some of the shell has been ablated away and does not significantly contribute to the areal density, the ratio between the final number of shell ions and the initial number of shell ions is less than unity, and is expressed in terms of the blowoff fraction f as $(N_{sf}/N_{s0}) = 1\text{-}f$. Making that substitution, as well as for the convergence ratio $C = R_{s0}/R_{sf}$, the convergence can be expressed in terms of the shell areal density and the blowoff fraction as $C^2 = (\rho R_{sf}/\rho R_{s0})/(1-f)$. In the case of the NIF exploding pushers, a blowoff fraction of $f = 0.6$ was determined to be reasonable, based on simulations, and a $\rho R_{sf}/\rho R_{s0}{\sim}$10-20 was measured. As such, the convergence was estimated to be $C{\sim}$5-7, in good agreement with the convergence ratio of $C \sim 6$ inferred from fuel ρR and x-ray emission measurements.

Returning to the fuel ρR discussion, the inference of convergence and ion density from fuel ρR is complicated under circumstances when the assumption of mass conservation is no longer valid.[31] In Chapter 3, the ion density was inferred from the fuel ρR as $n_i = n_{i0}(\rho R_f/\rho R_{f0})^{3/2}$, where n_{i0} and ρR_{f0} are the initial gas ion density and initial fuel ρR, respectively. However, when the fuel loses mass (e.g. due to significant transport of fuel ions into the shell), the relationship is modified, so that $n_i = n_{i0}(1-f_{fuel})^{1/2}(\rho R_f/\rho R_{f0})^{3/2}$, where f_{fuel} is the fraction of fuel ions that have escaped.

Thus, if the fuel has lost a significant fraction of its mass ($f_{fuel} \gtrsim 0.5$), for a given measurement of fuel ρR, the ion density will actually be *greater* than the naively estimated value (assuming $f_{fuel} = 0$). This fuel mass loss is one consequence of ion kinetic effects, which lead to the escape of thermal and suprathermal ions from the fuel into the shell. The fuel mass loss fraction is likely related to the Knudsen number N_K, and it can be reasonably expected that for $N_K > 1$, this effect will be substantial. It may be possible to estimate the fraction of fuel ions that have escaped on the basis of experimental performance relative to hydrodynamic simulations, or through the direct use of a kinetic-based model. For more details, see Ref. [31].

X-Ray Emission

Table A.9. Measured x-ray emission size P0 (contour of 10% of maximum brightness for N121128) in comparison to LILAC-simulated minimum shell radius (R_{min}). The measured magnitude of the second Legendre mode, the dominant asymmetry in the implosion, quantifies the deviation in core shape from 1D.

Shot	Measured X-Ray P0 (μm)	LILAC R_{min} (μm)	Measured X-Ray P2/P0
N110131	89	47	-0.24
N110722	115	67	-0.33
N120328	182	66	-0.10
N121128	168	84	-0.13
N130129	94	64	-0.09

X-ray emission gives a sense of the core size around bang time and may be compared to the simulated shell convergence. The x-ray core size measured by gated x-ray imaging diagnostics hGXI[32] and GXD[33] are shown in Table A.9 in terms of the zeroth Legendre mode radius P0. The LILAC-simulated minimum shell radii are also shown for comparison. In each implosion, LILAC predicts a smaller minimum core size than observed in the x-ray images (though care must be taken to ensure that this comparison is valid). This result suggests that LILAC overestimates the amount of compression, supporting the interpretation of the fuel ρR data across the entire data set. Additionally, the x-ray images indicate a consistent Legendre P2 asymmetry, with the magnitude P2/P0 ranging from 9% to 33% oblate. Though this asymmetry does not necessarily impact the shock convergence that drives fusion production in these implosions, it can alter fuel density profiles around bang time in a way that 1D codes such as LILAC cannot replicate. As described in Chapter 3, the minimum shell radius is used to estimate the Knudsen number in these implosions.

Bang Times

Measured bang times are compared to LILAC and DRACO predictions in Figure A.9. Uncertainties in the pTOF-measured DD-neutron bang time is ~120 ps, while the uncertainty in the D^{3}He-proton bang time measurements is ~100 ps. Uncertainty in the x-ray bang time is ~100 ps. Measured bang times generally track and agree with LILAC and DRACO predictions, especially the nuclear bang times. The overall trend indicates that LILAC and DRACO capture the overall 1D dynamics of energy coupling to these shock-driven implosions fairly well.

A.8 References

1. R. P. Drake, *High-Energy-Density Physics*, (Springer Press, New York, 2006).

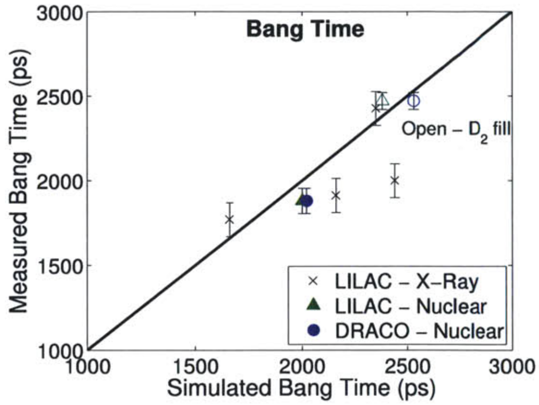

Figure A.15. Measured DD (open), D^{3}He (filled) or x-ray (X) bang times versus corresponding LILAC and DRACO bang times for exploding pusher implosions.

2. M. J. Rosenberg, H. G. Rinderknecht, N. M. Hoffman *et al.*, "Exploration of the transition from the hydrodynamiclike to the strongly kinetic regime in shock-driven implosions," Phys. Rev. Lett., **112**, 185,001 (2014).
3. W. Seka, H. A. Baldis, J. Fuchs *et al.*, "Multibeam stimulated brillouin scattering from hot, solid-target plasmas," Phys. Rev. Lett., **89**(17), 175,002 (2002).
4. V. Y. Glebov, C. Stoeckl, T. C. Sangster *et al.*, "Prototypes of national ignition facility neutron time-of-flight detectors tested on omega," Rev. Sci. Inst., **75**, 3559–3562 (2004).
5. F. H. Séguin, J. A. Frenje, C. K. Li *et al.*, "Spectrometry of charged particles from inertial-confinement-fusion plasmas," Review of Scientific Instruments, **74**(2) (2003).
6. C. Stoeckl, V. Y. Glebov, S. Roberts *et al.*, "Ten-inch manipulator-based neutron temporal diagnostic for cryogenic experiments on omega," Rev. Sci. Inst., **74**(3), 1713–1716 (2003).
7. F. H. Séguin, J. L. DeCiantis, J. A. Frenje *et al.*, "Measured dependence of nuclear burn region size on implosion parameters in inertial confinement fusion experiments," Physics of Plasmas, **13**(8), 082704 (2006).
8. D. K. Bradley, P. M. Bell, O. L. Landen *et al.*, "Development and characterization of a pair of 30-40 ps x-ray framing cameras," Rev. Sci. Inst., **66**(1), 716–718 (1995).
9. M. D. Cable and S. P. Hatchett, "Neutron spectra from inertial confinement fusion targets for measurement of fuel areal density and charged particle stopping powers," J. Appl. Phys., **62**(6), 2233–2236 (1987).
10. J. Delettrez, "Thermal electron transport in direct-drive laser fusion," Can. J. Phys., **64**, 932 (1986).
11. P. Amendt, J. D. Colvin, R. E. Tipton *et al.*, "Indirect-drive noncryogenic double-shell ignition targets for the national ignition facility: Design and analysis," Phys. Plasmas, **9**(5), 2221–2233 (2002).
12. G. Dimonte and R. Tipton, "K-l turbulence model for the self-similar growth of the rayleigh-taylor and richtmyer-meshkov instabilities," Physics of Fluids, **18**(8), 085101 (2006).
13. J. A. Frenje, C. K. Li, F. H. Séguin *et al.*, "Measuring shock-bang timing and ρr evolution of d^{3}he implosions at omega," Phys. Plasmas, **11**(5), 2798–2805 (2004).
14. H. G. Rinderknecht, H. Sio, C. K. Li *et al.*, "First observations of nonhydrodynamic mix at the fuel-shell interface in shock-driven inertial confinement implosions," Phys. Rev. Lett., **112**, 135,001 (2014).
15. H. G. Rinderknecht, private communication (2014).
16. F. H. Séguin, C. K. Li, J. A. Frenje *et al.*, "Using secondary-proton spectra to study the compression and symmetry of deuterium-filled capsules at omega," Phys. Plasmas, **9**(6), 2525–2537 (2002).
17. S. Kurebayashi, J. A. Frenje, F. H. Séguin *et al.*, "Using nuclear data and monte carlo techniques to study areal density and mix in d$_2$ implosions," Phys. Plasmas, **12**, 032,703 (2005).
18. S. Atzeni, "2-d lagrangian studies of symmetry and stability of laser fusion targets," Computer Physics Communications, **43**(1), 107 – 124 (1986).
19. J. T. Larsen and S. M. Lane, "Hyades - a plasma hydrodynamics code for dense plasma studies," J. Quant. Spectrosc. Radiat. Transfer, **51**(12), 179–186 (1994).
20. B. Yaakobi, T. Boehly and P. Audebert, "Focusing x-ray spectrograph for laser fusion studies," Review of Scientific Instruments, **61**(7), 1915–1919 (1990).

21. D. G. Hicks, C. K. Li, F. H. Séguin *et al.*, "Charged-particle acceleration and energy loss in laser-produces plasmas," Phys. Plasmas, **7**(12), 5106–5117 (2000).

22. F. H. Séguin, J. L. Deciantis, J. A. Frenje *et al.*, "D^3he-proton emission imaging for inertial-confinement-fusion experiments (invited)," Rev. Sci. Inst., **75**(10), 3520–3525 (2004).

23. N. Hoffman *et al.*, "Validating kinetic models in a fluid code using data from high-knudsen-number capsule implosions," Bull. Am. Phys. Soc., **58**(16) (2013).

24. M. J. Rosenberg *et al.*, "Utilization of nif diagnostic development shots for investigation of ion kinetic effects in direct-drive exploding-pusher implosions," to be submitted to Phys. Plasmas (2014).

25. J. Delettrez, R. Epstein, M. C. Richardson *et al.*, "Effect of laser illumination nonuniformity on the analysis of time-resolved x-ray measurements in uv spherical transport experiments," Phys. Rev. A, **36**(8), 3926–3934 (1987).

26. R. C. Malone, R. L. McCrory and R. L. Morse, "Indications of strongly flux-limited electron thermal conduction in laser-target experiments," Phys. Rev. Lett., **34**, 721–724 (1975).

27. J. P. Matte, T. W. Johnson, J. Delettrez *et al.*, "Electron heat flow with inverse bremsstrahlung and ion motion," Phys. Rev. Lett., **53**(15), 1461–1464 (1984).

28. A. Sunahara, J. A. Delettrez, C. Stoeckl *et al.*, "Time-dependent electron thermal flux inhibition in direct-drive laser implosions," Phys. Rev. Lett., **91**(9), 095,003 (2003).

29. K. Molvig, N. M. Hoffman, B. J. Albright *et al.*, "Knudsen layer reduction of fusion reactivity," Phys. Rev. Lett., **109**(095001) (2012).

30. J. R. Rygg, J. A. Frenje, C. K. Li *et al.*, "Observations of the collapse of asymmetrically driven convergent shocks," Phys. Plasmas, **15**, 034,505 (2008).

31. N. M. Hoffman, private communication (2014).

32. S. Glenn, J. Koch, D. K. Bradley *et al.*, "A hardened gated x-ray imaging diagnostic for inertial confinement fusion experiments at the national ignition facility," Rev. Sci. Inst., **81**(10E539) (2010).

33. G. A. Kyrala, S. Dixit, S. Glenzer *et al.*, "Measuring symmetry of implosions in cryogenic *Hohlraums* at the nif using gated x-ray detectors (invited)," Rev. Sci. Inst., **81**(10E316) (2010).

Appendix B

Discussion of Fusion Product Linewidth Measurements

Measurements of the linewidth of fusion product spectra have been used extensively for measurements of ion temperature averaged over the period and location of fusion burn, as was discussed in Chapters 2 and 3, as well as in Appendix A. In this appendix, more details of the linewidth measurement are presented, including discussions of possible non-thermal contributions to the spectral width (e.g. from bulk plasma flows).

B.1 Doppler Width Measurements from OMEGA Exploding Pusher Experiments

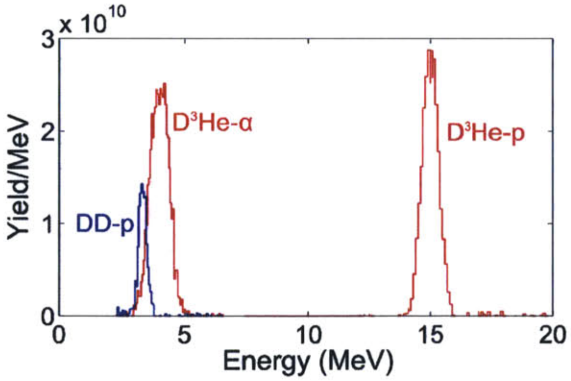

Figure B.1. Fusion-product spectra of DD protons, D^3He alphas, and D^3He protons obtained using the magnet-based charged particle spectrometer CPS2 on an implosion with 0.67 mg/cm^3 D^3He (OMEGA shot 69064). These spectra are used to infer the burn-averaged ion temperatures from the width of the spectral lines.

As was shown previously, the width of fusion product spectra (e.g. those shown in Figure B.1 for an exploding pusher implosion on OMEGA) is used to infer ion temperature, as the Doppler width $\sigma_D^2 \propto T_i$ (e.g. those shown in Figure B.2). Practically speaking, the spectral width that is measured by charged-particle spectrometers is a convolution of instrumental broadening, Doppler broadening, and any other sources of broadening from within or around the implosion. For the purposes of this discussion, and is reasonably true of the exploding pusher implosions described herein, the non-Doppler, non-instrumental sources of broadening can be ignored (except, possibly, for bulk flows, which are discussed in Section B.2). Thus, for a given measurement, the (useful) Doppler broadening component is inferred from the total measured spectral width, assuming a Gaussian spread for each component, as $\sigma_{tot}^2 = \sigma_D^2 + \sigma_{inst}^2$, where σ_{inst} is the instrumental broadening.

The charged-particle detectors used in this work are the wedge range filter (WRF) proton

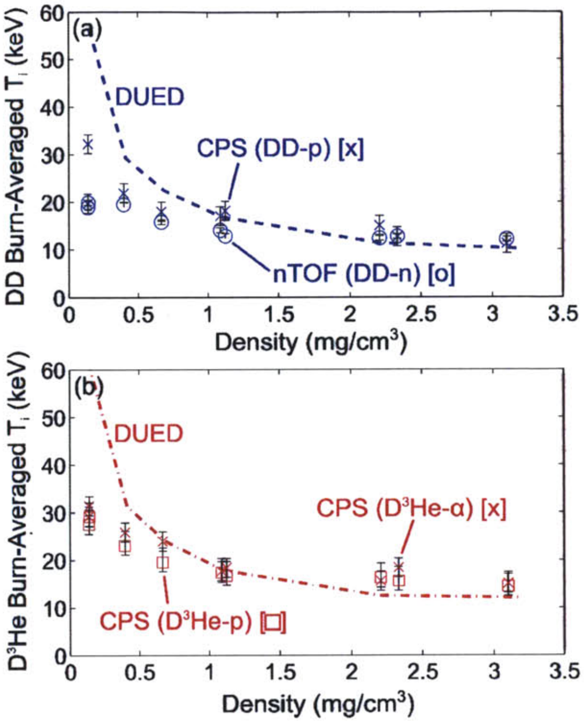

Figure B.2. Measured (a) DD- and (b) D^{3}He-burn-averaged ion temperatures as a function of initial D^{3}He gas density. The DD-burn-averaged T_i measured by the nTOF DD-n Doppler width (blue circles) are in good agreement with the average of DD-burn-averaged T_i inferred from CPS1 and CPS2 (blue x) DD-proton spectra, and increase gradually with decreasing initial gas density. The CPS-measured D^{3}He-proton T_i (red squares) are in good agreement with the CPS1-measured D^{3}He-α yields (red x) and increase more rapidly than the DD-burn-averaged T_i at low density. The DUED-simulated burn-averaged ion temperatures for both reactions are increasingly discrepant with the measured ion temperatures at low initial gas density as the implosions become more kinetic.

spectrometers and the charged particle spectrometers (CPS), which were introduced in Chapter 2. For the WRFs, the instrumental broadening for D^{3}He-proton spectra is determined based on the actual spectra measured during calibration runs on LEIA. The total linewidth is measured by both the WRF ($\sigma_{WRF,tot}$) and the surface barrier detector (SBD) ($\sigma_{SBD,tot}$). After subtracting in quadrature the known instrumental broadening of the SBD ($\sigma_{SBD,inst}$), the actual spectral width of the D^{3}He-p line produced by LEIA is calculated, as $\sigma^2_{LEIA} = \sigma^2_{SBD,tot} - \sigma^2_{SBD,inst}$. Thus, the instrumental broadening of the WRF is determined to be $\sigma^2_{WRF,inst} = \sigma^2_{WRF,tot} - \sigma^2_{LEIA}$. Typically, $\sigma_{WRF,inst}$~150 keV for Al WRFs and ~220 keV for Zr (broadband, BB) WRFs, though these quantities can be readily reconfirmed using LEIA calibrations.

The instrumental width for CPS is based primarily on the spread in particle trajectories entering the finite-width aperture in front of the magnet. As such, a delta function distribution of particles in energy space will be transmitted to a spread of locations on the CR-39, and thus interpreted to have different energies. This energy response function consists of a "boxcar" shape, with a width σ_w related to the physical width of the aperture. The instrumental broadening $\sigma_{CPS,inst}$ that is imparted on a spectrum of finite width is, to zeroth order, related to this boxcar width as $\sigma^2_{CPS,inst} = \sigma^2_w/12$.[1] A more sophisticated treatment[2] has directly quantified the effective additional broadening imparted by convolving a spectrum of finite width with the boxcar function. It was determined that the effective instrumental broadening deviates from the simple equation above when the boxcar width becomes larger than the total measured linewidth. A 3rd order polynomial fit has determined that, to within 0.4%, rather than $\sigma^2_{CPS,inst} = \sigma^2_w/12$, the relation is actually $\sigma^2_{CPS,inst} = \sigma^2_w/[12.02 - 0.398\sigma^2_w/\sigma^2_{tot} + 0.0373(\sigma^2_w/\sigma^2_{tot})^2 - 0.00664(\sigma^2_w/\sigma^2_{tot})^3]$.[2] Having calculated the instrumental width, the Doppler width is determined in the usual way as $\sigma^2_D = \sigma^2_{tot} - \sigma^2_{CPS,inst}$.

B.1.1 Verification of CPS Aperture Width for Calculating Instrumental Broadening

The boxcar width of the CPS response and, therefore, the instrumental broadening, is a strong function of the width of the aperture at the from of the CPS magnet. Thus, in order to make accurate measurements of the Doppler width (and, more directly, the total fusion yield) from the CPS-measured spectra, it is important to have confirmation of the aperture or "slit" that was used. Recently, a technique was developed to use the x-rays produced in the implosion itself to produce an image of the slit opening using radiochromic film (RCF).[3] That work has produced expected widths of the slit image for each slit used in both CPS1 and CPS2. Sample images of CPS slits from the OMEGA exploding pusher experiments is shown in Figure B.3, and a summary of the measured slit image widths from the different experiments, in comparison to the expected slit image width, is shown in Table B.1. For many cases, the measured width of the image on the RCF agreed with expectations; however, in some instances, notably for the 1 mm slit for both CPS1 and CPS2, the resulting image was smaller than expected. Given that CPS-measured yields were in good agreement with other diagnostics (see Figure A.6), it is unlikely that an erroneously-identified slit was used. Moreover, for inferring a the generally high (>10 keV) ion temperatures in these exploding pusher implosions from the Doppler width, the instrumental broadening is typically small in comparison to the total measured linewidth and, therefore, does not significantly impact the inferred temperature.

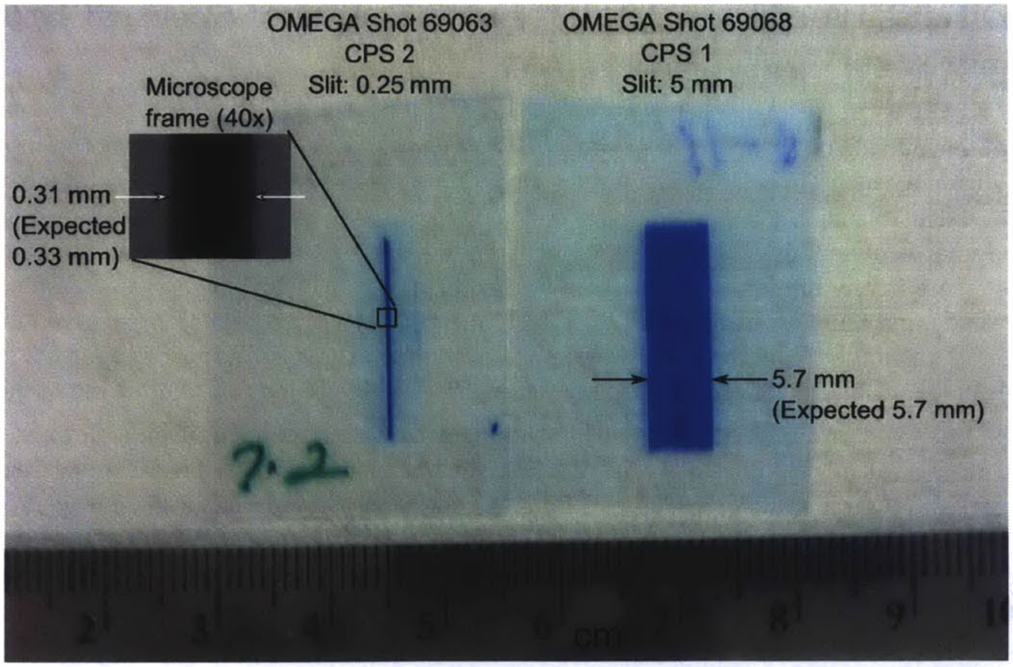

Figure B.3. CPS slit images on radiochromic film from OMEGA exploding pusher experiments. The width of the slit image is used to confirm that the slit used on a given shot was identified correctly. In these cases, the CPS2 slit from shot 69063 and the CPS1 slit from shot 69068 show a measured width in agreement with the expected width.

Table B.1. CPS slit image widths from OMEGA exploding pusher experiments. The 0.25 mm, 3 mm, and 5 mm slits produced images of the expected size, though the 1 mm slits produced images smaller than expected.

Shot	CPS1 Slit Width (mm)			CPS2 Slit Width (mm)		
	Nominal	Expected	Measured	Nominal	Expected	Measured
69055	1	1.13	0.63	0.25	0.33	0.33
69057	1	1.13	0.60	0.25	0.33	0.37
69058	1	1.13		0.25	0.33	
69059	0.1	0.11	0.08	0.1	0.13	0.27
69060	1	1.13	0.61	0.25	0.33	0.31
69061	1	1.13	0.64	0.25	0.33	0.34
69063	1	1.13	0.64	0.25	0.33	0.31
69064	1	1.13	0.64	0.25	0.33	0.34
69066	1	1.13	0.64	0.25	0.33	0.29
69067	5	5.7	5.6	1	1.31	0.76
69068	5	5.7	5.7	3	3.9	4.0
69069	5	5.7	5.7	1	1.31	0.77
69070	5	5.7	5.7	1	1.31	0.76

B.2 Discussion of Flow Velocity as a Source of Spectral Broadening

Another potentially significant source of spectral broadening, which is typically ignored in measurements of ion temperature from fusion-product Doppler widths, is bulk flows. Bulk flows can impart additional width to fusion-product spectra in a manner that is quite similar to the temperature-related Doppler broadening.[4,5] Flow-related broadening can "masquerade" as thermal broadening and cause errors in the inference of ion temperature from the linewidth. This degeneracy between thermal broadening and flow broadening effectively means that, strictly speaking, a given linewidth-inferred temperature is really an upper limit on the actual burn-averaged ion temperature, though using multiple reactions there are ways to constrain the possible impact or magnitude of bulk flows.

For the purposes of analyzing linewidths, the most troublesome form of bulk flows is random, turbulent motion, at all angles relative to the detector line of sight, which produces spectral broadening in a characteristic Gaussian shape, similar to the Gaussian spectrum generated by thermal Doppler broadening.[5] As such, there can be a degeneracy between thermal-related spectral broadening and turbulent-flow-related spectral broadening. In contrast, bulk flows in a single direction simply translate the spectrum in energy space,[6,4] while bulk flows in the radial direction produce, to first order, Gaussian-like broadening in a manner similar to random, turbulent flows, but for large flow velocity significantly distort the spectral shape into something much flatter.[6] Going forward, this discussion is restricted to the simple case of random, turbulent flows, with the understanding that radial bulk flows could have a similar impact on the spectrum (though when the radial flow velocity approaches the ion thermal velocity, the distortion in spectral shape will make it easier to distinguish the two sources of broadening and resolve the degeneracy).

Following the discussion by Murphy,[5] for two fusion-product ions A and B, the thermal Doppler width of the product A spectrum is[7]

$$\sigma_D^2 = \frac{2m_A kT_i \langle E_A \rangle}{m_A + m_B}, \tag{B.1}$$

where m_A and m_B are the masses of each ion and E_A is the birth energy of product ion A. In order to calculate the spectral broadening due to random, turbulent motion, first consider the shift in energy due to bulk motion $\Delta E_A = 2E_A v_z / v_A$, where v_z is the plasma velocity along the detector line of sight and v_A is the velocity of particle A. Averaging over angle yields a spread of energy shifts characterized by

$$\sigma_K^2 = m_A^2 v_A^2 \langle v_z^2 \rangle, \tag{B.2}$$

and the total linewidth (ignoring instrumental broadening) is equivalent to the quadrature sum of these contributions, as

$$\sigma_A^2 = \sigma_D^2 + \sigma_K^2 = \frac{2m_A kT_i \langle E_A \rangle}{m_A + m_B} + m_A^2 v_A^2 \langle v_z^2 \rangle = \frac{m_A^2 v_A^2}{m_A + m_B} \left[kT_i + (m_A + m_B) \langle v_z^2 \rangle \right]. \tag{B.3}$$

Among the terms in brackets on the right-hand side, kT_i represents the thermal contribution and $(m_A + m_B)\langle v_z^2 \rangle$ represents the flow contribution. A few observations are noteworthy: (1) under permutation of A and B, for a given reaction, $\sigma_A = \sigma_B$, signifying that both products will have the same linewidth, regardless of flow velocity,[1] and (2) that for *different* reactions with a different sum of $m_A + m_B$, the presence of flows will impact the linewidth in proportionately different ways, i.e. that $(m_A + m_B)\langle v_z^2 \rangle / kT_i$, the ratio of flow to thermal contributions, depends on $m_A + m_B$, with heavier reactions affected more strongly by flows.

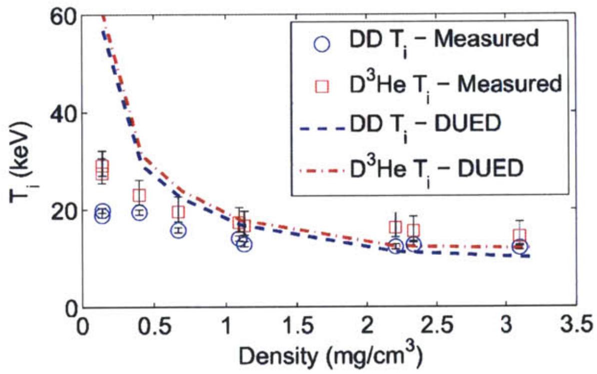

Figure B.4. Measured and DUED-simulated DD and D^{3}He burn-averaged ion temperatures, inferred from spectral linewidths assuming only thermal Doppler broadening, as a function of initial gas density. The use of multiple reactions allows for possible characterization of random bulk flows.

This last property suggests that by measuring the spectral widths of different reactions, it may be possible to estimate, or at least place an upper bound on, the magnitude of flow velocities. While Murphy[5] uses the examples of DT-neutrons and DD-neutrons, for this discussion the analogous (at least mass-wise) D^{3}He-protons and DD-neutrons are used. As was presented in Chapter 3 and is shown again in Figure B.4, the linewidths of the D^{3}He-p and DD-n spectra were used to infer burn-averaged ion temperatures in the OMEGA exploding pusher experiments.[8] Figure B.4 shows the measured linewidth-inferred temperature as a function of initial gas density, in comparison to the burn-averaged ion temperatures predicted by DUED.[9] The DUED values are direct burn-averaged ion temperatures and by definition do not consider the impact of flows on fusion-product spectral widths. The subtle difference predicted by DUED between D^{3}He- and DD-burn-averaged ion temperatures reflects spatial and temporal gradients in the ion temperature, as, in comparison to the DD reaction, the D^{3}He reaction is more temperature-sensitive and, thus, is weighted more strongly by the hotter regions of the fuel.

---

[1] This is a consequence of the fact that, for a given reaction with two products, the energy of each product is inversely related to its mass, i.e. that $m_A E_A = m_B E_B$ or, alteratively, $m_A^2 v_A^2 = m_B^2 v_B^2$.

The small differences between the observed D^{3}He- and DD-burn-averaged ion temperatures in the experimental data could reflect these temperature gradients in the actual implosion, or they could be a result of random bulk flows.[2] Unfortunately, both effects go in the same direction, preferentially broadening the D^{3}He-p spectrum more than the DD-n spectrum; this degeneracy between temperature gradients and flows is less of a concern for DT and DD, whose reactivities have a fairly similar temperature dependence. Based on the observed difference between the D^{3}He- and DD-burn-averaged ion temperatures, an upper limit can be set on the flow velocity, corresponding to the ratio of apparent ion temperatures.

In general, the relationship between the "apparent" ion temperature $T_{i,app}$, the "actual" ion temperature T_i, and the random flow velocity is[5]

$$kT_{i,app} = kT_i + (m_A + m_B)\langle v_z^2 \rangle. \tag{B.4}$$

With multiple reactions 1 and 2, with different total mass $M = m_A + m_B$ for each (M_1 and M_2), the random flow velocity and actual ion temperature can be solved. Using the example of D^{3}He as reaction 1 ($M_1 = 5m_p$ and DD as reaction 2 ($M_2 = 4m_p$),

$$\langle v_z^2 \rangle = \frac{kT_{i,app1} - kT_{i,app2}}{M_1 - M_2} = \frac{kT_{i,appD3He} - kT_{i,appDD}}{m_p} \tag{B.5}$$

and

$$kT_i = \frac{kT_{i,app1} - \frac{M_1}{M_2} kT_{i,app2}}{1 - \frac{M_1}{M_2}} = 5kT_{i,appDD} - 4kT_{i,appD3He}. \tag{B.6}$$

For the example of OMEGA D^{3}He-filled exploding pusher shot 69055, the inferred or apparent ion temperatures are $T_{i,appD3He} = 14.5$ keV and $T_{i,appDD} = 12.2$ keV. Assuming that the entire difference is due to random flows sets an upper limit on the flow velocity of $\sqrt{\langle v_z^2 \rangle} < 470 \mu\text{m/ns}$. However, it is highly likely that a large fraction of the difference between D^{3}He- and DD-burn-averaged ion temperature measurements is due to (actual) temperature gradients in the fuel.

Given measurements of the fusion yield, ion density, ion temperature, fusion burn volume, and burn duration, it is possible to check the consistency of each of those measurements (including the temperature), as the equations for total yield are

$$Y_{DD} = \frac{n_D^2}{2} \langle \sigma v_{DD} \rangle (T_{i,DD}) V_{burn,DD} \tau_{burn,DD} \tag{B.7}$$

and

$$Y_{D3He} = n_D n_{3He} \langle \sigma v_{D3He} \rangle (T_{i,D3He}) V_{burn,D3He} \tau_{burn,D3He}. \tag{B.8}$$

For the purposes of this exercise, based on the OMEGA exploding pusher data, n are inferred from fuel ρR or convergence measurements, σv is calculated based on the measured ion temperature of each reaction, V_{burn} is calculated as $4/3\pi R_{50}^2$, where R_{50} is radius containing 50% of the fusion reactions, and τ_{burn} is the FWHM of the reaction history. These measurements were discussed in

---

[2] It is also possible that, especially for the more "kinetic" implosions, that the ^{3}He ions and D ions are not at the same temperature. This effect could introduce yet another degeneracy into this problem, causing the D^{3}He reaction to occur between ions at a greater temperature than the DD reaction. For the sake of this discussion, this possibility is ignored.

Chapter 3 or Appendix A.

As an example, consider shot 69055. The measured yields were $Y_{DD,measured} = 2.81\times10^{10}$ and $Y_{D3He,measured} = 3.41\times10^{10}$, while the expected yields based on equations B.7 and B.8 were $Y_{DD,expected} = 5.37\times10^{10}$ and $Y_{D3He,expected} = 1.47\times10^{10}$. The expected and measured yields are of the same order, which suggests that the measurements are reasonably consistent with each other; however, the measured DD yield is about a factor of 2 lower than expected, while the measured D^3He yield is about a factor of 2 higher than expected. If this discrepancy were interpreted only through the lens of ion temperature, one might conclude that the measured $T_{i,DD}$ were erroneously high (i.e. should be lower) and that the measured $T_{i,D3He}$ were erroneously low (i.e. should be higher). This would actually increase the burn-averaged temperature difference between DD and D^3He. It is plausible that suppression of the high-energy ion tail, which more strongly impacts D^3He reactions, would preferentially cause a narrowing of the D^3He-p spectrum, as yet another effect on the linewidth.

An important, general question going forward is: is there a way to distinguish between broadening due to temperature and broadening due to flows? Can other measurements be brought to bear, beyond simply the fusion-product spectra, in order to break the degeneracy? Is there a way using only the spectra themselves to be able to say definitively that a difference in apparent ion temperatures between different reactions is a consequence of temperature gradients, as opposed to flows? To break the degeneracy between temperature gradient effects and flow velocity effects in the relative linewidths of D^3He and DD fusion products, PCIS images of the fusion burn profiles of both reactions may be used to estimate the ion temperature profile and deduce the magnitude of temperature gradients.

To conclude, a summary of different physical effects and their impact on fusion product linewidths is summarized in Table B.2. This is intended as a starting point for future efforts to break the many degeneracies and to be able to resolve the different effects.

Table B.2. Mechanisms that impact fusion product spectral widths and their effects on the absolute and relative Doppler widths of different reactions.

Mechanism	Effect
Temperature gradients	*Real* D^3He Doppler-inferred T_i larger than DD Doppler-inferred T_i
Random flows	Spectra broadened, *apparent* T_i larger, D^3He affected more than DD
Multi-T_i ions	*Real* D^3He Doppler-inferred T_i larger than DD Doppler-inferred T_i[3]
Knudsen tail loss	Spectra narrowed, *apparent* T_i smaller, D^3He affected more than DD

B.3 References

1. D. G. Hicks, *Charged-Particle Spectroscopy: A New Window on Inertial Confinement Fusion*, Ph.D. thesis, Massachusetts Institute of Technology (1999).
2. H. G. Rinderknecht, private communication (2013).
3. C. J. Waugh, M.sc. thesis, Massachusetts Institute of Technology (2014).
4. M. Gatu Johnson, D. T. Casey, J. A. Frenje *et al.*, "Measurements of collective fuel velocities in deuterium-tritium exploding pusher and cryogenically layered deuterium-tritium implosions on the nif," Physics of Plasmas, **20**(4), 042707 (2013).

---

[3] Assuming that ^3He ions are hotter than D ions due to shock heating

5. T. J. Murphy, "The effect of turbulent kinetic energy on inferred ion temperature from neutron spectra," Physics of Plasmas (1994-present), **21**(7), 072701 (2014).
6. B. Appelbe and J. Chittenden, "The production spectrum in fusion plasmas," Plasma Physics and Controlled Fusion, **53**(4), 045,002 (2011).
7. H. Brysk, "Fusion neutron energies and spectra," Plasma Physics, **15**(7), 611 – 617 (1973).
8. M. J. Rosenberg, H. G. Rinderknecht, N. M. Hoffman *et al.*, "Exploration of the transition from the hydrodynamiclike to the strongly kinetic regime in shock-driven implosions," Phys. Rev. Lett., **112**, 185,001 (2014).
9. S. Atzeni, "2-d lagrangian studies of symmetry and stability of laser fusion targets," Computer Physics Communications, **43**(1), 107 – 124 (1986).

Appendix C

Discussion of Ion Transport and "Diffusion" Under Long Mean Free Path Conditions

Ion transport or "diffusion" is a key consideration in the discussion of ion kinetic effects, such as presented in Chapter 3 and Appendix A. In the reduced ion kinetic (RIK) model, this was one of the principal effects found to be responsible for diminished fusion yields under conditions of long ion-ion mean free paths (λ_{ii}) or large Knudsen numbers ($N_K \equiv \lambda_{ii}/R_{shell}$). This effect can be understood as the transport of thermal ions out of the hot fuel region, or, alternatively, as the blurring of an otherwise sharp interface between fuel and shell ions (e.g. versus a pure hydrodynamic model without ion diffusion). This transport effect is especially important for long mean free path conditions, but under such conditions, the definition of "diffusion" breaks down – how can a collisional process such as diffusion occur in a collisionless plasma? A framework for discussion of these issues is presented in this appendix.

C.1 Ion Transport in the Fuel

In general, diffusion is considered to be a random walk process as, at each collision, the particle direction is randomized. Thus, particles spread out in position according to the relation $R^2 = D\tau$, where R is the average net distance traveled, D is a diffusion constant, and τ is the duration of time. As was shown in Appendix F, the diffusion constant D depends on the velocity of the diffusing particle (v) and the average distance between collisions, the mean free path (λ), as $D = \frac{1}{3}\lambda v$. This process is predicated on the randomizing effect of collisions,[1] and the picture of diffusion becomes hazy when particles are not expected to undergo collisions over the spatial extent of the particle fluid, i.e. when λ becomes larger than the system size. This issue is illustrated directly in the case of shock-driven implosions with low initial gas density, high temperatures, and $N_K>1$, as described in Chapter 3. For these implosions where the ion-ion mean free path (λ_{ii}) for D^{3}He fuel ions is greater than the radius of the fuel itself, how can a diffusion-like process be assessed?

Consider the example of OMEGA exploding pusher shot 69067, where the average ion-ion mean free path of fuel ions is λ_{ii}~900 μm, while the radius of the fuel-shell interface is R_{shell} ~90 μm, so that the Knudsen number N_K~10. If a diffusive process were transporting the ions from the center of the fuel region to the fuel-shell interface via a random walk (ignoring for now the fact that no collisions would occur over that distance), it would take an average ion $\tau_{diff} = R_{shell}^2/D$

---

[1] For the purposes of this discussion, ignore the fact that this diffusion picture, predicated on discrete large-angle collisions spaced out at intervals of λ, is somewhat different than the typical picture of transport in a plasma, which instead occurs over many small-angle collisions.

~20 ps to reach the fuel-shell interface (variables as defined in Appendix F). However, given that no collisions actually occur over that distance, the diffusion picture is not necessarily valid.

It is likely more accurate to consider instead the crossing time $\tau_{cross} \equiv R_{shell}/v_{th}$, the amount of time it takes for a thermal ion at velocity v_{th} to travel in a straight-line path the distance R_{shell} to the fuel-shell interface. For the case of shot 69067, with an ion temperature of 28 keV, the average ion thermal velocity is ~1500 μm/ns, and τ_{cross}~60 ps. That is, the time for an ion to travel directly from the center of the implosion to the fuel-shell interface is *longer* than the supposed diffusion time in this regime where the diffusion picture is invalid. Clearly, it is impossible for an ion to diffuse out of the fuel faster than it can do so on a straight-line path, and the true "ion transport time" in the fuel should be taken as the crossing time. In the case of shot 69067, it is still the case that the crossing time τ_{cross} (~60 ps) is shorter than the burn duration τ_{burn} (~120 ps), so that ions can freely stream out of the fuel over the time during which fusion production occurs. As such, these implosions are still appropriately described as well into the kinetic regime.

Comparing τ_{diff} and τ_{cross}, it is apparent that $\tau_{cross}>\tau_{diff}$ and, therefore, that the diffusion time calculation is inappropriate, when $N_K>3$. It is likely the case that diffusion as a concept is inappropriate at Knudsen numbers smaller than that, for $N_K\sim1$. This discussion so far has only considered what happens to the ions within the hot fuel; however, at the interface between the fuel and the shell, a diffusion picture becomes appropriate once again.

C.2 Ion Diffusion at the Fuel-Shell Interface

While under conditions of $N_K>1$ within the fuel itself, the diffusion picture breaks down, ion behavior at the interface between hot, light fuel ions and (relatively) cool, heavy shell ions can be accurately described by a diffusive process. When considering transport across the interface, the relevant mean free path is no longer that between two fuel ions, but is instead the mean free path for a fuel ion colliding with a shell ion. For example, the mean free path for a 28 keV D ion ($Z = 1$, $A = 2$) on an average SiO$_2$ shell ion ($Z = 10$, $A = 20$) fluid at a density of 5×10^{21} cm^{-3} (based loosely on the shell ion density in HYADES simulations of OMEGA shot 69067) is $\lambda_{D,shell}\sim30$ μm, a factor of 30 shorter than the mean free path for collisions among fuel ions. As such, a diffusion model is likely valid when considering the propagation of fuel ions into the shell. An appropriate picture of ion transport under such conditions, with extremely long mean free paths within the fuel, but modest mean free paths between fuel and shell ions, is as follows: fuel ions stream freely out of the fuel, but encounter collisional conditions upon reaching the fuel-shell interface, at which point they diffuse through the high-Z shell plasma.

Another important consideration is the opposite effect: the propagation of high-Z shell ions into the hot fuel region. Consider a shell O ion ($Z = 8$, $A = 16$) propagating into an average-ion D^{3}He ($Z = 1.5$, $A = 2.5$) fluid at a fuel ion density of 4×10^{21} cm^{-3} and a fuel ion temperature of 28 keV. The mean free path for O ion collisions with D^{3}He in the fuel is ~30 μm, based on a collision rate for slow O test ions (subscript 1) colliding with fast D^{3}He field ions (subscript 2) of

$$\nu_{slow1,fast2} = 6.8\times10^{-8} f_2 n_i\,(\mathrm{cm}^{-3})\left(\frac{1}{T_i\,(\mathrm{eV})}\right)^{3/2} Z_1^2 Z_2^2 \frac{A_2^{1/2}}{A_1}\left(1+\frac{A_2}{A_1}\right)\ln\Lambda_{12}\ \ \mathrm{s}^{-1}, \tag{C.1}$$

where n_i (T_i) is the ion density (temperature) of the D^{3}He fuel. Thus, the mean free path for collisions across the fuel-shell interface is ~30 μm both for fuel ions entering the shell and for shell ions entering the fuel. As this distance is fairly small relative to the implosion size, a diffusion model can be reasonably applied to the interface, though it is largely inapplicable to the fuel itself.

Using models of ion diffusion implemented in hydrodynamic codes, such as through the reduced-ion-kinetic (RIK) model, it will be possible to predict the extent of this diffusive effect. Clever experiments with different fuel and/or shell composition, to vary the mean free path of ion-ion collisions across the interface, can probe this effect. Measurements of the spatial burn profiles of the fuel ions themselves (possibly quenched by significant diffusion of high-Z shell ions into the outer regions of the fuel), and/or of reactions between shell ions and fuel ions (such as a CD shell with a ^{3}He or T fuel), can further elucidate diffusion across the interface.

C.3 References

Appendix D

Thomson Scattering Data from Laser-Foil and Magnetic Reconnection Experiments

A compendium of Thomson scattering data, from single laser-foil and dual laser-foil (magnetic reconnection) experiments, expanding on those which have been shown already in Chapter 5,[1] are presented in this appendix. In particular, the Thomson scattering spectra, which were previously only presented for one of six shots, are shown in their entirety. A table summarizing the assumed and inferred quantities based on fitting the measured spectra to the modeled form factor are also presented.

As was discussed and presented in Chapter 5, streaked Thomson scattering spectra were obtained on six shots, three in the single-bubble configuration and three in the dual-bubble (reconnection) configuration, as shown in Figure D.1. In each experiment, a 5-μm CH foil was irradiated by one or two 351 nm (3ω) beams in a 1-ns pulse with 500 J/beam and SG4 phase plates, producing an 800 μm spot size with a 4th-order supergaussian profile. For the dual-beam reconnection experiments, laser spots were separated by 1.2 mm. The 30-J, 3-ns Thomson-scattering probe beam was incident at a 79° angle relative to the foil normal, nearly parallel to the foil surface, while the detector was at 37° to the normal, such that the scattering angle was 63° and the scattering vector 21° to the foil normal. In each of the three shots for both the single-bubble and colliding-bubbles experiments, the Thomson scattering volume was located at a different region relative to the bubble(s). Streaked spectral images from each of the six shots are shown again in Figure D.2.

Snapshots in time are assessed by taking lineouts of the streaked spectra. These spectra are presented in Figures D.3-D.8, with the time of each spectrum indicated. The electron and ion temperatures inferred from fitting the measured spectra to the form-factor curves, as well as other fixed or adjustable inputs to the Thomson scattering model, are shown in Table D.1. As discussed in Chapter 5, the spacing between the two peaks in the spectrum is primarily sensitive to the electron temperature T_e, while the height of the plateau between the peaks is most sensitive to the ion temperature T_i. The bulk plasma velocity along the probe beam direction V_{par} causes a shift in the centroid of the Thomson scattering feature relative to the probe wavelength of 263.5 nm. The relative drift velocity u_d between electrons and ions along the scattering vector manifests as a difference in height between the two peaks. The electron density n_e most strongly dictates the total number of scattered photons, or the magnitude of the spectrum, though the magnitude was not used in fitting the spectra. Thus, fitting the spectral shape constrains V_{par}, u_d, and, as presented in Chapter 5 and published in *Physical Review E*,[1] T_e and T_i.

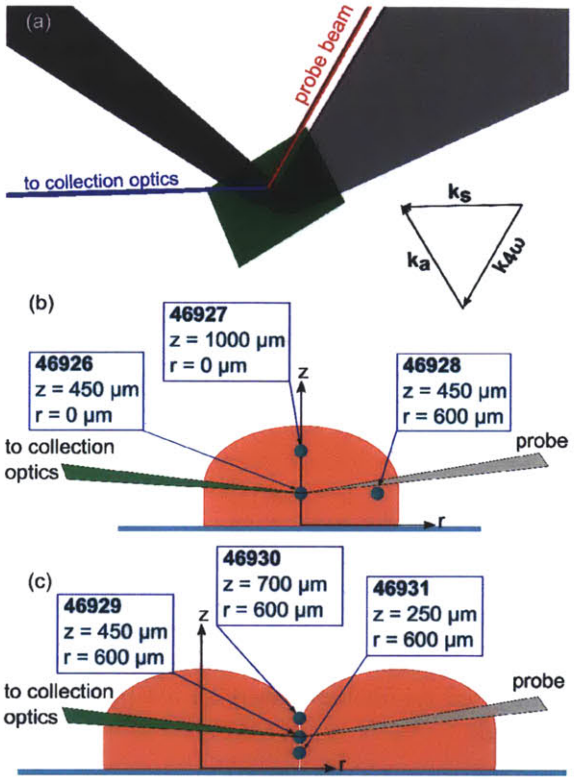
(a)
probe beam
to collection optics
k_s
k_a
$k_{4\omega}$
(b)
46927
z = 1000 μm
r = 0 μm
46926
z = 450 μm
r = 0 μm
46928
z = 450 μm
r = 600 μm
z
to collection optics
probe
r
(c)
46930
z = 700 μm
r = 600 μm
46929
z = 450 μm
r = 600 μm
46931
z = 250 μm
r = 600 μm
z
to collection optics
probe
r

Figure D.1. Experimental setup for the Thomson-scattering experiments (a). A dual laser-foil (colliding bubbles or reconnection) setup is depicted, as was used in three of the experiments. The other three used a single laser. In these experiments, the Thomson-scattering probe beam was incident at a 79° angle relative to the foil normal (z-axis), nearly parallel to the foil surface, while the detector was at 37° to the normal, such that the scattering angle was 63° and the scattering vector 21° to the foil normal. Locations probed are shown for (b) single bubble experiments and (c) reconnection experiments.

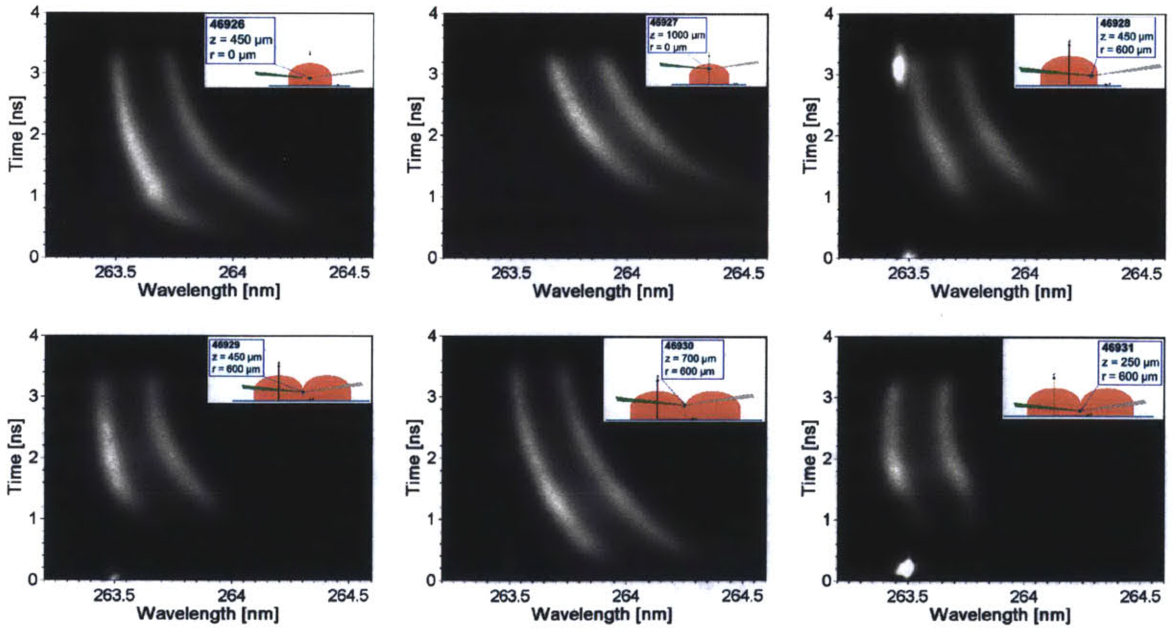

Figure D.2. Streaked Thomson scattering spectra from single bubble experiments (top) and interacting bubble experiments (bottom), at the locations depicted in Figure D.1. Lineouts of the streaked spectra, to generate time-dependent spectra (integrated over 120 ps), are shown in Figures D.3-D.8.

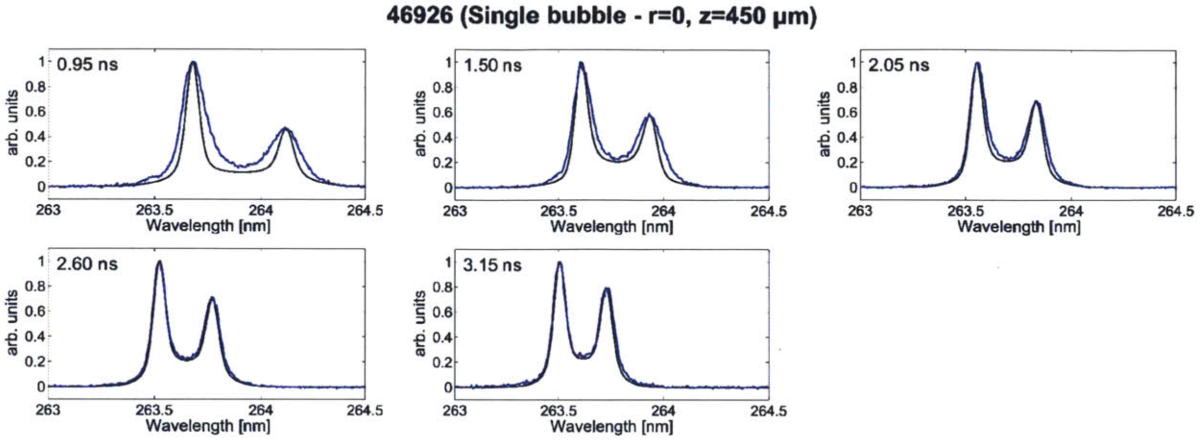

46926 (Single bubble - r=0, z=450 μm)

Figure D.3. Measured (blue) and best-fit modeled (black) Thomson scattering spectra obtained on OMEGA shot 46926, at times between 0.95 ns and 3.15 ns after the onset of the drive laser in this single-bubble experiment. The spectra have been integrated over 0.12 ns around the indicated times. The incident probe beam wavelength was $\lambda_0 = 263.5$ nm. These spectra capture plasma conditions at (r=0, z=450 μm). The assumed and inferred plasma conditions on the basis of this modeled spectrum are summarized in Table D.1. The modeled form factors have been convolved with a Gaussian of $\sigma = 0.023$ nm to account for instrumental broadening in the measured spectra.

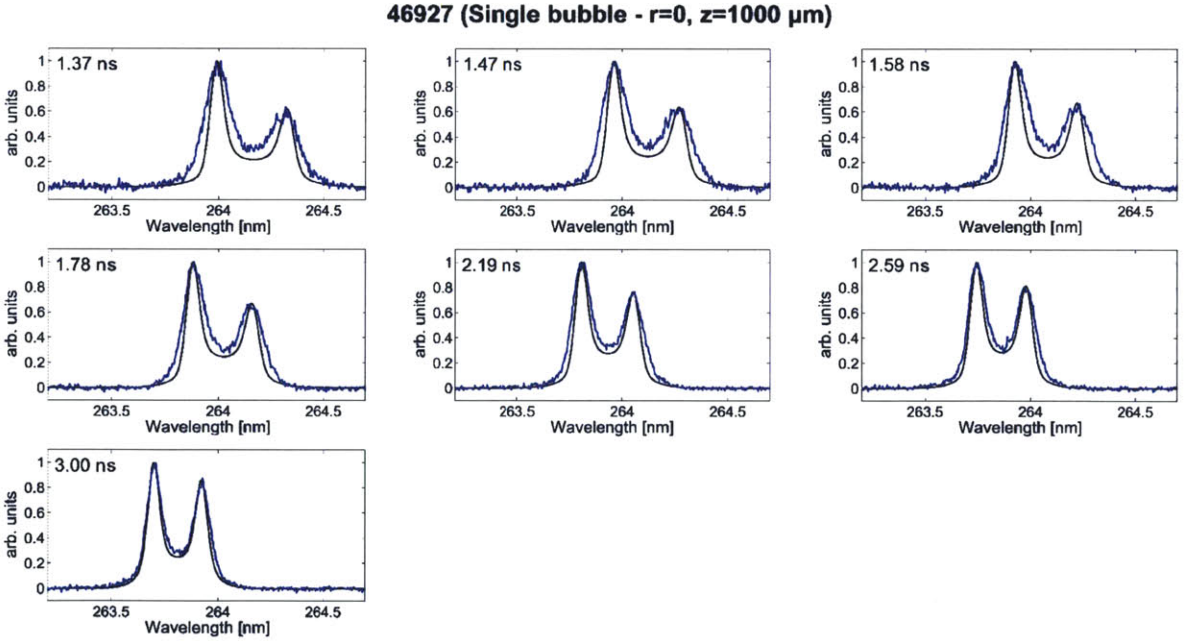

46927 (Single bubble - r=0, z=1000 μm)

Figure D.4. Measured (blue) and best-fit modeled (black) Thomson scattering spectra obtained on OMEGA shot 46927, at times between 1.37 ns and 3.00 ns after the onset of the drive laser in this single-bubble experiment. The spectra have been integrated over 0.12 ns around the indicated times. The incident probe beam wavelength was $\lambda_0 = 263.5$ nm. These spectra capture plasma conditions at (r=0, z=1000 μm). The assumed and inferred plasma conditions on the basis of this modeled spectrum are summarized in Table D.1. The modeled form factors have been convolved with a Gaussian of $\sigma = 0.023$ nm to account for instrumental broadening in the measured spectra.

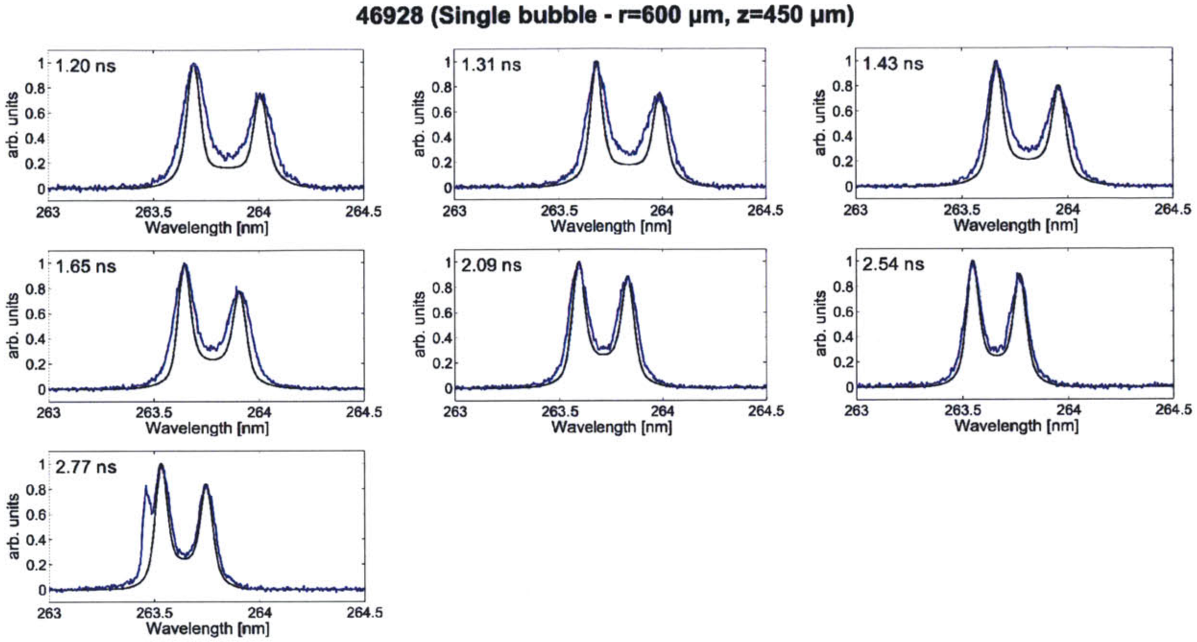

Figure D.5. Measured (blue) and best-fit modeled (black) Thomson scattering spectra obtained on OMEGA shot 46928, at times between 1.20 ns and 2.77 ns after the onset of the drive laser in this single-bubble experiment. The spectra have been integrated over 0.12 ns around the indicated times. The incident probe beam wavelength was $\lambda_0 = 263.5$ nm. These spectra capture plasma conditions at (r=600 μm, z=450 μm). The assumed and inferred plasma conditions on the basis of this modeled spectrum are summarized in Table D.1. The modeled form factors have been convolved with a Gaussian of $\sigma = 0.023$ nm to account for instrumental broadening in the measured spectra.

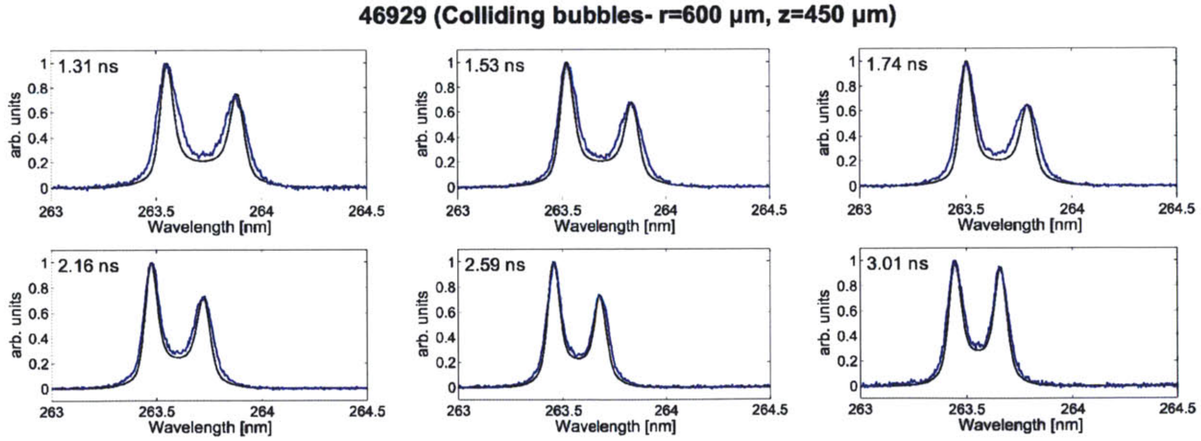

Figure D.6. Measured (blue) and best-fit modeled (black) Thomson scattering spectra obtained on OMEGA shot 46929, at times between 1.31 ns and 3.01 ns after the onset of the drive lasers in this colliding-bubbles experiment. The spectra have been integrated over 0.12 ns around the indicated times. The incident probe beam wavelength was $\lambda_0 = 263.5$ nm. These spectra capture plasma conditions at (r=600 μm, z=450 μm). The assumed and inferred plasma conditions on the basis of this modeled spectrum are summarized in Table D.1. The modeled form factors have been convolved with a Gaussian of $\sigma = 0.023$ nm to account for instrumental broadening in the measured spectra.

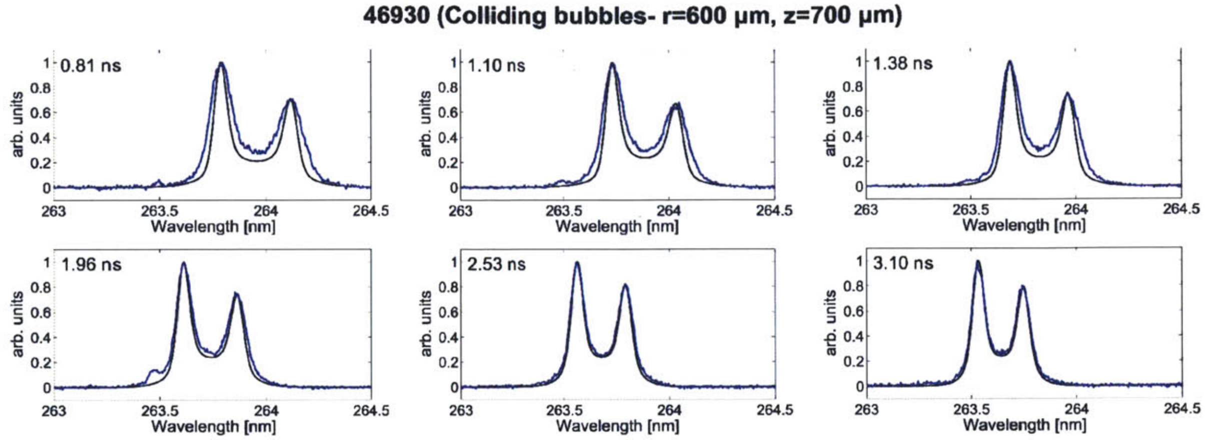

Figure D.7. Measured (blue) and best-fit modeled (black) Thomson scattering spectra obtained on OMEGA shot 46930, at times between 0.81 ns and 3.10 ns after the onset of the drive lasers in this colliding-bubbles experiment. The spectra have been integrated over 0.12 ns around the indicated times. The incident probe beam wavelength was $\lambda_0 = 263.5$ nm. These spectra capture plasma conditions at (r=600 μm, z=700 μm). The assumed and inferred plasma conditions on the basis of this modeled spectrum are summarized in Table D.1. The modeled form factors have been convolved with a Gaussian of $\sigma = 0.023$ nm to account for instrumental broadening in the measured spectra.

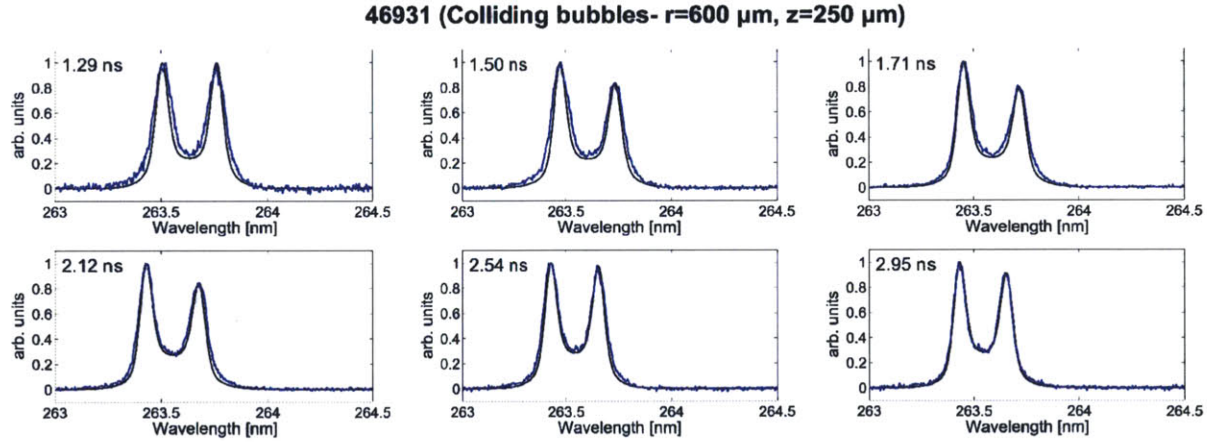

Figure D.8. Measured (blue) and best-fit modeled (black) Thomson scattering spectra obtained on OMEGA shot 46931, at times between 1.29 ns and 2.95 ns after the onset of the drive lasers in this colliding-bubbles experiment. The spectra have been integrated over 0.12 ns around the indicated times. The incident probe beam wavelength was $\lambda_0 = 263.5$ nm. These spectra capture plasma conditions at (r=600 μm, z=250 μm). The assumed and inferred plasma conditions on the basis of this modeled spectrum are summarized in Table D.1. The modeled form factors have been convolved with a Gaussian of $\sigma = 0.023$ nm to account for instrumental broadening in the measured spectra.

Table D.1. Time-dependent plasma conditions assumed or inferred from Thomson scattering spectra, including the electron density n_e, plasma flow velocity along the probe beam direction V_{par}, relative drift velocity between electrons and ions u_d along the scattering vector, and the electron and ion temperatures T_e and T_i. The ion population is 1:1 C:H. Time is measured from the onset of the drive lasers, and the spectra have integrated over 0.12 ns around the indicated time. The electron density is assumed, based on simulations (though as the magnitude of the spectrum is not used, it has only a small impact on the form factor). The plasma flow and relative electron-ion drift velocities are adjusted to optimize the form-factor fit, as are the electron and ion temperatures. Error bars for the electron and ion temperatures, the data which were actually reported, are based on the amount each parameter can be varied while maintaining a reasonable fit between the modeled form factor and the measured spectrum.

Time (ns)	n_e (cm^{-3})	V_{par} (μm/ns)	u_d (μm/ns)	T_e (keV)	T_i (keV)
46926 (Single bubble - r=0, z=450 μm)					
0.95	4.43×10^{20}	-830	880	1.10±0.20	0.60±0.19
1.50	3.69×10^{20}	-565	550	0.53±0.10	0.44±0.09
2.05	2.88×10^{20}	-400	300	0.41±0.06	0.28±0.07
2.60	2.46×10^{20}	-305	260	0.33±0.04	0.20±0.05
3.15	2.10×10^{20}	-240	150	0.27±0.04	0.15±0.05
46927 (Single bubble - r=0, z=1000 μm)					
1.37	1.06×10^{20}	-1350	580	0.60±0.16	0.45±0.15
1.47	1.08×10^{20}	-1270	540	0.50±0.13	0.43±0.15
1.58	1.09×10^{20}	-1180	430	0.46±0.12	0.36±0.14
1.78	1.09×10^{20}	-1070	400	0.40±0.10	0.32±0.11
2.19	1.00×10^{20}	-885	240	0.32±0.08	0.25±0.09
2.59	0.93×10^{20}	-745	170	0.29±0.06	0.22±0.08
3.00	0.87×10^{20}	-640	110	0.28±0.04	0.16±0.07
46928 (Single bubble - r=600 μm, z=450 μm)					
1.20	1.06×10^{20}	-720	300	0.65±0.17	0.26±0.16
1.31	0.91×10^{20}	-690	310	0.61±0.13	0.27±0.17
1.43	1.29×10^{20}	-640	210	0.49±0.11	0.29±0.15
2.65	1.34×10^{20}	-570	210	0.37±0.10	0.24±0.12
2.09	1.22×10^{20}	-435	100	0.32±0.08	0.21±0.10
2.54	1.00×10^{20}	-330	80	0.28±0.05	0.15±0.08
2.77	0.91×10^{20}	-290	120	0.26±0.04	0.14±0.06
46929 (Colliding bubbles - r=600 μm, z=450 μm)					
1.31	1.19×10^{20}	-450	330	0.63±0.10	0.41±0.12
1.53	1.33×10^{20}	-370	410	0.55±0.08	0.37±0.11
1.74	1.34×10^{20}	-305	410	0.45±0.09	0.30±0.10
2.16	1.19×10^{20}	-205	260	0.33±0.06	0.23±0.08
2.59	0.98×10^{20}	-140	110	0.28±0.04	0.16±0.06
3.01	0.83×10^{20}	-110	40	0.26±0.04	0.16±0.06
46930 (Colliding bubbles - r=600 μm, z=700 μm)					
0.81	0.74×10^{20}	-930	460	0.68±0.17	0.40±0.16
1.10	1.19×10^{20}	-790	430	0.48±0.12	0.38±0.13
1.38	1.34×10^{20}	-670	270	0.41±0.09	0.29±0.11
1.96	1.21×10^{20}	-490	240	0.34±0.06	0.23±0.08
2.53	0.94×10^{20}	-365	150	0.30±0.04	0.17±0.05
3.10	0.78×10^{20}	-290	160	0.26±0.03	0.14±0.04
46931 (Colliding bubbles - r=600 μm, z=250 μm)					
1.26	1.18×10^{20}	-275	0	0.37±0.07	0.20±0.09
1.50	1.33×10^{20}	-215	150	0.38±0.06	0.23±0.08
1.71	1.34×10^{20}	-175	190	0.38±0.05	0.25±0.07
2.12	1.21×10^{20}	-110	140	0.32±0.04	0.23±0.06
2.54	1.00×10^{20}	-85	20	0.28±0.03	0.18±0.05
2.95	0.85×10^{20}	-90	70	0.27±0.02	0.18±0.04

D.1 References

1. M. J. Rosenberg, J. S. Ross, C. K. Li *et al.*, "Characterization of single and colliding laser-produced plasma bubbles using thomson scattering and proton radiography," Phys. Rev. E, **86**, 056,407 (2012).

Appendix E

Proton Radiography Data from Magnetic Reconnection Experiments

A compendium of proton radiography data, including experimental setup and images, from laser-plasma magnetic reconnection experiments, some of which have been shown already in Chapter 6, are presented in this appendix. Data from the asymmetric magnetic reconection experiments – both 15-MeV- and 3-MeV-proton images – including experiments not discussed previously as well as repeated experiments, are shown in Section E.1 and discussed in Section E.6 in comparison to data showing the interaction of parallel magnetic fields. Images from the reconnection experiments using TNSA backlighting on OMEGA-EP, using protons at a variety of energies, are presented in Section E.2 and the data are discussed further in Section E.3. Data from additional experiments not previously discussed, with side-on radiography of reconnection experiments on OMEGA using monoenergetic proton backlighting, are shown in Section E.4. Finally, data from experiments probing the collision of parallel magnetic fields, using both 15-MeV and 3-MeV protons, are shown in Section E.5, and discussed further in Section E.6.

E.1 Monoenergetic Proton Radiography Images from Asymmetric Magnetic Reconnection Experiments on OMEGA

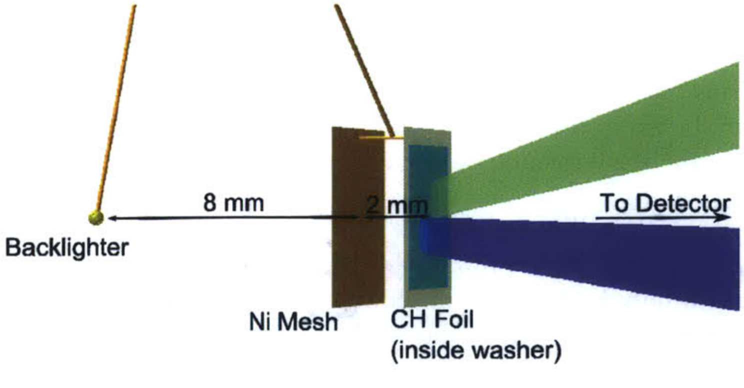

Figure E.1. To-scale depiction of experimental setup for asymmetric reconnection experiments on OMEGA. The two interaction beams are shown, but the backlighter drive beams have been hidden for clarity.

Experimental setup parameters from the asymmetric magnetic reconnection experiments on OMEGA are shown in Table E.1, and a depiction of the experiment (with backlighter beams turned off) is shown in Figure E.1. All experiments used a 60-μm thick, 150-μm period Ni mesh, positioned 2 mm away from the subject CH foil (5 μm thick, 4x4 mm in lateral dimension) toward the backlighter and 8 mm away from it. For all experiments, the backlighter-subject distance was 1.0 cm, while the distance from the backlighter capsule to the detector package was 27 cm for shots 61729-61733 and 28 cm for shots 64608-64611, such that the magnification was M = 27 or M = 28. On shots 61729-61733, two experiments were fielded on opposite sides of the backlighter capsule, with detector packages in OMEGA ports TIM 4 and TIM 6. All laser beam durations were 1 ns.

Table E.1. Experimental setup parameters for asymmetric magnetic reconnection experiments on OMEGA, including the OMEGA shot number, detector port position, backlighter laser energy, interaction laser energies, backlighter DD yield (DD-n measured by nTOF), backlighter D^3He yield (D^3He-p measured by PTD), and sample time for 15-MeV-protons relative to the interaction laser onsets.

Shot	Det. Loc.	BL Laser E (kJ)	Int. Laser E (kJ)	Y_{DD}	Y_{D^3He}	15-MeV-p Sample Time (ns)
61729	TIM 4	11.4	0.48/0.49	8.1×10^8	3.1×10^8	0.6/0.6
61729	TIM 6	11.4	0.49/0.48	8.1×10^8	3.1×10^8	0.3/1.0
61730	TIM 4	12.0	0.49/0.49	5.8×10^8	3.4×10^8	0.6/1.3
61730	TIM 6	12.0	0.50/0.49	5.8×10^8	3.4×10^8	0.4/1.0
61731	TIM 4	11.7	0.48/0.48	7.5×10^8	2.7×10^8	0.6/1.3
61731	TIM 6	11.7	0.49/0.48	7.5×10^8	2.7×10^8	0.3/1.7
61732	TIM 4	11.9	0.48/0.49	6.1×10^8	2.2×10^8	1.0/1.3
61732	TIM 6	11.9	0.49/0.49	6.1×10^8	2.2×10^8	0.3/1.7
61733	TIM 4	11.6	0.49/0.49	5.5×10^8	1.7×10^8	1.0/1.3
61733	TIM 6	11.6	0.49/0.50	5.5×10^8	1.7×10^8	1.3/1.3
64608	TIM 6	11.4	0.51/0.49	5.5×10^8	1.3×10^8	0.6/1.0
64609	TIM 6	11.7	0.52/0.50	4.7×10^8	1.3×10^8	1.0/1.0
64610	TIM 6	11.3	0.50/0.49	4.0×10^8	1.0×10^8	1.0/1.7
64611	TIM 6	11.5	0.50/0.49	4.1×10^8	0.7×10^8	1.3/1.7

The complete set of 15-MeV- and 3-MeV-proton radiography images from the asymmetric magnetic reconnection experiments is shown in Figure E.2. Like in Chapter 6, these images are presented in terms of the duration of time that the two plasma bubbles have been interacting and the degree of asymmetry in terms of the relative laser onset delay. A second set of images, corresponding to duplicates of some of the experiments, is shown in Figure E.3. These images demonstrate excellent repeatability, both in the experimental setup and execution and in the acquisition of the proton radiography data.

In all cases, as was explained in Chapter 5, while the 15-MeV-proton radiography images preserve the grid structure, the 3-MeV protons are smeared out and appear as a nearly-continuous fluence of protons, with only hints of the mesh apparent. The 3-MeV-proton radiography images are obtained slightly later in time, due to the ~0.2 ns longer flight time for 3-MeV protons in comparison to 15-MeV protons over the 1 cm distance between the backlighter capsule and the plasma. Because the 3-MeV protons sample the experiment later in time, the plasma bubbles are larger in radius and also generally have a stronger path-integrated magnetic field strength and more total magnetic flux when the 3-MeV protons arrive. Additionally, as a consequence of having a lower energy, these protons are more strongly deflected by the magnetic fields and produce structures in the proton radiography images that appear to have a larger radius. These 3-MeV-proton radio-

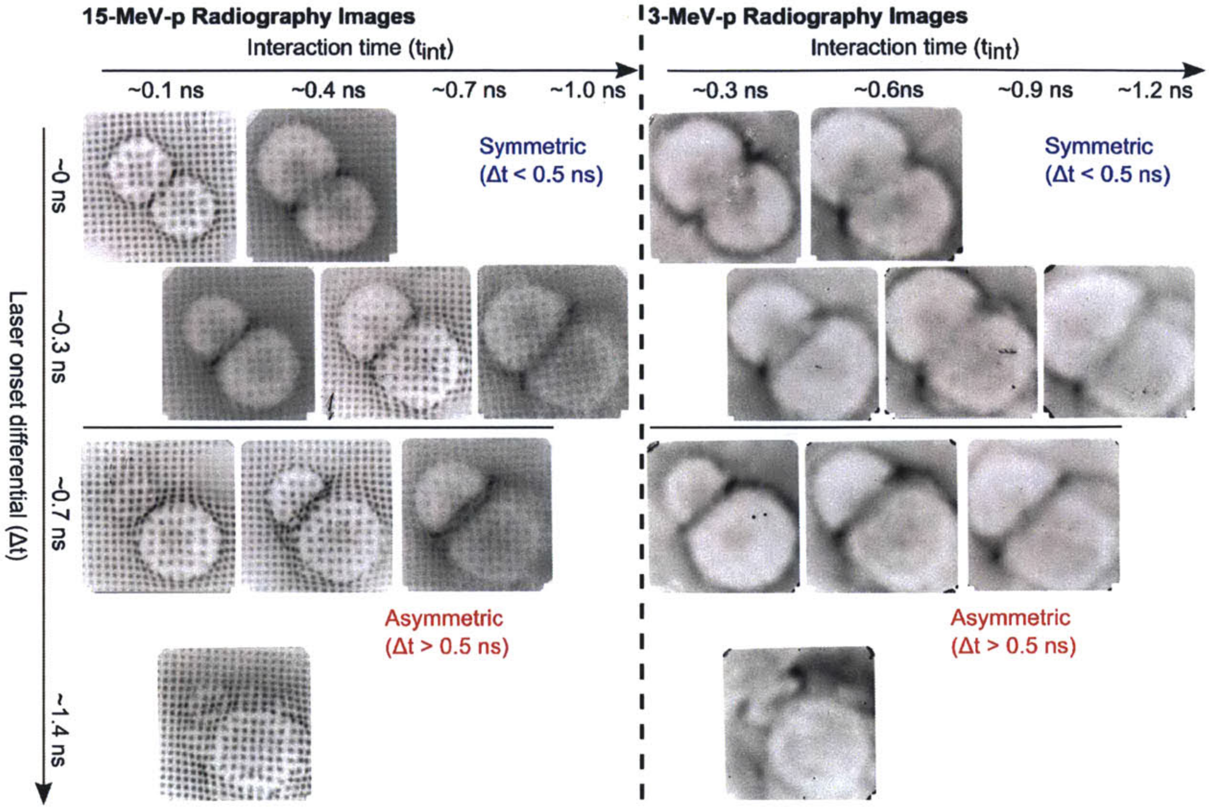
15-MeV-p Radiography Images
Interaction time (t_{int})
~0.1 ns
~0.4 ns
~0.7 ns
~1.0 ns
3-MeV-p Radiography Images
Interaction time (t_{int})
~0.3 ns
~0.6ns
~0.9 ns
~1.2 ns
Symmetric
(Δt < 0.5 ns)
Asymmetric
(Δt > 0.5 ns)
Laser onset differential (Δt)
~0 ns
~0.3 ns
~0.7 ns
~1.4 ns

Figure E.2. Monoenergetic 15-MeV-proton and 3-MeV-proton radiography images at different times in asymmetric magnetic reconnection experiments on OMEGA, in terms of how long the two plasma bubbles have been interacting (increasing $t_{int.}$ to the right) and the degree of asymmetry (increasing Δt down). Each image has a field of view at the foil 3.6 mm on a side.

graphs show similar structures as the 15-MeV-proton radiography images, with the fluence in the interaction region reflecting the annihilation of magnetic fields due to reconnection.

The 3-MeV-proton radiography images provide corroborating evidence that the path-integrated magnetic field maps shown in Chapter 6 are interpreted properly in the interaction region. While the 15-MeV-proton image for the asymmetric experiment at $\Delta t = 0.7$ ns and $t_{int} = 0.4$ ns shows a fairly broad proton fluence feature in the interaction region, the 3-MeV-proton image shows a narrower feature. Considering that the 3-MeV protons are deflected more strongly than the 15-MeV protons by whatever magnetic fields are present at the interaction region, this result demonstrates that the protons piled up in the interaction region do not " cross over", signifying weaker magnetic fields and their annihilation due to reconnection.

The 3-MeV-proton image in the symmetric images in Figure E.2 (t_{int}~0.6 ns, top row) also show hints of a plasma jet emerging from the reconnection region. This type of jet feature was previously reported in experiments on OMEGA-EP using high-resolution backlighting. The effective resolution of the 3-MeV-proton images obtained on OMEGA is sufficient to resolve the overall jet structure, and its appearance is qualitatively similar to that observed in the OMEGA-EP experiments described in Chapter 5.

A summary of the magnetic-field data obtained in these experiments is presented in Table E.2.

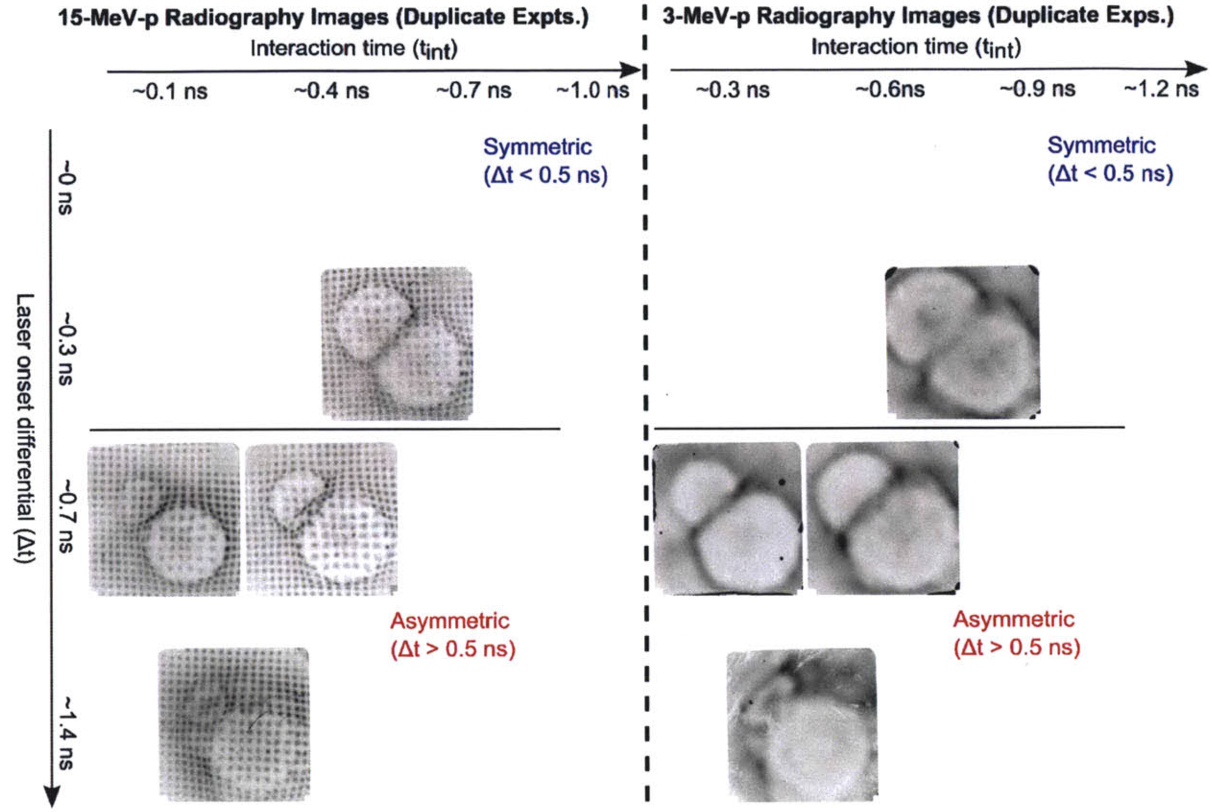

Figure E.3. Monoenergetic 15-MeV-proton and 3-MeV-proton radiography images from duplicate asymmetric magnetic reconnection experiments. The similarity between these images and their counterparts in Figure E.2 demonstrate excellent experimental repeatability.

E.2 Proton Radiography Images from Magnetic Reconnection Experiments on OMEGA-EP

A summary of experimental conditions for proton radiography of magnetic reconnection experiments on OMEGA-EP is shown in Table E.3, including backlighter and subject laser energies and durations, experimental timing, and relevant distances, and a depiction of the experiment is shown in Figure E.4. The experiments used a 12 μm thick, 5x5 mm CH foil. The backlighter foil targets consisted of 10 μm thick Au foils, separated by 2 mm by a cylindrical washer from a 5 μm thick piece of Ta to shield the backlighter foil from x-rays produced in the main drive. The face-on backlighter foil was parallel to the CH foil and 8 mm away from it. The side-on backlighter foil was perpendicular to the CH foil and 8 mm from its center (5.5 mm from its edge), and offset 1 mm laterally from the plane of the CH foil in the direction of the expanding plasma bubbles. For both face-on and side-on radiography, the RCF detector packs were 12 cm from the CH foil, such that the magnification was M = 16. The interaction lasers had a duration of 1 ns, while the side-on backlighter ("sidelighter") beam had a duration of 10 ps and the face-on backlighter ("backlighter") beam had a duration of 1 ps.

Face-on and side-on proton radiography images at a variety of proton energies, based on the energy of greatest sensitivity on that particular piece of radiochromic film, are shown in Figures E.5 and E.6, respectively. These images are presented in terms of the duration of time since the

Table E.2. Magnetic field data for asymmetric magnetic reconnection experiments on OMEGA, including the OMEGA shot number and detector port position (see Table E.1), path-integrated field strength through the perimeter of plasma bubbles 1 and 2, total magnetic flux at the perimeter of plasma bubbles 1 and 2, total magnetic flux in the interaction region of the plasma bubbles, and duration of time that the plasma bubbles have been interacting (t_{int}).

Shot-Loc.	$\lvert\int \mathbf{B}\times\mathbf{dl}\rvert_{per,1}$ MG μm	$\lvert\int \mathbf{B}\times\mathbf{dl}\rvert_{per,2}$ MG μm	$\Phi_{per,1}$ MG μm mm	$\Phi_{per,2}$ MG μm mm	Φ_{int} MG μm mm	t_{int} (ns)
61729-T4	85±10	90±10	34±6	39±5	54±6	0.04
61729-T6	25±5	110±10	8±2	59±7	43±7	0.02
61730-T4	80±10	115±15	25±5	75±9	75±9	0.33
61730-T6	25±5	110±15	9±2	59±7	56±8	0.04
61731-T4	75±10	120±15	22±5	80±9	69±9	0.35
61731-T6	30±10	90±15	14±4	62±7	58±8	0.06
61732-T4	110±15	115±15	57±8	72±8	64±6	0.53
61732-T6	25±10	90±15	7±3	55±4	48±5	0.08
61733-T4	120±15	125±15	67±9	78±9	51±7	0.50
64608-T6	85±10	110±15	43±7	68±8	56±7	0.20
64609-T6	150±20	120±15	75±10	52±8	64±8	0.38
64610-T6	120±15	115±15	61±13	75±11	74±10	0.72
64611-T6	120±15	100±20	65±12	70±13	47±8	0.85

onset of the interaction lasers. The different images mostly reflect the varying sensitivity of protons of that particular energy to the electric and magnetic field structures, though there is also a slight difference in sample time related to the proton time of flight (35-MeV protons arrive ~75 ps earlier than 15-MeV protons).

By virtue of the exponentially decaying proton spectrum, a significantly higher fluence of protons is incident on the lower-energy films than the higher-energy films. As a result, for the face-on radiography, with a 190 J, 1 ps backlighter laser, many of the lower-energy films (numbers 1 through 3 – 4.7, 7.1, 8.9 MeV) are saturated, and even the film sensitive predominantly to ~10.5-MeV protons is partially saturated. At the other extreme, the higher-energy films (numbers 10 through 12 – 42.5, 51.0, 60.9 MeV) have too little proton signal to reveal any features in the image. For the side-on radiography, with a 835 J, 10 ps backlighter laser, the proton spectrum is overall lower in energy and weaker in proton fluence. There are no useful images at proton energies >25 MeV, as the proton fluence is too weak, and films with proton energies as low as 9 MeV produce non-saturated images.

E.3 Additional Discussion of Data from Magnetic Reconnection Experiments on OMEGA-EP

Additional discussion of reconnection data from OMEGA-EP, expanding on that presented in Chapter 6, is discussed in this section.

In this work, high-resolution proton radiography has produced images of magnetic fields and dynamics in the magnetic reconnection of colliding laser-produced plasma bubbles of unprecedented detail and clarity. In these experiments, simultaneous proton backlighting and sidelighting has

Table E.3. Experimental setup parameters for magnetic reconnection experiments on OMEGA-EP, including the OMEGA-EP shot number, backlighter laser energy (1 ps duration), sidelighter laser energy (10 ps duration), interaction laser energies (1 ns duration), and sample time for 24-MeV-protons relative to the interaction laser onsets.

Shot	BL Laser E (J)	SL Laser E (J)	Int. Laser E (J)	24-MeV-p Sample Time (ns)
12567	195	390	934/934	0.9/0.9
12568	189	833	948/952	1.3/1.3
12569	189	833	912/930	0.3/0.3
12570	190	839	913/923	1.8/1.8
12571	186	838	921/909	0.3/1.3

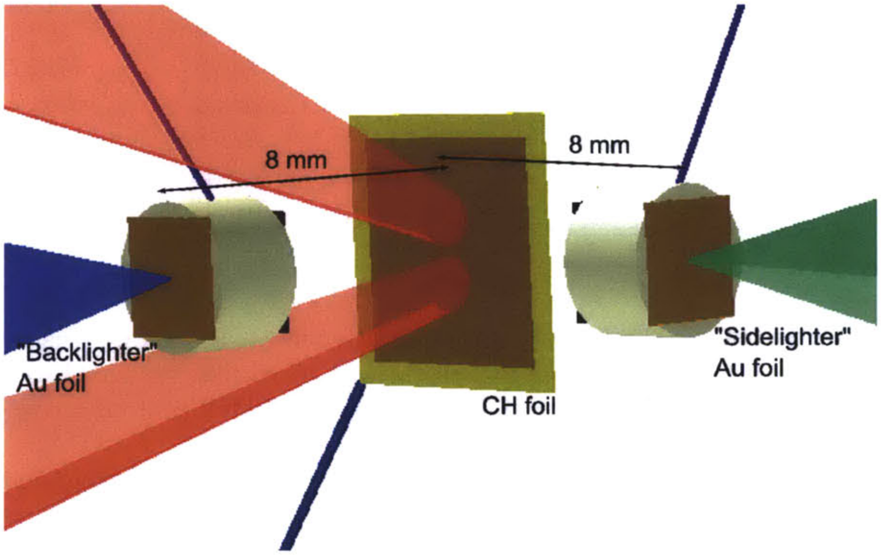

Figure E.4. To-scale depiction of experimental setup for magnetic reconnection experiments on OMEGA-EP.

allowed for imaging of electric and magnetic field structures in both the in-plane and out-of-plane directions. These images provide new insight into field structures and dynamics around both individual laser-produced plasma bubbles and their interaction, where magnetic reconnection and the hydrodynamic collision of plasma in the high-energy-density regime[1,2] occurs.

For the purposes of this discussion and to hone in on particularly compelling data, Figure E.7 shows the most revealing face-on (top) and side-on (bottom) radiography images. The fluence modulations across the images are largely due to the deflection of backlighter protons by electric and (predominantly) magnetic fields around the laser-produced plasma bubbles and in their interaction. As in Chapter 5 the times indicated are between the onset of the interaction beams and the arrival of ~10-24-MeV backlighter protons. Some aspects of the timing on each experiment were verified using the ultra-fast x-ray streak camera (UFXRSC),[3] which measures the relative timing between the backlighter and sidelighter beams.

The face-on images reveal several features relevant to magnetic reconnection and laser-produced

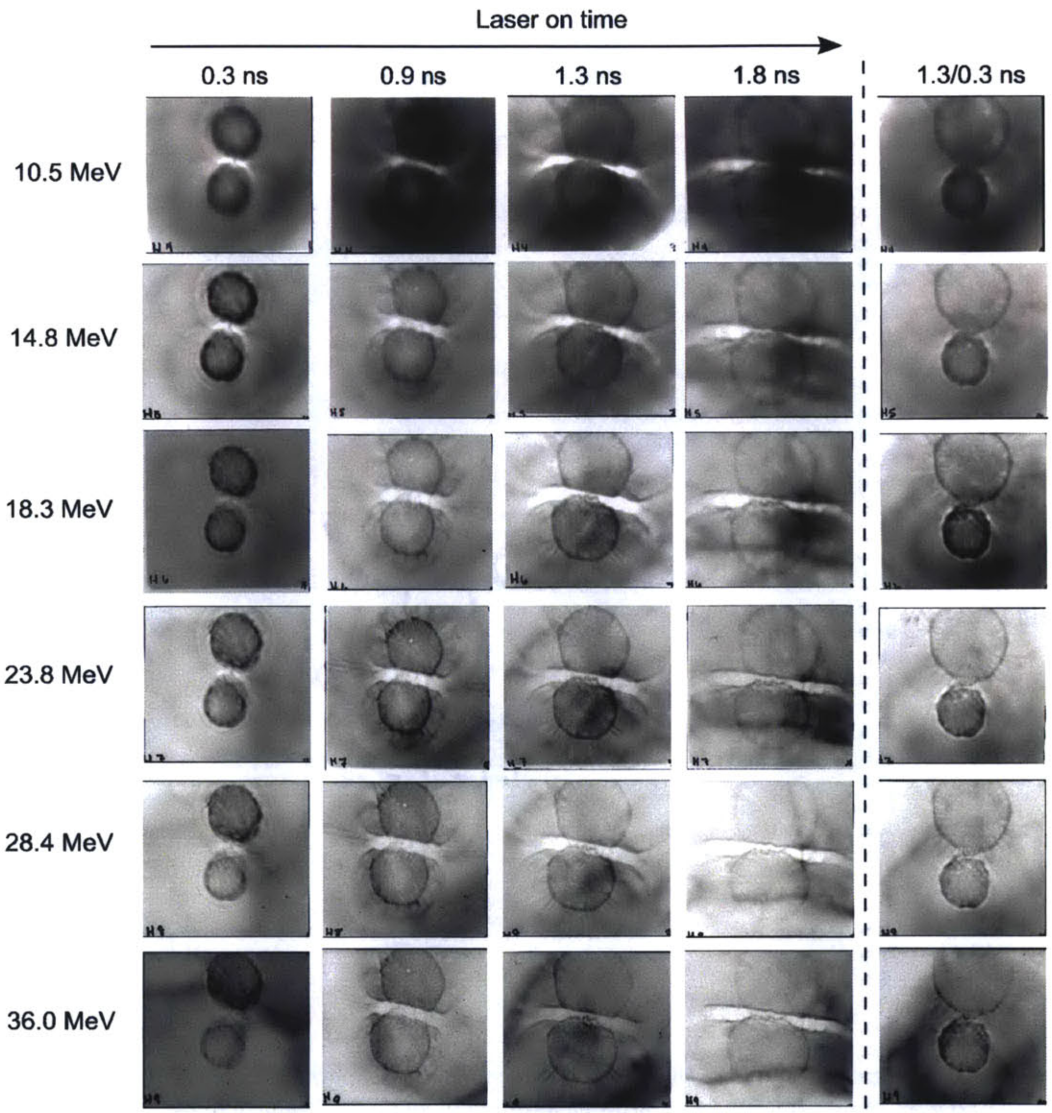
Laser on time
0.3 ns
0.9 ns
1.3 ns
1.8 ns
1.3/0.3 ns
10.5 MeV
14.8 MeV
18.3 MeV
23.8 MeV
28.4 MeV
36.0 MeV

Figure E.5. Face-on proton radiography images of reconnection experiments on OMEGA-EP at different times relative to laser onset. Images using protons of different energies obtained on each shot are shown. The sharper images were obtained by microdensitometer scan with a red filter, while the fuzzier images were obtained from a simple, flatbed scanner, with one color component (red, blue, or green) selected. Contrast has been optimized in each individual image to enhance proton fluence structures. Each image has a field of view at the foil 3.7 mm on a side.

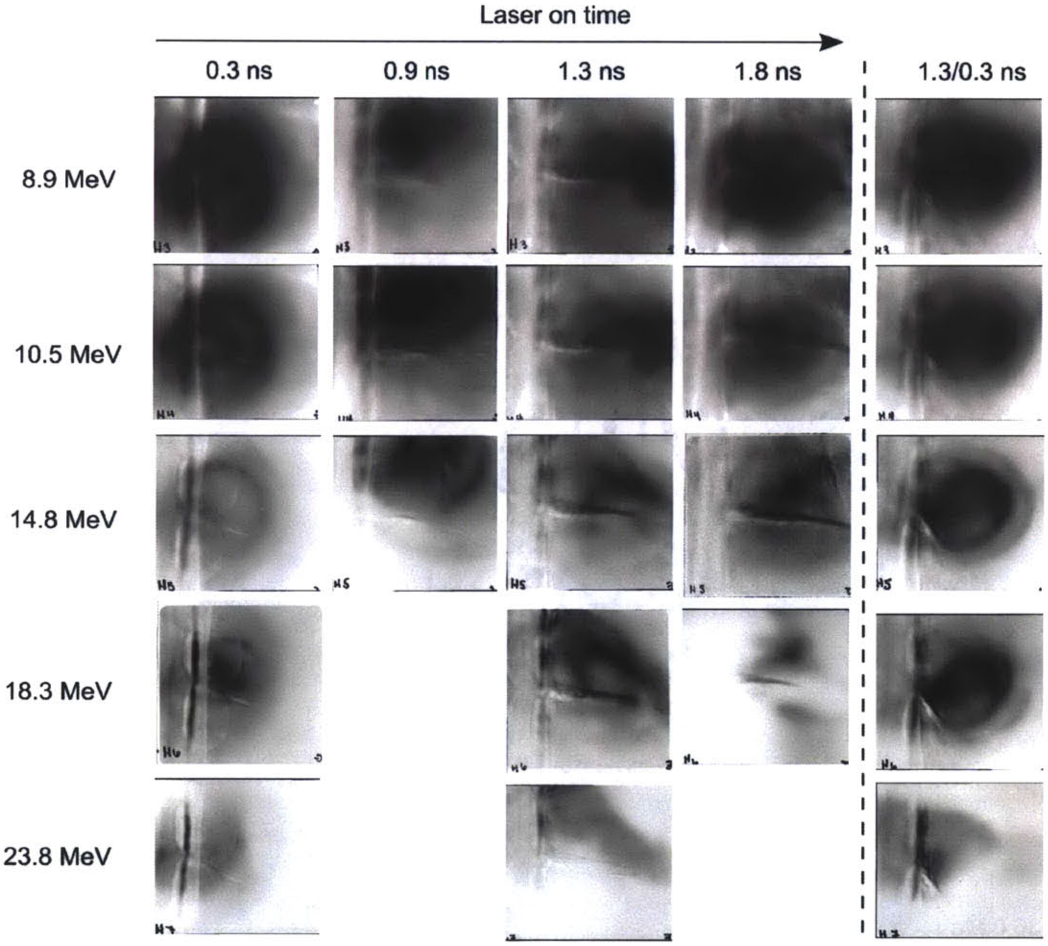
Laser on time
0.3 ns
0.9 ns
1.3 ns
1.8 ns
1.3/0.3 ns
8.9 MeV
10.5 MeV
14.8 MeV
18.3 MeV
23.8 MeV

Figure E.6. Side-on proton radiography images of reconnection experiments on OMEGA-EP at different times relative to laser onset. Images using protons of different energies obtained on each shot are shown.The sharper images were obtained by microdensitometer scan with a red filter, while the fuzzier images were obtained from a simple, flatbed scanner, with one color component (red, blue, or green) selected. Contrast has been optimized in each individual image to enhance proton fluence structures. Each image has a field of view at the foil 3.7 mm on a side.

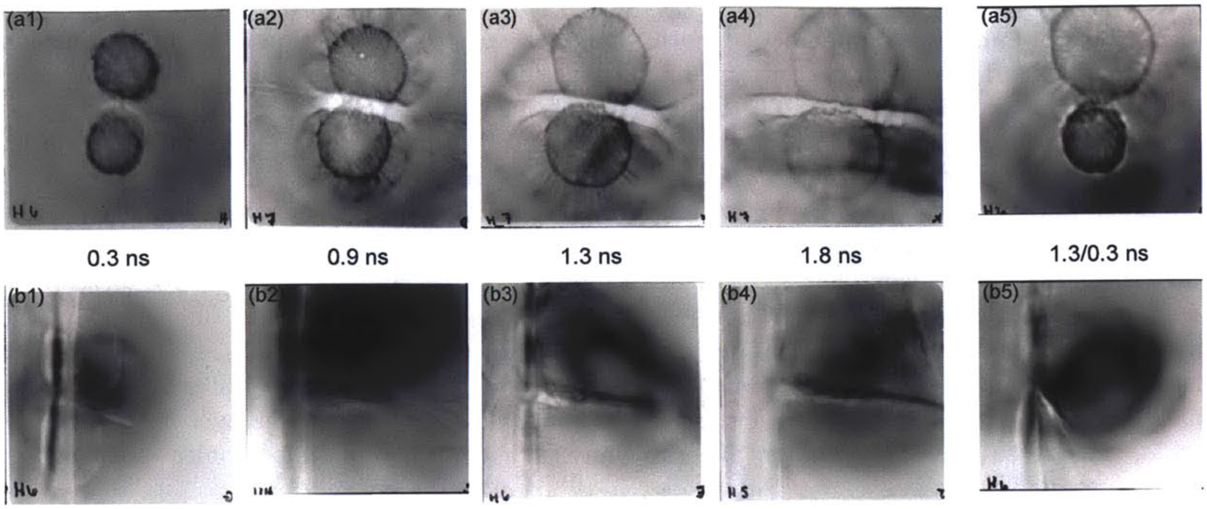

Figure E.7. Proton radiography images at different times relative to the onset of the interaction beams, for both (a) face-on and (b) side-on radiography, with dark areas representing greater proton fluence. Contrast has been optimized differently in each image to reveal details. The times indicated are between the onset of the interaction beams and the arrival of backlighter protons. The alphanumeric labels at the bottom-left of each film denote the position in the film stack and the proton energy of greatest sensitivity on that film: H4 (10.5 MeV), H5 (14.8 MeV), H6 (18.3 MeV), and H7 (23.8 MeV). Each image has a field of view at the foil ~3.7 mm on a side.

plasmas, some of which have been already discussed in the main text. The most readily apparent feature is the pileup of protons in a circular pattern due to their inward deflection by ~MG azimuthal magnetic fields at the bubble perimeters. These fields are generated by the Biermann battery mechanism, arising due to non-parallel gradients in electron density and electron temperature, with $\partial B/\partial t \propto \nabla T_e \times \nabla n_e$. The deflection due to magnetic fields is evident in the interaction region as well by a strong deficit of protons along a flat sheet where the plasma bubbles collide. Here the plasma bubbles are flattened against each other and the protons are deflected back toward the bubble centers due to the strong magnetic fields piled up just outside the current sheet. This region of strong magnetic fields lengthens at a rate of approximately 1500 μm/ns. Also apparent near the interaction region are in-plane jets, especially prominent at 0.9 ns (a2), and a "double-Y"-shaped structure, produced by lines of ~0.1 MG magnetic fields extending outward from the reconnection region at 1.3 ns (a3).

The coronae of the plasma bubbles also contain features of laser-produced plasmas that are revealed in more detail than have been observed in previously-reported experiments.[4–6] The images at 0.3 ns show a halo of proton fluence of diameter ~1600 μm at the outer corona in both the face-on (a1) and side-on (b1) images, suggestive of a radial electric field generated by the electron pressure gradient at the bubble perimeter. A skin of electric field of thickness ~60 μm and magnitude ~2×10^8 V/m is inferred from the proton deflection. The flare-like features at 0.9 ns (Figure E.7(a2)) may represent interchange phenomena, which have been observed previously[5], or the onset of the Weibel instability. Radial spokes of proton fluence at 1.3 ns in Figure E.7(a3) and (a5) may be the result of Weibel-related current filaments at the plasma bubble perimeters, where large temperature gradients are present. The periodicity of this structure is 8° and the magnetic field magnitude is of order 0.05 MG. Filamentary structures due to possible radial currents have been observed in proton radiography of inertial confinement fusion implosions.[7]

The side-on images primarily show the out-of-plane jet produced by the hydrodynamic collision of the plasmas bubbles – perpendicular both to the foil and to the direction of bubble expansion at the midplane. This jet and its entrained field structures extend farther from the foils with time, with an estimated velocity of ~1100 μm/ns, a Mach number of M~4 relative to a sound speed of 290 μm/ns for a T_e~1 keV CH plasma. While earlier in time (e.g. at 1.3 ns in (b3)) the jet field structure appears somewhat turbulent, by 1.8 ns it has become much more uniform with a consistent upward deflection of sidelighter protons, suggesting a plane of magnetic fields in the direction of jet propagation with B ~0.02 MG. These fields may have been advected from the magnetized plasma collision. For an ion number density of 10^{20} cm^{-3}, a length of 3 mm, a width of 2.5 mm, and a height of 0.2 mm, the out-of-plane jet contains ~85 J of kinetic energy. In the asymmetric experiment (b5), the jet appears at a steep angle relative to the foil, 34°, in contrast to the near-90° propagation of the jets in the symmetric experiments. This jet propagation suggests that the reconnection current sheet is similarly angled, with the reconnection layer not parallel to the foil surface as inferred in similar experiments with asymmetric plasma bubbles (see Chapter 6).[8]

The large-scale proton fluence features illustrate the bulk magnetic fields around the interacting plasmas. Unlike in previous work using grid-based monoenergetic proton radiography,[9,8] where the deflection of discrete proton beamlets was used to infer directly the proton-path-integrated magnetic field strength, the path-integrated magnetic fields in these experiments are estimated qualitatively by means of matching structures in synthetic proton images to the data. A set of 24-MeV-proton images (a1-a3) and their synthetic analogs produced using proton ray-tracing (b1-b3) through hypothesized field structures (c1-c3) are shown in Figure E.8. The synthetic images are optimized to match the measured separation of the plasma bubbles, the radii of the proton pileup features, the length and width of the proton deficit region at the center, and the chord length of the circular pileup feature where it intersects the deficit region. The artificial field structures give a qualitative picture of the extent and geometry of the path-integrated field structures in the experiment.

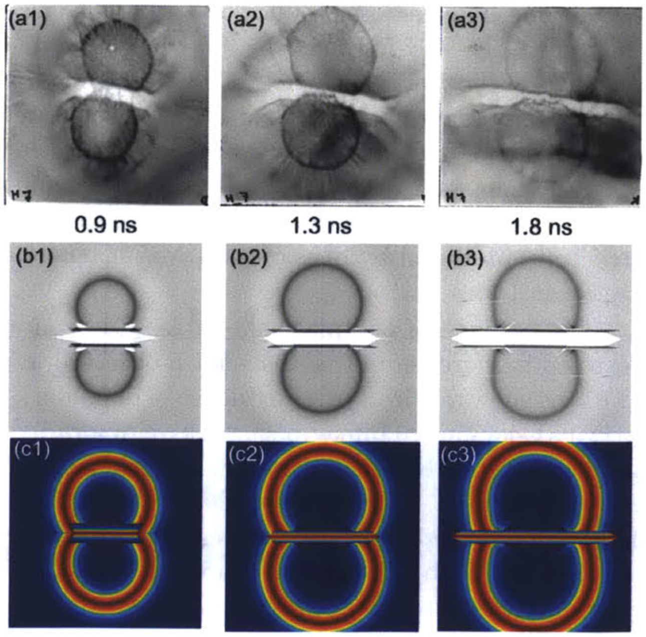

Figure E.8. Face-on proton images from Figure E.7 (a2-a4) at different times relative to the onset of the interaction beams (a1-a3) and synthetic images (b1-b3) produced from magnetic field structures (c1-c3).

The inferred path-integrated magnetic field structure is an expanding radially-Gaussian annulus with a σ~180 μm. The peak path-integrated magnetic field strength is 150 MG μm, comparable to that measured in prior experiments.[5,8] With a scale height in the hundreds of microns, the magnetic field strength is of order 0.5 MG. The expansion speed of the magnetic field annulus is ~500 μm/ns between 0.9 and 1.3 ns, but then slows to ~150 μm/ns between 1.3 ns and 1.8 ns, while the laser is off. As the interaction proceeds, the layer of magnetic fields in the reconnection region becomes compressed and elongated, such that by 1.8 ns the field layer piled up outside the current sheet is longer (1700 μm) than the diameter of the plasma bubbles (~1500 μm). In order to produce the near-uniform deficit of protons, the field structure in the interaction region is a Gaussian profile in the vertical direction.

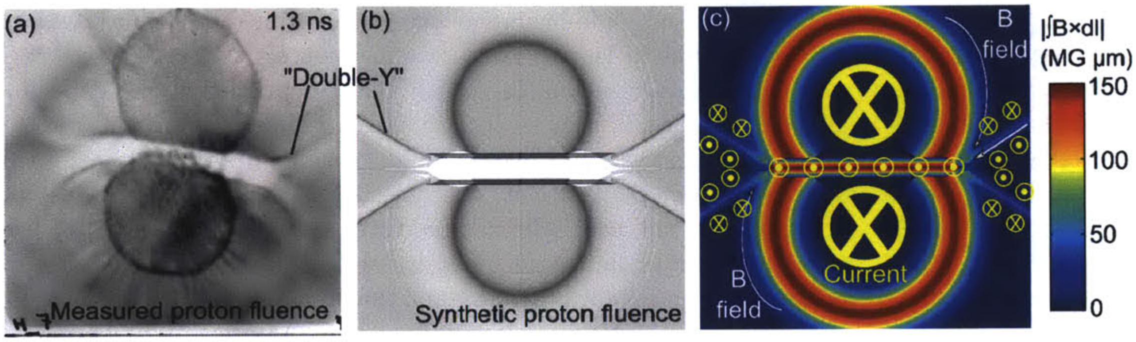

Figure E.9. (a) 24-MeV proton radiograph and (b) synthetic proton image produced from (c) artificial path-integrated field map. The "double-Y" feature in the proton fluence image is generated by lines of magnetic fields distinct from the original azimuthal field structure and appear to follow typical electron flow patterns around the separatrix associated with Hall reconnection. Out-of-plane currents consistent with these in-plane magnetic field structures are indicated.

The "double-Y" feature in the proton fluence image at 1.3 ns reflecting magnetic fields and flows around the magnetic separatrix in a geometry reminiscent of electron currents in two-fluid reconnection. This structure corresponds to lines of magnetic field roughly in the same direction as the bulk magnetic field structure (clockwise relative to each bubble), though not part of the original annulus of magnetic flux, as shown in Figure E.9. The artificial path-integrated magnetic field structure (Figure E.9c), inferred by matching large-scale proton fluence features in a synthetic proton fluence image (Figure E.9b) to features in the measured image (Figure E.9a), illustrates how these lines of magnetic field stream out from the edge of the reconnection region. The "double-Y" field structure follows the pattern of a magnetic separatrix as it emerges from the edges of the highly compressed reconnection layer. This feature is ~500 μm long, such that between t = 0.9 ns and 1.3 ns, it lengthened at a velocity of ~800 μm/ns, about half as rapidly as the propagation of the electron jet. The half-angle of this feature relative to the current sheet is 25°, implying a normalized reconnection rate of 0.4, of a similar magnitude to models of collisionless reconnection.

This separatrix magnetic field structure is consistent with a reversal of out-of-plane currents of a similar magnitude to that in the electron jet (see Chapter 6), as expected in two-fluid reconnection. The pattern of currents illustrated in Figure E.9c, with the reconnection (out-of-plane) current sheet matching the direction of the outflow-side current and opposing the inflow-side current, is observed in simulations of two-fluid reconnection.[10] The path-integrated magnetic field strength inferred from the "double-Y" proton fluence structure is $|\int \mathbf{B}\times d\mathbf{l}|$ ~30 MG μm, about 25% of that in the reconnection region, with an approximate B ~0.06 MG for an out-of-plane scale height *dl* ~500 μm. This field is self-consistent with an out-of-plane current ~1.5 kA over a 50 μm in-plane length scale. The magnitude of this out-of-plane current is of the same order as that carried by the electron jets, as described in Chapter 5, suggesting that they are part of the same system of currents, though the jet appears earlier in time and is ejected at a greater velocity. This electron current may also have an in-plane component oriented roughly along the separatrix, as is expected in the two-fluid reconnection picture; however, the backlighter protons are not sensitive to in-plane components of the current.

E.4 Side-On Monoenergetic Proton Radiography Images from Magnetic Reconnection Experiments on OMEGA

In an experiment not previously discussed, side-on monoenergetic proton radiography was used to investigate out-of-plane field structures in laser-plasma reconnection experiments on OMEGA. Experimental setup parameters are summarized in Table E.4 and a depiction of the experiment (with backlighter beams turned off) is shown in Figure E.10. These experiments used a 60-μm thick, 150-μm period Ni mesh, positioned 1 mm away from the edge of the subject CH foil (50 μm thick, 5x5 mm in lateral dimension) and perpendicular to it. The mesh was placed on the backlighter side of the subject foil, 8 mm away from the backlighter. The distance from the backlighter to the center of the subject foil, at the midpoint of the beam spots, was 1.15 cm, while the distance from the backlighter capsule to the detector package was 28 cm, such that the magnification was M ~24. All laser beam durations were 1 ns.

Table E.4. Experimental setup parameters for side-on radiography of magnetic reconnection experiments on OMEGA, including the OMEGA shot number, detector port position, backlighter laser energy, interaction laser energies, backlighter DD yield (DD-n measured by nTOF), backlighter D^{3}He yield (D^{3}He-p measured by PTD), and sample time for 15-MeV-protons relative to the interaction laser onsets.

Shot	Det. Loc.	BL Laser E (kJ)	Int. Laser E (kJ)	Y_{DD}	Y_{D^3He}	15-MeV-p Sample Time (ns)
64612	TIM 6	11.4	0.49/0.50	5.0×10^8	0.9×10^8	0.6/0.6
64613	TIM 6	11.3	0.49/0.50	4.7×10^8	0.9×10^8	1.3/1.3

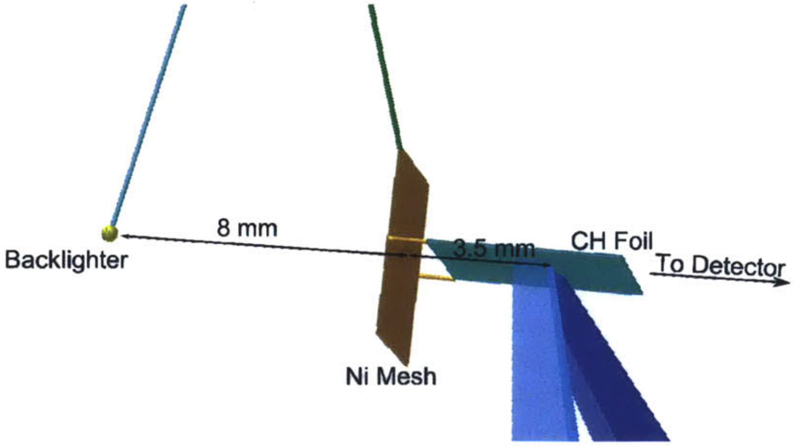

Figure E.10. To-scale depiction of experimental setup for side-on radiography of magnetic reconnection experiments on OMEGA. The two interaction beams are shown, but the backlighter drive beams have been hidden for clarity.

A cartoon of the experimental geometry and proton radiography images are presented in Figure

E.11. The field structures appear fairly weak, such that very little proton fluence modulation is observed in the 15-MeV-proton radiographs. The 3-MeV-proton radiography images, particularly that at $t_{int} = 0.9$ ns shows evidence of fields near each bubble as well as the interaction region, where the collision of the two bubbles produces a hydrodynamic jet perpendicular to the plane of the CH foil. Similar to the experiments on OMEGA-EP, these experiments demonstrate that electric and/or magnetic fields are entrained in the flow of these hydrodynamic jets, even though the jets themselves are not a product of the interaction of magnetic fields.

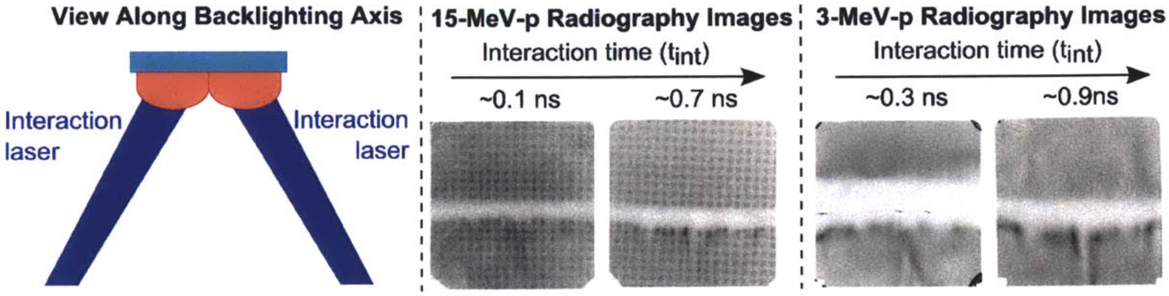
View Along Backlighting Axis
Interaction laser
Interaction laser
15-MeV-p Radiography Images
Interaction time (t_{int})
~0.1 ns
~0.7 ns
3-MeV-p Radiography Images
Interaction time (t_{int})
~0.3 ns
~0.9ns

Figure E.11. Cartoon of experimental geometry and side-on monoenergetic 15-MeV-proton and 3-MeV-proton radiography images at different times in magnetic reconnection experiments on OMEGA, in terms of how long the two plasma bubbles have been interacting (increasing $t_{int.}$ to the right). Each image has a field of view at the foil 3.6 mm on a side.

E.5 Monoenergetic Proton Radiography Images from Colliding Parallel Magnetic Fields Experiments on OMEGA

A summary of experimental conditions for proton radiography of colliding parallel magnetic fields on OMEGA is shown in Table E.5, including backlighter and subject laser energies, experimental timing, and relevant distances, and a depiction of the experiment (with backlighter beams turned off) is shown in Figure E.12. As discussed in Chapter 6, all experiments used a pair of 5 μm thick CH foils centered around the center of the target chamber, offset 0.5 mm from the center and parallel to each other, but aligned so that the backlighting axis passed through opposing edges of each foil. The backlighter capsule was 1.0 cm from the center (or the interaction point of the plasma bubbles), while the detector package was 28 cm from the backlighter, such that the magnification was M = 28. Two 60-μm thick, 150-μm period Ni meshes were used, one with each foil. The mesh for the backlighter-side foil was positioned 2 mm away from its foil toward the backlighter (7.5 mm from the backlighter), while the mesh for the detector-side foil was positioned 2.5 mm away from its foil toward the detector (13 mm from the backlighter). All laser beam durations were 1 ns.

The complete set of 15-MeV-proton radiography images and currently-processed 3-MeV-proton radiographs are shown in Figure E.13. A summary of the magnetic-field data obtained in these experiments is presented in Table E.6.

E.6 Additional Discussion of Magnetic Field and Reconnection Data on OMEGA

Additional discussion of data from magnetic reconnection and colliding parallel magnetic field experiments on OMEGA, expanding on that presented in Chapter 6, is discussed in this section.

Table E.5. Experimental setup parameters for asymmetric magnetic reconnection experiments on OMEGA, including the OMEGA shot number, detector port position, backlighter laser energy, interaction laser energies, backlighter DD yield (DD-n measured by nTOF), backlighter D^3He yield (D^3He-p measured by PTD), and sample time for 15-MeV-protons relative to the interaction laser onsets.

Shot	Det. Loc.	BL Laser E (kJ)	Int. Laser E (kJ)	Y_{DD}	Y_{D^3He}	15-MeV-p Sample Time (ns)
68605	TIM 6	10.7	0.49/0.49	5.6×10^8	1.6×10^8	0.6/0.6
68607	TIM 6	10.8	0.50/0.49	5.1×10^8	1.2×10^8	1.0/1.0
68608	TIM 6	10.8	0.50/0.50	5.3×10^8	1.4×10^8	1.3/1.3
68609	TIM 6	10.9	0.50/0.50	4.9×10^8	1.3×10^8	0.3/1.0
68610	TIM 6	10.9	0.50/0.50	4.7×10^8	1.2×10^8	0.6/1.3
68611	TIM 6	10.9	0.50/0.50	5.2×10^8	1.2×10^8	1.0/1.7
68612	TIM 6	10.9	0.50/0.50	5.3×10^8	1.2×10^8	0.3/0.3
68613	TIM 6	10.7	0.49/0.49	4.6×10^8	1.2×10^8	1.0/1.3

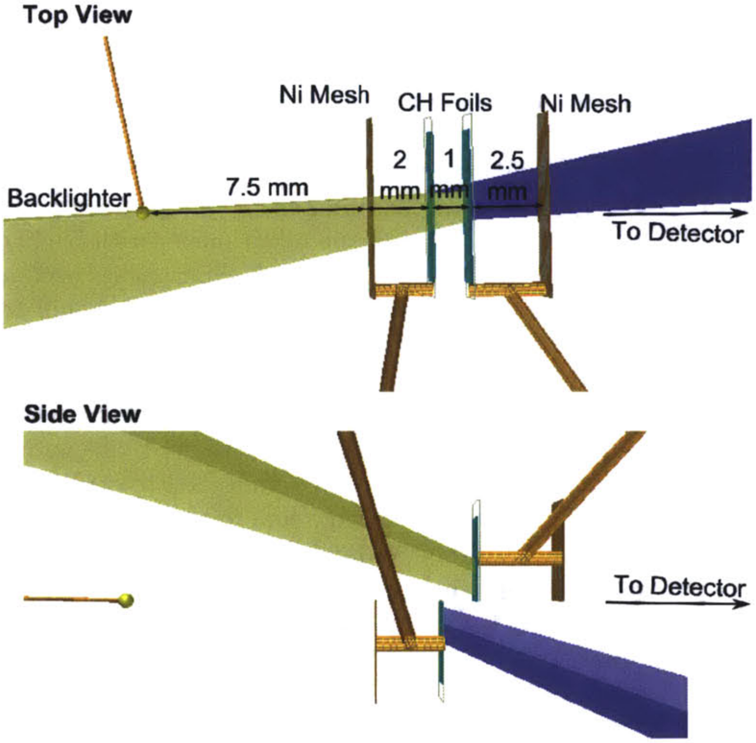

Figure E.12. To-scale depiction of experimental setup for colliding parallel magnetic fields experiments on OMEGA. A top view and side view are shown. The two interaction beams are shown, but the backlighter drive beams have been hidden for clarity.

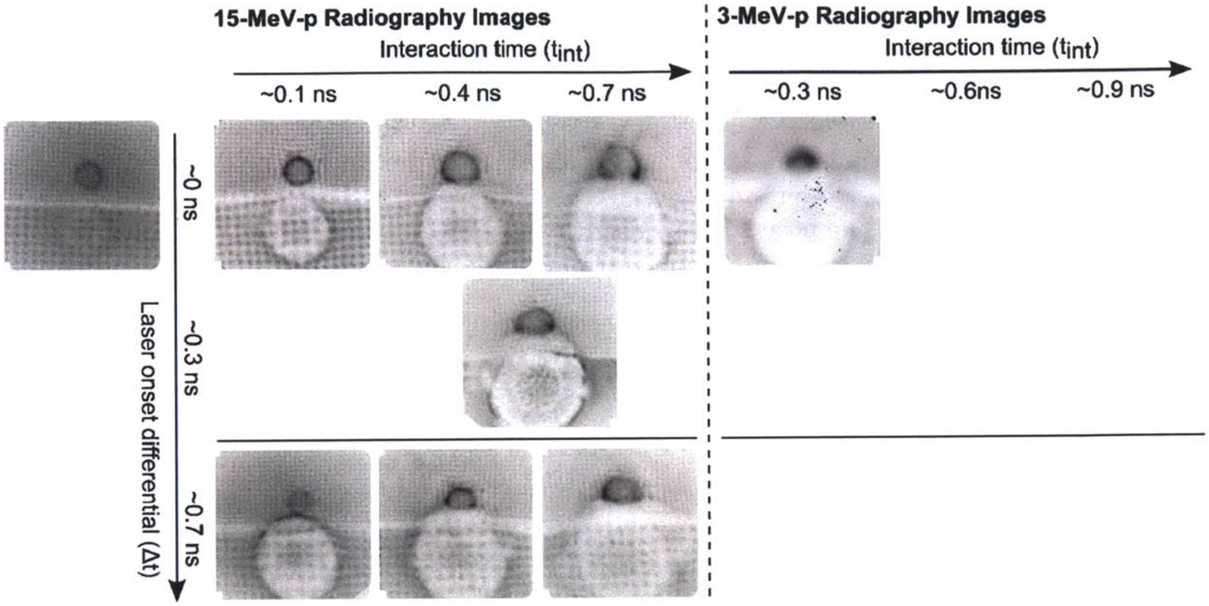
15-MeV-p Radiography Images
Interaction time (tint)
~0.1 ns
~0.4 ns
~0.7 ns
3-MeV-p Radiography Images
Interaction time (tint)
~0.3 ns
~0.6ns
~0.9 ns
~0 ns
~0.3 ns
~0.7 ns
Laser onset differential (Δt)

Figure E.13. Monoenergetic 15-MeV-proton and 3-MeV-proton radiography images at different times in colliding parallel magnetic fields experiments on OMEGA, in terms of how long the two plasma bubbles have been interacting (increasing $t_{int.}$ to the right) and the degree of asymmetry (increasing Δt down). Each image has a field of view at the foil 3.6 mm on a side. The image at the far left is ~0.3 ns before the bubbles interact. The image at moderate symmetry was obtained with one mesh (bottom foil) missing.

Table E.6. Magnetic field data for colliding parallel magnetic fields experiments on OMEGA, including the OMEGA shot number and detector port position (see Table E.1), path-integrated field strength through the perimeter of plasma bubbles 1 and 2, total magnetic flux at the perimeter of plasma bubbles 1 and 2, total magnetic flux in the interaction region of the plasma bubbles, and duration of time that the plasma bubbles have been interacting (t_{int}).

Shot-Loc.	$\lvert\int\mathbf{B}\times\mathbf{dl}\rvert_{per,1}$ MG μm	$\lvert\int\mathbf{B}\times\mathbf{dl}\rvert_{per,2}$ MG μm	$\Phi_{per,1}$ MG μm mm	$\Phi_{per,2}$ MG μm mm	Φ_{int} MG μm mm	t_{int} ns
68605-T6	75±10	65±10	24±7	18±7	50±13	0.04
68607-T6	110±20	90±15	50±8	37±8	74±15	0.38
68608-T6	130±30	80±20	65±10	31±8	79±14	0.67
68609-T6	50±20	120±30	6±3	55±8	85±16	0.04
68610-T6	50±10	110±30	21±5	58±10	73±13	0.33
68611-T6	60±10	90±20	28±6	52±10	70±10	0.72

Experiments inverting the geometry of typical laser-plasma reconnection experiments can produce a collision of plasmas with parallel magnetic fields (shear angle ∼0), which complement experiments studying the reconnection of anti-parallel magnetic fields.[9,8] In concert, these multiple campaigns provide insight into the impact of the hydrodynamic collision of laser-produced plasmas on magnetic field dynamics and reconnection over a variety of shear angles and symmetries across the interaction region. As discussed in Chapter 6, the experiments with parallel fields highlight magnetic field deformation and compression in a configuration where magnetic flux annihilation is unlikely to occur. The collision and interaction process of multiple plasma regions each carrying magnetic fields is universal, and occurs at any magnetically-separated boundary. This phenomenon in $\beta\sim10$ plasmas is especially relevant to planetary magnetopauses[11–13] and the heliopause.[14]

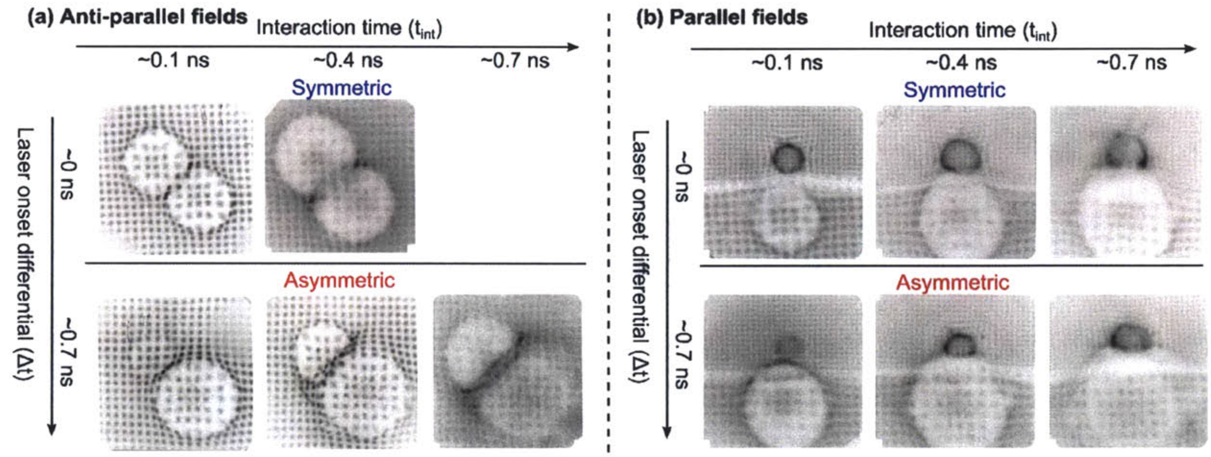

Figure E.14. 15-MeV-proton images at different times relative to the onset of the two interaction beams in (a) anti-parallel and (b) parallel magnetic field experiments. The horizontal axis represents how long the two plasmas have been interacting (increasing $t_{int.}$ to the right) for symmetric ($\Delta t = 0$) and asymmetric ($\Delta t = 0.7$ ns) experiments. Darker indicates more protons.

To make a direct comparison between the reconnection of anti-parallel magnetic fields and the collision of parallel magnetic fields, 15-MeV-proton images of colliding, laser-produced plasmas are shown in Figure E.14. As were discussed separately in Chapter 6, these images demonstrate the deflection of proton beamlets due to magnetic fields concentrated at the perimeter of the plasma bubbles and in their interaction, in (a) anti-parallel and (b) parallel magnetic fields experiments. In the anti-parallel experiments, the magnetic fields are universally oriented clockwise with respect to each bubble, deflecting protons (moving out of the page) away from the bubble centers. In the collision region, the magnetic fields are oriented in opposite directions, and the images show distortion of the proton fluence structure due to the deformation and annihilation of magnetic fields. In the parallel experiments, the plasma bubble at the top half of each image has azimuthal magnetic fields that are oriented counterclockwise when looking from the detector toward the backlighter, and the proton beamlets are deflected radially inward. The plasma bubble at the bottom half of the image has a similar orientation to in the anti-parallel experiments, such that the magnetic fields are oriented clockwise and the protons are deflected radially outward. This effect has been observed previously in laser-foil experiments with lasers incident on opposite sides of the same foil, but with no interaction between the plasma bubbles.[15] Where the plasma bubbles collide, the magnetic fields are parallel, both deflecting protons upward.

In the parallel magnetic fields experiments, the grid structure on each side of the image has a different apparent size due to the different magnifications of the two pieces of mesh. The mesh for the smaller-appearing bubble is 1.3 mm from the backlighter, while the mesh for the larger-appearing bubble is 0.75 mm from the backlighter. In some experiments, a light strip (few protons) appears in the center of the image, possibly due to the overlap of the two meshes, preventing proton transmission, or a slight charging of the mesh itself, which could create an electric field that deflects protons away from the edge of the mesh.

The time axes in Figure E.14 are the duration of time since the plasmas began to interact ($t_{int.}$) and the difference in onset time between the two interaction beams (Δt). Experiments at Δt = 0 are symmetric, even though one bubble appears smaller and the other appears larger in the parallel experiments, due to the magnetic deflection. Experiments at Δt = 0.7 ns are asymmetric, with the larger-appearing bubble actually larger in both the anti-parallel and parallel experiments, as it has had more time to expand. The timing was confirmed by the proton temporal diagnostic (PTD), which measures the absolute time of proton emission from the backlighter.[16]

These images illustrate the expansion of azimuthal magnetic field structures around the laser-produced plasma bubbles and most importantly demonstrate the deformation and, in the anti-parallel experiments, annihilation of the field structures in the plasma bubble collision. In the parallel experiments, the later two images in both the symmetric and asymmetric configuration show that the proton pileup ring in the collision region is perturbed and flattened. This feature indicates that the magnetic fields are frozen in to the plasma as it is being reshaped by the interaction with the opposing bubble. The asymmetric experiments in particular illustrate this deformation, and the stronger effect may be due to a more forceful collision. In the anti-parallel experiments, this region is characterized both by flattening of the proton fluence structures and also a shortening of the apparent beamlet deflection, signifying magnetic field annihilation and reconnection.

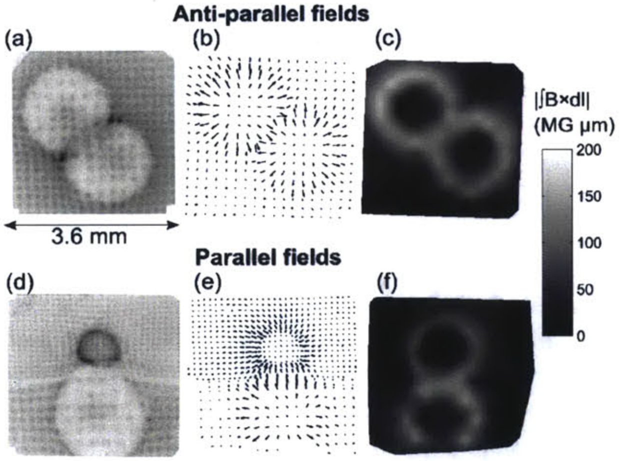

Figure E.15. (a,d) 15-MeV-proton radiography images, (b,e) beamlet deflection map, and (c,f) contour plot of the local magnitude of the path-integrated magnetic field strength inferred from beamlet deflections, for interacting symmetric plasma bubbles at t_{int}=0.4 ns, with anti-parallel (top row) and parallel (bottom row) magnetic fields. Anti-parallel experiments show less magnetic flux in the interaction region, due to magnetic reconnection, while parallel experiments do not, and instead may show a slight enhancement of the path-integrated magnetic field strength due to flux pileup.

The inference of proton-path-integrated magnetic field strength through the plasma from the beamlet deflection in experiments with both anti-parallel and parallel interacting magnetic fields is illustrated in Figure E.15. Figures E.15a and E.15d show the radiography images from which proton beamlet deflections (Figures E.15b and E.15e) and the path-integrated magnetic field strength (Figures E.15c and Figure E.15f) are inferred. Though the anti-parallel and parallel images appear rather different due to the geometry of the different experiments, the magnitude and structure of proton beamlet deflection and therefore the magnitude and structure of the path-integrated magnetic field strength at the plasma bubble perimeters are approximately equal. In the interaction regions, where the anti-parallel experiments show a reduction in total magnetic flux in comparison to the bubble perimeters, due to magnetic reconnection, the parallel experiments show no magnetic flux annihilation, and may exhibit an increase in path-integrated magnetic field strength due to flux compression. This is especially true of the symmetric parallel experiments. These results are discussed quantitatively below.

The resulting maps of path-integrated field strength inferred from each of the radiography images in Figure E.14 are shown in Figure E.16. The anti-parallel fields experiments show significant annihilation of magnetic flux in the collision region, while the parallel fields experiments universally show negligible change in the total magnetic flux, despite the observable deformation of frozen-in field structures in the collision of the plasma bubbles. In some parallel experiments, the interpretation of the field structure in the interaction region is complicated by mesh overlap, though sufficient information is present in the images to infer the bulk magnetic field magnitude at slightly poorer resolution.

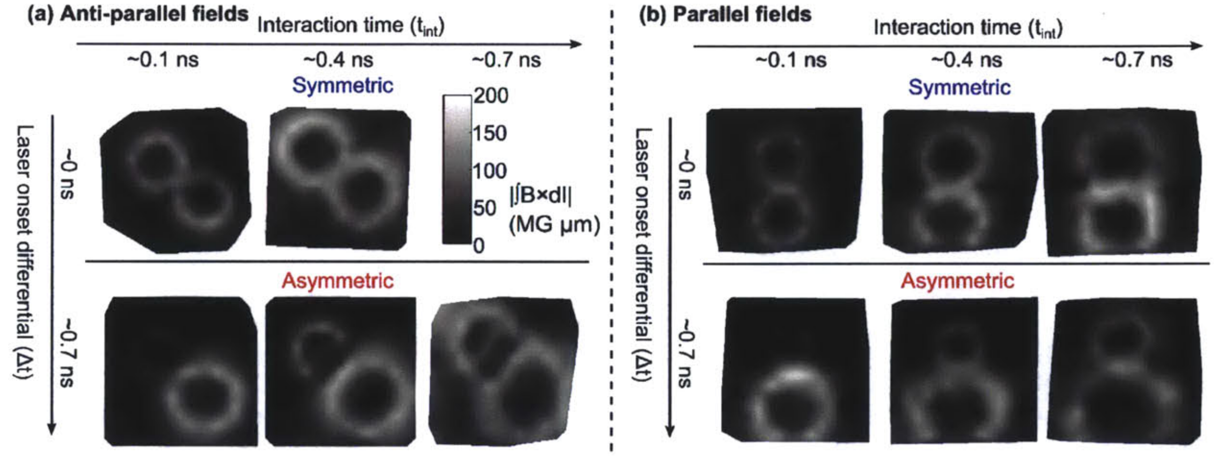

Figure E.16. Magnitude of path-integrated magnetic field strength inferred from 15-MeV-proton images at different times relative to the onset of the two interaction beams in (a) anti-parallel and (b) parallel magnetic field experiments. As in Figure E.14, the horizontal axis represents how long the two plasmas have been interacting for both symmetric ($\Delta t = 0$) and asymmetric ($\Delta t = 0.7$ ns) experiments.

Maps of path-integrated magnetic field strength shown in Figure E.16 have been analyzed to quantify the annihilation – or lack thereof – of magnetic flux in the interaction region. Figure E.17 shows a lineout of the field-strength map in symmetric anti-parallel and parallel experiments at $t_{int} = 0.4$ ns. The lineout is taken with finite width, approximately the size of the ribbon of magnetic flux around each plasma bubble, to smooth out the finite resolution of the beamlet grid. The lineout is divided into discrete segments corresponding to the perimeter and interaction region of each plasma bubble, and the line-integral of path-integrated field strength in each segment equals the magnetic flux, as $\Phi = \int [|\int \mathrm{B} \times \mathrm{d}l|] dx$, where dx is along the lineout direction. As labeled in Figure E.17, the flux in the perimeter of the upper (lower) bubble is identified as Φ_A (Φ_D), while the flux in the interaction region of the upper (lower) bubble is identified as Φ_B (Φ_C). It should be noted that the spatial resolution associated with these lineouts is only as small as the grid spacing, 150 μm, and in the interaction region of the parallel experiments, where the mesh structure is more complicated, it is somewhat larger, ~200-300 μm. The anti-parallel experiment shows a significantly reduced path-integrated magnetic field strength in the interaction region due to magnetic reconnection, while the parallel experiment indicates a slight enhancement, possibly signifying flux compression in the absence of reconnection.

The total flux around the bubble perimeters and in the interaction region is computed and compared to deduce the amount of flux annihilated. Defining the perimeter flux and interaction-

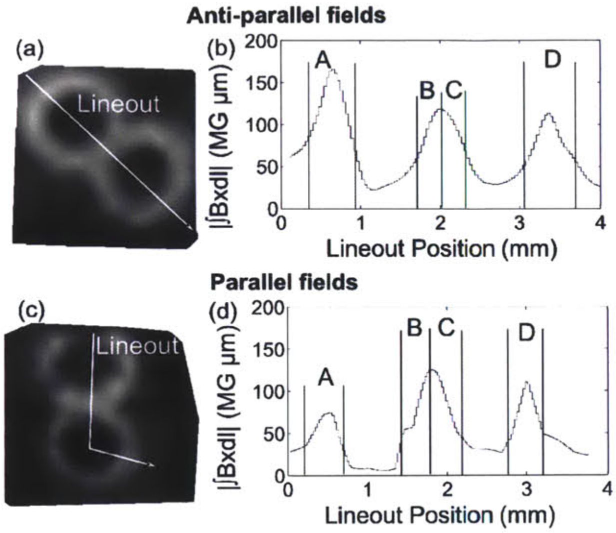

Figure E.17. Lineout of the path-integrated field map for (a-b) anti-parallel and (c-d) parallel interacting magnetic fields. Magnetic flux is inferred from the line-integrated sum of path-integrated magnetic field strength in the upper bubble perimeter (A), the interaction region of each bubble (B) and (C) and the lower bubble perimeter (D). The amount of flux annihilated is deduced by comparing these quantities.

region flux as

$$\Phi_{per.} = \Phi_A + \Phi_D \tag{E.1}$$

and

$$\Phi_{int.} = \Phi_B + \Phi_C, \tag{E.2}$$

the flux annihilated can be defined as the difference between them,

$$\Delta\Phi_{ann.} = \Phi_{int.} - \Phi_{per.}, \tag{E.3}$$

and the fraction of flux annihilated is therefore

$$f_{ann.} = 1 - \frac{\Phi_{int.}}{\Phi_{per.}}. \tag{E.4}$$

This definition assumes that in the absence of reconnection, the total flux in the interaction region would equal the flux at the perimeters, that the difference between the perimeter flux and the interaction-region flux is due to reconnection. Error in the inferred flux arises due to uncertainty in the mesh orientation and spacing and the magnitude of beamlet deflection, the definition of boundary regions, and non-uniformity in field strength across the plasma bubble.

For the anti-parallel data shown in Figure E.17a-b, the total magnetic flux at the bubble perimeters was $\Phi_{per.}$=128±13 MG μm mm, while the flux in the interaction region was $\Phi_{int.}$=64±8 MG μm mm, suggesting that $\Delta\Phi_{ann.}$= 64±15 MG μm mm, or 50±8% of flux was annihilated by magnetic reconnection.The rapid rate of magnetic flux annihilation in anti-parallel experiments, ~100 MG μm mm/ns ~$10V_{A0}|\int \mathrm{B}\times\mathrm{dl}|$, indicates that flux pileup may be amplifying the local magnetic field strength, Alfvén speed, and reconnection rate. Conversely, in the parallel experiments shown in Figure E.17c-d, the perimeter magnetic flux was $\Phi_{per.}$=87±11 MG μm mm, while the flux in the interaction region was $\Phi_{int.}$=74±15 MG μm mm, such that the net flux annihilated is consistent with zero. This result demonstrates that for the interaction of parallel magnetic fields, at a shear angle of ~0, magnetic reconnection does not occur and the magnetic flux is simply advected and compressed.

The amount of flux annihilated normalized to the possible amount of flux annihilated – defined as twice the flux in the smaller bubble – is shown as a function of interaction time for both anti-parallel and parallel experiments in Figure E.18. For colliding anti-parallel magnetic fields, >50% of the available magnetic flux is annihilated in the interaction region due to magnetic reconnection. For colliding parallel magnetic fields, the fraction of flux annihilated is consistent with zero to within experimental uncertainty, in both symmetric and asymmetric experiments.

Figure E.18. Fraction of possible magnetic flux annihilated as a function of interaction time for anti-parallel (blue circles) and parallel (red squares) colliding magnetic fields. For the parallel experiments, both symmetric (filled) and asymmetric (open) experiments show negligible annihilation of magnetic flux, while anti-parallel experiments show >50% flux annihilation.

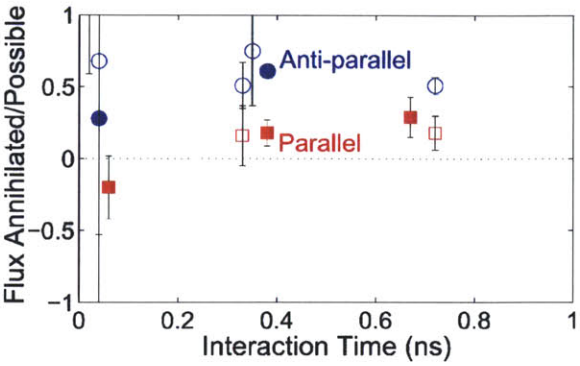

These experiments effectively mimic the collision of magnetic fields at the Earth's dayside magnetopause, where the solar-wind-carried magnetic field interacts with the magnetosphere. The average plasma β is ~1-5, of similar order to the laser-produced plasmas. Furthermore, the interaction of magnetic fields has been observed to occur at a variety of shear angles, and reconnection was found to be weaker at smaller magnetic shear.[17] An additional correlation was observed in asymmetric configurations at the magnetopause, where small-shear-angle reconnection was suppressed in the presence of a large pressure or β gradient across the current sheet.[18,19] These observations are confirmed by the results of the present experiments, where reconnection of magnetic fields at small shear angles is negligible. Future experiments may probe a variety of magnetic shear angles between perfectly anti-parallel ($\theta = 180°$) and perfectly parallel ($\theta = 0$), to study reconnection in a regime similar to the dayside magnetopause, where the solar-wind magnetic field orientation varies and interacts with the Earth's magnetic field at a continuum of shear angles, in a β>1 plasma.

E.7 References

1. R. C. Davidson, *Frontiers in High Energy Density Physics*, (National Academies Press, Washington, DC, 2003).
2. R. P. Drake, *High-Energy-Density Physics*, (Springer Press, New York, 2006).
3. C. Stoeckl *et al.*, Bull. Am. Phys. Soc., **52**(67) (2007).
4. C. K. Li, F. H. Séguin, J. A. Frenje *et al.*, "Measuring *e* and *b* fields in laser-produced plasmas with monoenergetic proton radiography," Phys. Rev. Lett., **97**, 135,003 (2006).
5. C. K. Li, F. H. Séguin, J. A. Frenje *et al.*, "Observation of the decay dynamics and instabilities of megagauss field structures in laser-produced plasmas," Phys. Rev. Lett., **99**, 015,001 (2007).
6. S. L. Pape, P. Patel, S. Chen *et al.*, "Proton radiography of magnetic fields in a laser-produced plasma," High Energy Density Physics, **6**, 365–367 (2010).
7. F. H. Séguin, N. Sinenian, M. Rosenberg *et al.*, "Advances in compact proton spectrometers for inertial-confinement fusion and plasma nuclear sciencea)," Review of Scientific Instruments, **83**(10), 10 (2012).
8. M. J. Rosenberg *et al.*, "A laboratory study of asymmetric magnetic reconnection in strongly-driven plasmas," submitted to Nat. Commun. (2014).
9. C. K. Li, F. H. Séguin, J. A. Frenje *et al.*, "Observation of megagauss-field topology changes due to magnetic reconnection in laser-produced plasmas," Phys. Rev. Lett., **99**, 055,001 (2007).
10. M. A. Shay, J. F. Drake, B. N. Rogers *et al.*, "The scaling of collisionless, magnetic reconnection for large systems," Geophysical Research Letters, **26**(14), 2163–2166 (1999).

11. T.-D. Phan, G. Paschmann, W. Baumjohann *et al.*, "The magnetosheath region adjacent to the dayside magnetopause: Ampte/irm observations," J. Geophys. Res., **99**(A1), 121–141 (1994).
12. A. Masters, J. P. Eastwood, M. Swisdak *et al.*, "The importance of plasma β conditions for magnetic reconnection at saturn's magnetopause," Geophys. Res. Lett., **39**(L08103) (2012).
13. M. Desroche, F. Bagenal, P. A. Delamere *et al.*, "Conditions at the expanded jovian magnetopause and implications for the solar wind interaction," J. Geophys. Res., **117**(A07202) (2012).
14. M. Opher, J. F. Drake, K. M. Schoeffler *et al.*, "Is the magnetic field in the heliosheath laminar or a turbulent sea of bubbles?" Astrophys. J., **734**(71) (2011).
15. R. D. Petrasso, C. K. Li, F. H. Seguin *et al.*, "Lorentz mapping of magnetic fields in hot dense plasmas," Phys. Rev. Lett., **103**, 085,001 (2009).
16. J. A. Frenje, C. K. Li, F. H. Séguin *et al.*, "Measuring shock-bang timing and ρr evolution of d^{3}he implosions at omega," Phys. Plasmas, **11**(5), 2798–2805 (2004).
17. L. Scurry, C. T. Russell and J. T. Gosling, J. Geophys. Res., **99**(A8), 14,811–14,814 (1994).
18. T. D. Phan, J. T. Gosling, G. Paschmann *et al.*, "The dependence of magnetic reconnection on plasma β and magnetic shear: Evidence from solar wind observations," Astrophys. J. Lett., **719**, L199–L203 (2010).
19. J. T. Gosling and T. D. Phan, "Magnetic reconnection in the solar wind at current sheets associated with extremely small field shear angles," Astrophys. J., **763**(L39) (2013).

Appendix F

Formulary and Discussion of Relevant Parameters in Kinetic Effects and Magnetic Reconnection Experiments

Key physical quantities in the discussion of kinetic effects in ICF implosions (Chapter 3) and magnetic reconnection experiments (Chapters 5 and 6) – and the formulas used to calculate them – are presented in this appendix.

F.1 Formulary of Parameters Relevant to Ion Kinetic Effects in ICF Implosions

A discussion of the importance of ion kinetic effects centers on the time and length scales over which a hydrodynamic description of the plasma is valid. In general, when the ion-ion mean free path λ_{ii} is much smaller than some relevant system size, gradient scale length, or, in the context of numerical simulations, the typical zone size, the hydrodynamic picture applies. Similarly, when the ion-ion collision time τ_{ii} is much shorter — or the timescale for ion diffusion out of the system τ_{diff} is much longer – than typical implosion timescales, hydrodynamics is a valid assumption. However, when those relations are not true, hydrodynamics becomes invalid and ion kinetic effects are expected to be important, as was demonstrated in experiments discussed in Chapter 3.

Calculation of all of these parameters originates with the calculation of the frequency of ion-ion collisions ν_{ii}. The following calculations assume a two-ion-species plasma (labeled by subscripts 1 and 2), characterized by a total ion density n_i and a single ion temperature T_i, as based on calculations in the 2009 NRL Plasma Formulary. The Maxwellian-averaged collision frequency between ions of species 1 and ions of species 2 is given by

$$\nu_{12} = \frac{\sqrt{2}}{3\sqrt{\pi}} n_2 \left(\frac{Z_1 Z_2 e^2}{4\pi\epsilon_0}\right)^2 \frac{4\pi}{m_1^{1/2} T_i^{3/2}} \left(\frac{m_2}{m_1 + m_2}\right)^{1/2} \ln\Lambda_{12}, \tag{F.1}$$

where n_2 is the number density of the background ions, Ze (m) is the respective ion charge (mass), T_i is the ion temperature in energy units (assumed to be the same for both ion species), and $\ln\Lambda_{12}$ is the Coulomb logarithm for collisions of ion species 1 and 2. This equation can be simplified for a two-species plasma as

$$\nu_{12} = 2.145 \times 10^9 f_2 \frac{n_i\,(\mathrm{cm}^{-3})}{10^{21}} \left(\frac{1}{T_i\,(\mathrm{keV})}\right)^{3/2} Z_1^2 Z_2^2 \sqrt{\frac{A_2}{A_1}\frac{1}{A_1 + A_2}} \ln\Lambda_{12} \quad \mathrm{s}^{-1}, \tag{F.2}$$

where f_2 is the fraction of ion species 2, n_i is the total ion number density, Z (A) is the respective ion charge (mass) in units of the proton charge (mass). The Coulomb logarithm Λ_{12} is evaluated as

$$\Lambda_{12} = 23 - \ln\left(Z_1 Z_2 \left(f_1 Z_1^2 + f_2 Z_2^2\right) \frac{n_i\,(\mathrm{cm}^{-3})}{(T_i\,(\mathrm{eV}))^{3/2}}\right). \tag{F.3}$$

As a concrete example, for a D^{3}He plasma, the total collision time for a D ion is computed using Equation F.2 as the inverse of the sum of collision frequencies for D on D collisions (subscripts 1 = D, 2 = D) and D on ^{3}He collisions (subscripts 1 = D, 2 = ^{3}He),

$$\tau_{D,total} = 1/\left(\nu_{DD} + \nu_{D3He}\right). \tag{F.4}$$

The ion-ion mean free path for a D ion is the product of the collision time for a D ion in this plasma and the D ion thermal velocity,

$$v_{th,D} = \sqrt{\frac{2kT_i}{m_D}}, \tag{F.5}$$

as

$$\lambda_D = \tau_{D,total} v_{th,D}. \tag{F.6}$$

A similar calculation can be performed for ^{3}He ions with the appropriate choices of species 1 and 2 in the ν_{12} calculations. For much of the work in Chapter 3 and Appendix A, the ion-ion mean free path in a D^{3}He plasma is taken to be the geometric mean of the individual mean free paths for D ions and ^{3}He ions, with

$$\lambda_{ii} = \sqrt{\lambda_D \lambda_{^3He}}. \tag{F.7}$$

The average ion-ion mean free path λ_{ii} is compared to the minimum shell radius R_{shell} to describe the hydrodynamic or kinetic regime of an ICF implosion. When $\lambda_{ii} \ll R_{shell}$, the implosion is hydrodynamic; when $\lambda_{ii} \gtrsim R_{shell}$, the implosion is kinetic. This condition is described by the Knudsen number N_K, the ratio of ion mean free path to minimum shell radius,

$$N_K \equiv \lambda_{ii}/R_{shell}. \tag{F.8}$$

For $N_K \ll 1$, ion mean free path effects should be negligible; for $N_K \gtrsim 1$, ion mean free path effects are important.

The diffusion coefficient and diffusion time can also be calculated from the mean free path and thermal velocity of a given ion. Using again the deuteron ion example, the diffusion coefficient for a deuteron, following the discussion above, is given by

$$D_D = \frac{1}{3}\lambda_D v_{th,D}. \tag{F.9}$$

The characteristic time for a deuteron to diffuse out to the fuel-shell interface over a distance R_{shell} is therefore

$$\tau_{diff,D} = R_{shell}^2/D_D. \tag{F.10}$$

For an equimolar D^{3}He gas, the ion diffusion time is taken as the geometric mean of ion diffusion times for D and ^{3}He, as

$$\tau_{diff} = \sqrt{\tau_{diff,D}\tau_{diff,^3He}}. \tag{F.11}$$

The average ion diffusion time τ_{diff} is compared to characteristic implosion timescales, for example the duration of fusion burn τ_{burn}, to determine the importance of ion diffusion over that period. When $\tau_{diff} \gg \tau_{burn}$, ion diffusion is negligible over the duration of fusion burn. However, when

$\tau_{diff} \lesssim \tau_{burn}$, ion diffusion is a significant effect. These conditions are summarized in the parameter R_τ, the temporal analogue of the Knudsen number, defined as

$$R_\tau \equiv \tau_{burn}/\tau_{diff}. \tag{F.12}$$

Like the Knudsen number, $R_\tau \ll 1$ signifies conditions where ion diffusion is minimal, while $R_\tau \gtrsim 1$ describes conditions where ion diffusion is important.

Related to the discussion of ion diffusion and ion kinetic effects more broadly, it is often of interest to consider the behavior of ions corresponding to the Gamow peak energy for fusion reactions, as was discussed in Chapter 3. The ions around the Gamow peak energy are those principally responsible for fusion, and the behavior of those ions most directly relates to the resulting fusion yield. The most probable center-of-mass (COM) energy for fusion reactions between ion species 1 and 2 is

$$\epsilon_{Gp12} = 6.2696\,(Z_1 Z_2)^{2/3} \left(\frac{A_1 A_2}{A_1 + A_2}\right)^{1/3} T_i^{2/3}, \tag{F.13}$$

where T_i is given in keV.[1] This is a center-of-mass energy, from which the laboratory-frame energy of individual ions can be estimated. Generally, as discussed in Chapter 3, the energy of reactant ions corresponding to a center-of-mass energy around ϵ_{Gp} is typically a few times greater than the thermal energy.

The COM Gamow peak energy can be related to the energy of individual reactant ions as follows. Assume, for simplicity, that the reacting ions have the same individual energy $E_1 = \frac{1}{2}m_1 v_1^2 = \frac{1}{2}m_2 v_2^2 = E_2$. As the Gamow peak energy is the COM energy of the reacting ions, it can be expressed as $\epsilon_{Gp} = \frac{1}{2}m_r v_r^2$, where $m_r = m_p A_1 A_2/(A_1 + A_2)$ is the reduced mass and $v_r \sim v_1 + v_2$ is the (non-relativistic) relative velocity, assuming a head-on collision.[1] Solving for one of the reactant velocities, $v_2^2 = v_1^2(m_1/m_2)$ yields

$$\epsilon_{Gp} \sim \frac{1}{2} m_r v_1^2 \left(1 + 2\sqrt{\frac{m_1}{m_2}} + \frac{m_1}{m_2}\right), \tag{F.14}$$

or, solving for v_1,

$$v_1^2 \sim \frac{2\epsilon_{Gp}}{m_r\left(1 + 2\sqrt{\frac{m_1}{m_2}} + \frac{m_1}{m_2}\right)}. \tag{F.15}$$

Therefore, the energy of reactant ion 1 (E_1) is

$$E_1 = \frac{1}{2} m_1 v_1^2 \sim \epsilon_{Gp} \frac{m_1}{m_r} \frac{1}{\left(1 + 2\sqrt{\frac{m_1}{m_2}} + \frac{m_1}{m_2}\right)}. \tag{F.16}$$

For DD reactions, where $A_1 = A_2 = 2$, the D ion energy that, in a head-on collision with an identical D ion at the same energy, produces a COM energy equivalent to the Gamow peak energy is $E_1 = \frac{1}{2}\epsilon_{Gp}$. For D^{3}He reactions, with $A_1 = 2$ and $A_2 = 3$, $E_1 = 0.51\epsilon_{Gp}$. As this calculation assumed a head-on collision of reactant ions, these individual ion energies represent a near minimum of possible ion energies. Collisions at smaller angles of incidence allow for higher individual ion energies to produce the same COM energy. For example, collisions at 90 degrees give individual ion energies that are nearly equal to the Gamow peak energy. For $T_i \sim$10 keV, the Gamow peak energy is 29.1 keV for DD reactions and 49.1 keV for D^{3}He reactions, so that the reacting ions each typically have an energy several times the thermal energy.

---

[1] A head-on collision minimizes the individual ion energy required to produce a center-of-mass energy at the Gamow peak energy.

To approximate the collision frequency for a Gamow-peak ion among the thermal plama, the collision rate for "fast" ions of species 1 (i.e. ions likely to be responsible for fusion) in a field of slower ions of species 2 is

$$\nu_{fast1,slow2} = 9.0 \times 10^{-8} f_2 n_i \,(\mathrm{cm}^{-3}) \left(\frac{1}{\epsilon_i\,(\mathrm{eV})}\right)^{3/2} Z_1^2 Z_2^2 \left(\frac{1}{A_1^{1/2}} + \frac{A_1^{1/2}}{A_2}\right) \ln\Lambda_{12} \quad \mathrm{s}^{-1}, \qquad \text{(F.17)}$$

where ϵ_i is the energy of the fast reactant ion. When a suitable collision rate has been calculated, an effective Gamow-peak ion-ion mean free path can be estimated using the prescription of equations F.4-F.7. The mean free path for ions colliding at a center-of-mass energy equivalent to the Gamow-peak energy is typically several times that for ions around the thermal energy, and thus are more susceptible to escaping the hot fuel region of an ICF implosion.

A table summarizing typical plasma conditions after shock convergence in an exploding pusher experiment, as described in Chapter 3 and Appendix A, is presented in Table F.1. These conditions are based on OMEGA shot 69055, a 2.2-μm-thick, 854-μm diameter $\mathrm{SiO_2}$ shell, with a nominally 23 atm equimolar $\mathrm{D^3He}$ fill pressure, imploded by 14.6 kJ of laser energy in a 0.6-ns pulse. This implosion, by virtue of having $N_K{\sim}0.3$ and $R_\tau{\sim}0.15$, is considered to be in the hydrodynamic-like regime.

F.2 Formulary Relevant to Magnetic Reconnection Experiments Using Laser-Produced Plasmas

Several parameters are used identify regimes of magnetic reconnection on the basis of collisionality, and balances between magnetic, thermal, and ram pressure. For the purposes of this discussion and the calculation of those parameters, the plasma consists of an electron fluid at density n_e and temperature T_e and an ion fluid of average charge Ze, mass $m_i = Am_p$, number density $n_i = n_e/Z$ (preserving quasi-neutrality), mass density $\rho = n_i m_i$, and temperature T_i. The extent of the plasma is over a length scale L, with a magnetic field strength around the reconnection region B, driven together at a flow velocity V. A Coulomb logarithm $\ln\Lambda$ is used, with a constant value of ~8 chosen to be representative of a typical value in laser-plasma experiments.

As was discussed in Chapter 4, in the single-fluid Sweet-Parker model of magnetic reconnection, the width of the reconnection current sheet, which helps set the regime of collisionality, is dictated by the resistivity of the plasma. For an electron temperature in eV, the Spitzer resistivity in mks units (Ωm), following the discussion in the NRL Plasma Formulary, is given by

$$\eta = 0.000103 Z \ln\Lambda / T_e^{3/2}. \qquad \text{(F.18)}$$

The Lundquist number S is the ratio of resistive to Alfvén timescales,

$$S = \sqrt{\mu_0 L V_A / \eta}, \qquad \text{(F.19)}$$

where the Alfvén speed V_A is defined as

$$V_A = B/\sqrt{\mu_0 \rho} = B/\sqrt{\mu_0 n_i A m_p}. \qquad \text{(F.20)}$$

The Lundquist number determines the relative importance of Alfvénic to magnetic diffusive processes and is conceptually similar to the magnetic Reynolds number Rm, the ratio of resistive to

Table F.1. Plasma parameters relevant to experiments studying ion kinetic effects in ICF, based on the above discussion, using the example of OMEGA shot 69055.

Parameter [symbol (units)]	Value	Comments
Ion density [n_i (cm^{-3}]	2.42×10^{22}	Total ion density of both ions
Ion temperature [T_i (keV)]	13.5	T_i assumed same for both species
Charge of ion 1 [Z_1]	1	Deuteron charge inproton charge e
Charge of ion 2 [Z_2]	2	^{3}He charge in proton charge e
Mass of ion 1 [A_1]	2	D mass in units of proton mass m_p
Mass of ion 2 [A_2]	3	^{3}He mass in units of proton mass m_p
Coulomb logarithm 1-1 [$\ln\Lambda_{11}$]	11.5	Coulomb log for D on D collisions
Coulomb logarithm 1-2 [$\ln\Lambda_{12}$]	10.3	Coulomb log for D on ^{3}He collisions
Coulomb logarithm 2-1 [$\ln\Lambda_{21}$]	10.3	Coulomb log for ^{3}He on D collisions
Coulomb logarithm 2-2 [$\ln\Lambda_{22}$]	9.4	Coulomb log for ^{3}He on ^{3}He collisions
Collision rate 1-1 [ν_{11} (s^{-1})]	3.01×10^{9}	Maxwellian-avg. D-D collision rate
Collision rate 1-2 [ν_{12} (s^{-1})]	1.19×10^{10}	Maxwellian-avg. D-^{3}He collision rate
Collision rate 2-1 [ν_{21} (s^{-1})]	7.91×10^{9}	Maxwellian-avg. ^{3}He-D collision rate
Collision rate 2-2 [ν_{22} (s^{-1})]	3.22×10^{10}	Maxwellian-avg. ^{3}He-^{3}He collision rate
Ion 1 thermal speed [$v_{th,1}$ (μm/ns)]	1140	Deuteron thermal velocity
Ion 2 thermal speed [$v_{th,2}$ (μm/ns)]	930	^{3}He thermal velocity
Ion 1 collision time [$\tau_{1,total}$ (ps)]	67	Deuteron total collision time
Ion 2 collision time [$\tau_{2,total}$ (ps)]	25	Deuteron total collision time
Ion 1 mean free path [λ_1 (μm)]	77	Maxwellian mfp for D-ion collisions
Ion 2 mean free path [λ_2 (μm)]	23	Maxwellian mfp for ^{3}He-ion collisions
Ion mean free path [λ_{ii} (μm)]	42	Geometric mean of λ_1 and λ_2
Minimum shell radius [R_{shell} (μm)]	130	Min. radius of fuel-shell interface
Knudsen number [N_K]	0.3	Ratio λ_{ii}/R_{shell}
Ion 1 diffusion coeff. [D_1 (μm^2/ps)]	29	Deuteron total diffusion coefficient
Ion 2 diffusion coeff. [D_2 (μm^2/ps)]	7	^{3}He total diffusion coefficient
Ion 1 diffusion time [$\tau_{diff,1}$ (ps)]	580	D diffusion time to shell boundary
Ion 2 diffusion time [$\tau_{diff,2}$ (ps)]	2360	^{3}He diffusion time to shell boundary
Ion diffusion time [τ_{diff} (ps)]	1170	Geometric mean of $\tau_{diff,1}$ and $\tau_{diff,2}$
Fusion burn duration [τ_{burn} (ps)]	180	Average of DD and D^{3}He burn durations
R parameter [R_τ]	0.15	Ratio τ_{burn}/τ_{diff}
Gamow peak ener. 1-1 [$\epsilon_{Gp,11}$ (keV)]	36	Most likely COM energy for DD fusion
Gamow peak ener. 1-2 [$\epsilon_{Gp,12}$ (keV)]	60	Most likely COM energy for D^{3}He fusion
Gamow peak ener. 2-1 [$\epsilon_{Gp,21}$ (keV)]	60	Most likely COM energy for ^{3}HeD fusion
Gamow peak ener. 2-2 [$\epsilon_{Gp,22}$ (keV)]	103	Most likely COM energy for ^{3}He^{3}He fusion

flow timescales,

$$Rm = \sqrt{\mu_0 LV/\eta}. \tag{F.21}$$

For large magnetic Reynolds numbers, advection of the magnetic field is much more rapid than magnetic diffusion. For large Lundquist numbers ($>10^4$), the reconnection current sheet is prone to instability and breaking up into multiple X-points or plasmoids (magnetic islands). This is a analogous to the fluid Reynolds number, which, when large, signifies the dominance of flow versus diffusive processes in a fluid and correlates with a susceptibility to turbulence. The Lundquist number is related to the width of the Sweet-Parker current sheet δ_{SP}, as discussed in Chapter 4, as

$$\delta_{SP}/L = 1\sqrt{S}. \tag{F.22}$$

This scale width of the current sheet in a single-fluid, magnetohydrodynamics (MHD) picture is compared to other relevant length scales to determine whether reconnection takes place in the collisional, single-fluid regime or the collisionless, two-fluid (decoupled electrons and ions) regime.

When the ions are effectively coupled to the electrons and to the magnetic field over the width of the current sheet, and the flow of field lines follows the entire plasma fluid, reconnection occurs in the single-fluid MHD regime. Conversely, when the current sheet width is small enough that ions and electrons are decoupled and the field lines follow only the electron fluid, reconnection is said to take place in the two-fluid regime. The scale lengths describing the coupling of ions either to the electrons or to the magnetic field lines themselves are the ion inertial length (often called the ion skin depth) d_i or the ion gyroradius ρ_i. The ion skin depth depends simply on the frequency of ion plasma oscillations as

$$d_i = c/\omega_{pi}, \tag{F.23}$$

where the ion plasma frequency ω_{pi} is

$$\omega_{pi} = \sqrt{\frac{n_i Z^2 e^2}{m_i \epsilon_0}}. \tag{F.24}$$

The radius of ion Larmor orbits perpendicular to the magnetic field is determined by the thermal velocity of the ions perpendicular to the magnetic field (note that the value used here is a factor of $\sim\sqrt{2}$ lower than in Section F.1)

$$v_{th,i\perp} \sim \sqrt{kT_i/m_i} \tag{F.25}$$

and the ion gyrofrequency

$$\omega_{ci} = ZeB/m_i \tag{F.26}$$

as

$$\rho_i = v_{th,i\perp}/\omega_{ci}. \tag{F.27}$$

When $\delta_{SP} \gg d_i$ or $\delta_{SP} \gg \rho_i$, the ions are strongly bound to the field lines over the scale of the reconnection region, and a single-fluid reconnection occurs. However, when $\delta_{SP} \lesssim d_i$ or $\delta_{SP} \lesssim \rho_i$, two-fluid reconnection effects become important. It is notable that d_i and ρ_i are somewhat related parameters, as the ion inertial length is equivalent to the ion gyroradius for an ion whose speed is equal to the Alfvén speed. The near equivalency in the treatment of these parameters in the context of reconnection (i.e. that both are used as scale lengths to determine single-fluid versus two-fluid reconnection), is based on the Sweet-Parker model where magnetic energy is directly equivalent to kinetic energy of the ion outflow. More generally, the parameters are related via the ion plasma β_i, the ratio of ion thermal pressure to magnetic pressure, as

$$\rho_i/d_i \sim \sqrt{\beta_i}, \tag{F.28}$$

where

$$\beta_i = \frac{n_i k T_i}{B^2/2\mu_0}. \tag{F.29}$$

This quantity is also equivalent to the ratio of thermal to Alfvén speeds, as

$$\beta_i = \left(\frac{v_{th,i}}{V_A}\right)^2. \tag{F.30}$$

The β parameter is used more broadly to describe the relative importance of different types of energy within the system. It is typically invoked as the ratio of total (electron and ion) thermal pressure to magnetic pressure, as

$$\beta = \beta_e + \beta_i = \frac{n_e k T_e}{B^2/2\mu_0} + \frac{n_i k T_i}{B^2/2\mu_0}. \tag{F.31}$$

When $\beta \gg 1$, the magnetic energy is negligible in comparison to the thermal energy, and hydrodynamic processes dominate dynamics related to the magnetic field. As discussed in Chapters 5 and 6, this condition is present in magnetic reconnection experiments using laser-produced plasmas. Similarly, the "ram pressure beta", β_{ram}, is defined as the ratio of ram pressure to magnetic pressure, as

$$\beta_{ram} = \frac{\frac{1}{2}\rho V^2}{B^2/2\mu_0}. \tag{F.32}$$

For $\beta_{ram} \gg 1$, the magnetic energy is insignificant in comparison to the bulk kinetic energy of the plasma fluid. Under this circumstance, as was the case in experiments described in Chapter 5, Chapter 6, and Appendix E, the magnetic field is simply advected with the fluid and does not appreciably influence the dynamics of the system. Under these conditions, it is said that a reconnection between colliding plasmas at high β_{ram} is strongly driven, as the magnetic fields are squeezed together faster than they can naturally rearrange themselves. This is made more apparent by the equivalence between β_{ram} and the ratio of flow to Alfvén velocities, as

$$\beta_{ram} = \left(\frac{V}{V_A}\right)^2. \tag{F.33}$$

The analogies between β and β_{ram}, as well as relationships between relevant scale velocities (thermal, flow, Alfvén) (equations F.30 and F.33), are evident.

A table summarizing typical conditions for laser-plasma magnetic reconnection experiments, as described in Chapters 5 and 6, as well as in Appendix E, is presented in Table F.2. These conditions are based on the perimeter of an expanding plasma bubble produced by the interaction of a 500-J, 1-ns laser pulse with a 5-μm CH foil, ~0.6 ns after laser onset.

F.3 References

1. S. Atzeni and J. Meyer-Ter-Vehn, *The Physics of Inertial Fusion: Beam Plasma Interaction, Hydrodynamics, Hot Dense Matter*, International Series of Monographs on Physics, (Oxford University Press, 2004).

Table F.2. Plasma parameters relevant to magnetic reconnection experiments using laser-produced plasmas, based on the above discussion.

Parameter [symbol (units)]	Value	Comments
Ion charge [Z]	3.5	Average charge of CH plasma
Ion mass [A]	6.5	Average mass of CH plasma
Electron density [n_e (cm^{-3})]	7×10^{19}	Electron density of both ions
Mass density [ρ (g/cm^3)]	2.2×10^{-4}	$\rho = n_i m_i = (n_e/Z)Am_p$
Electron temperature [T_e (eV)]	650	At plasma bubble perimeter at ~0.6 ns
Ion temperature [T_i (eV)]	260	At plasma bubble perimeter at ~0.6 ns
Magnetic field strength [B (T)]	50	At plasma bubble perimeter (~0.5 MG)
Current-sheet length [L (μm)]	800	Approximate length of collision interface
Flow velocity [V (μm/ns)]	450	Plasma bubble expansion speed
Coulomb logarithm [$\ln\Lambda$]	8	Approximate $\ln\Lambda$ (not directly calculated)
Plasma resistivity [η (Ωm)]	1.74×10^{-7}	Spitzer resistivity
Alfvén speed [V_A (μm/ns)]	100	Ion Alfvén speed
Lundquist number [S]	550	Speed of Alfvén vs. diffusive processes
Magnetic Reynolds number [Rm]	2600	Speed of flow vs. diffusive processes
Sweet-Parker width [δ_{SP} (μm)]	34	Single-fluid current sheet width ($L/\sqrt{S}$)
Ion plasma frequency [ω_{pi} (rad/s)]	8×10^{12}	Frequency of ion plasma oscillations
Ion inertial length [d_i (μm)]	37	Length scale for electron-ion decoupling
Ion gyrofrequency [ω_{ci} (rad/s)]	3×10^{9}	Frequency of ion Larmor orbits
Ion Larmor radius [ρ_i (μm)]	24	Radius of ion orbits in magnetic field
Ion thermal Beta [β_i]	0.8	Ion thermal pressure/mag. pressure
Electron thermal Beta [β_e]	7.3	Electron thermal pressure/mag. pressure
Total thermal Beta [β]	8.1	Total thermal pressure/mag. pressure
Ram pressure Beta [β_{ram}]	22	Flow ram pressure/mag. pressure

Appendix G

Description of Simulation Terms

Terms and aspects of physics used in simulations of ICF implosions and laser-plasma experiments generally, as discussed primarily in Chapters 3 and 6, are described in this appendix and in the numerous references.

Simulation of Laser Propagation and Absorption

Most simulation codes treat laser absorption by inverse bremsstrahlung near the critical surface, allowing for some losses due to refraction (e.g. DUED[1] and the hydrodynamic simulation underlying the RIK model). Some codes (e.g. LILAC[2] and DRACO[3]) additionally model scattering of laser energy by SBS, SRS, or two-plasmon decay, and thus reduce the overall fraction of energy coupled to the simulated implosion. Codes that do not model these scattering processes (including DUED and HYADES[4]) allow the fraction of absorbed laser energy to be set at the beginning of the simulation to match the average laser absorption fraction measured in the experiment.

Many ICF codes use 3D ray tracing to simulate the propagation of laser beams in a plasma. In general, these models treat the full spatial extent of the laser beam and divide the beam into smaller beamlets so as to capture the non-perpendicular angle between the 1D radial dimension away from the capsule center and the propagation direction of beamlets at the perimeter of the laser beam.[5] The propagation of the laser beamlets proceeds according to the eikonal equation $\frac{d}{ds}\left(\eta\frac{d\mathbf{r}}{ds}\right) = \nabla\eta$, where ds is a differential path length, $\mathbf{r}$ is the beamlet position, and $\eta(\mathbf{r},t) = \sqrt{1 - n_e(\mathbf{r},t)}$ is the index of refraction, with n_e the electron density normalized to the critical density. This model therefore treats the refraction and propagation of the full cylindrical laser beam up to the critical density surface, with some laser energy refracted away from the implosion.

In addition to inverse bremsstrahlung absorption and the LPI processes described above, some ICF simulation codes also account for the process of cross-beam energy transfer (CBET), where the overlap of multiple laser beams in a plasma induces Brillouin scattering and the transfer of laser beam power from one to another.[6] This process, in addition to refraction and previously-discussed LPI, prevents efficient coupling of laser energy to the implosion in direct-drive implosions when power is transferred from the ingoing ray of one beam to the outgoing ray of another beam. Models of CBET are included in some direct-drive ICF codes, including LILAC and DRACO.[7,8] In DRACO simulations of polar-direct-drive exploding pushers on NIF (Chapter 3), CBET was required on high-power implosions to capture the implosion symmetry. CBET has actually been harnessed to determine the symmetry of indirect-drive implosions,[9] based on the overlap of many beams near the laser entrance hole of indirect-drive hohlraums.[10,11] By tuning the wavelength separation between beams directed toward the equator and beams directed toward the end of the hohlraum, the relative amount of laser energy in each ring of beams and, consequently, the symmetry of the implosion is controlled. CBET has been included in LASNEX[12] simulations of NIF implosions.

Energy Transport

Treatment of the transport of energy from the critical surface to the ablation surface, and throughout the implosion, is another aspect of ICF simulations that can vary from code to code. Many codes use a flux-limited model of electron thermal conduction, which limits the rate of energy transport, based on a Spitzer-Harm heat flux, to a fraction f of the free-streaming limit.[13] A typical value of this flux limiter is $f = 0.06$. Flux limiters have been used in LILAC, DRACO, DUED, HYADES and the hydrodynamic simulation used in the RIK model. Another treatment of electron thermal conduction includes the use of a non-local model.[14–16] This Fokker-Planck-based approach[17] captures electron thermal flux under conditions of long mean free path or sharp gradients, where the Spitzer model does not necessarily apply. This non-local electron transport model was required to match implosion dynamics in exploding pusher implosions on NIF.[8]

Opacity and Equation of State

Two important parameters as they relate to simulations of ICF implosions are the different material opacities (i.e. how materials respond to radiation) and equations of state (i.e. how materials respond to hydrodynamic pressure). Opacities are dictated by atomic physics models used to determine population levels and thus the strength of absorption lines, emission lines, and continuum features in different energy bins of radiation. The assumption of local thermodynamic equilibrium (LTE) underpins one such opacity model, where the radiation temperature is equal to the electron temperature of the plasma. Many codes, including DUED, use non-LTE models, with a more sophisticated atomic physics package and therefore different opacities and radiation transport. Equations of state – a relationship between density, temperature, and pressure – typically deviate from the simple ideal gas approximation.[18] The SESAME equation of state tables have been widely used in ICF hydrodynamic codes and determine the compressibility of shell and fuel plasmas under extreme conditions.

G.1 References

1. S. Atzeni, "2-d lagrangian studies of symmetry and stability of laser fusion targets," Computer Physics Communications, **43**(1), 107 – 124 (1986).
2. J. Delettrez, "Thermal electron transport in direct-drive laser fusion," Can. J. Phys., **64**, 932 (1986).
3. D. Keller, T. J. B. Collins, J. A. Delettrez *et al.*, "*DRACO* - a new multidimensional hydrocode," Bull. Am. Phys. Soc., **44**(37) (1999).
4. J. T. Larsen and S. M. Lane, "Hyades - a plasma hydrodynamics code for dense plasma studies," J. Quant. Spectrosc. Radiat. Transfer, **51**(12), 179–186 (1994).
5. M. Temporal, S. Jacquemot, L. Bonnet *et al.*, "A three-dimensional ray-tracing code dedicated to x-ray laser amplification simulation," Physics of Plasmas, **8**(4) (2001).
6. R. K. Kirkwood, B. B. Afeyan, W. L. Kruer *et al.*, "Observation of energy transfer between frequency-mismatched laser beams in a large-scale plasma," Phys. Rev. Lett., **76**, 2065–2068 (1996).
7. I. V. Igumenshchev, D. H. Edgell, V. N. Goncharov *et al.*, "Crossed-beam energy transfer in implosion experiments on omega," Physics of Plasmas, **17**(12), 122708 (2010).
8. P. W. McKenty, F. J. Marshall, M. Hohenberger *et al.*, "Evaluation of the effects of cross-beam energy transfer in nif polar-drive exploding-pusher experiments," Bull. Am. Phys. Soc., **58**(16) (2013).
9. P. Michel, L. Divol, E. A. Williams *et al.*, "Tuning the implosion symmetry of icf targets via controlled crossed-beam energy transfer," Phys. Rev. Lett., **102**, 025,004 (2009).

10. J. Moody, P. Michel, L. Divol *et al.*, "Multistep redirection by cross-beam power transfer of ultrahigh-power lasers in a plasma," Nature Physics, **8**(4), 344–349 (2012).
11. E. L. Dewald, J. L. Milovich, P. Michel *et al.*, "Early-time symmetry tuning in the presence of cross-beam energy transfer in icf experiments on the national ignition facility," Phys. Rev. Lett., **111**, 235,001 (2013).
12. G. B. Zimmerman and W. L. Kreur, "Numerical simulation of laser-initiated fusion," Comments Plasma Phys. Control. Fusion, **2**(51) (1975).
13. R. C. Malone, R. L. McCrory and R. L. Morse, "Indications of strongly flux-limited electron thermal conduction in laser-target experiments," Phys. Rev. Lett., **34**, 721–724 (1975).
14. V. N. Goncharov, O. V. Gotchev, E. Vianello *et al.*, "Early stage of implosions in inertial confinement fusion: Shock timing and perturbation evolution," Phys. Plasmas, **13**(1), 012,702 (2006).
15. N. B. Meezan, R. L. Berger, L. Divol *et al.*, "Role of hydrodynamics simulations in laser-plasma interaction predictive capability," Physics of Plasmas, **14**(5), 056304 (2007).
16. S. X. Hu, V. A. Smalyuk, V. N. Goncharov *et al.*, "Validation of thermal-transport modeling with direct-drive, planar-foil acceleration experiments on omega," Phys. Rev. Lett., **101**, 055,002 (2008).
17. G. P. Schurtz, P. D. Nicola and M. Busquet, "A nonlocal electron conduction model for multidimensional radiation hydrodynamics codes," Physics of Plasmas, **7**(10) (2000).
18. S. X. Hu, B. Militzer, V. N. Goncharov *et al.*, "Strong coupling and degeneracy effects in inertial confinement fusion implosions," Phys. Rev. Lett., **104**, 235,003 (2010).